

Real-Time Control of Tokamak Plasmas: from Control of Physics to Physics-Based Control

THÈSE N° 5203 (2011)

PRÉSENTÉE LE 4 NOVEMBRE 2011
À LA FACULTÉ SCIENCES DE BASE
CRPP - PHYSIQUE DU TOKAMAK TCV
PROGRAMME DOCTORAL EN PHYSIQUE

ÉCOLE POLYTECHNIQUE FÉDÉRALE DE LAUSANNE

POUR L'OBTENTION DU GRADE DE DOCTEUR ÈS SCIENCES

PAR

Federico Alberto Alfredo FELICI

acceptée sur proposition du jury:

Prof. N. Grandjean, président du jury
Dr O. Sauter, Dr T. Goodman, directeurs de thèse
Dr E. Joffrin, rapporteur
Dr Ph. Müllhaupt, rapporteur
Prof. H. Zohm, rapporteur



ÉCOLE POLYTECHNIQUE
FÉDÉRALE DE LAUSANNE

Suisse
2011

An electronic version is available for download from either
<http://library.epfl.ch/theses/?nr=5203>

or

<http://dx.doi.org/10.5075/epfl-thesis-5203>

Please cite this publication as:

F. Felici, “Real-time control of tokamak plasmas: from control of physics to physics-based control”, *PhD thesis no.5203, École Polytechnique Fédérale de Lausanne (EPFL), CH-1015 Lausanne, Switzerland, October 2011.*

e-mail: federico.felici@epfl.ch, ffelici@gmail.com

This document was created using L^AT_EX.

Document version: Final.

Lausanne, October 24, 2011

©2011 by Federico Felici

*Men at some time are masters of their fates:
The fault, dear Brutus, is not in our stars,
But in ourselves, that we are underlings.*

William Shakespeare (1564 - 1616)
The Tragedy of Julius Ceasar, Act I, Scene 2, 230-233

Abstract

Stable, high-performance operation of a tokamak requires several plasma control problems to be handled simultaneously. Moreover, the complex physics which governs the tokamak plasma evolution must be studied and understood to make correct choices in controller design. In this thesis, the two subjects have been merged, using control solutions as experimental tool for physics studies, and using physics knowledge for developing new advanced control solutions.

The TCV tokamak at CRPP-EPFL is ideally placed to explore issues at the interface between plasma physics and plasma control, by combining a state-of-the-art digital real-time control system with a flexible and powerful set of actuators, in particular the electron cyclotron heating and current drive system (ECRH/ECCD). This unique experimental platform has been used to develop and test new control strategies for three important and reactor-relevant tokamak plasma physics instabilities, including the sawtooth, the edge localized mode (ELM) and the neoclassical tearing mode (NTM). These control strategies offer new possibilities for fusion plasma control and at the same time facilitate studies of the physics of the instabilities with greater precision and detail in a controlled environment.

The period of the sawtooth crash, a periodic MHD instability in the core of a tokamak plasma, can be varied by localized deposition of ECRH/ECCD near the $q = 1$ surface, where q is the safety factor. Exploiting this known physical phenomenon, a *sawtooth pacing* controller was developed which is able to precisely control the time of appearance of the next sawtooth crash. It was also shown that each individual sawtooth period can be controlled in real-time. A similar scheme is applied to H-mode plasmas with type-I ELMs, where it is shown that pacing regularizes the ELM period. The regular, reproducible and therefore predictable sawtooth crashes obtained by the sawtooth pacing controller have been used to study the relationship between sawteeth and NTMs. It is known that post-crash MHD activity can provide the “seed” island for an NTM, which then grows under its neoclassical bootstrap drive. Experiments are shown which demonstrate that the seeding of 3/2 NTMs by long sawtooth crashes can be avoided by preemptive, crash-synchronized EC power injection pulses at the $q = 3/2$ rational surface location. NTM stabilization experiments in which the ECRH deposition location is moved in real-time with steerable mirrors have shown effective stabilization of both 3/2 and 2/1 NTMs, and have precisely localized the deposition location that is most effective. Studies of current-profile driven destabilization of tearing modes in TCV plasmas with significant amounts of ECCD show a great sensitivity to details of the current profile, but failed to identify a stationary region in the parameter space in which NTMs are *always* destabilized. This suggests that transient effects intrinsically play a role.

Next to instability control, the simultaneous control of magnetic and kinetic plasma profiles is another key requirement for advanced tokamak operation. While control of kinetic plasma profiles around an operating point can be handled using standard linear control techniques, the strongly nonlinear physics of the coupled profiles complicates the problem significantly. Even more, since internal magnetic quantities are difficult to measure with sufficient spatial and temporal resolution – even after years of diagnostic development – routine control of tokamak plasma profiles remains a daunting and extremely challenging task.

In this thesis, a model-based approach is used in which physics understanding of plasma current and energy transport is embedded in the control solution. To this aim, a new lightweight transport code has been derived focusing on simplicity and speed of simulation, which is compatible with the demands for real-time control. This code has been named RAPTOR (RApid Plasma Transport simulatOR). In a first-of-its-kind application, the partial differential equation for current diffusion is solved in real-time during a plasma shot in the TCV control system using RAPTOR. This concept is known in control terms as a *state observer*, and it is applied experimentally to the tokamak current density profile problem for the first time. The real-time simulation gives a physics-model-based estimate of key plasma quantities, to be controlled or monitored in real-time by different control systems. Any available diagnostics can be naturally included into the real-time simulation providing additional constraints and removing measurement uncertainties. The real-time simulation approach holds the advantage that knowledge of the plasma profiles is no longer restricted to those points in space and time where they are measured by a diagnostic, but that an estimate for any quantity can be computed at any time. This includes estimates of otherwise unmeasurable quantities such as the loop voltage profile or the bootstrap current distribution. In a first closed-loop experiment, an estimate of the internal inductance resulting from the real-time simulation is feedback controlled, independently from the plasma central temperature, by an appropriate mix of co- and counter- ECCD.

As a tokamak plasma evolves from one state to another during plasma ramp-up or ramp-down, the profile trajectories must stay within a prescribed operational envelope delimited by physics instabilities and engineering constraints. Determining the appropriate actuator command sequence to navigate this operational space has traditionally been a trial-and-error procedure based on experience of tokamak physics operators. A computational technique is developed based on the RAPTOR code which can calculate these trajectories based on the profile transport physics model, by solving an open-loop optimal control problem. The solution of this problem is greatly aided by the fact that the code returns the plasma state trajectory sensitivities to input trajectory parameters, a functionality which is unique to RAPTOR. This information can also be used to construct linearized models around the optimal trajectory, and to determine the active constraint, which can be used for time-varying closed-loop controller design.

This physics-model-based approach has shown excellent results and holds great potential for application in other tokamaks worldwide as well as in future devices.

keywords: Tokamak, TCV, plasma control, ECRH/ECCD, MHD control, sawteeth, NTMs, ELMS, profile control, transport modeling, real-time signal processing, real-time simulations, state observers, finite element methods, partial differential equations, optimal control, plasma scenarios, RAPTOR.

Version Abrégée

L'opération stable et à haute performance d'un plasma dans un tokamak nécessite le traitement simultané de plusieurs problèmes de contrôle du plasma. De plus, les lois de physique qui gouvernent l'évolution du plasma doivent être étudiées et comprises pour faire les choix appropriés dans la synthèse des contrôleurs. Dans cette thèse, les deux sujets ont été unifiés, en utilisant des solutions de contrôle comme outil expérimental pour des études de physique, et en utilisant les connaissances de la physique pour le développement des schémas de contrôle avancés.

Le tokamak TCV, au CRPP-EPFL, est idéalement placé pour explorer les problèmes à l'interface entre physique et contrôle des plasmas, en combinant un système de contrôle numérique moderne avec un ensemble d'actionneurs puissants et flexibles, tels que le système de chauffage à résonance cyclotronique des électrons (ECRH/ECCD). Cette plateforme expérimentale unique a été utilisée pour développer et tester des nouvelles méthodes de contrôle pour trois instabilités importantes dans le but de réaliser un réacteur à fusion basé sur le tokamak: la "dent-de-scie" (sawtooth), le "Edge Localized Mode" (ELM), et le "Neoclassical tearing mode" (NTM). Ces stratégies de contrôle offrent des nouvelles possibilités pour le contrôle des plasmas de fusion et facilitent l'étude de la physique de ces instabilités, avec plus de précision et détail, grâce à un environnement contrôlé.

La période des dents-de-scie, une instabilité MHD périodique dans le coeur du plasma, peut être variée avec la déposition localisée de ECRH/ECCD en proximité de la surface $q = 1$, ou q est le facteur de sécurité. En exploitant ce phénomène physique, un algorithme pour "synchroniser" les dents-de-scie a été développé qui est capable de contrôler précisément l'instant de l'apparition de la prochaine dent-de-scie. De même, il a été montré que chaque dent-de-scie peut être contrôlé individuellement. Un schéma similaire a été utilisé pour contrôler les ELMs de type-I dans un plasma en mode-H, en montrant qu' en "synchronisant" les ELMs on arrive à régulariser le temps de leur apparition. Les dents-de-scie reproductibles obtenues à travers cette méthode ont aussi été utilisées pour étudier la relation entre dents-de-scie et NTMs. Des expériences ont montré que la déstabilisation des NTMs du type 3/2 peut être prévenue en appliquant des pulses de puissance ECH sur la surface rationnelle du mode, synchronisé avec le moment de la dent-de-scie. Les études de stabilisation des NTMs avec l'application localisée de ECRH à l'aide des lanceurs, asservis en temps réel, ont démontré la stabilisation des modes du type 2/1 et 3/2 avec puissance localisé et contrôle de l'angle du lanceur. L' étude de la déstabilisation des NTMs due au profil de densité de courant plasma n'ont pas mené à une condition opérationnelle dans laquelle les NTMs sont systématiquement déstabilisés. L'apparition des NTMs étant plus probable dans des phases d'évolution des profils, il est probable que

des effets temporaires jouent un rôle important.

À part le contrôle des instabilités, le contrôle simultané des profils magnétiques et cinétiques du plasma est une autre condition fondamentale pour l'opération avancée d'un tokamak. Même si le contrôle des profils cinétiques autour d'un point d'opération est abordable avec des outils de contrôle linéaire, la physique couplée des profils magnéto-thermiques est fortement non-linéaire, ce qui complique le problème. De plus, vu que les quantités magnétiques à l'intérieur du tokamak sont difficiles à déterminer avec une résolution temporelle et spatiale suffisante – même après plusieurs années de développement – le contrôle des profils dans un tokamak reste un grand défi.

Dans cette thèse, la compréhension physique du transport de courant et d'énergie dans le plasma est utilisée directement au coeur de la solution de contrôle. À cette fin, un nouveau code de transport a été construit, focalisé sur la simplicité et la rapidité d'exécution, et compatible avec les contraintes du contrôle en temps réel. Ce code a été nommé RAPTOR (RAPid Plasma Transport simulatOR). Comme première application, RAPTOR a été utilisé pour simuler la diffusion du profil de densité de courant dans TCV en temps réel, en résolvant l'équation différentielle partielle qui gouverne son évolution. Cette méthode est connue dans le domaine du contrôle comme un *observateur d'état*, et est appliqué à la reconstruction des profils tokamak pour la première fois. La simulation donne une estimation basée sur la physique du problème, qui peut être utilisé pour contrôle en rétroaction ou pour des fins de supervision. Les diagnostics qui sont disponibles peuvent être inclus de façon naturelle afin de diminuer les incertitudes dans la modélisation. Un grand avantage des simulations en temps réel est que plusieurs quantités, y compris des quantités qui ne sont pas mesurables (courant de bootstrap, profil de tension) peuvent être calculées sur des grilles de temps et d'espace arbitrairement choisies. Dans une première expérience, l'inductance interne du plasma a été contrôlée en rétroaction indépendamment de la température centrale, à l'aide de ECCD dans la direction co- et contre-courant.

Quand le plasma dans un tokamak évolue d'un état à un autre, typiquement pendant la phase d'initiation ou de terminaison du plasma, les trajectoires suivies par les profils dans le temps doivent rester dans un espace opérationnel limité par des limites physiques et techniques. La détermination de la séquence de commandes des actionneurs appropriées pour naviguer dans cette espace est traditionnellement fait à la main, selon l'expérience des opérateurs d'un tokamak. Ici, une nouvelle méthode est développée, basée sur RAPTOR, pour calculer ces trajectoires en se basant sur un modèle physique du transport, en résolvant un problème de contrôle optimal à boucle ouverte. La solution de ce problème est facilitée par le fait que les dérivées des trajectoires des profils par rapport aux paramètres de la trajectoire d'entrée sont connues – une fonctionnalité qui est unique à RAPTOR. Cette information peut aussi être utilisée pour construire un modèle linéarisé autour de la trajectoire optimale, et pour déterminer les contraintes actives sur cette trajectoire, ce qui peut être utilisé pour construire des contrôleurs en boucle fermée.

Cette approche basée sur la physique a donné d'excellents résultats avec un vaste potentiel d'applications dans d'autres tokamaks ainsi que pour des expériences futures.

Mots clés: Tokamak, TCV, contrôle des plasmas, ECRH/ECCD, contrôle MHD, dents-de-scie, NTMs, ELMs, contrôle des profils, modélisation de transport, traitement des signaux, simulations en temps réel, observateurs d'état, méthodes des éléments finis, équations différentielles partielles, contrôle optimal, scénarios plasma, RAPTOR.

Sinossi

Operare un tokamak in modo stabile ed efficace richiede la soluzione simultanea di una moltitudine di problemi di controllo automatico. Inoltre, la fisica che governa l'evoluzione del plasma in un tokamak deve essere studiata e compresa in modo da prendere le giuste decisioni nella progettazione di algoritmi di controllo. In questa tesi, i due argomenti sono stati combinati, usando soluzioni controllistiche come strumento sperimentale per studi di fisica, ed utilizzando conoscenza della fisica per sviluppare nuovi metodi di controllo avanzati.

Il tokamak TCV, all'CRPP-EPFL, è in una posizione ideale per studiare problemi all'interfaccia fra fisica e controllo del plasma, in quanto combina un moderno sistema di controllo digitale con un insieme di attuatori potenti e flessibili, quali i sistemi di riscaldamento ed iniezione di corrente alla frequenza ciclotronica degli elettroni (ECRH/ECCD). Questa piattaforma sperimentale, unica al mondo, è stata utilizzata per sviluppare e testare nuove strategie di controllo per tre instabilità importanti in vista di un reattore a fusione, incluso il "dente di sega", il "Edge Localized Mode" (ELM) ed il Modo Tearing Neoclassico (NTM). Queste strategie di controllo offrono nuove possibilità per il controllo di plasmi di fusione, ed allo stesso tempo ne facilitano lo studio, fornendo un ambiente controllato precisamente nel quale effettuare esplorazioni dettagliate.

Il periodo dei denti di sega, una instabilità magneto-idrodinamica che si ripete periodicamente al centro del plasma in un tokamak, può essere controllato dalla deposizione localizzata di ECRH/ECCD vicino alla superficie $q = 1$, dove q rappresenta il *safety factor* (fattore di sicurezza). Utilizzando questo fenomeno fisico ben noto, è stato sviluppato un algoritmo per sincronizzare i denti di sega, in grado di controllare precisamente l'istante di apparizione del prossimo dente di sega. È stato mostrato che ogni dente di sega può essere controllato individualmente. Lo stesso schema di controllo è stato utilizzato anche per controllare gli ELM di tipo I in un plasma in modo H, ed ha mostrato che sincronizzando gli ELM si arriva a regolarizzare il momento della loro apparizione. I denti di sega a periodo regolare, ottenuti grazie al nuovo metodo sono stati utilizzati per studiare il rapporto fra denti di sega e NTM. È stato dimostrato sperimentalmente che l'apparizione di NTM del tipo 3/2 può essere prevenuta con l'applicazione di potenza ECH sulla superficie razionale del modo, sincronizzato con l'istante nel quale appare il dente di sega. Studi di stabilizzazione di NTM, usando ECRH con iniettori controllati in tempo reale, hanno dimostrato la stabilizzazione di modi 2/1 e 3/2 per mezzo dell'applicazione di potenza localizzata precisamente grazie al controllo di specchi mobili del sistema d'iniezione. Studi di destabilizzazione degli NTM dovuta al profilo di densità del plasma non hanno portato ad una condizione operativa nella quale gli NTM sono sistematicamente destabilizzati. Visto che l'apparizione degli NTM è più probabile durante la fase di evoluzione del pro-

filo, è possibile che essa sia dovuta in parte ad effetti transitori.

Oltre al controllo di instabilità, il controllo simultaneo di profili magnetici e cinetici è un'altra condizione fondamentale per il controllo operativo avanzato di un tokamak. Anche se il controllo dei profili cinetici nelle vicinanze di un punto nello spazio d'operazione è realizzabile con strumenti di controllo lineare, l'accoppiamento fisico dei profili magneto-termici è fortemente nonlineare, il che complica il problema in modo significativo. Inoltre, visto che le grandezze magnetiche all'interno di un tokamak sono difficili da determinare con una risoluzione temporale e spaziale sufficiente – nonostante molti anni di sviluppo – il controllo dei profili in un tokamak resta una sfida.

In questa tesi, la comprensione della fisica del trasporto di corrente e di energia nel plasma è utilizzata al cuore dell'algoritmo di controllo. A tale scopo, è stato creato un nuovo codice di trasporto orientato verso la semplicità e rapidità d'esecuzione, compatibile con i requisiti per la simulazione in tempo reale. Questo codice è stato chiamato RAPTOR (RAPid Plasma Transport simulatOR). Come prima applicazione, RAPTOR è stato impiegato per simulare la diffusione del profilo di corrente dentro TCV in tempo reale, risolvendo l'equazione differenziale parziale che governa la sua evoluzione. Questo metodo è conosciuto nell'ambito del controllo automatico come un *osservatore di stato*, ed è stato applicato per la prima volta al problema di ricostruzione dei profili in un tokamak. La simulazione fornisce una stima basata sulla fisica del problema, che può essere utilizzata per controllo in retroazione o per supervisione. Le diagnostiche disponibili possono essere incluse in modo semplice e naturale in modo da ridurre le incertezze di modellizzazione. Un grande vantaggio delle simulazioni in tempo reale è che molte grandezze, incluse grandezze non-misurabili, possono essere calcolate su delle griglie numeriche scelte arbitrariamente. In una prima verifica sperimentale, l'induttanza interna del plasma è stata controllata in retroazione indipendentemente dalla temperatura centrale, utilizzando ECCD nella direzione co-corrente e contro-corrente.

Durante l'evoluzione da uno stato ad un altro, tipicamente nella fase di accensione o di terminazione del plasma, le traiettorie temporali seguite dai profili devono restare in uno spazio operativo delimitato da limiti fisici ed ingeneristici. La scelta della sequenza di comandi degli attuatori appropriata per navigare questo spazio viene tradizionalmente fatta a mano, basandosi sull'esperienza degli operatori di un tokamak. Qui è stato sviluppato un nuovo metodo, basato su RAPTOR, per calcolare le traiettorie ottimali usando un modello fisico del trasporto e risolvendo un problema di controllo ottimo ad anello aperto. La soluzione di questo problema è facilitata dal fatto che le derivate delle traiettorie dei profili rispetto ai parametri della traiettoria d'ingresso sono conosciute – una funzionalità che è unica a RAPTOR. Questa informazione può anche essere utilizzata per costruire un modello linearizzato intorno alla traiettoria ottimale, per determinare i limiti attivi su ogni segmento della traiettoria, informazione che può essere utilizzata per la sintesi di controllori ad anello chiuso.

Questo approccio basato sulla fisica ha dato ottimi risultati con un vasto potenziale d'applicazione, sia in altri tokamak esistenti, sia in quelli futuri.

Parole chiave Tokamak, TCV, controllo del plasma, ECRH/ECCD, controllo MHD, denti di sega, NTMs, ELMs, controllo dei profili, modellizzazione del trasporto, trattamento di segnali, simulazioni in tempo reale, osservatori di stato, metodi degli elementi finiti, equazioni differenziali alle derivate parziali, controllo ottimo, scenari plasma, RAPTOR.

Contents

| | |
|--|------------|
| Abstract | v |
| Version Abrégée | vii |
| Sinossi | ix |
| Contents | xvi |
| 1 Introduction | 1 |
| 1.1 Thermonuclear fusion plasmas | 2 |
| 1.1.1 The fourth state of matter | 2 |
| 1.1.2 Conditions for fusion reactions and plasma confinement | 3 |
| 1.2 The tokamak device | 5 |
| 1.2.1 Magnetic field and coil systems | 5 |
| 1.2.2 Auxiliary heating and current drive systems | 7 |
| 1.2.3 Tokamak parameters | 8 |
| 1.3 Control problems in tokamaks | 10 |
| 1.3.1 Control of bulk plasma quantities | 10 |
| 1.3.2 Plasma shape and strike point control | 11 |
| 1.3.3 MHD instability control | 12 |
| 1.3.4 Plasma profile control | 13 |
| 1.3.5 Safety, prediction and disruption avoidance | 14 |
| 1.3.6 Integrated control | 14 |
| 1.4 Motivation for this thesis | 15 |
| 1.5 Outline of this dissertation | 16 |
| 1.5.1 Other work carried out during this thesis | 18 |
| 2 The TCV tokamak | 19 |
| 2.1 Overview | 19 |
| 2.2 The TCV ECH/ECCD system | 22 |
| 2.2.1 Second harmonic ECH/ECCD | 22 |
| 2.2.2 Third harmonic ECH system | 24 |
| 2.3 Main diagnostics used in this thesis | 25 |
| 2.3.1 Magnetic diagnostics | 25 |
| 2.3.2 Electron diagnostics | 25 |
| 2.3.3 X-ray diagnostics | 26 |

CONTENTS

| | | |
|----------|---|-----------|
| 2.3.4 | Post-shot analysis tools | 28 |
| 2.4 | Real-time control systems | 28 |
| 2.4.1 | The “Hybrid” Plasma Control System | 29 |
| 2.4.2 | The “SCD” digital real-time control system | 30 |
| I | Control of physics | 33 |
| 3 | Control of Sawteeth and ELMs | 35 |
| 3.1 | Sawtooth physics and control | 35 |
| 3.1.1 | The sawtooth instability | 35 |
| 3.1.2 | Sawtooth control methods | 36 |
| 3.2 | Sawtooth period pacing by EC power | 39 |
| 3.2.1 | Basic principle | 39 |
| 3.2.2 | Methodology | 40 |
| 3.2.3 | Experimental results | 41 |
| 3.2.4 | Discussion | 45 |
| 3.2.5 | Sawtooth locking | 46 |
| 3.2.6 | Pacing with sawtooth destabilization | 48 |
| 3.2.7 | Sawtooth pacing and locking in high-performance plasma scenarios | 49 |
| 3.3 | ELM pacing and real-time control by EC power | 50 |
| 3.3.1 | Introduction and motivation | 50 |
| 3.3.2 | Experimental setup | 51 |
| 3.3.3 | ELM pacing | 52 |
| 3.3.4 | TCV the singing tokamak | 54 |
| 3.3.5 | Individual ELM control | 56 |
| 3.3.6 | Pure integrator model for the ELM period | 58 |
| 3.3.7 | ELM kicking or ELM pushing? | 58 |
| 3.4 | Conclusions | 59 |
| 4 | Triggering, preemption and suppression of NTMs in TCV | 61 |
| 4.1 | Introduction | 61 |
| 4.1.1 | (Neoclassical) tearing mode fundamentals | 61 |
| 4.1.2 | NTM control capabilities developed on TCV | 63 |
| 4.1.3 | Overview of this chapter | 64 |
| 4.2 | Neoclassical tearing mode physics | 64 |
| 4.2.1 | The Modified Rutherford Equation | 64 |
| 4.2.2 | Experimental observation of tearing modes | 69 |
| 4.2.3 | Triggering mechanisms: TMs vs NTMs | 70 |
| 4.3 | Tearing mode triggering in plasmas with ECCD | 71 |
| 4.3.1 | Current profile driven tearing modes in TCV plasmas | 71 |
| 4.3.2 | Transient profile effects in tearing mode triggering | 75 |
| 4.4 | Stabilization of NTMs in plasmas with ECCD | 77 |
| 4.4.1 | Overview of NTM stabilization and preemption experiments on other tokamaks | 78 |

| | | |
|-----------|---|------------|
| 4.4.2 | Stabilization with EC deposition on the outside and inside of the mode location | 79 |
| 4.4.3 | Stabilization efficiency dependence on β and ECCD | 80 |
| 4.4.4 | Observation of “fuzzy” marginally stable islands | 84 |
| 4.5 | Sawtooth - triggered NTMs in low q_{95} TCV plasmas | 86 |
| 4.5.1 | NTM triggering by stabilized sawteeth | 87 |
| 4.5.2 | Preemption and suppression of sawtooth triggered NTMs | 89 |
| 4.5.3 | Outlook: combined Sawtooth control and NTM preemption in ITER | 93 |
| 4.6 | Conclusions | 93 |
| 5 | Feedback control of kinetic plasma profiles in TCV | 95 |
| 5.1 | SISO control of TCV kinetic plasma parameters | 95 |
| 5.1.1 | SISO PI control with anti-windup | 95 |
| 5.1.2 | Control of Soft-X ray emission peak by launcher angle control | 96 |
| 5.1.3 | Feedback control of central pressure in transport barriers by EC power feedback | 98 |
| 5.1.4 | Control of central electron temperature by EC power in variable shape TCV plasmas | 99 |
| 5.1.5 | Feedback control of the plasma beta | 100 |
| 5.2 | MIMO control of soft X-ray profile peak and width | 102 |
| 5.2.1 | Control problem and plasma | 102 |
| 5.2.2 | System identification | 103 |
| 5.2.3 | State controller design | 105 |
| 5.2.4 | Results | 105 |
| 5.3 | Conclusions | 106 |
| II | Physics-based control | 109 |
| 6 | Tokamak profile dynamics and control | 111 |
| 6.1 | Introduction | 111 |
| 6.2 | Tokamak ideal MHD equilibrium | 112 |
| 6.3 | Flux surface quantities and averaging | 114 |
| 6.4 | Poloidal flux diffusion | 115 |
| 6.4.1 | The flux diffusion equation | 115 |
| 6.4.2 | Non-inductive current sources | 116 |
| 6.4.3 | Boundary conditions | 118 |
| 6.4.4 | Other quantities related to the poloidal flux | 118 |
| 6.5 | Transport of particles and energy | 120 |
| 6.5.1 | Particle transport | 121 |
| 6.5.2 | Energy transport | 121 |
| 6.5.3 | Sources | 122 |
| 6.5.4 | Boundary condition | 123 |
| 6.5.5 | Other quantities related to the electron temperature profile | 123 |
| 6.6 | Coupling between equilibrium and transport | 124 |
| 6.7 | Tokamak simulations | 125 |

CONTENTS

| | | |
|----------|---|------------|
| 6.7.1 | Classification of tokamak equilibrium and transport codes | 125 |
| 6.7.2 | Integrated tokamak simulation codes | 126 |
| 6.8 | Tokamak operating scenarios | 126 |
| 6.9 | Profile control | 128 |
| 6.9.1 | Feedforward profile control | 128 |
| 6.9.2 | Feedback profile control methods | 129 |
| 6.10 | Motivations and outlook for Part II | 130 |
| 7 | The RAPTOR code | 133 |
| 7.1 | Introduction | 133 |
| 7.1.1 | Relation to previous work | 133 |
| 7.2 | Reduced physics model | 134 |
| 7.2.1 | Fixed equilibrium assumption | 134 |
| 7.2.2 | Parametrized heating and current drive sources | 135 |
| 7.2.3 | Ad-hoc transport model and losses | 136 |
| 7.2.4 | Neoclassical conductivity and bootstrap current | 137 |
| 7.2.5 | Summary of equations | 138 |
| 7.3 | Spatial discretization | 139 |
| 7.3.1 | Finite elements | 139 |
| 7.3.2 | Computing quantities related to the profile state | 141 |
| 7.4 | Interpretative mode | 141 |
| 7.4.1 | Time discretization | 141 |
| 7.4.2 | Benchmarking vs ASTRA | 142 |
| 7.5 | Predictive-RAPTOR | 143 |
| 7.5.1 | Algorithm | 143 |
| 7.5.2 | Trajectory sensitivity | 144 |
| 7.5.3 | A simulation example | 145 |
| 7.5.4 | Analysis of locally linearized profile dynamics | 151 |
| 7.6 | Outlook: extending the physics of RAPTOR | 153 |
| 7.6.1 | Extending the kinetic profile transport models | 154 |
| 7.6.2 | Time-dependent equilibrium | 154 |
| 7.6.3 | Sawteeth, NTMs and other MHD | 154 |
| 8 | Real-time simulation of tokamak plasma profiles | 155 |
| 8.1 | Advantages and applications of real-time simulations | 155 |
| 8.2 | Real-time simulation of TCV current density profile | 159 |
| 8.2.1 | Real-time estimates of the kinetic profiles | 159 |
| 8.2.2 | Implementation on the TCV digital control system | 161 |
| 8.2.3 | Results and comparison to off-line ASTRA and LIUQE | 161 |
| 8.2.4 | Discussion and possibilities for improvement | 166 |
| 8.3 | Feedback control of l_i and T_{e0} using RT-RAPTOR | 168 |
| 8.3.1 | Experimental set-up | 168 |
| 8.3.2 | Controller design | 169 |
| 8.3.3 | Results | 169 |
| 8.3.4 | Discussion and outlook | 170 |
| 8.4 | Further developments of real-time simulation | 171 |

| | | |
|-----------|--|------------|
| 8.4.1 | Incorporating internal diagnostics using a closed-loop observer . . . | 171 |
| 8.4.2 | Adaptation of model parameters | 172 |
| 8.4.3 | Disturbance estimation and fault detection | 173 |
| 8.4.4 | Real-time simulations on ITER and other tokamaks | 173 |
| 8.5 | Conclusion | 174 |
| 9 | Optimization of actuator trajectories | 175 |
| 9.1 | Introduction | 175 |
| 9.1.1 | Background and motivation | 175 |
| 9.1.2 | Advantages of Predictive-RAPTOR for optimization studies | 176 |
| 9.1.3 | Relation to previous work | 177 |
| 9.2 | Formulation and solution of the optimal control problem | 179 |
| 9.2.1 | Control vector parametrization | 179 |
| 9.2.2 | Cost function definition | 180 |
| 9.2.3 | Actuator trajectory constraints | 182 |
| 9.2.4 | State trajectory constraints | 182 |
| 9.2.5 | Formulation of the optimal control problem | 183 |
| 9.2.6 | Solution using Sequential Quadratic Programming | 184 |
| 9.3 | Optimization of ramp-up to hybrid plasma q profile | 185 |
| 9.3.1 | Plasma scenario and transport model | 185 |
| 9.3.2 | Introductory example: optimization with two degrees of freedom . | 186 |
| 9.3.3 | Complete optimization of hybrid plasma ramp-up scenario with constraints | 190 |
| 9.4 | Input trajectory classification and consequences for feedback control . . . | 193 |
| 9.5 | Outlook | 196 |
| 9.5.1 | Extension of open-loop optimal trajectory studies | 196 |
| 9.5.2 | Transport parameter fitting to experimental data | 197 |
| 9.5.3 | Closed-loop feedback controller design | 198 |
| 9.5.4 | Real-time predictive simulations | 199 |
| 9.6 | Conclusion | 199 |
| 10 | Conclusions | 201 |
| 10.1 | Control of Physics | 201 |
| 10.2 | Physics-based control | 203 |
| A | The SCD control system | 207 |
| A.1 | TCV multi-system real-time control | 207 |
| A.1.1 | Control hardware layout and system combinations | 207 |
| A.2 | SCD operation in practice | 209 |
| A.2.1 | Simulink block diagram preparation | 209 |
| A.2.2 | Input/output handling | 210 |
| A.2.3 | C-code building and compilation | 211 |
| A.2.4 | TCV shot cycle | 212 |
| A.2.5 | Operational experience | 213 |
| A.2.6 | Overview of developed algorithms | 213 |
| A.3 | Improved TCV hybrid controller | 214 |

CONTENTS

| | | |
|----------|--|------------|
| A.3.1 | Basic hybrid controller emulation | 214 |
| A.3.2 | IOH control | 217 |
| B | Real-time signal processing algorithms | 219 |
| B.1 | Real-time spline fitting | 219 |
| B.2 | Profile peak, width, gradient information | 220 |
| B.3 | Inversion radius detection by DMPX correlation analysis and bayesian filtering | 221 |
| B.4 | Sawtooth crash detection | 223 |
| B.5 | MHD mode detection | 224 |
| B.6 | Phase-Locked loop for NTM control | 225 |
| C | Mathematical derivations | 229 |
| C.1 | Derivation of the 1D transport equations | 229 |
| C.1.1 | Derivation of the poloidal flux diffusion equation | 229 |
| C.1.2 | Derivation of the particle transport equation | 232 |
| D | Details of the RAPTOR code | 235 |
| D.1 | Implementation using finite elements | 235 |
| D.1.1 | Finite Element Method | 235 |
| D.1.2 | Finite element matrix expressions | 236 |
| D.1.3 | Numerical integration using Legendre-Gauss quadrature | 237 |
| D.2 | Interpretative mode | 239 |
| D.2.1 | Program workflow | 239 |
| D.2.2 | Algorithm breakdown | 239 |
| D.3 | Predictive mode | 241 |
| D.3.1 | Newton iterations | 241 |
| D.3.2 | Convergence studies | 242 |
| D.4 | Discretization of the optimization problem | 243 |
| D.5 | Importing MHD equilibria from CHEASE | 246 |
| D.5.1 | CHEASE output definitions | 246 |
| D.5.2 | RAPTOR quantities in terms of CHEASE outputs | 246 |
| E | TENEX: kinetic profiles from X-ray diagnostics | 249 |
| | Acknowledgements | 251 |
| | Glossary | 253 |
| | Bibliography | 273 |
| | Curriculum Vitae | 275 |

Chapter 1

Introduction



Figure 1.1: Artist's impression of gravitationally confined thermonuclear reactors (top) and fossil-fueled late 19th century human lighting systems (below). *Vincent van Gogh, Starry night over the river Rhone. Arles, France, 1888.*

Nuclear fusion is the most basic energy production mechanism in the universe. A starry night is, romanticism aside, a dazzling display of countless fusion reactors, tirelessly burning their hydrogen nuclei and converting them into helium, releasing energy in the process. The energy released by our own star, the sun, is what makes our earth habitable and our existence possible.

Taming this fundamental process and exploiting it to power the growing needs of humanity would represent a historic breakthrough. A safe, non-polluting and abundant source of energy could propel mankind beyond the fossil-fueled spark of the industrial revolution and provide perspective for human development thousands or millions of years into the future. These potential advantages have been the driving force behind more than 50 years of civilian research in controlled nuclear fusion and appear ever more appealing at

a time of rising oil prices, concern over anthropogenic climate change and renouncement of nuclear fission technology.

In the early days of fusion research in the 1950's, it was believed that achieving controlled fusion was within grasp. Understanding of plasmas, the state of matter in which nuclear fusion reactions can occur, progressed rapidly and experimental successes were booked in confining hot plasmas by magnetic fields. Unfortunately, early estimates were overly optimistic, and generations of scientists have been continually beset by the discovery of new instabilities and transport mechanisms which limited the fusion performance of experimental devices, and a definitive solution has not been found to this date. Arguably, the most promising approach today is represented by the tokamak, a magnetic confinement configuration which so far retains the world record in fusion power production, and tokamak devices have dominated the experimental fusion community for the past 30 years.

While the fusion community has been the realm of plasma physicists, uncontested experts in describing and understanding the complexity of the plasma medium, it was recognized early on that the active suppression of plasma instabilities, particularly in tokamaks, is a key requirement for achieving fusion. These instabilities must be detected using dedicated sensors (diagnostics), and acted appropriately upon using the available actuators (e.g. plasma heating systems). When formulated like this, the fusion problem becomes a *control* problem, which can be approached by the tools of the control engineer. Cross-fertilization between the two communities has occurred throughout fusion research history, growing in frequency as experiments have evolved from table-top setups with few controlled parameters to football-field-sized one-of-a-kind facilities with thousands of subsystems.

This thesis fits within this multidisciplinary nature of the controlled fusion problem, and contains elements of physics and control engineering. It is the firm belief of this author that such a combined approach continues to bear great advantages and that multiple competences will be required to solve today's and tomorrow's problems in fusion research.

1.1 Thermonuclear fusion plasmas

1.1.1 The fourth state of matter

While in its gaseous, liquid or solid state, matter consists of positively charged nuclei surrounded by negatively charged electrons, forming neutral atoms as basic building blocks. The electrons normally prevent other nuclei from coming into close proximity to the atom's nucleus. The first requirement for nuclear fusion reactions to occur is that the nuclei must be free to encounter other nuclei, thus they must have been stripped of their electrons. This occurs naturally when a gas' temperature is raised beyond the limit where ionization takes place: atomic collisions can then cause electrons to become detached from the nuclei, and these free electrons then cause an avalanche, ionizing the majority of atoms. This transition generally occurs within a small temperature range (around 10,000K for many gases), and can therefore be approximately described as a phase transition into the *plasma* state. Most observed matter in the universe consists of plasmas, most importantly in the form of (high-density) stars but also in (low-density) interstellar plasma.

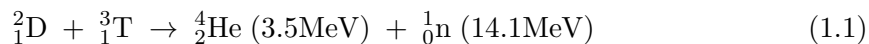
In this state, the kinetic energy of the charged particles exceeds the potential energy

of their electrostatic (Coulomb) attraction and, under certain conditions, collective effects mediated by electromagnetic interactions dominate over single particle collision effects. In a plasma, particles collide quasi-elastically by their electrostatic repulsion or attraction. In the case of two ions, that electrostatically repel each other, it is possible that the ions come sufficiently close to each other that they tunnel through the Coulomb potential barrier into the region where the strong nuclear force dominates, and two ions fuse. This is an exothermal reaction as long as the product nucleus is iron or lighter, and in most cases produces a heavier element (plus possibly some neutrons). The probability that fusion reactions occur depends on the ion temperature and is only significant in excess of 1keV, or approximately 10 million degrees Kelvin.

A fortuitous consequence of the charged nature of the particles in a plasma is that their behavior can be influenced by external electromagnetic fields thanks to the Lorentz force $\mathbf{F} = q(\mathbf{E} + \mathbf{v} \times \mathbf{B})$ where q is the particle's charge, \mathbf{v} is the particle's velocity and \mathbf{E} , \mathbf{B} are the electric and magnetic fields, respectively. As a consequence of the Lorentz force, charged particles tend to follow orbits around magnetic fields lines, as illustrated in Figure 1.2. Since the plasma can also carry electrical currents, electromagnetic fields can be created by the plasma itself, in addition to any fields imposed externally, which complicates the picture. Self-consistent models of plasmas are difficult to formulate, since they must take into account at the same time statistical mechanics to describe particle positions and velocity probabilistically, as well as Maxwell's laws to describe electromagnetic effects. Another inherent difficulty in studying plasmas is the wide range of spatial and temporal scales of interest. For spatial scales, this ranges from the electron Larmor radius (the radius of an electron orbit around a magnetic field line, $\sim 10\mu\text{m}$ in magnetically confined fusion (MCF) plasmas) to the length of field lines themselves which can be hundreds of meters long for open field lines in some configurations. On temporal scales we must be concerned with intervals ranging from the electron cyclotron frequencies (period of electron orbit around a field line, $\sim 1/100\text{GHz} = 10\text{ps}$ for MCF plasmas), to the time needed for resistive effects to manifest themselves, which can be several hundreds of seconds for plasmas at fusion-relevant temperatures.

1.1.2 Conditions for fusion reactions and plasma confinement

In order for fusion reactions to occur in significant numbers, a plasma must at the same time be sufficiently dense and at the optimum temperature where the fusion probability, or cross-section, between the fusion reactants is maximal. Out of all possible fusion reactions the one with the largest cross-section is that of the reaction between Deuterium (${}^2_1\text{D}$) and Tritium (${}^3_1\text{T}$), two isotopes of Hydrogen with one proton and 1 and 2 neutrons, respectively:



A large fusion reaction rate alone is not sufficient for net positive energy generation: at the same time the energy must be confined for a sufficiently long time such that the power required to maintain the plasma at the required temperature remains as small as possible. This is expressed by the *energy confinement time* (τ_E) defined as the ratio between plasma total energy and power losses. The well-known Lawson criterion stipulates the conditions under which a plasma ignites, i.e. when the fusion power is sufficient to maintain the plasma in the burning regime, and is written as a condition on the "triple" product $nT\tau_E$,

where n is the density and T is the temperature of the plasma:

$$nT\tau_E \geq 3 \times 10^{21} \text{m}^{-3} \text{keVs}. \quad (1.2)$$

It turns out that, for D-T fusion reactions, choosing $T \approx 20 \text{keV}$ corresponds to a minimum required $n\tau_E > 1.5 \times 10^{20} \text{m}^{-3} \text{s}$ to reach ignition. Therefore, efforts have focused on obtaining a value as high as possible for this product.

To this aim, two alternative routes have been developed in mainstream fusion research. The first is to reach very high densities, at the cost of having a rather low confinement time. This approach is referred to as *inertial* confinement fusion, and is practically achieved by compressing small capsules about 1mm in diameter using powerful lasers. The state of the art in this line of research is represented by the NIF facility in Livermore, USA which is planned to achieve ignition within a few years (Lindl et al. 2011). A complementary approach is to create relatively low density plasmas, but to keep their thermal energy confined for a longer time. As plasmas can be confined using magnetic fields, this line of research is referred to as *magnetic* confinement fusion. Plasmas of densities $n > 10^{20} \text{m}^{-3}$ and confinement times $\tau_E > 1.5 \text{s}$ are typically required in this case.

Several different approaches for magnetic confinement fusion have been devised, differing in the geometric configuration of the magnetic fields used to contain the plasma. Globally, one can distinguish between devices in which the entire magnetic field is generated by external coils, and devices in which (part of) the magnetic field is generated by electrical currents in the plasma itself. Examples of the first case includes stellarators (Lyon et al. 1990), (Boozer 1998) and magnetic mirrors (Ryutov 1988), (Burdakov et al. 2010), while the latter category is represented mainly by tokamaks and pinches. At the time of invention of the tokamak¹ concept in the Soviet Union at the end of the 1960's (Artsimovich 1972), the results greatly exceeded those of competing devices. Stimulated by this early progress, tokamaks have rapidly grown during the '70s and '80s to become the most promising concept to obtain plasmas in controlled thermonuclear conditions. Efforts worldwide have culminated in the production of 16MW of total fusion power, achieved in 1997 in the Joint European Torus, the world's largest tokamak situated in Culham, UK (Jacquinot et al. 1999). Present-day tokamaks have demonstrated the feasibility of the temperatures and densities required for break-even and ignition, the confinement time remaining the parameter to be increased further (Figure 1.3). As the confinement time increases with device size and total plasma current, the worldwide magnetic fusion community has come together around a single, large device constituting the next generation of tokamaks. The ITER tokamak, currently under construction (Figures 1.6,1.7), is designed to exceed the break-even condition and produce ten times more fusion power than the required input power. It is scheduled to achieve its first plasma at the end of 2019 at the time of writing ((Shimada et al. 2007)).

Paradoxically, the main reason for the tokamak's success is also the cause of its greatest problems. The plasma current, while responsible for creating a stable magnetic configuration in which charged plasma particles are confined, is the source of magnetic plasma energy that can drive unwanted phenomena. Current-driven (but also pressure-driven) instabilities limit the maximum confinement achievable in a tokamak, either causing a global loss of plasma stability and subsequent extinction of the plasma, or locally enhanc-

¹Russian acronym which translates to Toroidal Chamber for Magnetic Confinement

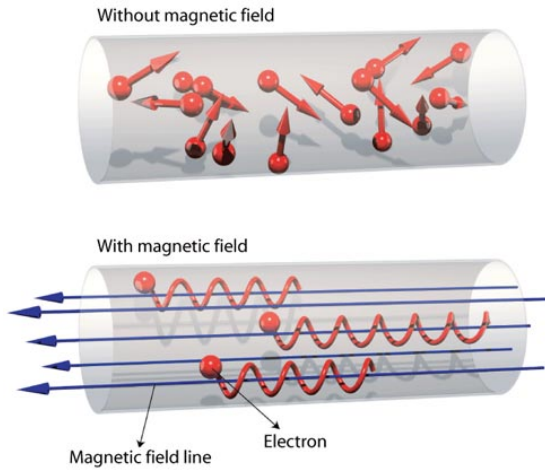


Figure 1.2: Magnetic confinement of charged particles by a magnetic field. *Image:EFDA*

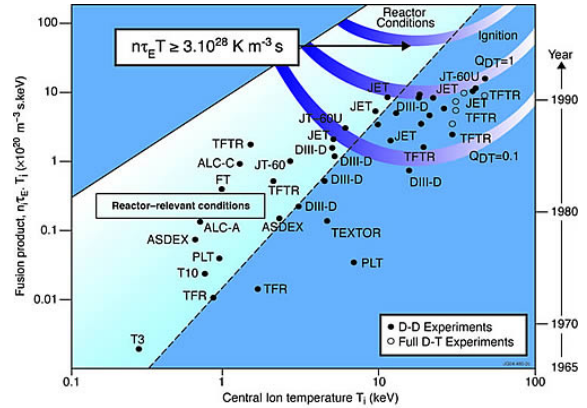


Figure 1.3: Achieved triple product on different tokamaks *Image:EFDA*

ing transport of energy from the plasma core through the plasma edge. More fundamentally, the position and shape of the plasma must be actively controlled to maintain the plasma in place and avoid it touching the vessel walls. Some of these instabilities can be suppressed by appropriate actions using some of the available actuators in the tokamak. As such, *plasma control* has emerged as an essential component of tokamak physics understanding and operation. Basic tokamak operation requires only a few, relatively simple feedback loops to be in place to control a small number of global plasma quantities but, as operational boundaries were expanded, new challenges presented themselves. The next section will describe the tokamak in some more detail after which an overview of the various tokamak control problems will be given.

1.2 The tokamak device

1.2.1 Magnetic field and coil systems

In a tokamak, a plasma is confined by a torus- (donut-) shaped axisymmetric magnetic field configuration. A schematic diagram of the main magnetic field and current configuration in a tokamak is shown in Figure 1.4. The main field component in a tokamak is the field in the toroidal direction (around the torus) which is generated by a set of identical toroidal field coils (arranged in the poloidal plane, i.e. the plane perpendicular to the toroidal direction). Alone, the toroidal field cannot confine a plasma: it can be shown that drifts due to the magnetic field gradients and curvature would lead to opposite vertical drifts for the differently charged species, leading to charge separation and loss of the plasma due to the resulting electric fields. A second, typically 10 times weaker, poloidal magnetic field is generated by a toroidal current flowing inside the plasma itself. The combination of poloidal and toroidal fields lead to helically wound field lines. This way, particles gyrating around the field lines while slowly drifting downwards tend to spend as much time moving away from the field line as moving towards it: charge separation is reduced and individual particles are confined.

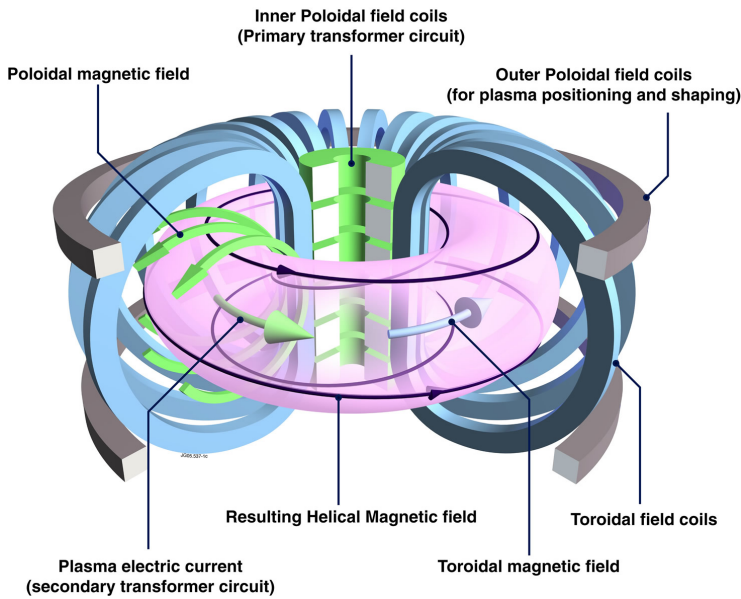


Figure 1.4: Illustration of the tokamak concept. The main toroidal field is generated by toroidal field coils. Plasma current is induced by the primary (Ohmic) transformer coils. Poloidal field coils control the plasma position and shape. *Image: EFDA*

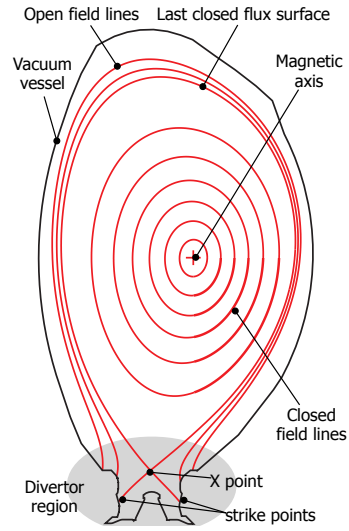


Figure 1.5: JET plasma equilibrium, showing flux surface distribution with open and closed field lines in the poloidal plane, and divertor region with strike points.

To maintain the plasma in a stable equilibrium, an additional set of coils generating a poloidal magnetic field (PF coils) must be used. The combination of poloidal field generated from the plasma and the coils outside is used to control the plasma vertical and horizontal position in the poloidal plane, as well as to define the shape of the plasma via the last closed flux surface, i.e. the last surface where the field lines close on themselves.

Since plasma current is necessary for confinement, it must be sustained for the duration of the plasma, preferably in steady-state to ensure economical operation of a power plant and to avoid cyclic stresses on the components. The easiest way to sustain a plasma current is to drive it inductively using the Ohmic coil (often referred to as the primary transformer coil, or Central Solenoid (CS), see Figures 1.4, 1.7). This has the important side effect of resistively heating the plasma through the Joule effect. The plasma current, being the secondary circuit of a transformer in which the Ohmic coil is the primary, is proportional to the Ohmic coil current ramp rate. Since the Ohmic coil current cannot be ramped indefinitely, the time during which plasma current can be inductively sustained is inherently limited by the *flux swing*: the integral of inductive voltage over time which the Ohmic coil can provide. To maximize the availability of a tokamak-based fusion reactor, alternative means must be found to drive the plasma current non-inductively. Part of this non-inductive current can be provided by the plasma self-generated *bootstrap* current, and additional current can be provided by auxiliary current drive injection systems which will be described below.



Figure 1.6: Concrete pouring for the foundation of the ITER tokamak building, 9th August 2011. *Photo: F4E*

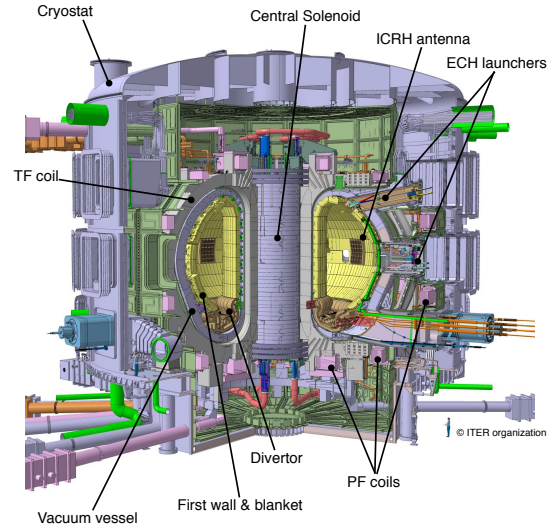


Figure 1.7: Cutout view of the ITER tokamak illustrating the main subsystems. Notice the size of the human figure on the lower right-hand side. *Image: ITER organization, 2011*

1.2.2 Auxiliary heating and current drive systems

A fundamental property of plasmas, which can be derived by studying Coulomb collisions, is that their resistivity scales as $\eta \sim T_e^{-3/2}$ where T_e is the electron temperature. This means that, in contrast to metals and most other materials, plasmas become less resistive as their temperature is increased. This sets a fundamental limit to the temperatures which can be achieved through Ohmic heating alone: for temperatures above $\sim 1\text{keV}$, Ohmic power becomes practically useless. Auxiliary heating systems have therefore been developed to heat plasmas beyond this limit, as well as to inject additional current.

- Neutral Beam Injectors (NBI) inject beams of neutral particles into the plasma. As they are neutral, they are initially not affected by the magnetic field until the particles ionize in collisions with plasma particles, while imparting their kinetic energy to the plasma. Neutral Beams injecting tens of megawatts have been successfully used and provide the bulk heating of many tokamaks worldwide. One of their main disadvantages is the size and complexity of the injectors, as well as the difficulty to vary where the heat and current are deposited. NBIs also inject momentum, causing the plasma to rotate globally which can have important physical consequences.
- Ion Cyclotron Heating and Current Drive (ICRH/ICCD) uses low-frequency RF waves ($f \sim 40\text{MHz}$) which couple to the ion cyclotron frequency or a hybrid frequency of a given ion species in the plasma. While the RF sources use conventional technology, the waves must be driven directly at the plasma/vacuum interface since they do not propagate in vacuum or low-density plasmas. This can cause problems related to the plasma/antenna interface. Specially designed antennas have been tested on tokamaks over the years (see Figure 1.9).

- Lower Hybrid Heating and Current Drive (LHCD) is yet another method for plasma heating, relying on resonant coupling to a wave in the plasma. LHCD is technologically and conceptually simple on the source side ($f \sim 5\text{GHz}$), and is able to drive significant amounts of current which can be easily controlled. It also requires an antenna placed in proximity to the plasma, providing similar engineering challenges as ICRH.
- A final auxiliary heating method is that of Electron Cyclotron Heating and Current Drive (ECRH/ECCD). These waves resonate with the electron cyclotron motion around the field lines, heating the electrons and driving bulk current. RF waves of frequencies in the 100GHz range have the advantage that they propagate through vacuum and can therefore be injected from antennas placed farther from the plasma. Their optical properties are also such that steering/focusing mirrors can be used to precisely direct the location of absorption and current drive in the desired location inside the plasma. This allows great operational flexibility which has motivated the installation of ECRH systems on many tokamaks around the world. A disadvantage is their relative inefficiency at driving current, as well as the fact that the electrons are heated instead of ions (as would be useful to stimulate fusion reactions – though this is also the case for LHCD)

Experience gained using auxiliary heating & current drive systems in tokamaks around the world has resulted in the inclusion of NBI, ICRH and ECH systems in the ITER design (Wagner et al. 2010), where each will have its own role in the sustainment and control of the plasma. Together with the coil system, they constitute important actuators or control levers through which desired plasma behavior for optimal tokamak operation can be achieved.

1.2.3 Tokamak parameters

A number of key quantities can be identified which define a tokamak plasma. These are the quantities which should be controlled to reach the desired point in the tokamak operational space. Before discussing the different control problems related to the tokamak, the main quantities are introduced here. Starting with the main physical parameters of the tokamak, we define the major radius R_0 as the radial position of the geometric centroid of a typical plasma, and the vacuum toroidal field B_0 as the magnetic field strength at R_0 on the midplane, in the absence of a plasma. The minor radius a is half of the distance between maximum and minimum radial location of the edge of the plasma. These parameters define, largely, the engineering characteristics of a tokamak.

Some macroscopic plasma quantities can also be defined. The most important ones are the total **plasma current** I_p , and the normalized pressure factor β : the ratio of thermal pressure to magnetic field pressure. Many different definitions of β exist depending on the choice of how to average the pressure. One often-used choice is

$$\beta = \frac{\langle p \rangle}{B_0^2/2\mu_0} \quad (1.3)$$

where $\langle p \rangle = \frac{1}{V} \int_V p \, dV$ is the volume-averaged pressure. Another important measure is



Figure 1.8: Internal view of the TCV tokamak (Lausanne, CH. $R_0 = 0.88\text{m}$, $a = 0.25\text{m}$). Note the large number of ports and protective carbon tiles. This photo was taken just after the tiles had been cleaned.

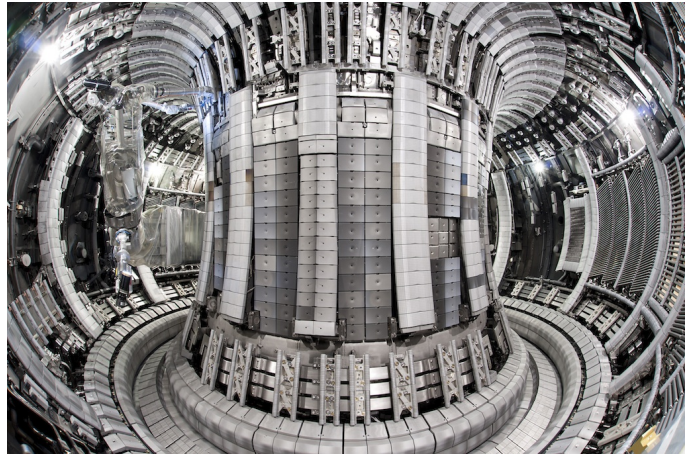


Figure 1.9: View of the inside of the JET tokamak (Culham, UK. $R_0 = 2.96\text{m}$, $a = 1\text{m}$) in May 2011, after installation of the ITER-like wall. Note the ICRH antennas on the right, and the divertor below, and the remote manipulation arm on the left. [Image: EFDA-JET]

the poloidal β , defined by normalizing the pressure by the poloidal magnetic field

$$\beta_p = \frac{\langle p \rangle}{B_p^2 / 2\mu_0} \quad (1.4)$$

where $B_p = \mu_0 I_p / \oint d\ell_p$ and the integral is taken over the last closed flux surface. Another normalized form of β which allows one to express the proximity to tokamak stability limits is

$$\beta_N = \frac{\beta[\%]}{I[\text{MA}]/a[\text{m}]B[\text{T}]} \quad (1.5)$$

The maximum achievable limit for β_N for typical tokamak plasmas but neglecting the effect of a conducting wall is given by the Troyon limit (Troyon et al. 1984) $\beta_N < 3.4$.

Apart from the global quantities defined above, a number of spatially dependent quantities play a role. This is discussed in more detail in Chapter 6, but an introductory treatment is given here. In a tokamak, the closed helical magnetic field lines define a set of nested flux surfaces on which the pressure is approximately constant. By defining a radial coordinate corresponding to each flux surface, we can define 1-dimensional (radial) profiles of important quantities which are constant on a 3D flux surface. By taking suitable averages over a flux surface, quantities which are not necessarily constant flux-surface quantities can also be expressed as 1D profiles. We start by defining the **safety factor**

$$q = \frac{\partial \Psi}{\partial \Phi} \quad (1.6)$$

where Ψ is the poloidal flux and Φ is the toroidal flux. For now, it suffices to state that q represents how many toroidal periods a field line covers for one poloidal period. As such, it indicates the degree of helicity of magnetic field lines, with smaller q indicating

a greater degree of helical twist. It is a key indicator of the plasma stability and defines different regimes of confinement. The shape of the q profile defines the spatial variation of the magnetic field line twist over the plasma, and is the result of the internal distribution of current density due to the spatially varying resistivity, itself governed by the plasma temperature. The q and current density profiles are referred to as the **magnetic profiles**.

Apart from the q profile, the spatial distributions of plasma **temperature** and **density** for different species are important, as they directly define the plasma β and the rate of fusion reactions. One can define the electron and ion temperatures and densities as T_e , T_i , n_e , n_i , respectively, and one can extend the definitions to any other ion species present. In some cases, the **rotation** profile, i.e. the profile of toroidal and poloidal average plasma velocity can also play an important role. The ensemble of these profiles is often referred to as the **kinetic profiles**.

1.3 Control problems in tokamaks

The combination of plasma bulk and profile quantities defined above uniquely define a point in the tokamak operational space referred to as a **plasma scenario** (Gomezano et al. 2007). Each plasma scenario has its distinct properties, advantages and disadvantages which will be discussed in some more detail in Section 6.8. It is however important to realize, at this point, that the overall objective of plasma control is to steer the plasma towards the desired operational point, staying clear of stability and operational limits, and to maintain the plasma at the desired operational point for the duration of the discharge. The various control problems described below represent particular aspects of this global issue. An extensive overview of plasma control problems for non-plasma physics experts was presented in (Pironti et al. 2005) and (Pironti et al. 2006).

1.3.1 Control of bulk plasma quantities

Virtually all existing tokamaks have some form of active control over the plasma position, current, density, and internal energy. These global parameters define macroscopic characteristics of the plasma, and must each lie within given ranges in order for the plasma to exist at all.

Position control is achieved, in its simplest form, by a linear combination of PF coils generating a magnetic field which creates a net (Lorentz) force on the plasma in the required direction to maintain the plasma at a given reference location. Variations in the plasma position are derived based on a set of magnetic probe measurements, which sense the perturbation in the magnetic field caused by the displacement of the plasma. Additionally, the vertical position is unstable for plasmas that are vertically elongated (higher than they are wide in the poloidal plane), and without active feedback control (Lazarus et al. 1990) an elongated plasma would depart vertically. Out of all control issues involving coils, vertical control poses the most stringent requirements on the coil characteristics in terms of dynamic response and maximum current. Lively research has been conducted on this topic and some advanced controllers have been designed taking into account the nonlinear properties of superconducting coils and power supplies, (Favez et al. 2005).

The plasma current is proportional to the Ohmic coil ramp rate which governs the inductive voltage, but at the same time depends on the resistivity. To ensure that the desired plasma current is obtained even while the plasma resistivity varies (e.g. due to temperature variations), a feedback loop is used to adjust the Ohmic current ramp rate depending on the error between the measured plasma current and its reference value. The current is measured by integrating the magnetic field over a poloidal loop around the plasma.

The plasma density is controlled by adjusting the aperture of gas valves or the timing of pellet injection system. In some cases, the pumping rate can also be adjusted providing an additional degree of control. Density is usually measured by interferometric means and compared to a reference value.

Finally, the total plasma energy can be controlled in feedback (though this is not always necessary) by adjusting the injected auxiliary power levels. One important aspect in controlling the plasma heating power is the appearance of the H-mode (high confinement mode), an enhanced confinement regime in which the transport of plasma energy through the edge is reduced. This regime forms spontaneously while increasing the heating power and is now the baseline high-performance scenario for tokamaks.

All the above control problems are considered to be solved and constitute a basic requirement for tokamak operation. They are typically implemented as PID (Proportional, Integral, Derivative) controllers where the actuator command is a linear combination of the error signal, its integral and its derivative. This standard control method stems from the '60s and is widely used and well-known in industrial applications.

1.3.2 Plasma shape and strike point control

Beyond the basic quantities described above, it is also desirable to control the position of the **Last Closed Flux Surface** (LCFS), i.e. the location of the plasma boundary in the poloidal plane. This is done by adjusting the distribution of current in the PF coils which, if more than four are available, can be used to control the shape independently from the plasma position. Plasma shape control is important not only for safety reasons (to prevent part of the last close flux surface to intersect the wall) but also to ensure correct coupling with auxiliary heating system antennas close to the plasma (ICRF,LH). The shape of the plasma also has an effect on the confinement of energy and particles and can be optimized to achieve better performance (Moret et al. 1997). Finally, the strike points in diverted plasmas (Figure 1.5) should be controlled to be at the correct location with respect to the divertor target plates to avoid power deposition in locations where it can do damage.

Control algorithms for shape control are dominated by the multivariable, distributed nature of the problem. Often, a set of gaps (minimum distance between the LCFS and a given point on the wall) is defined yielding a discrete set of control variables. Shape control has been an active area of research for many years, and is usually integrated with plasma position and current control (sharing the PF coils as common actuators). A recent overview can be found in (Ariola et al. 2008) and (Ambrosino et al. 2005). This problem is now also considered solved and standard analysis and design techniques exist. Problems, if any, are related to optimization of the required coil and sensor hardware in hostile plasma conditions. Shape control problems, or the wider field of *magnetic* control

of tokamak plasmas encompassing any control done using external magnetic coils, is a key discipline in plasma control albeit one which has reached a certain level of maturity. It is therefore not discussed further in this thesis.

1.3.3 MHD instability control

Let us imagine a tokamak plasma in which macroscopic quantities such as plasma edge and position have been controlled. When trying to increase the density, current and power towards conditions where the fusion triple product becomes significant, we can trigger so-called MHD modes, i.e. modes described by equations of Magneto-Hydrodynamics (Goedbloed et al. 2004), (Goedbloed et al. 2010), (Friedberg 1987). While these do not always cause an immediate problem for tokamak operation, they must be understood and controlled in order to optimize the plasma performance.

Out of the many existing MHD modes, four are operationally most relevant in tokamaks. They will be briefly mentioned starting from the edge region of the plasma and moving towards the inside.

- The **Resistive Wall Mode** (RWM) appears in high- β plasmas as a helical deformation of the plasma, peaked near the edge, due to resistive MHD and wall effects. As it limits the maximum achievable pressure in high- β_N plasmas, operational benefits can be obtained by controlling it. Active nonaxisymmetric coils close to the LCFS have been used in the past to control the RWM and increase the obtainable β_N limit (Chu et al. 2010).
- Examining the region just inside the LCFS, we encounter the **Edge Localized Modes** (ELMs), an exclusive feature of H-mode plasmas wherein the edge pressure gradients suddenly collapse causing a loss of part of the plasma energy and its deposition on the plasma facing components. Recent progress has been obtained in accessing ELM-free H-mode regimes, where the ELMs are entirely suppressed and replaced by more continuous channels for energy flow through the LCFS (Evans et al. 2004), (Suttrop et al. 2011). While these strategies are being assessed and validated for operation in reactor conditions, other methods for controlling the ELMs without achieving full suppression are being investigated. ELM control by power modulation of off-axis heating will be shown in Section 3.3 of this thesis.
- Moving towards the center of the plasma, we find **Neoclassical Tearing Modes**, or NTMs. These resistive MHD modes cause the otherwise nested surfaces to reconnect and form regions of so-called magnetic islands. While often not catastrophic they do degrade plasma confinement significantly and should be avoided if possible. Additionally, they may, in some situations, cause a global plasma disruption – events in which the entire plasma current drops to zero in a short time, causing thermal and mechanical stresses on machine components. The control of tearing modes can follow two paradigms. Either the operational regimes are chosen such that their appearance is avoided entirely, or they are stabilized if they appear. Fortunately, NTMs can be reduced in size and even completely suppressed by sufficient amounts of localized ECCD. The study of the physics and control problems associated with NTM control has seen much active research in the past years and a set of control

strategies have been devised for ITER – and included in the ITER ECH system design. The physics and control of these tearing modes in the TCV tokamak is the main topic of Chapter 4.

- Proceeding further towards the plasma center we can encounter the **Sawtooth** oscillation: a periodic, sudden relaxation (“crash”) of the core plasma pressure. Though not inherently problematic, and possessing some advantages such as fusion ash (He) and impurity removal, these crashes can serve as destabilizing trigger for NTMs which in turn decrease confinement. If they cannot be avoided, they must be controlled to avoid their coupling to NTMs, either by reducing the magnitude of the crash event or by taking appropriate action to prevent a large crash from triggering a tearing mode. These control strategies will be discussed more in depth in Chapter 3 and 4 which will present experiments on the TCV tokamak featuring a novel sawtooth control strategy as well as NTM preemption methods.

The state-of-the-art in MHD control is represented by the successful control of individual MHD instabilities in dedicated experiments. Many of the existing tools and control strategies are yet to be developed into routinely usable solutions for everyday tokamak operation.

1.3.4 Plasma profile control

With a given amount of auxiliary heat and injected current, the plasma profiles will evolve towards their self-consistent final equilibrium state. However, as mentioned, one would like to achieve a particular shape of the profiles, associated with a desired plasma scenario. This requires appropriate actions with the available actuators, most notably the auxiliary heating/current drive systems, which must be positioned and distributed such that they are compatible with the desired final stationary state. At the same time, the trajectory followed by the plasma profiles while evolving towards the stationary state is also important since it may transiently violate operational limits or trigger instabilities. Additionally, bifurcations may be present in the dynamic behavior of the plasma, such that a given stationary setting of the plasma actuators may not correspond to the same stationary state. The path followed during the evolution is therefore itself important and must be chosen carefully. Once the desired operational point is reached, it must be maintained throughout the duration of the flat-top avoiding drifts and disturbances to the plasma. At the end of the flat-top (or fusion burn) phase, measures must be taken to avoid exceeding any limits as the plasma current and heating are gradually decreased. As outlined above, the profile control problem can be split into the problem of defining the trajectory which the profiles should follow during their transient evolution towards/from their stationary state, and the question of how to maintain the desired profiles in time during the flat-top. These are conventionally referred to as open-loop and closed-loop profile control problems, respectively.

Profile control plays a fundamental role especially in so called *advanced* tokamak scenarios, where the q profile is actively tailored to a desired shape that has a positive influence on the plasma confinement. It is a subject which has received significant attention in the recent past and successes have been reported (Ferron et al. 2006), (Moreau et al. 2008), (Suzuki et al. 2008) in dedicated experiments. Still, routine use of profile

feedback control is far from being a reality. Plasma profile control will be the topic of Part II of this thesis.

1.3.5 Safety, prediction and disruption avoidance

The control problems described above can be considered control problems in the classical sense, where a desired operating point is to be tracked based on error measurements. Now, consider more global control issues pertaining to the overall monitoring of the tokamak plasma state. As in any complex system, one can define a set of normal operating modes, in which the system evolves in a predictable and well-understood way, even while a control system may be necessary to maintain the system within the required limits. At some point, however, it is possible that the deviation from these normal operating conditions becomes so large that one may speak of an anomaly, which could originate from a fault or other unexpected occurrence. This anomaly may bring the system (in this case the plasma) dangerously close to its operating limits. Standard control actions are then no longer appropriate and emergency actions must be taken to bring the plasma back into a controllable state, or, if that is not possible, the plasma must be terminated in safe manner. A particularly pertinent example in this respect is **disruption avoidance**. Disruptions, as previously mentioned, must be avoided as they can cause thermal and mechanical stresses on tokamak components. Though multiple reasons for disruptions can be identified (de Vries et al. 2011), most of them can be attributed to the plasma approaching a fundamental physical limit, beyond which some instability grows in an uncontrolled way. Monitoring the plasma state for proximity to known physical limits can provide early warning of approaching disruptions.

These important tasks are normally performed by a higher-level, supervisory control system which accepts information from several redundant sources to construct a picture of the plasma conditions. Most existing tokamaks today have some form of safety monitoring interlock system but a fully integrated system with the level of reliability required to satisfy ITER requirements is still to be developed. A desirable feature of this supervisory plasma control system is that it should be able to look forward in time, to **predict** the future behavior of the plasma based on the planned actuator inputs. This requires a simulation of the tokamak plasma to be done faster than real-time, while the shot is progressing. Physics models are required which are sufficiently simple to be executed rapidly, yet sufficiently accurate to correctly predict the plasma evolution. For a complex nonlinear system such as a plasma this is not an easy task and tokamak plasma prediction is yet in its infancy. New results in this direction will be presented in Part II of this thesis.

1.3.6 Integrated control

Many tokamak control problems have been separately addressed and solved to some extent in various experiments around the world. A challenging task remains to integrate all these disparate control strategies, which in many cases share actuators and sensors, and in some cases are in conflict with each other, into one single overall control strategy which accomplishes all the shot's objectives while satisfying all constraints. This is referred to as **integrated control** (Joffrin et al. 2003), (Humphreys et al. 2007).

Before concluding this section, it should be pointed out that, in a fully integrated tokamak shot control scheme, different control problems receive priority depending on

the phase of the discharge. In the initial and final phases, the transient evolution of profile and shape will be of greatest concern, while during the flat-top and burn phases the focus will be on burn control and MHD control while holding the reference operating point. This is illustrated schematically in Figure 1.10, which summarizes the control problems mentioned above.

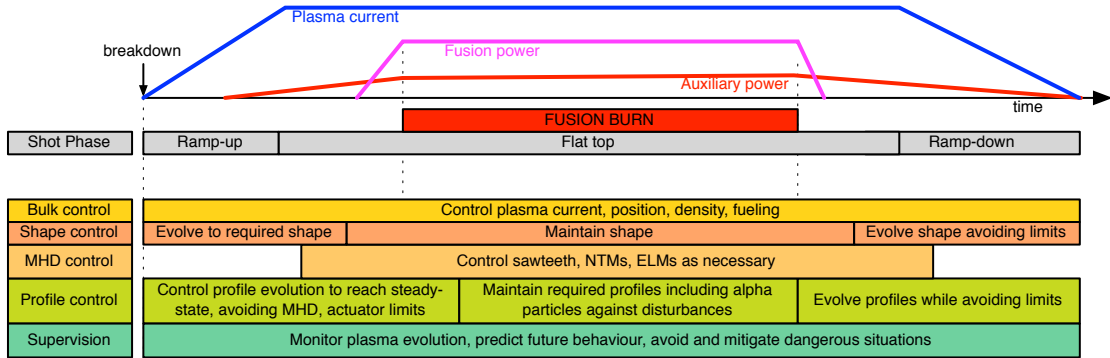


Figure 1.10: Schematic illustration of the time evolution of a burning plasma in a tokamak experiment, with illustration of the various control goals which are relevant in the various phases of the discharge.

1.4 Motivation for this thesis

The central theme of this thesis is the combination of physics and control in its application to tokamaks. This apparent dichotomy will manifest itself in two ways. On one hand, existing control methods will be experimentally applied to control various physical phenomena in a tokamak plasma. On the other hand, physics insight will be used to design advanced control solutions. The focus will be not only on how each aspect of the problem can learn and benefit from the other, but especially on how they can be merged to provide more than the sum of their parts.

The experimental work presented was performed on the TCV tokamak at CRPP-EPFL in Lausanne. On TCV, the recent development and commissioning of a new digital real-time control system has provided the opportunity to implement a large number of new control algorithms, with applications to both enhanced physics studies and development of general tokamak control solutions. As will be discussed in Chapter 2, TCV combines a great flexibility in available actuators, thanks to 16 independently powered PF coils and 7 independently steerable ECH/ECCD launchers, with multiple diagnostics having high spatial and temporal resolution. Now that this actuator and diagnostic flexibility has been matched with an equally flexible real-time control system, TCV has become the ideal platform for studying physics issues and control solutions for **MHD control** and **profile control**. The new opportunities provided by this unique experimental platform have been the fertile ground on which much of the work in this thesis has grown.

At the same time, the material in this thesis is strongly influenced by the idea that standard control engineering solutions alone are not sufficient to solve the strongly non-linearly coupled, multivariable tokamak profile control problem. Better approaches can

be obtained by including the physics understanding gained by years of tokamak theory and experiments, at a deep level, inside the profile control loop. Since modern computational platforms can numerically solve the equations governing tokamak profile evolution faster than the physical profile evolution itself, the application of **real-time tokamak simulations** provides ample opportunities for study and constitutes a major part of this work. At the same time, the physics-based model can be used in a numerical optimization scheme that can compute the **optimal actuator trajectories** required to reach a desired operating state. The model also provides the necessary information for predicting the future evolution of plasma profiles.

1.5 Outline of this dissertation

This first chapter has provided an introduction to nuclear fusion, plasma physics and the tokamak concept, and highlighted some of the main control problems which must simultaneously be solved during a tokamak discharge.

- Chapter 2 will describe the TCV tokamak where all the experimental work reported in this thesis was carried out. The magnetic coil system, main diagnostics and heating systems will be described, and particular attention will be devoted to the TCV real-time control systems, including the new digital control system which has been extensively used to obtain the experiments described in the following chapters. More technical details about the new control system are also given in Appendix A

The remainder of this thesis is divided into two main parts. The first shows experimental applications of real-time control algorithms to control the plasma behavior on TCV, and consists of three chapters:

- Chapter 3 will focus on **sawtooth control** and will present a new experimental method of using EC heating and current drive to accurately control the occurrence of individual sawtooth crashes during a tokamak discharge. The first results of this work have recently been published as (Goodman et al. 2011), (Lauret et al. 2011) and this thesis provides a more extended account of the method, results and analyses. A very similar method has also been successfully applied to **ELM control** using off-axis EC power, as will be shown at the end of the chapter.
- Chapter 4 will present technical developments in TCV NTM real-time control capabilities, and show experimental results on **triggering and control of NTM**, in particular making use of real-time control algorithms to enhance the experimental possibilities. Triggering conditions for NTMs originating from large sawtooth crashes are experimentally investigated both in high-current, low q_{95} plasmas and also in lower current plasmas. NTM control demonstrations and stability studies are performed by using the real-time control system to detect the mode appearance and act appropriately on the EC actuators to stabilize the mode. These results have partially been presented as (Sauter et al. 2010) and (Coda et al. 2010)
- The final chapter of the first part (Chapter 5) shows several experimental demonstrations of closed-loop control of plasma kinetic profile quantities using the ECRH

system. In particular, control of the peak and width of X-ray emission profiles, of plasma central temperature for variable-shaped plasmas, and of poloidal beta is shown. The EC power is used as an actuator, as well as the EC deposition location by varying the EC injection angles. Part of this work has been published in (Paley et al. 2009) and part is presented here for the first time.

Some technical details pertaining to real-time signal processing algorithms used mainly in Part I of the thesis are given in Appendix B.

Part II focuses on a new physics-model-based framework for real-time tokamak profile reconstruction, optimization and prediction, and revolves around a newly developed code named RAPTOR. The framework presented in this part of the thesis has been presented as conference contributions on two occasions (Felici et al. 2010b), (Felici et al. 2011a) and published in journal publications as cited below.

- Chapter 6 describes in some detail the **physics of tokamak profiles** and their dynamic evolution. An overview of present tokamak equilibrium-transport simulation methods is also given. While most of this introductory material represents previous work, a new measure for profile stationarity is introduced in this chapter, quantifying the degree to which a plasma profile has relaxed to a steady state by a scalar value.
- Chapter 7 describes the new **RAPTOR** (Rapid Plasma Transport simulatOR) code, a **lightweight 1D profile evolution code** focused on execution speed while maintaining key physics. The necessary simplifications to the full-physics model are introduced, as well as both interpretative and predictive modes of operation. Appendix D contains further technical details about the code implementation and numerics. The code is successfully benchmarked against the ASTRA transport code in interpretative and in predictive mode.
- Next, Chapter 8 introduces a first application of this new code for **Real-time current density profile simulations** on TCV. The implementation of the code on the real-time TCV control system is explained, as well as a method to estimate the required kinetic profiles in real-time from diagnostic data. The real-time current density profile simulations give information about hitherto unmeasurable quantities including loop voltage profile, q profile, and bootstrap current fraction. The real-time reconstructed data is shown to compare favorably to established post-shot analysis tool results. The real-time estimate of the internal inductance is used in a closed-loop controller demonstrating simultaneous control of the (coupled) plasma temperature and internal inductance using the TCV EC system as actuator. Part of this chapter has been published as (Felici et al. 2011b).
- The final chapter (Chapter 9) shows another application of the RAPTOR code. It is used to solve the **open-loop plasma profile control** problem, computing the optimal actuator trajectories to reach a desired operating point. The problem is formulated as an optimal control problem and solved using well-known numerical techniques. For the first time, optimal control techniques are applied to a self-consistent

coupled model of poloidal flux and electron temperature transport, obtaining new insights on possibilities of steering tokamak profiles during their transient evolution. The material in this chapter has recently been submitted for publication (Felici et al. 2011).

1.5.1 Other work carried out during this thesis

During the time frame allocated for this thesis the author had the pleasure of participating in other scientific work. It has not been included in this dissertation for brevity's sake, but is listed here nevertheless for completeness.

- During three visits to the National Institute for Fusion Science (NIFS) in Japan in 2008 and 2009, control systems were developed for feedback control of the ECH polarization on LHD (Large Helical Device). A laboratory test was published as (Felici et al. 2009a) and a successful experimental demonstration in LHD plasmas was published in (Felici et al. 2010a).
- To analyze EC polarization control methods, in view of the installation of fast polarizers in the TCV EC transmission line (Silva et al. 2011), a code was developed to compute the polarization state of an EC wave as it propagates through several reflecting mirrors, including grooved polarizers. This work is unpublished, but will be published as an internal report (Felici 2011). The code has also been used for guiding the design of rectangular polarizers for Dynamic Nuclear Spectroscopy applications (Alberti et al. 2011).
- A wiki-based internal website for the CRPP was developed (2007). It currently consists of about 2000 unique pages, collaboratively developed and maintained by CRPP staff. It has become the central repository for TCV hardware/software documentation, manuals, project planning, and administrative information. It has greatly facilitated the harmonization and centralization of information shared across the laboratory (Schlatter 2009, Appendix G).

Chapter 2

The TCV tokamak

This chapter describes the TCV tokamak at CRPP/EPFL in Lausanne, Switzerland. All the experimental work presented in this thesis was done on this device. Special attention will be devoted to the control systems used, as well as providing an overview of the most relevant diagnostics and actuators.

2.1 Overview

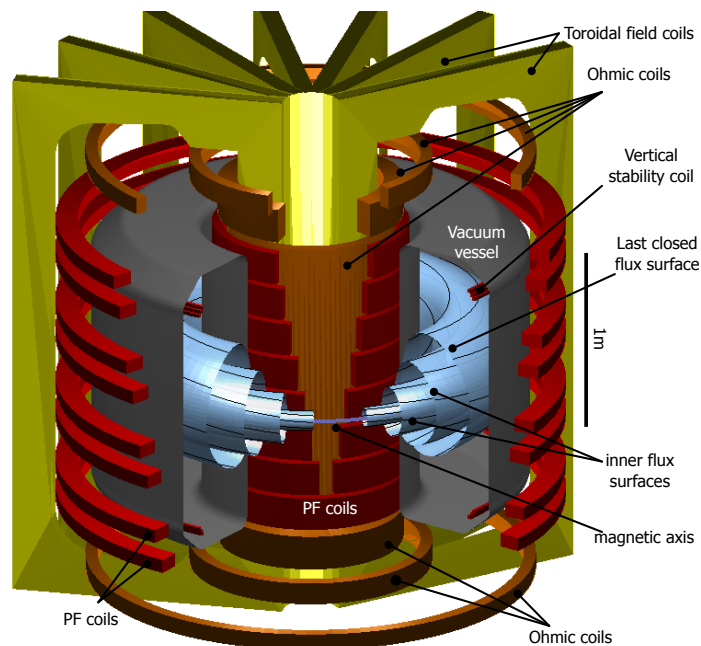


Figure 2.1: Cutout view of TCV showing poloidal and toroidal field coils, ohmic coils, vacuum vessel and nested plasma flux surfaces with magnetic field lines. Numerous access ports are cut in the vacuum vessel (not shown)

The Tokamak à Configuration Variable (TCV) (Hofmann et al. 1994), commissioned in 1992, is an experimental tokamak characterized by a high degree of operational flexibility.

Figure 2.1 shows a cutout view of the magnetic coil system, consisting of 16 PF coils, 7 coils forming the Ohmic transformer primary, 16 TF coils as well as two internal (fast) coils placed inside the vessel for vertical position control. The coil layout is also shown in a poloidal cut in Figure 2.2. One of the unique features of TCV is the fact that the 16 PF coils are controlled by 16 independent power supplies, which allows one to tune the poloidal field and to obtain a large number of unique plasma cross-sectional shapes including both limited (e.g. Fig.2.3) and diverted (e.g. Fig.2.2) configurations.

Another unique feature of TCV is the high power and current drive capabilities provided by a flexible Electron Cyclotron Resonance Heating and Current Drive (ECRH/ECCD) system. The ECRH/ECCD system consists at present of 6 gyrotrons of 500kW each, whose power is injected from the low field side for second harmonic X-mode (X2) heating and current drive (82.7GHz), as well as 3 other gyrotrons, also 500kW each, delivering power from the top of the vessel providing third harmonic X mode (X3) heating (118GHz). Each X2 launcher, as well as the combined launcher for all X3 gyrotrons, has an independently steerable mirror which allows the ECH/ECCD deposition location to be scanned and controlled in real-time during a plasma shot. Each X2 launcher can be rotated between shots, allowing variation of the ECH/ECCD configuration. The X3 launcher can be displaced radially between shots, allowing one to optimize the launch configuration for a particular plasma. A poloidal cut of TCV is shown in Figure 2.3, highlighting the range of available injection angles in the poloidal plane, the radial excursion of the X3 launcher, as well as showing the vacuum vessel and PF coil layout. More details on the ECRH/ECCD system are provided in Section 2.2.

The inside of the TCV vacuum vessel is covered (90%) with graphite tiles, thus the main impurity in TCV plasmas is carbon. Every time the TCV vacuum vessel has been exposed to air, a baking procedure is executed to remove impurities (e.g. O₂, N₂, Ar) accumulated in the wall, followed by boronization. Between each plasma shot, the first wall is cleaned by a Helium glow discharge.

The main device parameters, listed in Table 2.1, situate TCV in the mid-range of worldwide tokamaks (by size), with a higher than average power density given the significant ECH power compared to the plasma volume. Another specificity is the relatively long pulse length with respect to the current redistribution time, facilitating studies of stationary and steady-state scenarios.

Some areas of focus of the TCV scientific program are listed below.

- Studies of plasma shaping effects on transport, MHD and edge physics, including effects of elongation and triangularity and innovative divertor configurations (Weisen et al. 1997), (Hofmann et al. 2001), (Pochelon et al. 2001), (Weisen et al. 2002), (Scarabosio et al. 2007), (Camenen et al. 2007a), (Camenen et al. 2007b), (Piras et al. 2010b).
- Physics of steady-state plasmas with high non-inductive current drive fractions and transport barriers. (Henderson et al. 2004), (Goodman et al. 2005), (Sauter et al. 2005), (Coda et al. 2007), (Turri et al. 2008), (Udintsev et al. 2008). Significant achievements include a world record fully ECCD-driven plasma (210kA) (Coda et al. 2000) and 100% bootstrap current sustained plasmas (Coda et al. 2008).
- H-mode, both in Ohmic and EC-heated plasmas, with ELMing regimes ranging

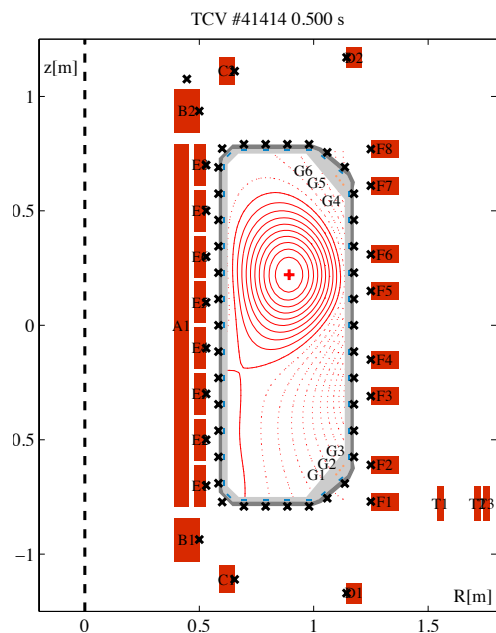


Figure 2.2: Poloidal view of TCV tokamak showing the poloidal field coil system and magnetic diagnostics. Ohmic coils labeled A-D, PF coils labeled E-F. Internal field coils G (3 turn each, shown separately). Positions of magnetic field probes (rectangles) and flux loops (\times) are also shown. Flux contours and magnetic axis for a “standard shot” (L-mode diverted plasma), is also shown.

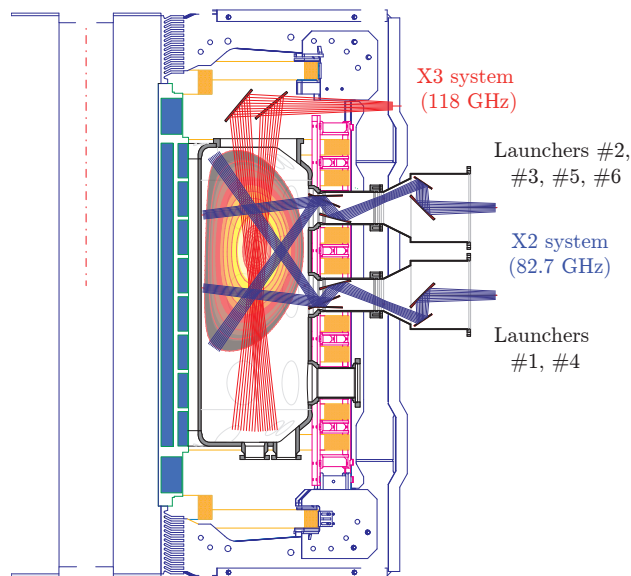


Figure 2.3: Poloidal view of the TCV tokamak showing the PF coils, toroidal field coil, as well as low-field-side launched X2 and top-launched X3 ECRH/ECCD systems. The steering ranges in the poloidal plane are also shown. In addition to the movement in the poloidal plane, the X2 launchers can be rotated toroidally to allow ECCD.

from type-I to type-III to a quiescent ELM-free scenario with high-power X3 heating (Martin et al. 2003), (Martin et al. 2006), (Porte et al. 2007).

- Edge physics, focusing on scrape-off-layer physics and ELM power deposition on strike points (Pitts et al. 2001), (Pitts et al. 2003), (Pitts et al. 2007)
- High-energy electron physics, in particular studying suprathermal electrons and runaway generation as a result of high-power ECH/ECCD (Coda et al. 2003), (Klimanov et al. 2007)
- Studies of plasma rotation in the absence of external momentum inputs in various scenarios (Scarabosio et al. 2006), (Bortolon et al. 2006), (Duval et al. 2010), (Camenen et al. 2010).
- Advanced plasma control focusing on vertical stability of highly elongated plasmas (Hofmann et al. 1998) (Hofmann et al. 2000) and, more recently, real-time plasma control using the ECRH/ECCD system (Paley et al. 2007), (Paley et al. 2009), (This Thesis)

| | |
|---|---|
| Major radius | 0.88m |
| Minor radius | 0.25m |
| Maximum plasma height | 1.45m |
| Maximum toroidal field | 1.54T |
| Plasma current achieved | $I_p \leq 1\text{MA}$ |
| elongation achieved | $0.9 \leq \kappa \leq 2.8$ |
| triangularity achieved | $-0.8 < \delta < 1$ |
| Typical/Max. shot duration | 2s/ 4s |
| Inter shot delay | > 400s |
| Energy confinement time | < 50ms for H-modes |
| Current redistribution time | $\sim 150\text{ms}$ for heated plasmas |
| Central electron temperature | $T_{e0} < 15\text{keV}$ (EC heated) |
| Central ion temperature | $T_{i0} < 1\text{keV}$ |
| Density range | $0.5 \cdot 10^{19}\text{m}^{-3} \leq n_e \leq 20 \cdot 10^{19}\text{m}^{-3}$ |
| PF coils | 8+8, copper, water cooled |
| TF coils | 16, copper, water cooled |
| Ohmic flux swing | 3.4Vs |
| Installed power | 220MVA |
| Electron-Cyclotron heating/current drive system | 4.5MW: $6 \times 500\text{kW}$ @ 82.7GHz (X2/O2), 3 \times 500kW @ 118GHz (X3) |

Table 2.1: Some parameters of the TCV tokamak, as of 2011

A wide variety of diagnostics is available, the most important of which will be highlighted in Section 2.3. Finally, the real-time control systems presently installed on TCV will be described in some detail in Section 2.4.

2.2 The TCV ECH/ECCD system

This section describes the ECH/ECCD system in some detail, focusing on some technical aspects which will be important in later chapters of this thesis. A recent overview of the system is given in (Goodman et al. 2008). A bird’s eye view of the hardware components is shown in Figure 2.4.

2.2.1 Second harmonic ECH/ECCD

The second harmonic X- or O-mode (X2/O2) system consists of six Gycom gyrotrons with nominal RF power output of 500kW each, at a frequency of 82.7GHz. This corresponds to a second harmonic cold resonance at a field of $B = 1.47\text{T}$, situated near the magnetic axis for nominal magnetic fields. By lowering the field the resonance layer can be moved to the high field side, allowing further operational flexibility.

Transmission line

Attached to each gyrotron is a Matching Optics Unit (MOU) which modifies the optical properties of the outgoing beam so as to have a Gaussian shape, and sets the polarization of the EC wave with a set of two moveable grating mirror polarizers. These polarizers can be rotated between shots to adjust the polarization of the EC beam to correspond to X or O mode (or a combination of both) at the last closed flux surface for a given

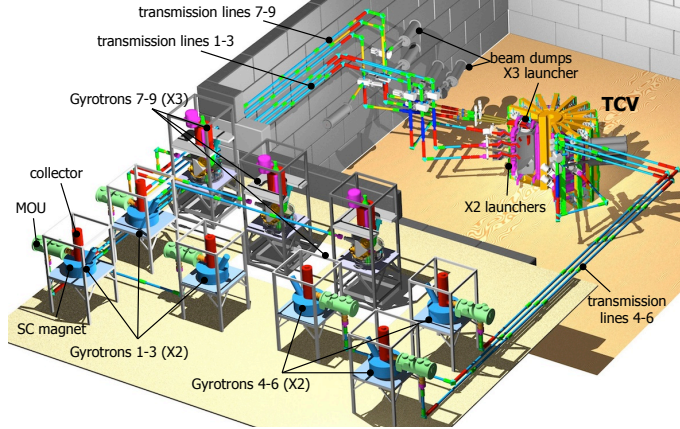


Figure 2.4: Bird's eye view of the TCV ECH system (2011), showing the 9 gyrotrons, transmission lines and launchers.

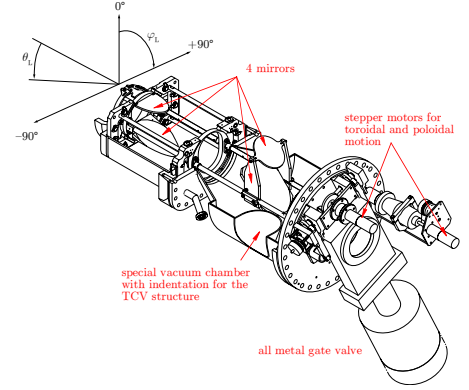


Figure 2.5: Drawing of X2 launcher, showing the 3 fixed mirrors and 1 (final) real-time steerable mirror. The EC power enters the launcher from the bottom-right. Steering angle conventions are also indicated.

equilibrium. At the exit of the MOU, the EC wave is coupled to the HE11 mode in a corrugated waveguide, along which it propagates until reaching, after a series of miter bends, an EC launcher installed in the torus.

Launchers

Each launcher consists of four mirrors, the last one of which (at the front, close to the plasma) can be steered in real-time. By varying the inclination of this final mirror, the injection angle of the EC beam into the plasma can be varied. This mirror can be moved rapidly during the shot providing real-time EC steering capability. The transfer function of the mirror mechanics is approximately described by a well-damped second order system with a resonance at 13Hz, limiting the speed with which the mirror position can be changed.

There are two “equatorial launchers”, (#1,4) installed in equatorial ports ($z = 0$) and four “upper launchers” (#2,3,5,6) installed in upper ports ($z = 0.46\text{m}$), as shown in Fig.2.3. The available ECH/ECCD configurations are determined by the steering range of the mirrors (extremes of the vacuum beam paths are also shown in Fig.2.3) as well as by the geometry of the plasma. The injection geometry is best described in a spherical “launcher” coordinate system (cf. Fig. 2.5): θ_L is the angle of the EC ray leaving the final mirror with respect the axis of the launcher (in the horizontal plane, pointing radially inward towards the tokamak vertical axis), and φ_L is the angle of the plane containing the optical axis of the launcher mirrors, with $\varphi_L = 0$ corresponding to a downward pointing beam ($\theta_L > 0$). The “launcher poloidal angle” θ_L is mechanically constrained between 8° and 45° and can be steered rapidly during the shot. The “launcher toroidal angle” φ_L can be chosen arbitrarily, but can only be varied between shots ($-180^\circ \leq \varphi_L \leq 180^\circ$). Typical configurations are co- or counter- ECCD in the horizontal plane ($\varphi_L = \pm 90^\circ$) and pure ECH (on-axis) for plasmas with axis at $z = 23\text{cm}$: $(\theta_L, \varphi_L) = (38^\circ, -180^\circ)$ for equatorial launchers and $(\theta_L, \varphi_L) = (38^\circ, 0^\circ)$ for upper launchers.

Power supplies

The gyrotrons are grouped into two “clusters” of three gyrotrons each. Cluster A (gyrotrons #1-3) and Cluster B (gyrotrons #4-6). Gyrotrons of the same cluster share a common power supply and will have the same nominal output power at any point in time. Individual gyrotrons can however be deselected or fired into a dummy load if not required. Recalling the launcher configuration, each cluster consists of one equatorial and two upper launchers.

Due to technical reasons of the gyrotron, there are constraints as to how rapidly its power can be varied when starting from or returning to the off-state. In particular, the power range between 0 and approximately 180kW can not be crossed faster than 700 μ s, and the same range in reverse can not be traversed faster than 300 μ s to avoid current and voltage overshoots. Between 180kW and full power (500kW), the power can be varied at any speed, in practice being limited by the transfer function of the power supply itself which, damps oscillations above ~ 25 kHz. Under very special conditions the gyrotrons can generate an on-off modulation at up to 15kHz for a short (up to 600ms) period.

Plasmas for EC heating

The second harmonic system is most often used for heating and current drive in L-mode plasmas or at the edge of H-mode plasmas, since the X-mode cutoff density $4 \times 10^{19} \text{m}^{-3}$ is lower than the central density in typical H-mode plasmas. Up to 100% absorption can be obtained except for very low density cases. Second harmonic fundamental O-mode heating is possible in H-mode plasmas albeit with reduced absorption, or the O-X-B electron Bernstein wave heating scheme can be used, albeit within a very small operational window (Mueck et al. 2007). Most H-mode experiments however rely on the third harmonic system described below. Occasionally, the X2 system is also used for ECH-assisted plasma startup.

2.2.2 Third harmonic ECH system

The third harmonic (X3) ECH system allows heating of high density plasmas, including H-modes. The X3 system has three CRPP-CEA-Thales 500kW gyrotrons at 118GHz, giving a third harmonic cyclotron resonance slightly on the low-field side for nominal magnetic field strength. All three use the same power supply and are injected from the top of the vessel using a single launcher. The radial position of this launcher can be varied between shots (maximum range shown in Figure 2.3) and the poloidal injection angle can be varied during the shot. The EC ray propagation is almost parallel to the resonance surface in order to increase the single-pass absorption. The absorption fraction and deposition location therefore depend sensitively on the injection angle. Real-time feedback using a dedicated analog system has been employed to maximize the absorbed power (Alberti et al. 2005).

The ECRH system is integrated into the TCV plant control system (TCVPC) and can be routinely operated by a single specially-trained gyrotron operator during TCV experiments.

2.3 Main diagnostics used in this thesis

Without giving a complete overview of TCV diagnostics, the main systems which were used in this thesis are briefly described below. Some commonly used diagnostics-based post-shot analysis tools for equilibrium reconstruction and ray tracing are also presented.

2.3.1 Magnetic diagnostics

The TCV magnetic diagnostic system consists of a set of flux loops, magnetic field probes and saddle coils. The location of flux loops and field probes is shown in Figure 2.2. There are four poloidal arrays of 38 magnetic probes each, placed inside the vessel in 4 toroidal sectors separated by 90° . They measure the time derivative of the magnetic field tangential to the vessel, and analog integrators are used to obtain an estimate of the magnetic field. A complementary toroidal probe array is used for analyzing the toroidal composition of magnetic perturbations. 61 flux loops placed around the vessel and near each coil are used to measure the poloidal flux. Some flux loops must circumvent diagnostic ports and are thus not perfectly circular, so not all flux loops are always considered. 24 saddle coils placed around the vessel complement the magnetic system by providing estimates of non-axisymmetric error fields. Since no Rogowski coil is installed on TCV, the plasma current is obtained by trapezoidal integration of the discrete magnetic probe measurements. A diamagnetic loop (DML) measures the total magnetic energy and is used as an extra constraint in equilibrium reconstruction. Further details on the magnetic diagnostic system are given in (Moret et al. 1998), (Piras et al. 2010a). Magnetic probe signals and flux loops are used for plasma control, MHD analysis and are available in the digital real-time control system as well.

2.3.2 Electron diagnostics

Thomson scattering system

The TCV Thomson scattering system (Franke 1997) measures the local electron density and temperature on 35 points along the path of 1-3 Nd:YAG lasers, vertically traversing the vacuum vessel at $R = 0.9\text{m}$. The diagnostic has an integration time of few nanoseconds but repetition rate of $\sim 20\text{ms}$, where the operator can choose to fire all lasers simultaneously, every 50ms for better statistics in low-density plasmas. The diagnostic has recently been upgraded to enhance the spatial resolution at the edge in order to study the dynamics of eITB and H-mode pedestal profiles (Pitzschke 2011). The density measurements are cross-calibrated against FIR measurements, described below. The Thomson scattering diagnostic is widely used as basis for post-shot analysis of profiles, profile gradients, thermal energy content, confinement time, and for subsequent EC ray-tracing analysis.

Multichord Far InfraRed interferometer (FIR)

A multichord Mach-Zender far-infrared $\lambda = 214\mu\text{m}$ interferometer (Barry et al. 1997) measures the line-integrated density along 14 radially separated vertical viewing lines, with time resolution limited by the acquisition diagnostics at 20kHz. The central viewing line at $R = 0.9\text{m}$ is used in the control system as the density measurement, to be feedback controlled using the gas valve as the actuator. Line-averaged density estimates can be

obtained by knowledge of the equilibrium, and localized profile can be inferred by inversion using (e.g.) Thomson scattering profiles as basis functions (See also Section 8.2.1 of this thesis).

Electron Cyclotron Emission diagnostics

A second-harmonic ECE system is installed, with viewing lines at $z = 21.2\text{cm}$ and $z = 0\text{cm}$ on both high field side (Blanchard et al. 2002) and the low-field side (Klimanov et al. 2005) (Udintsev et al. 2007). An extra viewing window is provided by an EC launcher, identical to those used for ECH/ECCD system, which can be steered to view the ECE signals obliquely as well as in the poloidal plane (Goodman et al. 2008). One of these viewing lines must be chosen per field side. The system measures radiated power in the electron cyclotron range of frequencies between 60GHz and 110GHz, with notch filters used to prevent power from the 82.7GHz gyrotrons from affecting the measurements. The ECE radiation temperature (T_{ECE}) can, potentially, provide localized measurements of the electron temperature. However, due to the relatively low density in TCV plasmas (to avoid cut-off), the optical thickness for EC radiation is often low. Therefore, the measurements are often affected by the non-thermal electron population (in particular for EC current drive plasmas with significant numbers of supra-thermal electrons) and/or third harmonic emission. In these cases the measurement is no longer localized, and the radiation temperature can significantly differ from the local electron temperature. However, the ECE system can be used to infer asymmetric deformations of the electron distribution function in velocity space (Goodman et al. 2007), which are an indication of EC-driven current.

2.3.3 X-ray diagnostics

X-ray emissions constitute the main radiative loss mechanism for the plasma electron energy, and are caused by the sum of bremsstrahlung losses (acceleration due to Coulomb collisions), line radiation (emission by bound electrons transiting to a lower energy state) and recombination radiation (free electron becoming bound by ions). The soft X-ray emissions in the keV photon energy range originate from electrons in the thermal range of common TCV plasmas, and the emission intensity depend on both electron temperature, density and impurity content. Several TCV X-ray diagnostics are discussed below.

Duplex Multiwire Proportional X-ray detector (DMPX)

The Duplex Multiwire Proportional X-ray detector (DMPX) (Sushkov et al. 2008) provides line-integrated X-ray measurements in the range 1 – 30keV with high spatial and temporal accuracy (8mm horizontal resolution at the midplane, 200kHz sampling rate). The diagnostic is installed below the TCV vessel, has a Beryllium filter and is filled with gas (typically Helium) in the transit tube. The viewing lines of the diagnostic are shown in Figure 2.6. Two detectors are placed one above the other, such that incoming photons traverse additional filters before reaching the bottom detector, resulting in a different observed spectrum. For simplicity, and since only the top chamber is used in the majority of cases, this diagnostic will be referred to as simply “MPX”. This diagnostic has been connected to the TCV digital control system and is used throughout this thesis for various

applications such as determination of the sawtooth period, inferring the temperature profile in combination with FIR density measurements (Sec.8.2.1) as well as detecting MHD activity, determining the sawtooth inversion radius and NTM properties (Appendix B).

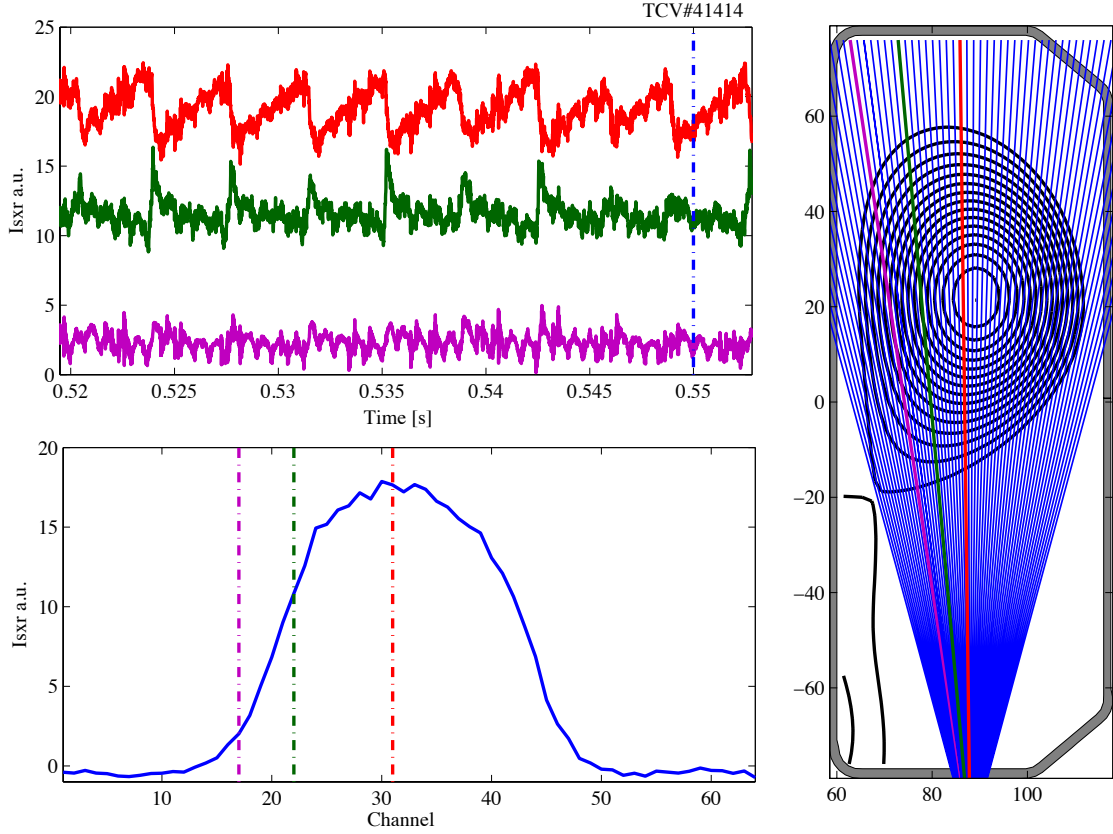


Figure 2.6: Typical signals, profile, and viewing lines for the MPX diagnostic. Sawtooth crashes are clearly visible in the central chord (red) and the heat pulse propagating out is visible in the (off-axis) green chord. Flux surfaces from a LIUQE reconstruction are also shown (Sec.2.3.4)

Tomographic soft X-ray diagnostic (XTOMO)

A soft X-ray system with 200 chords from 10 different cameras is installed allowing tomographic reconstruction of localized X-ray emissions in the poloidal plane. The signals are acquired at 200kHz, allowing the study of the temporal evolution of MHD activity, particularly sawteeth, and to analyze the spatial structure of tearing modes (Chapter 4). At present this diagnostic can only be used for post-shot analyses.

Multi-foil X-ray temperature diagnostic (XTe)

A single-chord X-ray measurement with different thickness Beryllium filters allows determination of the electron temperature, following the theory in (Donaldson 1978). The method assumes a Maxwellian velocity distribution and that there are no significant high Z impurities. In this case the ratio between two measurements can be related to the slope

of the electron distribution function in velocity space, from which the bulk temperature can be inferred. The calculations necessary to convert the raw X-ray measurements into a temperature estimate are nonlinear but not computationally intensive, and have been implemented in the new digital TCV real-time control system. The real-time central temperature estimate thus obtained is used in two applications in Chapters 5 and 8 of this thesis.

2.3.4 Post-shot analysis tools

Some important post-shot analysis codes used in TCV are described here.

Equilibrium reconstruction

After each shot, the magnetic properties of the plasma are calculated using an in-house Grad-Shafranov equilibrium solver called LIUQE¹ (Hofmann et al. 1988). The code computes the current density distribution inside the vacuum vessel to minimize the least-squares error between measured and reconstruction flux loops and magnetic probe data, taking into account the measured coil currents while satisfying the Grad-Shafranov equation. The number of degrees of freedom is reduced by expanding the plasma $p'(\psi) = \partial p / \partial \psi$ and $TT'(\psi)$ profiles (see a more detailed discussion in Section 6.2) into a small number of basis functions. The result is further constrained by the measured toroidal flux given by the DML (diamagnetic loop) diagnostic and can also be constrained by the electron pressure profiles measured by Thomson scattering.

Ray tracing

To determine the power and current density distribution resulting from the injected EC waves in the plasma, ray-tracing codes are commonly used. The most routinely used code in TCV at this time is TORAY-GA (Kritz et al. 1982), (Matsuda 1989). This code, like any ray tracing code, uses a geometric description of the launch points and wave vectors of the EC rays, and propagates them through the plasma under the WKB approximation (i.e. that gradient scale lengths are much longer than the wavelength). A quasilinear approximation of the plasma hot dielectric tensor is used to calculate local absorption and current drive efficiencies. This results in accurate and benchmarked results for the power deposition location and distribution. However, the current drive distribution is underestimated in amplitude and spatial broadening. More complete calculations using full Fokker-Planck modeling can be done, but is not performed routinely (Harvey et al. 2002), (Nikkola et al. 2003). The plasma description going into TORAY is calculated based on Thomson scattering density and temperature profiles, coupled to a refined MHD equilibrium, starting from the LIUQE result using the CHEASE code (Lutjens et al. 1996).

2.4 Real-time control systems

At present, two control systems exist on TCV. The first is the original control system installed on TCV. It is still very much used today and is referred to as the “Hybrid”

¹EQUIL spelt backwards

control system. The second is the new, fully digital, distributed control system named “SCD” (Système de Contrôle Distribu  ). It is an experimental system which is used for advanced control experiments and is envisaged to replace the old system entirely in the future.

More details about the simultaneous use of the two systems, including a diagram of the connections between Hybrid and SCD control systems are shown in Figure A.1 in the appendix.

A general overview of both systems is given here and more details can be found in Appendix A.

2.4.1 The “Hybrid” Plasma Control System

This system consists of a set of analog matrix multipliers, the coefficients of which are digitally programmable and can be switched during the TCV shot (hence the denomination “Hybrid”). It is introduced here since it still forms the backbone of TCV control, and also since a digital emulation of the system exists in the new system for backward compatibility and benchmarking.

- The diagnostic signals necessary for real time control (magnetics, gas, coil currents) are first passed through the A matrix, which has ~ 120 diagnostic signals inputs, and generates estimates of quantities to be controlled (“observables”) as linear combinations of the input signals. The set of observables in the standard mode of operation is I_p , the PF coil currents, the difference between the currents in two sets of Ohmic coils, the vertical position estimator zI_p , radial position estimator, elongation estimator and the line-integrated density. These observables are then subtracted from reference signals coming from a waveform generator (wavegen), yielding 24 error signals.
- These error signals are fed to P , I , and D circuits containing analog implementations of proportional gain, integrator and derivative terms. The outputs of these circuits are then passed to the G_2 , G_1 and G_3 matrices respectively. Not only do these define the Proportional, Integral and Derivative gains, they also assign each error signal to a set of actuators. The ensemble of the outputs of the G matrices represent actuator requests.
- Finally, the actuator command signals are passed through an M matrix which takes care of decoupling of the mutual inductances and compensating for resistive voltage of the coils. In other words, it ensures that the response of each individual coil current to a voltage command is that of a pure integrator.

The hybrid system has proven very robust during almost 20 years of TCV operation, but its capabilities are limited by the fact that it cannot perform any nonlinear operations, other than gain switching. It also has a limited number of output channels meaning the number of actuators which can be simultaneously controlled is limited: in particular the parameters of the TCV ECRH system could not be controlled in real-time and were, for the majority of TCV operational history, controlled by feedforward reference waveforms.

These limitations, coupled to the increasing capabilities of digital platforms, have prompted the development of new TCV control systems based on a fully digital architecture. One such system is the “DSP” system, developed to replace some functionality of the PID controller in the existing hybrid system. It is presently being tested for use as a fast vertical control system. For all other control applications, a modular, massively multichannel (~ 200 channels), distributed control system has recently been developed. It has spawned a host of new applications and results, and it is the work-horse behind the experiments described in this thesis. This system is described below.

2.4.2 The “SCD” digital real-time control system

The “Système de Contrôle Distribué” (Distributed Control System), or SCD, was developed during the course of 2008-2010 as an addition to, and future replacement of, the hybrid control system. It features multiple communicating nodes, each with a large number (> 96) of input channels. The architecture is described best in (Paley et al. 2010) which also contains first results of commissioning during plasma experiments. This section describes the main features of this control system and more details can be found in Appendix A and in internal documentation.

Architecture

The system consists of 4 modular nodes, each having a Linux PC. Some nodes are connected to a compact-PCI (cPCI) crate hosting one or more D-tAcq² ACQ-196 acquisition cards with 96ADCs each, and output cards containing 16 or 32 DAC channels, each. The Linux operating system has been modified to allow real-time operation by suspending interrupts during the plasma shot, preventing any processes from interfering with the real-time execution of the controller code. At each time step, the real-time software polls to check whether new data from the ADCs has been written to a pre-specified location in memory. If this is the case, one time step of the real-time code is executed and the DAC output values are written to another memory location. The software then waits again for the next ADC cycle to complete. Each ADC cycle is externally triggered by a physical clock, ensuring synchronization with the main TCV timers.

Each node also contains a reflective memory card. This represents a physical, addressable memory to which the operating system can write data. However each card is connected to all the other cards via a fiber-optic ring. The embedded reflective memory software ensures that when something is written to a location on the reflective memory by one node, the data is automatically copied to all other nodes, effectively giving all the nodes a partially shared memory. Data which should be shared between nodes can be written to this shared memory and read by any other node that needs it. Care has been taken to avoid read/write conflicts by allowing reading and writing from/to the reflective memory only on alternate clock cycles. Moreover, each node has its own assigned space in the reflective memory space – to which only it can write – so that data is not overwritten by accident. At the same time, all the nodes can read the whole memory, so all of that data is available to all the nodes at all times. Using reflective memory eliminates the need to set up a dedicated message passing scheme in the real-time control system, as all nodes

²www.d-tacq.com

can be configured independently and the algorithm design only has to decide to which location in memory each piece of shared data is assigned.

The current connectivity of the nodes to the diagnostics is shown in Figure 2.7. At present, two nodes out of the four available are installed in separate locations in TCV and connected to different diagnostics and actuators. The other two nodes are not presently used; one node serves as backup and the other as a purely “computational node”, having no independent input-output capabilities and only receiving and sending information via the reflective memory. It is envisaged to use this node in the future for real-time equilibrium reconstruction.

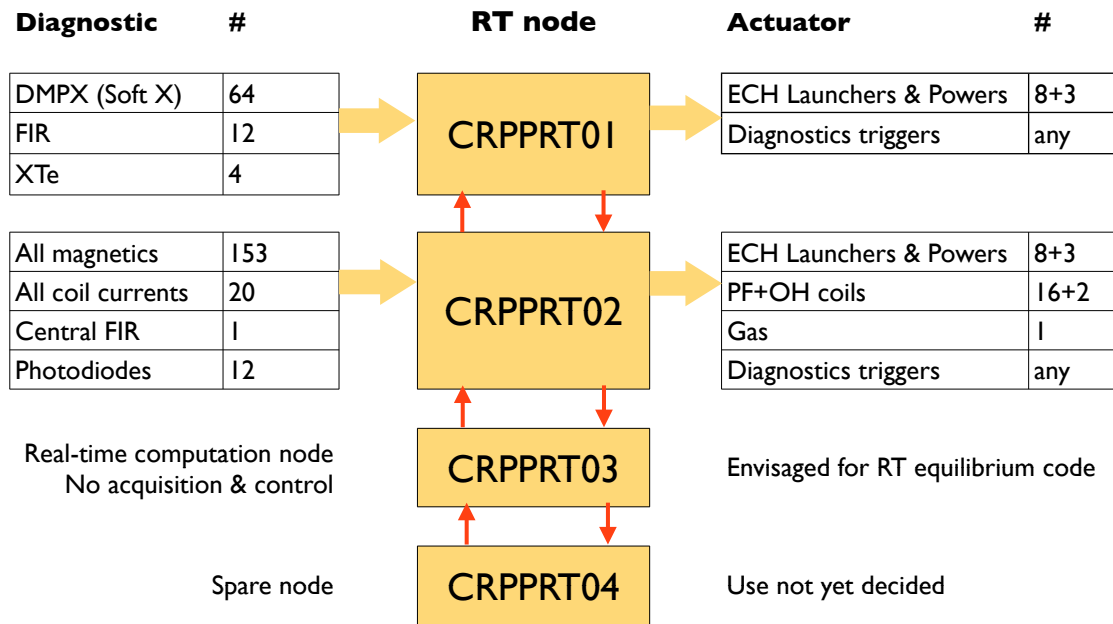


Figure 2.7: Diagram of the 4 SCD control system nodes and their respective connections to diagnostic signals and actuators. The integration with other real-time systems is shown in Figure A.1 in the Appendix. (Status August 2011)

Real-time algorithm development

Real-time algorithms for the SCD control system can be programmed entirely using the SIMULINK® block programming language³. SIMULINK block diagrams corresponding to each controller node can be designed and tested using the included SIMULINK simulation options, even using data acquired during previous shots. Furthermore the reflective memory inter-node communication is simulated. Once the block diagrams are complete, they are automatically translated to C code which is then compiled for the target real-time PCs.

This capability has allowed rapid development of a large variety of algorithms. On one hand, a vast library of standard signal processing functions is available including filters, matrix operations and linear algebra – while on the other hand, controllers can be tested in

³ www.mathworks.com

open-loop with previous shot data allowing rapid debugging and testing. Dedicated blocks can be made to interface with diagnostics and actuators, to implement calibrations, limits etc. – these can be reused across different algorithms. Importantly, it is also possible to test controllers in closed-loop using a model of the tokamak/plasma system implemented in SIMULINK. More details about algorithm development and operational workflow can be found in Appendix A.2

Applications

Starting from initial tests in 2008-2009 and continuing after being commissioned in July 2010, the SCD control system has seen a number of successful applications. Many of these are the subject of this thesis, while others have been published elsewhere. In chronological order:

- Feedback control of sawtooth period using launcher angles (Paley et al. 2009), (Paley et al. 2009)
- Control of kinetic plasma profiles (Paley et al. 2009), (This thesis, Ch. 5)
- Triggering of Thomson and Charge Exchange diagnostics based on real-time event detection (ELMs, Sawteeth) (Pitzschke 2011), (Duval et al. 2010)
- Real-time destabilization, suppression, and preemption of NTMs (This Thesis, Ch.4)
- Real-time pacing of the sawtooth period by EC power (Goodman et al. 2011), (This Thesis, Sec.3.2)
- Real-time control of the ELM period by edge X2 heating (Rossel et al. 2011), (This Thesis, Sec.3.3)
- Real-time poloidal flux profile simulation and control of current and temperature profile parameters (Felici et al. 2011b), (This thesis, Sec.8.2)

Since the SCD control system has proven its usefulness and forms a valuable addition to the TCV experimental program, its development will certainly continue and bring new applications in the future.

Part I

Control of physics

Chapter 3

Control of the period of Sawteeth and ELMs by EC power modulation

This chapter presents new experimental results obtained on TCV by applying the possibilities offered by the digital real-time control system to a previously well-studied physical phenomenon: the sawtooth. A new method for its control has been devised and tested, offering precise and reliable control of the time of the sawtooth crash. First, the sawtooth instability will be introduced from a phenomenological point of view. Then, existing methods for the control of the sawtooth instability are reviewed. Section 3.2 presents the new approach, including experimental results and a discussion of the applicability of this control methodology on other tokamaks. Section 3.3 will show that this same technique can also be applied to another instability: the Edge Localized Mode (ELM).

3.1 Sawtooth physics and control

3.1.1 The sawtooth instability

The sawtooth instability is a fundamental instability of tokamaks which has been observed on practically all devices, and was first reported on the ST tokamak (Goeler et al. 1974). Physically, the sawtooth results from the instability of the $m = 1/n = 1$ kink mode in MHD when there is a central region with $q < 1$. The instability manifests itself as a fast (Alfvén time scale) “crash” causing expulsion of core particles and energy, and magnetic reconnection in the center, eventually resulting in a redistribution of current, particles and energy inside a so-called “mixing radius”. The physics of sawteeth has been extensively studied (see, e.g. (Hender et al. 2007) for a recent overview). While the sawtooth instability is detrimental to core confinement, it may be necessary in fusion plasmas to prevent accumulation of thermalized alpha particles (helium ash) and impurities in the plasma core. Tokamaks naturally tend to develop $q < 1$ surfaces at high enough current unless significant off-axis heating/current drive is applied; therefore, sawteeth are part of routine tokamak operation. The sawtooth period, i.e. the time between two subsequent crashes, is influenced by a number of physical effects. In general, we may separate

stabilizing effects, which tend to increase the sawtooth period, and destabilizing effects, tending to shorten the period.

Sawteeth have been shown in the past to be correlated with the appearance of neoclassical tearing modes, (Sauter et al. 1997), (Westerhof et al. 2002), (Sauter et al. 2002a), for which they provide the seed island needed to trigger the linearly stable modes. In particular, sawteeth are predicted to be the main source of seed islands in standard ITER H-mode discharges (Sauter et al. 2002b), (Sauter et al. 2010). For this reason, their control is important and has been an active and lively area of research over the last decade.

3.1.2 Sawtooth control methods

This section provides a brief overview of the principles of sawtooth control as well as existing (feedback) control methods. A recent extensive review is given in (Chapman et al. 2007), (Chapman 2011).

Sawtooth crash criterium

Sawteeth are often modeled using the well-known Porcelli model (Porcelli et al. 1996) (Sauter et al. 1999b). This model consists of a set of crash criteria, with the sawtooth crash occurring as soon as one of the criteria is met. Following (Chapman 2011), the critical criterium which determines the sawtooth period in plasmas with auxiliary heating is written as

$$s_1 > \max \left(s_{crit} = \frac{4\delta W}{\xi_0^2 \epsilon_1^2 R B^2 c_\rho \bar{\rho}}, s_{crit}(\omega_*) \right) \quad (3.1)$$

where s_1 is the magnetic shear at the $q = 1$ surface, $s_{crit}(\omega_*)$ depends on the pressure gradient and δW is a rather complicated term representing the stability of the internal kink mode and is a sum of MHD, trapped particle and passing energetic particles effects. The key result from recent theoretical and experimental studies has been the elucidation of the mechanisms responsible for stabilization and destabilization of sawteeth by different actuators, acting on different terms of Eq.(3.1).

Control by fast-ion effects: NBI and ICCD

One way to affect the sawtooth period is by changing the δW term in the numerator of Eq.(3.1). Since this term partly depends on the fast ion distribution in velocity space, this quantity can be manipulated by fast-ion generating auxiliary systems like NBI (Angioni et al. 2002) and ICRH (Graves et al. 2009). Depending on the direction and deposition location of the driven ion population, and depending on trapped particle effects, a stabilizing or destabilizing effect can be obtained. The picture is also complicated by the fact that driven current (eg NBCD or ICCD) also affect the shear and critical shear evolution. While this stabilization mechanism is very important in tokamaks like JET or Tore Supra, and real-time control results have recently been reported (Lennholm et al. 2011), it is not discussed further in this thesis as TCV currently lacks such heating systems.

Control by magnetic shear: varying EC deposition location

Another widely explored actuator for changing the sawtooth period is the deposition location of locally absorbed ECH or ECCD. The main effect of the deposited power and/or current is to retard or accelerate the increase of s_1 following a sawtooth crash depending on the deposition location with respect to the $q = 1$ surface. Deposition just on the outside of the $q = 1$ surface has a stabilizing effect, while just inside it destabilizing. This effect is very sensitive on the deposition location but is well reproduced in transport simulations, which have been shown to model TCV sawtooth experiments with remarkable accuracy (Angioni et al. 2003).

The key idea underlying control by varying the evolution of the magnetic shear is illustrated schematically in Figure 3.1. In this sketch, a threshold (i.e. the critical shear, assumed to be a constant value for simplicity) is reached more or less rapidly depending on the rate of growth of the quantity of interest (i.e. the shear). Moving the EC deposition location is equivalent to retarding or accelerating the s_1 evolution with respect to the “natural” rate of growth. It should be emphasized that this picture is highly simplistic, and that in reality both the critical shear threshold and the shear value itself evolve simultaneously, on different time scales, under the influence of EC heating and other actuators. Note, in particular, that the distance from the crash threshold may not be approximately linear, in contrast to what is shown.

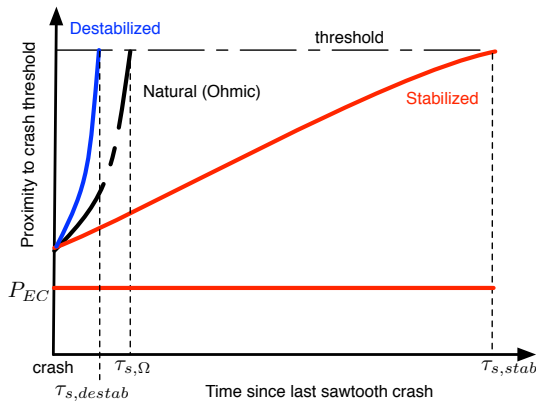


Figure 3.1: Schematic illustration of sawtooth stabilization/destabilization by altering the shear time evolution after a sawtooth crash. The crash threshold is shown as a constant value, but is in reality evolving in time as well.

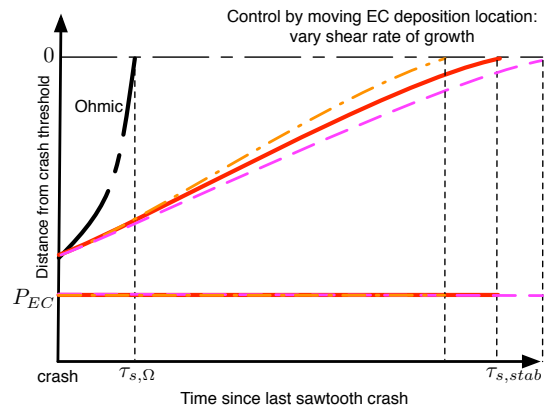


Figure 3.2: Schematic illustration of controlling the sawtooth period by changing the EC deposition location: the shear rate of change is altered and thus the time after each crash when it intersects the threshold again.

Feedback control by varying EC injection angle

The sensitivity of the sawtooth period to the EC deposition location has been exploited to control the sawtooth period in feedback during the plasma evolution, in tokamaks where the location can be changed in real-time. Contrary to experiments in which the various actuators were used to merely *affect* and study the sawtooth period, the goal of feedback control is to obtain a target sawtooth period as precisely and as rapidly

as possible. For this purpose the sawtooth period must be determined in real-time and appropriate commands need to be sent to the various actuators involved in order to obtain the reference period. In the case of control using the EC angle, the period is fed to a controller which adjusts the EC launcher angle, changing the EC deposition location.

Experiments on Tore Supra (Lennholm et al. 2009) show that in the presence of ICRH-created fast ions, ECCD can shorten the sawtooth period significantly, and a “search and maintain” controller is used to seek the ECCD deposition location such that the short sawteeth are obtained, and then maintain this position thereafter. Experiments on TCV, reported in (Paley et al. 2009), lacking a source of fast ions, show a more continuous variation of the attainable sawtooth period. By using a Proportional-Integral (PI) controller, intermediate sawtooth values could be obtained. The nonlinear dependence of the sawtooth period on the ECCD deposition location, as known from earlier work (Angioni et al. 2003), presents difficulty in using standard linear PI controllers, as the change of sawtooth period per unit launcher angle (affecting the EC deposition location) is not constant. To compensate for this, a gain-scheduling approach was used where the controller gain was set high in the region where the sawtooth period varies only slightly, and low when the high-sensitivity region is reached. Using this controller, a reference sawtooth period was obtained during the shot. An alternative approach is provided by using an extremum-seeking controller, programmed to maximize the sawtooth period. This controller is interesting also because the same algorithm could be obtained to minimize the period instead.

A systematic design and simulation of launcher angle-based control of the sawtooth period is presented in (Witvoet et al. 2011). This work also highlights the fact that, while these approaches have been relatively successful, they carry the inherent disadvantage that the speed at which the sawtooth period can be varied is constrained by the mechanical properties of the EC launcher, which is usually the slowest element in the control loop. In TCV, the time constant of the EC launchers is of the order $\sim 100\text{ms}$, which is longer than the typical crash period $1\text{ms} \leq \tau_{saw} < 40\text{ms}$ but still much less than the total shot time (2s).

Another related control strategy, investigated in simulations for ITER (Zucca 2009) also allows to change the sawtooth period by changing the relative location of absorption with respect to the $q = 1$ surface. However, due to the smaller relative spot size (size of the deposition region w.r.t the machine size) of ITER EC beams, and due to the large variation of the $q = 1$ location expected between two subsequent crashes, good stabilizing results can only be obtained by tracking the $q = 1$ surface location in real-time to maintain the same relative $\Delta\rho = \rho_{abs} - \rho_{q=1}$. This requires accurate, real-time knowledge of the $q = 1$ surface from coupled equilibrium-profile reconstruction codes, or by emerging methods such as described in Chapter 8. Additional feedback loops could then be used to control $\Delta\rho$ in order to obtain a requested sawtooth period value. In ITER, typical timescales for movement of the mechanical launchers ($< 100\text{ms}$) is expected to be similar to today’s experiments, while the sawtooth period will be orders or magnitude longer (several seconds). The limitation on the launcher period is therefore less stringent.

Still, another actuator is available that is yet much faster than any mechanical launcher. By varying the *power* of the ECRH, very rapid variations of the stabilizing/destabilizing effect can be obtained. This alternative is explored in the next section.

3.2 Sawtooth period pacing by EC power

In this section, a new and alternative sawtooth control method using ECH is presented. The main motivation for this experimental work was to investigate feedback control methods for sawteeth involving the EC power which, with typical time constants of 1ms or less, can be varied much more rapidly than the deposition location. This opens up the possibility to investigate control on time scales smaller than the sawtooth period itself. Interesting and surprising new results have been obtained in these experiments, and first results have been presented in (Goodman et al. 2011).

3.2.1 Basic principle

The main idea underlying the new control method is the knowledge that, when EC power is used to stabilize the sawteeth, the effect of the heat and current deposited in proximity to the $q = 1$ surface is to retard the growth of s_1 , thus retarding the time at which the crash threshold is attained. It is therefore expected that if the EC power is suddenly decreased or removed during the sawtooth cycle, the sawtooth will appear soon thereafter, where “soon” is a time scale related to the ohmic sawtooth period i.e. the natural time scale of evolution of the profiles. This idea is illustrated in Figure 3.3. Before the power is removed, the evolution follows that for a standard “stabilized” sawtooth (red –), but after the power is removed, the shear quickly grows and the threshold is reached soon thereafter (blue, –). This fact can be exploited to control the sawtooth period by controlling the time at which the EC power is removed, as illustrated in Figure 3.4: choosing the time interval τ_{set} after the last sawtooth crash at which the power is removed, the sawtooth can be induced at a desired time, i.e. *paced*.

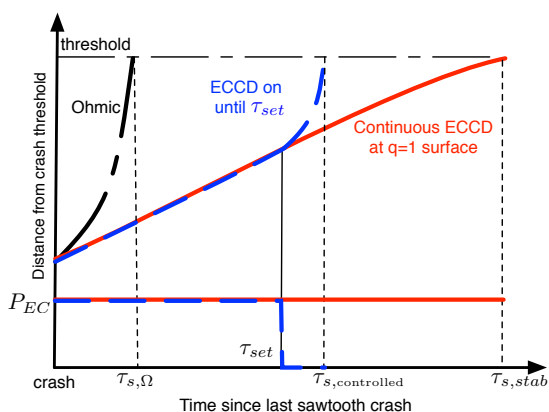


Figure 3.3: Illustration of sawtooth period pacing: if stabilizing EC power near $q = 1$ is removed at a time τ_{set} after the last crash, during the stabilized sawtooth cycle, the crash criterion is reached more rapidly.

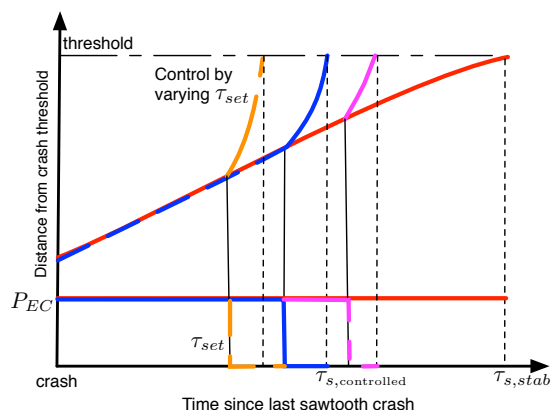


Figure 3.4: Sawtooth period control by varying τ_{set} . In theory, arbitrary values between the Ohmic period and the fully stabilized period can be obtained by this method.

3.2.2 Methodology

With the SCD control system (see Sec.2.4.2) connected to an X-ray diagnostic and the X2 power supplies, TCV experiments were performed to test this principle. A sawtooth pacing algorithm was prepared for this purpose. It uses a sawtooth trigger sent by a sawtooth detector at the occurrence of each crash. This sawtooth detector is described in more detail in Appendix B.4. The sawtooth pacing algorithm starts a timer whenever the crash trigger arrives. This timer increments until the threshold interval τ_{set} is reached. Before τ_{set} is reached, the EC power is maintained at some high value. After it is reached, the power is reduced or removed, until the next sawtooth trigger arrives. At this point the timer is reset, the EC power setting is increased again and the sequence begins anew.

Figure 3.5 illustrates the working of the sawtooth pacing algorithm in an actual experiment. The figure shows the time evolution of the MPX trace and the derived sawtooth trigger signal (gray vertical lines). The upper panel shows the resulting time-evolution of the X2 power command (red) and obtained power (blue). One can see how the parameter τ_{set} determines the relative time at which the EC power is switched off, while the time of subsequent EC switch-on time is dictated by the following sawtooth crash.

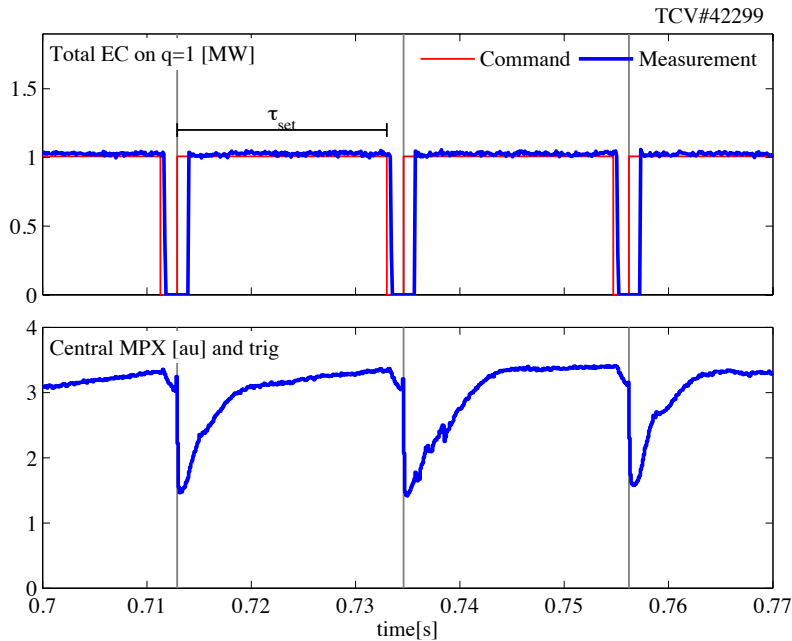


Figure 3.5: Example of X2 power traces and MPX signal evolution during sawtooth pacing experiments. The X2 power is reduced (switched off in this case) at a time τ_{set} after the previous detected crash (gray vertical lines), causing the sawtooth crash shortly afterwards. Note that for the technical reasons described in Section 2.2 the EC power can not be switched on or off too rapidly, resulting in a slight delay $\sim 700\mu\text{s}$ delay between the command and measured power in switch-on, and a much shorter delay before switch-off

Algorithm parameters such as τ_{set} and the maximum and minimum level of P_{EC} can also be varied in real-time, either by pre-programmed waveform references, or even in feedback as in experiments which will be described later. In the majority of experiments, $P_{EC,\min}$ and $P_{EC,\max}$ were set to 0 and 450kW per gyrotron, respectively. This gives the

3.2. Sawtooth period pacing by EC power

maximum possible power excursion and is expected to be most effective in triggering a sawtooth crash at the desired time.

The plasma target was chosen as $z = 0.02\text{m}$, $B_\phi = 1.25\text{T}$, $q_{95} = 2.2$, $\kappa = 1.5$, $\delta = 0.3$, $I_p = 330\text{kA}$. The lower-than-nominal field results in high-field side absorption for the X2 ECH system as illustrated in Figure 3.6. Both top and equatorial launchers were used, to provide both higher power and a modest amount of co-current drive; this gives a longer maximum sawtooth period (Angioni et al. 2003).

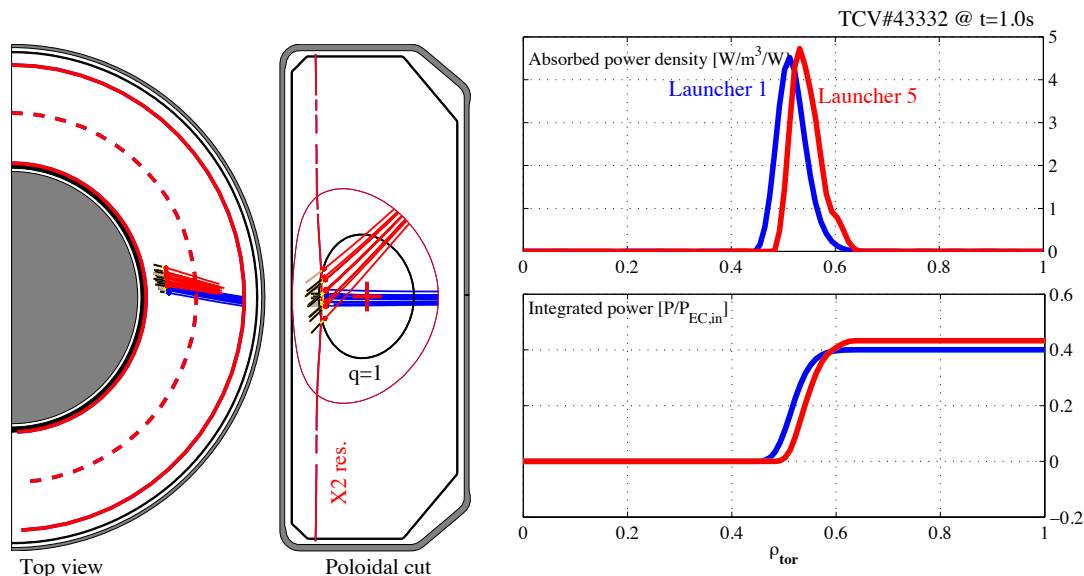


Figure 3.6: TCV and EC injection setup for sawtooth pacing shots. High field side absorption leads to a narrower absorption region of the EC power, so longer sawtooth periods can be reached. Both configurations with only equatorial launchers (blue) and equatorial + upper launchers were tested (blue+red). The $q = 1$ surface estimate from LIUQE is also shown, though experience suggests its size is slightly overestimated.

Since the sawtooth period is very sensitive to the precise deposition location for this kind of experiment, it was necessary to always begin a series of shots with one shot featuring a sweep of magnetic field and plasma current while keeping their ratio constant (constant q). This amounts to radially displacing the EC resonance surface allowing one to precisely scan the relative location of deposited power with respect to the $q = 1$ surface and to determine the optimum period for these experiments. This optimum was chosen to be slightly outside of the $q = 1$ surface, yielding cleanly-shaped regular sawteeth (e.g. compare Fig. 3.5 and Fig. B.6 on p.225). Experiments always begin with an initial phase of $\sim 100\text{ms}$ (~ 10 confinement times) with constant EC power to allow the bulk profiles respond to the presence of localized EC power before a pacing experiment is started. Note that the Ohmic power input in these plasmas is $\sim 300\text{kW}$ whereas the EC power is between $500 - 1000\text{kW}$.

3.2.3 Experimental results

Many TCV shots with sawtooth pacing were performed during the 2011 experimental campaign. Some key results were published in (Goodman et al. 2011). In the interest

of keeping this presentation compact, some highlights – representative of the observed plasma behavior – are listed below.

Sawtooth pacing demonstration

One of the first demonstrations of sawtooth pacing is shown in Figure 3.7. This plot shows, on the top panel (a), the time evolution of the average of seven central MPX chords, as well as the sawtooth trigger signal (gray lines) from the sawtooth detector. The middle panel (b) shows the time evolution of the power near the $q = 1$ surface, showing a series of dips at a fixed time τ_{set} after the previous sawtooth crash. The period of each sawtooth is plotted (red circles), together with the τ_{set} value (solid line), in the bottom panel (c). In this shot, a value of $\tau_{set} = 20\text{ms}$ was chosen, and the next sawtooth crash was consistently observed approximately 1ms thereafter. Note the remarkable regularity of the sawteeth even though the density during this shot was slightly decreasing, as evidenced by the lower peak MPX signal towards the end of the shot.

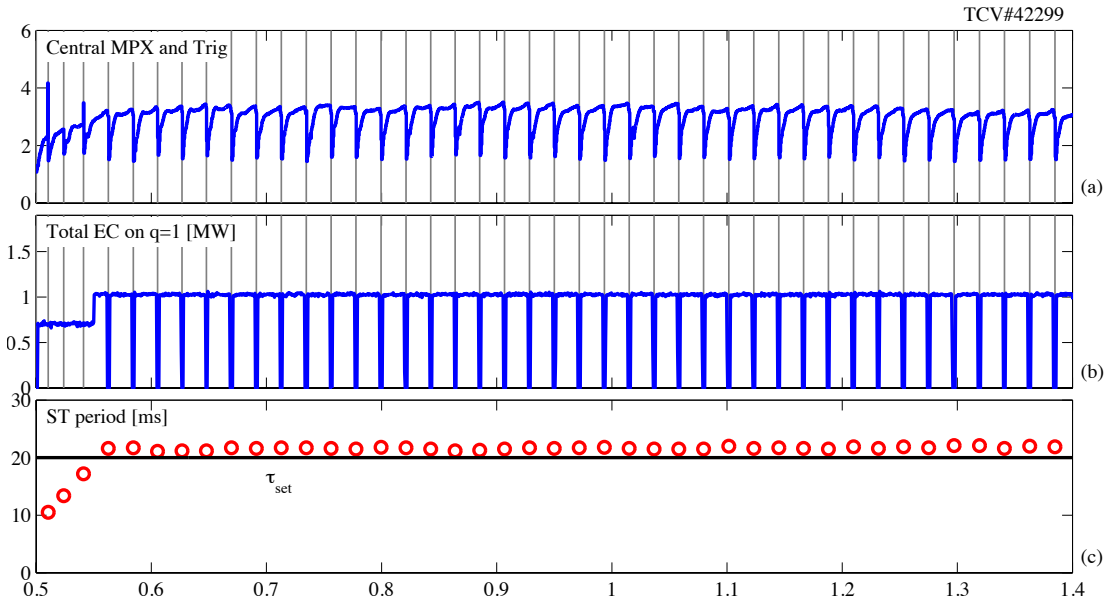


Figure 3.7: Typical TCV shot with sawtooth pacing. 20ms after each sawtooth crash, the EC power is briefly turned off until the next sawtooth. Highly regular sawtooth crashes are obtained with an average period of 21.6ms. The natural (Ohmic) sawtooth period is $\sim 2\text{ms}$ in these plasmas.

Individual sawtooth pacing

With this degree of control over the sawtooth crash time, it is natural to investigate how much variation in sawtooth period can be imposed from one sawtooth to the next. With this in mind, a sequence of τ_{set} values was programmed so that a new value is set after each sawtooth crash. Effectively, this amounts to requesting an individual period for each crash. The result can be appreciated in Figure 3.8. Indeed, the sawtooth period can be changed quite radically from one sawtooth to the next. This shows that each sawtooth cycle can

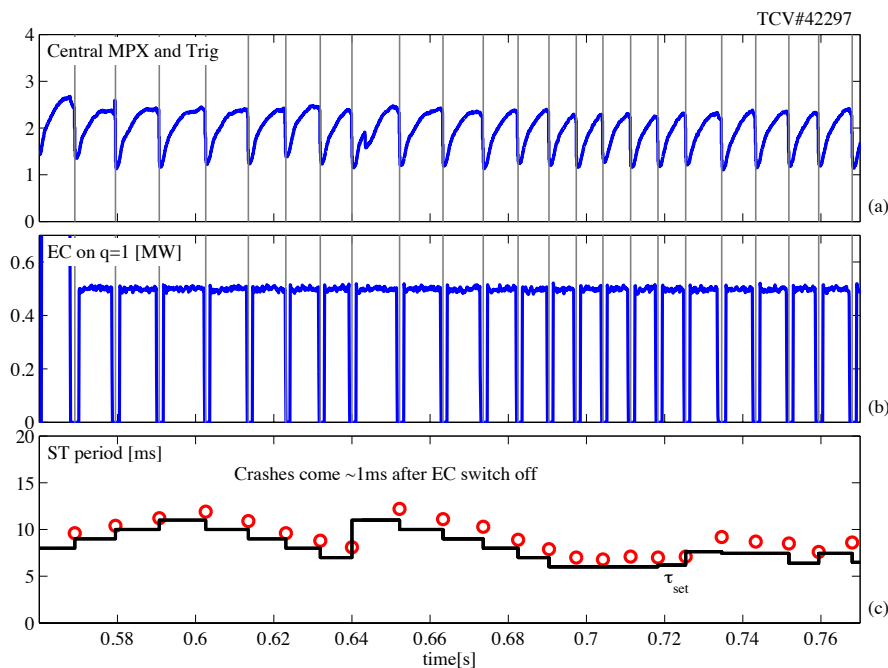


Figure 3.8: Shot evolution for rapidly varying sequence of τ_{set} values, showing the immediate response of each sawtooth crash time.

be controlled independently; that is, the sawtooth cycle has essentially no “memory” of previous crashes.

Crash delay dependence on sawtooth period

Having seen that a crash of arbitrary length (between the ohmic and maximum stabilized period) can be triggered by removing the EC at the appropriate time, we can study how the delay between the EC power removal and the sawtooth crash (referred to from hereon as the *crash delay*) depends on τ_{set} . Intuitively, examining Figure 3.4, one would expect the crash delay to be shorter as we approach the threshold, as there is less distance to cover to the threshold. To investigate this, two dedicated shots were carried out in which sawteeth over a range 2ms to 20ms were triggered in a fashion very similar to that used to generate Fig. 3.8. The maximum EC power was 1MW in these shots. The crash delay (in this case the temporal difference between the EC power removal command¹ and the sawtooth crash) is plotted as a function of τ_{set} for all these crashes in Figure 3.9. The data indicates that the crash delay increases from 1ms to approximately 1.6ms when τ_{set} is increased from 2 to 20ms. This contradicts the simple picture of Fig.3.4. This view therefore has to be refined somewhat. An effect which is likely to play a role is the simultaneous evolution of both $s_{1,crit}$, which evolves on a local confinement time scale, and s_1 , which evolves on a local current redistribution time, upon removal of the EC power. Detailed transport modeling of these experiments should shed more light on these observations, but is beyond the scope of this thesis.

¹the command timing is used here, despite the short delay between command and measured EC switch-off noted in Figure 3.5

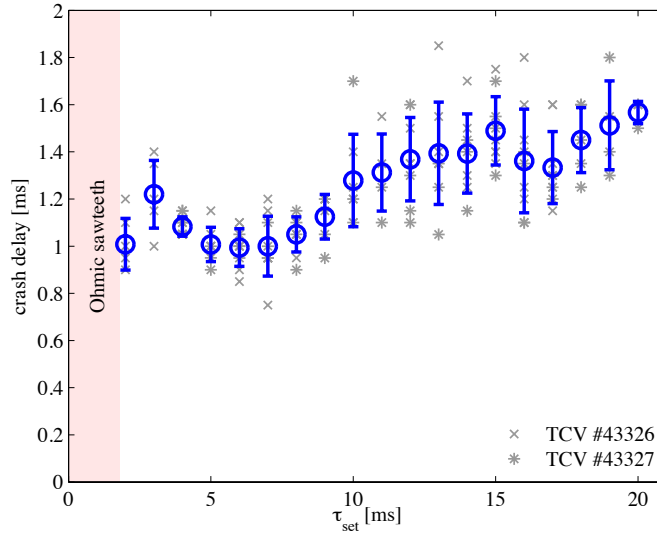


Figure 3.9: Crash delay as a function of τ_{set} , indicating (surprisingly) that one has to wait a longer time for the crash to occur for longer sawteeth.

Insensitivity of pacing to $q = 1$ maximum power change

Another interesting effect is shown in Figure 3.10. In this shot, two gyrotrons were initially directed at the $q = 1$ surface for constant-period pacing with $\tau_{set} = 10$ ms. At some point, one of the gyrotrons arced resulting in only half the power being injected thereafter. Surprisingly, the sawtooth pacing result is not affected. The only visible difference is the lower MPX signal (due to the lower temperature) and slightly shorter crash delay. This can be explained by the fact that the sawtooth period during pacing was sufficiently low in this case to be shorter than the maximum sawtooth period obtainable with only one gyrotron.

Pacing stabilized sawteeth

In the experiments shown so far, the EC power responsible for the pacing was the sole actuator available for lengthening of the sawteeth. In most other tokamaks, NBI, ICRH and fast (α) particles have an independent stabilizing effect on the sawtooth instability. It is therefore interesting to investigate how the sawtooth pacing paradigm demonstrated here performs if a constant sawtooth stabilizing influence is present. This is simulated in TCV by a dedicated experiment in which only one gyrotron is used for pacing, while a second is maintained continuously stabilizing near the $q = 1$ surface. This gives “natural” sawtooth periods of 7ms rather the standard Ohmic period (2ms). This effectively moves the operational window for sawtooth pacing. Sawtooth periods shorter than this new natural period cannot be obtained, but the extra power allows longer periods to be reached². If one assumes, as discussed earlier, that the crash delay is somehow related to the “natural” period before pacing, one expects the crash delay to be longer in these

² Future experiments are envisaged in which EC pacing is applied to destabilize previously stabilized sawteeth by moving the deposition location slightly to the inside of the $q = 1$ surface.

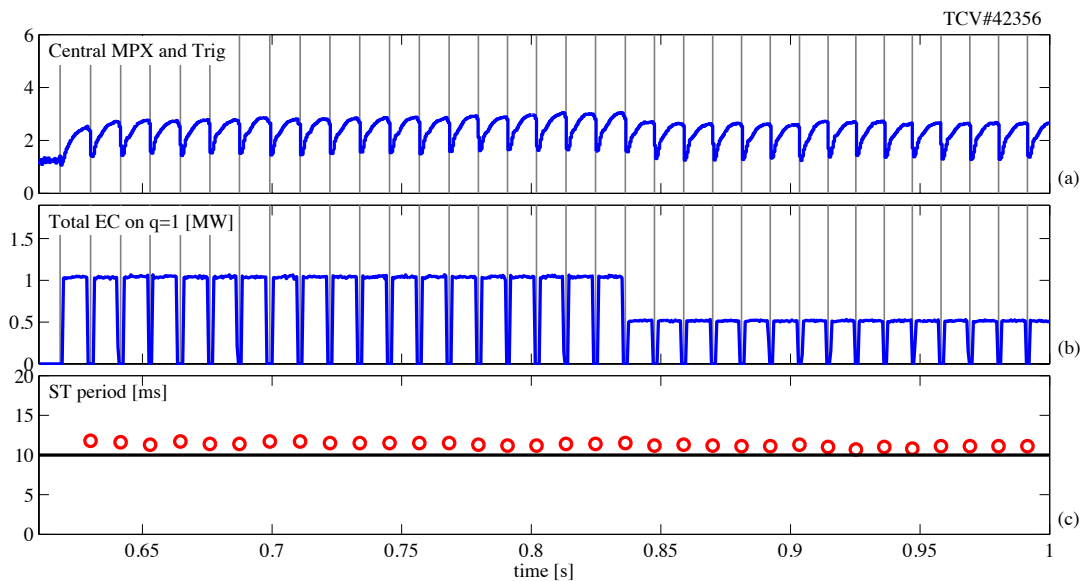


Figure 3.10: Loss of half of the EC power during pacing does not affect the sawtooth period as long as the lengthened sawtooth period with the reduced power is not shorter than τ_{set}

experiments. Indeed, examining Figure 3.11 confirms this expectation, showing a longer, but also more irregular crash delay.

3.2.4 Discussion

The sawtooth pacing experiments done so far demonstrate an advanced degree of control over the period of individual sawteeth, and observations globally match our understanding of the plasma physics underlying the sawtooth crash dynamics.

It is also worth mentioning some operational issues learnt while performing sawtooth pacing experiments. Since the real-time detection of the sawtooth crash is used to determine the timing of EC switch-on and switch-off, errors in sawtooth detection may lead to unwanted effects. It is instructive to consider two alternatives:

- If a sawtooth is detected where there is none (which is typically the case for a “false positive” sawtooth crash occurring early in the cycle, e.g. Fig.3.8 at $t = 0.645$ s), the algorithm resets the counter for the EC switch-off time without turning off the power. This means that the effective time during which the EC power is on is longer than required, and the eventual period of the following *true* crash is longer. This may be a problem in the case where pacing is used to avoid long sawteeth that may trigger a tearing mode as studied in the next chapter. False detections may be prevented by improving the sawtooth detector, e.g. assessing the likelihood that a sawtooth crash occurs at a given time and rejecting false positives which may come early in the cycle.
- If a true sawtooth crash is erroneously not detected (a “false negative” or “missed” sawtooth), there are two scenarios. If the algorithm misses the sawtooth crash triggered by the removal of EC power after τ_{set} , the algorithm does not know that

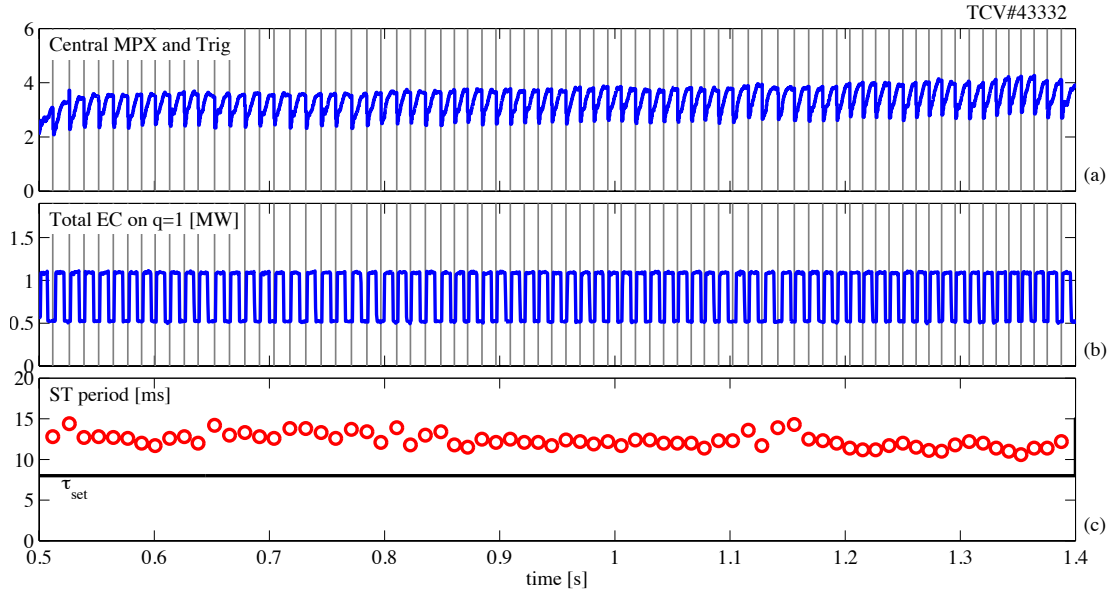


Figure 3.11: Sawtooth pacing under the stabilizing influence of one CW gyrotron. As visible in (b), the EC power is never completely removed but one gyrotron remains active throughout the shot. The crash delay is longer, and more variable than in shots with full EC power modulation.

the EC should be switched on again. In this case the EC power will stay off, and the next sawtooth will be of natural type, i.e. shorter. It may take several other crashes until the detector actually detects one of these shorter (smaller) sawteeth at which time the EC is switched on again. To prevent this occurrence, a “safety” mechanism has been included in the algorithm which, if no crash detection trigger has been sent yet, automatically sends a fake crash trigger at a fixed time after the EC switch-off time. This time is chosen slightly longer than the typical crash delay, but shorter than the Ohmic sawtooth period in order to prevent a short intermediate crash. This system has been shown to successfully protect the experiment evolution against such an occurrence, but needs to be tuned appropriately for different “natural” periods.

3.2.5 Sawtooth locking

In the sawtooth pacing experiments shown so far, it is important to note that the EC switch-off time is always referenced to the last sawtooth. This means that the pacing sequence is constantly synchronized with the plasma and the relative timing of the EC on- and off- time is moderated by the sawtooth crashes themselves. An alternative approach, which exploits the same physical principle, is to use a pre-programmed modulated EC power trace in the expectation that the sawtooth period will automatically adjust itself, or “lock” to the period of the modulation. The advantage of pacing with respect to locking is that in the pacing method the only parameter to be chosen is τ_{set} , owing to the inherent synchronization with the plasma. In the locking approach, both the *duty cycle* and *period* of the power trace have to be chosen appropriately such that the sawtooth cycle will lock to the power trace. This will not happen for any arbitrary parameter combinations of these two parameters, as shown in simulations (Witvoet et al. 2011). An advantage of

locking lies mainly in its simplicity since there is no need for real-time sawtooth detection or control system. Experiments to test the locking principle were carried out on TCV as follow-up to the sawtooth pacing experiments (Lauret et al. 2011). A complete discussion of the results and relative merits of pacing versus locking is outside the scope of this thesis, but some salient experimental results are shown.

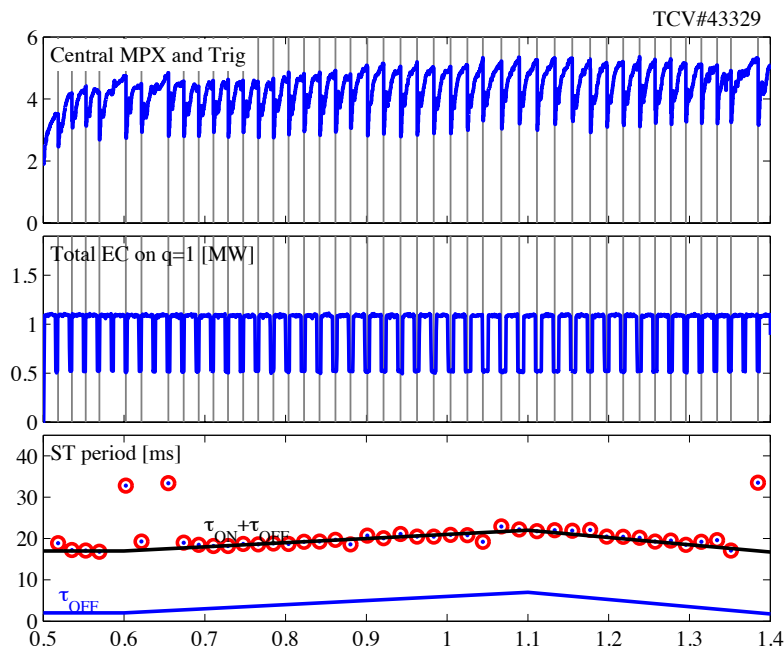


Figure 3.12: Example of sawtooth pacing with variable off-time. If the off-time is too short, the plasma may not have time to reach the crash threshold and ends up “skipping” one sawtooth.

Figure 3.12 shows a first example of sawtooth locking, where the EC power was pre-programmed to stay on for a time τ_{on} and off for a time τ_{off} . The latter parameter, τ_{off} was slowly varied during the shot. In this shot, only one gyrotron of 500kW was used for sawtooth locking while the other (also 500kW) was kept on constantly, as in the pacing experiment shown in Fig.3.11. One can observe that the sawtooth period indeed does lock to the EC modulation period, shown in black. Note also that when τ_{off} is too short, the sawtooth crash may not occur when the power is removed (for example at $t = \{0.6, 0.65, 1.38\}$). In this case the power is switched back on before the “point of no return”, apparently providing sufficient stabilization for the sawtooth crash to be delayed until the next switch-off. This also provides an interesting and challenging benchmark for transport-based sawtooth simulations.

Another typical example of sawtooth locking is shown in Figure 3.13. This shows a more complete experiment, which included an initial phase of full-power CW sawtooth stabilization with two gyrotrons (0.4-0.6s) followed by a period with only one CW gyrotron. This pinpoints the range between which the period can be controlled: [10ms – 40ms]. Steps of the modulation period (c) are imposed starting at $t = 0.7\text{s}$ keeping a constant duty cycle. This results in the sawtooth period successfully locking to the modulation waveform for the first two steps, but this synchronization is lost for the last step. In this case, one can observe a second crash occurring during the time when the modulating

gyrotron is off. Evidently, the duty cycle is too small for this setting of the period and locking is, initially, not achieved; however, the last four sawteeth appear to have locked to the period again. This transient behavior is also interesting to study from a first-principle point of view, work which has been partly presented in (Witvoet et al. 2011). Further studies of sawtooth locking are also interesting from a system theoretical point of view, since sawtooth locking can be seen as a special case of injection locking for limit cycles in nonlinear dynamical systems.

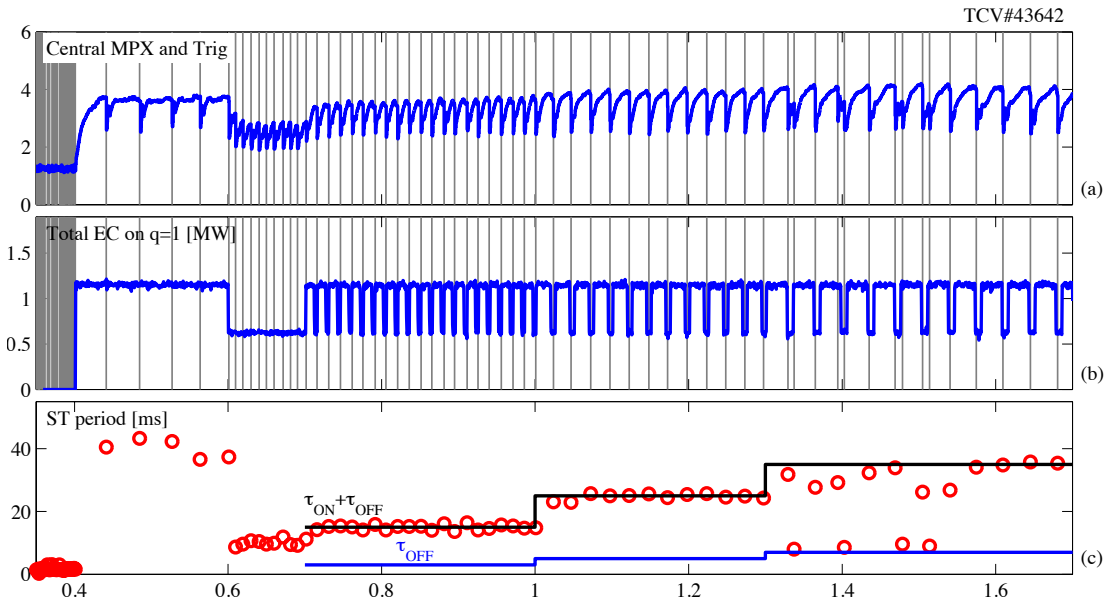


Figure 3.13: Example of successful locking for low modulation periods, but transient loss of synchronization for longer modulation periods. Shorter sawtooth crashes are observed after the EC off-time exceeds a certain length.

3.2.6 Pacing with sawtooth destabilization

Though not yet tested experimentally, it should be noted that the sawtooth pacing paradigm is not limited to the case of lengthened sawteeth by EC on the outside of $q = 1$ surface. A similar destabilization scheme can also be considered, as illustrated in Figure 3.14. In this case, the EC deposition is located just on the inside of the $q = 1$ surface, where the EC causes a more rapid time evolution of s_1 and more shorter sawtooth periods. In this case, the power command is opposite with respect to Fig.3.3 and Fig.3.4: power is added at a given time after each sawtooth crash to accelerate the s_1 evolution and stimulate a crash. This additional technique would allow one to choose the range of sawtooth period between the shortest destabilized period and the longest stabilized period.

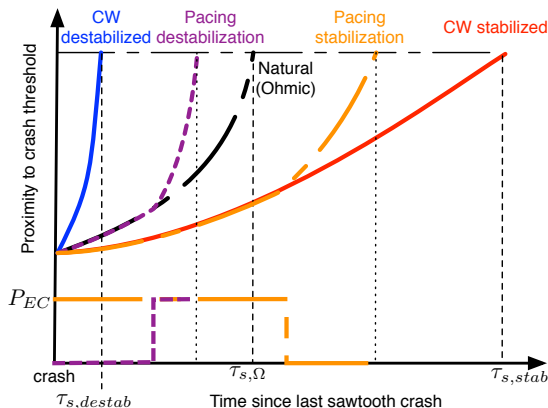


Figure 3.14: Illustration of sawtooth pacing for destabilized and stabilized sawteeth. For destabilized sawteeth, power on the inside of the $q = 1$ surface is added, which causes the shear growth rate to accelerate and the sawtooth to appear sooner. For stabilized sawteeth, the stabilizing power is removed. Note that the EC power deposition location is different for the two techniques.

3.2.7 Sawtooth pacing and locking in high-performance plasma scenarios

To conclude this section, we mention the operational advantages offered by sawtooth pacing in high-performance (burning) plasmas. As mentioned previously, and as will be studied more in-depth in the next chapter, sawtooth crashes often provide the seeding event for NTMs, therefore they must be kept as short as possible to ensure that this coupling does not occur. Sawtooth destabilization (shortening) methods are therefore being assessed for ITER. However, should these shortening methods not be adequate or should the operating space still be constrained by sawtooth-NTM coupling, sawtooth pacing strategies may provide a solution. The advantage is that the sawtooth, rather than being a semi-random uncontrollable event, becomes precisely controlled and the timing of each individual sawtooth crash is known in advance. This means that preemptive action can be taken around the time of the sawtooth crash in order to *prevent* the sawtooth crash from triggering an NTM. This action can be localized in time such that it does not require continuous preemptive action. This will be discussed further in the next chapter.

For large tokamaks with other actuators than ECH/ECCD, it is important to note that sawtooth pacing can be performed with other actuators as well. As long as their presence has a stabilizing effect on the sawteeth (Graves et al. 2005), (Lennholm et al. 2011), their removal will trigger a sawtooth soon thereafter. This is a promising strategy and one that should be evaluated on present tokamaks – in particular since removing the power may induce an unwanted transition from H to L mode.

Another important motivation is that advance knowledge of the sawtooth crash time facilitates physics studies, allowing one to take better statistical averages over equal-length sawteeth, but also to trigger diagnostics based on the crash time (Duval et al. 2010), (Pitzschke 2011) in order to measure at a precise relative time with respect to the crash. This opens up new opportunities for detailed experimental investigation of sawtooth crash dynamics. Finally, the ability to precisely tune the sawtooth period is very useful in studying the physics of NTM-sawtooth coupling and locked-mode disruptions

triggered by large sawteeth.

3.3 ELM pacing and real-time control by EC power

3.3.1 Introduction and motivation

Based on the results obtained with sawtooth pacing, described in previous paragraphs, it is natural to investigate whether similar results can be obtained for another repetitive instability of the plasma: the Edge Localized Mode (ELM). The ELM is a periodic expulsion of significant fractions of the total plasma energy through the edge, which can cause strong transient heat loads in plasma-facing components. For this reason, ELM mitigation and control is a crucial issue for operation of large tokamaks and is currently at the forefront of worldwide research activity in view of ITER. ELMs occur in H-mode plasmas, in which reduced edge transport causes steep gradients in the plasma temperature and density, known as the “edge pedestal”, which trigger localized instabilities responsible for the sudden loss of energy. This energy and particles are ejected and eventually strike plasma facing components. During an ELM, the edge pedestal collapses only to grow again immediately afterwards, and the cycle repeats. A recent detailed study of TCV edge profile evolution during ELMs can be found in (Pitzschke 2011).

During other recent TCV experiments (not directly related to this thesis) (Rossel et al. 2011), it has been observed that X2 heating close to the edge ($\rho \sim 0.9$) of centrally X3-heated TCV H-mode plasmas featuring ELMs has the effect of increasing the ELM frequency for type-I ELMs and reducing the energy released per ELM. Also, the ELM frequency was observed to increase further when heating closer to the edge, at constant injected power, even though the absorbed power is lower due to incomplete first-pass absorption near the edge. This goes against standard understanding of type-I ELM behavior, which are normally observed to decrease in frequency when the total power is decreased. Though a full explanation of this phenomenon is currently lacking, intuitively one may understand that heating close to the edge pedestal has a more immediate effect on the local pedestal property evolution and therefore causes the critical thresholds for the ELMs to be reached sooner. Alternatively, the localized heating may cause a different mode than usual to become unstable and trigger the ELM. In any case, edge heating provides a mechanism for affecting the edge stability, enabling studies of whether modulated, periodic application of edge EC power at constant heating location can be used to control or regularize the ELMs as was the case for the sawteeth.

This work is related to previous efforts to pace the ELM period by externally applied perturbation. A well-known example hereof is that of vertical kicks, where the ELMs synchronize with vertical perturbations of the plasma position induced by vertical position control coils (Degeling et al. 2003b). In these experiments, edge currents were invoked to explain the observations. ELM pacing by fast pellet injection has been shown on ASDEX Upgrade (Lang et al. 2004). Preliminary results on synchronization of the ELM period with modulated edge ECH were reported in ASDEX-Upgrade (Horton et al. 2004) but no follow-up studies were presented.

While recent focus on ELM control has focused on complete ELM suppression strategies using resonant magnetic perturbations (Evans et al. 2004), (Suttrop et al. 2011), ELM pacing is nonetheless appealing for several reasons. First of all, it does not require

installation of in-vessel coils, which pose many engineering difficulties – particularly in a burning plasma environment – but instead relies on an EC system present on most tokamaks for other reasons. While not observed to suppress the ELMs entirely, ELM pacing by EC may provide a mechanism for regularizing the ELMs and avoiding transient large ELMs which determine high peak loads. The experiments reported in (Rossel et al. 2011) have shown that the increased frequency is sufficiently large to compensate for the additional power, such that the energy released per ELM is lower, reducing the peak heat load on plasma facing components. Perhaps more importantly, ELM pacing experiments provide a stringent testbed for existing ELM models and can be used to confirm our understanding of edge pedestal physics along the lines of (Burckhart et al. 2010), (Pitzschke 2011). A full study and discussion from the physics point of view is not included in this thesis, but the experimental method and some highlights of the results will be given in this section.

3.3.2 Experimental setup

Standard TCV H-mode plasmas have core density above the second harmonic cutoff which precludes central X2 heating. These plasmas are therefore centrally heated by top-launched X3 heating. Despite the edge density pedestal and relatively flat density profile, edge heating with X2 is possible in some circumstances if the density is low enough. The H-mode plasmas presented in this section were of a particular configuration such that part of the LCFS presents itself perpendicularly to an EC beam injected from the equatorial launchers, avoiding problems related to refraction. Additionally, the increased flux expansion near the X-point allows for a very localized deposition location for a given beam width. The plasma and EC configuration are displayed in Figure 3.15. This configuration allows the EC beam to propagate inwards and reach the X2 resonance. This allows one to access deposition radii between $\rho_\psi = 0.8$ and $\rho_\psi = 1$, limited on the inside by the X2 cutoff (depending on density) and on the outside by the plasma edge (according to TORAY calculations). Only the two equatorial launchers can be used in this configuration, therefore the maximum injected X2 power is 1MW. In all the experiments presented in this section, 1MW of X3 heating is used, starting at $t = 0.3$ s. This leads to an initial H-mode phase with low-frequency (~ 100 Hz), type-I ELMs. At $t = 0.55$ s, 700kW of additional edge X2 is added at $\rho_\psi \sim 0.9$, increasing the frequency to approximately 300Hz. Further X2 power modulation or real-time control experiments begin only after $t = 0.7$ s, after the plasma density has become sufficiently stationary. Other parameters of these discharges are $I_p = 295$ kA, $q_{95} = 2.3$, $\kappa = 1.65$, $\delta = 0.2$, $B_0 = 1.42$ T, $n_{e0} = 5 \times 10^{19}$ m⁻³, $T_{e0} = 2$ keV.

A similar control algorithm was used as in the sawtooth experiments, again allowing one to flexibly vary the timing and power levels of injected EC power with respect to the occurrence of individual ELMs. The algorithm is run on the real-time node CRPPRT02 at its maximum clock rate of 50kHz (20 μ s sample time). This is done to maximize the temporal accuracy of the overall algorithm, in which fractions of milliseconds play a role when considering 2-3ms ELM periods. As the ELM signature is very clear from H $_\alpha$ photodiode signals, a simple ELM detector was built based on this signal alone. An ELM trigger is sent if the difference between the current value of the H $_\alpha$ signal and its value 10 samples (=200 μ s) earlier is more than a threshold value. After each trigger, a new trigger can only be sent after 500 μ s or more to prevent multiple triggers from the same ELM.

This simple ELM detector has proven very robust and reliable for the plasma studied here.

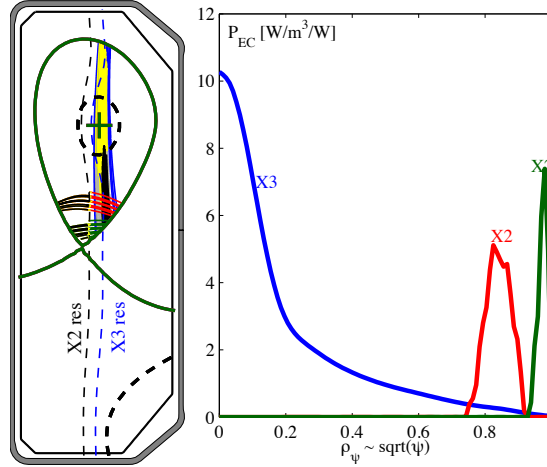


Figure 3.15: TORAY ray-tracing calculations of ECH setup during ELM pacing shots. Top-launched third harmonic (X3) power (blue) is absorbed mainly in the center, while second harmonic heating can be deposited at the edge between $\rho = 0.8$ and $\rho = 1$ depending on the injection angle.

3.3.3 ELM pacing

Recall from Section 3.2.1 that sawtooth pacing, for lengthened sawteeth, relies on removing the stabilizing influence of the localized ECCD after a given time. ELM pacing relies on the opposite effect: triggering the ELM by adding more (destabilizing) EC power, increasing the edge gradients, a given time after the last ELM. This is illustrated in Figure 3.16, which shows a short time segment of one ELM pacing experiment. The H_α signal shown in the lower panel is used to detect the occurrence of each individual ELM (gray vertical lines). At this time the EC power is switched to a lower level of 200kW per gyrotron (this level is chosen for the technical reasons mentioned in Section 2.2) giving 400kW in total. At a given time τ_{set} after the ELM occurrence, the EC power is switched back to a higher level of 450kW per gyrotron (900kW total), more than doubling the power deposited near the edge. The high-power phase ends at the time of the next ELM occurrence. This control scheme is conceptually similar to what would be used for sawtooth destabilization, as illustrated in Figure 3.14. The rationale for this control scheme is that increasing power yields to faster ELM destabilization. If the opposite were the case, as in Type-III ELMs, the opposite control scheme (similar to sawtooth pacing with lengthened sawteeth) should be employed. A similar study with Type-III ELMs has not been performed but should yield interesting insights as well.

Some salient features and results of ELM pacing can be appreciated by examining figure 3.17. In this carefully designed shot, two sequences of ELM pacing with a fixed value of τ_{set} (red curve in panel (c)) were used for ELM pacing, resulting in the EC waveform and H_α signals shown in panels (a) and (b), respectively. After each ELM pacing phase (yellow background), a fixed-power phase (blue background) follows with the power level fixed at the mean power of the previous (ELM pacing) phase. In other words, between 0.9 and 1.2s the X2 power was the same as the mean power of the ELM

3.3. ELM pacing and real-time control by EC power

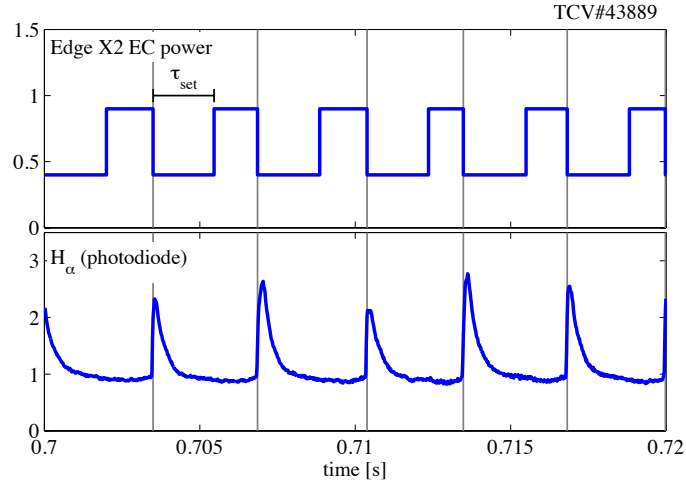


Figure 3.16: Illustration of edge X2 power waveforms for real-time ELM pacing experiments. The ELMs are clearly visible as brief spikes of light emitted from the plasma edge, detected by the H_α diagnostic. The EC power is switched to a low level (400kW) just after each detected crash (gray line). After a pre-programmed time τ_{set} the power is increased to 900kW and subsequently reduced at the next ELM.

pacing phase (0.7 – 0.9s), and between 1.4s and 1.7s it was the mean of the ELM pacing phase (1.2 – 1.4s).

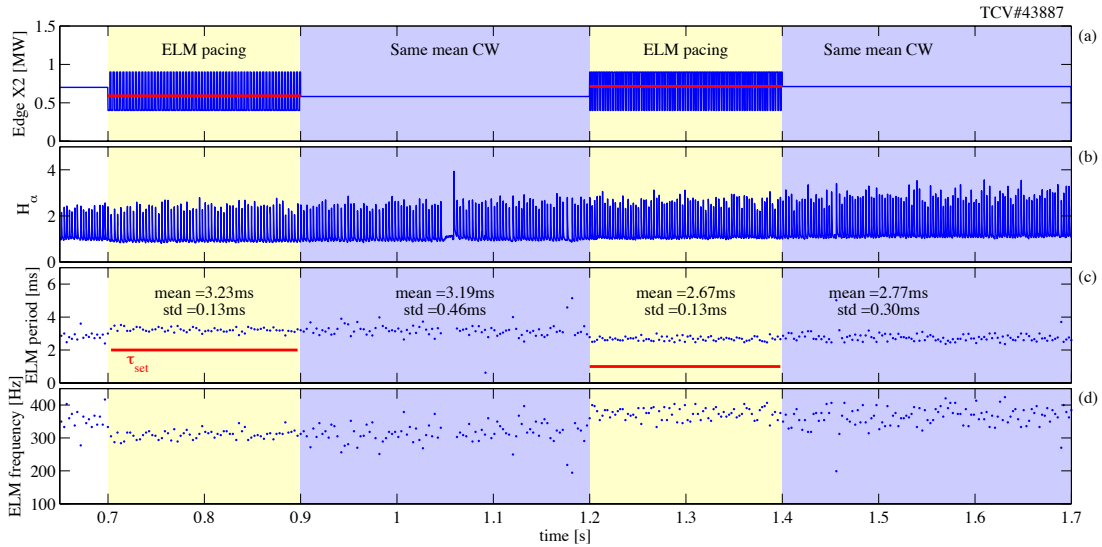


Figure 3.17: ELM pacing experiment, alternating phases of real-time ELM pacing (yellow) with phases of CW power (blue) at the same mean frequency as the preceding pacing phase (a). The H_α signal (b) shows regular ELMs, and one short ELM-free phase at $t = 1.05$ s. The ELM period (c) is shown to be significantly more stable during pacing. The ELM frequency is also plotted (d).

The first clear observation is that the ELM period is significantly regularized during ELM pacing, i.e. the standard deviation during pacing periods being smaller than in the corresponding CW power phases. Furthermore, decreasing τ_{set} has the effect of lowering

the ELM period. This results in a shorter phase of lower power, and the high power phase starting sooner in the ELM cycle; this results in the threshold being reached earlier. Note also that higher (mean) power still corresponds to higher frequency, confirming the type-I character of these ELMs. Note also the brief ELM-free phase occurring at $t \approx 1.05$ s. These phases cause sudden increase of the density (due to sudden removal of the ELM as a particle exhaust mechanism) and are terminated by a larger ELM. Though not systematically studied, as yet, it was observed that ELM-free phases are more likely to appear during phases with variable-frequency ELMs and CW edge power, and were less likely to appear during ELM pacing.

A second, similar experiment was done where feedback control was used to obtain a requested ELM frequency. In this setup, τ_{set} was varied during ELM pacing phases based on the difference between the requested and obtain ELM period. Note that while the control references were issued in terms of frequency, the control algorithm works based on the ELM period. The control law for τ_{set} can be written as

$$\tau_{set,k} = \tau_{set,k-1} + K_i T_s (\tau_{ELM,ref} - \tau_{ELM,meas}) + (\tau_{ff,k} - \tau_{ff,k-1}) \quad (3.2)$$

where k is the discrete-time sample index, T_s is the sample time and K_i is a gain which can be set. $\tau_{ff,k}$ is a sequence of pre-programmed feedforward values. This results in an integral-type control where the value of τ_{set} is incremented proportionally to the error. Alternatively, the ELM period can be controlled by feedback control of the edge (CW) power. To this aim, a controller structurally identical to 3.2 was used, replacing τ_{set} with P_{X2} .

The use of feedback control allows one to study the effect of using ELM pacing compared to using CW power to obtain the same ELM period. The time evolution of this shot is shown in Figure 3.18. The first part (until $t = 1.2$ s) shows clearly that the standard deviation is more than doubled for the same mean ELM period in case of power feedback with respect to ELM pacing using τ_{set} feedback. It should be mentioned, though, that the feedback gain during the ELM pacing phase was rather low so τ_{set} does not vary strongly. A correct choice of the feedforward value for τ_{set} results in the reference frequency being reached nevertheless, so feedback would not have been necessary. Note that the final phase is strongly influenced by an ELM-free phase appearing at $t \approx 1.41$ s, and this phase was excluded when computing the statistical mean and standard deviation.

These results confirm the earlier conclusion that ELM pacing reduces the ELM period variability and at the same time demonstrate the possibility to control the ELM period in feedback by varying the parameters of the additional heating.

3.3.4 TCV the singing tokamak

Interestingly, but perhaps not surprisingly, the steady frequency of the ELMs can be heard as a distinct and well-defined audible tone in the TCV experimental hall during these plasmas. This is attributed to the response of the fast vertical control coils to the ELMs. Each ELM crash causes a perturbation in the measured plasma vertical position (either due to a true shift in position, or due to direct perturbation of the measurements) which is fed back to the internal (G) coil current. This in turn causes a force (via eddy currents) in the vessel, causing the latter to vibrate at a frequency equal to the ELM frequency.

3.3. ELM pacing and real-time control by EC power

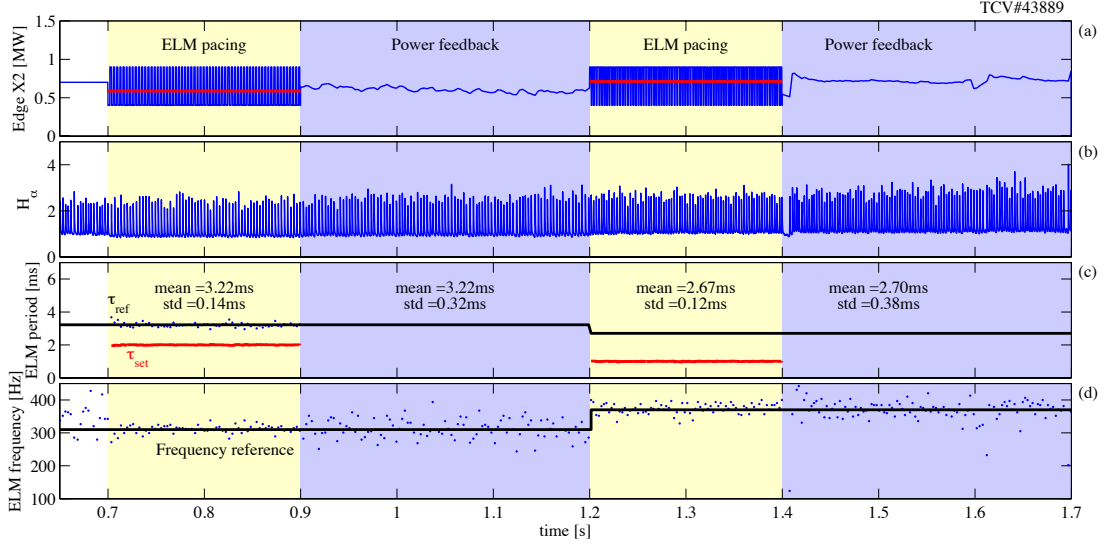


Figure 3.18: ELM pacing experiment with feedback control of the ELM period. alternating phases of real-time ELM pacing control (yellow) with phases of CW power (blue), with feedback control of τ_{set} respectively P_{EC} in each phase.

With this knowledge, further experiments were done during which the frequency references for the ELMs were chosen such that their ratios are always integer powers of $2^{\frac{1}{12}}$. This way, each frequency corresponds to an interval on a twelve-tone equal temperament scale, close (though not exactly equal) to that found on a classical piano. For example, choosing a root frequency $f_0 = 220\text{Hz}$ corresponding to the A (*La*) just below the piano central C (*Do*), the major fifth (E (*Mi*) natural), being seven half-tones above the root, has the frequency $f_{major5th} = 220 \times (2^{\frac{1}{12}})^7 = 329.6 \approx \frac{3}{2} \times 220\text{Hz}$. By choosing an appropriate time evolution of reference frequency requests in time, the TCV tokamak was made to perform a number of different tunes, notably the first notes of “Frère Jacques” and a four-note extract of the 4th movement of Beethoven’s 9th Symphony (popularly known as “Ode to Joy”, also used as European Anthem).

These two performances can be appreciated in Figures 3.19 and 3.20, respectively. The frequency is controlled by continuously adjusting τ_{set} during ELM pacing performed as above. In choosing the gain, a trade-off had to be made between the speed of the response and the amount of variability introduced by the feedback itself. The obtained ELM periods and frequencies are plotted in, respectively panels (a) and (b). The audible sound heard in the TCV building was recorded using a microphone, and a spectrogram of the time period of interest is shown in panels (c). The spectrogram is polluted by other sounds made by the TCV equipment, in particular the power supplies, but a hint of the time evolution can nevertheless be discerned. For comparison, a spectrogram of the FPS coil current (power supply commanding the G coil) is also plotted, showing increased activity at frequency components matching the ELM frequency request. For illustrative purposes, piano keys corresponding to the plotted frequencies are also shown. Note that in order to fit the tune into the range of ELM frequencies attainable by this method, the frequency of the “Do” note was transposed to 300Hz and 250Hz for Figs.3.19 and 3.20 respectively, resulting in a transposition of the relative scale.

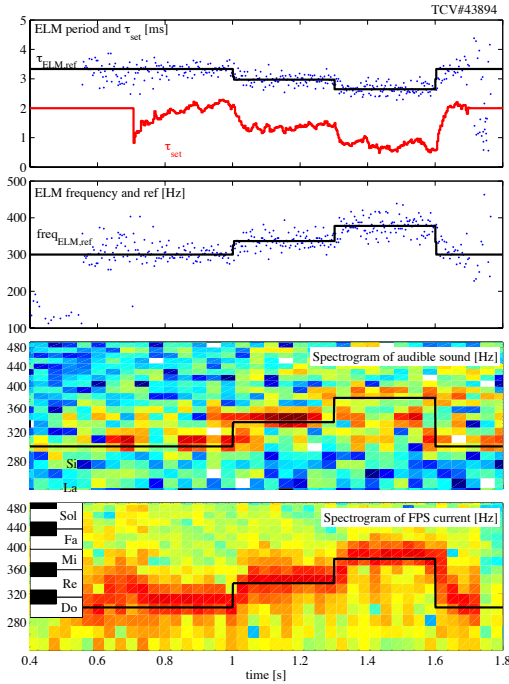


Figure 3.19: TCV performance of “Frère Jacques” by ELM frequency feedback control using the ELM pacing method

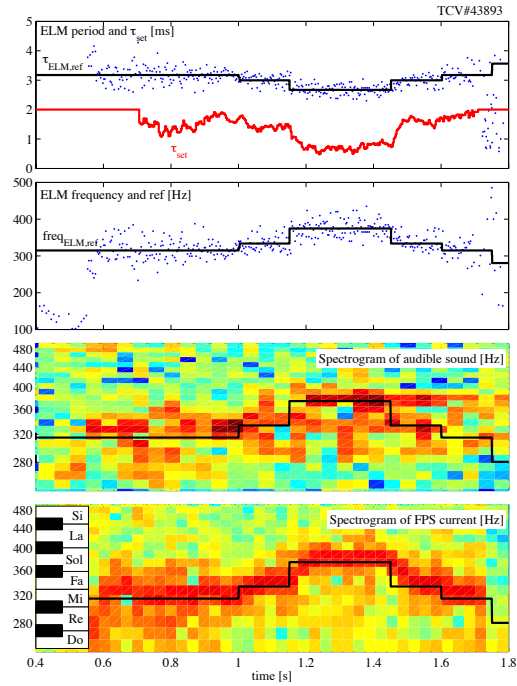


Figure 3.20: TCV performance of Beethoven’s 9th Symphony by ELM frequency feedback control using the ELM pacing method

Other tunes can be played on request as long as the notes lie within the obtainable interval of ELM frequencies: between 250Hz and 400Hz, corresponding to less than one octave, and the total playing time does not exceed the duration of the TCV ELMy H-modes (typically ~ 1 s).

3.3.5 Individual ELM control

After this brief musical intermezzo, we return to a more detailed analysis of ELM pacing. As done for the sawtooth crashes (shown in Fig.3.8), a sequence of τ_{set} values is issued which changes after each ELM. Figure 3.21 shows the time evolution for this shot, with the repeating sequence of τ_{set} values, and ensuing ELM period shown in Fig.3.21(c). The bottom panel shows the time evolution of line-integrated density and central MPX chord during this same shot, showing that neither n_e nor the temperature vary significantly. The H_α signal in Fig.3.21(b) is color-coded corresponding to each repeating sequence. These time intervals are displayed in one figure in Fig.3.22, giving a sense for the repeatability of the ELM period sequence for these shots.

For this shot, we compute the mean and standard deviation of the ELM period for each ELM reference in the repeating τ_{set} sequence. The result is shown in Figure 3.23, showing that indeed, just like for sawteeth, each ELM is independently controlled from the previous one. While chaotic behavior in ELM time series was reported in (Martin et al. 2002) (Degeling et al. 2003a), these results show that the period of an individual ELM can be deterministically controlled by external power. In this sense, apparently the

3.3. ELM pacing and real-time control by EC power

ELM cycle also has no direct “memory” of previous ELMs, though this does not exclude some underlying chaotic behavior of higher order.

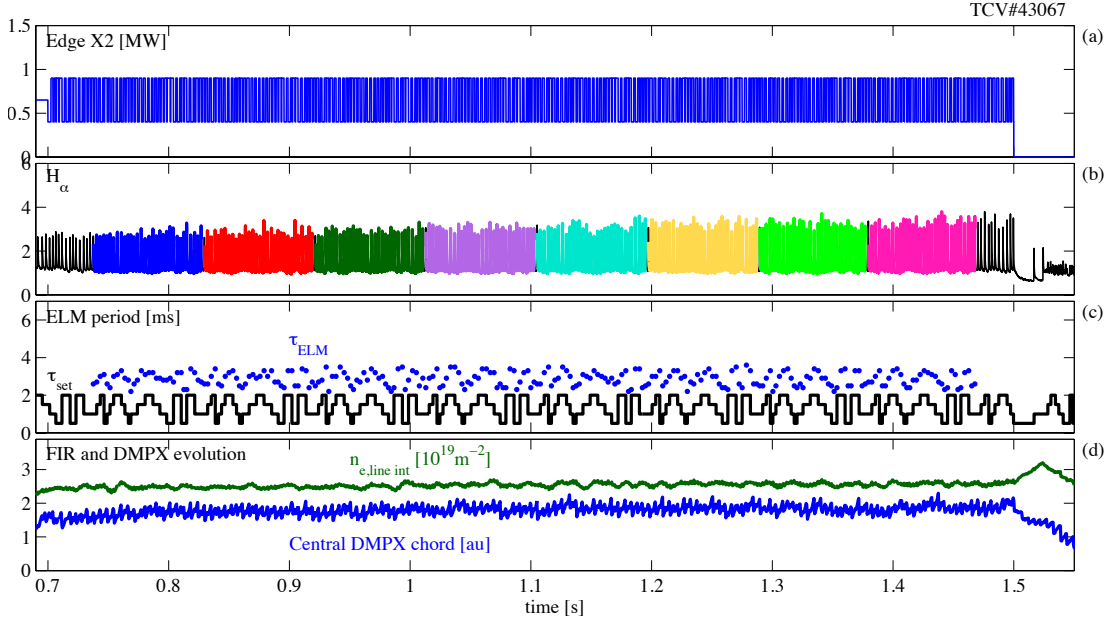


Figure 3.21: Individual ELM pacing experiment. A repeating sequence of τ_{set} is programmed, where the value switches after each ELM occurrence. This leads to 8 sequences of 32 ELMs each (each sequence shown in a different color in panel (b)). The ELM period and τ_{set} sequence is shown in (c). Plasma density and x-ray emission measurements (d) show only a slight variation in density and temperature.

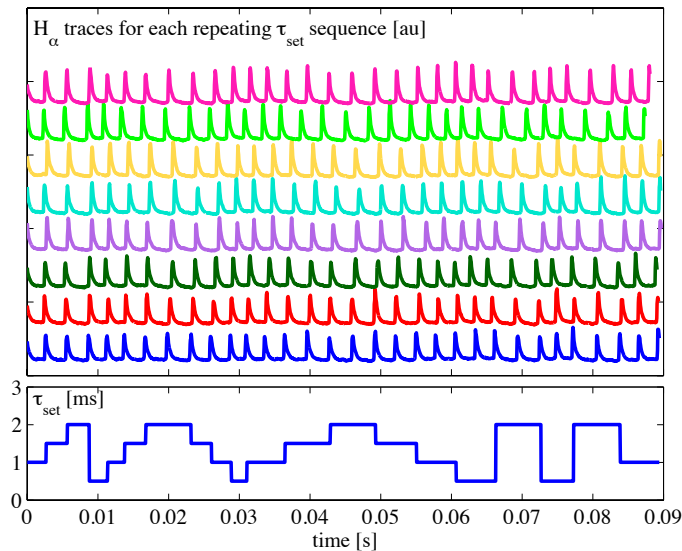


Figure 3.22: Detailed view of the 8 sequences in Fig. 3.21 showing the repeatability of the ELM sequences, and the independence of each individual ELM.

3.3.6 Pure integrator model for the ELM period

Recall the observation in Figure 3.17 that there is a relatively small difference in ELM period between the ELM pacing and CW phases. Conversely, Fig. 3.18 showed that very similar mean power levels yield the same ELM period for pacing and CW power injection. This suggests that, approximately, the ELM period does not depend on the detailed time-history of the X2 power but only on the average power during the ELM. A simple model that would capture this effect assumes that the ELM period is proportional to the total energy (integrated power) injected by X2 during each ELM cycle. This energy is computed for the j th ELM as

$$E_{X2,j} = \int_{t_{j-1}}^{t_j} P(t)dt = P_L\tau_{set,j} + P_H(\tau_{ELM,j} - \tau_{set,j}) \quad (3.3)$$

where t_j is the time of occurrence of the j th ELM, $\tau_{ELM,j} = t_j - t_{j-1}$ and P_L and P_H are the levels of X2 power during the first (low power) and second (high power) phase, respectively.

This hypothesis is tested by plotting, in the lower panel of Figure 3.23, the mean total injected energy $\langle E_{X2,j} \rangle$ where the average is taken over the 8 sequences in Fig. 3.22.

The bar graph also shows the contribution of the low-power and high-power phase of the X2 power. The low power (blue) phase is completely determined by the value of τ_{set} , while the high-power contribution depends on the ELM period τ_{ELM} and may be variable. Remarkably, an almost constant total energy per ELM is found. This suggests that the edge acts approximately as a pure integrator, in the sense that it integrates the input power in time until a threshold energy of approximately $E_{lim} = 1.9 \pm 0.1$ kJ is reached.

With this knowledge (3.3) we can then derive

$$f_{ELM} = \frac{1}{E_{lim}} \langle P_{X2} \rangle_{ELM} \quad (3.4)$$

i.e. the ELM frequency is proportional to the mean injected X2 power. Finer scans of the mean power seem to confirm this over the range 400kW-900kW, though it clearly will not hold for $P_{X2} = 0$. Also, this model clearly does not include the effect of the central X3 heating. The relative success of this very simple model motivates the development of a slightly more complicated model which can include many features of the ELM control experiments described in this section. Further refinement of a model of this type, for example including X3 power, a finite time constant for the integrator and variability of the threshold could explain more of the observed features, including the reduced variability of the ELM period when pacing is applied.

3.3.7 ELM kicking or ELM pushing?

One may wonder at this stage as to the nature of the edge X2 stimulation of the ELM occurrence. Initially, one may think that the additional heating may have a “kick” effect on the pedestal, causing the ELM to appear suddenly due to transient effects. This terminology is used in previous vertical “kick” experiments: forcing ELM period synchronization with plasma vertical oscillations. However the analysis in this chapter shows that this is not the case here. In these experiments, the ELM is shown to be triggered after a given amount of energy has been deposited. The results were obtained for edge heating

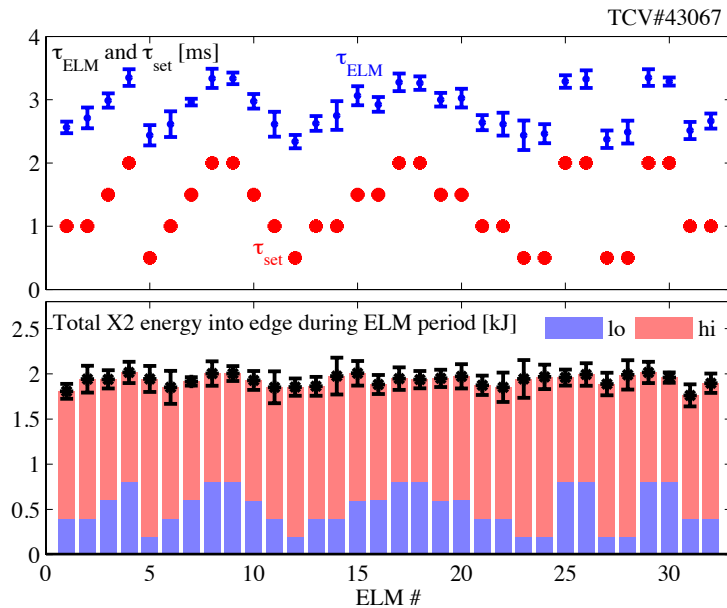


Figure 3.23: Top: statistical mean and standard deviation of ELM period (blue) for corresponding programmed value of τ_{set} (red). Bottom: Total integrated X2 power during ELM cycle, showing relative contributions of low power (blue) and high power (red) phases. Statistical averages are taken over the 8 repeating sequences shown in Figures 3.21 and 3.22.

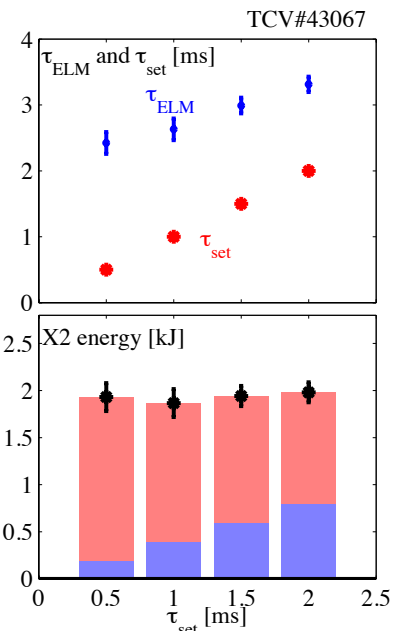


Figure 3.24: Same as Fig. 3.23 but binning all ELMs with the same τ_{set}

on TCV, but similar results can be expected for central heating, since the ELM frequency control relies on the global effect of ELM period decrease for power increase, a distinctive feature of type-I ELMs.

In the experiments shown, the deposited energy per ELM seems to be, to first order, independent of the rate at which the energy is deposited. Therefore we should perhaps speak of ELM “pushing”, whereby the pedestals have to be pushed a certain distance until a threshold. Pushing harder then simply means the threshold is reached faster.

3.4 Conclusions

The TCV experimental results and observations described in this chapter are summarized below. A sawtooth pacing technique has been introduced wherein the stabilizing influence of X2 power is removed a given time after the previous sawtooth crash, and reapplied as soon as the next crash is detected. It has been demonstrated that, using this technique, the period of individual EC-stabilized sawteeth can be precisely controlled from one sawtooth to the next. The time that one has to wait after the removal of the EC power until the appearance of the next sawtooth crash (the crash delay) increases with increasing sawtooth period. This crash delay also becomes longer and more variable if some stabilizing EC power is maintained. The sawtooth period has also been observed to lock to modulated EC power in a range of combinations of duty cycle and period, without requiring explicit synchronization of the EC power with the sawtooth crash times.

Upon the observation that edge X2 power increases the frequency of ELMs in X3

heated H-mode plasmas, ELM pacing techniques were developed and tested to study whether similar results could be obtained as for the sawteeth. An ELM pacing technique has been presented wherein the X2 power is reduced for a given period following an ELM crash, and subsequently increased again until the next ELM. This is the opposite of the sawtooth pacing, since the effect of X2 power is destabilizing in this case instead of stabilizing. It has been shown that ELM pacing can reduce the standard deviation of the ELM period by a factor 2, and that individual ELMs can be controlled this way. Finally, benefitting from the controlled nature of the ELM period, we now have been able to show that the total injected energy per ELM seems to be constant for the parameter range on TCV, indicating that the ELM frequency is proportional to the mean power through the edge.

Chapter 4

Triggering, preemption and suppression of neoclassical tearing modes in TCV

4.1 Introduction

4.1.1 (Neoclassical) tearing mode fundamentals

At high enough current and pressure, tokamak performance is theoretically limited by ideal MHD instabilities which render the confined plasma equilibrium globally unstable. In tokamak experiments, however, it soon became clear that other MHD phenomena, of a different nature, limit the plasma β at significantly lower values than the ideal limits (Rutherford 1973), (Carrera et al. 1986), (Callen et al. 1987), (Sauter et al. 1997). These modes were identified as *tearing* modes, of *resistive* MHD nature. Over the years, the understanding of the underlying physics has rapidly expanded, also revealing interesting parallels with astrophysical plasmas, and intensive research has been conducted on methods to avoid, suppress or otherwise mitigate their effects in tokamak plasmas.

Fundamentally, tearing modes appear due to the fact that at rational q surfaces, where magnetic field lines close upon themselves after a finite number of toroidal and poloidal turns, the forces preventing magnetic reconnection become sufficiently small that plasma resistivity can no longer be neglected and magnetic reconnection can take place. This leads to the plasma magnetic flux surfaces departing from their initial, nested state and to form “islands” in the poloidal plane, as illustrated in Figure 4.1. At the X-points of these islands, regions of the plasma which would otherwise be separated are in direct contact, so radial energy transport is locally enhanced with respect to the original situation. This destabilizes the mode further due to neoclassical effects as will be explained in Section 4.2. This neoclassical contribution has given rise to the nomenclature “Neoclassical Tearing Modes” or NTMs for short. This nomenclature serves to differentiate the main drive of the mode, but will be used interchangeably with “tearing mode” in this chapter since, as we shall see, it is not always easy to distinguish between the two.

Tearing modes are localized on a rational q surface, and are characterized by their poloidal and toroidal mode number, m and n , respectively, where $q_s = m/n$ is the q value at the rational surface. As higher mode numbers tend to be more stable, the low integer

ratios are most commonly observed in tokamaks, in particular the 2/1, 3/2, 4/3, and occasionally 3/1, 5/4 or 5/3. Higher order modes can be created by non-axisymmetric error fields but are generally a result of externally applied magnetic disturbances rather than plasma-driven instabilities.

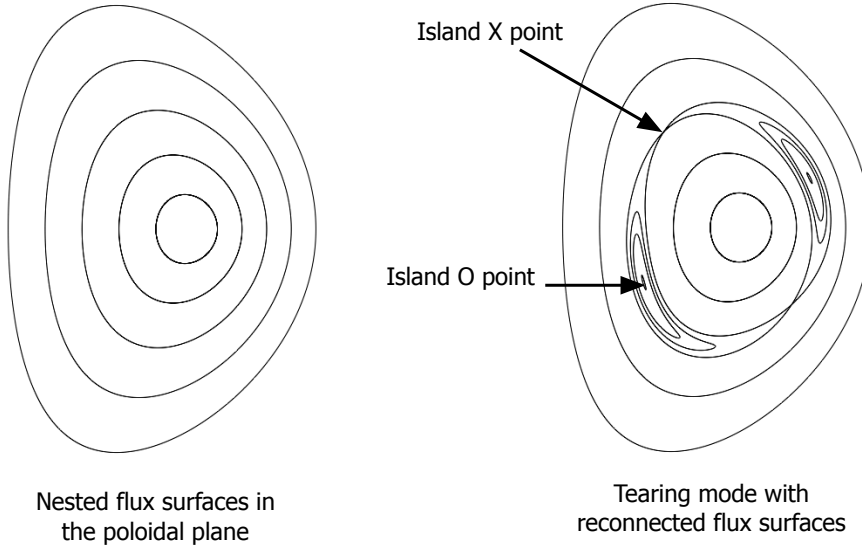


Figure 4.1: Illustration of flux surface shapes in the poloidal plane for standard (nested) configuration and reconnected configuration with a magnetic island with poloidal mode number $m = 2$.

Eventually, the NTMs, which rotate in the laboratory frame, may either saturate at a finite size and remain for the remainder of the stationary plasma phase, or may interact with external vessel structures, causing the mode rotation to slow down, and eventually lock to the static error field. The first case usually constitutes an unwanted situation as plasma confinement, thus the fusion performance, is degraded. The second case is even worse as it is usually followed by a plasma disruption, terminating the shot and causing mechanical stresses on the machine structure.

For these reasons, NTMs in plasmas should be avoided if possible, and mitigated when necessary. Several methods have been used to influence tearing mode appearance and evolution – the most promising of which is localized heating and current drive by Electron Cyclotron waves (EC). This has been the focus of intense studies on several tokamaks around the world (Zohm et al. 1999), (La Haye et al. 2006), (Isayama et al. 2009), as will be outlined in 4.2.3.

This chapter will present an overview of recent work carried out on TCV in the framework of NTM studies. While some studies on tearing modes have been carried out in the past on TCV, in particular regarding the triggering mechanism (Reimerdes et al. 2002) and shaping effects (Scarabosio et al. 2007) the flexibility of the TCV EC system has not yet been exploited for studies of tearing mode stabilization physics. Combined with the new digital control system, new control possibilities have been developed as will be discussed next.

4.1.2 NTM control capabilities developed on TCV

NTMs can be controlled by localized heating and current drive, most typically from an ECRH/ECCD system. Substantial research has been done on real-time tearing mode control, as real-time control of tearing modes will be essential for operation of ITER and other future tokamaks (Hender et al. 2007), (Sauter et al. 2010).

The introduction of the digital real-time control system, coupled to the flexible multi-beam ECH/ECCD system on TCV offered new possibilities for development of NTM control methodologies as well as for gaining a better understanding of the stabilization physics. To this aim, a suite of real-time control capabilities, similar to those developed on other tokamaks doing NTM experiments, was implemented in the new TCV controller.

Mode detection

The simplest way to determine the appearance of a tearing mode is to monitor the signals from a magnetic probe for signs of oscillations in the frequency range of interest. Since magnetic probe data is readily available on the TCV real-time control system, this approach was taken. The algorithms used are described in more detail in Section B.5. The amplitude of the oscillations is proportional to the square of the island width, so this can be used to detect growth or shrinking of the tearing mode during the plasma evolution. The real-time control system detects the presence of an NTM based on a threshold value of the MHD oscillation amplitude, including a minimum time during which the amplitude must be above this threshold. Similarly, the subsequent disappearance of the mode is also detected based on a (typically lower) threshold.

ECRH/ECCD system commands

A controller decides how the various actuators (in this case launcher angles and EC power for different gyrotrons) should react to the appearance/disappearance of a mode. Typically, the launcher angles are programmed to execute a sweep across the expected island location, and are programmed to stop once the island disappears. This simple control method is dubbed the “Scan and stop” algorithm. Additionally, gyrotron power can be increased or decreased. The details of the movement/power commands to execute are different for each experiment and are described for specific cases later in this chapter. One salient result of the use of this control system is that an $m = 2/n = 1$ mode was stabilized by sweeping the ECCD deposition location across the mode during a launcher angle scan.

Phase locking and modulated ECCD

As will be discussed later, modulated ECCD deposited in the O-point of an NTM has been theoretically and experimentally shown to be more effective when the island size is smaller than the ECCD deposition width (Maraschek et al. 2005). For this purpose, a real-time phase locking mechanism is required to generate an EC power command at the same frequency as the NTM. This has been done by implementing a digital Phase Locked Loop (see Appendix B.6) which can lock a (software) sinusoidal oscillator to an input (magnetic probe) oscillation with a pre-set phase offset. This allows one to generate an

EC power reference signal at an arbitrary phase difference with respect to the magnetic probe signal.

The modulated-ECCD capabilities were successfully tested in a plasma experiment, but not enough time was available for systematic studies of NTM stabilization efficiency. This is left as future work. Also, at this time, the PLL has been implemented based on one magnetic probe only – which is sufficient for modulated ECCD experiments. In the future, it would be possible to include a more complete complement of probe signals from the poloidal and toroidal probe array. The same PLL oscillator can be used to determine the relative phases of differently located magnetic probes, and a full spatial mode spectrum can be extracted allowing real-time detection of the n and m numbers.

4.1.3 Overview of this chapter

The remainder of this chapter is divided as follows. Section 4.2 will briefly review the physics behind the tearing modes, including a standard set of stabilizing and destabilizing effects discussed in the literature. In particular, different triggering mechanisms will be discussed. Next, Section 4.3 will show TCV experimental results obtained in studies of ECCD-dominated tearing modes, aimed at studying the physics of tearing mode destabilization by current profile effects. This is followed, in Section 4.4, by results on stabilization experiments using the ECH/ECCD system with real-time control of the steerable launchers. Finally, Section 4.5 will present NTM triggering, preemption and stabilization experiments for low q_{95} plasmas, where the NTM is triggered by long-period sawtooth crashes.

4.2 Neoclassical tearing mode physics

In this section we will briefly review the physics of Neoclassical Tearing Modes in tokamaks. A vast literature exists focusing on a multitude of physics effects affecting the tearing mode creation or evolution (see the review in (La Haye 2006)), but the focus of this section will be on the physics required to model the experimentally observed evolution of tearing modes in TCV. In this context, the Modified Rutherford Equation (MRE), discussed in Section 4.2.1, collects present physical understanding and has had considerable success in reproducing experimentally observed NTM evolution during tokamak experiments.

It should be noted that a more complete treatment of the tearing modes can be obtained from the full 3D resistive nonlinear MHD equations. This has been explored in recent work using numerical full-MHD codes such as NFTC (Popov et al. 2002b), (Popov et al. 2002a), XTOR (Maget et al. 2010) and NIMROD (Jenkins et al. 2010). Though the physics included in these codes is more complete, simulations at realistic plasma parameters remain numerically challenging and a satisfactory match to experimental observation is not always found.

4.2.1 The Modified Rutherford Equation

The Modified Rutherford Equation (MRE) is a nonlinear ordinary differential equation describing the evolution of the island width w in time. While it will be derived more fully

below, we can already write its general form

$$\frac{\tau_R}{\rho_s} \frac{dw}{dt} = \sum_i \rho_s \Delta'_i(w) \quad (4.1)$$

where τ_R is the local resistive time, ρ_s is the mode radial location in [m] and the various Δ' terms represent physical effects which independently affect the mode. Each term may depend on other plasma parameters and – as will be shown below – the plasma parameters themselves may also depend on the island width (w). This results in a complicated, nonlinearly coupled problem. In order to self-consistently simulate the evolution of a tokamak plasma with a tearing mode, the MRE must be solved in conjunction with other plasma (transport, equilibrium) evolution equations. If multiple modes exist at the same time in the plasma, one equation per tearing mode should be solved, including coupling terms. Additionally, one can solve an equation for the mode rotation frequency, which can also be used to simulate mode locking (Ramponi et al. 1999). The various terms governing the island width evolution will now be derived and discussed.

Classical tearing parameter

The most basic parameter is the so-called *classical* tearing parameter, so named because it is the result of classical tearing mode physics developed in (Furth et al. 1963), (Furth et al. 1973) and (Rutherford 1973). This parameter describes the natural tendency of a magnetic equilibrium to “tear” itself apart and spontaneously form magnetic islands. The energy for this process is made available by the external region (the region of plasma excluding the island), which can be regarded as satisfying ideal, inviscid, incompressible, massless MHD (cf. (Fitzpatrick 1995)). Assuming a cylindrical large aspect ratio tokamak and applying the energy principle in ideal MHD in this “outer” region, it can be shown that a helical flux perturbation of the form $\psi_1 = \psi_1(r) \exp(\gamma t + im\theta - inz/R)$ must satisfy

$$\frac{1}{r} \frac{d}{dr} r \frac{d\psi_1}{dr} - \frac{m^2}{r^2} \psi_1 - \frac{\mu_0 \frac{dj_0}{dr}}{B_\theta (1 - \frac{n}{m} q)} \psi_1 = 0 \quad (4.2)$$

Clearly, at the rational surface r_s such that $q_s(r_s) = m/n$ where the mode is localized, the last term develops a singularity. For this reason, the differential equation can be integrated independently on both sides of the singular layer, after which the values are set equal at the location of the layer. The resulting ψ_1 will therefore be, in general, non-differentiable at $r = r_s$, yielding a jump of magnetic energy from the outer to the inner layer. This provides a source of potential energy for magnetic reconnection. The rate of growth of the island is then directly related to the jump of logarithmic derivative

$$\Delta'_0 = \lim_{\epsilon \downarrow 0} \frac{\psi'_1}{\psi_1} \Big|_{r=r_s-\epsilon}^{r=r_s+\epsilon} \quad (4.3)$$

This term is called the classical tearing stability index. When positive, there is free energy available for magnetic reconnection to occur. It can also be shown that, for monotonic plasma profiles, it is the current gradient on the inside of the island which gives the main destabilizing contribution.

Since existing tokamak diagnostics measure poloidal fields rather than current densities, the current density gradient (which is related to the second spatial derivative of

the magnetic field) is rather difficult to resolve experimentally. For this reason, theory-experiment comparison for classical tearing stability are difficult to perform. At best, a global trend can be extracted from simulations and analytical/numerical evaluations of Δ'_0 for a set of plasma equilibrium variations.

In the linear theory, the exponential growth rate is proportional to $\gamma \sim (\Delta'_0)^{5/3}$. Adding nonlinear effects, (Rutherford 1973) derives a different, slower growth rate for the width of an existing island by linking Δ'_0 to the perturbed parallel helical currents in the inner layer via the *matching condition*. In what follows, we will derive the mode growth rate, following (Fitzpatrick 1995), (Hegna 1998). In the constant- ψ approximation, the perturbed flux is chosen constant in the inner layer ($\psi(r) = \Psi$). With this assumption, the matching condition is written as:

$$\Delta' \Psi = -2\mu_0 \oint \frac{d\zeta}{2\pi} \int_{r_{s-}}^{r_{s+}} \delta j_z \cos \zeta dr \quad (4.4)$$

where we have introduced the island coordinate ζ , which goes from 0 to 2π from one X point to the next. It is also useful to define a helical flux

$$\chi(r, \zeta) = - \int_{r_s}^r \left(1 - \frac{q}{q_s}\right) B_\theta dr + \psi_1(r) \cos \zeta \quad (4.5)$$

such that the contours of χ correspond to surfaces of constant perturbed magnetic flux. This can be exploited to define a perturbed flux surface label Ω

$$\Omega = \frac{\chi}{\Psi} = 8 \frac{(r - r_s)^2}{w^2} + \cos \zeta \quad (4.6)$$

We have introduced the island width w as the width of the region where reconnected island flux surfaces appear.

$$w = 4 \sqrt{\frac{R_0 q_s}{B_z s_s} \Psi} \quad (4.7)$$

where we have defined the magnetic shear at the rational flux surfaces $s_s = r q'_s / q_s$. The island O point corresponds to $(\Omega = -1, \zeta = \pi)$, the separatrix is the locus of $\Omega = 1$ and the X-point is located at $(\Omega = 1, \zeta = 0)$.

The growth rate of a magnetic island can now be derived from the perturbed Ohm's law.

$$\frac{\partial \Psi}{\partial t} \cos \zeta + \mathbf{B} \cdot \nabla \phi = -\eta \delta j_z \quad (4.8)$$

where η is the (neoclassical) plasma resistivity and ϕ is the perturbed electrostatic potential. The second term on the left hand side can be canceled by defining a flux surface average operator

$$\langle f(\sigma, \Omega, \zeta) \rangle_\zeta = \begin{cases} \oint \frac{f(\sigma, \Omega, \zeta)}{\sqrt{\Omega - \cos \zeta}} \frac{d\zeta}{2\pi} & \text{if } \Omega > 1, \\ \int_{\zeta_0}^{2\pi - \zeta_0} \frac{f(\sigma, \Omega, \zeta) + f(-\sigma, \Omega, \zeta)}{2\sqrt{\Omega - \cos \zeta}} \frac{d\zeta}{2\pi} & \text{if } -1 \leq \Omega \leq 1. \end{cases} \quad (4.9)$$

where σ is the sign of $(r - r_s)$, and $\zeta_0 = \cos^{-1} \Omega$. One can demonstrate that, for any function f , $\langle \mathbf{B} \cdot \nabla f \rangle_\zeta = 0$. Now we can rewrite (4.4), using the fact that

$$dr = d(r - r_s) = -\frac{w}{4\sqrt{2}} \frac{1}{\sqrt{\Omega - \cos \zeta}} d\Omega \quad (4.10)$$

yielding

$$\Delta'_0 = \frac{\mu_0}{2\sqrt{2}} \frac{w}{\Psi} \int_{-1}^{\infty} \langle j_z \cos \zeta \rangle d\Omega \quad (4.11)$$

Using these definitions, we can define the growth rate of a magnetic island. From the time derivative of (4.7)

$$\frac{dw}{dt} = \frac{w}{2\psi_1} \frac{\partial \Psi}{\partial t} \quad (4.12)$$

Multiplying (4.8) by $\langle \cos \zeta \rangle$ and taking the flux surface average, one can derive the growth rate of the “classical” magnetic island

$$\boxed{\frac{\tau_R}{r_s} \frac{dw}{dt} = r_s \Delta'_0} \quad (4.13)$$

where the resistive time $\tau_R = 0.82\mu_0 r_s^2 / \eta$ appears.

When $\Delta'_0 > 0$, the resistive instability develops spontaneously, in this case one conventionally speaks of *tearing* modes. In the case where $\Delta'_0 < 0$ the plasma is linearly stable and will not spontaneously depart from its equilibrium condition. Other sources of instability should then be considered and will be developed next.

Neoclassical effects

As mentioned in the introduction, the energy transport is locally enhanced due to the presence of magnetic islands, since $p(\Omega) = \text{cst}$. This means that a region of local pressure flattening appears at the magnetic island O point. The bootstrap current, the component of plasma current generated by neoclassical effects due to trapped particle orbits (Hinton et al. 1976), is proportional to the pressure gradient. Therefore, the local flattening of the pressure profile at the island O point results in a local reduction of the bootstrap current in this region. This perturbation will have the same helical structure as the magnetic island itself, and will be oriented in such a way that the magnetic field perturbation it creates has the same direction as the original field perturbation of the magnetic island itself, reinforcing it.

This effect is often referred to as the *bootstrap drive* of the island, and islands for which the size and growth are dominated by this effect are referred to as *neoclassical* tearing modes.

The effect can be derived by appropriately modifying the perturbed Ohm’s law (4.8). Following (Fitzpatrick 1995), the perturbed non-inductive current \tilde{j}_z is subtracted from the total perturbed current

$$\frac{\partial \psi_1}{\partial t} \cos \zeta + \mathbf{B} \cdot \nabla \phi = -\eta(\delta j_z - \delta \tilde{j}_z) \quad (4.14)$$

It can be shown that with this extra term, an extra contribution must be added to (4.13). The exact form depends on the choice of model for the perturbed bootstrap current as a function of the pressure gradient. A standard set of assumptions (Sauter et al. 1997), (Sauter et al. 2002b), gives

$$\boxed{\frac{\tau_R}{r_s} \frac{dw}{dt} = r_s \Delta'_0 + r_s \Delta'_{bs}} \quad (4.15)$$

where

$$\Delta'_{bs} = a_2 \beta_p (-L_{bs}) \frac{L_q}{-L_p} \frac{w}{w_d^2 + w^2} \quad (4.16)$$

Here, L_q and L_p are, respectively, the spatial gradient scale lengths of the q profile and p profile variation and L_{bs} is the scale length associated with the contributions of the profiles to the bootstrap current (Sauter et al. 2002b). The coefficient a_2 is of order unity.

A small island term w_d has been added, which ensures the neoclassical contribution goes to 0 in the small island limit. Physically, this is caused by the fact that for small islands, the flattening of the pressure gradient due to the presence of the island is not complete due to finite $\chi_\perp/\chi_\parallel$. The exact form of w_d can be derived from the local transport physics: (Fitzpatrick 1995), (Sauter et al. 2002b, Eq.6)

$$w_d = 5.1 \rho_s \left(\left(\frac{1}{\epsilon sm} \right)^{1/2} \right)^{4/3} \left(\frac{\chi_\perp}{\chi_\parallel} \right)^{1/3} \quad (4.17)$$

As the Δ'_{bs} term is positive for standard tokamak equilibria, this neoclassical contribution is destabilizing. Additionally, due to the dependence on the island size, this term provides an additional mechanism for NTM destabilization. A situation may arise where Δ'_0 , which depends on the magnetic equilibrium, is negative, while Δ'_{bs} , which depends on β_p , is positive for nonzero island size. In this case the NTM is *metastable*, and a “seed island” will grow to a saturated state under the influence of the Δ'_{bs} term. It has been shown that this is the situation in standard H-mode plasmas and is expected to be the case for the standard scenario of ITER (Sauter et al. 2002b). The triggering mechanism for metastable modes by seed islands will be discussed in more detail in Section 4.2.3.

Effects of localized heating and current drive

As has been discussed above, the bootstrap current term causes a reduction of local helical current and has a destabilizing effect on the islands. Exploiting the converse effect, adding helical current at the island O point location is theoretically expected to have a stabilizing effect on the island. Looking at (4.8), the extra driven current also appears in the \tilde{j}_z term, in addition to the bootstrap contribution. The perturbed current contribution consists of a heating component (additional Ohmic current caused by changing local conductivity) and a direct non-inductively driven current component. These effects can be grouped in Δ'_H and Δ'_{CD} term, respectively. The exact forms of Δ'_H and Δ'_{CD} depend on the ECH/ECCD power, the injection geometry (deposition width and location with respect to the island), as well as on the modulation (if any) of the deposited power with respect to the island O and X point. Analytical expressions giving fits of numerical data for these contributions have been calculated in (De Lazzari et al. 2009), (Lazzari et al. 2010).

Small island effects of geometry and polarization currents

A further effect, not considered in the cylindrical Δ' treatment, comes from the stabilizing effect of magnetic field curvature. This is referred to as the Glasser-Green-Johnson (GGJ) (Glasser et al. 1975) effect, and decreases with increasing island size. It is expressed in

large aspect ratio approximation as (Sauter et al. 1997), (Lütjens et al. 2001).

$$\Delta'_{GGJ} = 6.35\beta_p \frac{\epsilon^2}{s} \frac{L_q}{-L_p} \left(1 - \frac{1}{q^2}\right) \frac{1}{\sqrt{w^2 + 0.2w_d^2}} \quad (4.18)$$

Note the $\epsilon (= a/R_0)$ dependency, related to the fact that this term depends on β rather than β_p and $\beta = (\epsilon/q)^2\beta_p$. At the same time, the bootstrap contribution Δ'_{bs} is proportional to ϵ instead of ϵ^2 . This means that this term is usually small for conventional aspect ratio tokamaks and is more relevant for tight aspect-ratio (spherical) tokamaks (Buttery et al. 2002). Nevertheless, it plays a role in the details of small island stabilization.

Another effect is the polarization drift term (Wilson et al. 1996), (Waelbroeck et al. 2001), which arises physically due to the different response of electrons and ions to the rotating island in the plasma flow, and is frequency-dependent. The exact form of this term is still a source of debate, but it is often written as (Sauter et al. 1997), (Sauter et al. 2002b), (Poli et al. 2002):

$$\Delta'_{pol} = a_4\beta_p \left(\frac{L_q}{L_p}\right)^2 \rho_p^2 g(\epsilon, \nu_{ii}) \frac{w}{w^4 + w_p^4} \quad (4.19)$$

where ρ_p is the poloidal ion gyroradius and g is a function of order unity (see (Sauter et al. 2002b) for details). w_p is introduced to avoid large terms for $w \downarrow 0$. Following (Poli et al. 2002) we have $w_p = \sqrt{28}\epsilon\rho_p$ with ρ_p the poloidal ion larmor radius (Sauter et al. 2002b).

Coupling to other modes and to the conducting wall

When the island is sufficiently close to a conducting wall, the currents induced in the conductor have a drag effect, slowing the mode frequency (Nave et al. 1990), (Ramponi et al. 1999). This may in turn cause the island to grow and, at some point, the island may be seen to align itself to the static error field of the wall, fixing its position in the rest frame. It may then remain in place and grow further, either drastically degrading the confinement or causing a plasma disruption. MRE-type tearing mode analysis may therefore include a frequency-dependent Δ'_{wall} drag effect which represents the effect of the wall. Other modes may be present in the plasma as well, and may non-resonantly interact with each other and exchange energy. This can be reflected in additional Δ' -type terms as in (Sauter et al. 2002b), where the decay of a 3/2 mode is observed in the presence of a 4/3 mode.

4.2.2 Experimental observation of tearing modes

We now briefly turn to the practical question of how tearing modes in plasmas are observed. Most straightforwardly, the magnetic oscillation they produce is detected as an oscillating signal on magnetic probes placed inside the vessel. By performing spatial Fourier analyses, the poloidal and toroidal mode numbers can be inferred. The temperature fluctuations caused by the altered confinement can also be directly observed, most typically with localized ECE measurements or line-integrated soft-X ray measurements. These can then be used in real-time control applications to detect the phase and location

of the island (Gantenbein et al. 2000), (Berrino et al. 2005), (Park et al. 2006), (Oosterbeek et al. 2008). The flattening of the current density profile, caused by the loss of bootstrap current, was also observed using MSE diagnostics (Oikawa et al. 2005). More recently, visible camera emissions were used to reconstruct the 2D structure of the islands (Zeeland et al. 2008).

4.2.3 Triggering mechanisms: TMs vs NTMs

As briefly mentioned earlier, different Δ' terms in (4.1) can be most important depending on the plasma conditions, leading to qualitatively different triggering mechanisms for the mode. This is illustrated schematically in Figure 4.2. The first panel (a) shows an example where only the classical Δ'_0 plays a role, which may be the case in very low- β L-mode plasmas. In the case shown, the current density profile happens to be such that $\Delta'_0 > 0$ for $w = 0$. This means the island will spontaneously grow (positive dw/dt) until reaching the stable equilibrium w_{sat} (the saturated island size due to modification of the equilibrium current density profile by the island). No triggering event nor “seed” island is necessary in this case. Consider the contrasting situation shown in Fig.4.2b where $\Delta'_0(w = 0) < 0$, and the bootstrap term plays a more important role. In this case, there is a critical island width w_{crit} below which an island will self-stabilize and not grow. For islands of size $w > w_{crit}$, however, an island will evolve to the stable equilibrium corresponding to the saturated island size w_{sat} . This means that in this case an island will only grow starting from a “seed” island w_{seed} ; the plasma is metastable. The present understanding is that this seed island is provided by other events which cause perturbations in the internal plasma magnetic field, such as sawteeth or ELMs. The rightmost panel, Fig.4.2c, shows the mechanism of NTM self-stabilization, which occurs when the plasma β decreases due to the (further) confinement degradation or a reduction of the injected power. The Δ'_{bs} contribution decreases until the total curve satisfies $dw/dt < 0 \forall w$. The last point satisfying $dw/dt(w) = 0$ is the marginal island size, beyond which the island self-stabilizes. The effect of lowering the total curve can be obtained not only by decreasing the bootstrap contribution, but also by localized heating and current drive via the Δ'_H and Δ'_{CD} terms, which are negative, or by lowering the Δ'_0 term further by changing the current profile.

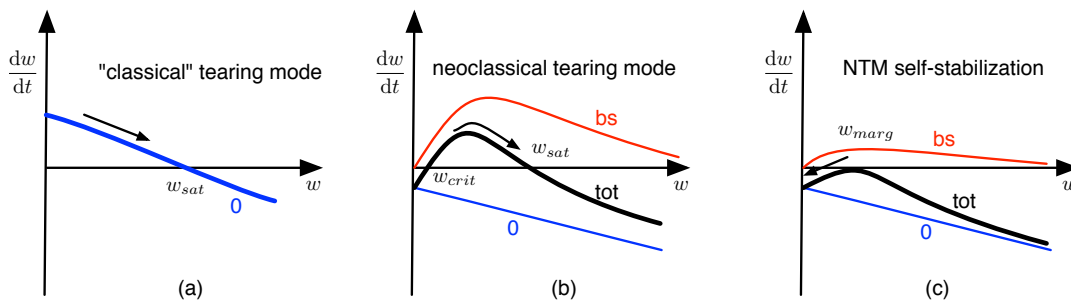


Figure 4.2: Schematic representation of different triggering methods for tearing modes, corresponding to the “classical” case (a) and the “neoclassical” case (b), depending on the relative importance of the classical tearing parameter Δ'_0 and the bootstrap term Δ'_{bs} . Also shown is the self-stabilization beyond the marginal island size when the right hand side of the MRE Eq.(4.1) is reduced (c).

One can distinguish between the two cases Fig.4.2a and Fig.4.2b by observing the

initial time evolution of the mode. If the mode grows from zero width, then we are dealing with a classical destabilization. If the mode appears suddenly, the mode appearance is caused by a seed island. A more detailed study of these two triggering mechanisms on TCV has been published (Reimerdes et al. 2002).

Fundamental questions still remain as to the physics of these “triggered” and “triggerless” tearing modes. Mode triggering by sawteeth is, at least phenomenologically, well understood. Longer sawtooth periods correlate with appearance of NTMs at lower β_N (Chapman et al. 2010), and, conversely, shorter sawtooth periods mean a higher beta limit for triggering NTMs, as shown on JET (Sauter et al. 2002a). This is the prime reason warranting research into methods to destabilize (shorten) the sawtooth period in ITER. Intuitively, one can relate this to a greater build-up of magnetic energy and subsequently more energy available to create seed islands. However, the details of the mechanism are not well understood and are still topic of scrutiny. Recent developments on sawtooth control, described in Chapter 3, provide a method to reliably create sawteeth with a precisely determined period, and offer new opportunities to study the triggering, avoidance and suppression mechanism for sawtooth-triggered tearing modes. This will be described further in Section 4.5.

The study of triggerless NTMs in DIII-D hybrid discharges has been the subject of a recent study (Turco et al. 2010), which correlates the appearance of the mode with a decrease in internal inductance. This indicates that the plasma current density profile evolution, on the (slow) current redistribution time scale, plays an important role in governing exactly when a mode will appear for discharges where β is above the NTM metastable limit. Very recent work reported in (Breslau et al. 2011) suggests that, at least in Spherical Tokamaks, the appearance of the seemingly triggerless modes is related to an infernal-type, nonresonant (1,1) mode appearing due to q_0 decreasing to values close to 1. At present, there is no understanding of what causes the apparently triggerless modes to appear. The fact that discharges can continue for many confinement times without developing a mode leads to the hypothesis that the q profile plays an important role, but attempts to explain this by a classical Δ'_0 dependence have so far been hampered by the sensitivity of Δ'_0 to details of the q profile through its first and second derivative, and that this level of detail cannot be resolved by existing current density profile diagnostics (Felici et al. 2009b). Some studies were carried out on TCV to reproduce such “triggerless” NTMs, thought to be caused by a slow evolution of the q profile, and some experimental observations and interpretations will be presented in 4.3.

4.3 Tearing mode triggering in plasmas with ECCD

4.3.1 Current profile driven tearing modes in TCV plasmas

Renewed interest for NTM studies on TCV has been the result of a series of “Swing-ECCD” experiments in 2005-2006. These experiments, described in (Cirant et al. 2006), (Zucca et al. 2009b), featured a periodic switching between co- and counter-ECCD phases. The experiments kept the total input power constant in order to study the effect on confinement caused by the local current density profile and magnetic shear variations. One interesting collateral result of these experiments was that during the co-ECCD phases of the discharge, at high local power, NTMs were repeatedly and reproducibly triggered.

As the main variation in the plasma is due to the current density profile, this led to the hypothesis that a local variation of the current density profile causes a variation of Δ'_0 such that the mode becomes unstable. This led to further experimental attempts to systematically study the effect of localized ECCD and to determine whether a reproducible method for TM/NTM destabilization could be found.

Plasma scenario

Plasma scenarios were used similar to those used in the mentioned Swing-ECCD experiments. However, instead of switching the ECCD direction, continuous co-ECCD was applied (as NTMs were observed during the co-ECCD phase).

Other typical parameters (which were not rigorously maintained, but serve as an indication) of these L-mode plasmas are $I_p = 120\text{kA}$, $B_T = 1.40\text{T}$, $q_{95} = 5.2$, $V_{loop} \approx 0.14\text{V}$, $\kappa = 1.3$, $\delta = 0.15$, $z_{ax} = 0.21\text{m}$, $n_{e0} = 1.2 \times 10^{19}\text{m}^{-3}$, $T_{e0} = 5\text{keV}$, $\beta_p = 0.75$. Though systematic transport modeling was not carried out, it appears these shots usually do not have much sawtooth activity, indicating a lack of (or very small) $q = 1$ surface. As such, the q profiles of some of these shots may resemble those of “hybrid” plasma scenarios (see Section 6.8), though no active effort was made to avoid sawteeth.

In these plasmas, varying amounts of co-ECCD were injected in different off-axis locations. The range of deposition location for ECCD was between $\rho_{tor} = 0.3$ and 0.5 , which is outside the $q = 1$ but inside the $q = 2$ surface for these plasmas.

Total injected EC power was between 1.0 and 1.5MW X2 from 3 upper launchers. With the given gyrotron configuration, approximately 30% non-inductive current fraction was obtained, split evenly between current drive and bootstrap current.

ECCD-destabilized NTMs

Time traces from a typical shot are shown in Figure 4.3. The left panels show a magnetic probe spectrogram and the time evolution of gyrotron power, launcher angle and mode amplitude. In this case, the deposition location was slowly varied inwards during the shot in order to perturb the current density profile. As seen in the spectrogram, there are no clear MHD events such as sawteeth, nor other mode activity, before the NTM onset. This further feeds the hypothesis that these modes are “triggerless” and do not have a seed island, as no seeding event is apparent.

At $t \approx 1.15\text{s}$ a mode appears, as witnessed from the dark red portion of the spectrogram. By careful examination, one can actually discern an initial phase of high-frequency activity followed by a longer stationary phase of low frequency activity. By decomposing the toroidal harmonics, one can see that the first high-frequency activity is actually an $n = 2$ mode, and poloidal probe analysis confirms that this is in fact a $3/2$ mode. Zooming in on the time of mode triggering one sees that the $n = 2$ mode grows initially, but its appearance is accompanied by the slower growth of an $n = 1$ component. At $t = 1.2\text{s}$ the $n = 1$ mode growth accelerates and the $n = 2$ mode disappears. The $n = 1$ mode is in fact a $2/1$ tearing mode which grows up to a saturated state.

In this particular shot, the mirror angles were controlled in real-time to increase (move the beam towards the magnetic axis) until the mode appears, and then reverse their direction and move the deposition location further outwards. This proves the meta-stable

character of the NTM: even returning to a deposition location further outside than at the beginning of the shot, the mode persists.

When the EC power is turned off, the mode disappears on a confinement time scale (\sim few ms) due to the disappearance of the bootstrap drive, similar to the case shown in Figure 4.2c.

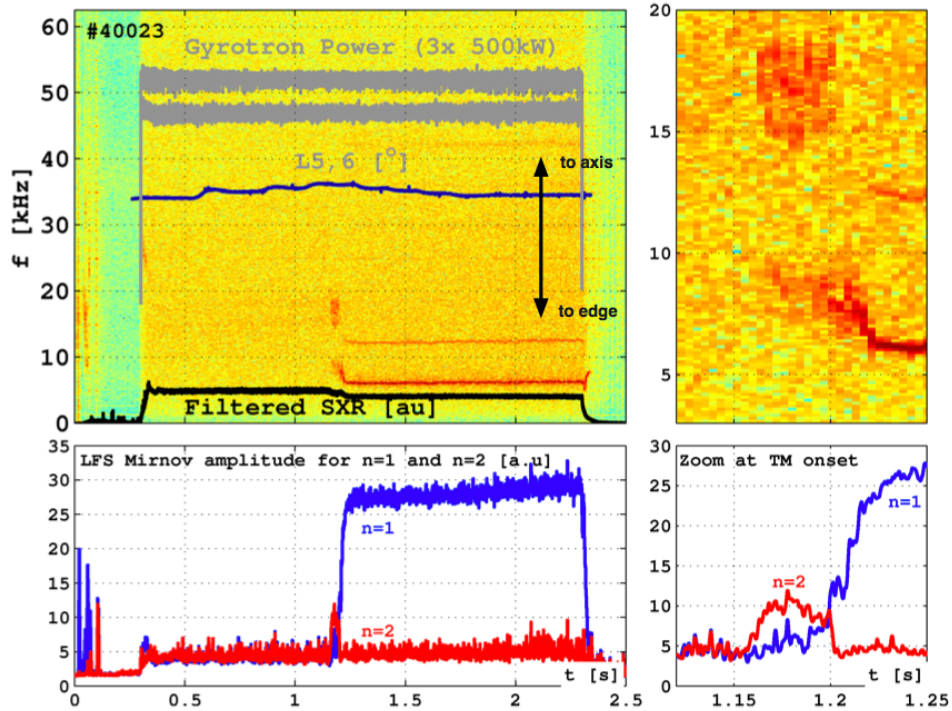


Figure 4.3: Top left: Typical NTM destabilization experiment using real-time control. The deposition location is moved towards the plasma core in steps. When the mode appears, this is detected by the control system and the mirror movement direction is reversed. The mode does not disappear, demonstrating the metastable nature of the NTM. Bottom left: $n = 1$ and $n = 2$ components of the spatially filtered Right: detail of tearing mode appearance, showing an $n = 2$ mode precedes the $n = 1$ growth.

Different NTM triggering mechanisms

The example shown above was an example of an attempt to systematically investigate under which circumstances NTMs are destabilized, several experiments were done during which the ECCD location was varied during the shot. On several occasions, 2/1 NTMs were triggered. The triggering mechanism was observed to belong to one of three categories, summarized in Figure 4.4.

- The first type, shown in Fig.4.4(a) resembles the scenario described in (Reimerdes et al. 2002). During this shot, a gyrotron beam was slowly sweeping inward from $\rho = 0.5$ towards $\rho = 0.25$. A very slow growth of the $n = 1$ component is observed, compatible with a slightly positive Δ'_0 . After some time, the growth accelerates, which can be explained by the fact that the Δ'_{bs} contribution (which increases due to

the more centralized heating) becomes sufficiently large that it changes the saturated island width to a different size.

- The second type, shown in Fig 4.4(b) and Fig 4.4(c), is a case where an $n = 2$ mode (possibly a $(3/2)$ mode) appears first, and an $n = 1$ mode grows slowly, maybe fed by nonlinear mode coupling (Raju et al. 2003), (Raju 2011), until the $n = 2$ disappears and the $n = 1$ mode grows to much larger size. It is also possible that both modes become unstable at the same time. The example in Fig 4.4(c) shows the same trend but with much shorter $n = 2$ phase.
- The third and final type (Fig 4.4(d)) was observed in the mentioned “Swing-ECCD” experiments. In the time frame shown, the ECCD was switched from counter- to co-ECCD at $t = 0.965$ s. Approximately 10ms later, a $2/1$ NTM grows rapidly but shrinks in size thereafter. This type of destabilization was not reproduced during the later experiments, which did not feature sudden ECCD direction switching. There are two possible explanations for this type of behavior: if it is a seed-island destabilized NTM, the seed island is initially larger than the critical island width, so that the island shrinks in the initial phases. It is not clear what provides this initial large seed island: a sawtooth is observed at the time of the NTM growth but similar sawteeth at other times during the plasma do not engender any strong MHD activity. Furthermore, while the growth is fast, it is still slower than the sawtooth crash time scales on which sawtooth-triggered tearing modes appear (examples will be given in Section 4.5). Another possible explanation is that the classical Δ'_0 becomes transiently very large, due to the localized current density perturbations induced by the ECCD sign switch. This is plausible, since the local current profile gradient can be rapidly varied by localized ECCD: numerical studies (Felici et al. 2009b), using a cylindrical Δ'_0 codes (which solves (4.2)) as well as the PEST III MHD stability code (Pletzer et al. 1994) also confirmed that the classical Δ'_0 stability can be radically varied by relatively small changes in the current density profile. This implies that the ECCD in these Swing-ECCD experiments was just at the right place for this to occur.

Two very similar plasmas

Unfortunately, despite efforts to find a systematic method to destabilize tearing modes in a stationary state, results were not clearly reproducible. An explicit search for a condition where NTMs were always triggered by appropriately choosing the ECCD deposition location and power combination was not successful. Even straightforward shot repetition occasionally showed different behavior. As an example, two shots, similar to the one shown above, were executed on the same experimental day, having exactly the same programmed settings for plasma parameters and EC deposition location. One of the plasmas develops an NTM after ~ 2 current redistribution times with stationary heating and current drive conditions ($\tau_{cert} \sim 150$ ms), while the other does not. An overview of the evolution of the main plasma parameters for both shots is shown in Figure 4.5. Panels (a) and (b) show the spectrogram of a magnetic probe, showing that one shot develops an NTM and the other does not. Subsequent panels (c)-(h) show the evolution of main plasma parameters.

4.3. Tearing mode triggering in plasmas with ECCD

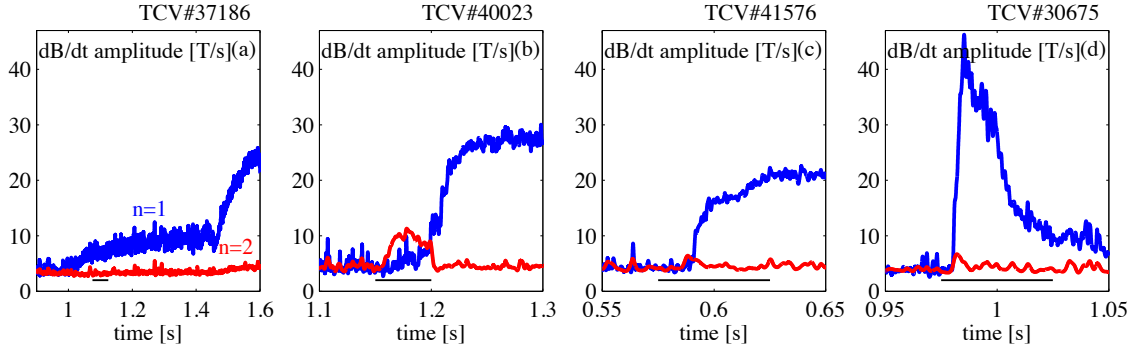


Figure 4.4: Different experimental observations of (N)TM triggering. Filtered amplitudes of $n = 1$ and $n = 2$ toroidal mode numbers are shown. We can distinguish (a) Classical tearing mode growth followed by NTM growth. (b) $n = 2$ destabilization followed by $n = 1$ growth and suppression of $n = 2$. (c) Similar to (b), but shorter time scales and shorter $n = 2$ phase. (d) Immediate strong $n = 1$ growth. Note the different time scales: the black line in each figure represents 50ms.

All parameters are identical, except for the XTe-measured temperature which is slightly lower for the shot with the mode. This is most likely due to a different impurity content, as a result of evolving wall conditions, and might explain the different plasma evolution.

Another interesting feature, visible in Fig.4.5 at the end of the shot, is the rate at which the mode disappears. Note the initial drop in $n = 1$ amplitude on a confinement time scale, due to the removal of ECCD power. From the point of view of the MRE, this is due to the β_p dependence in the Δ'_{bs} term. This phase is followed by another phase of slower mode shrinkage: in this case the mode size follows the residual $\Delta'_0(w)$ which can also be used to measure this dependence (as in (Reimerdes et al. 2002)).

In Figure 4.6 we focus on the region in time where the NTM appears in one case, but not in the other. Note in particular that small sawteeth are present in both plasmas, which disappear when the mode appears in shot #42099 Fig.4.6(h). Also, there is no clear trigger of the NTM as all sawteeth are of similar size and other parameters are constant during this phase of the shot. The triggering type is similar to the second case discussed in the previous paragraph, with a short period of $n = 2$ activity preceding the growth of the 2/1 island.

The most plausible explanation for the different behavior is that the slightly different temperature and impurity content causes the conductivity profile to be slightly different, resulting in a different evolution of the current density profile. This destabilizes a 3/2 mode, most likely with a small sawtooth crash creating a small seed island, which subsequently nonlinearly drives a small 2/1 mode. This mode then dominates and grows (neoclassically driven) to saturated size, damping the 3/2 mode in the process.

4.3.2 Transient profile effects in tearing mode triggering

After a substantial number of trial-and-error attempts, it was found that the most reliable way to get tearing modes by ECCD was to vary the deposition location during the shot; placing the ECCD at a fixed location and power, irrespectively of the deposition location, often did not trigger any modes. One should remember the original Swing-ECCD experiments which motivated these studies: in these experiments, the driven current profile was

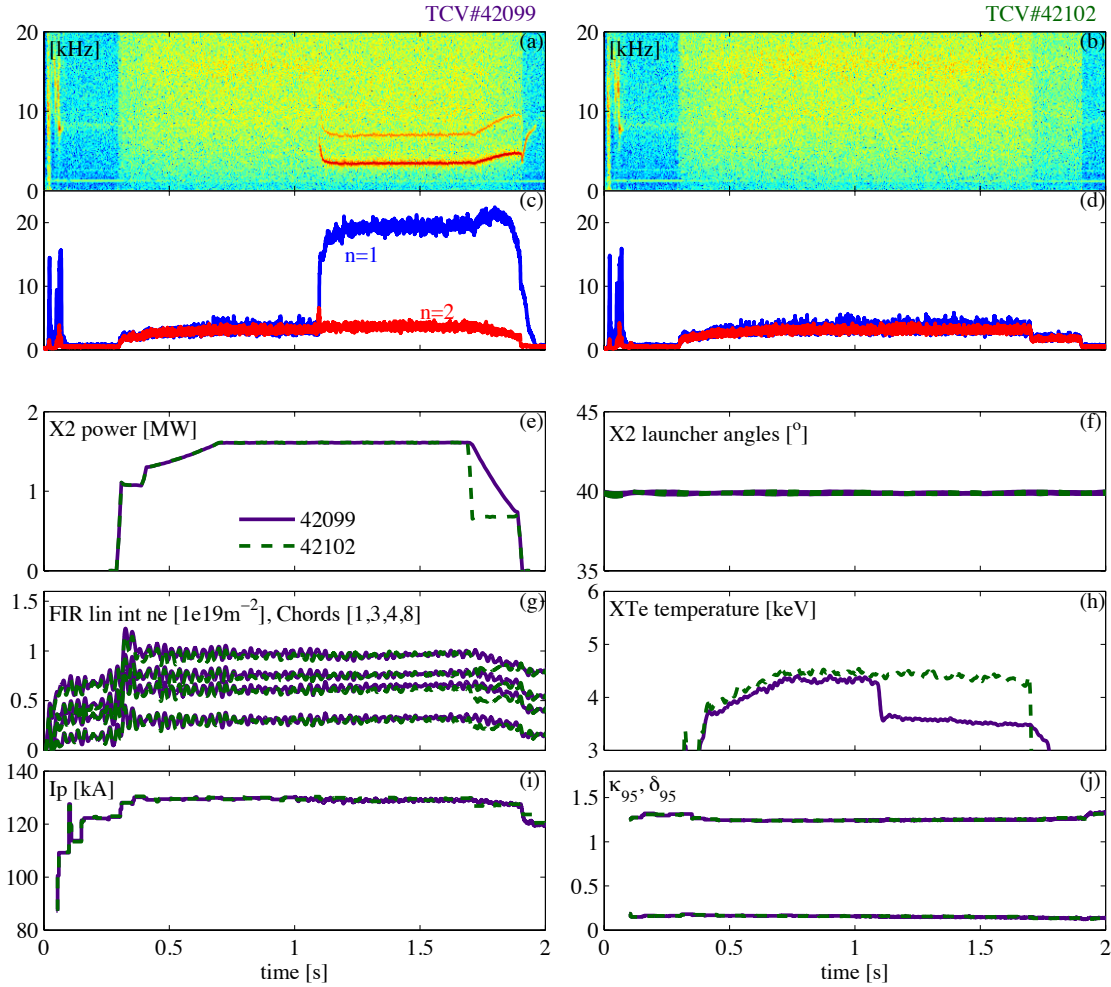


Figure 4.5: Two identically programmed shots, executed during the same experimental session. The first shot (TCV#42099, (a), blue) develops an NTM $t \approx 1.1$ s. The second (TCV#42102, (b), red) is identical in almost all respects, but no NTM is present. The only difference is a slight difference in temperature, probably due to different impurity content due to evolving wall conditions. Signals have been smoothed for clarity.

also transiently varying and NTMs were repeatedly triggered. This leads to the suspicion (which cannot be substantiated at this point) that the transience of the profiles somehow plays a role in the formation. Thus stationary profile states (at least in the TCV plasmas studies) are mostly stable to NTMs. However during their evolution towards a stationary state, they may or may not pass through a region in which the NTM is unstable. Physically, many effects could provide such a mechanism: Δ'_0 effects related to the current density profile derivative, but also effects related to the polarization term via (e.g.) poloidal currents, poloidal rotation, or others.

With such a complex formation mechanism, and with experimental results being determined by parameters of which the experimentalist has little control (e.g. the wall condition – despite inter-shot wall cleaning), systematic characterization of triggering conditions appears prohibitively difficult. This difficulty is not unique to TCV: similar

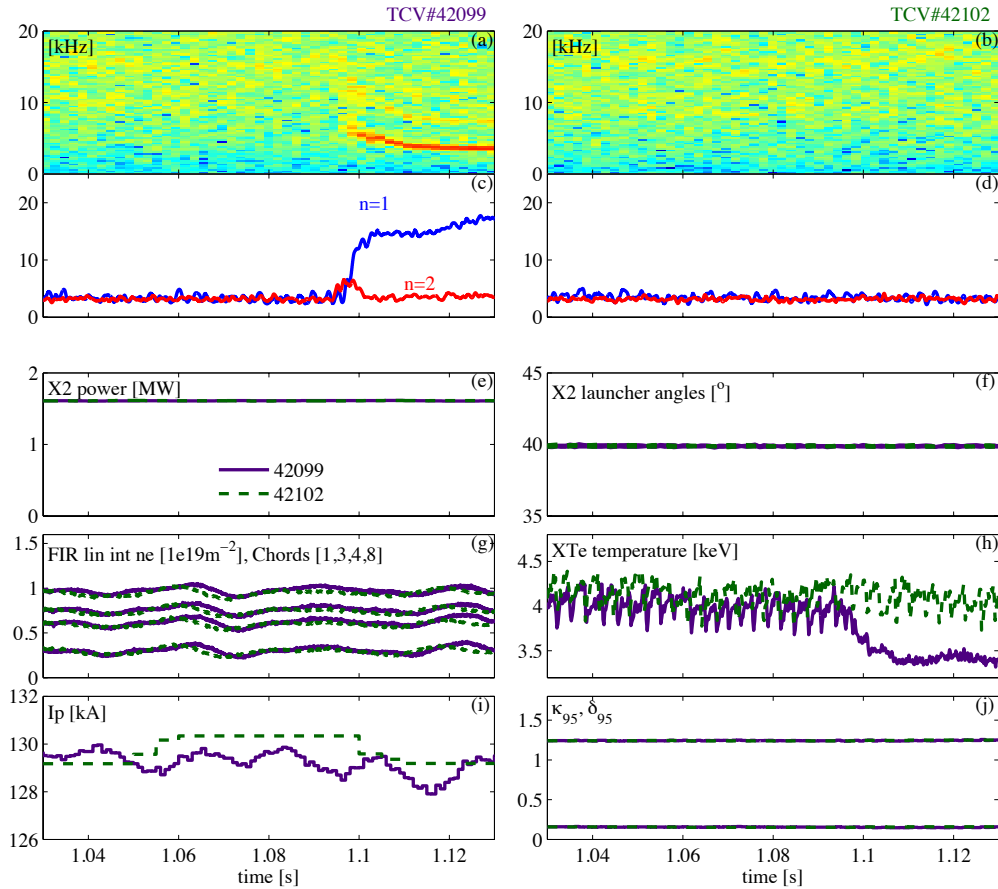


Figure 4.6: Zoom on the period when the NTM is triggered. $n = 2$ mode grows before $n = 1$ mode, and the sawteeth (h) that are present disappear. The I_p data was available at a different sampling rate for the two shots, but both had similar oscillations.

difficulties were encountered, for example, in (Turco et al. 2010), which also confirmed the role of the current density profile evolution on several current redistribution time scales. In subsequent experiments, therefore, focus was shifted to studies of NTM stabilization using ECRH/ECCD system, discussed in the next section.

4.4 Stabilization of NTMs in plasmas with ECCD

This section presents some NTM stabilization experiments carried out on TCV. Before proceeding, existing NTM control experiments on tokamaks around the world are briefly reviewed. Then, stabilization experiments in ECCD-dominated TCV plasmas will be discussed, concluding with modified Rutherford equation modeling of stabilization experiments.

4.4.1 Overview of NTM stabilization and preemption experiments on other tokamaks

ECCD stabilization of saturated NTMs was shown more than a decade ago in ASDEX-Upgrade experiments (Zohm et al. 1999), (Gantenbein et al. 2000). Since then, similar experiments have been repeated on many tokamaks, focusing on different aspects of the stabilization. ASDEX-Upgrade experiments focusing specifically on the effect of ECCD power modulation with respect to the island O and X point (Maraschek et al. 2007), (Zohm et al. 2007) have demonstrated that for a large ECCD deposition width with respect to the marginal island size the NTM stabilization efficiency can be improved by using modulated power.

These results have been confirmed by results obtained on JT-60U, starting from (Isayama et al. 2000) where complete suppression of an NTM in a high- β plasma was demonstrated. Additionally, using EC launcher angle steering, a destabilization of an existing island is shown due to misaligned ECCD (Isayama et al. 2007) and, as summarized in (Isayama et al. 2009), destabilization of a pre-existing island by X-point modulation has been observed as well as an enhancement of the ECCD stabilization efficiency by a factor 2 when modulating in the O-point.

Experiments on the DIII-D tokamak have addressed the onset and stabilization of 2/1 NTMs which are a key factor limiting the performance of high- β_N hybrid scenario (Petty et al. 2004a), (Petty et al. 2004b). Suppression algorithms have been developed (Humphreys et al. 2006) which are capable of searching and locking to the optimal conditions for NTM suppression, as well as preemptively applying ECCD to reach higher-beta operation (La Haye et al. 2005), (Prater et al. 2007). Later work (Volpe et al. 2009) combines an oblique-ECE diagnostic, viewing the island through a similar optical path through the plasma as the EC beam from the launcher, with EC power modulation, as well as active magnetic control of the toroidal phase of locked islands using non-axisymmetric coils to steer a locked mode to the appropriate location for stabilization by localized ECCD on the O-point. Experiments on DIII-D and ASDEX-Upgrade have, to date, relied on varying the toroidal field or the plasma position to change the ECCD deposition location with respect to the rational surface, and have not used real-time launcher angle steering as an NTM control parameter.

Work on the FTU tokamak (Berrino et al. 2005) shows development of a real-time control system incorporating multi-channel ECE data to detect the opposite-phase T_e oscillations characterizing an island position. Recent work on TEXTOR (Hennen et al. 2010) demonstrates a complete line-of-sight ECE method for NTM suppression, where the ECE signal used to detect the mode is obtained from the same physical beam line as used by the injected EC power. While this is technically challenging since it requires separating the (MW level) EC beam from the mW ECE signal, it has the advantage that alignment is automatically achieved without needing to rely on real-time equilibrium reconstruction and real-time ray-tracing. On the other hand this method is only applicable when the island is already formed, and requires an alternative method to determine the EC deposition appropriate for NTM preemption.

Specific application of an NTM control scheme for disruption avoidance, i.e. stabilizing a mode before it locks to the wall, has been shown recently in ASDEX-Upgrade experiments (Esposito et al. 2011).

These experiments have given confidence in predictions of NTM control strategies applicable for ITER, and have been used as a basis for designing the ITER ECH system (Zohm 2006), (La Haye et al. 2006), (Ramponi et al. 2008), (La Haye et al. 2009), (Sauter et al. 2010).

4.4.2 Stabilization with EC deposition on the outside and inside of the mode location

Based on the NTM triggering experiences described in the previous section, NTM control experiments were done on TCV in an attempt to verify existing NTM stabilization strategies and to explore routes for further detailed studies.

Real-time launcher angle control experiment

An essential requirement for an NTM control system is to be capable of depositing EC power on the island by moving the EC deposition location. This was tested successfully on a 2/1 NTM, destabilized in plasmas described by Section 4.3. Note that the mode location is not directly measured in these experiments. Instead, it is inferred indirectly by the effect that the applied ECH/ECCD has on the island width. This is similar to the search-and-suppress approach shown in (Humphreys et al. 2006). Upon detection of the mode, the deposition location of one of the gyrotrons responsible for creating the mode was first rapidly moved to a more off-axis location of $\rho \sim 0.7$ (the bulk of ECCD power was at $\rho = 0.3$). According to previous equilibrium reconstruction and ray tracing calculations, this corresponds to EC deposition just inside of the $q = 2$ surface location. The deposition location was then changed by sweeping the EC launcher angle, slowly moving across the mode towards the plasma surface. The resulting reduction in island size, and subsequent full suppression are shown in Figure 4.7(left). When the island disappearance is detected, the launcher angle is kept constant, hence the denomination “Scan and stop” for this control algorithm.

In a second experiment, the gyrotron power was switched off upon detection of the mode, and the angle was rapidly moved to a setting corresponding to a deposition location closer to the plasma edge than the mode. The power was then switched on again and the deposition location was slowly swept towards the expected mode location. When the island was stabilized (as detected from the magnetic signals), the launcher angle was again held constant. This sequence of events is illustrated in Figure 4.8 and the resulting island time-evolution is shown in Figure 4.7(right).

In Figure 4.9, the deposited EC power densities from both shots are combined to show the relative movement of the deposition location. The final deposition location for both EC beams is within one half beam width - illustrating that the tearing mode stabilization truly occurs when heating within the island and providing an experimental measurement of the island location.

Not only does this experiment validate previously investigated NTM stabilization approaches on TCV; it also shows a rare practical demonstration of 2/1 tearing mode stabilization by launcher angle steering, a feat that few tokamaks have demonstrated so far and that the ITER control system must also be able to accomplish routinely.

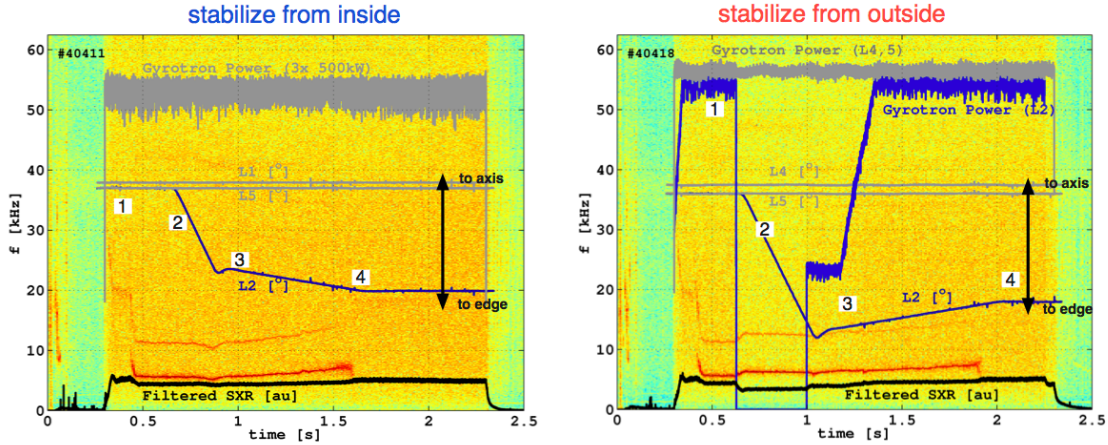


Figure 4.7: Stabilization of NTMs by sweeping the ECCD deposition location towards the island from both inside (left) and outside (right). An NTM is first created by three gyrotrons (total 1.5MW) injecting co-ECCD at approximately $\rho = 0.3$ (1). Some time after the magnetic island is detected, one of the launchers is moved towards the location of the island (2) and then slowly scanned towards the expected location (3). When the mode disappears, the angle is held constant (4). Note that when stabilizing from the outside (right panel) the gyrotron power is temporarily switched off to allow the launcher angle to go to the requested location without depositing power on the island. That in both cases the final angle stops just before reaching $\theta_L = 19^\circ$.

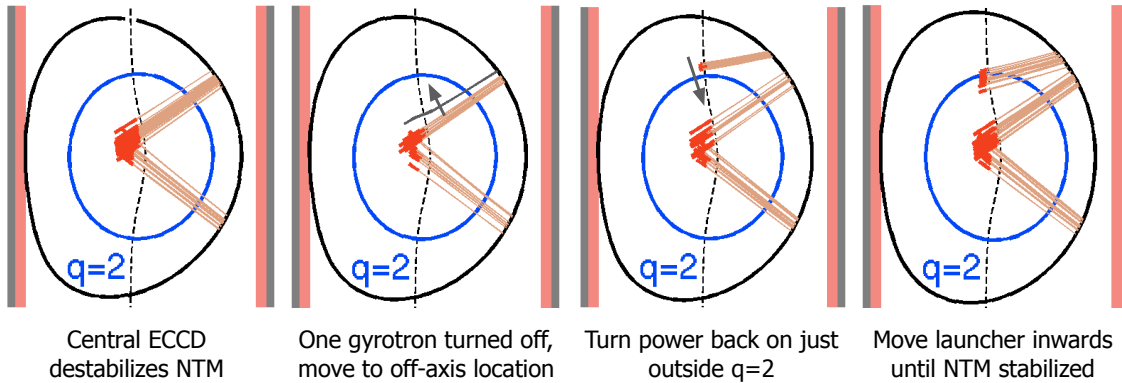


Figure 4.8: Sequence of EC ray aiming for NTM stabilization experiment shown in Fig.4.7 (right). The gray ray indicates the power is off during this phase, as the aiming moves across the mode surface to deposit power to the outside of the mode. EC ray paths were calculated using the TORAY ray-tracing code.

4.4.3 Stabilization efficiency dependence on β and ECCD

As explained in Section 4.2.3, for islands with negative Δ'_0 the MRE predicts a β -dependent stabilizing power above which the mode fully self-stabilizes – its size rapidly shrinking to zero. To investigate this, angle sweeps across $q = 2$ with fixed power, similar to those shown in the previous section, were carried out on plasmas with different β . This was achieved by stepping down the central ECCD power after the NTM is detected, waiting for a few confinement times for the β to decrease, and subsequently observing the time evolution of the island size while a separate EC beam was swept across the mode location. Note that the reduction in ECCD power also has an effect on the current density

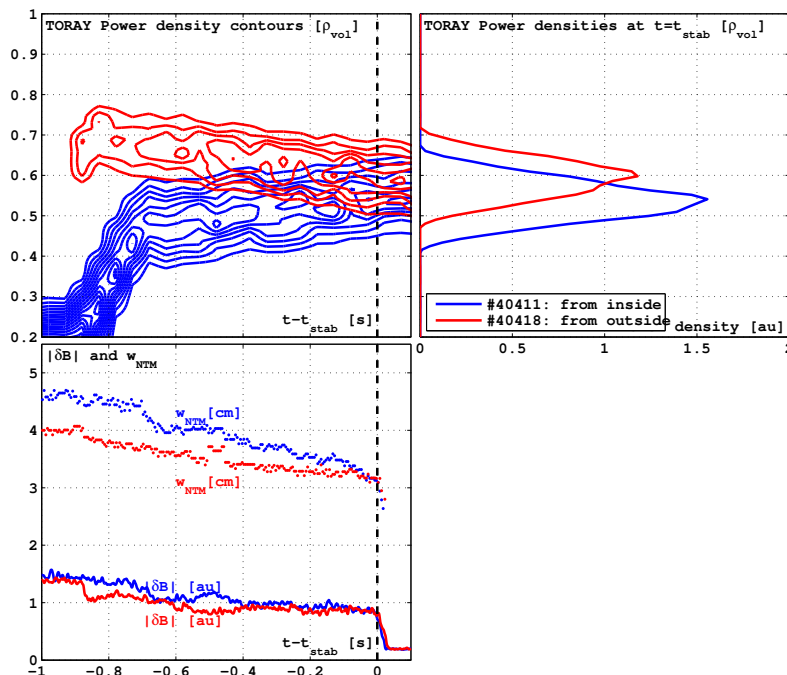


Figure 4.9: EC power density evolution as calculated by TORAY for the two shots shown in Figure 4.7. Also shown are the time evolution of the magnetic perturbation signal and magnetic island width. Notice that for both cases the island is completely stabilized when the island size reaches $w = 3.1\text{cm}$, so this is the marginal island size for these NTMs. The power densities at the time of the NTM stabilization are also shown, which can be seen to be approximately 1/2 beam width of each other. Also notice the larger w_{NTM} when the power is inside of the island rational surface and the β is therefore higher.

profile, of course, apart from its main effect on β .

The experimental results are shown in Figure 4.10. From the top-left panel, one can see that the mode amplitude settles to different sizes at $t = t_{NTM} + 0.1\text{s}$, corresponding to the different level of loss of the pressure-dependent bootstrap drive. Also shown are the T_e profiles (fits of Thomson scattering measurements) at the different times, as well as the TORAY-computed driven current densities. Note that the off-axis current drive contribution from the EC deposition near $q = 2$ is very small due to the small toroidal angle used in these experiments. It is therefore expected that current drive plays a small role in the NTM stabilization for these plasmas and that EC heating effects should be primarily considered.

Clearly, a different minimum island size is reached depending on the amount of central power. The red and green curves in the top-left panel of Fig.4.10 correspond to cases where the marginal island width is not reached and the mode is not fully stabilized. The blue and violet curves show two cases where power is sufficient for full suppression even though the deposition location has not yet been moved close to the island. One can also notice the small initial difference between the violet and green cases (TCV#41576 and TCV#41577, $t - t_{NTM} = 0.1$) but the subsequently very different time evolution of the island: in the violet case the island is rapidly extinguished whereas it persists in the green case. These two cases will now be further studied and modeled.

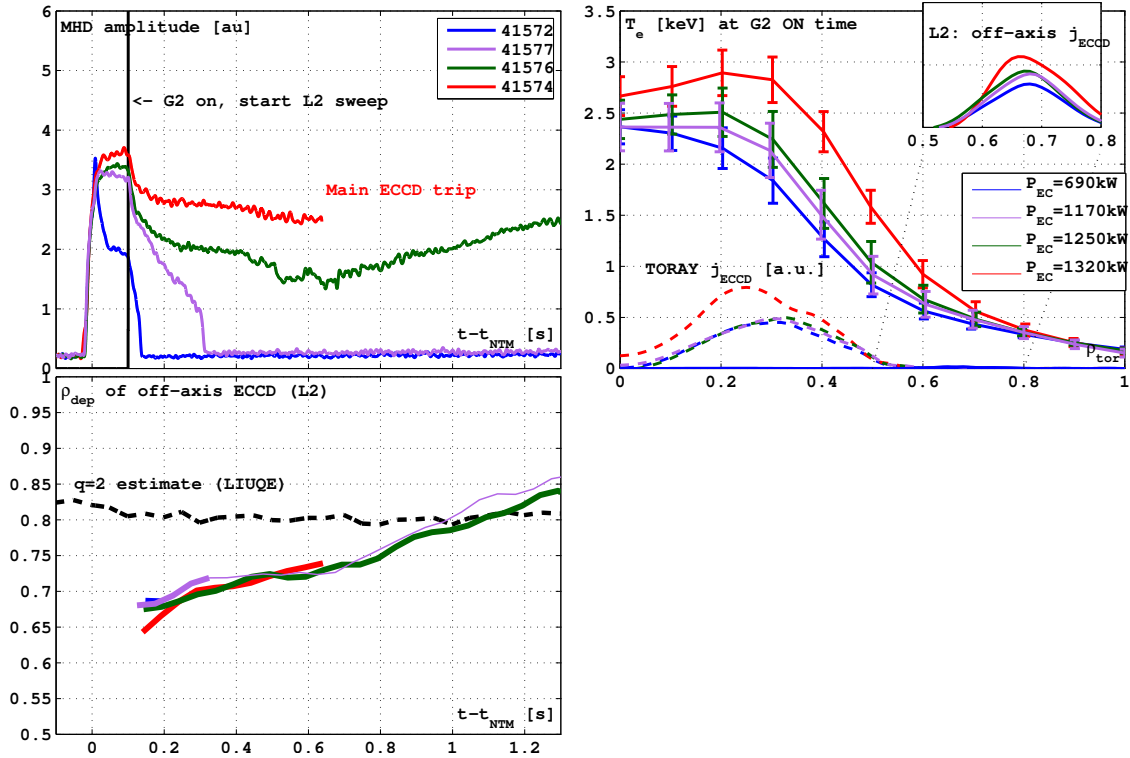


Figure 4.10: Several TCV shots in which the (near-central) ECCD power is reduced to different levels following the NTM appearance. A scan of ECCD power across the island is then executed with a separate gyrotron. Depending on the central power a different T_e i.e. different β is obtained which results in islands which are more or less resilient against stabilization attempts.

Modeling using the Modified Rutherford Equation

The examples above are also an excellent test case for modeling the effect of ECH on the island. For this purpose, a reduced form of the MRE was implemented, where only the main dependence of the various terms on w and β_p is retained. The objective of this exercise is to verify to what extent the TCV NTMs can be modeled using the MRE. A more exhaustive and systematic study is left as future work.

The simplified model has the form

$$\frac{\tau_r}{r_s} \frac{dw}{dt} = r_s \Delta'_0 + r_s \Delta'_{bs} + r_s \Delta'_{ggj} + r_s \Delta'_H \quad (4.20)$$

where the polarization term has been neglected, although it may play a role in the small island physics, it is not needed to explain most experimental observations, which is fortunate since it is extremely sensitive to the chosen model parameters and since it is not strictly needed to get qualitatively correct modeling results. The ECCD term has also been neglected since, as was mentioned, the toroidal injection and driven current is small. Due to the difficulty in modeling Δ'_0 based on first-principles, a simplified form from (Sauter et al. 1997) is used.

The various contributions are written as

$$r_s \Delta'_0(w) = \Delta'_0(0) - \alpha w, \quad (4.21)$$

$$r_s \Delta'_{bs}(\beta_p, w) = r_s a_{bs} \beta_p \frac{w}{w^2 + w_d}, \quad (4.22)$$

$$r_s \Delta'_{ggj}(\beta_p, w) = -r_s a_{ggj} \beta_p \frac{1}{\sqrt{w^2 + 0.2w_d^2}}, \quad (4.23)$$

$$r_s \Delta'_H = -r_s a_H P_{gyro}(t) F_H(w, w_{dep}, x_{dep}). \quad (4.24)$$

The function F_H , which defines the efficiency of localized heating depending on deposition width w_{dep} and deposition location x_{dep} with respect to the island, is taken from (De Lazzari et al. 2009), (Lazzari et al. 2010), choosing $w_{dep} = 1.5\text{cm}$ based on the TORAY power density. The free parameters of this model are $\Delta'_0(0)$, α , w_d and (a_{bs}, a_{ggj}, a_H) . Although first-principle equations exist which define many of these equations, this modeling was carried out by fitting these parameters to the time-evolution of the island width in time. Note also that the local profile effects L_p , L_q etc. are not taken into account.

One particular case, corresponding to the green curve in Figure 4.10, is shown in Figure 4.11. The gyrotron power $P_{gyro}(t)$ is taken from experimental measurements and the time evolution of $x_{dep} = r - r_{dep}$ is modeled as a linear dependence in time $x_{dep} = 0.15a(t - 1.2)$ where $a = 0.25\text{m}$ is the minor radius. This is based on the TORAY deposition location calculations in Fig.4.10c, assuming the island and EC deposition are aligned at the time of minimum island width. Note that this corresponds to a location slightly to the inside the LIUQE $q = 2$ surface location. This can be explained either by an island asymmetry effect or by a poor localization of the $q = 2$ surface location by the equilibrium reconstruction. A similar mismatch was observed in interpreting recent ASDEX upgrade experiments (Esposito et al. 2011).

The instantaneous island width is calculated based on the square root of the magnetic fluctuation amplitude as measured by one Mirnov signal, and has been scaled to match a separate reconstruction of the island width based on fitting a helical current perturbation to multiple magnetic measurements over a short time window. The poloidal beta (β_p) is taken from the LIUQE equilibrium reconstruction code. The free parameters in the MRE terms (4.21)-(4.24) are determined from a nonlinear fit of the experimental evolution of the island amplitude in time. Smoothing was applied where appropriate to remove measurement noise.

Figure 4.11 shows several distinct phases in the experimental island width evolution which are well reproduced by the modeling. Fig.4.11a shows the time evolution of experimental and simulated island size which qualitatively and quantitatively agree. Also β_p is shown, which visibly decreases at $t = 0.6\text{s}$ due to the appearance of the island and increases at $t = 0.7\text{s}$ when the off-axis gyrotron is switched on. At $t = 2.2\text{s}$ the auxiliary power is removed completely causing a sharp decrease in β_p and disappearance of the island on the confinement time scale $\tau_E \sim 1\text{ms}$, confirming the Neoclassical nature of the island. Fig.4.11b shows the time evolution of the various contributions of the right hand side of (4.20). The stabilizing contribution of Δ'_H is clearly visible, as well as the final stabilization due to the drop in the Δ'_{bs} term. The rightmost panels contain further information about the contributions of the various MRE terms at different interesting times during the plasma evolution. The saturated island size $w_{sat} = 5\text{cm}$ is shown in

Fig.4.11c where the black curve, representing the total dw/dt as a function of w , passes from a positive to negative value. The addition of the Δ'_H term causes the curve to shift down as shown in Fig.4.11d, reducing the saturated island size to $w = 3.6\text{cm}$. At $t = 2.2$, as shown in Fig.4.11e, the (red) bootstrap contribution halves therefore the total curve drops below 0. In this case the NTM is stable for any island size and the island width is quickly reduced. Finally Fig.4.11f shows the phase diagram of the time evolution of w and dw/dt , also showing relatively good agreement.

Some remarks are in order regarding effects which were intentionally neglected, but which may play a role. Firstly, the evolution of the profile terms L_p , L_q , L_{bs} etc, which appear in the full form of the MRE terms (4.16), (4.18), are not taken into account in this simplified modeling, while they will certainly vary as a result of the angle scan and do not appear in global terms through β_p . Furthermore, the Δ'_0 dependence on the profiles themselves is not taken into account, though it is expected to have a different effect when on the outside or on the inside of the island as originally predicted in (Westerhof 1990). Thirdly, comparing the experimental and simulated island evolutions in Fig.4.11a one notices the excessive effect of the EC power switch-off and switch-on on the island size. The simulated behavior shows rapid shrinkage and growth, of the island due the power addition and removal to be a Δ'_{bs} effect. However, in the experiment the effect seems to be smaller and less rapid indicating that unmodeled effects play a role.

In a second step, we attempt to validate the parameter values for the MRE terms obtained by fitting experimental data shown in Figure 4.11 (TCV#41576), by simulating a different shot (TCV#41577, corresponding to the violet curve of Fig 4.10). The result is shown in Figure 4.12. As can be observed from Fig. 4.12(a), the experiment shows a slow decrease of the drive between 0.8s and subsequent self-stabilization, which is not reproduced by the simple MRE simulation. This can simply be attributed to the fact that the difference in the experimentally determined β_p is very small between the two plasmas, and as all other parameters are kept the same there simply is no term in the model explaining the different island behavior.

The slow evolution of the mode, uncoupled from β_p , leads one to assume that localized profile effects due to L_p , L_q or L_{bs} are responsible. In previous work, it was also found necessary to include these terms to get satisfactory fits (Maraschek et al. 2003), (Koslowski et al. 2001), (La Haye et al. 1998). Qualitatively correct fits require accurate transport model reconstructions, which were not attempted in the scope of this study.

| TCV shot # | Figure | a_{bs} | a_{ggj} | a_H | w_d | Δ'_0 | α |
|------------|-----------|----------|-----------|-------|--------|-------------|----------|
| 41576 | 4.11,4.12 | 40.8 | 10.4 | 0.27 | 0.0331 | -29.7 | 795.6 |

Table 4.1: MRE Parameters for equations (4.21)-(4.24), obtained from a nonlinear optimization algorithm attempting to minimize the difference between experimental and simulated time evolution of the island width.

4.4.4 Observation of “fuzzy” marginally stable islands

The shot corresponding to the green curve in Figure 4.10 has an island evolution which comes very close to the marginal island size. When examining the time evolution of the magnetic signals more closely, an interesting phenomenon is observed, which is illustrated

4.4. Stabilization of NTMs in plasmas with ECCD

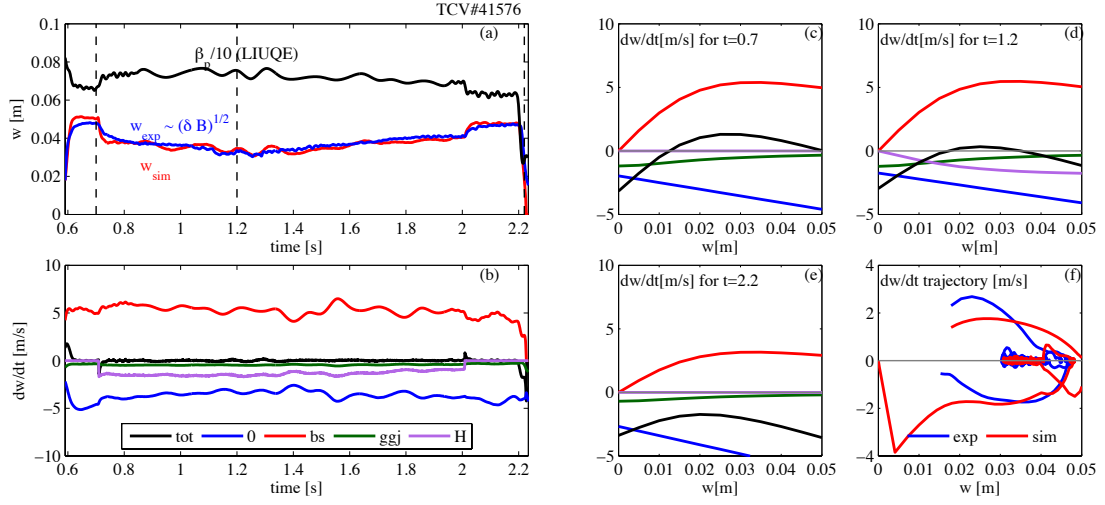


Figure 4.11: Modified Rutherford equation modeling of an evolving NTM, under partial stabilization by an ECH sweep across the island location. The EC power is insufficient to stabilize the island entirely, but the marginal island size is almost reached. The time evolution of experimental and simulated NTM width are shown (a), as well as the contributions of the various Δ' terms (b). Some plots of the $\Delta'(w)$ dependencies at different times of interest are shown in (c),(d),(e). Finally (f) shows the phase diagram of the island width evolution. The parameter values from the nonlinear optimization routine are listed in Table 4.1.

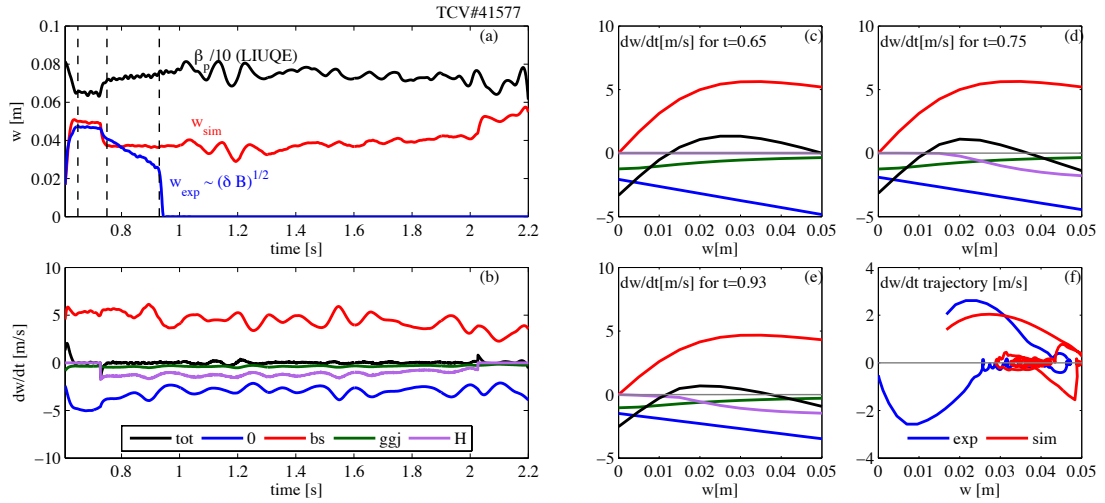


Figure 4.12: Fit of a different TCV shot with the same MRE model parameters as Figure 4.11. Clearly, the gradual decline and early stabilization of the mode at $t = 0.95$ s is not well reproduced. The gradual decline, without corresponding decrease in β_p , can most likely be attributed to unmodeled profile effects .

in Figure 4.13. When approaching the marginal island size, the frequency of the magnetic oscillation becomes less well defined. This is witnessed both by the spread in the power spectral density (top panel spectrogram and insert), and by computing the zero crossing times of the filtered magnetic signals. When examining the magnetic signals themselves in more detail, one can see that the signals transform from steady, coherent oscillations

(bottom panel, blue trace) to unsteady, variable-frequency oscillations (bottom panel, red trace). With hindsight, one can see that a similar spreading in frequency also occurs just before stabilization in the islands shown in Figure 4.7. This phenomenon has been observed very often in similar TCV experiments. If repeatable on other experiments, this observation may provide a practical additional diagnostic to infer proximity to the marginal island size.

Furthermore, if confirmed, the irregular nature of these oscillations may pose constraints on the signal-processing technique used to track the island phase during O-point ECCD power modulation experiments. The PLL (Phase-Locked-Loop) method used here (see Section B.6) was able to successfully track the NTM signature even in this “fuzzy” phase, but windowing techniques such as Fourier decomposition may have problems. This could be particularly troublesome since this may lead to a loss of stabilization efficiency when the island is small (when modulation is important) and just before reaching the marginal island size, smaller than which full self-stabilization is obtained.

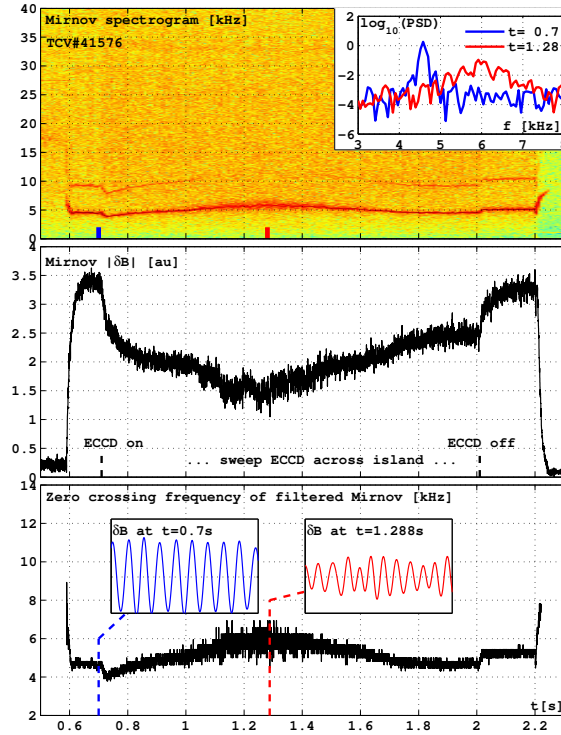


Figure 4.13: Observation of “fuzzy” NTMs when the island size is near the marginal island limit. The broadening of the frequency spectrum is apparent in the PSD (insert) at the two indicated times (blue/red). Note that the broadening occurs at signal amplitudes that are still well above the noise floor. Bandpass filtered time traces (lower panel) show the unsteady nature of the oscillations.

4.5 Sawtooth - triggered NTMs in low q_{95} TCV plasmas

As mentioned earlier in this chapter, one of the mechanisms for NTM destabilization, and the one most commonly observed in H-mode inductive scenarios, is a sawtooth crash. In (Chapman et al. 2010), it was shown that the β threshold for NTMs is lower for

longer period sawteeth, and sawteeth in ITER are expected to be long due to α particle stabilization.

In Section 3.2, a method was presented to precisely control the period of the sawteeth in TCV. It is natural, therefore, to use this control method to investigate the coupling between sawteeth and NTMs and under which condition NTMs are formed after a sawtooth crash.

This section will show experimental results of controlled lengthening of sawteeth by the sawtooth pacing method, and classification of ensuing MHD activity. Then, it will be shown how the post-crash MHD activity can be reduced by applying ECH on the rational mode location, hindering the formation of NTMs for a given sawtooth period. This technique is an important demonstration of using preemptive EC power to prevent the formation of an NTM, as alternative to stabilizing it once it has already formed.

4.5.1 NTM triggering by stabilized sawteeth

The plasmas used in the experiments shown in this section are of a different nature than those in the earlier part of this chapter. Here, plasmas are of the same type as those presented in Section 3.2, with low $q_{95} = 2.4$ and large $q = 1$ radius ($\rho \approx 0.5$). ECH and ECCD is applied near the (high-field-side) $q = 1$ surface (see Fig.4.18), at the correct location to get long stabilized sawteeth. The sawtooth pacing technique is applied (Goodman et al. 2011), temporarily switching off the EC power at a fixed time interval after each sawtooth crash, in order to trigger the crash at a given time.

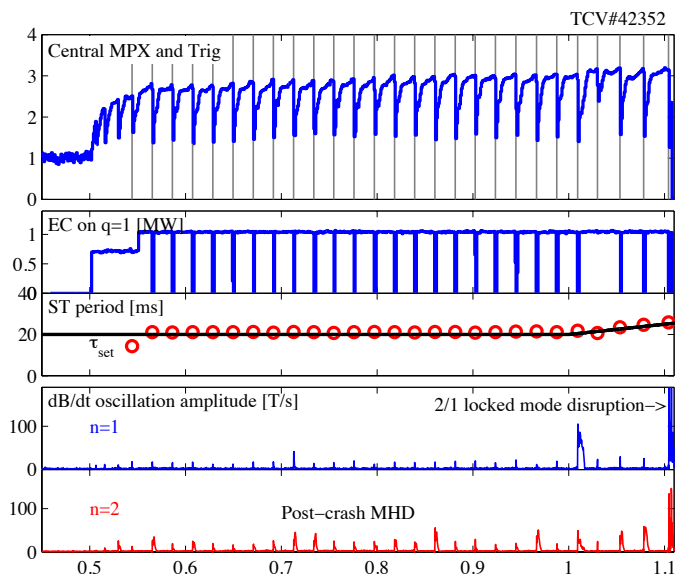


Figure 4.14: Example of sawtooth pacing shot with frequent post-crash MHD activity which disappears after a short time. Towards the end of the discharge, the sawtooth period is increased, causing more frequent and longer-lived post-crash MHD activity, until a 2/1 locked mode causes a disruption.

A first set of experiments was performed to explore eventual NTM behavior. A representative example is shown in Figure 4.14. This shot features regular sawteeth with a period of ~ 21 ms. From analysis of several toroidal harmonic components of the magnetic probe signals, it is apparent that some MHD activity follows each sawtooth crash. In this

particular shot, the sawtooth period was increased at the end of the shot, and the MHD activity and its longevity increases. When the sawtooth period exceeds 25ms, a $2/1$ mode is destabilized which immediately locks to the wall error field and causes the plasma to disrupt.

More detailed examples of post-crash MHD behavior are shown in another set of figures. Figure 4.15 shows another shot with regular 21ms sawteeth, in which alternating $n = 2$ and $n = 1$ post-crash modes dominate. For example, at $t = 1.065$ and $t = 1.17$, a long-lived $n = 2$ mode is visible, while at $t = 1.085$ and $t = 1.15$ the $n = 1$ component dominates and less $n = 2$ activity is visible. Detailed magnetic analysis, presented in (Canal 2011), shows that one or the other mode will dominate depending on the relative phase velocity of the modes just after the crash. After some time the modes may lock to each other in phase. Typically, if this locking occurs rapidly, within 300ms, the $2/1$ mode will dominate. If it occurs later, the $3/2$ mode will dominate.

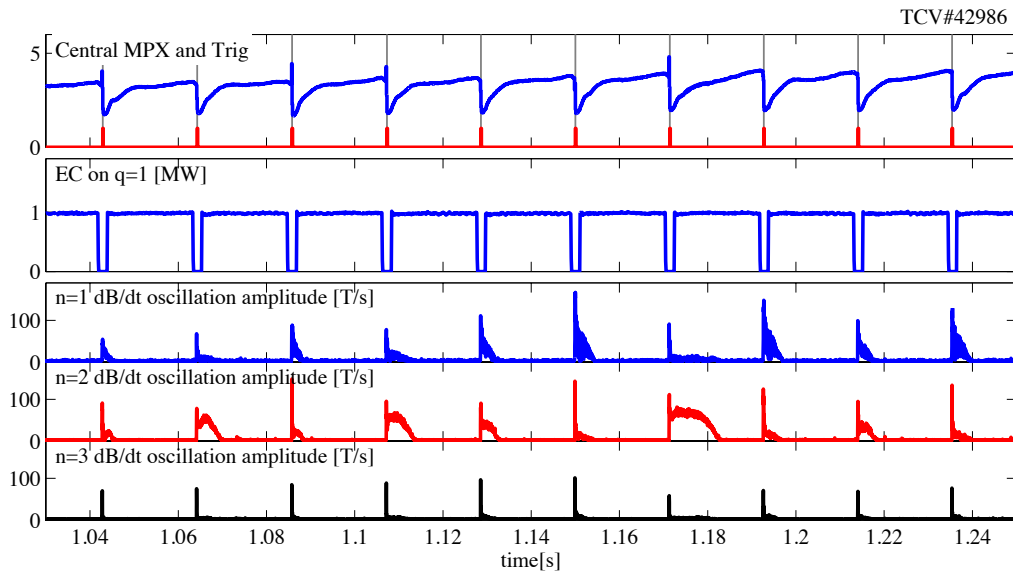


Figure 4.15: Typical evolution of post-crash MHD behavior occurring at otherwise similar stabilized sawteeth. In some cases the $n = 2$ component dominates but disappears rapidly. In other cases the $n = 1$ component is seen to dominate and the $n = 2$ contribution is smaller.

Figures 4.16 and 4.17 show two examples of the long-term evolution of the $3/2$ mode. This mode may either spontaneously disappear at the next sawtooth crash, or temporarily drop in size. The reduction in size is correlated to the appearance of an $n = 3$ toroidal component, indicating the presence of a $4/3$ mode. This suggests that a $4/3$ mode interacts nonlinearly with the $3/2$ modes, extracting some of its energy. This is reminiscent of the interaction between $3/2$ and $4/3$ modes reported on JET (Sauter et al. 2002b), JT60-U (Isayama et al. 2007) and the “FIR-NTM” (Frequently Interrupted Regime - NTM) on ASDEX-Upgrade (Maraschek et al. 2005).

If, on the other hand, the $n = 1$ component dominates, the plasma rapidly disrupts due to a locked $2/1$ mode. Note that this is a consequence of the choice of a low q_{95} , putting the $q = 2$ surface physically close to the wall. Other experiments (not shown here) with higher q_{95} were less susceptible to $2/1$ locked mode disruptions, and disruptions were

completely absent for $q_{95} > 3.5$ (Canal 2011).

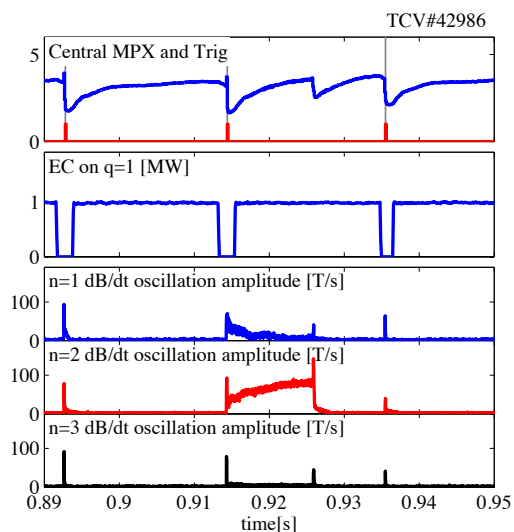


Figure 4.16: Example of a $3/2$ tearing mode appearing after a large sawtooth crash, but being stabilized at the next (smaller) sawtooth crash.

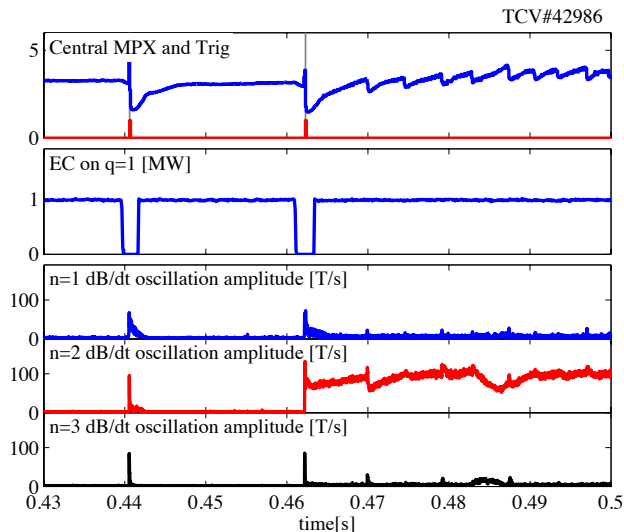


Figure 4.17: Example of a $3/2$ tearing mode appearing following a sawtooth crash. Note how the presence of post-crash $n = 3$ activity (e.g. $t = 0.47s$, $t = 0.483s$) correlates with a decrease of $n = 2$ amplitude. This is due to a $4/3$ mode interacting with the existing $3/2$ mode.

4.5.2 Preemption and suppression of sawtooth triggered NTMs

One of the motivations behind sawtooth pacing was that there is an advantage to knowing in advance when the seeding event for the NTM is likely to appear. This knowledge can then be used to take appropriate measures to prevent the seed island from growing into a fully formed NTM.

Simultaneous sawtooth pacing and NTM control

Using the TCV X2 system flexibility and the new control system, the sawtooth pacing controller (Section 3.2) was combined with an NTM controller (Section 4.4).

The ECH system configuration for this series of shots is shown in Figure 4.18. Sawtooth pacing with $\tau_{set} = 20ms$ is used in these experiments, yielding regular sawteeth with periods of approximately 21ms. This is done by two gyrotrons aimed close to the $q = 1$ surface.

Additionally, a separate gyrotron, aimed to deposit power at or near the location of the $q = 3/2$ surface, is programmed to briefly fire at the time when the “pacing” gyrotrons (near the $q = 1$ surface) switches off. This way, when the next sawtooth crash appears, power is being deposited at the location where the NTM might grow. The time interval during which this power is deposited can be varied, generally an interval longer than the typical decay time of post-crash MHD is chosen (typically $\sim 5ms$).

Separately, NTM suppression is triggered when MHD activity is present for a long enough time (to avoid triggering on short lived post-crash activity). In NTM suppression

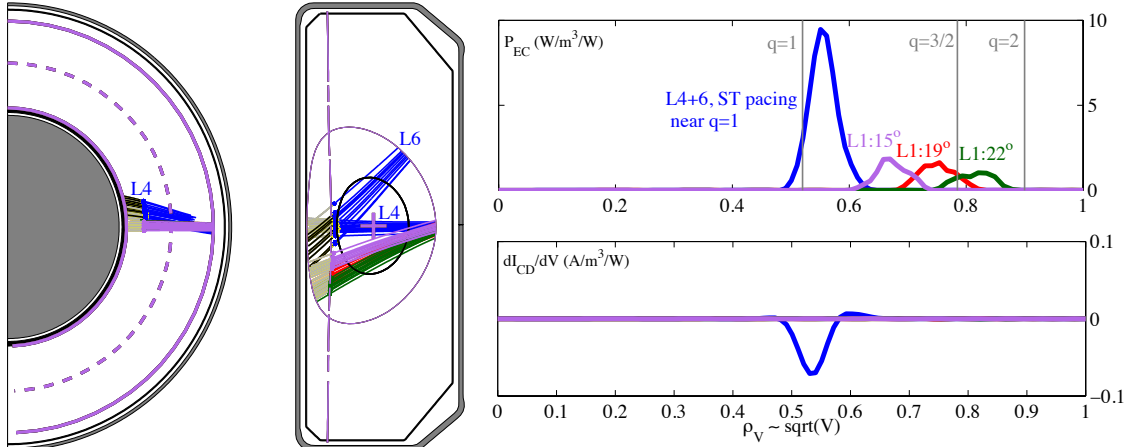


Figure 4.18: EC system and plasma set up for combined sawtooth pacing – NTM stabilization and preemption experiments. Launchers 4 and 6 (blue) were used for sawtooth pacing by deposition power near the $q = 1$ surface. Launcher 1, which can be individually controlled in power and angle, is used for off-axis heating (no ECCD) near the $q = 3/2$ surface.

mode, once a persistent mode is detected, the power of the pacing gyrotrons (L4+L6) is kept at its maximum value continuously, until the NTM disappears. In this case, the launcher is pre-aimed at the $3/2$ surface, or, alternatively, the launcher angle can be scanned towards the expected mode location as previously done in Section 4.4.2.

Note that with the present EC configuration setup it is also possible to deposit power on the $q = 2$ surface, which would extend the present experimental work to the important topic of $2/1$ mode preemption and stabilization. The low absorption at these far off-axis $q = 2$ locations and associated operational complications precluded the continuation of these studies within the time-frame of this thesis.

NTM preemption by pulsed EC power

Figure 4.19 shows a series of shots to test the effectiveness of preemptive EC power on the $3/2$ surface.

Proceeding from left to right, the first shot shows a baseline example in which no preemptive power was applied: the gyrotron aimed at the $3/2$ surface was activated only once NTMs had been triggered. The appropriate angle aiming was determined by ray tracing and experimentally, as will be shown next later. As can be observed, $3/2$ NTMs are occasionally destabilized and the gyrotron fires consequently. The $3/2$ mode repeatedly appears and disappears, but we can not conclude whether this is due to applied EC power or to the interaction with sawteeth (cf Figure 4.16 with its spontaneous $3/2$ mode disappearance).

The shot shown in the middle column shows an example where 200kW of EC power is preemptively deposited on the $3/2$ surface for up to 7ms after each crash. This does not lead to a reduction of the NTM activity. However, as soon as the preemptive power is removed (at $t = 1.3$ s) a $2/1$ locked mode disruption terminates the plasma. It should be noted that the density was increasing during this shot (as visible in the MPX trace) due to particle pump-in effects of the $3/2$ mode (this is not well understood). This may

4.5. Sawtooth - triggered NTMs in low q_{95} TCV plasmas

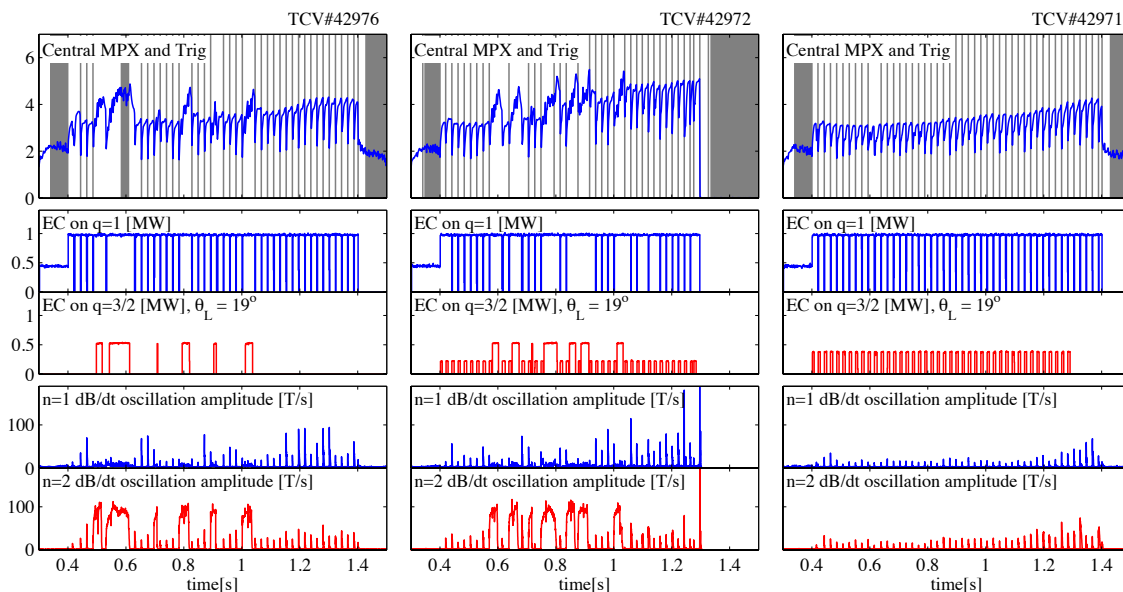


Figure 4.19: Preemptive NTM stabilization experiments during sawtooth pacing by gyrotron on $q = 1$. Left: no preemptive power is injected, and only NTM stabilizing power is injected on the 3/2 surface when MHD activity is detected. Center: 200kW are not sufficient to prevent appearance of 3/2 NTMs. Right: 320kW successfully prevent any 3/2 modes from appearing.

explain why no disruption was observed in the previous shot (on the left).

Focusing, finally, on the shot shown in the rightmost panels of Figure 4.19, we see the case where 320kW is preemptively injected on the 3/2 surface. In this shot, the MHD activity is much reduced and no 3/2 NTMs are formed. This seems to indicate the preemptive stabilization strategy is effective in this case. Note, also, that the preemptive power is removed at $t = 1.3\text{s}$ and that, at this point, the post-crash MHD activity is seen to increase somewhat (though this could also be related to the density increase).

Another series of shots investigates the effect of changing deposition location on the possibility of preempting 3/2 NTMs. These shots are shown in Figure 4.20. In the first shot (left), the EC was aimed to the outside of the expected $q = 3/2$ rational surface location ($\theta_L = 22^\circ$, see Fig.4.18). As can be observed, this also prevents any 3/2 NTM from forming, and the time evolution of the shot appears similar to that of shot TCV#42971 (Fig.4.19, right).

The central panels shows a different case in which no preemptive power is applied, but the gyrotron is initially aimed at the same location as before ($\theta_L = 22^\circ$). In this shot, a 3/2 NTM forms almost immediately. The NTM controller then kicks in, and is programmed to execute a slow inward angle sweep until the mode is stabilized. As can be observed, the MHD oscillation amplitude slightly decreases and disappears when the launcher angles reaches $\theta_L = 19.5^\circ$. Hereafter, the launcher is moved back to 22° and the shot resumes. Some short-lived 3/2 NTMs appear and the shot disrupts at $t = 1.2$ second due to a very fast 2/1 locked mode.

The right panels show a similar experiment, but with the launcher aiming initially too far on the inside on the mode surface location. 320kW of preemptive EC power is applied but is not successful in preventing the NTM formation. a 3/2 NTM forms at $t = 0.55\text{s}$

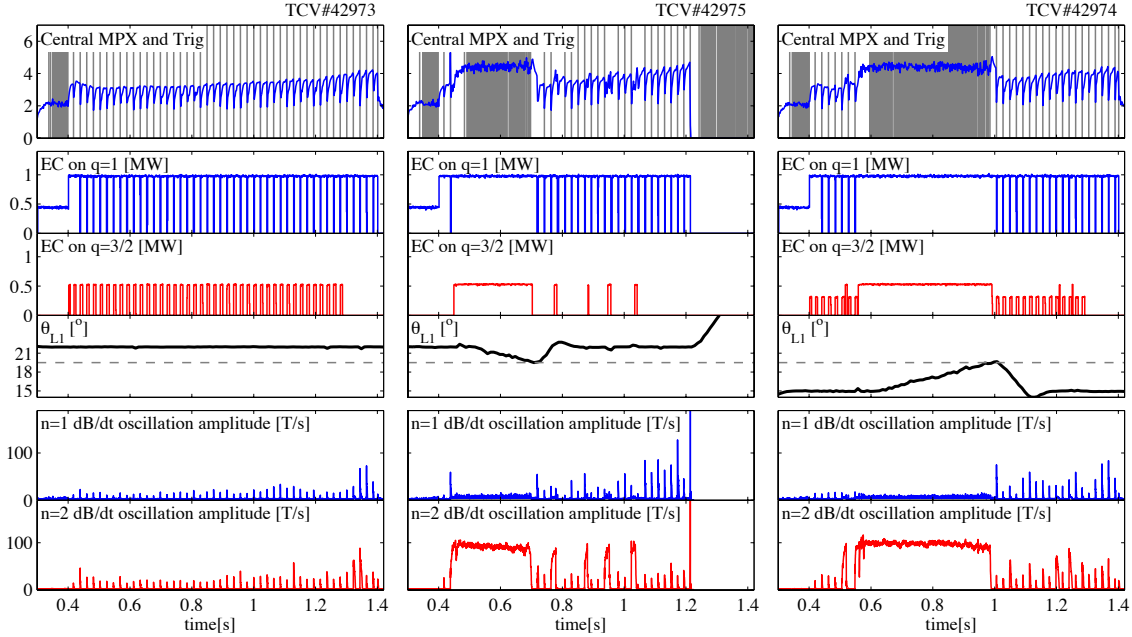


Figure 4.20: Preemptive stabilization experiments performed at different deposition locations. Left: Deposition to the outside of the $q = 3/2$ surface is effective at preventing $3/2$ NTMs from forming. Center: lack of preemptive measures cause $3/2$ NTM to appear, which is stabilized by a launcher angle sweep at $\theta_L = 19.5^\circ$. Right: power applied to the inside of the $3/2$ surface does not prevent NTM destabilization. The mode is subsequently stabilized by an angle sweep again when the launcher angle reaches $\theta_L = 19.5^\circ$.

and the NTM controller applies full power while sweeping the launcher angle towards the outside of the plasma. Again, the NTM is stabilized when the launcher angle reaches 19.5° .

This validates choosing $\theta_L = 19^\circ$ (in the shots shown in Figure 4.19) as close to the $3/2$ surface location. These results are similar to those shown in Fig.4.7 for a $2/1$ NTMs. The LIUQE estimate of the $3/2$ surface location (Fig.4.18) seems to confirm this, while suggesting that $\theta_L = 19^\circ$ puts the EC slightly to the inside of the mode. Note also that the power (500kW) in the first shot on the left (TCV #42973) was chosen to have the same absorbed power as 320kW at 17 degrees (right, TCV #42974) as calculated from TORAY ray tracing.

Now, the fact that power deposited on the outside is effective in preventing a seed island from forming an NTM can be explained from the ray-tracing calculations shown in Fig.4.18, where, based on the LIUQE $3/2$ surface location, some power indeed seems to be deposited inside the island in the case $\theta_L = 22^\circ$, in part due to the broadening of the deposition location. This is not at all the case for $\theta_L = 15^\circ$.

Some care has to be exercised in interpreting these results. Importantly, profile effects due to the applied power on the $3/2$ surface have not been considered. Thomson scattering measurements (not shown) indicate that the profiles (particularly the density profile) change depending on the amount and location of applied power. Having discussed previously how NTM stability can sensitively depend on (local) profile, these effects can not be excluded. However, they are extremely difficult to take into account in a comprehensive

analysis.

For completeness, it must also be stated that the experiments shown in this section were a selection of shots in which clear trends could be observed. Experimental reality was, unfortunately, less clear-cut. For example, shots were performed in which the relative timing of the $3/2$ preemptive power with respect to the sawtooth crash was varied. One would expect preemptive power to be less effective if it is not applied at the same time as the post-crash MHD activity, but this was not clearly observed. This may further point towards profile effects on the tearing mode stability. Additionally, shots exist in which (CW) preemptive stabilization is applied at the correct location, yet NTMs transiently appear nevertheless.

If anything, these experiments confirm the highly complex nature of tearing modes and the difficulty of finding a location in the operating space where they are either absent (so this regime can be operationally exploited), or omnipresent (such that NTMs may be systematically studied). Further experimental work should focus first on finding a stable, NTM-rich regime and then on studying the surrounding parameter space.

4.5.3 Outlook: combined Sawtooth control and NTM preemption in ITER

From the control point of view, the experimental results demonstrate the practical applicability of the sawtooth pacing + NTM preemption scheme advocated in Chapter 3. Contrary to other NTM preemption results (La Haye et al. 2005), (Prater et al. 2007) in which continuous power is applied, preemption was shown with pulsed power at the time of the sawtooth crash. With the ITER time scales, one can envisage the same EC actuators being used for other tasks when this preemptive stabilization is not necessary (in the absence of a seed island) and it being diverted to NTM preemption when necessary. Since the ITER launcher angles can be varied in fractions of a second, the same set of gyrotrons can be used to perform sawtooth pacing, depositing power near the $q = 1$ surface, and then switched off (to induce the sawtooth crash) and rapidly moved to the $q = 3/2$ and/or $q = 2/1$ surface location to preemptively suppress NTMs forming from the seed island. With time scales of several seconds for the sawtooth crash, there will most likely be enough time for such a scheme to be feasible. It would clearly require accurate real-time q profile simulation (Chapter 8) with equilibrium reconstruction and real-time ray tracing in order to align the launchers with the rational surface.

4.6 Conclusions

This chapter has shown some recent experimental results on NTM triggering, stabilization and preemption on TCV, making use of the flexible real-time ECH/ECCD system control possibilities. Studies of tearing mode triggering by influence on the current density profile by ECCD showed that islands were formed after several current redistribution times, confirming the link to the current density profile evolution. Different triggering mechanisms for $2/1$ tearing modes, were observed, which could be separated into directly Δ'_0 driven or preceded by a $3/2$ activity. The extreme sensitivity of NTM appearance to parameters of the plasma which are not under direct experimental control (in particular the wall condition) demonstrate the very sensitive nature of the triggering mechanism.

Difficulties encountered in finding a stationary plasma state that *always* has tearing modes leads to the suspicion that transient effects play a role in a more complete understanding of triggering in this type of tearing modes.

Stabilization experiments were also carried out, demonstrating the possibility to stabilize 2/1 and 3/2 NTMs by real-time steerable launchers depositing ECH/ECCD on the island location. “Scan and stop” NTM control algorithms were tested, whereby the launcher angles were moved in real-time across the expected mode location until the NTM disappears. The angles are then kept fixed at this optimum location. Stabilization by scanning the deposition location from both outside and inside the rational surface were shown to stabilize the island at the same position, to within a half-beam-width. In another set of experiments, the bulk ECCD power (not on-island) was reduced following the appearance of an NTM in order to investigate the dependence of the island resilience to stabilization efforts (by separate off-axis ECCD). It was shown that a small difference in power can make the difference between being stabilized or not, and that local profile effects, rather than global β_p effects, would be needed to explain the experimental observations within the framework of the Modified Rutherford Equation. These experiments also revealed that the oscillatory signature of the magnetic island becomes less regular as the island approaches the marginal island size, potentially providing a direct method to determine proximity to the stabilization threshold.

Separate experiments focusing on low q_{95} plasmas with long, regular, stabilized sawteeth were performed to investigate the seed island mechanism in destabilizing 3/2 or 2/1 NTMs. It was shown that either mode can be triggered, but that 2/1 modes often lock to the wall and cause disruptions in these low $q_{95} < 3$ plasmas. 3/2 modes are shown to interact with subsequent sawtooth crashes and 4/3 modes. NTM preemption and stabilization experiments show that 3/2 NTMs can be prevented by applying EC power near the 3/2 surface location for a brief interval around the seeding event caused by the sawtooth crash.

As a result of this work, a solid experimental framework now exists for future detailed studies on TCV using the real-time system to perform advanced tearing mode physics and control experiments.

Chapter 5

Feedback control of kinetic plasma profiles in TCV

This chapter presents experimental results of feedback control of kinetic profiles on TCV using the real-time capabilities of the ECH/ECCD system. The objective of these experiments was to investigate the operational use of feedback control techniques in plasma experiments, and to test whether established methods for linear controller design can be employed for kinetic profile control. Most of these experiments were done during testing and commissioning phases of the SCD control system, therefore the full complement of control capabilities was not available for all these experiments. This chapter is hierarchically ordered in increasing complexity. Starting from relatively simple controllers for a Single-Input Single-Output (SISO) plasma parameter control to Multiple-Input Multiple-Output (MIMO) plasma control problems.

5.1 SISO control of TCV kinetic plasma parameters

This section describes a series of TCV control demonstration experiments, performed in the early phases of development of the SCD control system and before a full system was available. In this context, the newly acquired control capabilities of the ECH system were exploited for control of internal plasma quantities, available through the MPX diagnostic (Section 2.3) connected to the CRPPRT01 node, the first node of the SCD control system to be commissioned. The controllers used in this section are quite rudimentary, focusing on tuning simplicity rather than control performance. This section begins by describing the typical controllers used. Then a number of experimental examples will be treated.

5.1.1 SISO PI control with anti-windup

The controllers in this section are mostly of the PI (Proportional-Integral) type (Ogata 2002), (Åstrom et al. 1997). This is a simple kind of controller with two tunable parameters (proportional gain and integral gain) which is capable of obtaining zero steady-state error. It is a reduced form of the more standard PID controller, without including a derivative term. The derivative term is not used in these applications, (though it would potentially yield better controllers) because of the noisy nature of the plasma measurements, which

would require careful design of the derivative term to avoid excessively oscillatory behavior. Also, most of the applications shown in this section rely mainly on integral control since the plant response time is very fast (of the order of the confinement time, $\sim 1\text{ms}$) with respect to the time scales on which the control has to act. In these preliminary experiments, controller response times of tens or hundreds of milliseconds were deemed adequate. A feedforward input term is also added, representing the baseline input around which the feedback loop should introduce variations.

The controller transfer function is written in the Laplace domain (neglecting the feedforward term) as

$$\frac{U(s)}{E(s)} = K_p + \frac{K_i}{s} \quad (5.1)$$

with $U(s)$ and $E(s)$ the Laplace transforms of the actuator command $u(t)$ and error signals $e(t)$, respectively. In the continuous-time domain this is equivalent to

$$u(t) = K_p e(t) + K_i \int_{t_0}^t e(t) dt \quad (5.2)$$

The controllers are implemented on a digital platform, in the discrete-time representation using the z -transform, including the feedforward term

$$u_k = \left(K_p + \frac{K_i T_s z^{-1}}{1 - z^{-1}} \right) e_k + u_{ff,k} \quad (5.3)$$

with T_s the sample time. A simplified schematic diagram is shown in Figure 5.1

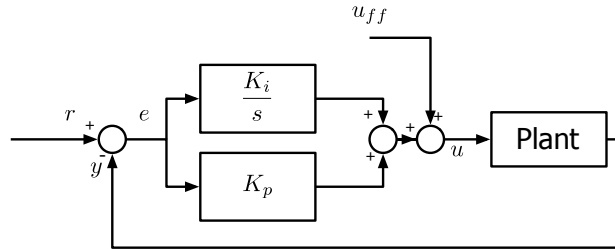


Figure 5.1: Schematic overview of a standard PI controller with additional feedforward input term.

When dealing with actuators with a limited range, it is important to stop the integrator accumulating when the actuator is saturated. Failure to do so can lead to unwanted oscillatory behavior and instability. The remedy is to implement so-called anti-windup scheme, setting the error going to the integrator term to zero when saturation of an actuator is detected.

5.1.2 Control of Soft-X ray emission peak by launcher angle control

In early tests of closed-loop feedback control, the ability to steer the ECH launchers in real-time was exploited to control the peak value in a line-integrated soft X-ray profile emission profile of the MPX diagnostic. The emission peak was determined by real-time spline fit of the MPX channels performed using an efficient real-time method described in Appendix B.1. A PI controller is used, acting on the error $e(t) = p_{ref} - p_{meas}$ with p_{meas}

5.1. SISO control of TCV kinetic plasma parameters

the measured peak value and p_{ref} the reference peak value. The controller parameters were initially tuned in a simplified closed-loop simulation which included a dynamic model of the launcher, the slowest element of the control loop (bandwidth $\sim 10\text{Hz}$). The controller gains were adjusted from shot-to-shot during the experiments and adequate values were found to be $K_p = -3^\circ$, $K_i = -52^\circ/\text{s}$ (note the negative gains because of the negative open-loop plant gain: an angle increase leads to a peak decrease).

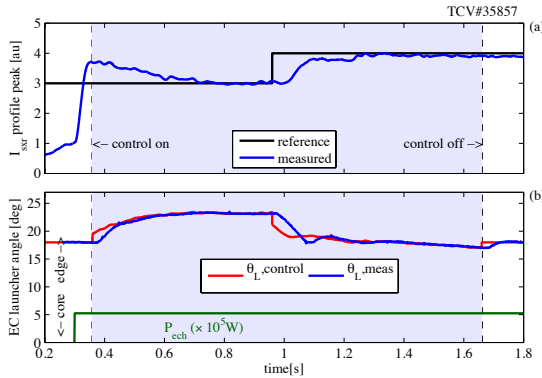


Figure 5.2: Demonstration of feedback control of the soft-X ray emission peak by control of the launcher angles.

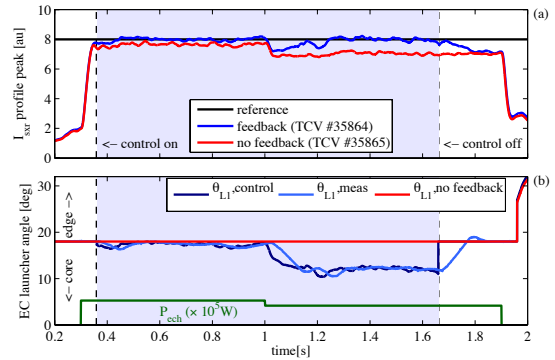


Figure 5.3: Comparison of controlled and uncontrolled cases. The gyrotron power is reduced during the shot, leading to a reduction of the X-ray profile peak (red curve). The controlled case shows recovery of the original peak level by moving the launcher towards the plasma center.

A demonstration of successful control with the mentioned gain values is shown in Figure 5.2. In this example a step command is issued, which is successfully tracked by moving the deposition location towards the interior of the plasma. A second example shown in Figure 5.3 illustrates how this control can reject disturbances, in this case a reduction of the gyrotron power halfway through the shot. The uncontrolled case shows a reduction of the X-ray peak, while in the controlled case the original peak reference level is recovered by the controller moving the launcher angle.

Since plasma heat diffusivity in a tokamak increases towards the edge, the relation between launcher angle and peak profile value is not linear: it flattens towards the center (zone of good confinement) and drops steeply when moving towards the edge. In control terms, this translates into an increasing open-loop plant gain when moving towards the edge. A choice of controller gains which is appropriate for heating close to the plasma center, may lead to instability when closer to the plasma edge. An example of this effect is shown in Figure 5.4, in which a ramp reference is issued. When moving sufficiently far away from the plasma center, the control loop becomes unstable and oscillations of the profile peak Fig.5.4(a) and actuator Fig.5.4(b) are observed. Additionally, the commanded high-frequency movement of the launcher is beyond the limit imposed on the launcher movement rate limits, therefore the launcher no longer tracks the commands correctly. By lowering the gains by a factor 2 in a second shot, Fig.5.5, the instability is suppressed, however the tracking error in the earlier phase of the shot is higher (Fig.5.5(a)). Further optimisation of the gains is certainly possible, for example by gain-scheduling based on the launcher angle.

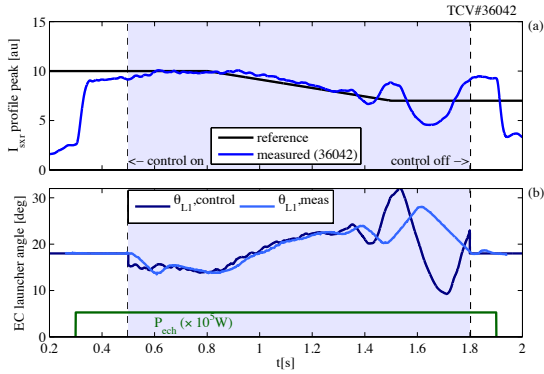


Figure 5.4: Ramp reference in X-ray profile peak followed by varying deposition location using a PI controller. At the end of the shot the loop becomes unstable because of the increasing open-loop plant gain when moving towards the edge.

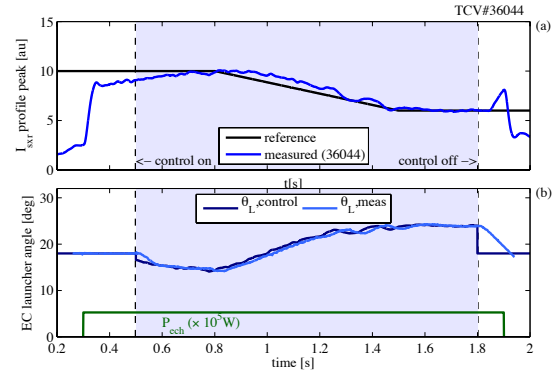


Figure 5.5: Similar experiment as the previous figure, but with controller gains reduced by a factor 2. The instability is suppressed at the expense of increasing tracking error.

5.1.3 Feedback control of central pressure in transport barriers by EC power feedback

As a demonstration of control in advanced scenarios, the peak-in-profile control demonstrated in the previous section was applied also to eITB plasmas. Control of the central pressure in these plasmas is particularly important since they operate close to ideal limits and internal disruptions can occur if these limits are exceeded.

In these experiments, EC power from two or three gyrotrons of one cluster (cluster B) was directed to drive current at $\rho = 0.35$ (as calculated with the TORAY ray tracing code). At the same time, one gyrotron from cluster A was directed to perform pure heating at $\rho = 0.25$, a location expected to be inside the barrier. Typical formation of eITB plasmas in TCV is as follows: 1) an ohmic plasma is created using standard I_p feedback control 2) off-axis ECCD is added and at the same time the Ohmic coil current set to a constant (zero inductive current). 3) additional heating in the center of the plasma is applied by an independent source of EC power, thus “feeding” the barrier exploiting the improved core confinement to get high central temperatures. The EC launcher set-up for these experiments is shown in Figure 5.6.

In these feedback control experiments, a PI controller is used with the same MPX spline-fit peak reconstruction as the previous section, commanding the power of the central gyrotron. Gains were set to $K_p = 100\text{kW}$ and $K_i = 5\text{MW/s}$ (note that the error has arbitrary units). The controller is activated after the barrier is fully formed and after 300kW central EC power has already been added. The reference is then programmed to hold the peak value at the time of the controller activation, followed by a step command as shown in Figures 5.7 and 5.8. The step-down command shown in Figure 5.7 is successfully followed by the controller. The second figure features, instead, a step-up command. In this case, the plasma is not able to obtain the required reference due to the saturation of the gyrotron power request. Additionally, MHD activity is triggered at increased gyrotron power (shown in gray on the top panels), causing the peak emission to drop periodically. This is an indication of approaching the limit of stable operation, beyond which the

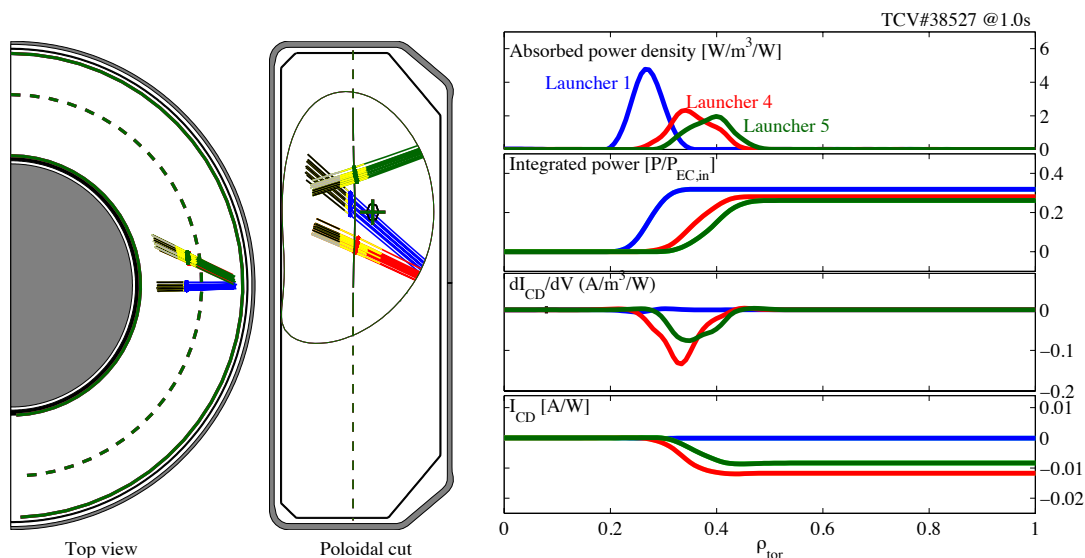


Figure 5.6: TORAY ray tracing results showing deposition location of different EC launchers for typical eITB plasmas. Off-axis ECCD provided by Launchers 4 and 5 is responsible for the formation of the reverse-shear q profile. Launcher 1 drives no current but serves to heat the interior of the barrier once it is formed. The plasma current is negative in this shot following TCV sign conventions, corresponding to co-ECCD for all gyrotrons.

plasma can not be forced by any controller. In interpreting these experiments, one must also remember that the MPX signal is strongly affected by the density, and weakly by the temperature. However, the electron temperature measurements from the Thomson Scattering system are shown in Figures 5.9 and 5.10, confirming the presence of an eITB and showing the effect of the peak control.

5.1.4 Control of central electron temperature by EC power in variable shape TCV plasmas

The TCV electron energy confinement in L-mode has been shown to increase with negative triangularity (Camenen et al. 2007b). Experiments attempting to elucidate the turbulence phenomena underlying the cause of this increased transport required two plasmas with similar T_e gradient scale lengths at opposite triangularities. This was achieved by implementing a feedback controller of the central EC power based on the XTe diagnostic measurement of the central electron temperature. This diagnostic was available in real-time at the time of these experiments and provides a more direct indication of the core temperature than the indirect measurement from the MPX.

The controller structure was again chosen as a simple PI controller, with parameters manually tuned to get reasonable results, without any systematic tuning attempts: $K_p = 100\text{W/eV}$, $K_i = 6\text{kW/eV/s}$. The result of the controller action is demonstrated in two shots shown in Figure 5.11. Here, the same reference T_e request is programmed for two plasmas of opposite triangularity. In both cases, the controller varies the EC power to obtain the requested central temperature. As can be observed from the (black) power traces, the power required for the same temperature is lower in negative triangularity plasmas, as expected. It should be noted that the positive triangularity case, with the

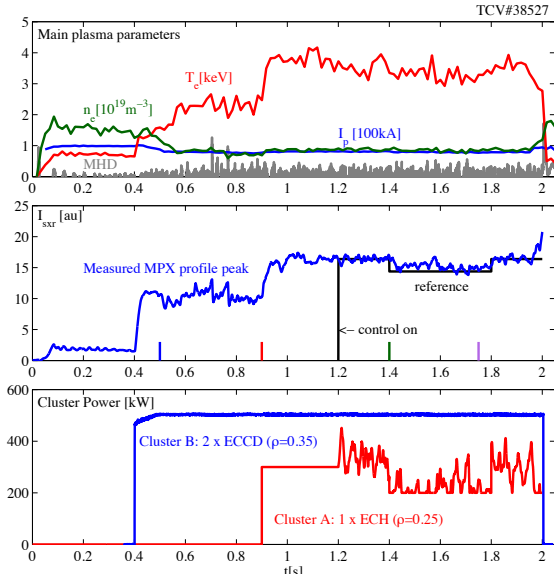


Figure 5.7: Demonstration of control of the soft-X ray emission peak during an eITB discharge. The controller initially holds the naturally obtained profile peak value, followed by a step-wise reduction. The response of the gyrotron power command is shown in the lower panel, showing that the power is reduced in response to the requested reduction of central emissions.

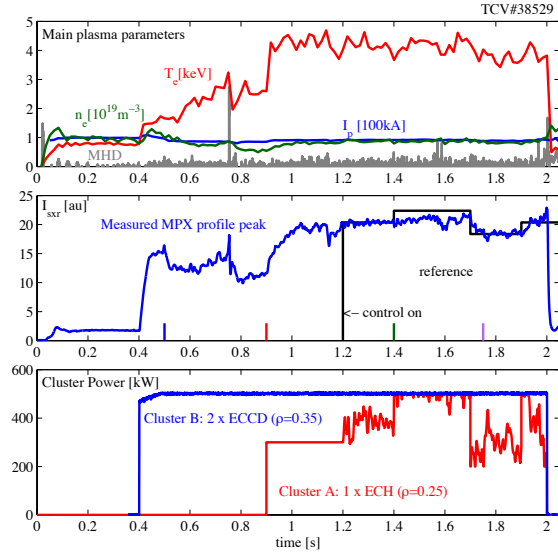


Figure 5.8: In another attempt of eITB emission peak control, an increase of peak emission level was requested. This peak is not attained because of the saturation of the gyrotron power at 500kW and the appearance of transient MHD activity, causing sudden confinement reduction and drop in emission peak.

lower confinement, required the use of an additional gyrotron since the requested temperature could not be reached with the same gyrotron set as in the negative triangularity case. This did not require any change in the controller which simply adjusted the power level until the requested temperature was reached.

5.1.5 Feedback control of the plasma beta

In the context of an ongoing project for development of observers of the plasma poloidal beta (β_p) and internal inductance based on diamagnetic loop (DML) and magnetic measurements (Sevillano et al. 2011), an observer for β_p was developed (outside the scope of this thesis) and tested with a closed-loop control experiment. In this experiment, two launchers deposited EC power on the plasma axis, with one gyrotron oriented to inject counter-ECCD and the other injecting co-ECCD. The power of the co-ECCD gyrotron was varied following an increasing staircase-shaped signal. The second gyrotron was feedback controlled to maintain β_p , using a PI controller acting on the β_p error with gains $K_p = 100\text{W}$ and $K_i = 260\text{MW/s}$. Note that a high integral gain is used making this an almost purely integral controller.

As can be observed in Figure 5.12, the controller automatically generates a complementary signal with respect to the feedforward-controlled gyrotron and achieves good control of β_p . The value of β_p as reconstructed (post-shot) from the LIUQE equilibrium code is also shown to be constant. As a side effect of increasing the co-ECCD power, the

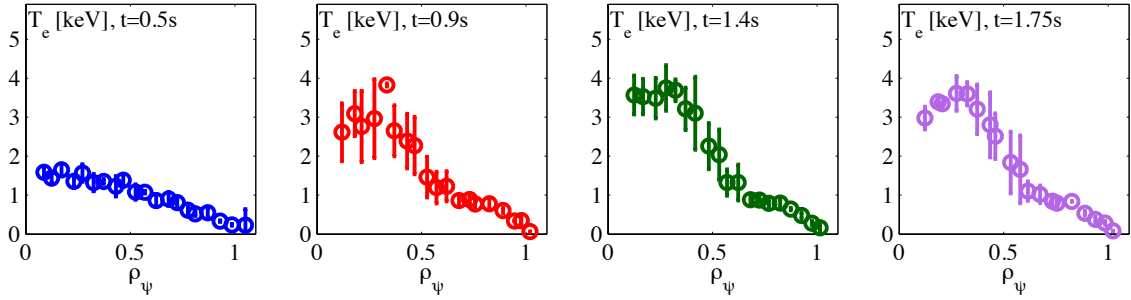


Figure 5.9: Thomson scattering T_e profile measurements at several times during TCV shot #38527, confirming the formation of an eITB, showing the reduction in central temperature as a result of the reduction in profile peak reference. Colors and times match the colors on the central panel of Figure 5.7

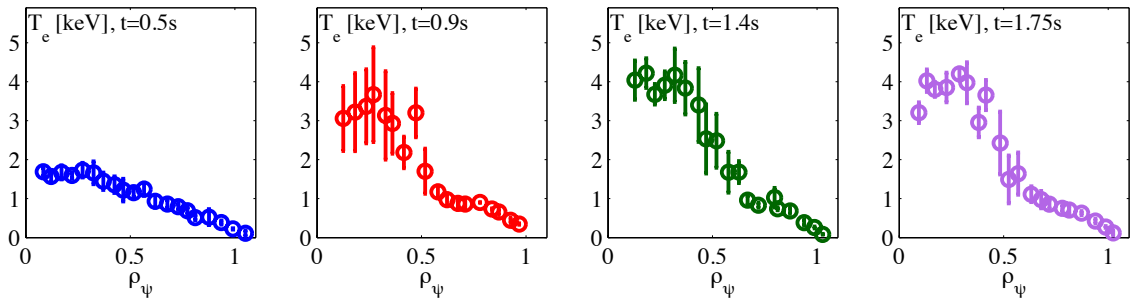


Figure 5.10: Thomson scattering T_e profile measurements at several times during TCV shot #38529, confirming the formation of an eITB, showing the reduction in central temperature as a result of the reduction in profile peak reference. Colors and times match the colors on the central panel of Figure 5.8

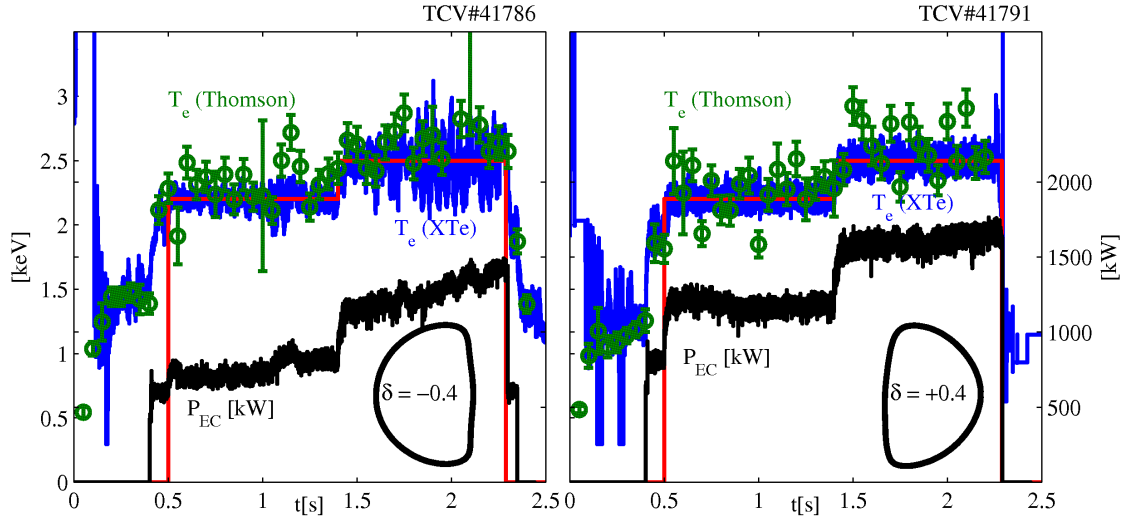


Figure 5.11: Feedback control of central electron temperature by on-axis EC power in two TCV plasmas of different triangularity. In both cases, the same step from 2.2keV to 2.5keV is requested (red). The controller changes the power in order to match the request, needing a much lower total power level in the negative triangularity case. Note the XTe temperature estimate is not reliable in the early phases of the shot.

current density profile peaks at the center, increasing the internal inductance. A similar experimental set-up is used in the experiments described in Section 8.3, where the internal inductance is simultaneously controlled in feedback.

5.2 MIMO control of soft X-ray profile peak and width

5.2.1 Control problem and plasma

Moving beyond SISO control, a demonstration of 2-parameter control was performed by actuating the peak and width of the MPX profile. As before, the peak is defined as the maximum of a spline fit of the MPX points. The width is defined as the integral of the MPX spline fit over all the channels looking at the plasma, divided by the peak. This controller was systematically designed using standard control tools and as such can be seen as an example application of these tools to plasma control problems. A linear controller is designed based on a linear model identified from data gathered during a dedicated identification experiment. The methodology resembles that of (Moreau et al. 2008) albeit of lower complexity and with one profile instead of multiple profiles.

The aim of these experiments was to demonstrate control of profile peak and width by varying the power of two gyrotrons aimed at different locations. Two degrees of freedom were provided by the power of two gyrotron clusters. Although additional flexibility would be provided by the freedom in simultaneously moving the EC launchers, this freedom was not exploited at this stage. Rather, two EC launchers were aimed at a fixed location in the plasma, one heating at $\rho = 0.2$ and the other heating at $\rho = 0.6$. Other parameters of this plasma are $I_p = 110\text{kA}$, $B_\phi = 1.43\text{T}$, $q_{95} = 7.5$, $\kappa = 1.4$, $\delta = 0.2$. The on-axis EC beam is expected to have a strong effect on the profile peak, while the off-axis EC beam is expected

5.2. MIMO control of soft X-ray profile peak and width

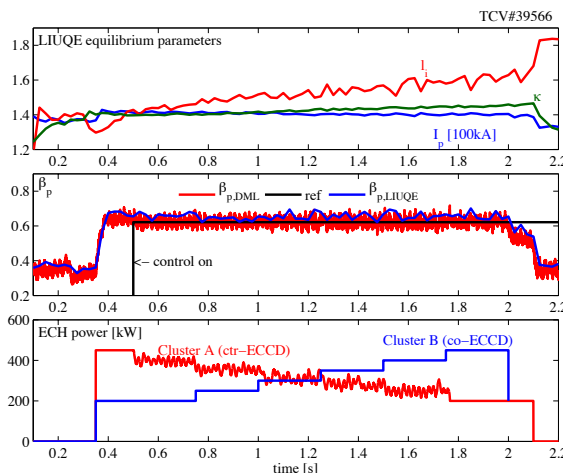


Figure 5.12: Demonstration of plasma β control. One gyrotron is commanded to increase power in step-wise fashion, while the other is controlled in feedback con maintain the same β as determined by the real-time DML observer. The internal inductance can be observed to increase at the same time due to the peaking current density profile caused by the injection of additional co-ECCD.

to broaden the profile. The flexibility in varying the profile is however somewhat limited by the inherent stiffness of plasma temperature profiles, i.e. the difficulty in changing their shape.

5.2.2 System identification

In a separate system identification experiment, the powers of the two gyrotrons were independently varied following a PRBN (Pseudo-Random Binary Noise) sequence, a standard type of signal used in the system identification literature because of its rich frequency content. The responses of peak and width as determined from the real-time spline fitting algorithm (see Section B.1) were collected and fed (after detrending) into a linear system identification routine which identified a linear 2-input 2-output transfer function (in state-space form) between inputs (gyrotron powers) and outputs (peak and width). After trying several model orders, a second order model was chosen. The linear model represents a linearization around a (mean) profile which is chosen as the average of all the profiles in the time sequence. As identification method, a subspace identification algorithm was used which has the advantage of being non-iterative and fast. In practice, identification and controller design could be done on-the fly between two shots as the procedure takes only a few seconds.

The output data and simulated output from the identified model are shown in Figure 5.13 where good qualitative match of the response is displayed. The step response of the identified model is shown in Figure 5.14, where the effect of each actuator can be discerned: the first gyrotron mainly influences the profile peak, while the second gyrotron mainly influences the width. Some cross effects are nevertheless visible.

One should be aware of the limited extent to which the profiles were varied in these experiments. The stiffness of the profiles in a given regime limit the extent to which the profile shape can be changed. However, this small variation is actually advantageous for linear controller design, as the small deviation helps keep the system within the range of

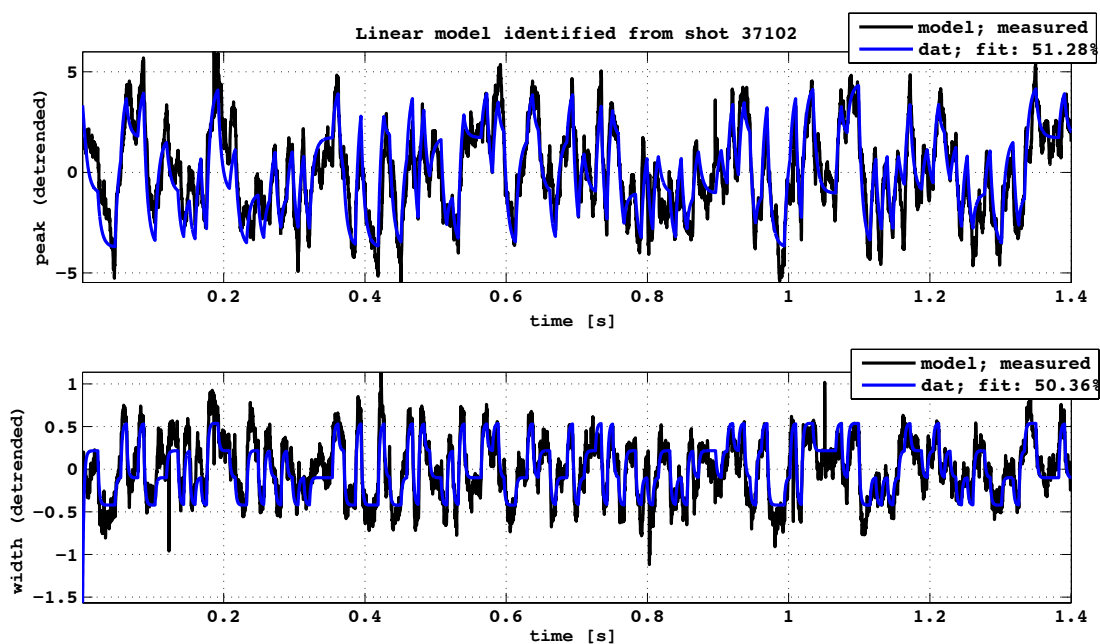


Figure 5.13: Measured profile peak and width, and simulated results from identified model.

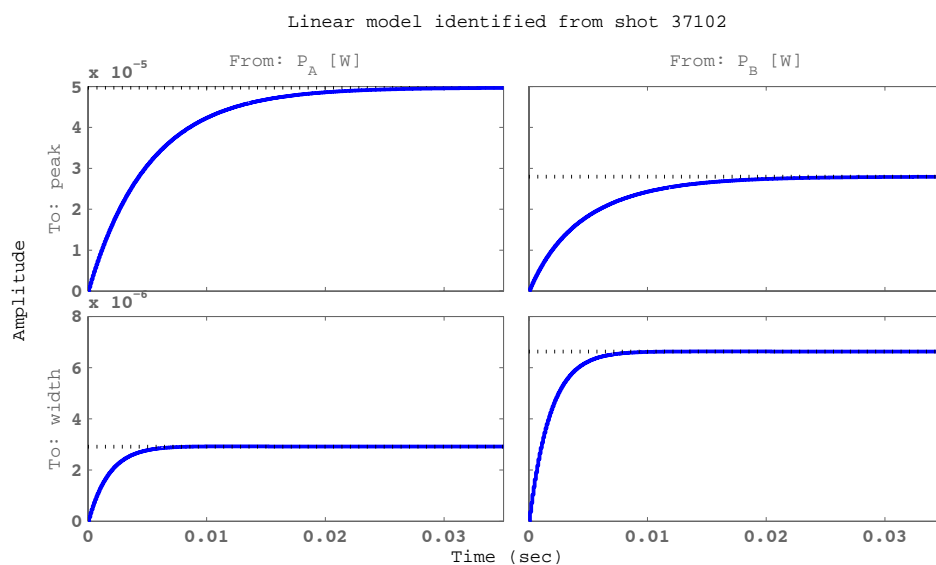


Figure 5.14: Step response of the identified linear model. The response of each output (rows) due to each individual input (columns) is shown. The diagonal terms are dominant, as the centrally aimed gyrotron in cluster A affects mainly the peak while the off-axis gyrotron in cluster B is the main one affecting the width, still having an important effect on the peak.

validity of the linearization.

5.2.3 State controller design

Based on the identified linear model, a state-space observer and controller, including disturbance rejection and zero-steady-state error reference tracking, is designed using standard design methods (Franklin et al. 2002).

The controller design was done in the discrete domain. First, an augmented state-space system is constructed, with the first two states being the peak and width, and the other two being the integral of the error. The observer eigenvalues were assigned by pole-placement within the unit circle:

$$p_{obs} = \{0.9850, 0.9867, 0.9883, 0.9900\}. \quad (5.4)$$

The controller was designed then using the LQR approach, which determines the control law $u = Kx$ with matrix K minimizing a cost function

$$J = \int (y^T Q y + u^T R u + 2y^T N u) dt \quad (5.5)$$

where y is the output of the closed-loop linear system, in essence allowing one to choose the relative importance of penalizing control effort vs output error. The weight matrices Q and R were chosen as diagonal matrices with constant coefficients along the diagonal, and $N = 0$. The values on the diagonals of Q and R were tuned in order to obtain a satisfactory step response. Note that in order for optimization problem to have a minimum, it is required that the matrix $\begin{bmatrix} Q & N \\ N^T & R \end{bmatrix}$ be positive definite.

One issue, not completely addressed in this design, was that anti-windup was not systematically integrated. This is not trivial for a coupled multivariable system (though literature exists). In this first design iteration, anti-windup was implemented only as a limit on the feedback path control signal, without taking the feedforward contribution into account.

5.2.4 Results

A successful demonstration of simultaneous peak/width feedback control is shown in Figure 5.15. The controller successfully tracks the independent steps of the profile parameter references that are prescribed, at least during the period between 0.8 and 1.4s. Limitations imposed on the feedback path of the control action cause the gyrotron powers to temporarily saturate at intermediate times (e.g. $t = 0.75s$), and absolute power limits cause saturation at 450kW and 200kW.

Note how the observed state is effectively a filtered version of the measured output. This is precisely the role of the state observer, in which noise is rejected according to the observer dynamics governed by the assigned eigenvalues. In this case, the noise in the width estimate is strongly suppressed while some oscillations are still visible in the peak estimate. Better tuning of the observer including information on the noise properties, as done by e.g. a Kalman filter, would improve this. In any case, the noise propagating to the actuator commands is small and no excessive oscillations in the power requests are visible.

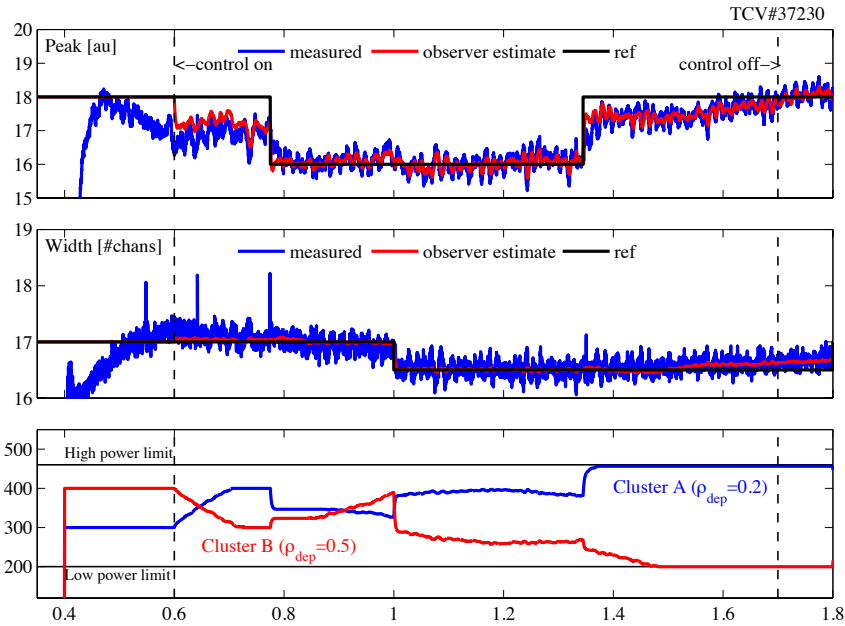


Figure 5.15: Demonstration of simultaneous control of MPX profile peak and width. Two independent step-changes in the references for both quantities are successfully tracked. Other parameters for this plasma: $I_p = 110\text{kA}$, $\kappa = 1.4$, $\delta = 0.25$, $z = 0.22\text{m}$. A similar figure was previously published in (Paley et al. 2009)

5.3 Conclusions

The kinetic profile control experiments presented in this chapter demonstrate the general applicability of linear control design methods for profile control using ECH/ECCD.

When the launcher angle was being used as an actuator, the slowest part of the control loop was the launcher dynamics. A PI controller was then usually sufficient to obtain the desired control action, but nonlinearities inherent in the profile response meant that a conservative choice for the linear control gain was necessary. In other experiments where the gyrotron power was used as an actuator, both the system and the actuator have sufficiently high bandwidth with respect to the control requirements that even conservative, almost purely integral controllers could be used to obtain satisfactory controller behavior.

Some routes for improvement are apparent. For example, gain-scheduling approaches could be used to handle the nonlinearities introduced by moving the EC deposition location, as done for sawtooth control experiments reported in (Paley et al. 2009). Furthermore, more advanced anti-windup schemes can be used to handle actuator saturation in such a way that the restricted actuator space is used to reach high-priority control objectives first.

Another issue which has not yet been addressed is how the control of (rapidly evolving) kinetic profiles is linked to the (slower) evolution of the current density profile. Their dynamics being coupled, the control problem becomes significantly more complicated. Also, since TCV lacks a diagnostic for the current density profile, feedback control can not be done with the existing tools. This motivates the work shown in Chapter 8, in

which real-time current density profile simulations are used as a numerical diagnostic to provide real time estimates of the magnetic profiles.

From a control point of view, when considering multiple profile simultaneously, the physics of profile evolution, which did not need to be discussed in this chapter, needs to be brought back into the discussion and analysis in the next part of this thesis. This next part will focus on real-time control methods for the coupled profiles of temperature and current density and represents an alternative, more model-based view of studying the problem.

Part II

Physics-based control

Chapter 6

Tokamak profile dynamics and control

The second part of the thesis will focus on methods to reconstruct and control in real-time the profiles of temperature and current density in a tokamak plasma. This is an infinite-dimensional (or distributed parameter) control problem, as the underlying physics governing the time evolution of these profiles is described by partial differential equations in space and time. As such, the problem is approached from a physical point of view: starting from a full set of equations describing the profiles, a simplified model is obtained which captures the salient features. This model is then used to solve three problems related to profile control: state observation, i.e. reconstruction of the full profiles based on a combination of measurements and models, an open-loop optimal control problem for the profiles, and a parametrized closed-loop control problem. A more complete description of the topics treated in this part will be postponed to Section 6.10 at the end of this first chapter. First, we will examine the physics of the profile control problem and some existing profile control solutions.

6.1 Introduction

Owing to its topology, a tokamak magnetic field confines plasma particles in the radial direction only. This results in the fact that many quantities are (approximately) constant on a flux surface, and that many plasma quantities are a function of the radial variable only. These plasma quantities are therefore studied in terms of their profiles, i.e. their radial dependence.

The first part of this chapter contains a detailed description of the physics model describing plasma profile evolution. It is a combination of 2-dimensional axisymmetric MHD tokamak equilibrium, with 1-dimensional transport of current density, particles and energy for different species. As such, it is commonly known as the 1.5D tokamak plasma model and has been a centerpiece of many tokamak simulations and control studies in the past 30 years. It has sometimes been referred to as a magneto-thermal model since it merges (electro)magnetic effects of currents and magnetic fields with thermodynamic quantities such as energy and pressure.

The model contains different elements which may be studied separately but are in-

trinsically coupled. In this chapter, these various elements will be gradually introduced, starting from the ideal MHD equilibrium in Section 6.2, and flux surface averaging in Section 6.3, the resistive current diffusion in Section 6.4 and particle and energy transport in Section 6.5. Coupling between equilibrium and transport will be the topic of Section 6.6. Some comments on today’s practice in tokamak simulation using 1.5D models will be given in Section 6.7. Based on this knowledge Section 6.8 describes a set of standard operating modes or “scenarios” for a tokamak plasma, focusing on their characteristics in terms of their q profile. We conclude this chapter by describing the state-of-the art in plasma profile control in Section 6.9. Much of the material of this chapter is a summary of previously known and well-understood ideas, and serves as an introduction to the remainder of Part II, a preview of which is given in Section 6.10.

6.2 Tokamak ideal MHD equilibrium

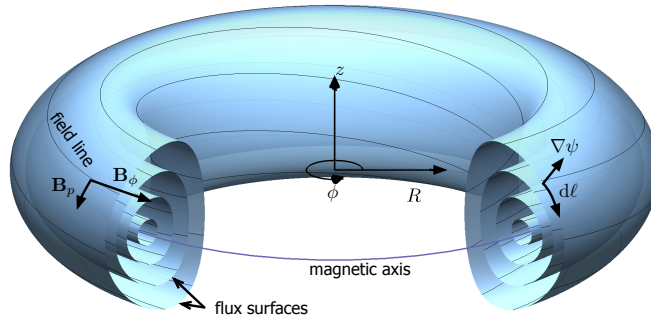


Figure 6.1: Coordinate system and definitions for various plasma quantities

The basic description of a tokamak plasma equilibrium starts with the static description of the spatial distribution of magnetic fields and currents which is introduced in this section. The present section is based largely on (Friedberg 1987) and (Pereverzev et al. 2002) and introduces the tokamak plasma axisymmetric MHD equilibrium as described by the Grad-Shafranov equation.

Let us start by introducing a cylindrical coordinate system (R, ϕ, z) where R is the distance between a given point and the vertical axis of the device, z is the vertical direction and ϕ is the corresponding angle to obtain a right-handed system. Decomposing the toroidal (parallel to \mathbf{e}_ϕ) and poloidal (orthogonal to \mathbf{e}_ϕ) components of the total magnetic field:

$$\mathbf{B} = \mathbf{e}_\phi B_\phi + \mathbf{B}_p \tag{6.1}$$

Defining the function ψ as the negative of the flux of the magnetic field through a disk of

radius R , perpendicular to \mathbf{e}_z ¹,

$$\psi(R, z) = - \int \mathbf{B} \cdot d\mathbf{A}_z \quad (6.2)$$

For the axisymmetric magnetic field of a tokamak this function does not depend on ϕ . With this definition, the poloidal magnetic field is related to the poloidal flux by the relation

$$\mathbf{B}_p = \mathbf{e}_\phi \times \frac{\nabla\psi}{2\pi R} \quad (6.3)$$

Clearly, the magnitude of the local poloidal field is $B_p = |\nabla\psi|/2\pi R$.

Loci of constant ψ in space define **magnetic flux surfaces**, and since it always holds that $\nabla\psi \cdot \mathbf{B} = 0$, a given magnetic field line always lies on a given flux surface.

Applying Faraday's law to (6.1) we obtain

$$\mu_0 \mathbf{j} = \mu_0 j_\phi \mathbf{e}_\phi + \nabla \times (B_\phi \mathbf{e}_\phi) = \mu_0 j_\phi \mathbf{e}_\phi + \frac{1}{R} \nabla(RB_\phi) \times \mathbf{e}_\phi \quad (6.4)$$

$$\mu_0 j_\phi = \nabla \times \left(\mathbf{e}_\phi \times \frac{\nabla\psi}{2\pi R} \right) = \frac{1}{2\pi R} R^2 \nabla \cdot \left(\frac{\nabla\psi}{R^2} \right) \equiv \frac{1}{2\pi R} \Delta^* \psi \quad (6.5)$$

Equation (6.5) above describes the relation between the spatial distribution of magnetic flux (and thus magnetic fields) and electrical currents. Now we add the constraint that the currents and fields inside the region where there is a plasma are such that this plasma satisfies the conditions for an MHD equilibrium. For this purpose, we introduce the momentum equation for stationary ideal MHD which reads

$$\mathbf{j} \times \mathbf{B} = \nabla p \quad (6.6)$$

where p is the plasma (total) pressure. This results in $\mathbf{B} \cdot \nabla p = \mathbf{j} \cdot \nabla p = 0$, i.e. that the pressure gradient is orthogonal to both the local current and the local magnetic field. Taking the component parallel to \mathbf{B} and applying some vector algebra we get

$$\mathbf{B} \cdot \nabla p = \left(\mathbf{e}_\phi \times \frac{\nabla\psi}{2\pi R} \right) \cdot \nabla p = \mathbf{e}_\phi \cdot \left(\frac{\nabla\psi}{2\pi R} \times \nabla p \right) = 0 \quad (6.7)$$

$$\mathbf{j} \cdot \nabla p = \frac{1}{R} (\nabla(RB_\phi) \times \mathbf{e}_\phi) \cdot \nabla p = \frac{\mathbf{e}_\phi}{R} \cdot (\nabla(RB_\phi) \times \nabla p) = 0 \quad (6.8)$$

From this we see that $\nabla p \parallel \nabla\psi$ and $\nabla(RB_\phi) \parallel \nabla\psi$ so $p(\psi)$ and $T(\psi) = RB_\phi$ are flux functions, i.e. constant on a flux surface.

Now evaluate the component of the momentum equation parallel to $\nabla\psi$:

$$\begin{aligned} \mu_0 \nabla\psi \cdot \nabla p &= \nabla\psi \cdot (\mu_0 \mathbf{j} \times \mathbf{B}) \\ &= \nabla\psi \cdot \left(-\mu_0 j_\phi \frac{\nabla\psi}{2\pi R} - \frac{\nabla T}{R} \frac{T}{R} \right) \end{aligned} \quad (6.9)$$

$$\mu_0 \nabla\psi \cdot \nabla\psi \frac{dp}{d\psi} = -\nabla\psi \cdot \left(\frac{\nabla\psi}{2\pi R} \frac{1}{2\pi R} \Delta^* \psi + \frac{\nabla\psi}{R} \frac{dT}{d\psi} \frac{T}{R} \right) \quad (6.10)$$

¹Different choices for the definition of ψ have been used in the literature, sometimes with opposite sign, other times with a factor $1/2\pi$. The opposite sign has the advantage having ψ to have the same sign as physical flux in the given coordinate system. The $1/2\pi$ term has the advantage that there are no 2π terms relating ψ to the poloidal field. In this thesis, we follow the convention from (Pereverzev et al. 2002). With this convention, the ψ has a minimum at the plasma magnetic axis for $I_p > 0$. The function ψ will loosely be referred to as the poloidal flux but one should be aware of the sign convention.

From which we obtain the famous Grad-Shafranov equation (Grad et al. 1958), (Shafranov 1958):

$$\Delta^* \psi = -4\pi^2 \left(\mu_0 R^2 \frac{dp}{d\psi} + \frac{dT}{d\psi} T \right). \quad (6.11)$$

The magnetic field and current density are written in terms of T and ψ as

$$\mathbf{B} = \mathbf{e}_\phi \frac{T(\psi)}{R} + \mathbf{e}_\phi \times \frac{\nabla\psi}{2\pi R} \quad (6.12)$$

$$\mu_0 \mathbf{j} = \frac{1}{R} \frac{dT}{d\psi} (\nabla\psi \times \mathbf{e}_\phi) + \mathbf{e}_\phi \frac{1}{2\pi R} \Delta^* \psi \quad (6.13)$$

The complete distribution of poloidal flux is given by the simultaneous solution of (6.11) in the plasma and vacuum regions (where $p = \mathbf{j} = 0$ in vacuum) and (6.5) in any other conducting elements including active poloidal field coils and passive structures such as the vacuum vessel. Based on the available information, we can distinguish several physical problems to be solved.

- Given the spatial distribution of $\psi(R, Z)$ and the functions $p(\psi)$ and $T(\psi)$, the problem of determining the currents in the active coils which yield the given $\psi(R, Z)$ is known as the *free boundary equilibrium problem*, and is commonly used to pre-determine the currents which will be required in the PF coils during a shot. An example of a computer code for this task is FBT (Hofmann 1988).
- With given currents and active and passive elements, and with given measurements of magnetic fields and/or magnetic fluxes at given points in time, the problem of determining $\psi(R, Z)$ and the functions $p(\psi)$ and $T(\psi)$ is known as the *equilibrium reconstruction problem* and is commonly solved during or after tokamak discharges to reconstruct the plasma equilibrium evolution in time during a discharge based on measurements. An example code which solves this problem is LIUQE (Hofmann et al. 1988), or the real-time equilibrium reconstruction codes EFIT (Ferron et al. 1998) or EQUINOX (Blum et al. 2008).

The Grad-Shafranov equation describes an equilibrium that is considered static in time. Indeed, any evolution of the equilibrium due to changing currents or pressure happens on the MHD time scale, which is comparable to the Alfvén time $\tau_A = a\sqrt{\mu_0\rho_m}/B_0$ (ρ_m is the mass density and a the device size) and is of order $\sim 1\mu\text{s}$ for fusion plasmas. In practice, the changes in equilibrium are dictated by the slower time scales of changes in the external coil currents, or internal changes in the profiles of $p(\psi)$ and $T(\psi) = RB_\phi$. These profiles vary due to radial transport processes in the plasma, which will be treated in the following sections.

6.3 Flux surface quantities and averaging

We have seen in the previous section that some quantities, in particular $p(\psi)$ and $T(\psi)$, are constant on a magnetic flux surface. This is not necessarily the case for other quantities of interest. For this reason, we need to introduce the notion of flux-surface-averaging, to

derive 1D equations involving quantities that are *not* constant on a flux surface. For a more extensive discussion, see the review in (Hinton et al. 1976).

Let us begin by defining the volume and poloidal area of a flux surface, which are obviously themselves flux functions.

$$V = \int dV = \int R d\phi \frac{d\psi}{|\nabla\psi|} d\ell_p = \int d\psi \oint \frac{d\ell_p}{B_p}, \quad (6.14)$$

$$A_\phi = \int \frac{d\psi}{|\nabla\psi|} d\ell_p = \int d\psi \oint \frac{d\ell_p}{2\pi R B_p} \quad (6.15)$$

with $d\ell_p$ an infinitesimal length in the poloidal plane along a flux surface. So

$$\frac{\partial V}{\partial \psi} = 2\pi \oint R \frac{d\ell_p}{|\nabla\psi|} = \oint \frac{d\ell_p}{B_p} \quad (6.16)$$

Now we define the total toroidal current inside a flux surface as

$$I_p(\psi) = \int \mathbf{j} \cdot d\mathbf{A}_\phi = \int j_\phi dA_\phi = \int j_\phi d\ell_p \frac{d\psi}{|\nabla\psi|} = \frac{1}{2\pi} \int^\psi d\psi \oint \frac{j_\phi d\ell_p}{R B_p}. \quad (6.17)$$

For quantities which are not constant on a flux surface, a flux-surface average can be defined as follows:

$$\langle Q \rangle = \frac{\partial}{\partial V} \int Q dV = \frac{\partial \psi}{\partial V} \frac{\partial}{\partial \psi} \oint Q \frac{R d\ell}{|\nabla\psi|} d\psi d\phi = \oint Q \frac{d\ell_p}{B_p} / \oint \frac{d\ell_p}{B_p} \quad (6.18)$$

This way, the infinitesimal increase of flux surface area per unit flux is, from (6.15)

$$\frac{\partial A_\phi}{\partial \psi} = \oint \frac{d\ell_p}{R B_p} = \langle 1/R \rangle \oint \frac{d\ell_p}{B_p} \quad (6.19)$$

Note that the toroidal current density is *not* a flux surface function. One possible definition of flux surface averaged toroidal current density (but not the only one!) is

$$\begin{aligned} \tilde{j}_{tor} &\equiv \frac{\partial I_p(\psi)}{\partial A_\phi} = \frac{\partial I_p}{\partial \psi} \frac{\partial \psi}{\partial A_\phi} \\ &= \int \frac{j_\phi d\ell_p}{R B_p} / \left(\langle 1/R \rangle \oint \frac{d\ell_p}{B_p} \right) = \frac{\langle j_\phi / R \rangle}{\langle 1/R \rangle} \end{aligned} \quad (6.20)$$

Another definition, which will be adopted for the rest of this thesis, is

$$j_{tor} \equiv R_0 \left\langle \frac{j_\phi}{R} \right\rangle. \quad (6.21)$$

6.4 Poloidal flux diffusion

6.4.1 The flux diffusion equation

Let us now introduce the poloidal flux diffusion equation, describing the radial diffusion of poloidal flux due to resistivity. First, define the toroidal magnetic flux as

$$\Phi = \int \mathbf{B} \cdot d\mathbf{S}_\phi = \frac{1}{2\pi} \int_V \mathbf{B} \cdot \nabla \phi dV = \frac{1}{2\pi} \int_V \frac{T}{R^2} dV \quad (6.22)$$

from which

$$\frac{\partial \Phi}{\partial V} = \frac{1}{2\pi} \frac{\partial}{\partial V} \int_V \frac{T}{R^2} dV = \frac{T}{2\pi} \langle 1/R^2 \rangle \quad (6.23)$$

This allows us to define a flux label based on the toroidal flux contained by a given flux surface:

$$\rho = \rho_{tor} = \sqrt{\frac{\Phi}{\pi B_0}} \quad (6.24)$$

which can be seen as a measure of an effective minor radius; one can easily see that for a cylindrical plasma with uniform B field, ρ_{tor} corresponds to the minor radius. On the magnetic axis $\rho = 0$, while at the plasma last closed flux surface $\rho = \rho_e$.

One can now derive a diffusion equation for the poloidal flux as a function of ρ . The derivation is shown in detail in Appendix C.1.1. The flux diffusion equation is a statement of Ohm's law, projected onto the direction parallel to the magnetic field, averaged over a flux surface.

$$j_{\parallel} = \sigma_{\parallel} E_{\parallel} + (j_{bs} + j_{cd}) \quad (6.25)$$

where E_{\parallel} is the parallel electric field, σ_{\parallel} is the conductivity and j_{bs} and j_{cd} are the non-inductive bootstrap and auxiliary current densities, respectively. Parallel quantities are defined as $j_{\parallel} = \langle \mathbf{j} \cdot \mathbf{B} \rangle / B_0$.

The j_{\parallel} and E_{\parallel} terms can be rewritten as functions of ψ , yielding the poloidal flux diffusion equation

$$\sigma_{\parallel} \left(\frac{\partial \psi}{\partial t} + \frac{\rho \dot{B}_0}{2B_0} \frac{\partial \psi}{\partial \rho} \right) = \frac{R_0 J^2}{\mu_0 \rho} \frac{\partial}{\partial \rho} \left(\frac{G_2}{J} \frac{\partial \psi}{\partial \rho} \right) - \frac{V'}{2\pi \rho} (j_{bs} + j_{cd}) \quad (6.26)$$

with

$$J = \frac{T}{R_0 B_0}, \quad (6.27)$$

$$G_2 = \frac{V'}{4\pi^2} \left\langle \left(\frac{(\nabla \rho)^2}{R^2} \right) \right\rangle, \quad (6.28)$$

$$V' = \frac{\partial V}{\partial \rho}. \quad (6.29)$$

Equation (6.26) is a parabolic PDE on the bounded spatial domain $0 \leq \rho \leq \rho_e$. Here, σ_{\parallel} is the (neoclassical) conductivity (Hinton et al. 1976). When the conductivity σ_{\parallel} is infinite, $d\psi/dt = 0$ and the poloidal and toroidal fluxes are frozen into each other (ideal MHD).

Note that J , (the normalized poloidal current function T), reflects the diamagnetic or paramagnetic effect of the plasma. G_2 is a geometric quantity depending only on the flux surface geometry. The non-inductive current sources j_{bs} and j_{cd} are described below.

6.4.2 Non-inductive current sources

The non-inductive current sources $j_{bs} + j_{cd}$ on the right hand side of (6.26) play a significant role in the overall distribution of poloidal flux, and are the primary means by which the current density profile can be controlled by external actuators.

Bootstrap current

The bootstrap current j_{bs} (Peeters 2000) arises physically because of trapped particles on banana orbits. These particles do not complete their periodic motion around the torus but oscillate back and forth in a magnetic mirror due to the varying magnetic field intensity along a field line. At a given spatial point one may count particles on banana orbits transiting either on the low field side or the high field side segment of their trajectory. In presence of a pressure gradient there are more particles on the side of increasing gradient, leading to a velocity space asymmetry in the trapped particle distribution. Due to collisions, this asymmetry spreads to the passing particle region, generating a current density proportional to the pressure gradient. The bootstrap current depends on the trapped particle fraction, which itself decreases with increasing aspect ratio, and on the collisionality.

An often-used closed-form expression for the bootstrap current is given by (Sauter et al. 1999a), (Sauter et al. 2002b) which represents accurate fits to numerical results obtained from the neoclassical physics describing the bootstrap current in a kinetic treatment. As such, this model includes all the physics of parallel neoclassical transport including Coulomb collisions (Hinton et al. 1976). This expression for $j_{bs} \equiv \langle \mathbf{j}_{bs} \cdot \mathbf{B} \rangle / B_0$ is given, assuming $n_e = n_i$ by²

$$j_{bs} = -2\pi J(\psi) R_0 p(\psi) \left[\mathcal{L}_{31} \frac{\partial \ln n_e}{\partial \psi} + R_{pe} (\mathcal{L}_{31} + \mathcal{L}_{32}) \frac{\partial \ln T_e}{\partial \psi} + (1 - R_{pe}) (\mathcal{L}_{31} + \alpha \mathcal{L}_{34}) \frac{\partial \ln T_i}{\partial \psi} \right] \quad (6.30)$$

Here $R_{pe} = p_e/p$ is the ratio between electron and total pressure and $\mathcal{L}_{31}, \mathcal{L}_{32}, \mathcal{L}_{34}, \alpha$ depend on the (local) trapped particle fraction and collisionality. One can observe from this equation the contribution of different gradients to the total bootstrap current.

Auxiliary current drive

The current and power density distributions generated by tokamak auxiliary systems (NBI, IC, EC, LH) arises through different physical mechanisms and also depends on the geometric and kinetic plasma properties. Specialized computer codes exist which calculate these distributions for a given plasma and injection geometry and system considered. For NBI, monte-carlo codes such as NUBEAM (Pankin et al. 2004) can be used, while for EC heating and current drive ray-tracing codes such as TORAY (Kritz et al. 1982), TORAY-GA (Matsuda 1989), TORBEAM (Poli et al. 2001), GRAY (Farina 2005) or C3PO - LUKE (Decker et al. 2004), (Peysson et al. 2008), which can also be used for LH waves, are widespread. Parametrized expressions are often used for practical purposes, when extreme accuracy and self-consistency are not required, as it turns out that many power and current density distributions can be approximately modeled by gaussian distributions.

²Note the factor 2π difference due to a different definition of ψ with respect to the reference

6.4.3 Boundary conditions

Now examine the boundary conditions for (6.26). By definition, the poloidal magnetic field vanishes on the magnetic axis ($\rho = 0$), therefore

$$\left. \frac{\partial \psi}{\partial \rho} \right|_{\rho=0} = 0. \quad (6.31)$$

The boundary condition at the outer boundary $\rho = \rho_e$ is given by the coupling between the plasma and the externally induced voltage from the Ohmic transformer primary. Writing the circuit equation for the plasma edge

$$U_{pl}|_{\rho_e} = -\frac{d}{dt} (L_{ext} I_p) + V_{OH} \quad (6.32)$$

where L_{ext} is the external inductance of the plasma, defined here as the induced voltage on the plasma boundary per unit plasma current. V_{OH} is the externally induced voltage from the Poloidal Field (PF) coil system. Taking the time integral of this expression and preemptively using (6.35) we obtain the following time-varying Robin condition for the boundary flux

$$L_{ext} \left[\frac{G_2}{\mu_0} \frac{\partial \psi(\rho, t)}{\partial \rho} \right]_{\rho=\rho_e} + \psi(\rho, t)|_{\rho=\rho_e} = \Psi_{OH}(t) = \int_{t_0}^t V_{OH} dt \quad (6.33)$$

Alternatively, the total plasma current can be imposed as a boundary condition, yielding the time varying Neumann condition.

$$\left[\frac{G_2}{\mu_0} \frac{\partial \psi}{\partial \rho} \right]_{\rho=\rho_e} = I_p(t). \quad (6.34)$$

One should note that this condition is imposed in simulations for practical purposes only. Physically, the induced plasma current I_p is a consequence of the externally induced voltage through V_{OH} in (6.32).

6.4.4 Other quantities related to the poloidal flux

From knowledge of the flux profile $\psi(\rho, t)$ and its spatial and temporal derivatives, a number of other profiles can be calculated which are important in many respects.

Plasma current and current densities

Let us start by writing the plasma current and defining a toroidal current density.

$$I_{pl}(\rho) = \frac{G_2}{\mu_0} \frac{\partial \psi}{\partial \rho} \quad \text{plasma current inside } \rho \text{ surface [A]} \quad (6.35)$$

$$j_{tor} \equiv R_0 \left\langle \frac{\mathbf{j} \cdot \mathbf{e}_\phi}{R} \right\rangle = \frac{2\pi R_0}{\mu_0 V'} \frac{\partial}{\partial \rho} \left(G_2 \frac{\partial \psi}{\partial \rho} \right) \quad \text{toroidal current density [A/m}^2\text{]} \quad (6.36)$$

Safety factor profile and magnetic shear

Two essential quantities governing the plasma stability and transport are the rotational transform ι (or its reciprocal, the safety factor transform q).

$$\iota = \frac{1}{q} \equiv \frac{\partial\psi}{\partial\Phi} = \frac{1}{2\pi B_0 \rho} \frac{\partial\psi}{\partial\rho} \quad (6.37)$$

and its normalized spatial rate of change, referred to as the magnetic shear s . Though various definitions are used, we define it here based on a radial label linked to the volume $\rho_V = \sqrt{V/V_e}$, with V_e the total volume, obtaining:

$$s = \frac{\rho_V}{q} \frac{\partial q}{\partial \rho_V} = \frac{2V}{q} \frac{\partial q}{\partial V} = \frac{2V}{\rho V'} \left(1 - \rho \frac{\partial^2 \psi}{\partial \rho^2} \left(\frac{\partial \psi}{\partial \rho} \right)^{-1} \right) \quad (6.38)$$

Poloidal field, magnetic energy and internal inductance

The magnitude of the poloidal magnetic field is given by

$$B_p = |\mathbf{B}_p| = \frac{|\nabla\rho|}{2\pi R} \frac{\partial\psi}{\partial\rho} \quad [\text{T}] \quad (6.39)$$

and is not constant on a flux surface. Note that we can also define, as in (Hinton et al. 1976), an average ‘‘cylinder-like’’ poloidal field (see also (C.13))

$$B_{po} = \frac{1}{2\pi R_0} \frac{\partial\psi}{\partial\rho} \quad [\text{T}] \quad (6.40)$$

such that $q = \rho B_0 / R_0 B_{po}$

The magnetic energy density of the plasma poloidal field is $B_p^2/2\mu_0$, from which we can derive the flux surface averaged poloidal magnetic energy density

$$w_i = \frac{\langle B_p^2 \rangle}{2\mu_0} = \frac{G_2}{2\mu_0 V'} \left(\frac{\partial\psi}{\partial\rho} \right)^2 \quad [\text{J/m}^3] \quad (6.41)$$

and from which we can obtain, by integration, the poloidal magnetic energy inside the flux surface ρ

$$W_i = \frac{1}{2\mu_0} \int_0^\rho \left(\frac{\partial\psi}{\partial\rho} \right)^2 G_2 d\rho \quad [\text{J}] \quad (6.42)$$

and the (non-normalized) plasma internal inductance

$$L_i = 2W_i / I_{pl}^2 \quad [\text{H}] \quad (6.43)$$

Voltage and electric field profiles

Toroidal loop voltage and parallel electric field are given by

$$U_{pl} = \frac{\partial\psi}{\partial t} \quad \text{Toroidal plasma loop voltage [V]} \quad (6.44)$$

$$E_{\parallel} = \frac{2\pi\rho}{V'} U_{pl} \quad \text{Parallel electric field [V/m]} \quad (6.45)$$

The heating of the plasma due to resistive dissipation is given by

$$P_{OH} = \frac{1}{2\pi R_0} U_{pl} j_{tor} \quad \text{Ohmic power density [W/m}^3\text{]} \quad (6.46)$$

Note that

$$\frac{\partial I_{pl}(\rho)}{\partial t} = \frac{G_2}{\mu_0} \frac{\partial U_{pl}}{\partial \rho} \quad (6.47)$$

therefore when $\frac{\partial U_{pl}}{\partial \rho} = 0$, i.e. when the plasma loop voltage profile is flat, the current density distribution stops evolving in time.

Measures of profile stationarity

Though not customarily defined in the literature, we introduce here a measure of the stationarity of the current density profile based on equation (6.47) above. We use the term “stationarity” and “stationary state” to avoid confusion with the conventional tokamak terminology where “steady state” refers to $U_{pl}(\rho) = \partial\psi/\partial t = 0$. In a stationary state the voltage profile is flat but not necessarily zero and the flux profile rigidly increases in time. Note that since the flux profile evolves on the slowest time scale of all internal plasma processes, if this profile has relaxed to a stationary state then all others have as well.

Formally, we can define a measure for the proximity to a stationary state of a given profile as the square norm of the profile time derivative.

$$f_{ss,I_{pl}} = \left\| \frac{\partial I_{pl}(\rho)}{\partial t} \right\|_2 = \left[\int_0^{\rho_e} \left(\frac{G_2}{\mu_0} \right)^2 \left(\frac{\partial U_{pl}}{\partial \rho} \right)^2 d\rho \right]^{1/2} \quad (6.48)$$

This scalar is zero for stationary profiles, and increasingly positive for increasingly transient profiles. As observed above, this turns out to be a weighted norm of the voltage profile derivative. One can similarly define stationarity factors for other profile quantities. Each can be written as other weighted norms of $\frac{\partial U_{pl}}{\partial \rho}$, and clearly a stationary state for *all* profiles is reached when the U_{pl} profile becomes flat

$$f_{ss,\iota} = \left\| \frac{\partial \iota(\rho)}{\partial t} \right\|_2 = \left[\int_0^{\rho_e} \left(\frac{1}{2\pi B_0 \rho} \right)^2 \left(\frac{\partial U_{pl}}{\partial \rho} \right)^2 d\rho \right]^{1/2} \quad (6.49)$$

$$f_{ss,w_i} = \left\| \frac{\partial w_i(\rho)}{\partial t} \right\|_2 = \left[\int_0^{\rho_e} \frac{I_{pl}^2}{V'} \left(\frac{\partial U_{pl}}{\partial \rho} \right)^2 d\rho \right]^{1/2} \quad (6.50)$$

In this sense, these scalar factors essentially represent (differently weighed) least-squares distances from the stationary state. The choice of weight depends on the importance that one attaches to stationarity of different profiles in different locations in the plasma.

6.5 Transport of particles and energy

In this section, the 1D equations for (flux profile averaged) transport of particles and pressure will be introduced.

6.5.1 Particle transport

For an arbitrary plasma species α , which may refer to electrons, main or impurity ion species, or fusion-born α particles, let n_α be the local particle density of the species and \mathbf{u}_α be the local velocity of the particles. The continuity equation for this species is stated as

$$\frac{\partial n_\alpha}{\partial t} + \nabla \cdot (n_\alpha \mathbf{u}_\alpha) = s_\alpha \quad (6.51)$$

Here s_α is a localized particle source.

We now wish to write an equation for the density associated with the particles contained inside a toroidal flux surface. The details are shown in Appendix C.1.2, and the final result is

$$\boxed{\frac{1}{V'} \left(\frac{\partial}{\partial t} + \frac{\dot{B}_0}{2B_0} \frac{\partial}{\partial \rho} \right) (\langle n_\alpha \rangle V') + \frac{1}{V'} \frac{\partial}{\partial \rho} \Gamma_\alpha = S_\alpha} \quad (6.52)$$

The particle fluxes Γ_α are determined by a complex interplay of phenomena which are beyond the scope of this treatment, but it is important to note that these fluxes can be both outward and inward, causing peaked density profiles even in plasmas without particle source in the plasma core.

6.5.2 Energy transport

In a similar manner as the particle transport equation, an equation for energy transport can be derived. Skipping the details, for which the reader can consult (Hinton et al. 1976), the result below is obtained:

$$\boxed{\frac{3}{2} (V')^{5/3} \left(\frac{\partial}{\partial t} - \frac{\dot{B}}{2B_0} \frac{\partial}{\partial \rho} \right) [(V')^{-5/3} n_\alpha T_\alpha] + \frac{1}{V'} \frac{\partial}{\partial \rho} \left(q_\alpha + \frac{5}{2} T_\alpha \Gamma_\alpha \right) = P_\alpha} \quad (6.53)$$

P_α is the net power to the species, and is itself a sum of multiple contributions. The convective and diffusive heat fluxes are given, respectively, in the general form

$$\Gamma_\alpha = -V' G_1 n_\alpha \left[\sum_{\beta \in \text{species}} \left(D_{n_\beta}^\alpha \frac{1}{n_\beta} \frac{\partial n_\beta}{\partial \rho} + D_{T_\beta}^\alpha \frac{1}{T_\beta} \frac{\partial T_\beta}{\partial \rho} \right) + D_E \frac{E_\parallel}{B_p} \right] \quad (6.54)$$

$$q_\alpha = -V' G_1 T_\alpha n_\alpha \left[\sum_{\beta \in \text{species}} \left(\chi_{n_\beta}^\alpha \frac{1}{n_\beta} \frac{\partial n_\beta}{\partial \rho} + \chi_{T_\beta}^\alpha \frac{1}{T_\beta} \frac{\partial T_\beta}{\partial \rho} \right) + \chi_E \frac{E_\parallel}{B_p} \right] \quad (6.55)$$

where G_1 is a geometric quantity defined as

$$G_1 \equiv \langle (\nabla \rho)^2 \rangle \quad (6.56)$$

The various transport coefficients $D_{x_\beta}^\alpha$, $\chi_{x_\beta}^\alpha$ quantify, respectively the particle and heat flux of species α due to a gradient in the profile of x_β , while D_E and χ_E represent (typically inward) fluxes due to parallel electric fields. These coefficients may themselves depend on ρ and are a function of other plasma quantities including the profiles themselves. Indeed,

giving quantitative estimates of these transport coefficients is one of the main challenges of fusion research.

First-principle plasma transport models have been the subject of continued and extensive research, but closed-form expressions for tokamak transport do not exist as yet. Various numerical codes exist which calculate the plasma transport coefficients (6.54), (6.55) for a given set of profiles under some approximations. Codes such as GLF (Hammett et al. 1990), are often used in conjunction with plasma transport simulations. These solve a set of partial differential equations derived from gyrokinetic equations and as such can be rather computationally involved. The linearized version of GLF, GLF23 (Waltz et al. 1997) is more efficient but still complicated. Alternatively, critical gradient models such as the Rebut-Laila-Watkins model (Rebut et al. 1989) can be used. The most computationally simple choice is to rely on direct ad-hoc transport models: closed-form expressions for transport coefficients derived from empirical scalings. Many possibilities exist, for example Coppi-Tang (Jardin et al. 1993), Bohm-Gyrobohm (Erba et al. 1998) or scaling law based (Witrant et al. 2007), (Ou et al. 2010a).

6.5.3 Sources

Particle sources and sinks

Particle sources include all gas injection systems including gas puffing, neutral beams and pellet injection, as well as particles released from the surrounding wall. This same wall may also act as a particle sink depending on the conditions; in any case a particle sink is provided by (cryo)pumping systems. Atomic processes are often also a source and sink of particles, but these are not considered in this thesis.

Energy sources and sinks

The electron energy sources are written as a sum of several contributions

$$P_e = P_{OH} + P_{e,aux} + P_{fusion} - P_{ei} - P_{e,rad} - P_{e,atomic}. \quad (6.57)$$

The electron-ion equipartition power P_{ei} is given by (Hinton et al. 1976):

$$P_{ei} = n_e \nu_{eq} (T_e - T_i) \quad (6.58)$$

where $\nu_{eq} = 0.041 T_{e[\text{keV}]}^{-3/2} \sum_{p \in \text{ions}} n_p [19] Z_p^2 / A_p$ is the neoclassical equipartition rate and Z_p and A_p are each ion species' charge and atomic mass number, respectively. Using $n_i = (Z_C - Z_{eff}) / (Z_C - 1) n_e$ and the definition of Z_{eff} :

$$Z_{eff} = \sum_{p \in \text{ions}} \frac{Z_p^2 n_p}{n_e}, \quad (6.59)$$

in the case of Deuterium plasmas with mainly Carbon impurity we can rewrite ν_{eq} as

$$\nu_{eq} = 0.041 T_{e[\text{keV}]}^{-3/2} \left(\frac{n_i}{A_i} + \frac{Z_C (n_e - n_i)}{A_C} \right) \quad (6.60)$$

Radiation losses (P_{rad}) can be split up into bremsstrahlung, line radiation and cyclotron radiation losses, the first of which is usually dominant in today's tokamaks. The bremsstrahlung radiation losses can be estimated using a simple formula (Wesson 2004)

$$P_{brems} = 5.35 \cdot 10^{-5} Z_{eff} n_e^2 T_e^{1/2}. \quad (6.61)$$

$P_{e,atomic}$ represents electron energy losses by atomic processes, such as impact ionization, and is not discussed here. P_{fus} , the fusion power transferred from the fusion-born α particles to the electrons, is also neglected in this treatment but will be a topic of intense scrutiny in the ITER experiment. The auxiliary powers going to the electrons, $P_{e,aux}$, are provided by the various auxiliary heating systems. Like the current drive, they are usually calculated by specialized codes as mentioned in Section 6.4.2.

Similarly, ion energy sources are written as

$$P_i = P_{i,aux} + P_{ei} - P_{i,rad} - P_{i,atomic} \quad (6.62)$$

6.5.4 Boundary condition

The central boundary condition for (6.53) is a natural Neumann condition at $\rho = 0$ to impose zero net flux

$$\left. \frac{\partial T_\alpha}{\partial \rho} \right|_{\rho=0} = 0. \quad (6.63)$$

The edge temperature should in principle be calculated self-consistently from edge and scrape-off-layer transport physics, but since this is very difficult to do accurately, in practice the edge temperature is usually externally imposed as

$$T_\alpha|_{\rho=1} = T_{\alpha,edge}(t) \quad (6.64)$$

Similar boundary conditions hold for n_α .

6.5.5 Other quantities related to the electron temperature profile

Thermal energy and confinement time

The total thermal energy of a species α in the entire plasma volume is given by

$$W_\alpha = \int_0^{\rho_e} k_B n_\alpha T_\alpha V' d\rho \quad (6.65)$$

where k_B is Boltzmann's constant.

Confinement times for particles and energy can be defined for each species, in general terms starting with

$$\frac{dW_\alpha}{dt} = -\frac{1}{\tau_{E,\alpha}} W_\alpha + P_\alpha \quad (6.66)$$

where P_α is the total (volume integrated) power input to the species α . The confinement time for the energy of each species is thus given by

$$\tau_{E,\alpha} = \frac{W_\alpha}{P_\alpha - dW_\alpha/dt} \quad (6.67)$$

The global energy confinement time is given by

$$\tau_E = \frac{\sum_{\alpha} W_{\alpha}}{\sum_{\alpha} P_{\alpha} - \sum_{\alpha} dW_{\alpha}/dt}, \quad \alpha \in \text{all plasma particle species} \quad (6.68)$$

which is sometimes written as

$$\tau_E = \frac{R_{pe} W_e}{P_{in} - R_{pe} dW_e/dt}, \quad (6.69)$$

where R_{pe} is the ratio of total energy to total electron energy and P_{in} is the total input power (canceling inter-species power flows).

Similarly, particle confinement times can be written as

$$\tau_{n,\alpha} = \frac{n_{\alpha}}{S_{\alpha} - dn_{\alpha}/dt} \quad (6.70)$$

Confinement scaling

To compare performance across different tokamaks and to extrapolate to future devices, confinement scaling laws have been derived which give the expected confinement for a given set of plasma parameters. An often-used scaling law for the energy confinement is the ITER-98 H-mode scaling (formally IPB98(y,2)), extracted by comparison of a multi-machine database.

$$\tau_{E,98} = 0.0562 I_p^{0.93} B_t^{0.15} n^{0.41} P_L^{-0.69} R^{1.97} \epsilon^{0.58} \kappa_a^{0.78} A_i^{0.19} \quad (6.71)$$

(units MA, T, 10^{19}m^{-3} , MW, m), where $P_L = P_{in} - dW/dt$, ϵ is the inverse aspect ratio, $\kappa_a = S_a/\pi a^2$ the effective elongation with S_a the plasma cross section area, and A_i the ion mass number (Doyle et al. 2007).

The experimental confinement time can then be compared to the confinement expected from the scaling law, giving a figure-of-merit for the “quality” of the confinement during given plasma discharge. To this end, the so-called H factor is defined as the ratio between the experimentally obtained energy confinement time and a given scaling, for example

$$H_{98} = \frac{\tau_{E,exp}}{\tau_{E,98}} \quad (6.72)$$

6.6 Coupling between equilibrium and transport

The equations for 1D transport (6.26), (6.52) and (6.53) contain terms depending on the 2D magnetic equilibrium governed by the Grad-Shafranov equation (6.11), i.e. $J = RB_{\phi}/R_0 B_0$, G_1 , G_2 and V . To study the coupled evolution of tokamak 2D equilibrium and transport, the 1D profile transport must be solved coupled with the 2D Grad-Shafranov equation. Therefore, this problem is often referred to as the 1.5D tokamak transport problem.

For this purpose, following (Pereverzev et al. 2002), we rewrite (6.11) such that it depends only on quantities known from solving the transport equations. Eliminating $\Delta^* \psi$ from (6.12), (6.13), and (6.11) we may write

$$\mathbf{j} = -2\pi\mu_0 R_0 \frac{dp}{d\psi} \mathbf{e}_{\phi} - 2\pi \frac{dT}{d\psi} \mathbf{B} \quad (6.73)$$

and taking the scalar product of this equation with (6.12):

$$j_{\parallel} = \frac{\langle \mathbf{j} \cdot \mathbf{B} \rangle}{B_0} = -\frac{2\pi}{B_0} \left(T \frac{dp}{d\psi} + \frac{\langle B^2 \rangle}{\mu_0} \frac{dT}{d\psi} \right) \quad (6.74)$$

Then, using the definition of ι (6.37), we can rewrite the source terms of the Grad-Shafranov equation as depending only on profile quantities.

$$\Delta^* \psi = 2\pi\mu_0 R_0 \left[\frac{J}{\langle B^2/B_0^2 \rangle} \left(j_{\parallel} + \frac{R_0 J}{B_0 \rho \iota} \frac{\partial p}{\partial \rho} \right) - \frac{R^2}{B_0 R_0 \rho \iota} \frac{\partial p}{\partial \rho} \right] \quad (6.75)$$

The coupled equilibrium+transport problem consists of iteratively:

1. Solving (6.75) for $\psi(R, Z)$ with given p and j_{\parallel} profiles.
2. Computing new estimates for G_1, G_2, V' , as well as J based on the new equilibrium
3. Using these to integrate the transport equations forward in time and obtain new estimate for $p(\rho), j_{\parallel}(\rho)$
4. Plugging these profiles back into the Grad-Shafranov equation and solving for a new equilibrium.

This can be done by a numerical iteration scheme such as outlined in (Blum 1989).

6.7 Tokamak simulations

6.7.1 Classification of tokamak equilibrium and transport codes

Over the years, many different type of codes solving some part of the coupled equilibrium-transport problem have been developed. This section serves to clarify some of the terminology and to aid in classification of the different codes.

Free boundary vs fixed boundary

We can distinguish between the free-boundary case (in which only the currents in the PF coils are provided, and the location of the LCFS has to be determined), and the fixed-boundary case (in which the location of the LCFS is prescribed). Free-boundary simulations are significantly more difficult since the vertical position is physically and numerically unstable and has to be feedback controlled.

Interpretative vs Predictive

Most transport codes have the option to set which transport equations are to be solved, as prescribed by the user. In many practical situations, the kinetic profiles and plasma boundary are known from diagnostic measurements. In this case one can solve only the flux diffusion equation to get the time-evolution of the current density distribution. This is commonly referred to as **interpretative transport modeling** and is routinely carried out as post-shot tokamak plasma analysis. When the energy transport equation (and possibly the particle transport equation), are solved as well, one speaks of **predictive plasma transport** simulations.

6.7.2 Integrated tokamak simulation codes

Some well-known and widely used tokamak simulation codes are listed below, categorized by fixed and free boundary

Fixed-boundary ASTRA (Pereverzev et al. 2002) is a modular system for running transport simulations, with great flexibility in defining which equations are solved and allowing the user to easily specify additional information by hand. CRONOS (Artaud et al. 2010) is a complete suite of codes for transport analysis and simulation, including integrated ray-tracing and neutral beam codes. JETTO (Genacchi et al. 1988) is another code, which has been widely used in the past. TRANSP and PTRANSF (Hawryluk 1980), (Budny et al. 2008), ONETWO (Pfeiffer et al. 1980) and BALDUR (Singer et al. 1988) are similar codes developed in the US.

Free boundary DINA (Khayrutdinov et al. 1993), CORSICA (Crotinger et al. 1997) and TSC (Jardin et al. 1986) are free boundary codes with simplified transport models. Recently DINA-CH has been coupled to CRONOS to obtain a more complete transport model description (Kim et al. 2009). Similarly TSC has been coupled to PTRANSF.

6.8 Tokamak operating scenarios

Different points in the tokamak operating space are interesting for different reasons. This allows one to distinguish between different tokamak operating modes commonly referred to as **plasma scenarios**. The literature on the different scenarios is vast, and the reader can consult the relevant chapters in the ITER physics basis (Doyle et al. 2007) (Gomezano et al. 2007) for a review. The discerning feature, determining the plasma scenario is the q profile, more precisely the degree to which it is monotonic or becomes flat or reversed near the center (see Figure 6.2).

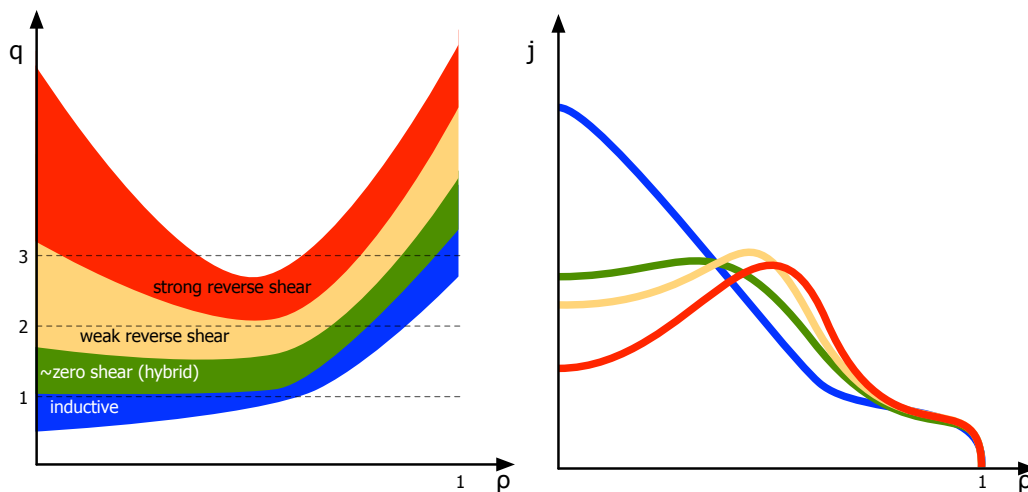


Figure 6.2: Typical ranges of q profiles and corresponding typical parallel current density profiles for different tokamak scenarios. Inspired by (Gomezano et al. 2007, Fig. 1)

More details of each scenario is given below.

- The (standard) **inductive H-mode** scenario has the objective of maximizing confinement by exploiting the favorable scaling of β with I_p , i.e. maximizing plasma current. This leads to a centrally peaked, predominantly ohmic current density profile and a monotonic q profile featuring a (possibly large) $q = 1$ surface and sawteeth. This is the most practical and promising scenario for obtaining $Q = 10$ in ITER, but has the disadvantage that most of the plasma current is driven inductively thereby making this an intrinsically short-pulse scenario. Additionally, the low central q and large $q = 1$ radius causes large sawtooth crashes which may trigger NTMs, which in turn may lock to the wall and cause a plasma disruption (Hender et al. 2007), as previously discussed in Part I of this thesis. This is particularly troublesome as inductive scenarios feature low q_{edge} and the $q = 2$ surface is physically close to the wall and the perturbed magnetic field may interact more easily with vessel currents.
- By driving a significant part of the plasma current non-inductively, off-axis, a centrally flat, broad q profile with $q > 1$ everywhere can be obtained with a large region of low magnetic shear. This is referred to as the **hybrid scenario** (Sips et al. 2002), (Luce et al. 2004), (Gomezano et al. 2004), (Sips et al. 2005) and has been shown to be favorable for confinement. Furthermore, the increased central pressure will drive bootstrap current which can contribute significantly to the total plasma current (typically up to $\sim 30\%$ in these scenarios). The absence of a $q = 1$ surface means there are no sawteeth, so the dominant source of triggering for NTMs is eliminated. Nevertheless NTMs are still observed in these scenarios (Joffrin et al. 2005), (Turco et al. 2010) so active MHD control remains necessary. Due to the larger non-inductive current fraction and lower I_p , the inductive flux consumption is lower and longer duration plasmas can be obtained this way.
- By driving even more off-axis current causing the q profile to reverse giving a region of negative magnetic shear, an internal transport barrier (ITB) – a region of locally reduced transport – can be formed (see (Connor et al. 2004) for a review). The locally reduced transport causes a steep gradient in the plasma pressure profile which in turn drives large amounts of off-axis bootstrap current. The sum of the non-inductive currents can be large enough to sustain 100% of the total current in which case a fully non-inductive steady-state plasma is obtained (Coda et al. 2007). Scenarios with reversed shear and/or transport barriers are referred to as **advanced scenarios**, typically having a high non-inductive current fraction of more than 50%, at least half of which can be bootstrap current. In these scenarios the nonlinear coupling between the temperature and current density profiles is important in determining the overall characteristics of the steady-state profiles because a large part of the current density is self-generated by the plasma. A disadvantage of ITB scenarios is that they must operate at high $\beta_N > 3.5$, close to ideal MHD stability limits (above the no-wall ideal limit), to be attractive for a reactor. Studies of advanced scenarios on TCV can be found in (Pietrzyk et al. 2001), (Goodman et al. 2005), (Sauter et al. 2005), (Coda et al. 2007), (Zucca et al. 2009a).

The next section will describe how to obtain the different scenarios by actively tailoring the q profile, an exercise known as profile control.

6.9 Profile control

Without active measures, a tokamak current density profile naturally becomes peaked because of the higher central temperature and the monotonic q profile of the standard inductive scenario forms. Off-axis current must be added to prevent the inward current diffusion in the hybrid scenario, and even more so in advanced scenarios. The quantity and location of auxiliary current drive and heating must be controlled in such a way that the sum of auxiliary (driven) current and pressure-gradient driven bootstrap current form a self-consistent stationary set of profiles. Moreover, the profiles must also be steered through the tokamak operating space, avoiding instabilities until the desired conditions are reached. This is the objective of profile control, which is introduced in this section.

While one generally refers to profile control as the combination of kinetic and current density profile control, emphasis is usually placed on current density profile control, for the reason that it is the slowest ($\tau_R \gg \tau_E$) and most difficult to change and because it globally affects the plasma scenario, as discussed. However the other profiles must simultaneously be controlled in order to obtain a consistent state, since they indirectly influence the current density profile (mainly by changing resistivity or bootstrap current).

Existing strategies for profile control can be roughly divided into two categories: feedforward and feedback control. Feedforward control tries to design a time evolution of tokamak actuator trajectories such that the desired profiles are obtained. In feedback control one measures the profiles and takes active measures to compensate from deviations with respect to a required reference. Both have been studied and progress so far is reviewed below.

6.9.1 Feedforward profile control

Feedforward control comprises efforts to steer the profiles towards their required state by pre-programmed time evolutions of tokamak actuator trajectory waveforms. One popular and well-known method to generate reversed-shear profiles in tokamaks is a fast current ramp-up with early heating (Söldner et al. 1997). The early heating increases the plasma conductivity, which prevents the ohmically induced plasma current from diffusing inwards in the early stages. If this induced off-axis current is not supplanted by non-inductive current (driven or bootstrap), this situation is only transient and the q profile will eventually become monotonic.

An alternative is, more simply, to add current drive to a pre-existing Ohmic plasma, as is commonly done in TCV to obtain eITB plasmas (Goodman et al. 2005). An advantage is that the formation can be studied in detail as it does not depend on detailed knowledge of the initial plasma evolution, which is difficult to diagnose. The disadvantage of this method is that one has to wait until the current has diffused such that the reverse-shear q profile is obtained. This is not always viable on tokamaks with long current redistribution times (with respect to the total shot time), or lacking sufficient current drive capabilities.

In the vast majority of cases, appropriate feedforward input trajectories are chosen by trial and error shaping of the reference commands to various plasma actuators, and measurements of the plasma evolution are used a-posteriori in determining whether the attempted feedforward reference was appropriate.

6.9.2 Feedback profile control methods

Feedback control methods differ from feedforward methods by the fact that real-time profile measurements are used to decide the appropriate actuator response to obtain the desired profiles. Early work by Firestone and Kessel numerically explored the opportunities of applying linear control theory to kinetic and current density profile control (Firestone et al. 1991a), (Firestone et al. 1991b). The particular importance of profile control for advanced scenarios was recognized and studied in (Moreau et al. 1999). An early practical example of current density profile control can be found in (Wijnands et al. 1997), in which the internal inductance, which is related to the peakedness of the current density profile, is feedback controlled by Lower Hybrid current drive on Tore Supra. This was later extended to a more integrated control of steady-state scenarios (Joffrin et al. 2007). Work reported in (Ferron et al. 2006) on DIII-D shows active control of the rate of decrease of the minimum value of q during the current ramp-up by varying the level of heating. JT60-U results show feedback control of the q profile using MSE measurements and LHCD actuators (Fujita et al. 2006). Recent work (Imbeaux et al. 2011b) demonstrates feedback control of the plasma scenario by identifying macroscopic features of each scenario to decide in which category the plasma falls at a given time in order to decide whether to add or remove off-axis current.

The most advanced approach from a control point of view is represented by the extensive work by Moreau and co-workers at JET (Joffrin et al. 2003), (Moreau et al. 2008). This method relies on linear dynamical models of the profile response to actuators for a given tokamak operating point to construct two-timescale linear controllers: one acting on the kinetic timescale (roughly the energy confinement time) and the other acting on the (slower) current diffusion time scale. For this purpose, linear dynamic models including the coupling between different profiles are identified from dedicated system identification experiments, a process which has been done for several experiments worldwide (Moreau et al. 2011).

The feedback control experiments described in (Moreau et al. 2008) represent the state-of-the-art in terms of complexity and completeness of the approach. Still, there are some limitations and disadvantages of this method. Firstly, while this method may be appropriate for the flat-top phase, it may have difficulties during transient (ramp-up, ramp-down, ITB formation, L-H transition ...) phases during which the dynamics (time scales, responses to actuators) may vary. Additionally, the identification method is a purely black-box approach and the model is identified from experimental data. The physics of the problem does not enter explicitly into the model structure (other than in the choice of separating the two time scales).

More model-based, control-oriented work has been recently performed by the group of Prof. Schuster at Lehigh, encompassing closed-loop controller design (Ou et al. 2010a), (Ou et al. 2010b), open-loop control (Xu et al. 2010a) and model parameter identification (Xu et al. 2010b). These activities represent a new effort in providing a solid foundation for current profile control and are soon to be tested in experiments (Barton et al. 2010). More work along this lines is provided in the remainder of this thesis.

6.10 Motivations and outlook for Part II

In the final section of this chapter we use the acquired background on tokamak profile dynamics and control to place the contributions of this thesis, which will follow in later chapters, in proper perspective.

In the previous section we introduced profile control as an essential tool for obtaining the attractive hybrid and advanced tokamak plasma scenarios. Some successful experimental developments in the literature have shown control of several parameters related to the profiles, usually by one or a few actuators controlling a set of observed parameters. The controllers were usually based on manual tuning, in simple cases, or on data-driven identified models. The *physics* of the profile control problem enters the control design only in qualitative understanding of what needs to be done. In particular, profile diffusion physics models play an indirect role in controller design at best, sometimes serving as simulation models to test various controllers.

Rarely does the profile diffusion enter directly in a real-time control scheme. This is not surprising since, as we have seen in this chapter, tokamak transport physics is very complex and a large spectrum of physical phenomena can affect the profile evolution in a myriad of ways. Control schemes used today are relatively simple relative to the complexity of the physical system to be controlled. On the other hand, many profile transport simulation codes exist, but most of them are purely physics-oriented: they have been designed to include as much physics as possible in order to reproduce experiments as accurately as possible, and are therefore relatively complex and CPU time consuming.

The core result of Part II of this thesis is the use of profile physics models in tokamak profile control loops. The next chapters will demonstrate applications of a lightweight, simplified model which incorporates the key elements of profile physics described in this chapter in a tractable and efficient manner.

The next chapter, Chapter 7, will introduce this new code, called RAPTOR (Rapid Plasma Transport simulatOR) and explain the main approximations in the physics as well as the choices in numerical implementation that make this code highly efficient in terms of computational time. The two subsequent chapters will present two applications offered by this type of code.

Chapter 8 shows how RAPTOR can be used to simulate the current density profile in tokamak plasmas in real-time. This amounts to solving the poloidal flux diffusion equation (6.26) using real-time diagnostics to determine the kinetic profiles governing bootstrap current and conductivity. Knowledge of the current density profile based on simulations has a number of advantages, primarily related to the fact that a-priori physics-based expectations of the current density evolution can be used to complement diagnostic measurements. The implementation of this scheme on TCV is discussed in detail, but generalizations and applicability to other tokamaks are also presented. The real-time reconstructed profile is used for a feedback control experiment in which both the internal inductance and the central electron temperature are controlled in real-time by a combination of ECH and ECCD in TCV.

Next, Chapter 9 will be devoted to a computational method to calculate optimal feedforward actuator trajectories for open-loop profile control based on a cost function and a set of constraints. The fact that calculations can be performed rapidly allows one to incorporate a profile simulation in a nonlinear optimization scheme which is then

tasked with finding actuator trajectories in time such that a desired profile is reached while simultaneously respecting both physics-based and engineering-based constraints. Prospects for enhancing the open-loop control by closed-loop trajectory controllers will be mentioned.

It should be noted that the development of the RAPTOR code was partly inspired by earlier work on a “control-oriented” model for the current density profile developed in (Witrant et al. 2007). Some possible applications were also mentioned in that paper. However since the development of that model, no actual applications have been reported.

Chapter 7

The RAPTOR code for simulating profile dynamics

7.1 Introduction

The problem of profile transport and control was described in detail in the previous chapter. At the end of the chapter, a motivation was given for using a simplified transport code which contains only the essential physics to solve problems where rapid profile evolution is required. The RAPTOR (RAPid Plasma Transport simulatOR) code was developed with this aim in mind: to provide a lightweight, simplified transport physics code, sufficiently fast to run very rapidly, including in real-time, yet sufficiently complex to contain the most important physics. As such, the RAPTOR code is much simpler and contains less physics than existing transport codes such as ASTRA and CRONOS. However by making the right choices of which physics to simplify, results comparable to these heavier codes have been obtained.

This chapter describes the main assumptions of the reduced physics model in Section 7.2. Information on the spatial discretization method used to discretize the equations is given in Section 7.3. As with many transport codes, RAPTOR can be used either in interpretative or in predictive code, and these two modes are described in Sections 7.4 and 7.5, respectively. The latter section also describes a unique feature of RAPTOR, namely that it returns not only the profile evolution but also the sensitivity of the profile evolution to a chosen set of parameters. This chapter is concluded, in Section 7.6, with an outlook on possible extensions of the RAPTOR model and code.

7.1.1 Relation to previous work

In (Witrant et al. 2007), a control-oriented model was introduced to model the poloidal flux and temperature profile. The model used in this thesis is, to some extent, similar to that model, but differs importantly in the modeling of the electron temperature profile. In the model from (Witrant et al. 2007) the T_e profile shape is parametrized with a set of 3 parameters, which are then each derived from global scaling laws; whereas the approach presented in this thesis solves directly the diffusion equation for T_e including a spatially dependent model of electron energy diffusivity that depends directly on magnetic shear and safety factor profiles. It imposes no restrictions on the T_e profile and

allows extension to more complex transport models. This is more realistic in the case of advanced scenarios with locally improved confinement and transport barriers. Moreover, the numerical scheme used to solve the coupled PDEs is different: finite differences and a mixed implicit-explicit integration method are used in (Witrant et al. 2007), compared to finite elements and a fully implicit method in the present work.

7.2 Reduced physics model

The RAPTOR code in its present form solves the 1D profile diffusion equations (6.26) and (6.53) for $\psi(\rho, t)$ and $T_e(\rho, t)$. The other kinetic profiles T_i, n_e and n_i are kept fixed. The reason for this choice is that the most important nonlinear coupling between plasma profiles during a tokamak discharge stems from the electron temperature-dependent resistivity and bootstrap current and the q profile-dependent confinement. What is more, actuators for temperature and current density are quite effective while the shape of the density profile is, in practice, less well controlled and globally follows a pre-defined evolution during a given discharge (sometimes under feedback control of particle injection/exhaust systems). Still, several more assumptions are made to yield a reduced model for the ψ and T_e profile evolution; these will be discussed below.

7.2.1 Fixed equilibrium assumption

As explained in Section 6.6, the standard practice in 1.5D transport codes is to simultaneously evolve the 1D profiles and the 2D Grad-Shafranov equilibrium. An important simplification used in the RAPTOR code is to not evolve the 2D equilibrium, but to assume the equilibrium is known. More precisely, the spatial distribution of iso- ψ surfaces on the (R, Z) plane is fixed. Additionally, we assume that the enclosed toroidal flux (6.22) is fixed, thereby fixing the spatial distribution of constant $\rho = \rho_{tor}$ surfaces $\rho_{tor}(R, Z)$. As a consequence, the geometric profile quantities G_1, G_2 and V' , as well as J (6.56), (6.27)-(6.29) are fixed in time. Also, the flux-surface-averaged trapped-particle fraction, which enters in the bootstrap current and current drive efficiency (Section 6.4.2), is a function of the magnetic geometry; therefore, it is fixed as well. Finally, the vacuum toroidal magnetic field B_0 is assumed fixed. These restrictions mean that we are, in practice, (i) neglecting variations in diamagnetic effects which cause variations of $J(\rho)$, (ii) neglecting effects due to changes in the flux surface shapes such as motional electric fields and varying geometries, which are primarily the result of varying Shafranov shift as β evolves, and (iii) assuming a fixed plasma boundary in time.

Note that this is a weaker statement than assuming the Grad-Shafranov equilibrium to be fixed, indeed we do allow the poloidal flux profile $\psi(\rho)$, and hence q, j_{tor} etc to change in time. We merely fix the flux surface *geometry* and enclosed *toroidal flux*. By choosing a reference equilibrium, we can treat arbitrary plasma shapes as long as they are not time-varying. Analysis of several plasma equilibria, shown in Figure 7.1, indicates that unless the plasma β varies significantly with respect to the reference, the change in poloidal current density and Shafranov shift will be limited and acceptable. Even a doubling of β results in a variation of G_2/J and V' of less than 10%.

To alleviate this restriction it is also possible, though not implemented yet, to use a time-varying but pre-calculated parametrization for G_1, G_2, \dots as a function of plasma

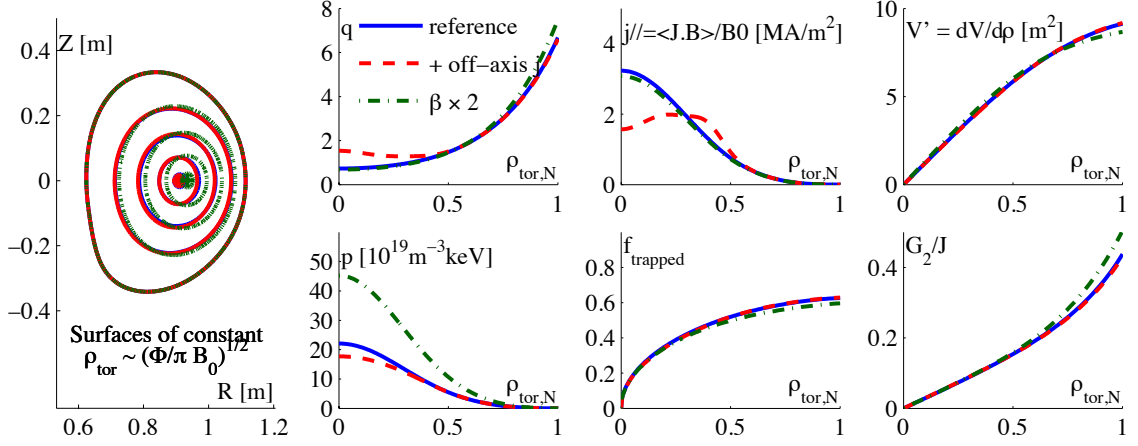


Figure 7.1: Set of three TCV equilibria illustrating the effect of assuming fixed flux surface geometry on the terms V' , G_2/J appearing in (6.26). A reference equilibrium (blue, $-$) is perturbed by redistributing current density to give a reversed-shear q profile (red, $--$), and by doubling the pressure, i.e. β (green, $\cdot-$). The variation in V' and G_2/J can be seen to be within 10% of their reference value. Also the trapped particle fraction, which governs the neoclassical contribution to j_{bs} , σ_{\parallel} and current drive efficiency, is hardly changed. The largest difference appears when changing the pressure through a change in Shafranov shift. The calculations were done using the fixed-boundary MHD equilibrium code CHEASE (Lutjens et al. 1996).

shape parameter such as elongation, Shafranov shift and triangularity. Alternatively, coupling to a Grad-Shafranov code can provide a consistent update of the magnetic equilibrium.

7.2.2 Parametrized heating and current drive sources

Common practice in transport physics codes is to recompute the power density and current density distribution at each simulation time step to reflect the changes due to the evolving plasma, using one of the codes mentioned in Section 6.4.2. These steps can often take a significant portion of the total computational time. In order to obtain a fast and lightweight code, the choice was made for RAPTOR to use only analytical parametrizations for heating and current drive sources. A simple but effective choice is to approximate power and current densities by weighted gaussian distributions which is the choice made for RAPTOR.

The power density to the electrons $P_{e,i}$ for the i th actuator is modeled as a Gaussian

$$P_{e,i}(\rho, t) = P_i(t) \exp\left\{\frac{-4(\rho - \rho_{dep,i})^2}{w_{dep,i}^2}\right\} / \int_0^{\rho_e} \exp\left\{\frac{-4(\rho - \rho_{dep,i})^2}{w_{dep,i}^2}\right\} V' d\rho \quad (7.1)$$

with w_{dep} the deposition width and ρ_{dep} the location of the peak of the deposition. As for the current density, at this stage only ECCD is modeled. The current drive efficiency is known to be proportional to T_e/n_e (Prater 2004) and at the same time decrease with increased trapped particle fraction. This effect is modeled heuristically in the expression below.

$$j_{cd,i}(\rho, t) = c_{cd} e^{\rho^2/0.5^2} \frac{T_e}{n_e} e^{-4(\rho - \rho_{dep,i})^2/w_{cd,i}^2} P_i(t) \quad (7.2)$$

The factor c_{cd} is a machine-dependent proportionality factor (units A/m⁵/eV/W) which can be chosen to scale the expression to experimentally obtained current drive values.

More complex parametrizations can be obtained by performing several runs of more complete codes for representative cases, parametrizing the resulting power and current densities based on the numerical results. It is worth noting that while the spatial distribution of EC and NBI deposition is relatively smooth and continuous with respect to plasma changes, LH and ICRF are much more sensitive to changes in the plasma and such parametrizations may prove to be more challenging.

7.2.3 Ad-hoc transport model and losses

RAPTOR, at present, solves only the energy transport equation for the T_e profile. To close the equations, expressions for the transport coefficients must be specified. A very simple model can be obtained by giving a closed-form expression for the heat diffusivity term χ_e (corresponding to $\chi_{T_e}^e$ in the notation of (6.55)) and setting all other coefficients to zero. In other words, the only driving term for electron heat flux is the electron temperature gradient, and convective transport is neglected. Though any analytical expression can be used, the model presently used in RAPTOR is a closed-form expression similar to that used in (Polevoi et al. 2002), (Albajar et al. 2005), (Garcia et al. 2010). It is constructed so as to reflect increasing confinement due to increasing I_p while having higher conductivity towards the plasma edge. A multiplicative term describes the confinement improvement due to low magnetic shear. The expression reads

$$\chi_e = \chi_{neo} + c_{ano}\rho q F(s) + \chi_{central}e^{-\rho^2/\delta_0^2} \quad (7.3)$$

where χ_{neo} is a (small) neoclassical diffusion term, chosen as a constant but which could be calculated from neoclassical physics. The anomalous diffusion is controlled by c_{ano} , and the presence of q in the anomalous diffusion term accounts for the lower transport at higher currents. $F(s)$ is a shear-dependent function to include the effect of improved confinement at low and negative magnetic shear, responsible for improved confinement (ic) scenarios (see Section 6.8):

$$F(s) = \frac{a_{ic}}{1 + \exp(w_{ic}(d_{ic} - s))} + (1 - a_{ic}) \quad (7.4)$$

here a_{ic} , w_{ic} and d_{ic} govern, respectively, the amount of confinement improvement, the sharpness of the transition and the value of the shear for which the transition takes place. The last term involving $\chi_{central}$ is an ad-hoc term representing a local confinement decrease at the center of the plasma, used to model the experimental observation that kinetic profiles are relatively flat near the center. It is consistent with sawtooth activity in the standard scenario and current hole effects in reverse shear scenarios (Fujita 2010). In this work we use $\delta_0 = 0.1$. An example of χ_e for a reversed-shear q profile is illustrated in Figure 7.2, showing the various terms of χ_e as well as $F(s)$ as a function of s .

Note that out of the seven transport model coefficients (χ_{neo} , c_{ano} , $\chi_{central}$, δ_0 , a_{ic} , w_{ic} , d_{ic}), the first can in principle be obtained from neoclassical calculations, the final three only affect detailed behavior of enhanced confinement regimes, and $\chi_{central}$, δ_0 have only a local effect on the central profile. The most important parameter in this model, having a global effect on confinement is the anomalous transport c_{ano} . This parameter was chosen

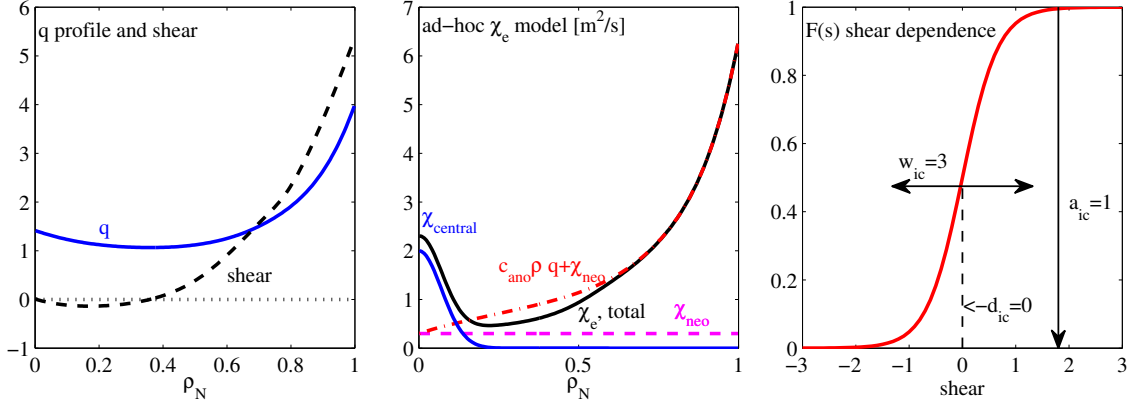


Figure 7.2: Illustration of ad-hoc electron transport model. Left panel: q and shear profile. Central panel: different components of Eq.(7.3), with and without shear enhancement factor F_s . Right panel: illustration of $F(s)$ vs s and dependence on parameters: d_{ic} , w_{ic} and a_{ic} .

by hand to yield reasonable profiles matching experimental observations, while no formal effort was made to quantitatively reproduce existing experiments. Note that c_{ano} could also be chosen to satisfy a confinement scaling such as the ITER scaling law (Doyle et al. 2007). H-mode pedestals are not modeled, thus the model can be used for L-mode only. Reduced transport at the edge can however easily be added by reducing the edge conductivity based on an analytical threshold for the transition.

As for direct loss terms for the electron energy appearing through P_e , sinks such as electron-ion equipartition losses, radiation losses and recombination have been neglected since the ion temperature evolution is not modeled.

7.2.4 Neoclassical conductivity and bootstrap current

The neoclassical conductivity and bootstrap current follow the equations given in (Sauter et al. 1999a), (Sauter et al. 2002b).

The neoclassical conductivity is factored as

$$\sigma_{\parallel}(\rho, t) = c_{neo}(\rho)\sigma_{Spitzer}(T_e(\rho, t)) \quad (7.5)$$

where the Spitzer conductivity is given by

$$\sigma_{Spitz} = \frac{1.9012 \cdot 10^4 T_e [eV]^{3/2}}{ZN(Z) \ln \Lambda_e}. \quad (7.6)$$

Here, $Z = Z_{eff}$ (6.59) is the effective charge and $N(Z) = 0.58 + 0.74/(0.76 + Z)$ depends weakly on Z (Sauter et al. 1999a). While Z_{eff} may in general vary spatially, it is chosen as a fixed quantity for the whole plasma, being difficult to diagnose accurately. The neoclassical correction c_{neo} depends on geometric effects as well as collisionality, but is, for now, evaluated only once for a given equilibrium and temperature profile. Variations in this neoclassical correction due to changes in collisionality (which are small) are therefore neglected in this model, although an extension would be straightforward as simple expressions for the collisionality as a function of T_e and n_e exist.

For the bootstrap current we use (6.30) which is rewritten, assuming $n_i = n_e$ and $\frac{\partial \ln T_i}{\partial \psi} = \frac{\partial \ln T_e}{\partial \psi}$ in a more convenient form involving derivatives of ρ .

$$j_{bs} = -\frac{2\pi J(\psi)R_0}{R_{pe}} \frac{\partial \rho}{\partial \psi} \left[\mathcal{L}_{31} \frac{\partial n_e}{\partial \rho} T_e + (\mathcal{L}_{31} + R_{pe}\mathcal{L}_{32} + (1 - R_{pe})\alpha\mathcal{L}_{34}) \frac{\partial T_e}{\partial \rho} n_e \right] \quad (7.7)$$

The assumption $\partial \ln T_i / \partial \psi = \partial \ln T_e / \partial \psi$ is appropriate because in cases where the T_e and T_i profiles have a very different shape (as is the case, for example, in electron transport barriers, or eITBs), the contribution of T_i to the bootstrap current is modest. One also has the option of assuming $\partial \ln n / \partial \psi = c_T \partial \ln T_e / \partial \psi$ with $c_T = 0.5$. This value is valid in transport barriers and has been shown to be due to the thermodiffusive pinch (Fable et al. 2006). Note that although this last assumption for the n_e contribution to the bootstrap current is inaccurate for non-eITB cases, the bootstrap contribution in such plasmas is in any case rather small. The coefficients α , \mathcal{L}_{31} , \mathcal{L}_{32} , \mathcal{L}_{34} are functions of ρ which depend on collisionality and geometric effects which, as was the case for c_{neo} , above, are kept fixed in this work and calculated once with representative profiles and equilibrium. Note also that $\mathcal{L}_{34} \approx \mathcal{L}_{31}$, allowing further gains in execution speed if necessary.

7.2.5 Summary of equations

Under the approximations described above, Eq. (6.26) becomes

$$\sigma_{\parallel} \frac{\partial \psi}{\partial t} = \frac{R_0 J^2}{\mu_0 \rho} \frac{\partial}{\partial \rho} \left(\frac{G_2}{J} \frac{\partial \psi}{\partial \rho} \right) - \frac{V'}{2\pi \rho} (j_{bs} + j_{aux}) \quad (7.8)$$

And the electron transport equation, in the form of (6.53) becomes

$$V' \frac{\partial}{\partial t} [n_e T_e] = \frac{\partial}{\partial \rho} G_1 V' n_e \chi_e \frac{\partial T_e}{\partial \rho} + V' P_e \quad (7.9)$$

The equations can be written in a more general form as

$$m_{\psi}(T_e) \frac{\partial \psi}{\partial t} = \frac{\partial}{\partial \rho} \left(d_{\psi} \frac{\partial \psi}{\partial \rho} \right) + f_{\psi}(\psi, T_e) + \sum_{i=1}^m S_{i,\psi}(T_e) P_i(t) \quad (7.10)$$

$$m_{T_e} \frac{\partial T_e}{\partial t} = \frac{\partial}{\partial \rho} \left(d_{T_e}(\psi, T_e) \frac{\partial T_e}{\partial \rho} \right) + f_{T_e}(\psi, \frac{\partial \psi}{\partial t}) + \sum_{i=1}^m S_{i,T_e} P_i(t) \quad (7.11)$$

This is a set of two coupled, nonlinear parabolic PDEs on $\Omega = \{t \in \mathbb{R}, \rho \in \mathbb{R} \mid t_0 \leq t \leq t_f, 0 \leq \rho \leq \rho_e\}$. The boundary conditions are given by (6.31), (6.33) or (6.34) and by (6.63), (6.64).

The various terms read

$$m_{\psi}(T_e) = \frac{\sigma_{\parallel}(T_e) \mu_0 \rho}{J^2 R_0} \quad (7.12)$$

$$d_{\psi} = \frac{G_2}{J} \quad (7.13)$$

$$f_{\psi}(\psi, T_e) = \frac{V'}{2\pi \rho} j_{bs}(\psi, T_e) \quad (7.14)$$

$$m_{T_e} = V' n_e \quad (7.15)$$

$$d_{T_e}(\psi, T_e) = G_1 V' n_e \chi_e(\psi, T_e) \quad (7.16)$$

$$f_{T_e}(\psi, \dot{\psi}) = V' P_{OH}(\psi, \dot{\psi}) \quad (7.17)$$

and $S_{\psi,i}$, $S_{T_e,i}$ are, respectively, $V'/(2\pi\rho)$ times the time-independent part of Eq.(7.2) and V' times the time-independent part of Eq.(7.1). The time-dependent inputs $P_i(t)$ represent actuator powers. In this form, the same actuator can have both a heating and current drive effect as is often the case.

Having described the physics assumptions, we turn to the question of how to efficiently solve the equations numerically.

7.3 Spatial discretization

We treat the spatial discretization of the PDE in this section and the time integration for each simulation mode (interpretative or predictive) in the next two sections.

7.3.1 Finite elements

RAPTOR differs from most 1D transport codes in the choice for spatial discretization of the PDE. While most codes use finite difference schemes, RAPTOR uses finite elements. This method has the advantage of allowing a flexible choice of basis functions, a natural implementation of a non-equidistant mesh as well as reduction of the order of spatial derivatives required through integration by parts. The infinite-dimensional PDEs (7.10) - (7.11) for the continuous functions $\psi(\rho, t)$, $T_e(\rho, t)$ are transformed into a set of finite-dimensional ODEs in the finite element coefficients by writing:

$$\psi(\rho, t) = \sum_{\alpha=1}^{n_{sp}} \Lambda_{\alpha}(\rho) \hat{\psi}_{\alpha}(t) \quad \text{and} \quad T_e(\rho, t) = \sum_{\alpha=1}^{n_{sp}} \Lambda_{\alpha}(\rho) \hat{T}_{e\alpha}(t) \quad (7.18)$$

where as finite element basis functions $\Lambda_{\alpha}(\rho)$ we choose non-periodic B-splines (de Boor 2001) having finite support, defined using a set of *knots*

$$\rho_j \in [\rho_1, \dots, \rho_{n_{kts}}] \quad (7.19)$$

with $0 = \rho_1 < \rho_2 < \dots < \rho_{n_{kts}} = \rho_e$.

One has the option of choosing splines of arbitrary order, but in this work cubic splines were chosen as this guarantees continuity up to the second derivative, ensuring continuity of, for example, current densities and magnetic shear. The set of basis functions is furthermore chosen such that all elements have zero derivative at $\rho = 0$. This ensures that the solutions automatically satisfy the Neumann boundary conditions (6.31) and (6.63).

Figure 7.3 shows an example of a $\psi(\rho)$ profile approximated as a sum of cubic splines (Fig.7.3a) on a non-equidistant set of 16 knots. Also shown are the q profile and j_{tor} profile computed directly from the spline representation of $\psi(\rho)$. One can clearly observe that j_{tor} , which is a function of the second derivative of ψ , is continuous but not differentiable if we choose third order splines. Note also that with this choice of splines the edge values are determined only by the first and last spline coefficients.

With this approximation, the PDEs (7.10), (7.11) are rewritten into ODEs: substituting (7.18) into (7.10) and (7.11), then projecting both equations onto a set of basis functions $\Lambda_{\beta}(\rho)$, and integrating by parts, the PDEs are recast into two matrix-vector

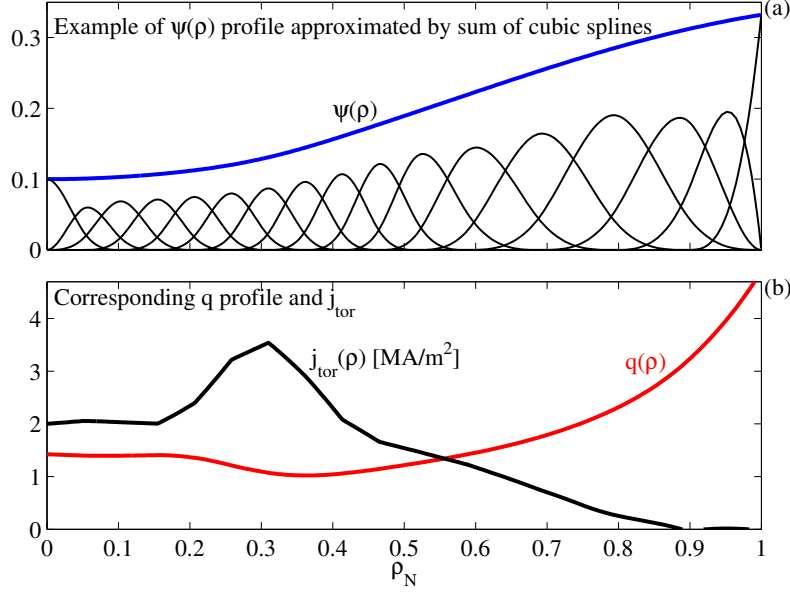


Figure 7.3: Illustration of an example $\psi(\rho)$ profile expressed as the sum of 18 non-periodic cubic splines defined by choosing a set of 16 non-equidistant knot points on the ρ grid. Fig.7.3a shows individual weighted splines and the resulting ψ profile following Eq.(7.18). Fig.7.3b shows corresponding q profile (6.37) and j_{tor} profile (6.36). Note that since $j_{tor} \sim \partial^2\psi/\partial\rho^2$, j_{tor} is continuous but not differentiable at the knot points with this choice of basis functions.

equations involving $\hat{\psi} = [\hat{\psi}_1, \dots, \hat{\psi}_{n_{sp}}]^T$ and $\hat{\mathbf{T}}_e = [\hat{T}_{e1}, \dots, \hat{T}_{en_{sp}}]^T$.

$$F = \mathbf{0} = -\mathbf{M}_\psi(\hat{\mathbf{T}}_e)\dot{\hat{\psi}} - \mathbf{D}_\psi\hat{\psi} + \mathbf{B}_\psi(\hat{\mathbf{T}}_e)\mathbf{u} + \mathbf{f}_\psi(\hat{\psi}, \hat{\mathbf{T}}_e) \quad (\psi \text{ evolution}) \quad (7.20)$$

$$G = \mathbf{0} = -\mathbf{M}_{T_e}\dot{\hat{\mathbf{T}}_e} - \mathbf{D}_{T_e}(\hat{\psi}, \hat{\mathbf{T}}_e)\hat{\mathbf{T}}_e + \mathbf{B}_{T_e}\mathbf{u} + \mathbf{f}_{T_e}(\hat{\psi}, \hat{\psi}) \quad (T_e \text{ evolution}) \quad (7.21)$$

Where $\hat{\psi}, \hat{\mathbf{T}}_e \in \mathbb{R}^{n_{sp}}$. Matrices $\mathbf{M}_\psi, \mathbf{D}_\psi, \mathbf{M}_{T_e}, \mathbf{D}_{T_e} \in \mathbb{R}^{n_{sp} \times n_{sp}}$; $\mathbf{B}_\psi, \mathbf{B}_{T_e} \in \mathbb{R}^{n_{sp} \times m+1}$ and vectors \mathbf{f}_ψ and \mathbf{f}_{T_e} have elements defined by equations (D.12) - (D.19). Note that \mathbf{M} and \mathbf{D} are sparse and have a band structure with bandwidth $2d + 1$ where d is the order of the chosen splines. Details on how the terms in the matrices are efficiently calculated are given in Appendix D.1.3. The input vector \mathbf{u} depends on the choice of boundary condition for the flux diffusion equation:

$$\mathbf{u}(t) = \begin{cases} [P_1(t), \dots, P_m(t), \Psi_{OH}(t)]^T & \text{if Eq.(6.33) is used} \\ [P_1(t), \dots, P_m(t), I_p(t)]^T & \text{if Eq.(6.34) is used} \end{cases} \quad (7.22)$$

In equations (7.20) and (7.21), the \mathbf{M} matrices represent *mass* matrices; the \mathbf{D} matrices are *stiffness* terms and the \mathbf{B} matrices are *input* matrices, translating how the influence of the input vector gets distributed over the profiles. Finally the \mathbf{f} terms are endogenous forcing terms, or sources, which are caused by the profiles themselves.

Using these definitions, the boundary conditions now appear explicitly either as terms in the input vector (7.22) or in the forcing function \mathbf{f}_{T_e} (D.19). Since we choose $T_{e,edge}$ to be a fixed prescribed value throughout this work, we do not include it in the input vector.

Having discussed the main equations and assumptions of the RAPTOR code, we now turn to the different modes of operation.

7.3.2 Computing quantities related to the profile state

It is important to realize that using finite elements we can calculate any related quantity, including all those listed in Sections 6.4.4 and 6.5.5 at any time t and location ρ , including spatial derivatives, directly from the spline coefficient vectors $\hat{\boldsymbol{\psi}}$, $\hat{\mathbf{T}}_e$.

In particular, quantities which could be obtained by applying linear (differential) operators to the ψ or T_e profile, can now be obtained at an arbitrary ρ by taking the inner product of the coefficient vector with another vector¹. To provide a few examples:

$$\iota(\rho, t) \approx \mathbf{c}_\iota^T(\rho) \hat{\boldsymbol{\psi}}(t), \quad (7.23)$$

$$j_{tor}(\rho, t) \approx \mathbf{c}_{j_{tor}}^T(\rho) \hat{\boldsymbol{\psi}}(t), \quad (7.24)$$

$$U_{pl}(\rho, t) \approx \mathbf{c}_\Lambda^T(\rho) \dot{\hat{\boldsymbol{\psi}}}(t), \quad (7.25)$$

$$T_e(\rho, t) \approx \mathbf{c}_\Lambda^T(\rho) \hat{\mathbf{T}}_e(t), \quad (7.26)$$

$$\frac{\partial U_{pl}}{\partial \rho}(\rho, t) \approx \mathbf{c}_{\Lambda'}^T(\rho) \dot{\hat{\boldsymbol{\psi}}}(t), \quad (7.27)$$

$$\frac{\partial T_e}{\partial \rho}(\rho, t) \approx \mathbf{c}_{\Lambda'}^T(\rho) \hat{\mathbf{T}}_e(t), \quad (7.28)$$

where the vector elements are given by

$$[\mathbf{c}_\iota(\rho)]_\alpha = \frac{1}{2\pi B_0 \rho} \frac{\partial \Lambda_\alpha}{\partial \rho}, \quad (7.29)$$

$$[\mathbf{c}_{j_{tor}}(\rho)]_\alpha = \frac{2\pi R_0}{\mu_0 V'} \left(\frac{\partial G_2}{\partial \rho} \frac{\partial \Lambda_\alpha}{\partial \rho} + G_2 \frac{\partial^2 \Lambda_\alpha}{\partial \rho^2} \right), \quad (7.30)$$

$$[\mathbf{c}_\Lambda^T(\rho)]_\alpha = \Lambda_\alpha, \quad (7.31)$$

and

$$[\mathbf{c}_{\Lambda'}^T(\rho)]_\alpha = \frac{\partial \Lambda_\alpha}{\partial \rho}. \quad (7.32)$$

7.4 Interpretative mode

RAPTOR can be run in interpretative mode, in which only the poloidal flux equation (7.20) is solved. The evolution of $T_e(\rho, t)$, as well as all other kinetic profiles required to compute the $\sigma_{||}$, j_{bs} and j_{aux} are assumed to be known, usually from experimental data. This section describes the numerical scheme for the time integration in this mode.

7.4.1 Time discretization

To discretize the continuous-time equation (7.20), a time grid $t = [t_0, \dots, t_k, \dots, t_M]$ is chosen. After combining the source terms $\mathbf{s}_\psi = \mathbf{B}_\psi(\hat{\mathbf{T}}_e) \mathbf{u} + \mathbf{f}_\psi(\hat{\boldsymbol{\psi}}, \hat{\mathbf{T}}_e)$ one can write a general Crank-Nicholson-type discretization scheme

$$\mathbf{M}_\psi(t_{k+\frac{1}{2}}) \left(\frac{\hat{\boldsymbol{\psi}}_{k+1} - \hat{\boldsymbol{\psi}}_k}{\Delta t} \right) = -\mathbf{D}_\psi(t_{k+\frac{1}{2}}) \left(\theta \hat{\boldsymbol{\psi}}_{k+1} + (1 - \theta) \hat{\boldsymbol{\psi}}_k \right) + \mathbf{s}_\psi(t_{k+\frac{1}{2}}) \quad (7.33)$$

¹More formally, we can obtain the projection of these profiles on the space \mathcal{V}_h spanned by the finite-element basis functions or their derivatives.

which is second-order accurate. For practical reasons, let us approximate the terms above in order to obtain the most stable numerical scheme requiring no iterations, at the expense of being less accurate. This is achieved by choosing

$$\mathbf{M}_\psi(t_{k+\frac{1}{2}}) \approx \mathbf{M}_\psi(t_k) = \mathbf{M}_{\psi,k}, \quad (7.34)$$

$$\mathbf{s}_\psi(t_{k+\frac{1}{2}}) \approx \mathbf{s}_\psi(t_k) = \mathbf{s}_{\psi,k}, \quad (7.35)$$

$$\mathbf{D}_\psi(t_{k+\frac{1}{2}}) = \mathbf{D}_\psi(t_k) = \mathbf{D}_\psi \quad (\text{time-independent}), \quad (7.36)$$

$$\theta = 1. \quad (7.37)$$

This gives the following difference equation, implicit in time:

$$(\mathbf{M}_{\psi,k} + \Delta t \mathbf{D}_\psi) \hat{\psi}_{k+1} = (\mathbf{M}_{\psi,k}) \hat{\psi}_k + \Delta t \mathbf{s}_{\psi,k} \quad (7.38)$$

This linear system is to be solved for each time step yielding an update $\hat{\psi}_{k+1}$. Note that the elements $\mathbf{M}_{\psi,k}$ and $\mathbf{s}_{\psi,k}$ of this linear system are all calculated based on the current time step, k , avoiding the need to iterate: a step forward in time to step $k+1$ is made based only on information available at time step k . Experience suggests that when the time step is taken sufficiently small with respect to the characteristic time scales of the equations, errors introduced by the approximations (7.34)-(7.37) are acceptably small. Each time step requires the solution of the linear system (7.38), the left-hand side of which contains a banded, positive definite, symmetric matrix such that the problem can be efficiently solved by LDL^T (Cholesky) decomposition (Golub et al. 1996).

7.4.2 Benchmarking vs ASTRA

To validate and benchmark the Interpretative-RAPTOR algorithm, we can compare simulation results to results from the ASTRA code. The results are shown in Figure 7.4.

Input data was chosen so as to provide a dynamically varying set of profiles. The total plasma current was prescribed as a triangular waveform varying from 100kA to 200kA as shown in Fig.7.4a. Additionally, a set of artificial T_e, n_e, T_i, n_i profiles were generated, all of which had a Gaussian shape and the temperature profiles were programmed to evolve in time following a square wave signal between 0.5 and 1.5keV as shown in Fig.7.4b. This data was then fed to Interpretative-RAPTOR, run using a given baseline plasma equilibrium. The same data was fed to ASTRA, using a parametrized shape for the LCFS based on the elongation, triangularity and minor radius of the baseline equilibrium. Recall that for ASTRA only the LCFS parameters are specified but the internal equilibrium is solved self-consistently, while for RAPTOR the entire equilibrium is static. Z_{eff} was set to 3.5 for both cases. The simulations were run for sufficient time for transient effects due to initial conditions to subside, and a final period of the simulation is compared.

One can observe an excellent agreement between all displayed quantities. Variations were found to be due to the different treatment of the equilibrium due to the fixed equilibrium assumption in RAPTOR. Nevertheless, remarkably good agreement is found in critical quantities such as q profile locations, which are virtually indistinguishable, even with large variations of T_e , and therefore β , by a factor 3.

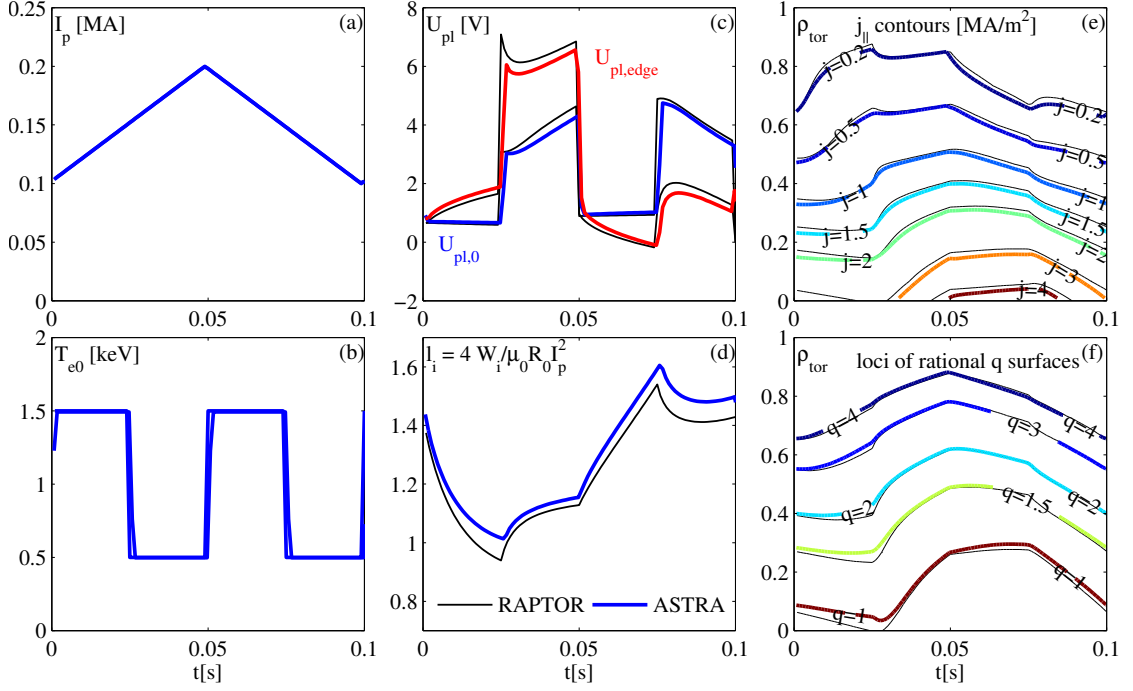


Figure 7.4: Benchmark simulations comparing RAPTOR and ASTRA results for artificial input profiles. A set of Gaussian temperature and density profiles were specified, which were scaled in time to a square-wave shaped central temperature time trace shown in (b). The colored traces represent ASTRA results and the black lines are the corresponding result from RAPTOR. One can see a very good match for the central and edge loop voltage (c), the internal inductance (d) and contour lines of j_{\parallel} (e) and q surface locations (f).

7.5 Predictive-RAPTOR

The predictive version of the RAPTOR code solves the coupled system (7.20), (7.21). The numerical scheme is different, owing to the stiff and strongly nonlinear nature of the equations. A fully implicit scheme is used as summarized below. Uniquely, the predictive-RAPTOR code returns not only the time evolution of ψ and T_e , but also sensitivities of the solution to a given set of parameters. This is discussed in some depth in Section 7.5.2.

7.5.1 Algorithm

For notational simplicity, equations (7.20)-(7.21) are recast in compact form by defining the state

$$x(t) = \begin{bmatrix} \hat{\psi}(t) \\ \hat{\mathbf{T}}_e(t) \end{bmatrix} \quad (7.39)$$

and combining both equations into

$$f = \begin{bmatrix} F(\dot{x}, x, u) \\ G(\dot{x}, x, u) \end{bmatrix} \quad (7.40)$$

thus obtaining

$$f(\dot{x}(t), x(t), u(t)) = 0 \quad \forall t \quad (7.41)$$

Here the bold notation for vectors and matrices has been dropped.

After defining a time grid $t = [t_0, \dots, t_k, \dots, t_M]$, the continuous-time equations (7.20)-(7.21) are discretized in time by choosing

$$\dot{x}(t_k) = (x_{k+1} - x_k)/\Delta t, \quad (7.42)$$

$$x(t_k) = \theta x_{k+1} + (1 - \theta)x_k, \quad (7.43)$$

and

$$u(t_k) = u_k. \quad (7.44)$$

We can then rewrite the discrete-time equivalent of (7.41)

$$\tilde{f}_k \equiv \tilde{f}(x_{k+1}, x_k, u_k) = 0 \quad \forall k \quad (7.45)$$

Varying θ between $\theta = 1$ and $\theta = 0$ allows one to vary between a fully implicit and fully explicit method. We choose a fully implicit method $\theta = 1$, which has advantages for such a stiff system since the time step can be taken quite large without risking numerical stability problems².

A disadvantage is that the nonlinear equation (7.45) must be solved iteratively. This is done by a series of Newton-Raphson iterations at each time step: with given x_k from the previous time step, and known u_k , a solution x_{k+1} to the nonlinear equation (7.45) is found. Details of how the Newton iterations are implemented, as well as a summary of the algorithm, are given in D.3.1. It is important to note that in the Newton step the Jacobian matrix $\mathcal{J}_{k+1}^k = \partial \tilde{f}_k / \partial x_{k+1}$ is computed and factored, and that this matrix will be important in calculating the state sensitivities as explained in the following section.

7.5.2 Trajectory sensitivity

When simulating the system of equations (7.10)-(7.11), it will be important to evaluate not only the evolution of the state x in time, but also the sensitivity of its evolution to a set of parameters. This information will turn out to be very useful for purposes described in Section 9.2, but in this section we will already describe how these sensitivities are computed numerically.

The definition of “parameters” is kept purposely general at this stage, but we may restrict ourselves to model parameters (for example one of the transport parameters appearing in (7.3)) or input parameters (affecting the temporal evolution of the actuator trajectories or initial conditions). It is important to distinguish between the model states (for example ψ) and model outputs (for example j_{tor}) on one hand, and parameters on the other. Parameters affect the time evolution of the simulation and are not a simulation result.

The sensitivity of the state evolution to a set of parameters can be computed using the so-called Forward Sensitivity Analysis method (Cacuci 1981). Differentiating (7.45)

²A similar choice is documented for the BALDUR code (Singer et al. 1988) which solves structurally identical equations. However, note that BALDUR uses the more conventional predictor-corrector method rather than full Newton steps

with respect to a vector of parameters $p \in \mathbb{R}^{n_p}$ we obtain the *forward sensitivity equation* with respect to p :

$$0 = \frac{d\tilde{f}_k}{dp} = \frac{\partial \tilde{f}_k}{\partial x_{k+1}} \frac{\partial x_{k+1}}{\partial p} + \frac{\partial \tilde{f}_k}{\partial x_k} \frac{\partial x_k}{\partial p} + \frac{\partial \tilde{f}_k}{\partial u_k} \frac{\partial u_k}{\partial p} + \frac{\partial \tilde{f}_k}{\partial p} \quad (7.46)$$

This linear matrix equation is recursively solved starting from the initial condition $\frac{\partial x_0}{\partial p}$, yielding $\frac{\partial x_{k+1}}{\partial p}$, for $k \in [1, \dots, M]$. We will now treat each of the terms in slightly more detail.

- The first term on the r.h.s. contains the Jacobian $\mathcal{J}_{k+1}^k = \frac{\partial \tilde{f}}{\partial x_{k+1}}$, which has already been computed and factored in the Newton step (D.34), the solution of (7.45).
- The second term contains the Jacobian $\mathcal{J}_k^k = \frac{\partial \tilde{f}}{\partial x_k}$, which has to be computed. However the expressions for the terms in this matrix have the same structure as those of \mathcal{J}_{k+1}^k , and can be obtained by substituting $\Delta t \rightarrow -\Delta t$ and $\theta \rightarrow (1 - \theta)$ in (D.29)-(D.33). This additional matrix can therefore be additionally computed with minimal effort. Note that there is no need to factor the matrix.
- The third term on the r.h.s. is nonzero only for input parameters, which affect the model evolution via the input trajectories, having nonzero $\frac{\partial u_k}{\partial p}$ for some k . Note that $\frac{\partial \tilde{f}_k}{\partial u_k}$ is related to the \mathbf{B} matrices in (7.20)-(7.21).
- The last term on the r.h.s., on the other hand, is nonzero only for model parameters, i.e. parameters which affect the model directly by altering the equations. Depending on the parameter considered, the appropriate form for $\frac{\partial \tilde{f}_k}{\partial p}$ can be derived analytically.

To compute the state sensitivities with this method one needs to evolve one ODE of the form (7.46) for each parameter in the parameter vector p . The additional computational burden for performing this calculation at the same time as evolving the main PDE is modest, as long as the number of parameters is not excessively large. Indeed, one has to be careful in correctly computing the various derivatives, but since the Jacobians are already known from the Newton iterations, this important step does not need to be repeated. In the following section we will provide a practical example of the information which can be obtained from the state sensitivities.

7.5.3 A simulation example

We now provide a simulation example to illustrate a typical run of Predictive-RAPTOR, for benchmarking as well as to point out some salient features. It will also serve as an example to demonstrate the usefulness of the state sensitivities. This example also serves as an introduction to the operationally relevant plasma current ramp-up scenarios which will be studied more in-depth in later chapters.

Simulation parameters

For this simulation and for all those presented in this thesis, unless specified otherwise, we use the same fixed 2D background equilibrium from an existing TCV shot with elongation

$\kappa = 1.4$ and triangularity $\delta = 0.3$. The other parameters of the simulation, including transport model parameters, are those listed in Table 7.1.

Table 7.1: Simulation parameters. See Eq.(7.3) for the meaning of the transport coefficients.

| Parameter | Value |
|------------------|------------------------------|
| Equilibrium | TCV#41083@1.0s |
| B_0 | 1.44T |
| R_0 | 0.88m |
| Z_{eff} | 3.5 |
| χ_{neo} | $0.5\text{m}^2\text{s}^{-1}$ |
| c_{ano} | $7.0\text{m}^2\text{s}^{-1}$ |
| a_{ic} | 1.0 |
| w_{ic} | 3.0 |
| d_{ic} | 0.0 |
| $\chi_{central}$ | $10.0\text{m}^2\text{s}$ |
| δ_0 | 0.15 |

For this first example, we choose $\Delta t = 0.5\text{ms}$ and $n_{kts} = 41$. These temporal and spatial grids are chosen to be overly dense at this stage: a more thorough investigation of the appropriate gridsize is carried out using a set of benchmarks presented in Appendix D.3.2.

Benchmarking vs ASTRA

To validate the implementation, a benchmark simulation is shown comparing the output of Predictive-RAPTOR to that of ASTRA. First, a simulation was run in Predictive-RAPTOR with the I_p and P_{aux} trajectories shown in Figure 7.5a. Then, the same I_p and P_{aux} , j_{aux} and plasma shape parameters were used in an ASTRA simulation, in which the transport model (7.3) has also been implemented. Again, in both cases, the input trajectory sequence was repeated several times to get rid of effects of initial conditions. The equations solved by ASTRA are identical to those in Predictive-RAPTOR except that ASTRA updates the internal Grad-Shafranov equilibrium and flux surface shapes while RAPTOR does not. Still, as shown in Figure 7.5, the results compare very well, except for some discrepancy at the center which is attributed to the changing flux surfaces. This, however, does not have a strong effect on the q profile evolution, which is the key parameter to be simulated.

Example of plasma trajectory evolution during ramp-up

Next, we simulate a current ramp-up from 80kA ($q_{95} \approx 13$) to 200kA ($q_{95} = 4.8$) in 25ms, followed by another 25ms period of flat I_p and a step of 1MW of EC power deposited at $\rho = 0.4$ ($w_{dep} = 0.35$), giving both a heating and current drive effect. These actuator input trajectories are plotted against time in Fig.7.6a. The remaining panels of Figure 7.6 show a collection of simulation outputs. Fig.7.6b shows contour plots of the rotational transform $\iota(\rho, t)$ in space (vertical axis) and time (horizontal axis), with superimposed contours showing the location of rational q surfaces. Similarly, Fig.7.6c and Fig.7.6d show

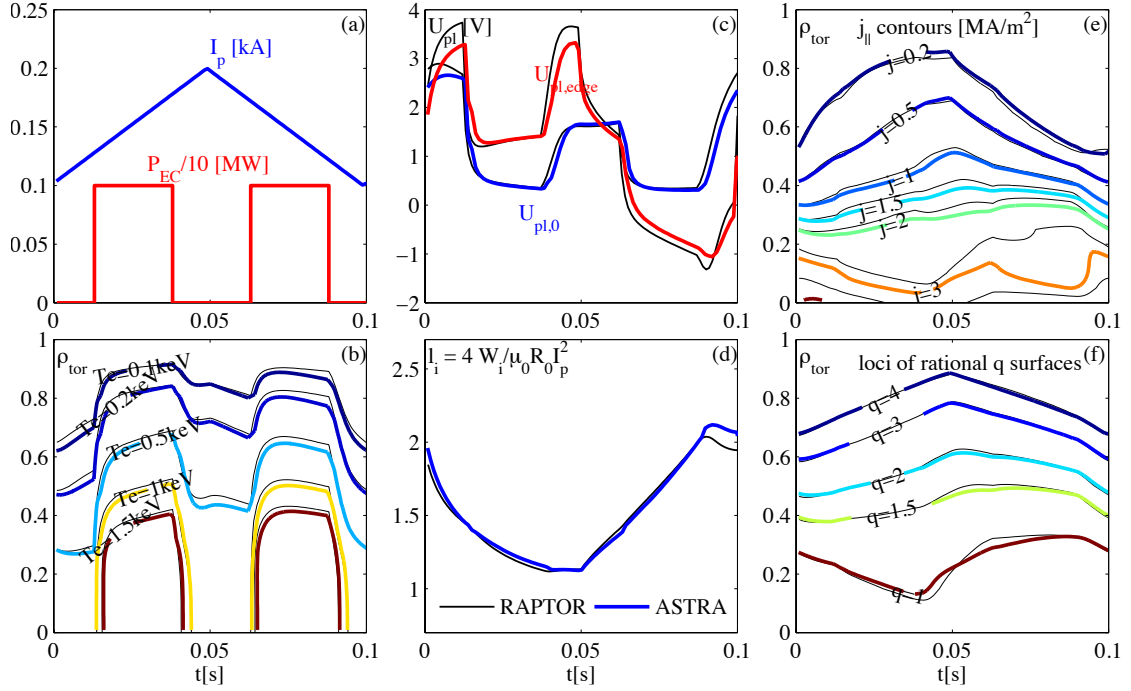


Figure 7.5: Benchmarking of Predictive-RAPTOR (black, thin) vs. ASTRA (color, thick), run with the same transport model and current drive profile. This confirms that the 1-D model used in Predictive-RAPTOR can reproduce the results of the 1.5D profile+equilibrium simulation from ASTRA.

the contours of electron temperature T_e and plasma loop voltage profile U_{pl} , respectively. The four rightmost panels show a collection of profiles at the final time of the simulation ($t = 50\text{ms}$). Fig.7.6e shows the current density profile, separated into Ohmic, auxiliary and bootstrap components. Fig.7.6f shows the safety factor profile and shear, Fig.7.6g shows the kinetic profiles T_e and n_e , as well as the loop voltage profile U_{pl} . Finally Fig.7.6h shows the power sources, separated into Ohmic and auxiliary power, as well as the thermal diffusivity profile χ_e .

Now let us examine some of the main features which are visible on these plots

- In the period before the auxiliary power switch-on, the q surfaces move in response to the diffusion of current in the plasma and the q profile drops slightly below 1 in the center. As the plasma is relatively cold ($T_e < 1\text{keV}$) the loop voltage is also relatively high and is higher at the edge of the plasma: the edge loop voltage, induced by the ohmic transformer, is effectively pulling the I_p ramp of plasma current at this stage.
- At $t = 25\text{ms}$, when 1MW of auxiliary power is added, the electron temperature can be seen in Fig.7.6c to rapidly increase on a confinement time scale of a few ms. There is also an effect on the q profile evolution, as witnessed by the discontinuity in the rational q surface evolution. The decreased resistivity causes a reduction in the overall loop voltage and, combined with auxiliary current drive, causes the current distribution to change with respect to the Ohmic profile. We can also witness

the lower loop voltage around $\rho = 0.3$ for $t > 25\text{ms}$ caused by the back-EMF (electromotive force) in reaction to the auxiliary current drive.

- The profiles at the final time $t = 50\text{ms}$, shown in the rightmost panels, feature a centrally flat q profile with $|s| < 0.5$ for $\rho < 0.46$. This state resembles that of the “hybrid” plasma scenario in terms of q profile, albeit with lower β and thus lower bootstrap current fraction (cf. Section 6.8), and excluding the important H-mode pedestal. However, examining the U_{pl} profile in Fig.7.6g shows that the profiles have yet to reach a stationary state. The central Ohmic current would peak further and the central q would drop if the simulation were allowed to continue beyond this time. Also, notice that the Ohmic power constitutes a small fraction of the total input power, the bulk of which comes from the auxiliary heating source. The thermal diffusivity profile, also shown in Fig.7.6h, is low in the region of low shear $\rho \sim 0.3$ but increases again due to the peaked central heat conductivity introduced, as explained in Section 7.2, to obtain a flat central T_e profile.

Illustration of state sensitivities

The example presented above also provides an opportunity to illustrate the concept of state sensitivities introduced in Section 7.5.2. In the present example we choose to define p precisely as the level of auxiliary power to be injected at $t = 25\text{ms}$. Therefore, $p = p_0 = 1\text{MW}$. This specific choice to parametrize the actuator inputs in time with a discrete parameter can be seen as a special case of *control vector parametrization*, a concept which will be generalized in Section 9.2.1.

At this point, we will simply examine the information given by the state sensitivity to this parameter $\partial x / \partial p$, which is an output of the Predictive-RAPTOR simulation. Recalling the definition of x (7.39) and the profile quantities which can be derived from x such as (7.23)-(7.28), we actually have knowledge of the sensitivities $\partial \iota(\rho, t) / \partial p$, $\partial j_{\parallel} / \partial p$, $\partial T_e / \partial p$ etc. From this information, we can approximate, to first order, the perturbed evolution of the profiles due to a perturbation δp with respect to p_0 , for example

$$\iota(\rho, t)|_{p=p_0+\delta p} \approx \iota(\rho, t)|_{p=p_0} + \frac{\partial \iota(\rho, t)}{\partial p} \delta p \quad (7.47)$$

Following this method, we compute the perturbed evolution of the various profiles for $\delta p = \pm 200\text{kW}$, shown in Figure 7.7. In these figures, the gray curves show the reference, unperturbed case $p_0 = 1\text{MW}$, identical to those shown in Figure 7.6. The blue and red curves show the profiles for $\delta p = +0.2\text{MW}$ and $\delta p = -0.2\text{MW}$ (Fig.7.7a), respectively. As one can see from Figure 7.7b-d, the profile evolutions are identical for $t < 25\text{ms}$. After this time, the additional or reduced auxiliary power causes a different evolution of the profiles.

Qualitatively, we notice that lower power (red) causes more peaked current density profile (Fig.7.7e), lower q profile in the center and higher shear (Fig.7.7f), lower T_e profile and higher loop voltage due to the increased plasma resistivity (Fig.7.7g). Conversely, more power (blue) causes a more reversed q profile with lower (negative) shear (Fig.7.7g), higher T_e and reduced loop voltage.

The computed variation in the profiles is, as mentioned, a linearization with respect to the original (unperturbed) profile evolution. We therefore also compare the perturbed

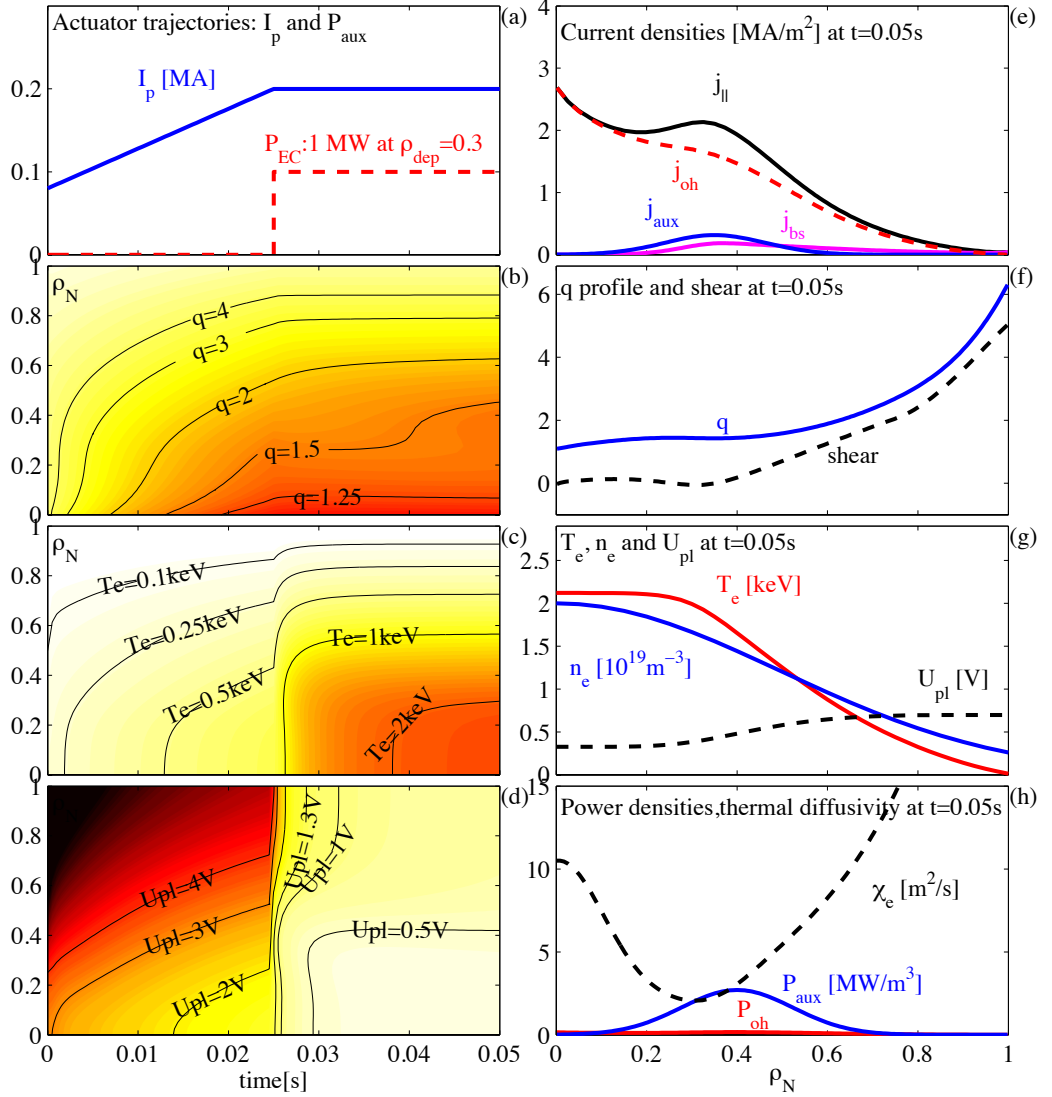


Figure 7.6: Example of tokamak plasma profile evolution during current ramp-up followed by auxiliary current drive switch-on (a), simulated using Predictive-RAPTOR. The temporal evolution of q , T_e and loop voltage U_{pl} profiles shown in space and time in (b),(c),(d), respectively, illustrates how the off-axis current drive creates a q profile slightly above 1 and results in increased plasma temperature and reduced plasma loop voltage. Various profiles at the end of the simulation period $t = 50ms$ are shown in (e),(f),(g),(h). It is observed that the bootstrap current plays a minor role in this plasma, and that the off-axis current results in a magnetic shear close to 0 in the region $\rho < 0.4$.

T_e profile evolution computed with this method to the result obtained from a (new) full nonlinear simulation, i.e. running a new Predictive-RAPTOR simulation again for $p_0 = 1.2MW$. The difference between the two T_e profiles obtained in this way is shown in Fig.7.7h, showing a maximum error of 5eV, which is remarkably small when compared to the typical central T_e values of $\sim 2keV$. Considering that δp is, in our example, 20% of p_0 , one can expect the local linearization to be even more exact for smaller perturbations.

It is important to realize that variation of this single (scalar) parameter impacts the

global evolution of the profiles in space and time, and that the differential variation in every plasma quantity at any point in space and time can be obtained, to first order, by simple operations from the sensitivities $\partial x/\partial p$, which in turn have been previously obtained at low computational cost, in parallel with the original simulation. In essence, $\partial x/\partial p$ is the gradient of the profile evolution trajectories with respect to p . The knowledge of these gradients will prove to be of crucial importance in later sections when we attempt to find a numerical optimum in a multi-dimensional parameter space.

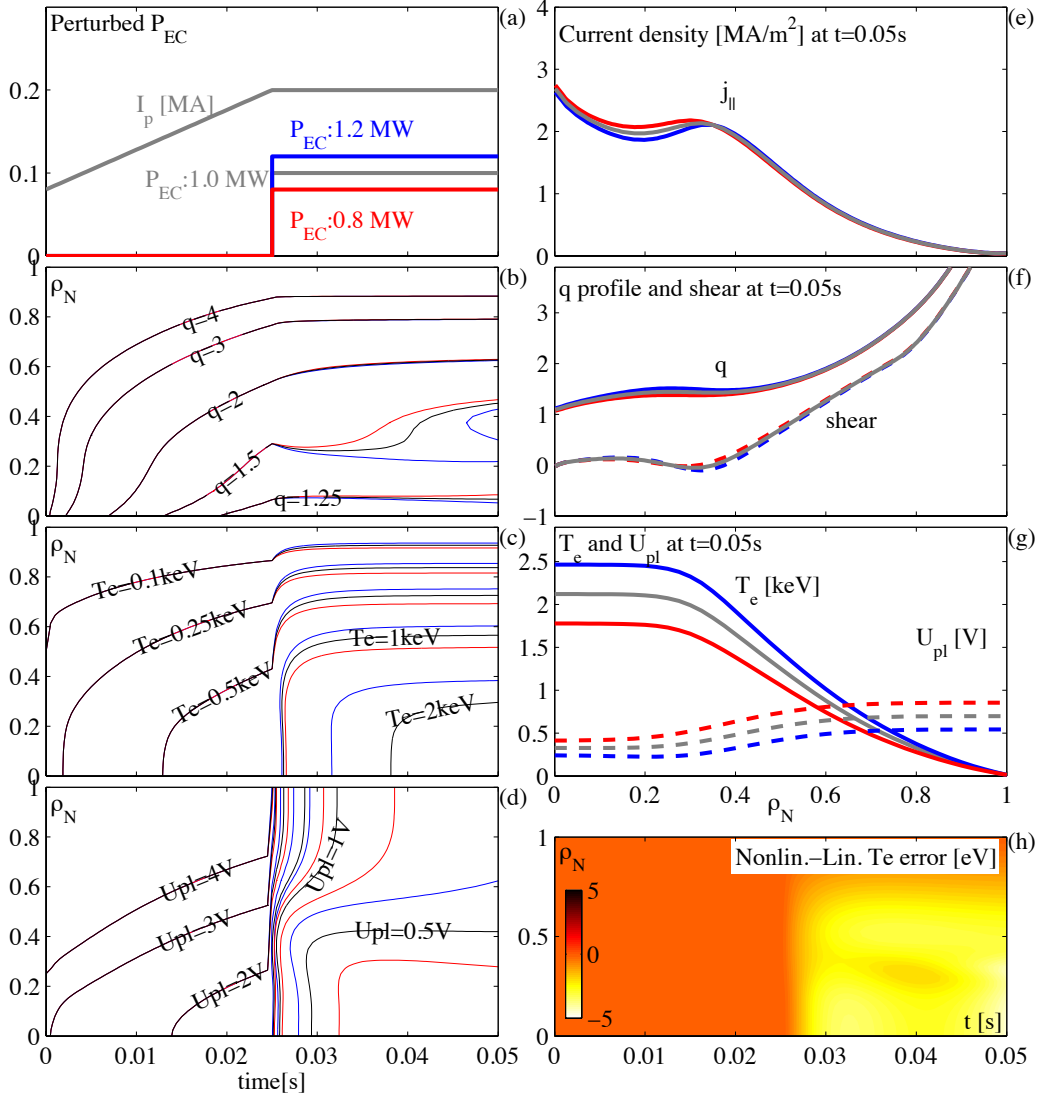


Figure 7.7: Perturbed profile trajectories for variations in the EC power level, calculated from the linearization of the nonlinear profile evolution shown in Figure 7.6. Gray curves show the nominal trajectories, while blue and red curves show, respectively, the trajectories for power variations of $\pm 200\text{kW}$ (a). The evolutions of constant q , T_e and U_{pl} surfaces is shown in (b),(c),(d), and the final profiles of $j_{||}$, q , magnetic shear s , T_e and U_{pl} are given in (e),(f),(g). The error in T_e of the linearized trajectories (blue curve) with respect to a new nonlinear simulation with $P_{EC} = 1.2\text{MW}$ is shown in (h).

7.5.4 Analysis of locally linearized profile dynamics

Let us consider another useful application of the knowledge of the Jacobian matrices, by further exploring the concept of local linearization and analyzing the linear models thus obtained.

Suppose an input actuator trajectory u_k^o (discrete-time notation is used) is given, then the profile state evolution x_k^o can be computed by Predictive-RAPTOR simulation. From knowledge of the Jacobian matrices, we can construct the local, linear model describing the linear dynamics of the profiles at a given time. The system is written in state-space form

$$\delta x_{k+1} = A_k \delta x_k + B_k \delta u_k \quad (7.48)$$

where $\delta x_k = x_k - x_k^o$ and $\delta u_k = u_k - u_k^o$. Matrices A_k and B_k are obtained by linearizing (7.41) around (x_k^o, u_k^o) . The linearization of the state equation $\tilde{f}(x_{k+1}^o, x_k^o, u_k^o) = 0$ (Eq.7.45) reads

$$0 = \frac{\partial \tilde{f}_k}{\partial x_{k+1}} \delta x_{k+1} + \frac{\partial \tilde{f}_k}{\partial x_k} \delta x_k + \frac{\partial \tilde{f}_k}{\partial u} \delta u_k \quad (7.49)$$

where the Jacobians on the nominal trajectory $(x_{k+1}^o, x_k^o, u_k^o)$ have already been calculated for the Newton step, from which one recognizes

$$A_k = - \left(\frac{\partial \tilde{f}_k}{\partial x_{k+1}} \right)^{-1} \frac{\partial \tilde{f}_k}{\partial x_k}, \quad B_k = - \left(\frac{\partial \tilde{f}_k}{\partial x_{k+1}} \right)^{-1} \frac{\partial \tilde{f}_k}{\partial u_k} \quad (7.50)$$

Note that $\frac{\partial \tilde{f}_k}{\partial x_{k+1}}$ is invertible in practice, a condition guaranteed by the existence of a unique solution of the physical problem. The model above is a **linear time-varying system**, consisting of a different linear model at each time step. A vast literature on these kind of systems exists, see for example (Khalil 2001).

To illustrate the diversity of behavior that is contained in this model, the dynamics of the linear systems obtained at each time step is studied. It should be stressed that such point-wise-in-time analysis of time-varying systems is by no means exhaustive and that other characteristics may be hidden. However this analysis highlights some of the fundamental difficulties in analyzing and studying the time-evolving tokamak profile dynamics from a control point of view.

The same plasma scenario and heating/current drive configuration is used as in the previous section, but this time the EC power is not increased step-wise but is gradually increased to its maximum (1MW) value. This provides a smoothly evolving plasma with increasing I_p and heating. The actuator trajectories and profile evolution at a number of instants during the evolution are shown in Figure 7.8(a)-(d). A standard method to visualize the dynamic behavior of a linear system is to plot its impulse response, i.e. the response of some system outputs to a delta function input (or a Kronecker delta, a single-sample pulse in the discrete domain). In the case of time-varying systems one will obtain time-varying impulse-response functions. The panels on the right show these impulse responses for pulses of I_p (Panels (e)-(h)) and P_{EC} (Panels (i)-(l)). Responses are shown of 4 different model outputs, from top to bottom the rotational transform at three radial locations $\rho = \{0, 0.3, 0.6\}$ and the central temperature T_{e0} .

The different impulse responses show dramatically different dynamic behavior as the plasma evolves from a cold low-temperature, low-current plasma to a hot, high temperature, high-current plasma. Not only does the response times become longer with increasing current diffusion time and confinement time, as is to be expected, but note also the initial negative response (known as non-minimum-phase behavior) of $\iota(\rho = 0)$ and $\iota(\rho = 0.3)$. Also, note the varying sign of the response for $\iota(\rho = 0.3)$ to an impulse in P_{EC} .

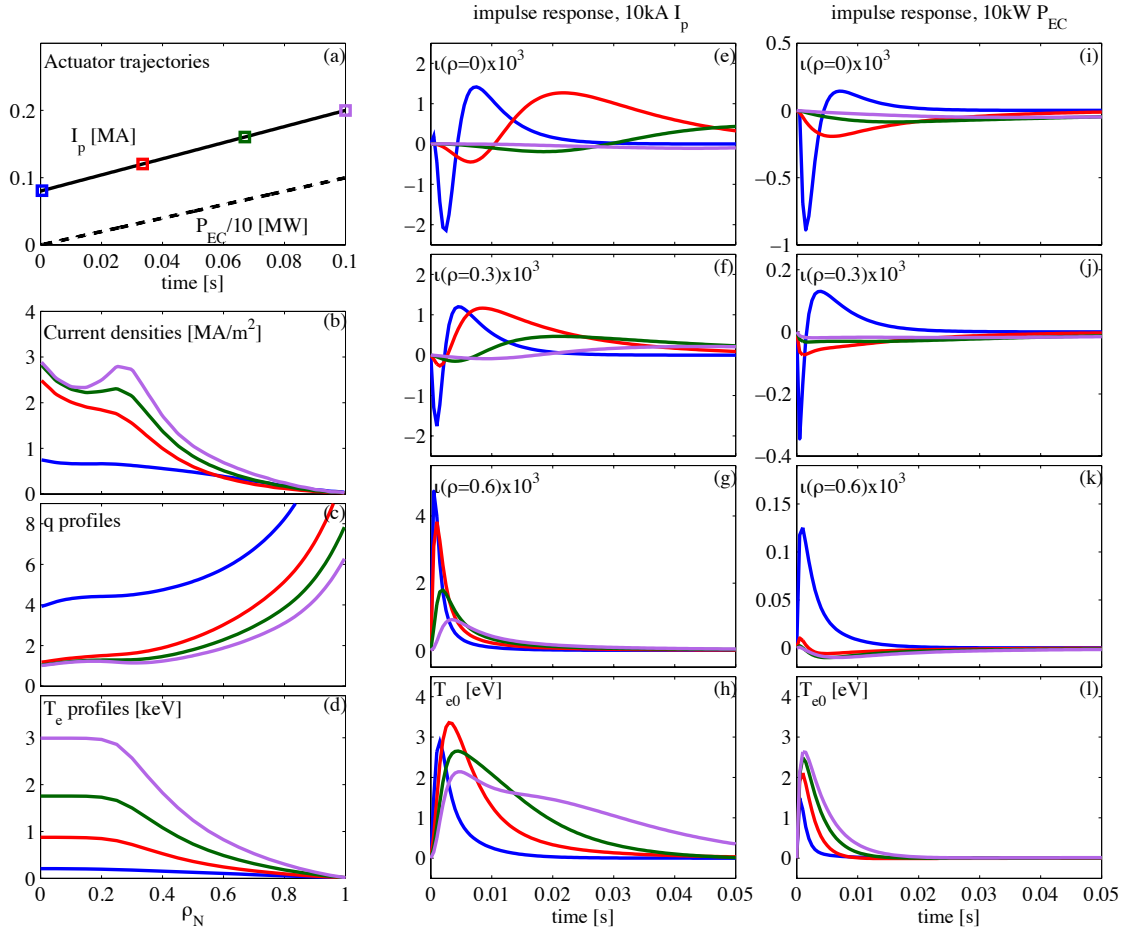


Figure 7.8: Impulse responses of local linear dynamic models at different times during a smooth plasma current and heating ramp-up. Actuator trajectories of I_p and $P_{EC}(\rho = 0.3)$ are shown in (a), profiles at indicated points in time are shown in (b)-(d). Impulse responses of ι (at radial locations $\rho = (0, 0.3, 0.6)$) and T_{e0} to: I_p (e)-(h) and P_{EC} (i)-(l) are shown. Different responses are visible depending on the state of the plasma.

Another way to visualize the variation in system dynamics is to plot the temporal evolution of the poles and zeros of the local linearizations. The poles are simply the eigenvalues of each A_k , while the zeros are the values of z for which the matrix $G_k(z) = C_k(Iz - A_k)B_k$ loses rank. In the complex z plane, poles z_p with absolute value smaller than 1 represent stable modes while $|z_p| > 1$ represents an unstable pole. The closer a pole is to $z = 1$, the longer the characteristic time scale. Unstable zeros, with $|z_0| > 1$ indicate non-minimum phase behavior, or initial undershoot, in linear systems and need to be taken into account in controller design.

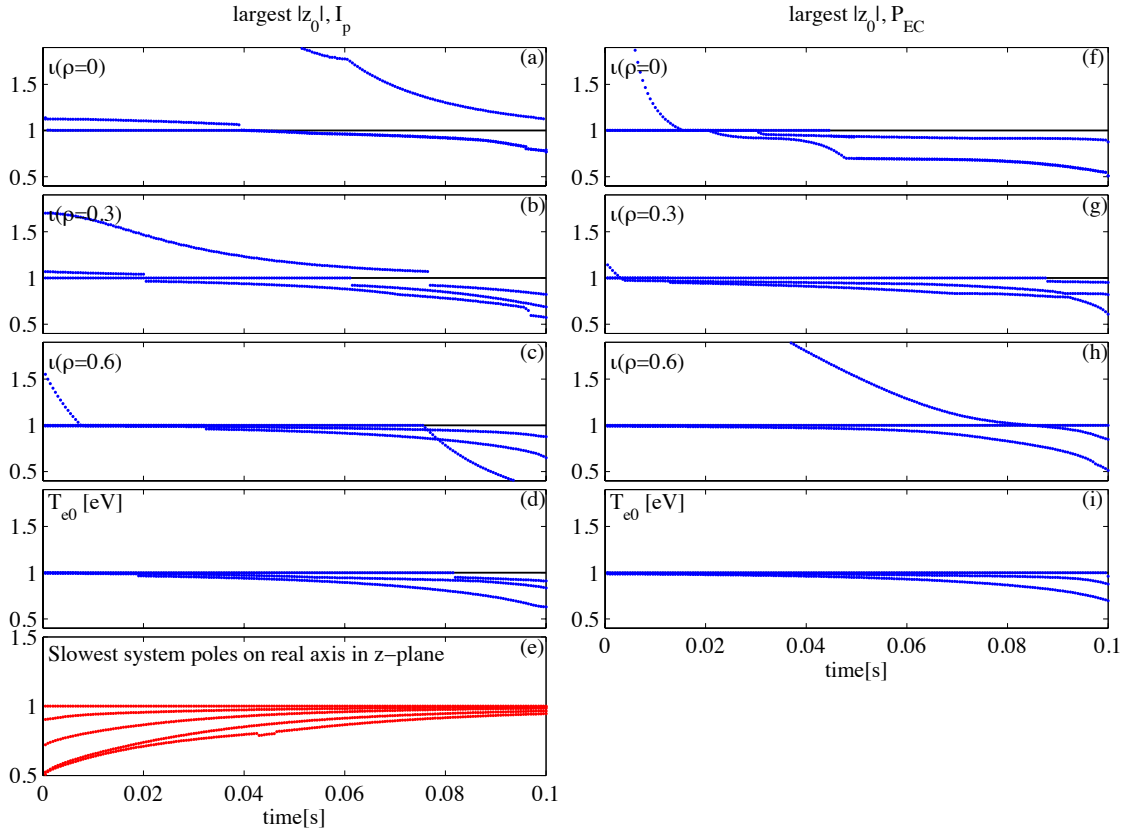


Figure 7.9: Loci of dominant zeros and poles of the linear models as a function of time. For the input-output channels corresponding to Fig.7.8 (e)-(h) and (i)-(l), the zeros with the largest absolute values are shown in, respectively, (a)-(d) and (f)-(i). Unstable zeros with $|z_0| > 1$, corresponding to non-minimum phase behavior, transiently appear and disappear from the mappings. The system poles are shown in (e), and become slower (closer to 1) as the current diffusion time increases.

This diversity in dynamics, depending on time, highlights some of the pitfalls of a purely linear analysis of the profile dynamics. The foregoing analysis represents a first useful application of the Jacobians obtained in computing the nonlinear evolution. More details on the consequences for feedback controller design will be discussed in Section 9.5.3.

7.6 Outlook: extending the physics of RAPTOR

The RAPTOR code was designed from the outset to be a simple, lightweight transport code and never intended to contain the complete physics models of heavier codes which have taken decades of development to reach their present stage. Nevertheless, in this final section of the chapter some additional elements which could be added to RAPTOR, without denaturing it, will be enumerated. Recall that since the numerical integrations are performed using Newton steps, the derivatives of all the analytical expressions included in the model must be specified and handled through propagation of the chain rule. While not posing a conceptual problem, this complicates the development of additional modules.

7.6.1 Extending the kinetic profile transport models

At present only the electron temperature equation is evolved. However, since the structure of the transport equations for ions and for particle density are very similar, it would be a straightforward extension to simulate these profiles. This would be useful in some cases; in particular, if fusion power is to be included in the simulations which may be particularly interesting for ramp-down scenarios. When additional profiles are introduced, kinetic profile coupling via equipartition power and nonlinear terms involving density and temperature in the transport equations must be addressed. More complete transport expressions (including edge pedestals for H-mode scenarios) are possible as well, but it should be remembered that closed-form (differentiable) expressions are preferable, to avoid having to use (computationally intensive) finite difference schemes to obtain the derivatives of transport with respect to the profiles.

7.6.2 Time-dependent equilibrium

Including a time varying Grad-Shafranov equilibrium into RAPTOR can be done in two steps, of increasing complexity. In a first, simplified approach, a pre-computed time evolution of the shape can be used to extract geometric terms which vary in time. These geometric profiles can also be parametrized as a function of global shape parameters κ , δ , Shafranov shift and their temporal evolution prescribed instead. A second, approach is to self-consistently solve the Grad-Shafranov equation with the profile evolution as done in many other codes. Handling a time-varying equilibrium increases the number of time-varying terms in the model and therefore the computational complexity. This additional complexity must be weighed against the foreseen advantages.

7.6.3 Sawteeth, NTMs and other MHD

At present, RAPTOR excludes any MHD events such as sawteeth and tearing modes. These could be added quite simply by using crash-threshold models to trigger a reconnection (e.g. following the Porcelli model, see Chapter 3), though care needs to be taken to properly propagate the parameter sensitivities across these discontinuous events. NTMs can likewise be modeled using the Modified Rutherford Equation (Section 4.2.1), and their effect on the confinement can be included.

In short, there are many opportunities for extending the range of physics covered by RAPTOR without excessive complexity. One must be careful however to include only the necessary equations in a given task, and one must bear in mind the original goal of the code: to provide a simple and fast transport model at the expense of completeness. As such, RAPTOR does not aspire to substitute or supersede existing codes, merely to complement them for specific tasks that have stringent speed constraints. Two such tasks are discussed in the coming chapters.

Chapter 8

Real-time simulation of tokamak plasma profiles

During a real-time simulation of a tokamak plasma, the plasma discharge is evolving (physically) inside the tokamak while at the same time evolving (numerically) inside a computer. By linking the physical reality with the numerical simulation in real-time, a better overall picture of the plasma state can be obtained. Real-time simulations of the plasma profiles are the topic of this chapter¹.

For the TCV tokamak, the real-time constraint places an upper bound on the time step needed to resolve the current redistribution time ($\sim 150\text{ms}$), so the target computation time per time step is a few ms. By careful design and programming, it was possible to implement the interpretative version of RAPTOR, described in Section 7.4, such that one time step takes less than 1ms. This has allowed real-time simulation of the current density profile on TCV, giving real-time information about the current density, q profile and related quantities, which can be used for control and other purposes.

Real-time simulations are not only interesting in their TCV implementation: all existing and future tokamaks can benefit from incorporating this approach in their control systems and the pilot implementation on TCV demonstrates that this is feasible. This chapter will start by describing the advantages and possible applications of real-time simulations in a general sense in Section 8.1, before moving on to the specific TCV implementation in Section 8.2. The results from the real-time simulation are used in a closed-loop feedback control experiment of the plasma internal inductance, shown in Section 8.3. Finally, an outlook on future improvements and uses of these real-time simulations is given in Section 8.4.

8.1 Advantages and applications of real-time simulations

The incorporation of a real-time simulation in an advanced tokamak control scheme is illustrated schematically in Figure 8.1. As can be observed, the physical tokamak (red) receives actuator commands from a control system. At the same time, a real-time simulation is evolved based on the same actuator commands, evolving its own internal estimate of (a subset of) the tokamak state. Real-time diagnostics feed auxiliary information about

¹Some parts of this chapter have been published in (Felici et al. 2011b).

the true plasma evolution to the simulation, thereby providing constraints to the simulation and compensate for modeling uncertainties. On the other hand, the physics-based state estimate can be used to compensate for measurement uncertainties and remove noise and (non-physical) measurement errors. Such a scheme is known in the control systems literature as a *state observer* (Sontag 1998). The parallel between real-time simulation and state observers will be discussed in more detail in 8.4.1.

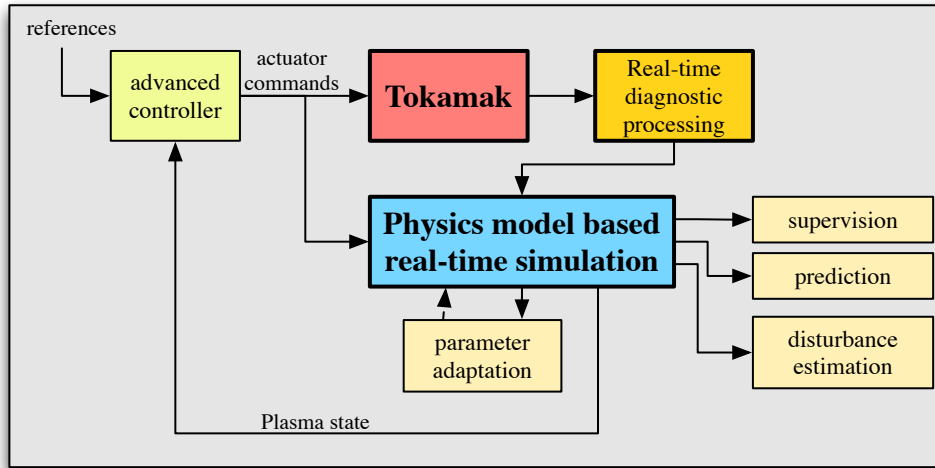


Figure 8.1: Diagram illustrating the envisaged role of a real-time simulation in a tokamak real-time control scheme. The real-time simulator simulates the plasma behavior based on the same inputs as the actual tokamak. Measurements from the available real-time diagnostics are, after pre-treatment, used to help the simulation converge to an accurate plasma state. Mismatches between measured and expected values can be used either to estimate disturbances, or to adapt the model parameters in real-time. Application of the plasma state knowledge to scenario monitoring, prediction and feedback control is also drawn.

Since state estimates, in today’s practice, are based exclusively on the available real-time diagnostics, knowledge of the state has been determined by the availability and spatial/temporal resolution of such diagnostics. The fundamental advantage in using a real-time simulation to obtain the plasma state lies in the exploitation of knowledge about the dynamic behavior of the plasma, as dictated by the physics, for the estimation of the plasma state. In other words, the expectation of how the profiles should be evolving based on our understanding of the underlying physics is taken into account in producing a estimate of physical quantities at any given point in space and time. The available real-time diagnostics can complement and improve the quality of this estimate but a real-time simulation, by itself, can yield information on an arbitrary spatial and temporal scale i.e. beyond the sample time and spatial resolution of diagnostic hardware. This concept is schematically illustrated in Figure 8.2.

The plasma state estimate thus obtained can then be used for a number of applications, which are illustrated below.

State feedback control Feedback control methods, for example the profile control methods described in (Moreau et al. 2008), rely on a sufficient quality measurement of the estimated state in order to work properly. Using the real-time simulated state

8.1. Advantages and applications of real-time simulations

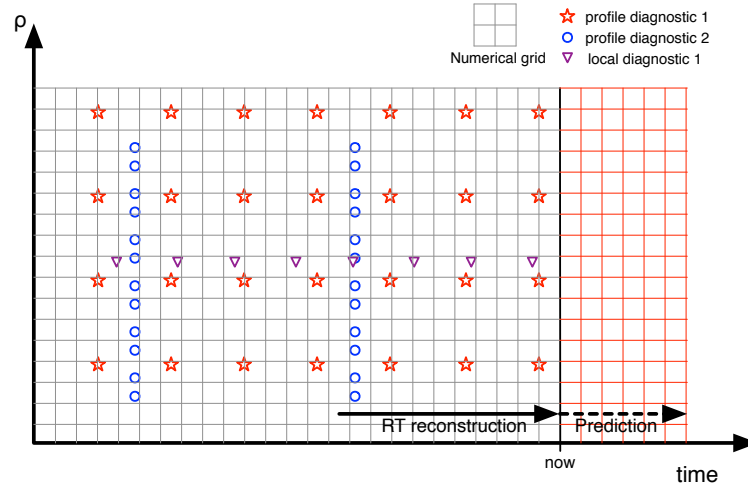


Figure 8.2: Illustration of how real-time simulation can provide information about the plasma state with spatial and temporal resolution determined by the numerical grid on which the simulation is run. Real-time diagnostics of arbitrary spatial and temporal resolution can be incorporated as additional constraints to compensate for model inaccuracies and noise. The knowledge of the plasma state at the current time can also be used in faster-than-real-time simulations to predict the state in the future.

as a basis for real-time control, rather than only relying on individual measurements from specific diagnostics, carries some important advantages. The state estimate is decoupled from the specificities of the diagnostics, which are different for each tokamak, increasing the portability of real-time algorithms, allowing their comparison across different machines. Furthermore, measurement noise present in the diagnostics is filtered out by the real-time simulation if this noise is not compatible with physically-expected, realistic variations in the measured signals. Finally, quantities which can not be directly measured can also be used for feedback control, for example the bootstrap current fraction can be used as a real-time controlled variable in advanced scenarios.

Physics model parameter estimation and adaptation In addition to estimating the plasma state as discussed above, other quantities can be estimated as well. Firstly, parameters in the physics model which are not precisely known may be estimated by incorporating redundant measurements. Secondly, further physics calculations can be performed which do not pertain to calculating the state but give auxiliary quantities of interest. One example is to evolve a sawtooth crash criterion model as presented in (Porcelli et al. 1996), (Sauter et al. 1999b), (see also Chapter 3) in real-time since all the quantities which go into the model are known from the plasma state. This would give real-time estimates of the proximity to the next sawtooth crash. Another example is to simulate the evolution of Neoclassical Tearing Modes (NTMs) by evolving the Modified Rutherford Equation (Sauter et al. 2002b) in real-time. This would allow one to predict, for example, the amount of ECCD required to stabilize an evolving NTM.

Supervision This broad category includes all high-level supervision activities performed by the control system to maximize the scientific output of the tokamak while maintaining safe operation. In particular, the plasma state can be compared to its expected evolution to check whether the plasma is still behaving in a well-understood and expected way. If it is not, this may indicate a new, unexpected phenomenon or, more simply, some piece of missing physics in the model. Since the design of any control system is based on expectations of the plasma response to actuator inputs, an indication that the system is not behaving within the model-based design parameters would be cause for concern and possibly a reason to terminate the plasma in a safe manner. Apart from the safety aspect, supervision can have the goal of rescheduling the evolution of the single tokamak experiment during the shot as needed.

Disruption avoidance One of the key outstanding issues for ITER concerns the need to avoid plasma disruptions as much as possible. As recent focus has shifted from disruption mitigation (Reux et al. 2010) to disruption prevention and avoidance, methods to determine the proximity to a disruption are being studied. Recent methods (Murari et al. 2009), (Rattá et al. 2010), (Zhang et al. 2011) use a variety of machine learning and statistical techniques to infer the proximity to a disruption and give advance warning. These methods rely on past shot data to “train” a classification algorithm, and are shown to be reasonably reliable but with degraded performance for new shots which were not used in training. These algorithms are purely data-driven and do not incorporate physical insight into the causes of disruptions, though much understanding exists (de Vries et al. 2011). Crucially, training shots with disruptions will not be available in ITER, as the objective is precisely to avoid disruptions in the first place. The real-time simulations proposed in this thesis open up the possibility of physics-based disruption prevention. A self-consistent estimate of the plasma state, in particular the q profile and pressure profile, can be compared to known (MHD) physics limits (Hender et al. 2007), and used to provide advance warning when entering a regime with increased risk of disruptions. Also, physics-based disruption prevention becomes independent of specific diagnostics and algorithms can easily be ported from one tokamak to another.

Prediction As a final application, we mention the use of real-time predictive simulations, i.e. faster-than-real-time simulations. This provides estimates of the *future* plasma state based on knowledge of future actuator inputs. In this case one may have to resort to predictive simulations of the type described in Section 7.5. This has important applications in predicting whether actuator saturations or safety limits are about to be exceeded. Taking this approach one step further, one can also optimize future actuator inputs by iteratively predicting the plasma state in a model-predictive control scheme as proposed in (Ou et al. 2007), (Ou et al. 2008).

The motivation and advantages presented here are valid for any tokamak, existing or planned. In this Chapter, the first implementation of a real-time simulation framework on an existing tokamak is presented. It serves as a pilot implementation towards deployment on other tokamaks as well.

8.2 Real-time simulation of TCV current density profile

Up to this point, the definition of which physical phenomena to simulate in real-time has not been stated explicitly. Indeed, any part of Tokamak physics could be simulated as long as a model is available which can be evolved sufficiently quickly. For the pilot implementation on TCV the decision was made to simulate the current density profile. This is for three reasons. First of all, the q profile is of prime importance for the plasma performance and macro-stability, since its shape determines the proximity to operational MHD limits, the presence of improved confinement (e.g. hybrid) regimes or transport barriers, and the appearance and location of tearing modes. Secondly, the physics of poloidal flux diffusion (Section 6.4), which governs the current density profile evolution, is relatively well understood and reliable physics models exist on which to base first-principle simulations. Simulation results, therefore, can be trusted. This is in contrast to the more complex phenomena governing anomalous plasma energy transport, for example, for which first-principle models are much less developed and understood as discussed in Section 6.5.2. Thirdly, the q profile happens to be a quantity which is difficult to measure with sufficient spatial and temporal accuracy in real-time, even after years of development of diagnostics dedicated to do so, such as Motional Stark Effect spectroscopy (MSE) or polarimetry.

Real-time simulation of the current density profile amounts to performing an interpretative transport simulation i.e. solving the poloidal flux diffusion equation (6.26). The interpretative version of RAPTOR, described in detail in Chapter 7, was developed specifically with this application in mind, and is referred to as RT-RAPTOR when used for this application. To solve (6.26) one needs to know the conductivity profile σ_{\parallel} and bootstrap current density profile j_{bs} , both of which depend on the kinetic profiles, as well as the current drive distribution j_{cd} , which is itself a function of the available current drive actuators. The current drive distribution is obtained, in this implementation, from the simple parametrization of Eq.(7.2). The first is obtained from real-time diagnostics as discussed below.

8.2.1 Real-time estimates of the kinetic profiles

In order to calculate the conductivity, bootstrap current and auxiliary current one needs to have estimates of the profiles of T_e , n_e and T_i in real-time. The details of how they are obtained will be different for each tokamak, depending on the available real-time diagnostics. We will now discuss the method implemented on TCV to provide these profiles from the available real-time diagnostic set.

Ideally, a tokamak equipped with real-time T_e , n_e and T_i profile diagnostics could feed this information directly to the real-time flux diffusion simulator. However, the ECE, Thomson scattering and Charge Exchange Recombination Spectroscopy systems available on TCV cannot provide real-time data at this time. We must therefore infer the profiles from other diagnostics that are available in real-time. In the TCV case they are 1) 14 line integrated density measurements from the FIR, 2) 64 soft-X ray chords from the MPX 3) 4 single-chord X-ray measurements with different thickness filters (see Section 2.3 for more details on these diagnostics). The method to combine these measurements into a T_e and n_e profile measurement has been named “TENEX” (TE and NE from X-rays).

As TCV plasmas have only direct electron heating, the ion temperature T_i plays a relatively modest role in the sustainment of the bootstrap current and ions store a relatively small and constant fraction of the total plasma thermal energy. Lacking a real-time diagnostic to measure the T_i evolution, we fix this profile and take the value during the initial, Ohmic phase of the discharge (before any auxiliary heating is applied), which yields, on average $T_i^{ohmic} \approx 0.7T_e^{ohmic}$ at the densities used in the discharges considered here.

The remaining problem is to estimate the T_e and n_e profiles. The centrally weighted electron temperature $T_{e0} = T_e(\rho = 0)$ is directly provided by the XTe diagnostic by taking the ratio between X-ray intensities measured with different thicknesses of Beryllium filters. This diagnostic has been calibrated against Thomson Scattering measurements in the past and is known to give a reasonable quality estimate. To estimate the T_e profile shape $\tilde{T}_e(\rho) \equiv T_e(\rho)/T_{e0}$, and the density profile $n_e(\rho)$, we rely on a combination MPX and FIR chords. As the SXR intensity has the dependence $I_{sxr} \sim n_e^2 T_e^\alpha$ where $\alpha \sim 0.5 - 1$, the n_e and T_e profiles can in theory be derived from a nonlinear mapping from these two measurements. We have chosen to construct this mapping using machine-learning based techniques which are discussed in more detail in Appendix E. In this approach, a set of shots with similar plasma shape is collected for which the n_e , T_e profiles are known from off-line post-shot Thomson Scattering data. Using this shot database, a neural network is constructed which maps the data of the MPX and FIR chords to profiles of $n_e(\rho)$ and $T_e(\rho)$. After training the network, it can be used in real-time to estimate these profiles from fresh XTe, MPX and FIR data.

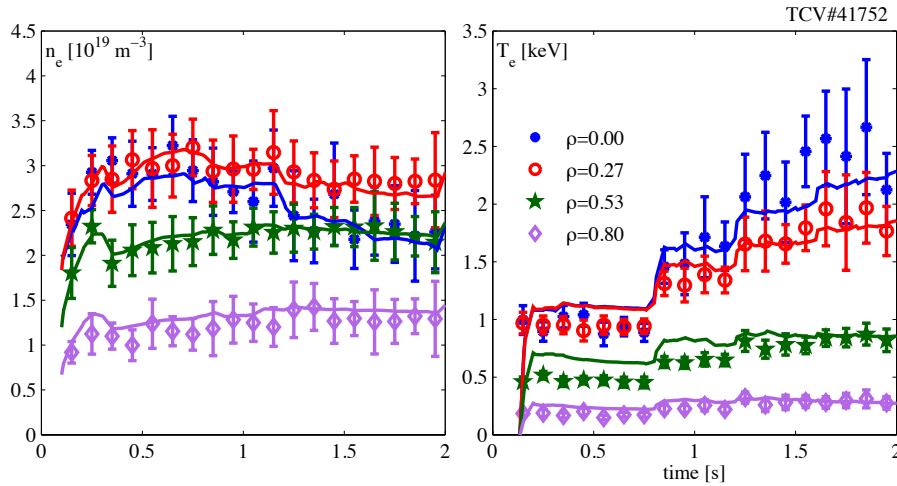


Figure 8.3: Comparison of post-shot fits of Thomson data for $T_e(\rho)$, $n_e(\rho)$ (points with errorbars) and real-time estimates (solid lines) using TENEX to reconstruct the profiles from interferometer and X-ray diagnostics. Note that the value of $T_e(0)$ is separately determined using a dedicated real-time diagnostic and only the profile shape is determined by mapping from the multichannel soft-X ray diagnostic. During this shot the EC heating power was increased in steps, causing an increase in T_e and a hollow density profile due to pump-out effects.

Profiles estimated by TENEX, in real-time, for one example shot are shown in Figure 8.3 and compared to Thomson scattering measurements for the same shot. We see that the T_e profile is relatively well reproduced by the neural network and the main dif-

difficulty resides in the estimation of $T_e(0)$ from the XTe diagnostic. On the other hand, both $n_e(0)$ and the n_e profile are well reproduced. We note here that this approach has been taken mainly because a direct T_e profile measurement is not available in real-time on TCV at this time. If such a measurement were available, the data could be used directly, avoiding the need for this scheme.

8.2.2 Implementation on the TCV digital control system

This section deals with the implementation of the RT-RAPTOR real-time simulation and the TENEX real-time kinetic profile reconstruction in the TCV digital control system described in Section 2.4.2.

The overall structure of the TCV implementation of the interpretative transport simulations is shown in Figure 8.4. Each of the four rectangles in the figure corresponds to a distinct hardware node which is described below

- The first node (RT01) has its ADCs connected to both FIR and MPX diagnostics in the TCV hall. On this node, both the TENEX diagnostic mapping and the RT-RAPTOR algorithm are hosted. Feedback controllers which use the data from RT-RAPTOR are also hosted in this node and will be discussed in Section 8.3. This node runs with a step time of $900\mu\text{s}$ which, for this hardware, is close to the limit of its computational capabilities (if need be, much more powerful hardware could be installed).
- The second node (RT02) is connected to the full set of magnetic and coil current measurements. A software replica of the hybrid analog TCV control system (Lister et al. 1997), which controls the plasma current, position, shape (partly) and density, runs here at a sample time of $100\mu\text{s}$. In these experiments, this node provides real-time estimates of plasma current and loop voltage. These quantities are written into the reflective memory at each time step and are thus available to other nodes, in particular RT01 where $I_p(t)$ is used as a boundary condition for RT-RAPTOR.
- The third node RT03 is connected to the network, reads selected data from the shared memory and displays it in real-time on a screen in the control room.
- The fourth node RT04 is left in stand-by but will be used to perform other tasks such as hosting a real-time Grad-Shafranov solver at a future date.

8.2.3 Results and comparison to off-line ASTRA and LIUQE

The RT-RAPTOR algorithm was first tested during several plasma shots on the TCV tokamak. The digital real-time control system was not controlling the TCV plasma, but running the simulation in the background using the real-time acquired diagnostic data. As mentioned in the previous section, the time step for the simulation and profile reconstruction was 0.9ms , more than two orders of magnitude below the TCV current redistribution time for heated plasmas ($\tau_{crt} \sim 150\text{ms}$). While this could be improved further by using higher performance CPUs and by parallelization, it was sufficient for the given application. A grid size of 41 equally spaced radial points was used, ensuring a largely sufficient spatial resolution with respect to the spatial scales of interest.

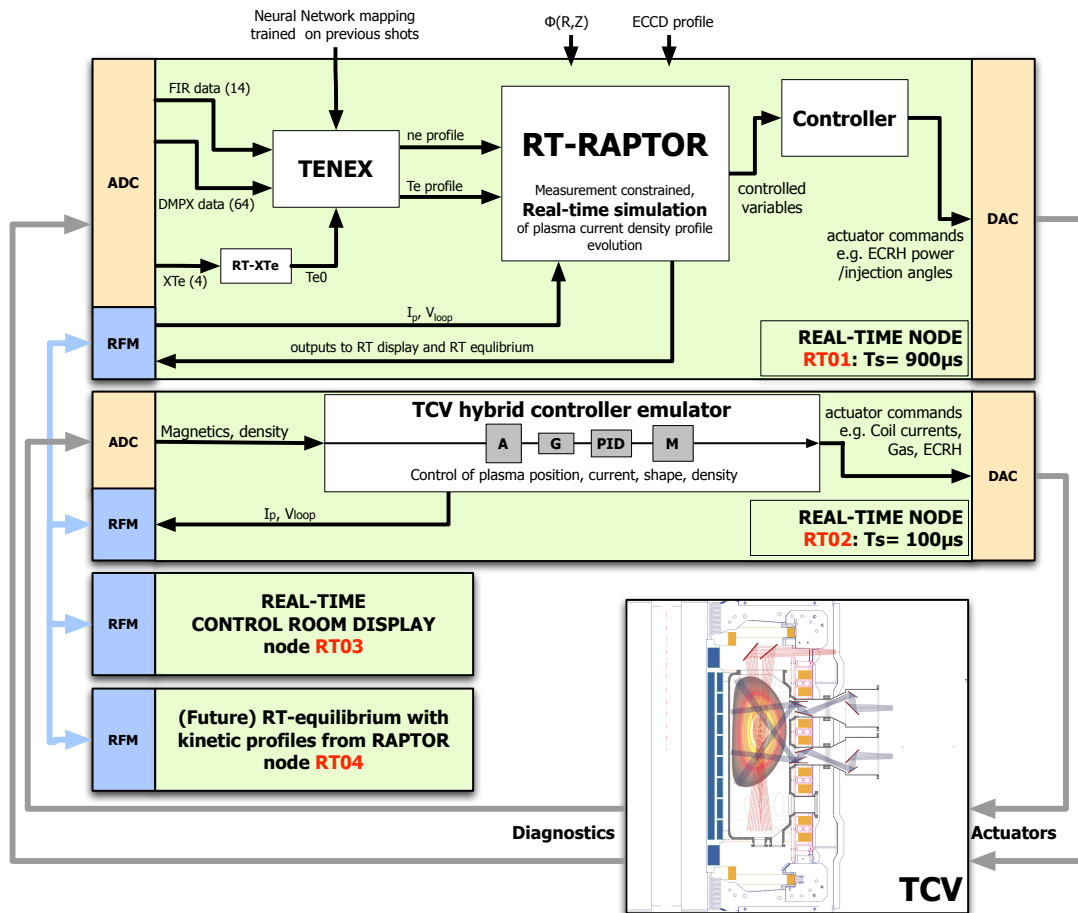


Figure 8.4: Diagram of the implementation of RT-RAPTOR in the distributed TCV digital control system. The main algorithm is run on node **RT01** which is connected to the profile diagnostics needed to reconstruct the T_e and n_e profiles. Measurement of I_p is provided by a second node (**RT02**) which runs a functionally identical copy of the TCV analog control system. As explained in detail in Section 2.4.2, each node is connected to a different set of actuators via ADCs and commands a different (sometimes overlapping) set of actuators via DACs. Information is exchanged via a real-time reflective (shared) memory (RFM). The third and fourth nodes (**RT03**, **RT04**) are now passively observing data generated from the other two nodes, but could be used for other applications in the future.

The boundary condition is given by the plasma current, which is available in real-time from node RT02. With this choice, the measurement of V_{loop} from a flux loop outside the vessel is redundant since it can also be obtained from the simulation as $U_{pl}(\rho, t)|_{\rho=\rho_e}$. This redundancy is used to allow RT-RAPTOR to adapt the value of Z_{eff} in real-time. The value of Z_{eff} is increased or decreased, depending on whether the plasma voltage is overestimated/underestimated (corresponding to too high/too low Z_{eff} , respectively). This is implemented into the real-time loop in the form of a parameter adaptation law for Z_{eff} , using the simple expression

$$Z_{eff,k+1} = Z_{eff,k} + \gamma[V_{loop,meas} - U_{pl}(\rho_e)]. \quad (8.1)$$

Here, γ is the adaptation gain which is tuned empirically. At this stage, a flat Z_{eff} profile is assumed. A more general discussion of this idea is given in Section 8.4.2.

To illustrate the capabilities and typical results of the code, we present two different types of shots. Time traces obtained in real-time are compared, where possible, to offline data obtained from (a) the off-line Grad-Shafranov equilibrium code LIUQE (Section 2.3.4) and (b) an off-line interpretative transport simulation performed using ASTRA. The boundary and plasma current used in the ASTRA simulations were taken from the LIUQE equilibrium data, while kinetic profiles were taken from Thomson scattering measurements.

Plasma current ramps

As a first and basic test of the current diffusion simulation, we present an example plasma in which the current is forced to diffuse by repeatedly varying the plasma current I_p between 240kA and 160kA with different linear ramp rates. We use this example to focus on some of the magnetic quantities calculated by RT-RAPTOR. A selection of the real-time data coming from the RAPTOR flux profile reconstruction is shown in Figure 8.5.

We mention four important events occurring during the evolution of this plasma:

- $t = 0.3s$: The control loop for elongation feedback is closed, bringing the plasma to the required elongation. This leads to transients in the coil currents which induce some sharp variations in loop voltage.
- $t = 0.4s$: The first current ramp is initiated, bringing the plasma current from 160kA to 240kA in 50ms, and simultaneously the ECH power is switched on, leading to increased temperature and decreasing loop voltage due to the lower plasma resistivity.
- $t = 1.0s$: A slower ramp-down is imposed, to bring I_p back to 160kA in 100ms. The lower current gives lower particle confinement such that a lower density is obtained, yielding higher temperature at constant auxiliary input power.
- $t = 1.6s$: An even slower ramp-up back to 240kA is performed in 200ms.

The profile of $I_{pl}(\rho, t)$ is plotted in Fig.8.5a for distinct values of ρ , showing how the change in I_p (controlled by feedback) diffuses into the plasma on the current redistribution time scale as expected. The values of T_{e0} obtained from the XTe diagnostic are shown,

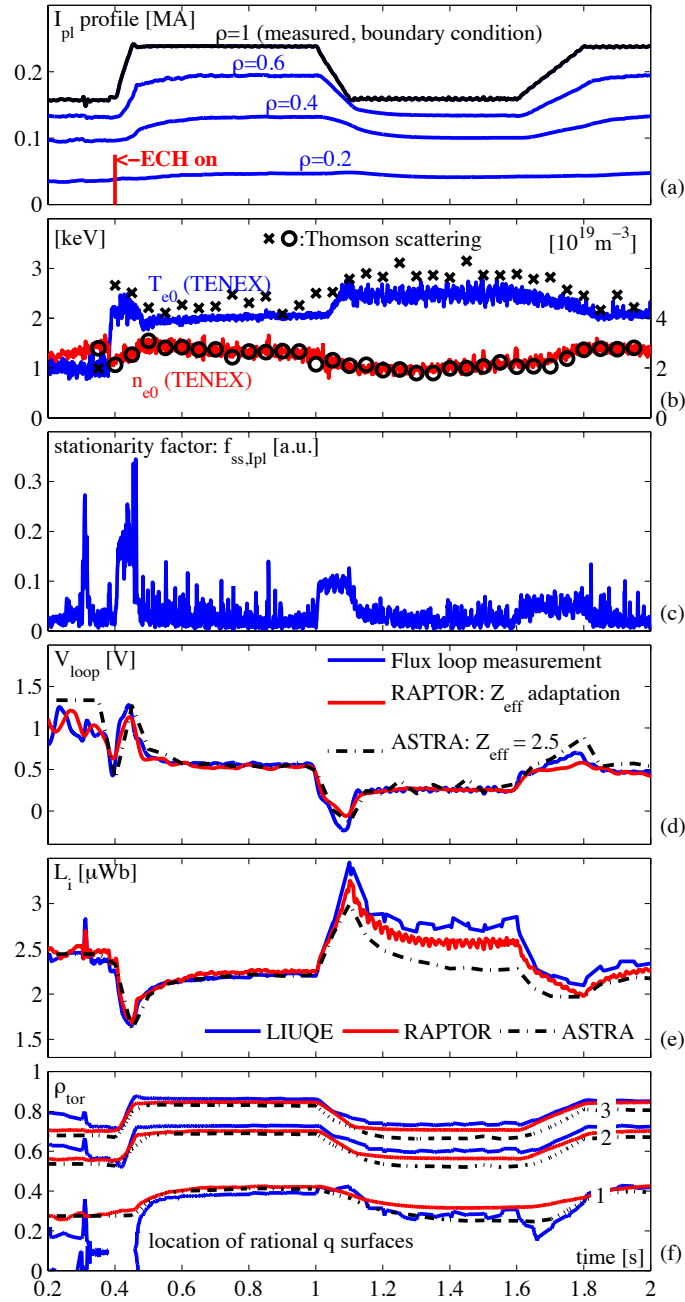


Figure 8.5: Illustration of real-time data output by the RAPTOR real-time simulation, on a shot with several changes of I_p (TCV#41479). Panel (a) shows the evolution of the $I_p(\rho)$ profile for different values of ρ . The edge value is constrained to the measured value as a boundary condition. The evolution of the profile for inner flux surfaces shows the inward diffusion of the plasma current. The second plot (b) shows the central T_e and n_e used for calculating the conductivity and bootstrap current. Also shown (c), is an indicator of the degree of stationarity of the I_p profile. Comparing V_{loop} (d), L_i (e) and the q (f) surface locations to measured data and off-line reconstructions using the LIUQE equilibrium code and ASTRA interpretative transport modeling shows that the real-time results are very close to those obtained post-shot.

in Fig.8.5b, to slightly underestimate the off-line Thomson measurements but are within reasonable margins of the measured values.

This plasma provides an opportunity to illustrate the degree of stationarity of I_{pl} as defined in (6.48). The reader should recall that it is the square norm of the profile $\frac{\partial}{\partial t} I_{pl}(\rho)$ which is related to the spatial derivative of the voltage profile. A high value of $f_{ss, I_{pl}}$ indicates that the I_p profile is evolving, while a zero value indicates it is stationary. In Fig.8.5c, one can clearly distinguish a phase of constant f_{ss} while the ramp-up is being performed, and a subsequent relaxation on the resistive time scale after I_p has reached its target value. Note the longer phase of increased $f_{ss, I_{pl}}$ corresponding to the lower current ramp rate at $t = 1.6$ s, and the shorter, higher peak in variability for the rapid current ramp at $t = 0.4$ s. Indeed, this quantity shows the degree to which the current profile has relaxed to a stationary state.

Figure 8.5d compares the loop voltage from RAPTOR, where Z_{eff} was adapted, to the measured loop voltage. This same loop voltage is also compared with the loop voltage from a post-shot interpretative transport simulation using ASTRA, with fixed $Z_{eff} = 2.5$, showing good agreement even in the transient phases. Finally, we also plot the internal inductance and radial location of rational q surfaces in Fig.8.5e,f. For the most part the real-time results show excellent agreement with the results from off-line analysis. The internal inductance estimates diverge somewhat during the second part of the shot, but this can be explained by the fact that the plasma shape (elongation) increases during this phase, in spite of the elongation feedback, due to one PF coil behaving unexpectedly for technical reasons from $t = 1.0$ s onwards. While this is taken into account in the equilibrium reconstruction from LIUQE, the RAPTOR result assumes a fixed equilibrium and is not aware of this change. Nevertheless, the estimate lies between the value estimated by LIUQE and ASTRA.

Auxiliary power steps

In a second shot we investigate confinement quantities, such as W_{kin} , τ_E and confinement scaling factors, by imposing the sequence of steps of second harmonic X-mode (X2) ECH heating power shown in Fig.8.6a. The kinetic profile reconstruction for this shot was previously illustrated in Fig.8.3. The power steps will yield changes to the plasma power balance, and RT-RAPTOR can be used to compute this power-balance in real-time as we will see.

The sequence of EC power steps cause a change in electron temperature and an increase in (electron) thermal energy (Fig.8.6b), but also increased conductivity leading to a redistribution of the current density and q surface locations (Fig.8.6f), and decreased loop voltage (Fig.8.6d) and Ohmic input power.

The value of Z_{eff} was, as in the previous example, adapted in real-time in order to match the measured loop voltage. The measured loop voltage is also compared to the value obtained from an off-line ASTRA simulation using Thomson profile data and a fixed value of $Z_{eff} = 2.5$, and shows a very similar evolution. The downward drift in the estimated Z_{eff} appears unrealistic (an increase is more likely with auxiliary power) but can be explained by errors in the T_e reconstruction. As can be observed from Figure 8.3, the initial T_e is overestimated whereas the final T_e is underestimated. This would explain why the adaptive algorithm compensates by initially increasing the Z_{eff} estimate and

decreasing it during the shot. This example illustrates that an accurate reconstruction of T_e is crucial for accurate estimation of Z_{eff} using this method. The noise in the confinement data can be explained as coming directly from the MPX diagnostic which is used in the determination of T_e , where the high-frequency oscillations largely result from sawteeth. Since the flux profile evolves on a slower time scale, the T_e oscillations in the simulations do not appear in the current density profile simulation, and no further filtering is necessary.

The extra auxiliary power causes a net decrease in confinement time as expected from known scaling laws (Fig.8.6c). Comparing the confinement time to the TCV L-mode scaling, which follows the Rebut-Lallia-Watkins scaling (Rebut et al. 1989), (Coda et al. 2000), reveals an $H_{TCV-Lmode} = \tau_E/\tau_{RLW}$ factor of just under 2 (Fig.8.6d) as is typically the case when the EC power is deposited inside of the $q = 1$ radius, as predicted in (Sauter et al. 2001). We stress again that the quantities shown here are now available in real-time during the shot, rather than post-shot from transport analysis, and could now be used for monitoring and control purposes.

8.2.4 Discussion and possibilities for improvement

All the real-time simulations shown above have given satisfactory results within error margins expected from diagnostics. Whenever the real-time simulation results have been compared to post-shot (offline) simulations, good agreement was obtained taking into account the different information available to the various methods. The experience gained operating this real-time interpretative transport code during TCV tokamak experiments, however, allows us to highlight a number of possible improvements to the system as presently implemented.

As illustrated in Section 8.2.1, TCV currently lacks a real-time T_e profile diagnostic and the reconstruction is done using indirect means, heavily relying on a single chord T_{e0} estimate and multi-chord X-ray wire chamber. This has often led to errors in the T_e profile estimate which is a crucial quantity strongly influencing conductivity, bootstrap current and confinement estimates. Particularly if these real-time simulations are to be applied to advanced scenarios with significant bootstrap current fractions, the correct determination of the T_e profile with steep gradients will be particularly important in order to simulate the correct current density profile (although, to some extent, this requirement may be alleviated by using an ad-hoc method to estimate the T_e gradients in these specific plasmas). Secondly, the simulation currently requires a number of similar shots to be performed beforehand, with an adequate range of heating and density conditions, to establish the neural network mapping from real-time diagnostics to kinetic profiles. A new shot database must be constructed if the plasma shape or position is significantly altered. It would be a major advantage to have a real-time T_e and n_e profile measurement of high spatial resolution to be able to improve on the results, entirely avoiding the neural-network based fits described in Section 8.2.1. Furthermore, any additional measurements of internal current profile quantities would provide extra constraints and redundancy in the system and yield improved current density profile estimates. Finally, time-varying equilibria could be included along the lines discussed in Section 7.6.2.

An outlook on how the present system could be extended and implemented on ITER and other tokamaks is given in Section 8.4.4.

8.2. Real-time simulation of TCV current density profile

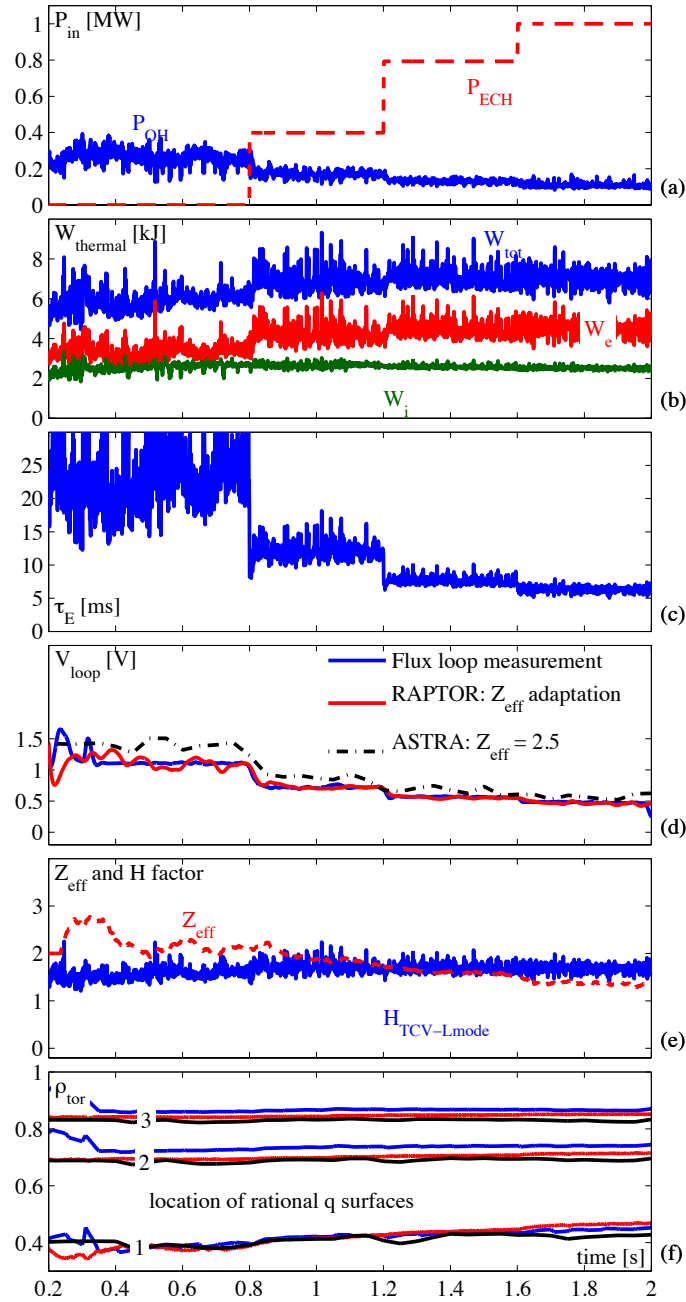


Figure 8.6: Illustration of several real-time signals available from the interpretative transport simulation done using RAPTOR during a TCV shot. During this particular shot, the ECH power is increased in steps and Ohmic power drops due to the decreased loop voltage (a). At the same time the plasma energy content is seen to increase (b). The confinement decreases as expected for heated plasmas (c) while the $H_{TCV-Lmode}$ scaling factor stays approximately constant. The loop voltage (d) is shown as measured by a flux loop, as tracked by RAPTOR by adapting Z_{eff} (e) and from off-line ASTRA simulations with fixed Z_{eff} . The movement of the rational q surfaces is also shown for RAPTOR, ASTRA and LIUQE. Other parameters for this discharge (TCV#41752) are $I_p = 240\text{kA}$, $\kappa = 1.5$, $\delta = 0.4$.

8.3 Feedback control of l_i and T_{e0} using RT-RAPTOR

The profile control experiments presented in Chapter 5 have demonstrated the applicability of feedback control techniques to control plasma temperature profile quantities. However, they fall short of showing the type of complete, integrated control of multiple profiles required for complete advanced scenario control. In particular, control of the current density is not addressed as a dedicated diagnostic is unavailable at the present time in TCV. The new possibilities offered by RT-RAPTOR, giving a real-time q profile estimate, open up the possibility to control (parameters of) the current density profile at the same time. A demonstration experiment is described in this section, demonstrating simultaneous control of temperature and current profile control quantities.

8.3.1 Experimental set-up

It was chosen to control the normalized internal inductance $l_i = 2L_i(\rho_e)/(\mu_0 R_0)$, being a global parameter indicating the degree of peakedness of the current density profile, and the central plasma temperature T_{e0} as measured by the XTe profile diagnostic. These two quantities were controlled by varying the power of two gyrotrons, oriented to drive current in co-, respectively counter-current direction in the same configuration as described for the β_p feedback control experiments in Section 5.1.5. With this setup, increasing the power of both gyrotrons has the main effect of increasing T_e while increasing the difference has an effect on l_i . The ECCD distribution from both launchers is shown in Figure 8.7.

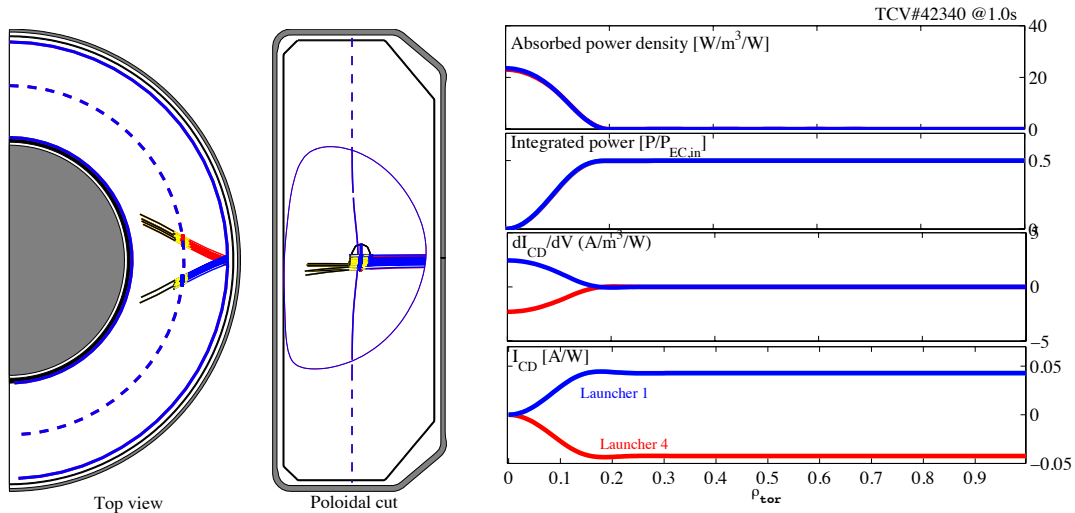


Figure 8.7: TORAY ray tracing calculations for the T_{e0} , l_i control experiments as well as the β_p control experiments of Section 5.1.5. Both gyrotrons deposit power on-axis and drive current in the opposite direction. The plasma current in this shot is negative in TCV sign conventions, therefore the beam from launcher 4 (red) drives co-current drive.

Contrarily to the β_p control experiments, the β_p observer was not used, relying instead on the XTe temperature estimate described in Section 2.3. The internal inductance was estimated from a RT-RAPTOR real-time flux profile simulation. As inputs to this simulation, the current drive distribution and efficiency must be specified for each gyrotron.

The spatial distribution was inferred from TORAY ray-tracing calculations and was approximately modeled as Gaussian profiles with at the plasma center with $w_{dep} = 0.3$. The efficiency (i.e. the c_{cd} parameters in Eq.(7.2)) was estimated by a preparatory shot in which the power levels were held at their minimum and maximum levels. The measured loop voltage in the experiment was then used to tune the current drive efficiency for each gyrotron such that the same simulated loop voltage was obtained for a fixed value of $Z_{eff} = 3.5$. The resulting coefficients were -1.4×10^{15} and 2×10^{15} A/(m⁵ eV W) for the counter- and co-gyrotron, respectively. This lower efficiency for counter-ECCD can be explained by the heating effect, which reduces the resistivity, inducing additional Ohmic co-current depending on the loop voltage.

8.3.2 Controller design

The controller design is based on a PI controller with 2 inputs and 2 outputs. The input is the vector of errors $e(t) = [T_{e0,ref} - T_{e0}, l_{i,ref} - l_i]^T$ and the output is the vector of power commands $u(t) = [P_{co-ECCD}, P_{ctr-ECCD}]^T$.

The action of the MIMO PI controller is written as in (5.3) with K_p and K_i now representing diagonal matrices with appropriate gains for the T_{e0} control loop and l_i control loop respectively. Approximate decoupling is obtained by a matrix

$$K_D = \begin{pmatrix} \frac{1}{2} & \frac{1}{2} \\ \frac{1}{2} & -\frac{1}{2} \end{pmatrix} \quad (8.2)$$

such that the final control law is, in the discrete domain (with sample time T_s),

$$u_k = K_D \left(K_p + \frac{K_i T_s z^{-1}}{1 - z^{-1}} \right) e_k. \quad (8.3)$$

It is easy to verify that K_D has the effect of (1) increasing both injected powers (first column) in response to an error in T_e and (2) changing the difference (second column) in response to an error in l_i . This decoupling is ‘‘approximate’’ in the sense that due to cross-coupling effects in the plasma, the injected power mean or difference will have an effect on both quantities, though the diagonal effect is dominant. A simplified anti-windup scheme was implemented which stops the integrator error accumulating on any of the two control loops in the case any actuator saturates. This is appropriate since saturation of one actuator precludes the possibility to achieve zero error on both actuators at the same time. More advanced anti-windup schemes could include a trade-off stating which error is more important. As for the feedback gains, dominantly integral controller settings were again used. For the T_{e0} loop: $K_{i,T_{e0}} = 2.5\text{MW/eV/s}$ and $K_{p,T_{e0}} = 200\text{W/eV}$. For the l_i control: $K_{i,l_i} = 20\text{MW/s}$, $K_{p,l_i} = 200\text{kW}$.

8.3.3 Results

An example of simultaneous control of both T_e and l_i is shown in Figure 8.8. Steps of reference T_{e0} , and (later) l_i are issued. In both cases, the controller responds appropriately by changing the powers in the co- and counter-ECCD clusters. The (off-line) Thomson scattering measurement-based estimates of the central temperature are also plotted, showing qualitative agreement even though the final temperature is somewhat overestimated

(or underestimated by the XTe diagnostic). A similar discrepancy was already noticed in Chapter 7 and is attributed to the line-integrated nature of the XTe measurement, which could be compensated for.

Note also how, when an increased temperature is required, the internal inductance momentarily increases ($t = 1.0\text{s}$). This can be explained by the higher central conductivity owing to the higher temperature, leading to further peaking of the current profile. The controller counteracts this by increasing the relative level of counter-ECCD. Note also that the loop voltage decreases in response to the step temperature increase. The controller gains could be tuned to make the response to the l_i step request have less overshoot, and a faster response. Still, this is satisfactory for a proof-of-principle experiment.

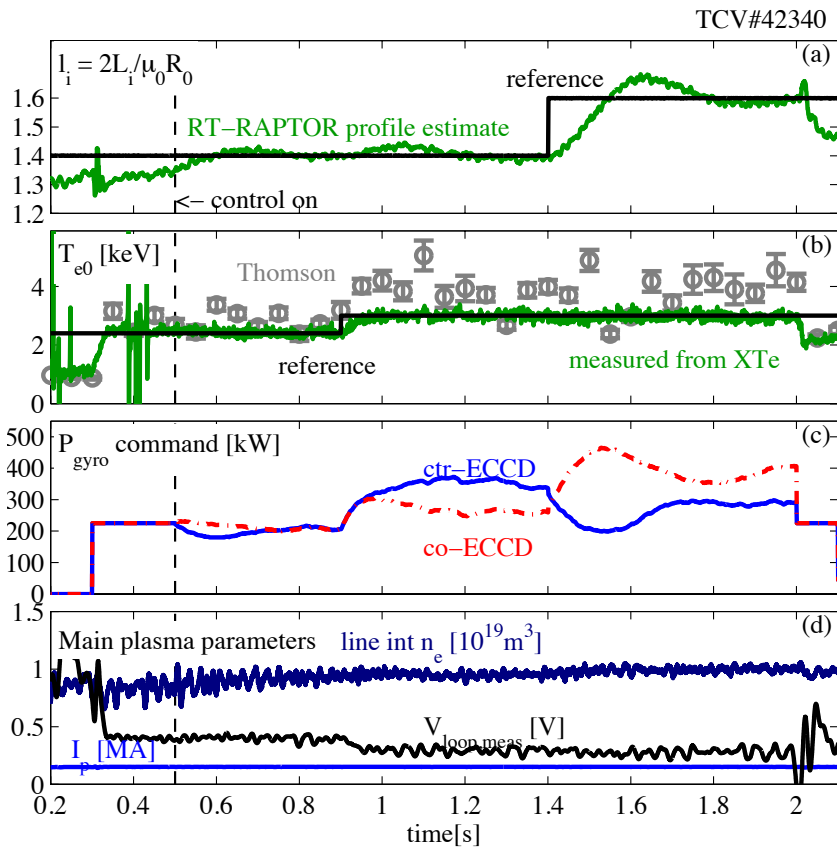


Figure 8.8: Successful simultaneous control of internal inductance (a) and central electron temperature (b) using a mix of co/counter ECCD on-axis. The relative amount of co/counter ECCD is controlled (c) by a feedback controller. Note the fast increase of the temperature at $t = 0.9\text{s}$, followed by a change in l_i on the current redistribution time scale ($t \sim 1.05\text{s}$) which is compensated by the controller. Other plasma quantities are also shown.

8.3.4 Discussion and outlook

The proof-of-principle experiment described above provide perspective for application of RT-RAPTOR for controlling more parameters of the current density profile. As described in previous sections, the entire q profile is available allowing control of magnetic shear,

q_0 , q_{min} and other parameters of interest for transport barrier and advanced scenario studies. TCV experiments can use the flexibility of real-time EC launcher steering as well as power control to tailor the q profile. Clearly, such experiments would rely strongly on the modeled current drive distribution as a function of power and EC injection angle, but substantial experience with eITB plasma modeling in TCV would aid in this effort. While the necessary work could not be carried out within the time frame of this thesis it would be an interesting path for future experimental studies.

8.4 Further developments of real-time simulation

Based on the initial results obtained on TCV, one can envisage several extensions to the real-time simulation paradigm; these are discussed in this section.

8.4.1 Incorporating internal diagnostics using a closed-loop observer

As was mentioned in the introduction of this chapter, the real-time simulations as those proposed in this chapter are known in control systems theory as dynamic state observers. Just as in our simulations, observers evolve the dynamic equations of the system to obtain a more reliable estimate of the system state. Linear model-based state observers for tokamak current density profiles were proposed in early work by (Morrow-Jones et al. 1993), and the possibility of using a nonlinear model like the one presented here was put forward in (Witrant et al. 2007), but to our knowledge neither had been implemented nor tested so far.

The standard way to handle measurements in the framework of state observers is to add a term to the equations which feeds back the error between measured system outputs and predicted system outputs with an observer gain. This is commonly known as a Luenberger observer.

Let $y(t) = C_\psi(\psi(t))$ be a real-time measurement of an internal quantity related to ψ , where C_ψ is an operator representing the diagnostic. We will assume in this initial treatment that C_ψ is a linear operator, which holds true, for example, for pitch angle measurements using MSE. Starting from (7.10), let $\bar{\psi}$ be the estimate of ψ in the observer (i.e. in the real-time simulation). The closed-loop observer equation for the flux profile can be written as

$$m_\psi \frac{\partial \bar{\psi}}{\partial t} = \frac{\partial}{\partial \rho} \left(d_\psi \frac{\partial \bar{\psi}}{\partial \rho} \right) + f_\psi(\bar{\psi}, T_e) + s_\psi + L \left(C_\psi(\bar{\psi}) - C_\psi(\psi) \right) \quad (8.4)$$

here s_ψ represents the sources (the summation term in (7.10)) and L represents the observer function (which may be a differential operator). Subtracting (7.10) from this equation, and neglecting (small) errors in the estimation of the source terms s_ψ one obtains

$$m_\psi \frac{\partial(\bar{\psi} - \psi)}{\partial t} = \left[\frac{\partial}{\partial \rho} \left(d_\psi \frac{\partial}{\partial \rho} \right) + LC_\psi \right] (\bar{\psi} - \psi) + (f_\psi(\bar{\psi}, T_e) - f_\psi(\psi, T_e)) \quad (8.5)$$

This is a diffusion equation for $(\bar{\psi} - \psi)$ also known as the *observer error equation* as it quantifies the deviation between the observed and true state. The last term on the

right hand side represents the error in estimated bootstrap current due to errors in the estimated ψ . The first term on the right hand side contains the same second order spatial operator as the original equation, with the addition of a combined operator LC_ψ of which L may be freely chosen.

In the present TCV implementation, where no internal measurements for the flux profile are available, we have $C_\psi = 0$ which is equivalent to using an open-loop observer, where $L = 0$. Since the system is stable (from the diffusive nature of the equations), the observer error will decay to zero asymptotically by the same stable dynamics that governs the overall profile evolution. This property is known in the literature as *asymptotic observability* (Sontag 1998, Ch. 6,7).

If measurements are available, this observer gain L can be chosen such that the observer error $(\bar{\psi} - \psi)$ converges to zero following a different time scale, governed by the operator $\left[\frac{\partial}{\partial \rho} \left(d_\psi \frac{\partial}{\partial \rho}\right) + LC_\psi\right]$. For example, if it is possible to choose L such that $LC_\psi = c \frac{\partial}{\partial \rho} \left(d_\psi \frac{\partial}{\partial \rho}\right)$ with c a scalar, then it is easily verified that for any $c > 0$ the eigenvalues of the diffusion operator in (8.5) will be larger (faster) than the original equation (7.10). The error will thus decay faster than the flux diffusion itself, and the time scale can be governed by c .

For linear systems, the principle of separability (Sontag 1998) guarantees that the observer error dynamics can be imposed by the observer gain, independently from the closed-loop error dynamics, dictated by the controller gain. For the nonlinear system at hand the picture may be more complicated and more advanced nonlinear analysis tools will need to be used.

Using a closed-loop observer allows us, in theory, to reduce the effects of measurement noise and an imperfect initial condition. This approach is natural when modeling errors are assumed to be small: the observer can then effectively filter out measurement noise. State observers for partial differential equations are extensively treated in (Smyslyhaev et al. 2010) which may be used as a starting point for further work in this direction.

8.4.2 Adaptation of model parameters

If high-quality, trustworthy measurements are available, but the parameters in the physics model are less well known, it may be more appropriate to adapt the model parameters in order to reduce the residual error. The key difference between the closed-loop observer of the previous section and the parameter adaptation approach is that in the first case one directly corrects the estimate of the state, while in the second case one corrects the parameters of the model generating the state estimate. We already mentioned in Section 8.2.3 the particular case of adapting the effective charge Z_{eff} by comparing the V_{loop} measurement with the simulated value. Of course the above methodology assumes that all the other model parameters and measurements are correct and that there is some redundancy in the available measurements. In practice, errors in, for example, the reconstruction of T_e would perturb our estimate of Z_{eff} . A more complete approach would attempt to make consistent estimations of all quantities including measurement and parametric uncertainties. Also, adding further redundant measurements increases the number of parameters which can be constrained and improves the quality of the reconstructions. Full analysis and development of this approach, along the lines of model adaptive control is beyond the scope of this thesis and is left as future work.

8.4.3 Disturbance estimation and fault detection

Finally, we discuss a third option for classifying a mismatch between measurements and simulations, that of a disturbance or fault. In the case of a disturbance, some unexpected or unmodeled effect causes the simulations and measurements to diverge. By assuming a particular structure for the disturbance, its magnitude and distribution can be computed from the residual error. Similarly, one can construct a typical signature of the residual which would arise from faults in a particular actuator or diagnostic. Correlating the occurring errors with the signature of each possible fault can aid in model-based diagnosis of problems in real-time. This field of model-based fault detection and identification (FDI) has been little explored for tokamaks to date but may be of great interest for the future.

It should be noted that the three approaches mentioned above can be treated in a unified manner by e.g. the Extended Kalman Filter method, where both the system states and parameters are estimated (Anderson et al. 1979). This has recently been proposed (Xu et al. 2010b) for estimating transport parameters. The full development of an adaptive, closed-loop state observer including disturbance rejection and fault detection is a very interesting avenue for research.

8.4.4 Real-time simulations on ITER and other tokamaks

Before concluding this section, let us consider how a real-time simulation on a tokamak like ITER might be implemented. Similar considerations hold for existing (large) tokamaks.

First of all, ITER will certainly have a real-time Grad-Shafranov equilibrium solver allowing a real-time update of the flux surface geometry based on magnetic measurements, without having to choose a fixed equilibrium. The Grad-Shafranov solver will provide the profiles G_2, V', J but, at the same time, the reconstructed current density profile can also be fed back into the real-time equilibrium code, providing a better profile than can be obtained from a purely diagnostics-based approach, since it is not limited by diagnostic spatial or temporal resolution. Additionally, any available real-time internal current density profile measurements such as MSE or polarimetry should be included in a closed-loop observer as outlined in Section 8.4.1, rather than fed directly to a q profile feedback controller. With knowledge of the (electron) density profile, real-time ray tracing could give the ECCD distribution providing more accurate and self-consistent current drive modeling. Self-consistent modeling of other heating sources such as NBI could also be included. While the combination of the above features would require significant computational effort, one should note that they can each be performed separately on different, dedicated computers, and require only exchange of the final results. As such, no technical obstacles are foreseen to deploying this technique to ITER.

The feasibility of the proof-of-principle implementation on TCV, with its relatively short time scales, shows that today's large tokamaks can certainly use this approach. Real-time equilibrium reconstructions codes (Section 6.2) exist and most tokamaks have multiple real-time diagnostics available (Felton et al. 2005), (Barana et al. 2007). The extra computational effort required to include time-varying flux surface shapes is non-negligible, but will be offset by the longer time scales of larger devices, making the implementation viable. For any tokamak, the accuracy of the real-time simulations will largely depend on the quality and availability of real-time kinetic profile measurements, which is a crucial condition for the method to be applicable.

In the introduction, we mentioned that the real-time simulation paradigm is applicable, in principle, to any profile including kinetic (T_e , n_e , ...) profiles, and would hold similar advantages as for the current density profile. However, kinetic profiles are more difficult to simulate in real-time, partly because they evolve more rapidly but especially because first-principle models are not yet sufficiently developed to allow accurate and rapid simulation. Ad hoc models could be used in these cases, as mentioned Section 7.2.3. These models would have to be tuned depending on the plasma scenario, but given the experience operating today's tokamaks, reasonable results can be expected. Fortunately, high-quality diagnostic measurements of kinetic profile quantities are often available, so a real-time simulation would be able to rely more heavily on the diagnostics and less on the model than would be the case for the current density profile. Though the TCV energy confinement times (~ 1 ms) probably preclude kinetic profile simulation on TCV with the present architecture, the time scales involved on today's large tokamaks, and even more so on ITER, are sufficiently long for kinetic profile simulations. Further research and better understanding of kinetic profile transport could also yield more tractable, accurate and general models.

Finally, real-time prediction and model predictive control, as mentioned in Section 8.1, requires faster-than-real-time predictive simulation capabilities, which may be beyond today's computing power for small tokamaks and may be at the limit of the capabilities for existing tokamaks. However for the ITER time scales this will most likely be possible, especially when relying on ad-hoc models as mentioned above and when simplifying the dynamical model, for example by local linearization. This will be discussed in more detail in Section 9.5.4.

8.5 Conclusion

This chapter has covered a first application of the capabilities of RAPTOR, showing a real-time simulation of the current density profile on TCV and highlighting some advantages of using real-time simulations for self-consistent plasma state estimation in other tokamaks. In essence, real-time simulations hold the promise to greatly improving the accuracy and consistency of plasma profile state estimates with multiple applications in control, supervision and prediction. The material of this chapter offers many opportunities for future research in these directions. The successful demonstration of sub-millisecond real-time solution of the nonlinear profile diffusion equations demonstrates the practical feasibility of the approach, and a demonstration of the used of computed quantities for feedback control opens perspectives for further TCV experiments with advanced, complete control of the current density profile of the complexity required for advanced scenario control in future tokamaks. Furthermore, the implementation of such a paradigm on another experiment would also be very interesting and instructive, and will benefit from the fact that the present implementation does not depend on specific diagnostics.

Chapter 9

Optimization of open-loop actuator trajectories for tokamak plasma profile control

The previous chapter presented an application of the fast RAPTOR code when used in interpretative mode to allow real-time simulation of plasma profiles. This chapter exploits the capabilities of the Predictive version of RAPTOR, which allows one to embed profile simulations in a nonlinear optimization scheme to determine optimal input trajectories in time. This will be the topic of the present chapter¹.

9.1 Introduction

9.1.1 Background and motivation

Across different tokamak experiments, the work of the tokamak physics operators has been to decide the time evolution of a set of externally controllable actuators, in order to achieve a given plasma profile evolution in time and reach a given plasma scenario (cf. Section 6.8). Typically, a tokamak operator programs a set of reference waveforms which are then fed into various actuators or control systems. The evolution of these reference waveforms in time is referred to, in this chapter, as the *actuator trajectories*, which may refer to direct actuators such as the power injected by various auxiliary heating systems, but also to a reference waveform such as the requested plasma current in time. We must distinguish here between *open-loop* trajectories and *closed-loop* trajectories, the difference being that the first are determined pre-shot whereas the latter are adapted in real-time, by a plasma control system (PCS) based on measurements of the actual plasma evolution. In this chapter we focus on open-loop actuator trajectories only. The choice of actuator trajectories required to reach the desired plasma profiles is traditionally the result of extensive experience gained during operation of a particular machine, and of a substantial number of trial-and-error attempts. The physics knowledge required to make the right choices is embedded in the operator's knowledge experience.

¹Part of the material in this chapter has been the topic of a conference presentation (Felici et al. 2011a) and has been submitted for publication (Felici et al. 2011)

This chapter presents a computational method to determine these optimal trajectories based on predictive plasma transport simulations. The problem is formulated in the form of a nonlinear optimization problem with a physics-dictated cost function and multiple constraints, and solved using a state-of-the-art nonlinear programming algorithm.

Having such a systematic design method is highly advantageous for several reasons. Given the complex physics underlying the profile dynamics, a physics-model-based methodology is expected to provide new and better trajectories, and provide them more rapidly and at lower cost in terms of machine time than can be obtained by experiments alone. Though validation on more complete transport codes and on experiments is essential, the computed trajectories can be used as a starting point. Secondly, this method is applicable to machines which are yet to be built, such as ITER, and can be helpful in designing trajectories in preparation of their operation. The environment of a large and costly installation will most likely preclude the possibility of extensive trial-and-error attempts and must rely on pre-validated scenarios.

New insight can also be obtained upon discovering unexpected actuator trajectories. Finally, since actuator and physics constraints are explicitly included in the trajectory design, the obtained trajectories can be analyzed with respect to their influence on the various constraints, and vice versa, as will be illustrated in Section 9.4.

As discussed in Section 6.5.2, tokamak transport models are notoriously complicated and often incomplete, therefore one must rely on approximate and ad-hoc models. It is important to realize that the correctness of the results obtained depends critically on these transport models. On the other hand, the results obtained with approximate transport models may well be qualitatively correct and can serve as a starting point for more refined optimization using more complete transport codes or by experiments. Furthermore, as we shall see, the tools presented in this chapter are also applicable to experimentally validate existing ad-hoc transport models, and to refine them where necessary.

As a first test of the method, the algorithm has been used to define the trajectories of plasma current and auxiliary power required to steer a plasma from a low-current, Ohmic phase, to a higher plasma current hybrid-type scenario using off-axis heating and current drive for a typical TCV plasma. The cost function is formulated in such a way that the loop voltage profile is as flat as possible at the end of the period of interest, indicating that a stationary situation has been reached. Constraints are included which limit the permitted actuator amplitudes and ramp rates, and ensure that $q > 1$ everywhere at all times (in order to avoid sawtooth crashes), and that a positive edge loop voltage is maintained (to avoid inducing negative edge currents). This will be treated in Section 9.3.

9.1.2 Advantages of Predictive-RAPTOR for optimization studies

The principle of optimizing actuator trajectories is illustrated schematically in Figure 9.1. A tokamak profile simulation evolves the plasma profiles in response to actuator inputs. An optimization algorithm then evaluates the cost function and constraint violations and computes a better set of actuator trajectories. The procedure is iterated until a satisfactory solution is found, which may require hundreds or thousands of iterations depending on the complexity. For precisely this reason, it is beneficial to have a lightweight physics model. Predictive-RAPTOR, the “predictive” version of the RAPTOR code introduced in Section 7.5, provides this rapid and efficient way to simulate the coupled evolution of

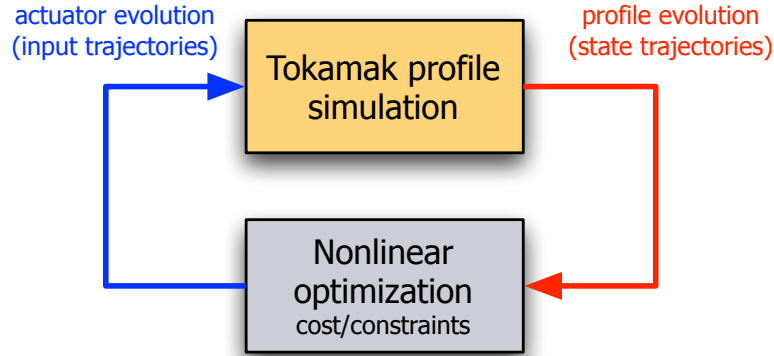


Figure 9.1: Schematic representation of the nonlinear optimization routine for actuator trajectory optimization.

the poloidal flux and electron temperature profiles, representing the key physics governing the global plasma profile evolution while keeping the computational burden tractable.

In this chapter, the cost function (denoted by J)² depends only on the state at a given final time. In order for the optimization algorithm to determine the next estimate for the actuator trajectories, it needs to know the descent direction, i.e. the direction in which it needs to modify the actuator trajectories in order to decrease the cost function. This is where the sensitivity calculations integrated in Predictive-RAPTOR, discussed in Section 7.5.2, show their usefulness: the cost function (and constraint) gradients can be computed directly from the state sensitivities. This is illustrated in Figure 9.2. The trajectory of the plasma state $x(t)$ in response to a given (unperturbed) actuator trajectory $u(t)$ is denoted by the purple trajectory, which ends at a given point in the state space at the final time, corresponding to a certain value of the cost function. In an analogous way to what was done in Section 7.5.3, let p be a parameter affecting the actuator trajectory $u(t)$. The state sensitivities $\partial x(t)/\partial p$ give information about the variation of the $x(t)$ trajectory in response to an infinitesimal parameter variation δp (blue curve), in particular the sensitivity of the final state $\partial x(t_f)/\partial p$. The variation in the cost function can then be calculated as

$$\delta J \approx \frac{\partial J}{\partial p} \delta p = \frac{\partial J}{\partial x(t_f)} \frac{\partial x(t_f)}{\partial p} \delta p \quad (9.1)$$

Here, $\frac{\partial J}{\partial p}$ is the cost function derivative for scalar p , but this can be generalized to vector-valued p , effectively giving the steepest descent direction for the cost function in parameter space. Analogous arguments hold for the constraints and constraint gradients, and a more thorough treatment is given in Sections 9.2.2 and 9.2.4.

9.1.3 Relation to previous work

When transient tokamak scenarios (in particular ramp-up and ramp-downs) are studied in simulations (see (Imbeaux et al. 2011a) for a recent example), the objective usually is to test transport models and to make predictions for ITER. The integrated modeling

²The notation J is standard in the optimization literature, but should not be confused with $J = RB_\phi/(R_0B_0)$ defined in Eq.(6.27)

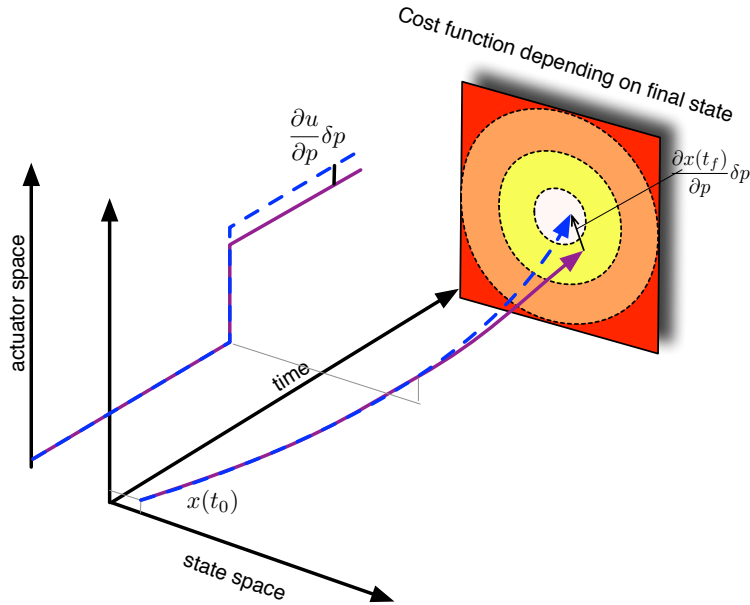


Figure 9.2: Illustration of how the knowledge of the state trajectory sensitivities with respect to an input parameter yield information about the cost function gradient.

tools used in this case are much more extensive and computationally intensive, and are therefore not very suited for integration into an optimization loop.

Partly due to the complexity of standard modeling tools, to date very few systematic attempts at computing open-loop trajectories for tokamaks have been made. A review of notable exceptions is given below.

Some recently published works (Ou et al. 2008), (Xu et al. 2010a) also describe a method to optimize tokamak actuator trajectories. While they includes constraints on the actuators, the proposed methods does not include state constraints (i.e. constraints on the internal plasma quantities). Additionally, they do not include any spatial evolution of the electron temperature profile, but assume a fixed profile shape for $T_e(\rho)$ which is scaled according to an empirical scaling law. While this is appropriate for some operating regimes and has the merit of avoiding the difficulty of modeling electron energy transport, it lacks the ability to model localized enhancement of energy confinement in advanced scenarios and only includes bootstrap current as a global effect.

On the other hand, the emphasis in (Xu et al. 2010a) is placed on a future real-time implementation of the optimization scheme in the framework of Model Predictive Control, as also proposed in (Ou et al. 2007), (Ouarit et al. 2011). Therefore, in (Xu et al. 2010a), much effort is put into reducing the dimensionality of the model by a Proper Orthogonal Decomposition method. In this work, we are less concerned with real-time performance and propose our scheme, at this stage of development, as an open-loop approach. This having been said, it shall be mentioned at the end of this chapter (Section 9.5.3) how real-time controllers can be built based on the open-loop optimal trajectories designed by the optimization algorithm. Similar ideas are proposed in (Ou et al. 2010a), (Ou et al. 2010b).

We move now to the main part of this chapter, describing the formulation and solution of the optimal control problem.

9.2 Formulation and solution of the optimal control problem

In this section the nonlinear, constrained, dynamic optimal control problem (Nocedal et al. 2006), (Bryson et al. 1975) for open-loop current profile control will be formulated. The solution to the problem will be the actuator trajectories that drive the plasma profile evolution such that it will give a minimum value for a chosen cost function while satisfying a given set of constraints. We will successively examine 1) the parametrization of the actuator trajectories in a discrete set of parameters, 2) a general formulation of various cost functions which can be employed, and 3) a formulation of constraints for both plasma state and inputs. Then we shall see how the full optimal control problem is formulated and solved using a nonlinear programming algorithm.

9.2.1 Control vector parametrization

In Section 7.5.3 a first example was shown of parametrizing the control input vector of actuator trajectories by a scalar parameter. In this section we extend this principle and describe what is referred to as *control vector parametrization*, i.e. parametrizing the continuous input functions in time $u(t) \in \mathbb{R}^r$ by a vector containing a discrete set of parameters $p \in \mathbb{R}^{n_p}$. To this end, the trajectory $u_i(t)$ for the i th actuator is written as

$$u_i(t) = \sum_j^{n_i} P_{ij}(t)p_{i,j}. \quad (9.2)$$

Here $P_{ij}(t)$ is a scalar function of time, typically chosen as a piecewise linear or piecewise constant function with a finite support and $\max P_{ij}(t) = 1$, although higher order polynomials, or any other reasonable function may be chosen as well. The scalar $p_{i,j} \in \mathbb{R}$ gives the weight of the associated function. n_i is the number of parameters which define the i th actuator trajectory, therefore by choosing

$$\underline{p}_i = [p_{i,1}, \dots, p_{i,n_i}]^T \quad (9.3)$$

and

$$\underline{P}_i(t) = \begin{bmatrix} P_{11}(t) & P_{12}(t) & \dots & P_{1n_i}(t) \end{bmatrix} \quad (9.4)$$

we can combine (9.2) for all actuators i in matrix form

$$u(t) = \begin{bmatrix} u_1(t) \\ u_2(t) \\ \vdots \\ u_r(t) \end{bmatrix} = \underbrace{\begin{bmatrix} \underline{P}_1(t) & 0 & \dots & 0 \\ 0 & \underline{P}_2(t) & \dots & 0 \\ \vdots & \vdots & \ddots & \vdots \\ 0 & 0 & \dots & \underline{P}_r(t) \end{bmatrix}}_{\mathbf{P}(t) \in \mathbb{R}^{r \times n_p}} \underbrace{\begin{bmatrix} p_1 \\ p_2 \\ \vdots \\ p_r \end{bmatrix}}_{p \in \mathbb{R}^{n_p}} \quad (9.5)$$

In summary, $p \in \mathbb{R}^{n_p}$ is the parameter vector and $\mathbf{P}(t) \in \mathbb{R}^{r \times n_p}$ is a time-varying matrix. This notion can be generalized further by assuming that only part of the input trajectory is defined by p , while another part is chosen independent of the parameters. In this case we may write

$$u(t) = \mathbf{P}(t)p + u_{fix}(t) \quad (9.6)$$

Note that

$$\frac{\partial u(t)}{\partial p} = \mathbf{P}(t), \quad \frac{\partial u(t)}{\partial t} = \frac{d\mathbf{P}(t)}{dt}p + \frac{du_{fix}}{dt} \quad (9.7)$$

The formulation allows a completely general description of each individual actuator trajectory. We can obtain the input trajectory parametrization used in the example in Section 7.5.3 by choosing:

$$\mathbf{P}(t) = \begin{bmatrix} \underline{P}_1 \\ 0 \end{bmatrix}, \quad \text{with } \underline{P}_1 = \begin{cases} 0 & \text{if } t < 25\text{ms} \\ 1 & \text{if } t \geq 50\text{ms} \end{cases} \quad (9.8)$$

$$u_{fix} = \begin{bmatrix} 0 \\ I_p(t) \end{bmatrix}, \quad \text{with } I_p(t) = \begin{cases} 80 + 4800t \text{ [kA]} & \text{if } t < 25\text{ms} \\ 200 \text{ [kA]} & \text{if } t \geq 50\text{ms} \end{cases} \quad (9.9)$$

Then

$$u(t) = \begin{bmatrix} u_1(t) \\ u_2(t) \end{bmatrix} = \begin{bmatrix} P_{aux}(t) \\ I_p(t) \end{bmatrix} \quad (9.10)$$

9.2.2 Cost function definition

Depending on the problem at hand, different cost functions can be formulated reflecting the different quantities which may need to be optimized. We write a generic form of the cost function here and will apply special cases in the examples that follow. Though a generalization is straightforward, we restrict ourselves here to cost functions depending only on the final input $u(t_f)$ and on the final state $x(t_f)$ or its derivative $\dot{x}(t_f)$ for simplicity.

In general, we may choose to penalize:

- Deviations from the final required rotational transform profile, using a weighted norm on the final error

$$J_\iota = \|\iota(t_f) - \iota_{ref}\|_{W_\iota}^2 \quad (9.11)$$

Where by the notation $\|f(\rho)\|_{W}^2$ we intend $\int_0^\rho [W(\rho)f(\rho)]^2 d\rho$.

Since $\iota(\rho, t_f) = \mathbf{c}_l^T(\rho)\hat{\psi}(t_f) = [\mathbf{c}_l^T, 0]x(t_f)$ this term depends only on the final state. Note that this form can be used either to assign a cost to the whole profile, or to certain points of interest such as the edge value $\iota_{edge} = 1/q_{edge}$, which is directly related to the total plasma current.

- The final loop voltage profile, which should be zero in particular cases such as steady-state scenarios.

$$J_{U_{pl}} = \|U_{pl}(t_f)\|_{W_{U_{pl}}}^2 = \|\dot{\psi}(t_f)\|_{W_{U_{pl}}}^2 \quad (9.12)$$

Since $U_{pl}(\rho, t_f) = \sum_\alpha \Lambda_\alpha(\rho)\hat{\psi}(t_f)$, this term depends on the time derivative of the state at the final time.

9.2. Formulation and solution of the optimal control problem

- The degree of stationarity, or distance from a stationary state (ss) profile, previously defined in (6.48), represented by the weighted norm of the loop voltage profile derivative

$$J_{ss} = \|\partial U_{pl}/\partial \rho|_{t_f}\|_{W_{ss}}^2. \quad (9.13)$$

Since $\partial U_{pl}/\partial \rho = \mathbf{c}_\Lambda^T \dot{\psi}(t_f)$, this term, like the previous one, depends on the time derivative of the state at the final time.

- The total consumption of ohmic flux, i.e. difference between initial and final value of Ψ_{OH} :

$$J_{\Psi_{OH}} = \Delta \Psi_{OH}^2 = [\Psi_{OH}(t_f) - \Psi_{OH}(t_0)]^2 \quad (9.14)$$

When the flux boundary condition is specified in terms of Ψ_{OH} (6.33), this can simply be obtained from the initial and final input values. If, instead, the boundary condition (6.34) is used, the Ohmic flux consumption is recovered using (6.33):

$$\Delta \Psi_{OH} = \Psi_{OH}(t_f) - \Psi_{OH}(t_0) = L_{ext}(I_p(t_f) - I_p(t_0)) - \psi(\rho_e, t_f) + \psi(\rho_e, t_0) \quad (9.15)$$

which depends only on the final and initial states. However, since the initial state is chosen a-priori, the input trajectories affect the flux consumption term through the final state.

- Finally we have the possibility to penalize deviations from a final desired temperature profile

$$J_{T_e} = \|T_e(t_f) - T_{e,ref}\|_{W_{T_e}}^2 \quad (9.16)$$

where, clearly, $T_e(t_f) = [0, \mathbf{c}_\Lambda^T]x(t_f)$

The total cost function is then written as

$$J = \nu_\iota J_\iota + \nu_{U_{pl}} J_{U_{pl}} + \nu_{ss} J_{ss} + \nu_{OH} J_{OH} + \nu_{T_e} J_{T_e} \quad (9.17)$$

with factors ν_ι , $\nu_{U_{pl}}$, ν_{ss} , ν_{OH} and ν_{T_e} setting the relative weight of each term. It is clear from these examples that other cost functions can readily be defined.

Cost function gradients

The cost function gradient evaluation is simplified by the fact that J is a function of $u(t_f)$, $x(t_f)$ and $\dot{x}(t_f)$ only. We can evaluate the cost function gradients by using the chain rule

$$\frac{d}{dp} J(p, x(t_f), \dot{x}(t_f), u(t_f)) = \frac{\partial J}{\partial p} + \left[\frac{\partial J}{\partial x} \frac{\partial x}{\partial p} + \frac{\partial J}{\partial \dot{x}} \frac{\partial \dot{x}}{\partial p} + \frac{\partial J}{\partial u} \frac{\partial u}{\partial p} \right]_{t_f} \quad (9.18)$$

Notice that

- The first term on the right hand side is zero in our case, since the cost function does not depend on the parameters explicitly.
- The terms $\left. \frac{\partial J}{\partial x} \right]_{t_f}$ and $\left. \frac{\partial J}{\partial \dot{x}} \right]_{t_f}$ are obtained by direct differentiation of the relevant terms in the cost function.
- The final state sensitivities $\frac{\partial x(t_f)}{\partial p}$ and $\frac{\partial \dot{x}(t_f)}{\partial p}$ are known from having solved (7.46).
- The last term on the right hand side is also calculated directly from the cost function definition, noticing that $\frac{\partial u}{\partial p} = \mathbf{P}(t)$ from (9.7)

9.2.3 Actuator trajectory constraints

The actuator constraints are formulated directly as constraints on (elements of) the parameter vector p . Upper or lower boundaries on the actuator values, as well as constraints on the actuator ramp rates, can be cast into linear inequality constraints.

$$A_{ineq}p \leq b_{ineq} \quad (9.19)$$

For example $\frac{\partial u(t)}{\partial t} \leq c$ translates to $\frac{\partial P(t)}{\partial t} p \leq c$.

9.2.4 State trajectory constraints

State trajectory constraints appear from physics considerations. In the present study, two constraints have been implemented, which can optionally be included in the optimization problem.

Note that state constraints are more difficult to implement, since they depend on the parameters through the system dynamics instead of directly, like the actuator inputs. If the constraints are active over an extended period of time, they must be evaluated for each time step, in which case the constraints can be written as one constraint per time point. However, this can yield an intractable amount of constraints if there are many time points. A way to alleviate this is to reformulate them as integral constraints (Teo et al. 1991). In this approach the i th state constraint of the form $c_i(t, x(t)) \leq 0$ is rewritten as

$$C_i = \left(\int_{t_0}^{t_f} (\max\{0, c_i(t, x(t))\})^2 dt - \epsilon \right) \leq 0 \quad (9.20)$$

where a small relaxation $\epsilon > 0$ is applied in order to ensure regularity of the constraint, i.e. to ensure that $\frac{\partial C_i}{\partial x} \neq 0$ when $C_i = 0$, which is a required property that a constraint must have in order to ensure a well-posed optimization problem (Nocedal et al. 2006).

We now discuss two particular cases of constraints which have been implemented. They have been chosen as representative of typical physical limits in Tokamak operation.

Constrain lowest q /highest ι value Recall from Section 6.8 that hybrid scenarios feature q profiles whose value is slightly above, but strictly not below one – to take advantage of improved confinement while avoiding sawtooth crashes which may trigger NTMs or disruptions. This can be imposed as a constraint on the rotational transform profile

$$\iota(\rho, t) < \iota_{lim} \quad \forall t \quad (9.21)$$

Where ι_{lim} is a scalar value slightly below 1. However this is not a scalar-valued constraint at each point time, as it depends on ρ as well. Let us therefore first reformulate the constraint from one on (ρ, t) into one dependent only on t , by writing

$$c_{\iota < \iota_{lim}}(t) = \int_0^{\rho_e} \max\{0, (\iota(\rho, t) - \iota_{lim})\} d\rho \leq 0 \quad \forall t \quad (9.22)$$

effectively integrating ι over the values of ρ for which the constraint is violated, and then writing the constraint as an integral constraint:

$$C_{\iota < \iota_{lim}} = \left(\int_{t_0}^{t_f} [c_{\iota < \iota_{lim}}(t)]^2 dt - \epsilon \right) \leq 0 \quad (9.23)$$

9.2. Formulation and solution of the optimal control problem

In this case, we do not need to take the maximum since $c_{\iota < \iota_{lim}}(t)$ is zero when the constraint is not violated.

Constrain edge loop voltage To avoid negative edge currents, which can have deleterious effects on MHD stability (Coda et al. 2008), we might want to avoid negative edge loop voltages. This is formulated as $U_{pl}(t)|_{\rho=\rho_e} \geq U_{pl,\min}$, where $U_{pl,\min}$ is the minimum allowed edge voltage. In integral form, this constraint reads:

$$\mathcal{C}_{U_{pl,e} < U_{pl,lim}} = \left(\int_{t_0}^{t_f} \max\{0, U_{pl,lim} - U_{pl}\}^2 dt - \epsilon \right) \leq 0 \quad (9.24)$$

State constraint gradients

The gradients of the constraints in integral form (9.20) are

$$\frac{d\mathcal{C}_i}{dp} = \int_{t_0}^{t_f} 2 \max\{0, c_i(t, x(t))\} \frac{\partial c_i(t, x(t))}{\partial x} \frac{\partial x(t)}{\partial p} dt \quad (9.25)$$

from which we can write the constraint gradients for our constraints (9.23),(9.24) as

$$\frac{\partial \mathcal{C}_{\iota < \iota_{lim}}}{\partial p} = \int_{t_0}^{t_f} 2c_{\iota < \iota_{lim}}(t) \left\{ \int_0^{\rho_e} \max\{0, (\iota(\rho, t) - \iota_{lim})\} \frac{\partial \iota}{\partial x} \frac{\partial x}{\partial p} d\rho \right\} dt \quad (9.26)$$

$$\frac{\partial \mathcal{C}_{U_{pl,e} < U_{pl,lim}}}{\partial p} = \int_{t_0}^{t_f} -2 \max\{0, U_{pl,lim} - U_{pl}|_{\rho=\rho_e}\} \frac{\partial U_{pl}}{\partial \dot{x}} \frac{\partial \dot{x}}{\partial p} dt \quad (9.27)$$

The terms $\frac{\partial \iota}{\partial x}$ and $\frac{\partial U_{pl}}{\partial \dot{x}}$ are readily evaluated from (7.23), (7.27). We notice again the state sensitivities $\frac{\partial x(t)}{\partial p}$ and $\frac{\partial \dot{x}(t)}{\partial p}$, obtained from (7.46).

9.2.5 Formulation of the optimal control problem

The complete, continuous-time optimization problem is finally written as

$$\min_p J(\dot{x}(t_f), x(t_f), u(t)) \quad (\text{cost}) \quad (9.28)$$

$$\text{such that} \quad (9.29)$$

$$f(\dot{x}(t), x(t), u(t)) = 0 \quad \forall t \in [t_0, t_f] \quad (\text{state}) \quad (9.30)$$

$$u(t) = P(t)p \quad (\text{control vector parametrization}) \quad (9.31)$$

$$A_{ineq}p \leq b_{ineq} \quad (\text{actuator limits}) \quad (9.32)$$

$$\mathcal{C}(x(t)) \leq 0 \quad (\text{state constraints}) \quad (9.33)$$

To solve the problem (9.28) - (9.33) numerically, we need to write the discrete-time equivalents of the cost function and constraints. These details are discussed in Appendix D.4.

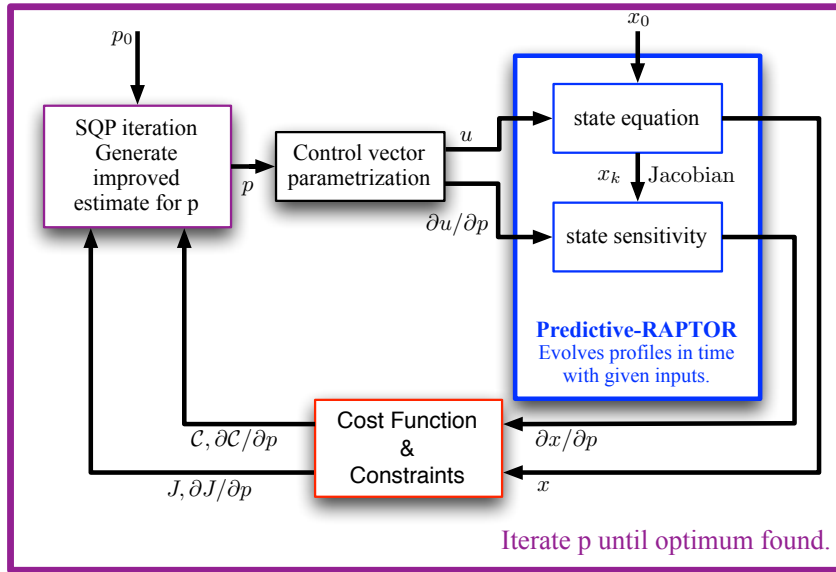


Figure 9.3: Schematic illustration of the nonlinear optimization algorithm described in this section. Starting from an initial guess of the parameter vector p_0 , the control vector parametrization maps the parameters to a set of input trajectories in time. Using these inputs, the state and sensitivity equations are evolved in time using the Predictive-RAPTOR code described in Section 7.5. The cost function and constraints, as well as their gradients, are evaluated as described in the present section, where the state sensitivities $\partial x/\partial p$ are used. The SQP solver then updates the parameter estimate as necessary until convergence criteria on the cost function, parameter vector variation and constraint violation are satisfied.

9.2.6 Solution using Sequential Quadratic Programming

Sequential Quadratic Programming represents a state-of-the art method for solving constrained nonlinear programming problems (Nocedal et al. 2006). The SQP algorithm sequentially solves a set of constrained quadratic optimization sub-problems obtained by quadratically approximating the cost function and linearizing the constraints. The estimate of the Hessian matrix of the cost function is obtained, in our case, using a quasi-Newton method. The SQP implementation in MATLAB^{®3} has been used, called using the `fmincon` function, which implements the algorithm as described in (Nocedal et al. 2006, Ch.18). An outline of the method is schematically depicted in Figure 9.3 but the interested reader is encouraged to consult the literature for details.

The SQP algorithm requires an estimate of the local gradient of both the cost function and constraint functions at the current estimate in the parameter space. For simple problems, it is possible to calculate the gradients using finite differences. However, in the case at hand, evaluating the gradient by finite differences requires n_p additional forward simulations to be run, one for each direction of the parameter space. For large amounts of parameters this would make the problem computationally intractable. A key advantage of the approach presented in this thesis is that the effort was made to calculate exact gradients based on the analytical equations. This effort pays off in the fact that the

³www.mathworks.com

problem becomes numerically tractable even for a large (~ 20) number of parameters. If a larger set of parameters is used, it may be worthwhile to use an adjoint sensitivity analysis method instead of the forward sensitivity analysis (Bryson et al. 1975). For adjoint methods, the time required to estimate the gradients is almost insensitive to the number of parameters. However, the adjoint problem must be formulated and solved separately. Nevertheless, since in our case we already have the Jacobian matrices calculated for the implicit Newton steps, the extra burden of solving the linear equations required for the forward sensitivity analysis is rather modest. For the runs presented in this chapter, a single evaluation of Predictive-RAPTOR (profile evolution in time plus sensitivities) takes a few seconds while a complete optimization takes a few minutes of computational time on a standard desktop PC, depending on the number of free parameters.

In general nonlinear optimization problems, one can never guarantee (except for a specific subset of problems) that a local optimum, as found by the SQP or any other algorithm, is also a global optimum. The risk of finding local (non-global) optima can be reduced by choosing different initial conditions, but especially by proper choice of algorithm and optimization parameters. Nevertheless, one must be aware of this fact when assessing solutions. In general, one can be satisfied if the optimization procedure yields an improvement over the initial condition, but a more optimal solution may always be hidden in a region of the parameter space that the algorithm did not explore.

9.3 Optimization of ramp-up to hybrid plasma q profile

In this section, we will apply the nonlinear optimization method outlined in the previous section to a realistic open-loop plasma profile control problem. Let us restrict ourselves, in this first application, to a particular type of plasma ramp-up scenario in order to fully illustrate the capabilities and potential of the methodology. We start by first examining the basic plasma scenario with its actuators and transport model. Then we study a simple example, in which the optimization is restricted to only two parameters. This illustrates the effect of different cost function weights and of adding constraints to the optimal solutions. Finally, a multi-parameter optimization is carried out to show the full capabilities of the algorithm. This section is concluded by illustrating a method for classifying parts of the input trajectories based on the constraints.

9.3.1 Plasma scenario and transport model

We focus again on a plasma ramp-up scenario similar to that shown previously in the simulation example, in Section 7.6. The plasma evolves from a cold, low-current plasma to a hotter, high-current plasma. The effect of EC heating and current drive is simulated by adding an off-axis power + current source as in Section 7.2.2. The boundary condition is specified through the plasma current I_p . Thus, there are two actuators, $I_p(t)$ and $P_{EC}(t)$.

The simulated plasma has characteristics close to the typical plasmas created in the TCV tokamak and the transport model coefficients in (7.1)-(7.4) are those in Table 7.1. This has allowed us to verify the code results based on experience, but it should be stressed that any Tokamak can be easily and realistically modeled in this way by adjusting equilibrium and transport coefficients.

The initial condition is chosen as an 80kA plasma with a parabolic current density profile $j_0(\rho) = j_0(1 - \rho_N)^2[\text{MA}/\text{m}^2]$, with 200eV central temperature and parabolic initial T_e profile $T_e(\rho, t_0) = 200(1 - \rho_N^2) + 20[\text{eV}]$. The (fixed) density profile is chosen as $n_e(\rho) = 2.0 \times 10^{19} \exp\{-\rho^2/0.6^2\}$. The plasma is simulated over a time period $[t_0, t_f] = [0\text{s}, 0.1\text{s}]$ with step size $\Delta t = 1\text{ms}$ and 16-point spatial grid with greater density of knot points near the center.

9.3.2 Introductory example: optimization with two degrees of freedom

We first focus on a simple case, in which the time-trajectories of the actuators are parametrized by only two parameters. This makes it possible to visualize the parameter space on a plane. The actuator trajectories are parametrized as piecewise linear functions with two segments, defined by the three time points $[t_0, t_c, t_f] = [0, 50\text{ms}, 100\text{ms}]$. The initial and final points (at t_0 and t_f) of the trajectories are fixed, and the value at the central time point t_c is allowed to vary. We choose $I_p(t_0) = 80\text{kA}$, $I_p(t_f) = 200\text{kA}$ (corresponding to $q_{95}(t_0) = 13$, $q_{95}(t_f) = 4.8$, respectively), $P_{EC}(t_0) = 0$, $P_{EC}(t_f) = 1\text{MW}$. The parameter vector is therefore simply

$$p = \begin{pmatrix} I_p(t_c) \\ P_{EC}(t_c) \end{pmatrix} \quad (9.34)$$

The entire input trajectory for both I_p and P_{EC} is thus defined by the choice of this parameter vector. From the plasma point of view, the two parameters decide, respectively, the amount of early current and the heating/current drive applied. Depending on the values chosen, we can have an initial current overshoot or undershoot, and more, or less, early heating and current drive.

Multi-objective unconstrained optimization

Since we have a parameter space of only two dimensions, we can perform a scan of these two parameters over a range of realistic values. This does not require nonlinear optimization of any sort, we simply repeat the simulation for a wide range of parameters corresponding to different actuator trajectories. For each parameter value, we store the ψ and T_e profiles evolution, as well as the values of the various cost function terms described in Section 9.2.2. We focus specifically on two cost function terms, J_{ss} and $J_{\psi_{OH}}$ describing, respectively, the degree of profile stationarity at the final time and the consumed Ohmic transformer flux at the final time. The contours of these two terms as a function of the parameters are plotted in Figure 9.4a. Visually, one can see that the optimum parameter value for which J_{ss} is minimized (the light region on the plot), is obtained for a slight current overshoot at $t = t_c$, with respect to the final 200kA, and little early heating power. This makes sense from the Tokamak physics point of view, since too much early heating (P_{EC}) would give a hot plasma earlier, with increased conductivity and current diffusion time; therefore it will take more time for the loop voltage profile to flatten. Moreover, a slight current overshoot can help flatten the central loop voltage more quickly when the current is subsequently reduced. The dashed lines in Figure 9.4a show contours of equal $J_{\psi_{OH}}$, decreasing with increasing power as can be expected: the lower resistivity due to early heating requires a lower voltage to sustain the same current, leading to a lower flux consumption.

9.3. Optimization of ramp-up to hybrid plasma q profile

Next, we run the nonlinear optimization routine and solve the (unconstrained) optimal control problem choosing the cost function of the form $J_{tot} = J_{ss} + \nu_{OH} J_{\Psi_{OH}}$. We vary the value of ν_{OH} so as to obtain optimal solutions for different weightings of flux consumption in the cost function. The set of solutions obtained is shown as markers in Fig.9.4a, with the blue circle corresponding to the choice $\nu_{OH} = 0$ (Flux consumption not important) and the red square corresponding to $\nu_{OH} = 80$ (High importance of flux consumption). Intermediate points are shown as black dots. One can clearly see that the first case visually matches the optimum of the J_{ss} contours, while increasing the importance of the flux consumption term causes the optimum to shift in the direction of the gradient of the $J_{\Psi_{OH}}$ contours.

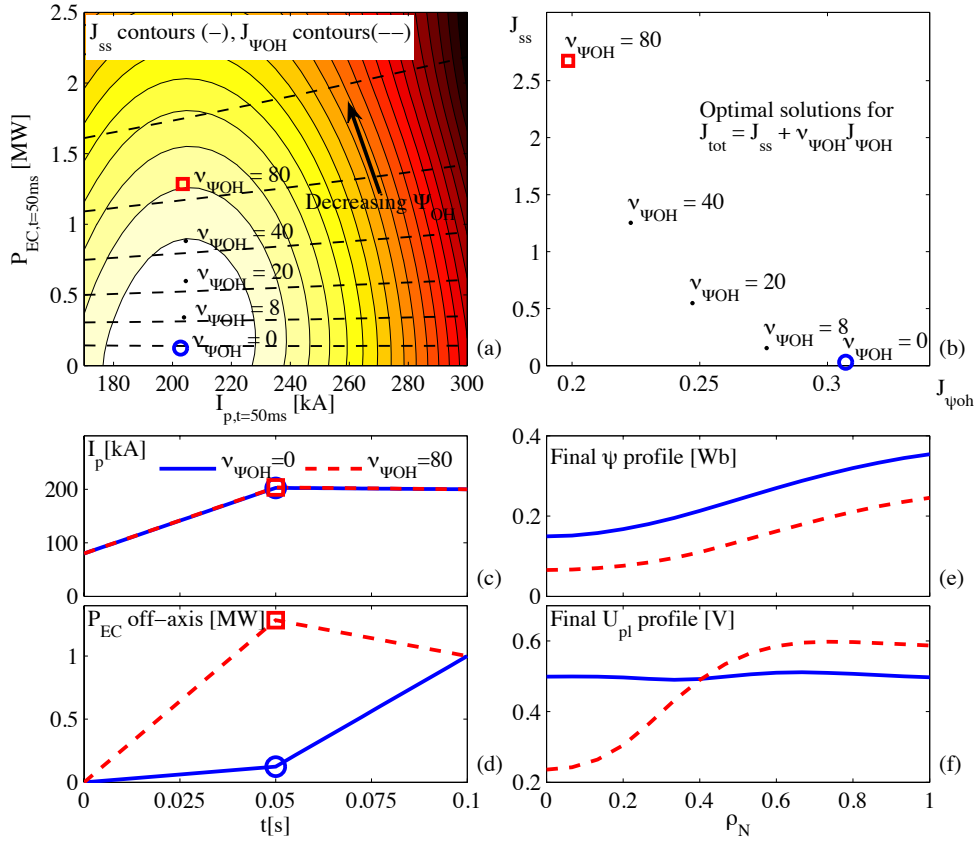


Figure 9.4: Illustration of nonlinear unconstrained optimization with two free parameters. The parameters represent the values of plasma current and auxiliary EC power halfway through a plasma current ramp-up. The cost function contours for J_{ss} (distance from stationary state, measured by voltage profile flatness) and $J_{\Psi_{OH}}$ (Ohmic flux consumption) are shown in (a), with J_{ss} having a local optimum in the parameter space corresponding to actuator trajectories (blue curves in (c),(d)) giving a maximally flat final loop voltage profile (f). The nonlinear optimization is run for different cost function weights representing a trade-off between final Ohmic flux consumption and loop voltage profile flatness. Several optimal solutions are found, with corresponding cost-function terms shown in (b). Clearly, a reduced flux consumption can be obtained only at the expense of a less flat final voltage profile (red traces).

The corresponding actuator trajectories for I_p and P_{EC} are shown for the two extreme cases in Figure 9.4c and 9.4d (blue: (—) $\nu_{OH} = 0$, red (---): $\nu_{OH} = 80$). The flux and

loop voltage profiles at the final time $t = t_f$ are also shown in Fig.9.4e and Fig.9.4f.

The values of the two cost function terms for the various optimal solutions are plotted in Figure 9.4b. When increasing the relative importance of one cost function term, the value of the other term decreases. This reflects the inherent trade-off between cost function terms in multivariable optimization problems like the present one. By varying the relative importance of the terms, one can obtain any solution lying on the curve connecting the points in Figure 9.4b. All these points are so-called Pareto-optimal solution points, i.e. for each point on this curve there does not exist a neighbouring point for which both cost function terms are lower. Improvement in one term must come at the expense of degradation in the other term. The curve connecting the points is known as a Pareto frontier (Grigorenko 2006). This example highlights the importance of carefully choosing appropriate cost function weights. Particularly when each cost function term represents a different physical quantity and/or when the minimum attainable value for the term is not zero, the choice of weights must be made with care.

Adding constraints on the profile evolution

A second example is now presented where the constraints described in Section 9.2.4 are included. Specifically, let us examine the effect of including the constraint $q \geq 1$, used to avoid sawteeth and $U_{pl,edge} \geq 0$, used to avoid negative edge currents. We also set $\nu_{OH} = 0$ such that $J_{tot} = J_{ss}$. Figure 9.5a shows exactly the same J_{ss} cost function level curves as Figure 9.4a, but the regions where constraints are violated are now marked in gray. One can observe a region of $U_{pl,edge} < 0$ appearing for excessive current overshoots: in this region, the edge voltage required to bring the plasma current back to its final value would be negative. Also, observe that the region of the parameter space corresponding to low early EC power violates the $q > 1$ constraint. In this region the EC does not provide sufficient off-axis ECCD current to maintain a broad q profile and a non-centrally-peaked current density profile.

The optimal solution calculated using the SQP algorithm for the constrained case, indicated with a red square in Figure 9.5a, lies just at the border of the $q > 1$ constraint, so this constraint is *active* at the optimal solution. The unconstrained case is also reproduced and corresponds to the optimum found in Section 9.3.2 for $\nu_{OH} = 0$ (blue circles).

In Figures 9.5b and 9.5c we compare the q profile evolution in space and time for the constrained and unconstrained cases. We can see that in the constrained case (b) the plasma evolves into a flat q profile and does not have a $q = 1$ surface during the simulation period. The unconstrained case (c) shows a more peaked q profile which quickly includes a $q = 1$ surface. Figures 9.5(d,e) show the trajectories for $I_p(t)$ and $P_{EC}(t)$ corresponding to these two cases with the constrained case (red, $-$) featuring more early heating when compared to the unconstrained case (blue, $-$). The final q and voltage profiles are shown in Figures 9.5(f,g). The condition $q > 1$ for the constrained solution is obtained at the expense of a less flat voltage profile.

The two examples shown allow us to illustrate an important concept from nonlinear optimization theory. A fundamental theorem of nonlinear optimization states that in the absence of constraints the cost function gradient must satisfy the first-order optimality condition $\partial J / \partial p = 0$ (Nocedal et al. 2006). This is obviously the case of the first example shown in Figure 9.4, where the optimum resides at the bottom of the valley of cost

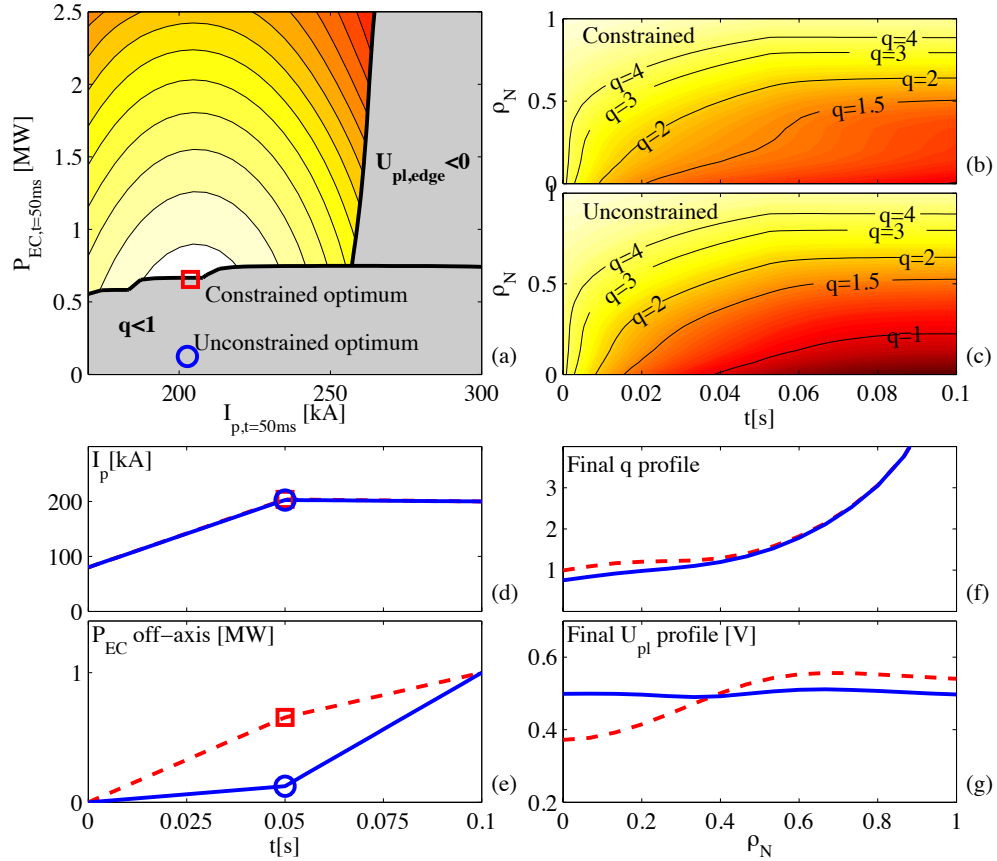


Figure 9.5: Illustration of different solutions to the optimal control problem depending on the presence of state constraints. The contour surfaces of J_{ss} (degree of stationarity), identical to those shown in Figure 9.4 are shown on the parameter space. Regions of the parameter space which would violate constraints on the q profile ($q > 1$) or the edge voltage $U_{pl,edge} > 0$ are shaded in gray. The unconstrained optimal solution from Fig.9.4 is compared to the constrained solution in (b-g), showing the temporal evolution of the q profiles (b,c), the corresponding actuator trajectories (d,e) and final q and loop voltage profiles (f,g). The formation of a $q = 1$ surface is prevented at the expense of being further away from a stationary situation, as demonstrated by the less flat U_{pl} profile for the constrained (red,--) case.

function contours. If constraints are present, then the optimal solution does not necessarily correspond to a point with zero gradient. In this case, however, the point must satisfy the Karush-Kuhn-Tucker (KKT) conditions (Nocedal et al. 2006), written in our notation as

$$\frac{\partial J(p)}{\partial p} + \nu^T \frac{\partial \mathcal{C}(p)}{\partial p} = 0 \quad \text{Primal feasibility} \quad (9.35)$$

$$\nu \geq 0 \quad \text{Positivity of Lagrange multipliers} \quad (9.36)$$

$$\mathcal{C}(p) \leq 0 \quad \text{Constraints satisfied} \quad (9.37)$$

$$\nu^T \mathcal{C}(p) = 0 \quad \text{Complementary slackness} \quad (9.38)$$

The geometrical interpretation of these conditions is that the cost function gradient and the gradient of the *active* constraints (i.e. constraints for which $\mathcal{C}_i(p)$ is equal to 0) must point in opposite directions. In other words, there exist no feasible points (i.e. points that satisfy the constraints) that correspond to a descent direction for the cost function in the neighborhood of a point satisfying the KKT conditions. This is illustrated in Figure 9.6. The Lagrange multiplier vector ν , which has as many elements as there are constraints, separates active from nonactive constraints. Elements of ν are zero if the constraint is not active (i.e. $\mathcal{C}_i(p) \neq 0$) as stated by the complementary slackness condition, and nonzero for active constraints.

By examining Figure 9.5a we can verify that these conditions are satisfied. The constrained optimum lies on the boundary of the $q \geq 1$ constraint region, so this constraint is active. The second constraint $U_{pl,edge} > 0$ is not active at the optimal solution. Additionally, since only one constraint is active in this case, the optimal point lies exactly at the point where the gradients of the cost function and of the active constraint are colinear and opposite.

These observations will be useful in Section 9.4 where we will examine the information about the optimal actuator trajectories that can be recovered by examining which constraints are active.

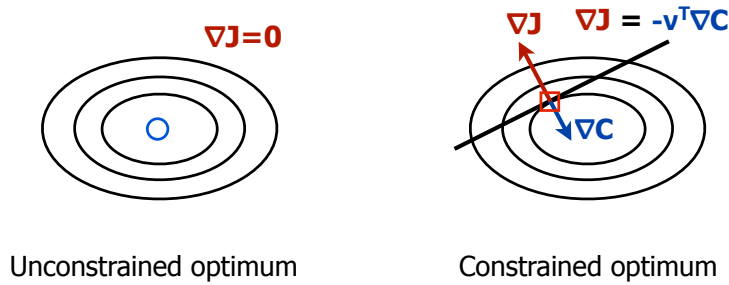


Figure 9.6: Schematic illustration of unconstrained (left) vs constrained right optima in cost function landscapes.

9.3.3 Complete optimization of hybrid plasma ramp-up scenario with constraints

In this section a more complete example of time-trajectory optimization, where the time trajectories are parametrized by a larger number of parameters, will be treated. This

provides more freedom in the choice of trajectories and allows the optimization to fully exploit the richness of the system dynamics. The plasmas simulated here are similar to those in the previous section, but in addition to a co-ECCD gyrotron at $\rho = 0.4$, a central heating source at $\rho = 0$ is added (no current drive). The initial and final values of the actuators have been fixed to $I_p(t_0) = 80\text{kA}$, $I_p(t_f) = 200\text{kA}$, $P_{ECCD}(t_0) = 0\text{MW}$, $P_{ECCD}(t_f) = 2\text{MW}$, and $P_{ECH}(t_0) = P_{ECH}(t_f) = 0\text{MW}$. The final values have been chosen such that a q profile with values $1.1 < q < 1.5 \forall \rho < 0.5$ is obtained when the profiles have relaxed to their final shape (verified in independent simulations over a longer time span). The cost function is defined as $J = J_{ss} + J_{\psi_{OH}}$. The optimization algorithm tries to find trajectories minimizing $J = J_{ss} + J_{\psi_{OH}}$, while satisfying the constraints $U_{pl,edge} > 0$ and $q(\rho) > 1.05$ at all times. The I_p ramp rate is constrained by $dI_p/dt \leq 8\text{MA/s}$ which represents a realistic value for TCV.

Local minima and regularization

The increased number of parameters n_p entails that a corresponding increase in the dimension of the parameter space \mathbb{R}^{n_p} to be searched, possibly increasing the risk of local minima. The existence of local minima is difficult to prove but is expected given the (strong) nonlinearities present in the system equations. Intuitively, one can imagine that parameters which affect the inputs at the initial phases of the simulation may have little effect on the final profiles. This will lead to ill-conditioning of the cost function Jacobian $\partial J/\partial p$ and associated numerical difficulties. One way to alleviate this problem is inspired by multi-grid methods: optimal solutions are computed for a small value of n_p first, after which the number of free parameters is increased. This is done as follows. First, we define the number of free time points per actuator, n_f , such that the total number of parameters is $n_p = n_f r$ (r is the number of actuators which is 3 in the present example). Then we solve the optimization problem with one free point on the time grid delimiting the piecewise linear segments (as in Section 9.3.2), and subsequently add a new intermediate point. This ensures that the solution which was found for the previous (coarser) parametrization can still be obtained with the new parametrization, and that the previous optimal solution should be used as a starting point. Thereby, we ensure that the new (larger) parameter space still contains the optimal point of the previous (smaller) parameter space, ensuring that the algorithm can always return to this point if no better solution is found. In Figure 9.7 it is shown that as the number of free points (n_f) is increased, the cost function value for the optimal solution will gradually decrease up to a point where a better value than the starting point cannot be found (solid blue line). In this case it makes no sense to increase the number of free parameters beyond this point.

When increasing the number of parameters, it is possible that the increasingly optimal trajectories (in the sense that they have lower cost function values) are in fact more optimal only for the very specific model which was used in solving the optimization problem. This problem is related to the problem of overfitting, commonly encountered in system identification or data fitting problems. One must always verify the generalization capabilities of the solution, i.e. ensure that the solution is appropriate also for models which are slightly perturbed with respect to the nominal one. Therefore, after each optimization is completed, we run 20 additional simulations using the same (optimal) input trajectory on a set of models with perturbed model parameters with respect to the nominal model

used in the optimization routine. In particular, the value of c_{ano} , governing the amount of anomalous transport in (7.3), has been perturbed by multiplying its nominal value ($7.0\text{m}^2/\text{s}$) by a random number picked each time from a Gaussian distribution with mean 1 and standard deviation 0.2. The results are summarized in Table 9.1 and the values of the cost function for this set of models is also displayed in Figure 9.7. The cost function value of the nominal model is seen to decrease monotonically as more degrees of freedom are added. The cost function mean standard deviation for the perturbed models, however, starts to increase if more than 3 points are chosen, indicating that the optimal solution for $n_f > 3$ relies excessively on the specific parameter set of the nominal model and generalizes poorly to models with slightly different parameters. This provides an important, additional criterion to decide the appropriate amount of freedom in the input trajectory parametrization. In this case $n_p = 3$ is the appropriate optimum.

Table 9.1: Nominal vs perturbed cost function values

| n_f | n_p | Nominal J | Perturbed: mean | median | min | max |
|-------|-------|-------------|-----------------|--------|--------|--------|
| 1 | 3 | 0.5540 | 0.5792 | 0.5637 | 0.4768 | 0.6889 |
| 2 | 6 | 0.2964 | 0.3579 | 0.3123 | 0.2943 | 0.4621 |
| 3 | 9 | 0.1780 | 0.2537 | 0.1956 | 0.1781 | 0.3495 |
| 4 | 12 | 0.1717 | 0.2464 | 0.1904 | 0.1718 | 0.3621 |
| 5 | 15 | 0.1684 | 0.2495 | 0.1884 | 0.1683 | 0.3805 |
| 6 | 18 | 0.1673 | 0.2635 | 0.1896 | 0.1672 | 0.4073 |

Results

The optimal solutions and corresponding profile evolutions for the values $n_f = \{1, 2, 3\}$, of Fig.9.7, are shown in Figure 9.8. We plot the actuator trajectories and the evolution of the q and T_e profiles for the different solutions. We can see how the additional freedom in the actuator trajectories allows a different control strategy. The rightmost panels Fig.9.8(g,h,i) show a steeper current ramp and earlier heating, leading to an early hot plasma exploiting the improved confinement of the reverse-shear condition. The q profile subsequently relaxes to a condition with a flatter final voltage profile and lower overall flux consumption than the other two cases. This shows that the freedom provided by $n_f = 1$ (Fig.9.8(a,b,c)) did not provide sufficient flexibility in the choice of actuator trajectories to fully exploit the system dynamics and there is still room to find better performing actuator trajectories. Increasing to $n_f = 2$ and then to 3 yields better results in this case. It is interesting to note the qualitatively different control strategy of the right case with respect to the other two cases.

One thing all strategies have in common is the initial current overshoot. This has been shown in practice to be advantageous for obtaining flat and broad q profiles in hybrid scenarios (Fujita et al. 2001), (Sips et al. 2002, Fig.2), (Joffrin et al. 2010). The fact that this has now been computed using a-priori knowledge, and not a result of experience, is encouraging. Other actuator trajectories found this way may yield performance benefits which were not known or expected or not yet tested before.

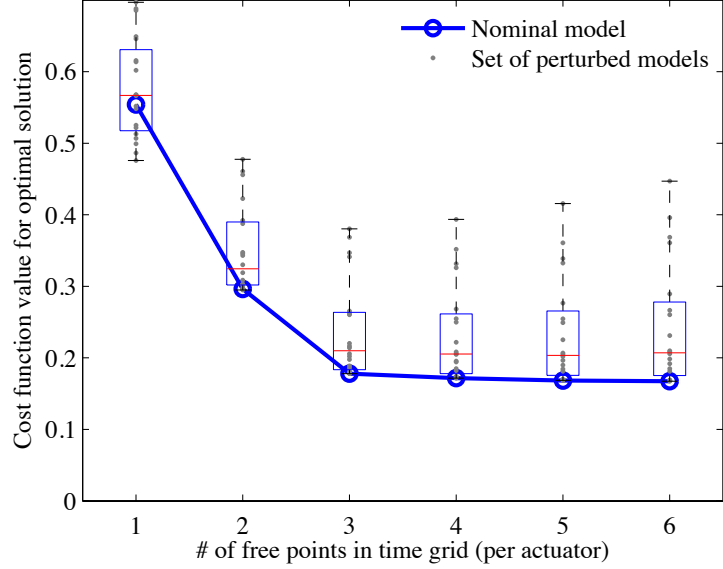


Figure 9.7: Cost function values for increasingly fine parametrization of the input trajectories, obtained by a larger number of free points in the time grid (n_f). The cost function value for the nominal model (solid, blue line) can be seen to decrease rapidly at first, and slowly later. Also shown (boxplot and gray dots) are the cost function values obtained when using the optimal trajectories found with the nominal model on a set of 20 perturbed models. The box indicates the 25th and 75th percentile interval, the red line is the median, and the error bars span from minimum and maximum.

9.4 Input trajectory classification and consequences for feedback control

In this section we will focus on additional information about the optimal input trajectories that can be obtained by examining the cost function and constraint gradients at the optimal solution. As discussed for the simple example in Section 9.3.2, constrained optimal points have gradients of the cost function pointing in opposite direction. Conversely, if the cost function derivative $\partial J/\partial p_j$ with respect to a particular parameter p_j is zero, the constraint gradients with respect to this parameter must also be zero. In other words, changing the value of p_j will not affect any active or inactive constraints.

With this idea in mind, another example is given here based on the one presented in the previous section. The only difference is that the $\iota \leq \iota_{lim}$ constraint has been removed and only the off-axis ECCD at $\rho = 0.4$ is used. Initial and final values for I_p and P_{ECCD} are again pre-set to $[80; 200]$ kA and $[0; 2.0]$ MW, respectively. The I_p ramp rate is again constrained by $dI_p/dt \leq 8$ MA/s. The trajectories are discretized by piecewise linear functions over 8 equal intervals, yielding a total of 7 free parameters per actuators, hence $n_p = 14$.

In Figure 9.9 the resulting optimal actuator trajectories are plotted for $I_p(t)$ and P_{ECCD} . Overlaid in green in Fig.9.9a, one can see the input trajectories corresponding to the steepest descent direction (i.e. the negative gradient of the cost function), i.e

$$u^*(t) = u^o(t) + k \frac{\partial u}{\partial p} \left(-\frac{\partial J}{\partial p} \right)^T = u^o(t) + kP(t) \left(-\frac{\partial J}{\partial p} \right)^T \quad (9.39)$$

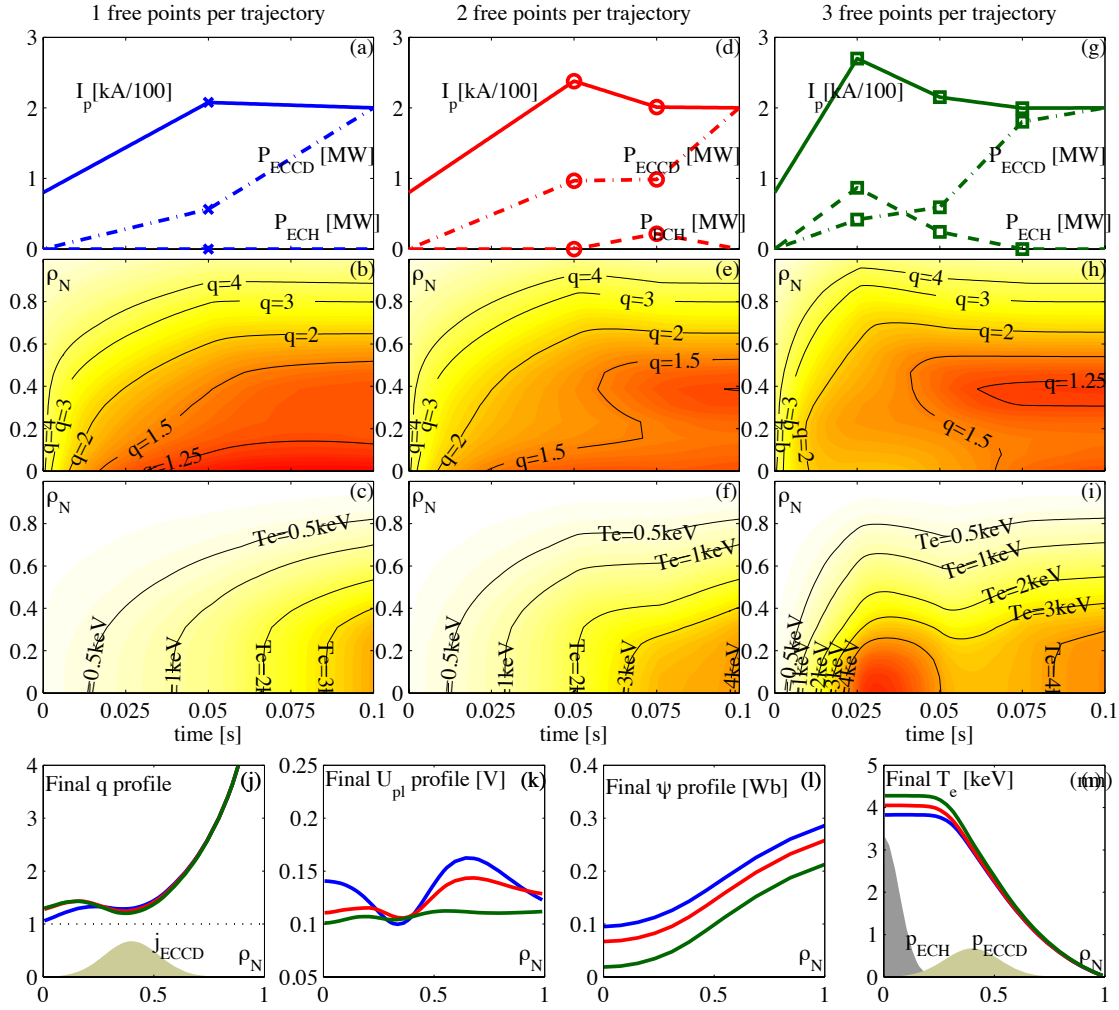


Figure 9.8: Results of constrained optimization with more degrees of freedom. Shown are the optimal actuator trajectories for I_p , P_{ECCD} and P_{ECH} , the q and T_e profile evolution for 1(a-c) 2(d-f) or 3(g-i) degrees of freedom per actuator, illustrated by the symbols in (a,d,g). The bottom panels (j-m) illustrate the final condition for the three cases, showing that more stationary profiles and lower flux consumption is obtained with 3 degrees of freedom (green curves). The spatial distribution of ECCD current density (j) and power densities are also shown (m) (amplitude not to scale).

where the scalar k has been chosen to provide adequate scaling in the figure for visualization. This indicates that varying the input trajectory in the “green” direction would decrease the value of the cost function.

In Figure 9.9b the same optimal $I_p(t)$ trajectory is plotted, but this time accompanied by the input corresponding to increasing constraint function value (red region), i.e. in the direction of the positive constraint gradient. Clearly, the green region in Fig.9.9a and the red region in Fig.9.9b match in the time interval denoted by (ii). This indicates that, in this region, the trajectory of I_p is constrained by the $U_{pl,edge} > 0$ constraint. This result matches intuition, since increasing the initial current overshoot or the final current undershoot requires stronger backwards “pull” by the Ohmic transformer coil. In the time interval denoted by (i) in Fig.9.9b, the situation is different. The cost function

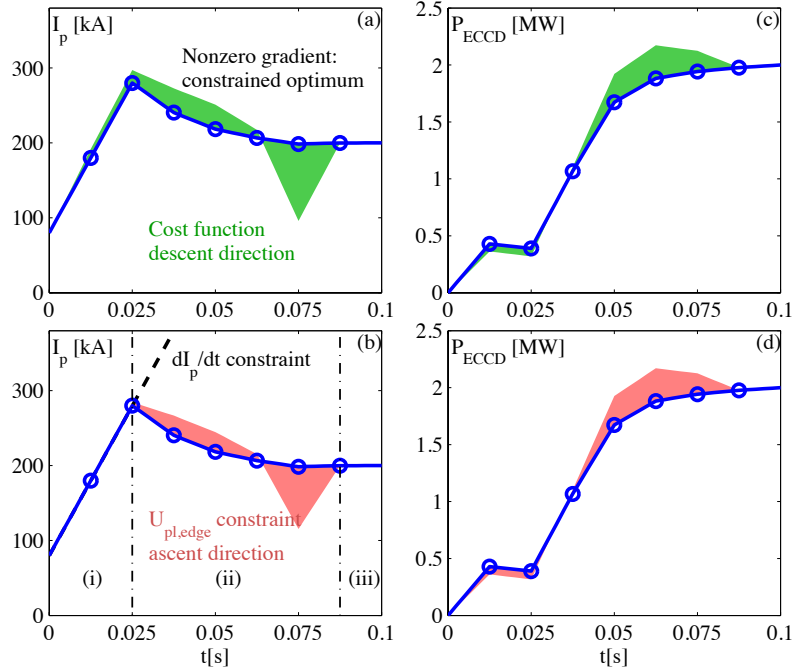


Figure 9.9: Sensitivity of actuator trajectories: moving the optimal actuator trajectory in the green direction would decrease the cost function value. However, moving into the red zone means violating a constraint. This gives information about which constraint is active at which time interval. The time interval indicated by (i), the constraint on the maximum ramp rate limits the current rise time. In (ii), the $I_p(t)$ trajectory is such that it obtains the best performance while *just* not violating the constraint on the edge voltage. The final interval (iii) is not limited by any constraints and is an unconstrained optimal arc.

gradient is nonzero in this segment while the cost function gradient for the $U_{pl,edge} > 0$ state constraint is zero. Indeed, the trajectory in this interval is constrained by the input constraint $dI_p/dt \leq 8\text{MA/s}$ as witnessed by the dashed diagonal line.

The final time interval (iii) belongs yet to another category. Since both cost function gradient and constraint gradients are zero in this region, the I_p trajectory is not constrained in this interval but has the optimum value corresponding to a minimum cost. i.e. changing the trajectory in this interval in any direction would give a performance degradation.

We now summarize the three classes in which we have categorized intervals of the input trajectories and discuss some consequences of this classification for feedback control. The classes are:

1. Input constrained arcs: The trajectory is directly constrained by an input bound, the actuator is working at the maximum of its capabilities.
2. State constrained arcs: The actuator trajectory is just at the limit of maximizing performance while not violating constraints.
3. Unconstrained arc: The actuator trajectory corresponds to maximum performance (minimum cost) and is not limited by possible the constraints.

Classifying input trajectories as above can have consequences for subsequent feedback control strategies. In an input constrained arc (i), there is little need for active feedback control as the system is limited by the actuators rather than other concerns. Along state constrained arcs (ii), however, the need for feedback control is more pressing. The inevitable mismatch between the model used for the optimization studies and the true system will mean that the system may be closer to safety limits than envisaged. These limits need to be monitored in real-time and active (feedback) measures need to be taken to ensure the constraints are satisfied, even at the cost of a less optimal performance. In the tokamak, this will typically be the case for ramp-up and ramp-down phases of the discharge. On unconstrained arcs (iii), the feedback control strategy may be yet different. As no constraints are at play, feedback controllers can be dedicated to maintaining the plant on its optimal performance trajectory. In the case of tokamaks this will typically be the case for flat-top stationary phases and closed-loop feedback control methods such as presented in (Moreau et al. 2008) are adequate.

Moreover, there is an important but subtle difference between the time intervals during which the actuator trajectories are constrained by state constraints and the actual times when the state constraints become active. It is very well possible that a particular state constraint is active only at one particular instant in time, referred to as the *junction* time. However due to the system dynamics including, for example, transport delay and diffusion, this point in time has a consequence for the actuator trajectories for an extended period before and after the junction time. The junction time can also be extracted from the open-loop optimal solution and this information can be explicitly incorporated in a feedback controller.

9.5 Outlook

The developed methodology, coupling the Predictive-RAPTOR code to a nonlinear optimization scheme, holds great potential for further studies and applications beyond the results already shown. This section will consider some future research directions that can be explored as a direct extension of the present work.

9.5.1 Extension of open-loop optimal trajectory studies

Since the tools presented are fully general and can be used for any tokamak geometry and distribution of current drive and heating actuators, it is possible to simulate and optimize scenarios of interest for any tokamak. In the near term, it is planned to study transport barrier formation in the TCV tokamak in more detail (Coda et al. 2007) and possibly obtain an actuator trajectory giving the final loop voltage close to zero more rapidly than is possible at present. Further work could include ITER scenarios with ramp-up and ramp-down simulations, including constraints on the internal inductance to stay within the limits specified by the vertical control system. Another possible application is to determine the power distribution in a set of actuators required to reach a prescribed q and T_e profile (i.e. the first and last terms of (9.17)), rather than focusing on profile stationarity and flux consumption as was done here. The set of constraints can also be extended to include constraints on internal inductance, MHD stability, magnetic shear profile, NTM stability criteria and more. The physics model used can also be extended

to include ion temperature profiles and density profiles, as well as alpha particles for burning plasmas. Similarly, the transport model can be enhanced to model H-modes, or modified to allow for non-diffusive transport processes such as sawtooth crashes, ELMs and other events. This additional physics would allow one to study, for example, ramp-down scenarios including conditions on the H-L transition and density limits.

An obvious extension is the coupling to a Grad-Shafranov solution code, thus evolving the 1D profiles and 2D magnetic equilibrium simultaneously, coming closer to full tokamak simulators such as DINA-CH/CRONOS, CORSICA and PTRANSP/TSC. This would require a major extension of the present work, or an adaptation of the mentioned codes so that they return the first-order sensitivities to actuator inputs, as the Predictive-RAPTOR code currently does. Additionally, computing the sensitivities for the coupled 1.5D equilibrium+transport problem is a far from trivial exercise, although intermediate models can be developed.

Of course, the applicability of these methods are restricted by the accuracy of the available physics models. Similarly, the initial conditions of the plasma affect the result of the optimization, requiring accurate descriptions of the initial phases of the plasma to yield unique solutions. As our understanding and quality of the physics models progresses, the results obtained will match reality more closely. On the other hand, by carefully validating the optimal trajectories for a range of physics models one can obtain trajectories which are less sensitive to the transport model. Testing these results in an experiment would lead to further advances.

9.5.2 Transport parameter fitting to experimental data

In order to obtain actuator trajectories which can be used on existing experiments, the model has to be tuned so that the model behavior, in particular that of the electron transport and current drive efficiency, matches the experimental evidence. Based on the tools developed in this chapter, the same nonlinear optimization routine can be used to determine the transport model parameters. In this case, experimental data is collected during a dedicated experiment with known actuator trajectories chosen to sufficiently excite the plasma profile dynamics. The parameter sensitivities as formulated in Section 7.5.2 can, without loss of generality, be evaluated for the transport model parameters instead of the input trajectories. The cost function can then be reformulated as the difference between simulated temperature and q profile (if available) and measured experimental profiles.

More precisely, let $u(t)$ be a chosen excitation (feedforward) input signal for a set of tokamak actuators, independent of p , and let p in this case be a vector of transport model parameters (for example $c_{ano}, w_{ic}, d_{ic}, a_{ic}, \chi_{central}$ in the ad-hoc model of Section 7.2.3). Let y_k be a set of measurements, at given times, of the profiles (kinetic and magnetic) obtained by exciting a tokamak with inputs trace $u(t)$ and let $\bar{y}_k(p)$ be the simulated measurements obtained by simulating the Predictive-RAPTOR model with parameter set p . Defining a cost function

$$J(p) = \sum_k \|y_k - \bar{y}_k(p)\|_2^2 \quad (9.40)$$

the problem of determining the transport parameters p can be formulated as the minimization problem

$$\min_p J(p) \quad (9.41)$$

A local minimum can be found by gradient descent, greatly aided by the fact that dJ/dp is known since

$$\frac{dJ}{dp} = \sum_k \left(\frac{\partial J}{\partial \bar{y}_k} \frac{\partial \bar{y}_k}{\partial x_k} \frac{\partial x_k}{\partial p} \right) \quad (9.42)$$

where $\frac{\partial \bar{y}_k}{\partial x_k}$ can be derived from a model for the diagnostic (i.e. how the plasma state appears in a given measurement) and $\partial x_k/\partial p$ is the state sensitivity computed using the method in 7.5.2.

This is a parameter identification problem for the transport model parameters. There are a number of conditions for the problem to have a unique solution, in particular, the input $u(t)$ must be chosen such that the system dynamics are sufficiently excited so that the measurements contain enough information to resolve the parameters. Also, the parameters themselves must be sufficiently independent in the way they appear in the measurements. This can readily be evaluated from the singular values of the matrix $\partial \bar{y}_k/\partial p$; a low condition number indicating that some of the parameters affect the outputs in a similar way, or not sufficiently. If this is the case, a more suitable parametrization of $\chi_e(p)$ needs to be chosen. With ample literature on the subject of (nonlinear) system identification (Ljung 1999) there is much scope for further work. As an intermediate step, this could be tested by using more complete physics models (such as GLF) and transport codes (ASTRA/CRONOS) as the “experiment”, and would provide a systematic method by which to fit an ad-hoc model to the results.

This approach can be thought of as a gray-box model identification approach. The structure of the model is given by the physics knowledge, and only the unknown parameters of the electron energy diffusion, (the physics of which is more complicated and less well understood), are estimated from the data. We can compare this approach to that of (Moreau et al. 2011), in which a black-box approach is used to identify the full model dynamics from experimental data; the present method has the advantage of using available physics knowledge where acceptable, and using data only to “fill the gaps”. Note that this can also be used to test if a given transport model structure is able to recover the experimental time evolution. The novelty in this approach is also that the dynamics of the system is taken into account in the ad-hoc model identification technique, whereas many existing methods fit transport coefficients based on stationary profiles only.

9.5.3 Closed-loop feedback controller design

The optimal open-loop actuator trajectory, calculated using the methods presented in this chapter, can be advantageous for feedback control design. As highlighted in Section 9.4, the optimal trajectories can be classified by which constraints (if any) bound them at different times. The optimal control strategy for each time segment may then be decided based on this information.

In Section 7.5.4, local linear models of the time-varying profile response were discussed. With knowledge of the optimal trajectory, the corresponding linear time-varying models can now be computed around this trajectory. Controller synthesis techniques for such models are well-established in the control literature (e.g. (Bryson et al. 1975)) and this literature may be used to design closed-loop controllers to keep the state trajectory on the optimal trajectory in the presence of model errors or disturbances, taking the time-varying nature of the system into account. Techniques such as LQR (Linear Quadratic

Regulator) control for time-varying systems can be used as recently shown in (Ou et al. 2010a). MPC (model predictive control) methods are also applicable in this case as they can naturally handle (linearized) state and input constraints. Recent work published in (Ou et al. 2010b) presents an example of robust linear time-invariant control design, where the time-varying part of the system is treated as an exogenous disturbance against which the controller should be robust. However the analysis of Section 7.5.4 suggests that care must be taken as the stability of plant zeros may vary during the evolution, as well as the sign of the response for some outputs. Systematic model-based controller design for these systems is a challenging and interesting research direction, in which model reduction may play an important role.

9.5.4 Real-time predictive simulations

As a related research opportunity we can consider *real-time prediction* of the plasma profile evolution, either based on the full nonlinear model or on the linearized model described above. In this case, real-time profile reconstructions would provide a starting point for a simulation of the profile dynamics based on the planned actuator trajectories, up to a finite time horizon. This could assist in identifying the imminent violation of a limit or the proximity to a state where disruptions are probable. The results presented in the previous chapter where an implementation of a transport model-based real-time flux profile evolution on the TCV tokamak is demonstrated, show that such calculations can indeed be done in real-time, certainly on a large tokamak like ITER, but also in present machines like ASDEX-Upgrade and JET.

There are multiple potential research opportunities as well as possibilities for testing these kind of closed-loop feedback control methods in practice. The final proof that these methods work can come only from application in a tokamak experiment. The open-loop actuator trajectories should be tested on the TCV tokamak in the near future.

9.6 Conclusion

In this chapter we have introduced a systematic methodology to optimize the open-loop actuator trajectories for tokamak plasma profile control. The optimization uses the RAPTOR model which includes the coupled dynamics of electron temperature and poloidal flux profiles, and includes non-inductive heating and current drive, bootstrap current, and a thermal transport model including local confinement enhancement at low shear. This physics model is implemented in the Predictive-RAPTOR code which, in addition to returning the time evolution of the plasma profiles in response to the actuator inputs, returns the sensitivity of the profile evolution with respect to some pre-defined model or input parameters.

A generic definition of possible cost functions has been introduced, allowing one to specify quantities to be minimized that are related to the final profiles of rotational transform, loop voltage, loop voltage spatial derivative and/or electron temperature. Constraints on the profile evolution can be included, and a constraint on the lowest allowable safety factor and on the lowest edge loop voltage have been implemented. The optimization itself is performed using the SQP (Sequential Quadratic Programming) method, a state-of-the art nonlinear programming algorithm. The SQP searches for an optimum

in the parameter space using the knowledge of cost function and constraint gradients derivatives with respect to the parameters.

The method has been illustrated by a number of examples of increasing complexity. All examples feature a plasma current ramp-up where one has the freedom of choosing the time evolution of plasma current and the power of a set of auxiliary heating and current drive actuators. While these examples have been chosen for their relative simplicity, for the sake of illustration, they exceed expectations in providing insight into the dynamics and optimization of tokamak plasma ramp-up scenarios. In particular, it follows from the optimization routine that early heating combined with an I_p overshoot is helpful to prevent the early formation of a $q = 1$ surface, which is important in order to reach hybrid scenarios with locally flat central q profile with $q > 1$. In addition, it shows that too much early heating is detrimental in obtaining an almost stationary profile at the end of the ramp-up and will lead to significant profile evolution during the flat top. These facts, which were known from experimental evidence, have been recovered as the result of the optimization. This provides confidence that other predictions may yield further insights that will help Tokamak operations. In addition, the examples presented in this chapter have shown that stationary situations, with flat loop voltage profile, can be obtained directly at the start of the current flat-top phase; that is, on a shorter time scale than the global current redistribution time by optimizing the ramp-up. This should be very useful for present experiments that have stationary scenarios with relatively long current redistribution times with respect to the total shot time, as the optimized trajectories would yield longer periods in stationary conditions.

An interesting insight is provided by these simulations through the classification of time segments of the actuator trajectories that depend on which constraint (if any) influences a particular segment. This has important consequences in subsequent feedback controller design; different feedback controller structures should be used for different phases of the discharge. These can be systematically designed taking constraints into account.

This chapter does not yet fully exhaust the broad research opportunities provided by the presented approach. Tests and validation on other tokamaks would be very valuable and relatively easy to implement. Future work will focus on 1) optimization of actuator trajectories to reach advanced scenario profiles with reverse shear, and 2) adding further constraints and increasing the complexity of the simulated physics model. Further applications in experimental validation of transport models have been described, as well as closed-loop controller design for transient phases of plasma evolution. Synergy and cross-validation with more complete transport models and with experiments are expected to be fruitful and yield interesting results in the future.

Chapter 10

Conclusions

Stable, high-performance operation of tokamak plasmas requires several plasma control problems to be handled simultaneously. Moreover, the complex physics which governs the tokamak plasma evolution must be studied and understood to make correct choices in controller design. In this thesis, the two subjects have been merged, using control solutions as experimental tool for physics studies, and using physics knowledge for developing new advanced control solutions.

The TCV tokamak in Lausanne offers a unique platform for investigating these issues, as it combines a flexible actuator set, consisting of 16 independent poloidal field coils and a powerful and flexible ECH and ECCD system with 7 real-time steerable launchers, with a modern digital controller receiving inputs from more than 200 diagnostic channels. This system has been extensively used for many recent applications (Paley et al. 2009), (Paley et al. 2009), (Paley et al. 2010), (Felici et al. 2011b).

10.1 Control of physics: applying real-time control to physics studies and plasma instabilities

Control of sawteeth and ELMs It is well known that the sawtooth period can be lengthened or shortened by localized EC deposition near the $q = 1$ surface (Angioni et al. 2003). A new control paradigm has been demonstrated in which the stabilizing power is periodically removed during the sawtooth ramp, which causes the sawtooth crash to appear soon thereafter. The timing of the EC removal is based on real-time detection of the previous sawtooth crash. This methodology, called *sawtooth pacing*, has been tested in TCV and has been shown to yield very regular and reproducible sawteeth, the period of which can be precisely controlled in the range between the natural (Ohmic) sawtooth period (without EC) and the maximum lengthened period (CW EC). Even more, each individual sawtooth crash was controlled independently of the previous one (Goodman et al. 2011), (Section 3.2).

Statistical analysis proves that the crash delay, i.e. the time between the removal of stabilizing power and sawtooth crash, increases with increasing crash period. Also, the crash delay increases and becomes more variable if not all of the stabilizing power is removed, simulating the stabilizing effect of α particles in a burning plasma. Alternatively, a similar method could be used for sawtooth destabilization, in which destabilizing EC

power (inside the $q = 1$ surface) is added at a given time after each crash to yield sawteeth shorter than the natural period. This has not yet been tested in experiments but is expected to give interesting results and new insight. The sawtooth pacing method provides a possible method for sawtooth control in burning plasmas in which the time of each sawtooth can be prescribed, allowing one to mitigate deleterious effects such as seeding of NTMs with preemptive ECCD.

ELM pacing It is shown that the pacing technique is also applicable to ELMs. In H-mode plasmas heated by X2 power at the edge, additional power leads to a decreasing ELM period for type-I ELMs. It is shown that ELM pacing, by adding power at a fixed time after the previous ELM, regularized the ELM period with respect to the case of continuous heating. This method has also been used to feedback control the ELM period by varying the delay between the last ELM and the EC power increase. The individual period of each ELM can be controlled independently, just like for the sawteeth, showing that both phenomena lack “memory” of past events (Section 3.3).

In addition to demonstrating new control methodologies with perspective for applications in burning plasmas, these experiments also provide a stringent testbed for physics models of sawteeth and ELMs.

NTM triggering and control Neoclassical tearing modes, which degrade confinement and can cause plasma disruptions, have been studied in TCV plasmas. Starting from plasmas with significant EC-driven current, investigations were carried out to elucidate the current-profile based classical tearing stability of $m/n = 2/1$ modes. Experiments showed that trigger events observed in TCV can be categorized as either 1) classical tearing destabilization with initial slow growth followed by faster growth driven by neoclassical effects, 2) $n = 2$ activity preceding a slowly increasing $n = 1$ signature, which suddenly accelerates in growth suppressing the $n = 2$ component and growing to a saturated NTM, or 3) fast growth with no apparent trigger, which subsequently decays rapidly. The latter was observed only in transient current profiles with time-varying localized ECCD and is believed to be due to a short-lived but strong classical destabilization.

NTM triggering in these plasmas is shown to be extremely sensitive to experimental conditions. In particular, NTMs were mostly found to be triggered in transient phases of the discharge (though occasionally even after 2-3 current redistribution times) i.e. no stationary condition was found in which the plasma is *always* unstable to tearing modes. It seems possible that transient effects related to the current density profile evolution may play a role in creating the conditions for NTMs to appear (Section 4.3).

Existing NTMs can be stabilized by applying EC power at the rational surface. Indeed NTM stabilization is the main objective of the ITER EC system with steerable launchers. In TCV, control demonstrations have shown successful stabilization of 2/1 NTMs by moving real-time steerable mirrors in response to detected MHD activity. When the MHD activity disappears, as a consequence of the island being stabilized due to EC deposition on the island, the launcher movement is stopped, maintaining the EC power on the location of the rational surface. With this methodology, a 2/1 NTM has been stabilized by sweeping EC power towards the mode surface location from both inside and outside. In both cases, the stabilization was observed at the same location, within a one-half beam width. Other experiments were done to test the possibility of stabilizing NTMs

in plasmas with different levels of EC power, changing both β and the current density profile. These experiments were modeled using a simplified form of Modified Rutherford equation with partial success: local profile gradient effects, which were not modeled, are likely to play a role in explaining the detailed time evolution of the mode (Section 4.4).

Furthermore, the sawtooth pacing method was applied to investigate sawtooth-triggered NTMs in low $q_{95} = 2.6$ plasmas under precise sawtooth period control, simulating the conditions of ITER inductive scenarios. Long, stabilized sawteeth were observed to generate post-crash MHD activity of $n = 1$, $n = 2$ and $n = 3$ signature, which occasionally destabilized $3/2$ NTMs or even $2/1$ NTMs, the latter of which rapidly locked to the wall and caused a disruption. The seeding of $3/2$ NTMs by post-crash MHD activity was successfully prevented by briefly applying EC power on the $q = 3/2$ rational surface at the time of each sawtooth crash (Section 4.5).

For these experiments, real-time control algorithms were developed, including modulated ECCD power capabilities, which will allow future studies of NTM physics and control. Already, the preemptive NTM stabilization provides a crucial proof-of-principle towards validating NTM control methods envisaged for ITER.

Kinetic profile control Linear control methods were used to control TCV kinetic profiles, mostly measured indirectly from a line-integrated x-ray measurement, in real-time. Manually tuned PI (proportional-integral) controllers were tested and were mostly successful at controlling one profile variable, for example the peak of a real-time spline fit or the plasma β_p . Multivariable controller design techniques based on a data-driven identified linear model were used to simultaneously control the x-ray profile peak and width. The experimental results show that these tools are generally applicable for controlling the plasma in the neighborhood of to a pre-established operating point. Gain-scheduling controller techniques were applied to compensate for changes in the amplitude of the response of the system. Owing to the complexity and nonlinear nature of the tokamak plasma, these methods fall short of completely solving the tokamak state control problem for a more general range of operating conditions.

10.2 Physics-based control: using physics knowledge for plasma state reconstruction and profile trajectory optimization

The key to complete control of a plasma scenario is to accurately know and precisely control both the magnetic and kinetic profiles in the plasma at all times, from ramp-up to flat-top and ramp-down. The profile evolution is described by a set of nonlinearly coupled partial differential equations, which show strongly varying dynamic responses at different stages of the plasma evolution. For this reason, the profile control problem is better approached starting from the (physics-based) nonlinear equations. At the same time, these equations are complex, as multiple effects play an important role, and simulation codes are often complicated and CPU intensive. For control purposes, a new, lightweight transport code was developed which solves the coupled evolution of the current density profile and electron temperature profile: the two most important profiles governing the time-evolution of the plasma. By making some simplifying assumptions, yet retaining

the principal elements of the physics model, a code was obtained which can simulate the plasma evolution on a standard computational platform faster than the physical plasma evolution. This code, named RAPTOR (RAPid Plasma Transport simulatOR) has been favorably benchmarked against the (more complete) transport code ASTRA (Pereverzev et al. 2002). It has been used in two applications so far, with ample perspective for further development.

Real-time simulation in TCV As a first application, RAPTOR has been used to simulate the time evolution of the current density profile in real-time in the TCV tokamak. The simulation requires a real-time estimate of the plasma kinetic profiles to compute conductivity and bootstrap current, which are extracted from real-time x-ray and interferometer signals by a nonlinear mapping using a neural network. A real-time estimate of the plasma current prescribes the boundary condition for the problem. ECCD sources are modeled by Gaussian profiles fitted to pre-calculated ray tracing results.

The real-time simulations are tested in shots with time-varying currents, showing that the results are similar to post-shot interpretative transport simulations with ASTRA using (offline) Thomson scattering profile data – which has been, to date, the most reliable source of information on TCV q profiles. The real-time profile estimates were used in a feedback control experiment demonstrating successful independent control of the internal inductance (a measure of current density profile peaking) and central electron temperature by balancing on-axis co- and counter-ECCD power.

Optimization of profile actuator trajectories Thanks to the speed of execution of the RAPTOR code, the predictive version (solving both current density profile and temperature profile using an ad-hoc transport model) was used as a basis for optimizing profile actuator trajectories. The objective is to determine what actuator trajectories are appropriate to steer the plasma profiles to an operating point, avoiding instabilities and other limits.

The optimization problem was formulated as a constrained finite-horizon optimization problem for the profile evolution equations, with a cost function depending on the final state and constraints on both the state and actuator trajectories, and solved using an SQP (Sequential Quadratic Programming) algorithm. The computation of the optimal solution is greatly aided by the fact that RAPTOR, unlike other transport codes, returns not only the time evolution of profile trajectories in response to actuator inputs, but also the sensitivities of the state evolution to the inputs, which are used to construct the cost function gradients at each iteration of the nonlinear optimization.

The optimization method has been applied to a plasma current ramp-up scenario with control of localized heating and current drive actuators and plasma current in time. The cost function was formulated in such a way as to minimize the loop voltage profile derivative at the final time, i.e. ensuring the plasma profiles have relaxed to a stationary condition at the end of the ramp-up, while penalizing Ohmic flux consumption. This is very important from an operational point of view, since long current redistribution times in large tokamaks mean that transient effects continue during a long portion of the discharge and instabilities can be expected at any time. Reaching a stable stationary condition at the end of the ramp-up guarantees that the discharge will remain stable throughout the remainder of the pulse if unperturbed. At the same time, conditions are

imposed on the q profile to avoid the formation of a $q = 1$ surface (yielding a *hybrid* tokamak scenario) and to avoid inducing counter-current at the edge by negative loop voltage.

The results of the optimization for the problem described above show that early current overshoot and moderate early central heating are beneficial for obtaining a stationary state. The fact that current overshoot is beneficial had already been observed experimentally, but has now been computed for the first time as a result of a tokamak profile evolution optimization (Chapter 9).

Prospective applications of RAPTOR Based on the encouraging results, one can envisage multiple directions for further deployment of the RAPTOR code in real-time simulation and control applications. It is important to note that RAPTOR is completely machine-independent and that deployment to other tokamaks would be straightforward.

A major advantage of real-time simulation is that it provides a natural unification of real-time diagnostic measurements and real-time equilibrium reconstruction into a self-consistent physics-based estimate of the plasma state. The spatial and temporal resolution of the information is no longer limited by diagnostic resolution, but can be chosen arbitrarily (within the limits of the available CPU time). Any available diagnostic information can be included at any time to improve the state estimate and remove uncertainties in the modeling. Conversely, the lack (or loss) of diagnostic information does not, however, render the estimation of the state impossible. Application on different tokamaks with different diagnostics can unify the q profile estimates across several devices, allowing control algorithms to be compared more easily. Scenario supervision and disruption prevention are particularly interesting applications due to their importance for ITER: while most of today's methods are purely data-driven, a physics-based estimate of disruption proximity can significantly improve these methods. Additionally, the estimated state can be used as basis for profile evolution prediction, i.e. to simulate the future time evolution of the plasma state, monitoring for approaching operational limits or optimizing future actuator trajectories in real-time.

Apart from the optimal trajectories, the RAPTOR-based optimization returns other important information as well. Notably, it specifies which constraint is active at any time during the plasma evolution, i.e. which constraint is at the limit of being violated. Different constraints are more important in different phases of a tokamak shot, different choices for feedback control strategies can be made based on this knowledge. Additionally, a local linearization of the system dynamics around any point along the (optimal) actuator trajectories is returned, which can be used for feedback controller design using model predictive control, linear parameter varying techniques, or other established methods. Optimization of plasma profile trajectory evolution can be applied to many other tokamak scenarios, most notably the ramp-down, and more complete physics models can be used to optimize the trajectories leading into (and out of) a stable burning plasma. Including models for sawteeth, NTMs, MHD limits, and other factors delimiting the tokamak operational space, a powerful, generic and machine-independent tool for model-based plasma shot preparation can be obtained with important applications in advanced plasma experiments in view of the Next Step.

Appendix A

The distributed real-time control system (SCD) in TCV

A.1 TCV multi-system real-time control

This appendix serves as a technical complement to Section 2.4 and contains information about the TCV control systems, in particular about the digital SCD system. Section A.1.1 describes the configuration of the SCD nodes with respect to other TCV control subsystems. Next, Section A.2 discusses some practical aspects of SCD operation, including algorithm development and integration with the TCV shot cycle. Finally, Section A.3 presents an example of a control algorithm, in particular the fully digital emulation of the Hybrid control system. Further real-time signal processing algorithms developed for the SCD in the scope of this thesis, are the topic of Appendix B.

A.1.1 Control hardware layout and system combinations

As described in Section 2.4, TCV presently uses both the Hybrid control system, part of the original TCV hardware, together with a new digital control system (SCD). The present state of the SCD system and its connection to legacy TCV control infrastructure is shown in Figure A.1. The hybrid system has also been upgraded with the possibility of using a DSP-based digital system instead of analog PIDs. The feedback paths are set by configuring a purpose-built summer/selector, which sets (for each channel) which of the three input signals (**Sum a**, **Sum b**, **Sum c**) are passed to the output. This way, different TCV subsystems can be controlled by different control systems. It should be noted that, at present, the fast vertical control loop, which requires a control bandwidth of approximately 100kHz, can only be run in the hybrid control system which has a very high bandwidth since it is based on analog electronics.

Three typical experimental configurations can be distinguished, though many variants exist:

Hybrid only In this configuration the SCD is not used and the entire TCV plasma is controlled by the hybrid system using standard control loops. The ECRH/ECCD system is exclusively controlled by feedforward signals from the wavegen.

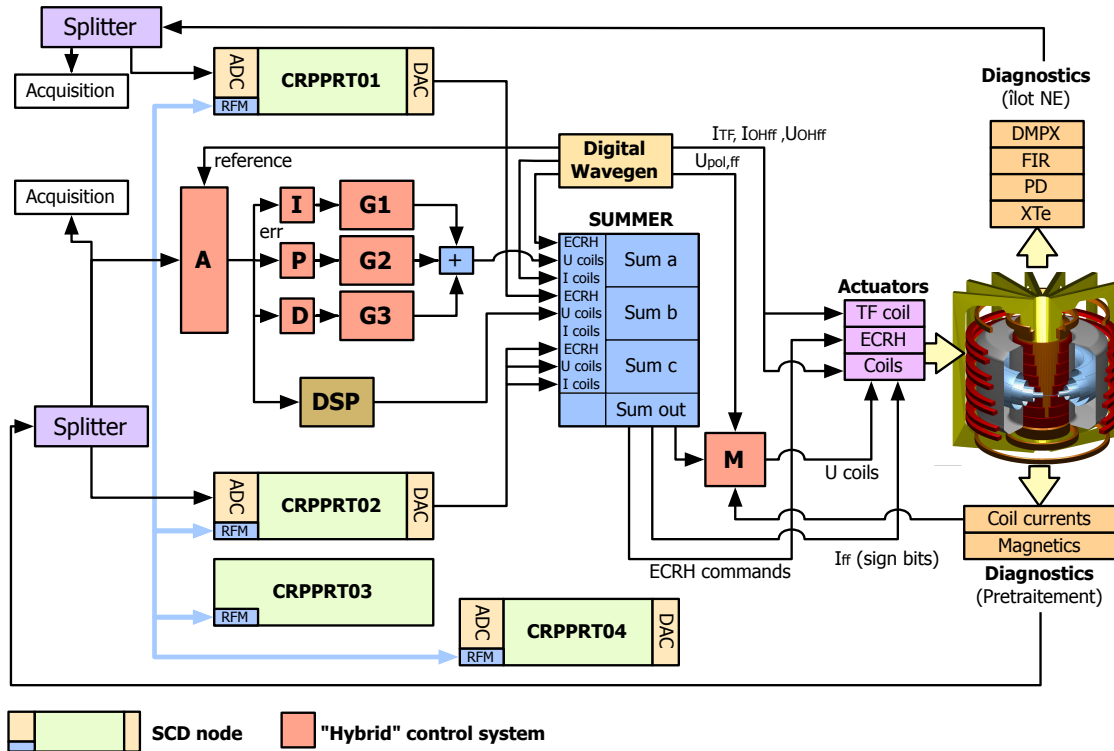


Figure A.1: Diagram of physical components of the TCV real-time control systems showing connections of “Hybrid” analog system, the DSP system and SCD nodes in a unified manner. This simplified diagram shows only the main connections and ignores some details, notably the disruption detector and protection systems (before the actuators) and the gas control (following the same path as the coil voltages (U coil)). See text for definition of acronyms. State as of August 2011.

Hybrid with SCD In this configuration, the Hybrid system controls the main TCV plasma (coils, gas, vertical position) while the SCD performs “advanced” control experiments, typically commanding the ECRH/ECCD system. These commands may come either from node RT01 or RT02. Most real-time control experiments described in this thesis are run in this mode.

Full SCD control In this case, the SCD takes over the entire control of TCV plasmas, except the fast vertical control system which is still handled by (one channel of) the hybrid system, and a restricted number of feedforward wavegen channels, which are still provided by the digital wavegen. For backward compatibility, the SCD runs an emulation of the hybrid controller, allowing the TCV operator to program the plasma in the same way. Enhancements to the control system, enabled by the digital control system, are implemented as additional functionalities. This improved digital version of the hybrid controller is discussed in more detail in Section A.3.

Some remarks are in order. To control the PF coils, both the voltage requests (U coils) and a set of coil polarity switches (I coils, indicating the direction of the next current sign switch) need to be sent to the power supplies. In the future, these polarity switches will be generated dynamically by the SCD, avoiding the need to prepare these values before

the shot, allowing more operational flexibility for coil control in view of full plasma shape feedback control.

Note also that the M matrix, which handles the coil mutual inductance decoupling and resistive voltage compensation (see Sec.2.4), is always in the coil voltage feedback path. When the SCD system is being used, a software version of the M matrix is included in the SIMULINK version of the hybrid controller in the CRPPRT02 node. In this operating mode, the hybrid M matrix is set to the identity matrix letting voltage requests pass through unchanged.

A.2 SCD operation in practice

This section briefly describes the steps to prepare a control algorithm for the SCD in practice, and explains the steps taken to convert the SIMULINK blocks to C and compile them for use in the real-time system¹. It assumes the reader is somewhat familiar with the SIMULINK block programming language.

A.2.1 Simulink block diagram preparation

A SIMULINK block diagram for use in the SCD consists of a single model file `tcv.mdl`, which follows a template structure, as well as one configuration file `load_params_CRPPRT0X.m` per active node (where X is the node number). An example of a SIMULINK model file with several subsystems is shown in Figures A.2 - A.5, and is described below.

- At the highest level, shown in Fig.A.2, each of the four SCD nodes is shown, with the inter-node connections to simulate the data passed across the RFM (Reflective Memory) when running the model in the SIMULINK environment. Each node has its own sample rate, which can be set via the block mask. Other parameters can be set via this same mask, including the node activation, the node sampling time and reserved RFM addresses. The overall SIMULINK simulation is run at a fixed sample time, corresponding to the smallest of all the node sample times. For reasons linked to the RFM implementation, see (Paley et al. 2010) for details, the sample times (also referred to as system period) of individual nodes must be odd integer multiples of this global sampling time.
- Each node block contains its own `rt_controller` sub-block, which contains the SIMULINK code which is to be converted to C and compiled for each node. As one can see in Fig.A.3, further input/output handling is done to allow the code to run in the SIMULINK environment. A dedicated input block retrieves previously acquired ADC data from the TCV database for a specified shot and another block retrieves reference wavegen traces (if any) from the TCV shot preparation data (see Section A.3 for further details on wavegen traces). The rate transition for the RFM I/O ensures the different sample rate across different nodes is properly simulated. Each `rt_controller` block has the same inputs (ADC, RFM, wavegen) and outputs (DAC, Memory, Digital Outputs, RFM). Since it is this block which is later converted to C,

¹It should be noted that much of the actual programming for the SCD was done by J.I. Paley (Paley et al. 2010), and that this work is documented in this thesis for completeness

these are the same inputs/outputs of the SIMULINK C-code wrapper to be discussed later.

- Examining the contents of the `rt_controller` block for CRPPRT02, we find in Figure A.4, algorithm-specific blocks for input/output handling (conversion to MKSA units, sorting) as well as the control algorithms themselves (in this case the improved TCV hybrid controller, discussed in Section A.3). Note how the input and output blocks are linked by custom-made blocks containing (parts of) control algorithms. These will be different for each node depending on the real-time task to be performed.
- Finally examining the interior of the TCV hybrid controller block we find an actual SIMULINK algorithm, with matrix multiplications, sources, summations etc. (Fig.A.5). Optionally, SIMULINK scopes or “to workspace” blocks can be used to examine the results of simulations on old data. Some rules apply as to what SIMULINK blocks can be used. In particular, only blocks which can be automatically converted to C can be used. This excludes the use of embedded MATLAB function blocks and continuous-time blocks.

An empty standard template is provided in which SIMULINK diagrams can be built. Alternatively, old diagrams can be used as a basis for new ones, since the SIMULINK model (.mdl) file and parameter files used in any previous shot can readily be retrieved from the database (a dedicated `mdsplus` tree).

A.2.2 Input/output handling

To allow maximum transparency for the SCD user, a library of common blocks is provided which handles standard input/output calibration and routing. This allows the user to focus on designing the control algorithm without having to deal with how to get the signal in and out of his/her routine. Some typical cases are mentioned below.

Calibrations

Calibration factors from volts to physical units, as well as cabling orders and other specificities for the various diagnostics are maintained in the TCV database. When the appropriate conversion block is included in the SIMULINK model, the block automatically looks up all necessary information in the database, keeping the calibration parameters up to date.

ECRH power and mirror control

An ECRH control block has been built which handles the conversions and safety protection mechanisms for the EC system. This allows the user to input any request of gyrotron power and mirror angle, and the block then converts this to DAC voltages taking system limitations and protection into account. It should be noted that this is only a first line of defense: all TCV hardware systems are designed to be self-protecting and independently shut down if incorrect or inappropriate commands are issued.

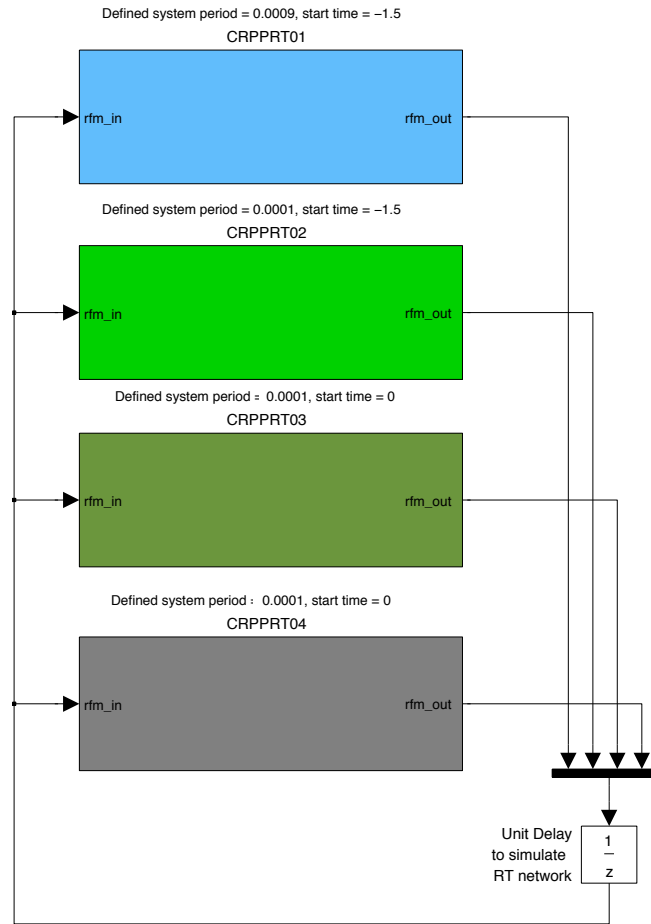


Figure A.2: Top-level view of SCD SIMULINK model file template. Each node is visible as a separately configurable block

In particular, there are technical limits on the minimum time during which a given voltage range on the X2 gyrotron cathodes can be traversed, which translates into power constraints as discussed in Section 2.2. Also, upper saturation limits on the voltage request are included, as well as the calibrated conversion formula from gyrotron output power to power supply voltage.

As for the poloidal mirror angles, physical limits are also implemented (typically 8 – 45 degree, but for some plasmas this is limited further by refraction and absorption considerations), and a lowpass filter is added to avoid sharp transients which may enhance wear of the mechanical components.

A.2.3 C-code building and compilation

When the control algorithm is ready and has been tested, a *build script* is run to individually convert each of the (active) `rt_controller` blocks into C code. This is done by the SIMULINK code building toolbox and produces the necessary `.c` and `.h` files.

The C code generated is then compiled into a shared object library file (`.so`) that

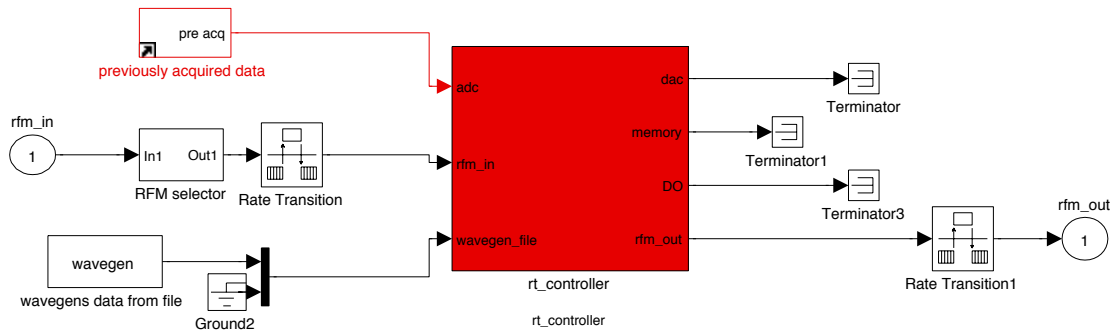


Figure A.3: Each node block contains an `rt_controller` block which contains the SIMULINK which will eventually be compiled to C code. The input/output handling is done to allow to test the control algorithm in the SIMULINK environment.

is copied across the network (via `ssh`) to each individual node. There, an executable is present which contains pre-compiled wrapper C code. This wrapper handles the I/O with the D-tAcq control hardware. It translates the acquired/read ADC and RFM values at the beginning of each time step into the appropriate SIMULINK-generated C-code variable and conversely maps the output from a SIMULINK-generated C code variable to the memory addresses for the DAC, RFM and Digital Outputs. As such, only the executable contains hardware-specific information such as device drivers, and the SIMULINK-generated `.so` is generic and interchangeable across hardware platforms. Finally, reference and feedforward time traces that are normally written to the `wavegens` are written to a binary file and also sent to the appropriate node.

A.2.4 TCV shot cycle

The compilation routine described in the previous section can be called manually, or is automatically called by the TCV Plant Control at the beginning of each TCV shot cycle when the SCD is selected. This builds, compiles and transfers the appropriate SIMULINK file found in a dedicated location in the file space. At the same time, configuration parameters in each node block mask are written to the database. This information is used just before the shot to set the physical triggers and clocks –which control the sample time of each SCD node– to the required values. Based on the experimental requirements, the summer/switch shown in Figure A.1 is configured as required.

The shot trigger command starts a fixed 13s-timer sequence and sends the plant into "fire-and-forget" mode, with software aborts disabled. Near the beginning of this timer sequence, seconds before the coil power supplies are energized, the executable is loaded, which itself loads both the `.so` containing the SIMULINK algorithm, and the `wavegen` binaries. Then, the interrupts to the Linux operating system on the active nodes are suspended, so that the processor and memory are entirely dedicated to performing the real-time task. When the triggers are received, the system performs its function and runs the control algorithm at the requested sample rate. When the shot is complete, the interrupts are resumed, the ADC/DAC/memory data that are stored in the node RAM is written to the TCV database, and the system returns to an idle state awaiting the next

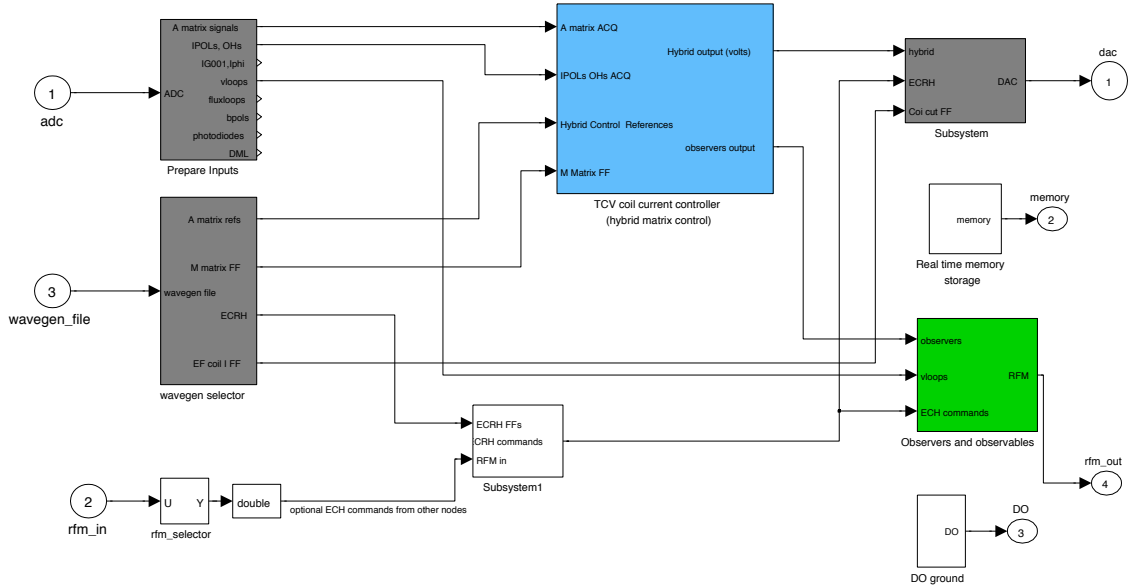


Figure A.4: Contents of an `rt_controller` block for CRPPRT02, showing several sub-blocks for input-output handling, calibrations and conversions, as well as the TCV hybrid controller emulation block.

shot. From this moment onwards, post-shot data can be analyzed and new SIMULINK simulations based on this ADC data can be run.

A schematic representation of the workflow for SCD operation is shown for the specific case of the RT-RAPTOR algorithm (Chapter 8) in Appendix D, Figure D.1.

A.2.5 Operational experience

The TCV set-up is such that the rapidity and flexibility of code development, debugging and testing allows an experienced RT control operator to modify controllers between shots. The previous shot data is available ~ 1 min after each shot, leaving about 10min before the next plasma during which SIMULINK simulations can be run, the results observed using SIMULINK scopes, and appropriate modifications made or settings changed in the algorithm.

In practice, the generated C-code has always behaved precisely as expected from simulations and the performance has been sufficient so that no dedicated algorithmic C-code development has ever been necessary for any of the experiments done with this system. This represents a unique experimental platform with a vast potential for further algorithm development, even by non-real-time specialists.

A.2.6 Overview of developed algorithms

Depending on the specific algorithm used in each node, the sample time of each node will be different. Table A.1 gives an overview of some mature applications which can be run on demand on the SCD nodes, specifying the sample time of each node and the Section of this thesis where each algorithm is discussed in more detail.

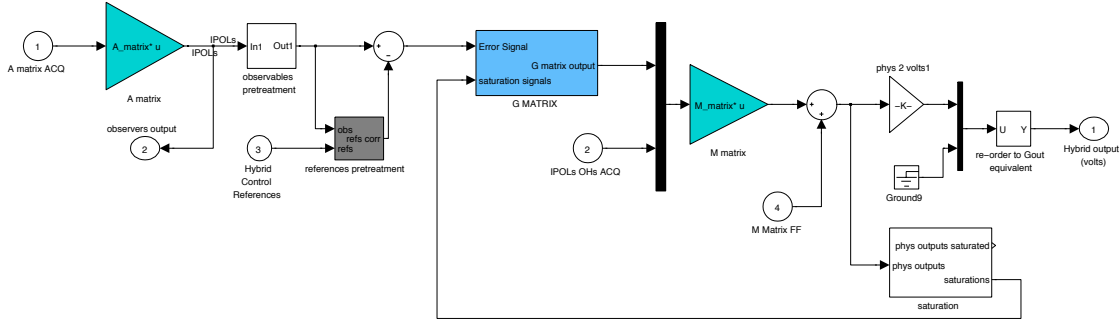


Figure A.5: Detailed view of the TCV hybrid controller emulation block, showing individual matrix multiplications. Some additional features, not available in the original hardware version, have been added such as anti-windup upon actuator saturation, and pre-treatment of observed variables and error signals.

| Algorithm | ref | CRPPRT01 | | CRPPRT02 | |
|---|-----------------|-----------------------------------|-------------|------------------------------|-------------|
| | | task | T_s | task | T_s |
| Sawtooth & NTM control | Sec.3.2, Ch.4 | Control logic, sawtooth detection | 100 μ s | NTM detection, phase locking | 20 μ s |
| ELM control | Sec.3.3 | idle | - | ELM detection and logic | 20 μ s |
| Kinetic profile control | Ch.5 Sec.B.1 | RT spline fitting & control | 100 μ s | idle | - |
| Real-time flux profile simulation + control | Sec.8.2 Sec.8.3 | RT-RAPTOR + feedback controller | 900 μ s | Hybrid controller | 100 μ s |
| Hybrid controller emulator | Sec.A.3 | idle | - | Improved hybrid controller | 100 μ s |

Table A.1: Example of roles of individual SCD nodes for real-time control algorithms presented in this thesis, showing a variety of node clock rates depending on application requirements

A.3 Improved TCV hybrid controller

The present section discusses one particular control algorithm, namely the software emulation of the existing (hardware) TCV hybrid control system. Some improvements to the existing system, made possible by the digital platform, are also discussed.

A.3.1 Basic hybrid controller emulation

Matrices and reference signals

To understand the details of the hybrid controller emulation, more details of the TCV shot preparation are helpful. TCV shots are prepared using an in-house software called MGAMS (Hofmann et al. 1990). Starting from a time sequence of basic plasma descriptors (I_p , B_ϕ , z , κ , δ , etc), the free-boundary code FBTE (Hofmann et al. 1988) computes the necessary PF coil currents required to obtain the requested equilibrium. The IOH coil ramp rate required to obtain the desired plasma current is included in the calculation to obtain the full set of OH and PF coil current trajectories and appropriate coil voltage

feedforward and sign bit sequences. These trajectories, together with reference and actuator feedforward trajectories for other controlled parameters (I_p , zI_p , radial position, density, κ) are stored in the shot database. Next, MGAMS calculates linear observers for the shape parameters based on the available magnetic measurements in the A matrix, as well as appropriate feedback gains and actuator configurations (i.e. which linear combination of coils is used to control a given shape parameter). This information is translated into a set of (possibly time-varying) coefficients for the A , G , and M matrices, both in “physics” (MKSA) units and in “physical” (volts) units; these are also stored in the shot database. When the hybrid controller is used, the physical coefficients are programmed into the analog matrices, and the time trajectories are programmed in the digital wavegen (c.f. Fig.A.5). Time-trajectories for power and launcher angles of the ECRH system, when used, are prepared by the gyrotron operator, and similarly stored in the database before being transferred to the wavegens.

The SIMULINK diagram for the hybrid controller was already shown in Figure A.5. One can observe the same basic components as the hybrid system, but replicated as SIMULINK blocks. The matrices are represented by SIMULINK matrix multiplication blocks. The (time-varying) coefficients of the matrices in MKSA units are themselves loaded from the TCV database location to which they were previously stored by MGAMS during shot preparation. The wavegen signals are loaded into a SIMULINK source block and are converted to binary files when the SIMULINK code is compiled and transferred to the various nodes, as described in the previous section.

PID Transfer function discretization

The P, I and D elements of the hybrid system must also be converted to a digital (discrete-time) representation in SIMULINK, attempting to match their transfer functions. The roll-off that was present in the analog circuits to filter out high-frequency noise does not need to be replicated in the digital system since, by nature, high frequency noise is not there if appropriate anti-aliasing filters are installed. For the proportional and integral terms, this is straightforward to achieve by taking a simple unit gain for the proportional term ($H(z)_P = 1$) and a bilinear transform (Tustin approximation) for the integrator, with transfer function

$$H_I(z) = \frac{1 + z^{-1}}{1 - z^{-1}}. \quad (\text{A.1})$$

The derivative term requires more care. The transfer function of the original analog electronics is, in the Laplace domain:

$$H_D(s) = \frac{s}{(1 + s\tau_{D1})(1 + s\tau_{D2})} \quad (\text{A.2})$$

with $\tau_{D1} = 1 \times 10^{-4}$ s and $\tau_{D2} = 1.02 \times 10^{-4}$ s. This means the frequency response rolls off starting from approximately 1.6kHz, which is a significant fraction of the Nyquist frequency (5kHz for the standard 10kHz sampling frequency). At these frequencies, the extra phase lag introduced by the 1-sample delay (which is inherently present in all digital systems) can no longer be neglected. Since the derivative term is usually only used for the (slow) vertical control loop (i.e. the vertical position control done by the PF coils instead of the fast coils), this phase lag appeared in early experiments as a reduced

vertical stability, which impeded the creation of very vertically unstable plasmas. The transfer function of the analog version of the PD controller for the slow vertical control loop is plotted for shot #40476 in Figure A.6 (blue). Discretizing the controller by the Tustin approximation and adding an extra 1-sample delay, one can see that the magnitude response is close, but a significant phase lag appears (red). To get rid of this phase lag, the D term of the controller is rewritten as

$$H_D(z) = \frac{1 - z^{-1}}{1 + \alpha z^{-1}} \frac{1 + \alpha}{T_s} \quad (\text{A.3})$$

The factor at the end is simply to get a unity time constant. The location of the denominator pole α can be varied, with $\alpha = 0$ yielding a simple 1-sample difference operator. Moving the pole in the region $-1 < \alpha < 0$ increases the phase lag but decreases the gain, while $0 < \alpha < 1$ yields a phase lead and higher gain. A family of frequency responses (green) can thus be obtained, a few examples are shown in Fig.A.6. The better phase response comes at the expense of a higher gain at high frequencies, i.e. less noise suppression. Tuning the value of α revealed that $\alpha = 0.2$ was appropriate, yielding good vertical stability even for elongated shots. One must nevertheless accept a performance degradation due to the reduced noise rejection. This is inherent to the choice of a digital design. This can be reduced by increasing the controller sampling time, but the presently used $100\mu\text{s}$ (10kHz) is already at the limit of the capabilities of this node for this algorithm. Alternatively, nonlinear control strategies can be envisaged. Remembering that the fast vertical control loop is still handled by analog control, it would be beneficial to reassess the entire design of the vertical control loop taking into account the digital-analog mix of the configuration.

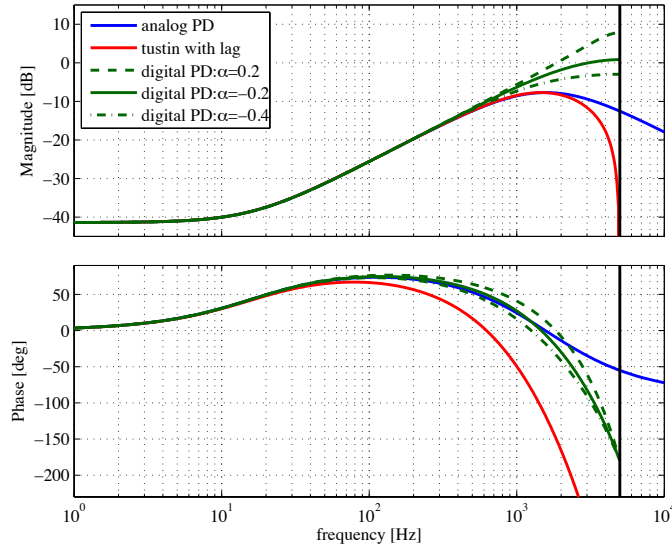


Figure A.6: Bode plot of the PD controller for the slow vertical stability loop, with gains from shot 40476. The analog transfer function implemented by the hybrid system (blue) is poorly approximated in the high-frequency phase response by a Tustin approximation (red) once a one-sample delay is taken into account. A redesign (green) of a purely digital PD controller with varying derivative pole yields a better phase response, at the cost of a higher gain close to the Nyquist frequency (black).

The next sections present other improvements which were implemented in the hybrid control emulator, exploiting the nonlinear digital capabilities of the new platform.

A.3.2 IOH control

In steady-state plasmas, the ohmic transformer coil current must be clamped to a fixed value such that the plasma current it induces is truly zero. This is done by feedback controlling the OH coil current to a constant reference value so as to offset any drifts due to changes in the coil resistance with time as well as currents induced in the ohmic coil by another conducting elements. This mode of operation is referred to as “IOH feedback”, in contrast to the standard operation of the OH coil, referred to as “ I_p feedback” in which its ramp rate is feedback controlled to obtain the desired plasma current. IOH feedback is also used to impose (usually small) ohmic perturbations to steady state plasmas (Sauter et al. 2005).

In the hybrid TCV controller, the OH coil feedback method is switched from one mode of operation to the other by pre-programmed switching of the controller matrix coefficients. The feedback path from the I_p error to the Ohmic coil voltage is removed and instead the OH coil voltage is controlled to obtain a pre-set reference current. Until now, this reference current had to be pre-programmed based on the *expectation* of what the OH coil current would be at the programmed switch time. This was usually done by performing one preparatory shot in which the I_p feedback control was kept during the entire duration of the shot and the appropriate reference value of I_{OH} was simply chosen as the measured value at the desired switching time for all later shots. During the course of subsequent shots, wall conditions and impurity content may change the plasma resistivity in the initial phase of the shot, resulting in a slightly different current at the time of switching from I_p - to IOH- feedback control. When the IOH feedback phase begins, the IOH current may experience a sudden jump to its pre-programmed reference which will cause a sudden spike in V_{loop} . This will propagate into the plasma and may strongly perturb the experiment or even cause a disruption. For this reason, during steady-state plasma experiments the IOH current had to be continuously monitored from shot to shot and the reference current had to be adjusted every few shots to avoid these jumps.

With the advent of the SCD system, such reference adjustments are no longer necessary. In the digital controller, an offset is added to the reference I_{OH} at the beginning of the IOH phase in order to match the value at the switch time, thus ensuring continuity in the OH coil current evolution. This improvement is now used routinely for steady-state shots, no longer requiring manual intervention. An example of the commissioning experiments for this technique is shown in Figure A.7. This figure shows two TCV shots both of which use IOH control in the time interval between $t = 1.0$ and $t = 1.2$ second (shaded region). Since this is a non-steady-state scenario, a ramp reference is programmed in order to maintain a nonzero V_{loop} and drive inductive current. In the first shot (red), the standard method is used, setting a reference trajectory for I_{OH} (panel Fig.A.7(c), dashed). At the beginning of the IOH feedback phase, the OH coil current is about 1.5kA lower than the first point of the reference. The current rapidly increases to match the reference, but in doing so creates a strong loop voltage which drives a strong current, Fig.A.7(a), which causes a plasma disruption. In the corrected case (using SCD), the original I_{OH} reference is shifted such that the first point matches the measured I_{OH} value Fig.A.7(d).

This gives the same loop voltage as what was programmed, but avoids unwanted V_{loop} transients. In this case the plasma does not disrupt (but I_p decreases, the loop voltage being lower than in the I_p feedback phase) and the shot carries on normally.

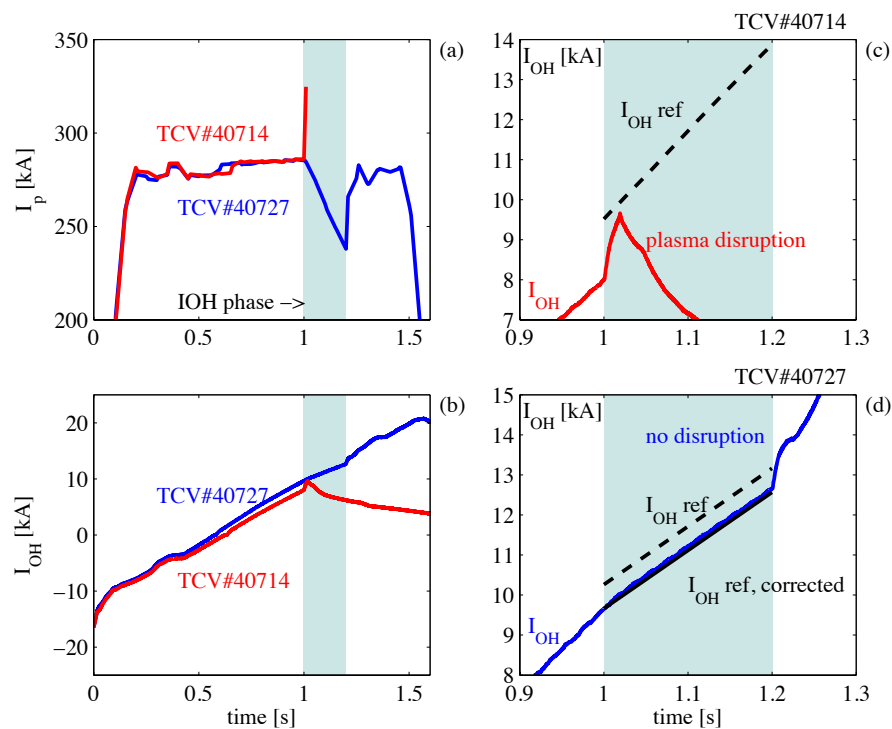


Figure A.7: Demonstration of improved IOH control by adjusting the reference OH coil current trajectory so as to start at the current value at the time of the switch from I_p to IOH feedback. For this non-steady state scenario, a ramp trajectory for I_{OH} was programmed.

Appendix B

Real-time signal processing algorithms

B.1 Real-time spline fitting

Profile diagnostics provide measurements at different (possibly line-integrated) spatial locations. When the spatial resolution of the diagnostic is high with respect to the feature one wishes to extract, spatial smoothing may be performed. To this end, a real-time spline fitting routine was developed. This routine exploits the fact that if the target domain on which the spline fitted values are to be computed is known in advance, the fitting operation can be rewritten into a single matrix multiplication.

To see how this works let the domain of the interpolation $x \in [a, b]$ be subdivided into n_s contiguous non-overlapping segments $x \in [x_i, x_{i+1}] \forall i = [1, \dots, n_s]$. Next, define n_s polynomials of degree n_p : $y_i(x) = \sum_{j=0}^{n_p} a_{ij}x^j$ that take value only on $[x_i, x_{i+1}]$. Then let $y(x)$ be the piecewise polynomial obtained by joining all n_s polynomials.

Now let $y_d, x_d \in \mathbb{R}^{n_d}$ be two vectors containing, respectively, n_d data points on the interpolation domain and their corresponding x coordinate. The problem of determining the minimum square-error interpolant function $y(x)$ can be formulated as the least-squares problem

$$\min_p \|y_d - Ap\|_2^2 \quad (\text{B.1})$$

where $p \in n_s n_p$ is a coefficient vector containing the a_{ij} s and the matrix $A \in \mathbb{R}^{n_d \times n_s n_p}$ is a block-diagonal matrix with block element of the form

$$[A]_{ii} = [x_i^0, x_i^1, \dots, x_i^{n_p}] \quad (\text{B.2})$$

Usually, constraints are imposed to ensure continuity up to a certain derivative at the boundary between the different segments. This can be rewritten as a constraint on the coefficient vector p .

$$Cp = 0 \quad (\text{B.3})$$

with $C \in \mathbb{R}^{n_c \times n_p}$ and n_c the number of constraints. for example a \mathcal{C}^0 constraint (continuity) at x_2 (boundary between y_1 and y_2) is written as

$$y_1(x_2) = y_2(x_2) \quad \rightarrow \quad \sum_{j=0}^{n_p} a_{1j}x_2^j - \sum_{j=0}^{n_p} a_{2j}x_2^j = 0 \quad (\text{B.4})$$

and a constraint on \mathcal{C}^1 (first derivative) is

$$y'_1(x_2) = y'_2(x_2) \quad \rightarrow \quad \sum_{j=1}^{n_p} a_{1j} j x_2^{j-1} - \sum_{j=1}^{n_p} a_{2j} j x_2^{j-1} = 0 \quad (\text{B.5})$$

Assuming there are fewer constraints than parameters, i.e. $n_c < n_p$, the constrained least-squares problem (B.1), (B.3) can be solved by computing an orthogonal basis for N for $\ker C$ (i.e. the null space of C , which can be computed by e.g. QR decomposition (Golub et al. 1996)). Then, write $p = Nv$ such that $CNv = 0$ for all vectors $v \in \mathbb{R}^{n_p - n_c}$. Finally one can solve the (unconstrained) least squares problem

$$\min_v \|y_d - ANv\|_2^2 \quad (\text{B.6})$$

for example by computing the pseudo-inverse $P = (AN)^+$, the least-squares solution is $v = Py_d$.

Note that in order for a unique solution v to exist, AN must be a square or tall matrix (more rows than columns). This translates to the constraint $n_d \geq (n_p - n_c)$ which can always be satisfied for a given n_d by either decreasing the number of segments or polynomial order (lower n_p), or by adding constraints (increasing n_c).

We can now compute the polynomial coefficients of the least-squares spline interpolant to the data with a single matrix multiplication. As a last step, the values of the spline on a new set of x points is calculated by the product Dp (with matrix D of similar structure to A , but evaluated at different x values). Note also that derivatives of the spline at any point can be calculated as well, by another product denoted $D'p$

Finally the values of the interpolated spline at the required values of x are obtained directly from the original data y_d by

$$y = (DNP)y_d \quad (\text{B.7})$$

Note that the matrix (DNP) can be pre-calculated based solely on the knowledge of a) the structure and order of the piecewise polynomial b) the x coordinates of the data points (x_d) , and c) the new x points on which the interpolated spline is to be evaluated. If this is known beforehand, spline interpolation therefore reduces to this single matrix multiplication, which can easily be done in real-time. Real-time spline fitting of the 44 central channels of the 64 chord DMPX diagnostic (external channels are excluded as they are often polluted by wall effects) has been implemented for X-ray profile control experiments described in Chapter 5. A typical result is shown in Figure B.1. Note that the smoothness of the spline can be adjusted by choosing a different number of piecewise polynomials.

B.2 Profile peak, width, gradient information

Based on the real-time spline interpolation routine described above, the location of the profile peak, maximum gradient and minimum gradient can also easily be extracted. This is done simply by computing the gradients, which is also a matrix multiplication as explained in the previous section, and finding for zeros and maxima of these gradients. A typical result was already shown in Figure B.1, but is more clearly demonstrated in Figures

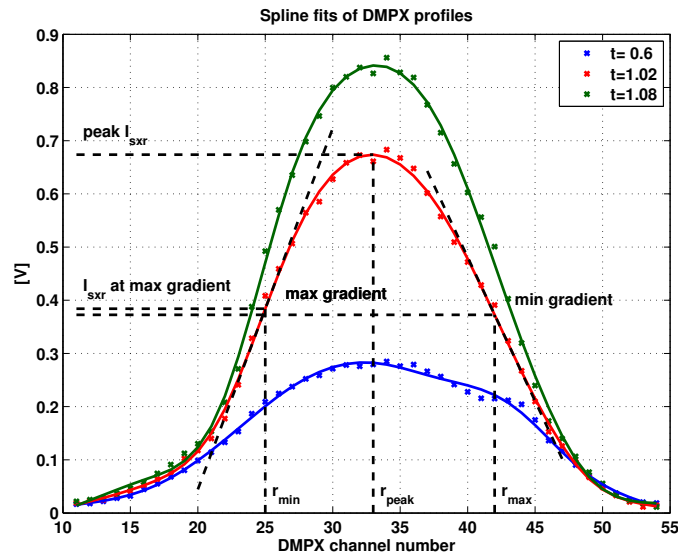


Figure B.1: Example of spline fitted DMPX profile channels, with identification of location of minimum gradient and maximum gradient, profile peak and width.

B.2 and B.3, showing spline fitted DMPX traces over time during an eITB shot, featuring an oscillatory regime (Udintsev et al. 2008), (Turri et al. 2008) due to the interplay between MHD and transport barrier dynamics. This causes the central temperature to oscillate in a slow, periodic fashion as witnessed by the X-ray emissions. The figures illustrate how the real-time spline interpolation is able to give information about the peak location, peak value, and location of maximum and minimum gradient locations. This information is available in real-time and can be used for feedback control or other purposes.

B.3 Inversion radius detection by DMPX correlation analysis and bayesian filtering

A typical signature of a sawtooth crash is a heat wave propagating out from the plasma core as the central temperature collapses, temporarily increasing the temperature outside the inversion radius. This sawtooth inversion radius is roughly defined as the location at which the temperature gradient before a sawtooth crash and after a sawtooth crash is the same. It is an indication of the $q = 1$ surface although they may not always coincide.

Real-time information about the inversion radius gives an estimate of the evolution of the $q = 1$ surface size during a shot. Since reliable localized temperature measurements are not available in real-time on TCV, the inversion radius is estimated instead from line-integrated X-ray channels from the DMPX diagnostic.

A simple but effective method to estimate the sawtooth inversion radius is to compute the correlation of adjacent DMPX channels over a time window close to the sawtooth crash time. Channels in the central region will have the typical sawtooth shape, while in the outside region they will have an “inverted” shape as illustrated in the top panel of Figure B.4. This shot featured a plasma current ramp, causing the $q = 1$ radius, and thus the inversion radius, to vary during the shot.

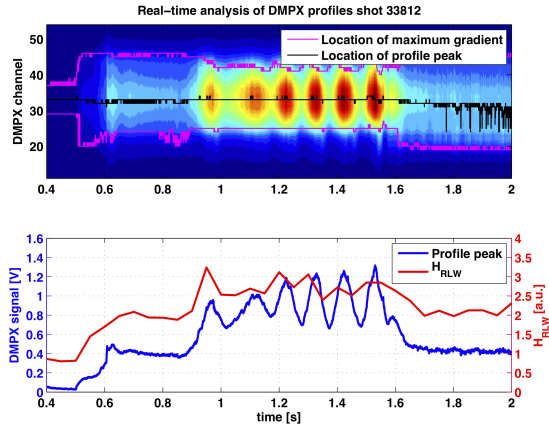


Figure B.2: Top: Time evolution of DMPX line-integrated X-ray emissions during an oscillating ITB plasma. The location of the profile peak and location of maximum and minimum gradient, as determined by the real-time spline fitting algorithm, is also shown. Below: Time evolution of peak DMPX signal and H_{RLW} (confinement enhancement factor w.r.t. RLW scaling law)

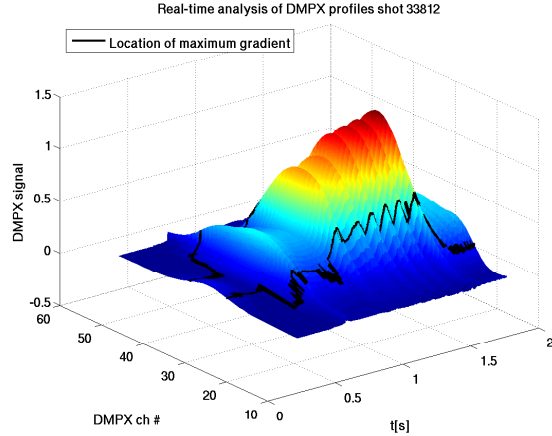


Figure B.3: 3D view of DMPX profile evolution and real-time determined minimum and maximum gradient location and value.

The DMPX signal values for all channels are stored in a time-windowing buffer and the correlation between each channel and its neighbour is continuously computed. Based on the time of occurrence of a sawtooth crash, the computed correlation over a time window around the sawtooth event (shown in pink in Fig.B.4) is sampled, giving one correlation estimate per sawtooth event. This correlation is shown in the second panel of Fig.B.4 and shows positive correlation between the central channels, correlation between outer channels on both sides, and two thin regions of low correlation separating the two. This indicates the inversion radius location, which is computed by taking the second spatial difference among the correlations. The correlation dip will then show up as a sharp peak (with strong second derivative) as witnessed in the lower panel of Fig.B.4, giving an estimate of the DMPX channel on which the inversion takes place.

Second difference of correlations shown in the bottom panel of Fig. B.4 is polluted by noise. When estimating the inversion channel by simply taking the maximum, an artifact due to this noise is sometimes selected, as shown in the bottom panel of Fig. B.5 (red dashed line). To alleviate this, Bayesian filtering was applied to remove solutions that are statistically unlikely.

Simply put, bayesian filtering solves the problem of estimating a state x_k given a noisy measurement d_k . The solution is to weigh the measurement by the probability of the state, given past measurements:

$$p(x_k|d_k) \sim p(d_k|x_k)p(x_k|d_{k-1}) \quad (\text{B.8})$$

The question is how to construct this a-priori probability $p(x_k|d_{k-1})$. The simplest choice is to assume that the next state will be “close” to previous one: choosing a Gaussian with

fixed width w .

$$p(x_k|d_{k-1}) = \exp\left(-\frac{4(x_k - (x_{k-1}|d_{k-1}))^2}{w^2}\right) \quad (\text{B.9})$$

The estimated state $(x_k|d_k)$ is finally chosen as the one with maximum probability density. This simple approach exploits the fact that the sawtooth inversion radius varies slowly with respect to the sampling time. The effect of filtering the correlation map can be appreciated in the middle panel of Fig. B.5, and the maximum computed from the filtered data (bottom panel) is seen to be free of outliers which affected the unfiltered data.

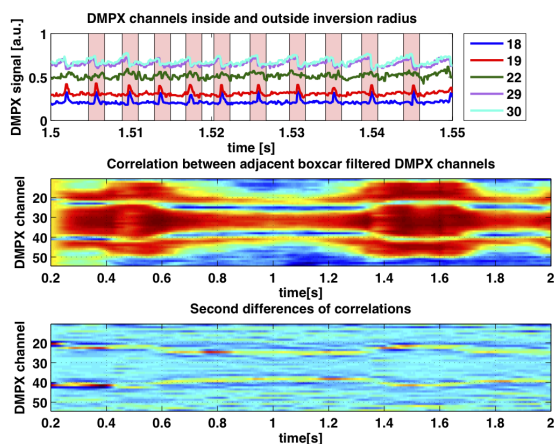


Figure B.4: Top: Typical DMPX central and off-axis channels, pink regions indicate time windows for correlation analysis. Middle: correlation of adjacent DMPX channels (red:high, blue:low). Bottom: second difference of correlation highlights inversion channel location. TCV#35075

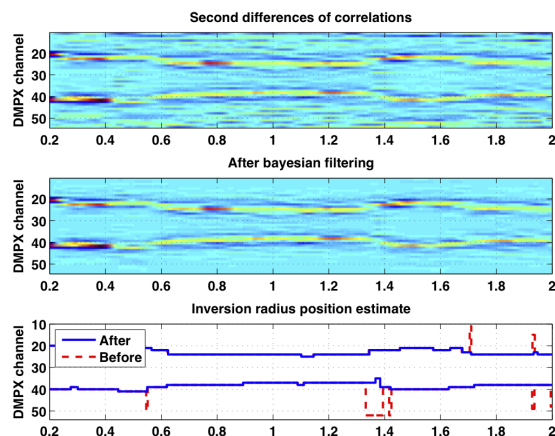


Figure B.5: Top: noisy estimate of inversion channel location from correlation analysis. Middle: After bayesian filtering removing statistically improbable inversion radius locations. Bottom: Comparison between location of maximum in raw and filtered cases. TCV#35075

B.4 Sawtooth crash detection

Sawtooth crashes appear as very recognizable, sudden crashes of the core X-ray emissions, as previously visualized in the top panel of Fig. B.4. The rapid crashes dominate the high-frequency component of the signal, and therefore a very simple method for their detection can be based on a highpass (or bandpass) filter followed by a threshold. This method was used in the sawtooth crash detector for the inversion radius location described in Section B.3.

However, for applications such as diagnostic triggering of sawtooth pacing, a trigger at the same time as the crash time is required. In many cases, the phase lag introduced by the high-pass filter may be unacceptable: instantaneous or near-instantaneous crash detection is necessary based on sample-by-sample analysis. Though this boils down to a discrete-time filter in the end, the design philosophy is different. Additionally, because of the variety of sawtooth periods and crash amplitudes observed on TCV, crash thresholds should be adapted to the plasma parameters. A real-time sawtooth detector of this type

was developed outside the scope of this thesis in the context of diagnostic triggering (Duval et al. 2010), (Piras 2011), and is briefly described here for completeness.

The detector uses the input from a single (or average) trace, referred to as y_k of the central x-ray emission, typically but not necessarily from the DMPX diagnostic, and detects a crash based on simultaneous fulfilment of two conditions

1. The value of the signal must cross an absolute threshold v_k in the negative direction.
2. The (negative) difference between two samples ($y_{k-1} - y_k$) in time exceeds a given relative threshold level r_k

The two thresholds are adapted in real-time based on the slow-scale evolution of y_k . First, an envelope for y_k is determined by storing the maximum and minimum values attained by y_k over several previous sawtooth crashes. v_k is then set to some relative value between this maximum and minimum. The difference threshold r_k is set to some fraction of the difference between this minimum and maximum. In practice, this provides an empirical criterium for a crash: the instantaneous change must be sufficiently abrupt and the loss of signal during after the crash must be sufficiently large in order to be classified as a crash.

This method successfully rejects (does not detect) “fake” crashes that occasionally occur at the beginning of the sawtooth cycle: in this case the signal is either not yet above the v_k threshold and the first criterium is not satisfied, or these crashes are too slow so the second criterium is not satisfied.

An illustration of the sawtooth detector is given in Figure B.6. Showing the first criterion (a) and second criterion (b) being satisfied simultaneously only for “real” sawtooth crashes. One can also see how the threshold is continually adapted to follow the global evolution of the sawtoothing signal.

A disadvantage of the present algorithm is that it is slow to adapt between very large (stabilized) sawteeth and very short (Ohmic) sawteeth, and often misses the first few Ohmic sawteeth, since the threshold values are calculated over previous sawtooth periods. Recently, a wavelet-based approach has been presented (Berkel et al. 2011), which, due to its inherent multi-scale nature, may be able to simultaneously detect both small and large sawteeth without the need of adaptation.

B.5 MHD mode detection

This subsection covers the detection of MHD activity in real-time on TCV. This information is used in NTM control schemes to detect the presence of a mode. The detection is based on a single magnetic probe which is, by default, connected to the CRPPRT02 node. It is, in reality, the mean of two toroidally opposite magnetic probes (sectors 3b and 11b). When the probe signals are used for standard applications, (e.g. shape control, or equilibrium reconstruction), their values are averaged in order to attenuate $n = 1$ oscillations due to, for example, sawtooth crashes. However, this also prevents the reliable detection of $(m/n=2/1)$ NTMs. To remedy this, different gains are set on the preamplifiers of these two toroidal sectors, such that the combined signal is dominated by one physical probe only. This signal gives a typical oscillatory signal in case of “MHD” activity.

The detection of coherent MHD activity from this oscillating signal can be done in a straightforward manner by bandpass filtering the magnetic signal and determining its

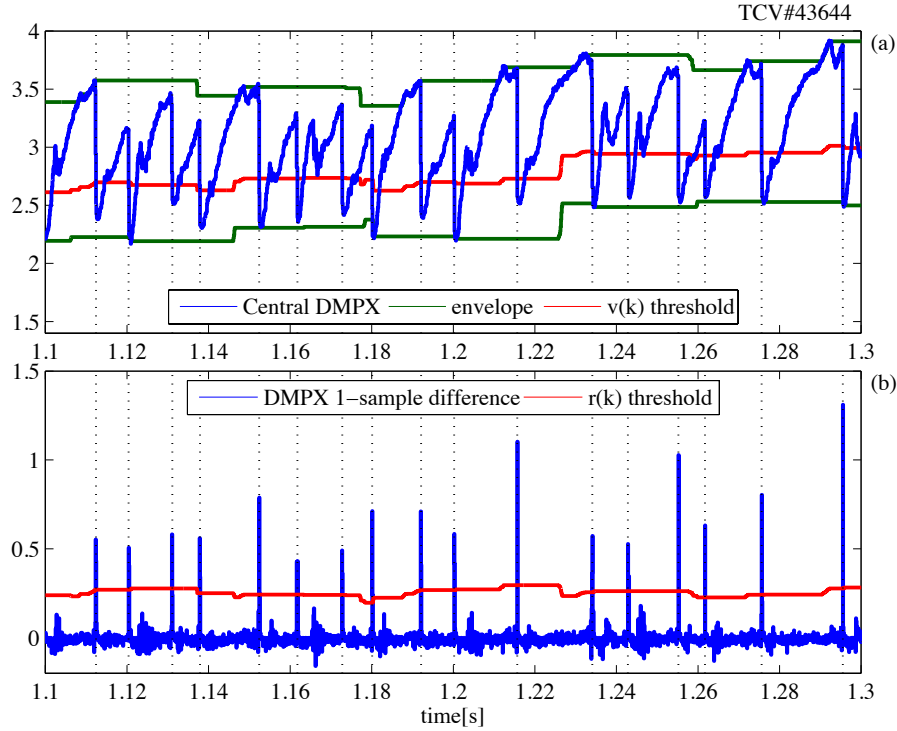


Figure B.6: Illustration of instantaneous sawtooth crash detector. A crash is detected (dotted vertical lines) when, simultaneously, (a) the DMPX signal drops below the red $v(k)$ threshold level and (b) the 1-sample difference exceeds a threshold (red r_k)

RMS power. A simple filter equation to estimate the instantaneous RMS power is

$$y_{rms}(t) = L(s)\sqrt{[B(s)y(t)]^2} \quad (\text{B.10})$$

where B_p is the bandpass filter – with appropriate passband for the signal of interest – and $L(s)$ is a lowpass filter with bandwidth lower than the lower limit of the passband of $B(s)$. Assuming a sinusoidally shaped signal, which is approximately true for MHD modes, the amplitude is then simply $y_{ampl} = \sqrt{2}y_{rms}$.

The appearance of an NTM is detected by a threshold on y_{ampl} . A subsequent disappearance of the mode is detected by comparing it with a (lower) threshold.

B.6 Phase-Locked loop for NTM control

In addition to determining the amplitude, a phase-locked loop can be used to determine the frequency of the mode, and to generate a signal with a specified relative phase. This is described in this section. First, the bandpass filtered magnetic signal is normalized by dividing it by y_{ampl} (calculated as shown above), yielding the normalized signal $\bar{y}(t)$. Then, this signal is fed to the Phase Locked Loop (PLL). The PLL is described by the

equations

$$\omega(t) = kL(s)[y_n(t)c(t)] \quad (\text{B.11})$$

$$\omega_l(t) = \omega(t) + \omega_0 \quad \text{loop frequency} \quad (\text{B.12})$$

$$\phi(t) = \int \omega_l(t)dt \quad \text{loop phase} \quad (\text{B.13})$$

$$c(t) = \cos(\phi(t)) \quad \text{PLL oscillator output} \quad (\text{B.14})$$

Here $L(s)$ is another lowpass filter with frequency lower than the bandpass region, and k is a scalar feedback gain, and ω_0 is the rest frequency of the PLL. A PLL is a nonlinear feedback system, and its working can be understood by considering an input signal $y_n(t)$ of the form

$$y(t) = \sin(\omega_c t), \quad (\text{B.15})$$

where ω_c is the ‘‘command’’ frequency. Then $y_n(t)c(t) = \sin(\omega_c t) \cos(\omega_l t) = \frac{1}{2}(\sin((\omega_c + \omega_l)t) + \sin((\omega_c - \omega_l)t))$. By appropriately choosing the bandwidth of $L(s)$, the first, high-frequency component is rejected and we have $\omega(t) = k \sin((\omega_c - \omega_l)t)$. Now if ω_c and ω_l are sufficiently close, we can linearize the expression such that $\omega(t) \approx k(\omega_c - \omega_l)t$. This will cause $\omega(t)$ to change in the direction such that the difference $\omega_c - \omega_l$ is reduced, causing the loop to eventually lock to the original signal when $\omega_l = \omega_c$ and therefore $\omega = \omega_c - \omega_0$. Evidence of this locking is that $\omega(t)$ stops varying in time, i.e. its derivative becomes small.

The locking range, quality, robustness, and other properties depend sensitively on the choice of k , ω_0 and $L(s)$. Roughly, the bandwidth of $L(s)$ defines a region around ω_0 to which the PLL can lock, while k comprises a trade-off between speed of locking and robustness against noise.

The exact phase difference between the locked signal $c(t)$ and the original signal $y(t)$ is, in this case, a function of the frequency due to the properties of the PLL and the phase lag induced by the bandpass filter. When the phase needs to be known exactly, for example to generate a power modulation signal with an exact phase difference with respect to the magnetic signal to use in modulated-ECCD experiments, some extra effort is needed: one takes the original signal $y(t)$ and multiplies it by (independently) $c(t)$ and its quadrature signal $s(t) = \sin(\phi(t))$, then lowpass filters the result. If $y(t)$ and $c(t)$ have the same frequency, i.e. the PLL is locked, then the result is $\cos(\phi_l)$ and $\sin(\phi_l)$, respectively, where ϕ_l is the instantaneous phase difference between $y(t)$ and $c(t)$. This is then recovered by $\phi_l = \tan^{-1}(\sin(\phi_l)/\cos(\phi_l))$. Based on this phase difference, other signals of arbitrary phase difference with respect to the original signal can be generated.

An example of a working PLL, implemented in SIMULINK and executed on node RT02 at 50kHz during a TCV NTM control experiment, is shown in Figure B.7. Panel (a) shows the original signal and the amplitude estimate. Note the appearance of an NTM at $t \approx 1.1$ and its disappearance at $t = 1.9$. Just below (b), the normalized and bandpass filtered signal is shown. Panels (e) and (f) show a smaller time interval of these traces, indicated by a vertical dashed line in (a-d). Figure B.7c shows the ‘‘locking indicator’’ signal, as discussed above this is the time derivative of the $\omega(t)$ signal. When this is close to zero, the PLL is locked. This can also be observed by comparing the mode frequency as it appears in a spectrogram (d) with the PLL frequency $\omega_l(t)$ (black line). When the PLL is locked, the frequency is observed to follow the mode frequency. Also, note how the

B.6. Phase-Locked loop for NTM control

loop tracks the varying frequency just before the mode's disappearance. Finally, (g) and (h) show the generated signals with, respectively, 0° (cos) and 90° (sin) phase difference with respect to the original probe signal. These have then been combined to generate an ECH power reference signal. The system is working and has been tested in plasma experiments, but not yet exploited for systematic investigations. Experimental results using this system will be the topic of future studies.

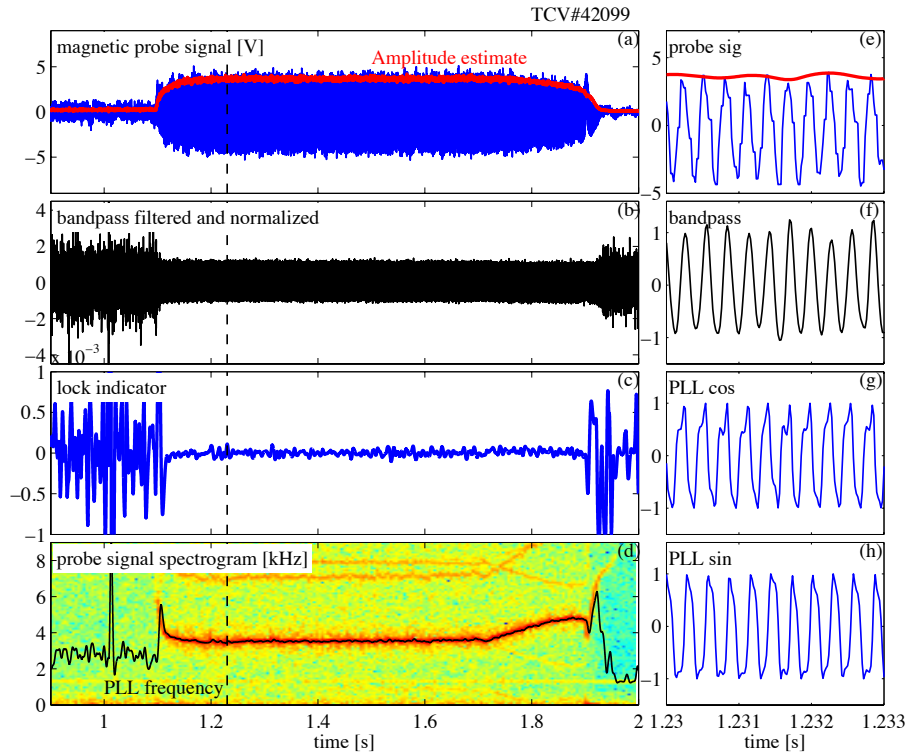


Figure B.7: Example of spline fitted DMPX profile channels, with identification of location of minimum and maximum gradients, profile peak and width. Some aliasing is observed in the spectrogram.

Appendix C

Mathematical derivations

C.1 Derivation of the 1D transport equations

C.1.1 Derivation of the poloidal flux diffusion equation

We will here derive the poloidal flux diffusion equation, describing the temporal evolution of the poloidal flux under the assumption of static background flux surfaces. We will follow (Hinton et al. 1976) (with some more detail) and use the notation and definitions in (Pereverzev et al. 2002).

Preliminaries

In this section we will use the useful relation

$$\begin{aligned}
 \langle \nabla \cdot \mathbf{F} \rangle &= \frac{\partial}{\partial V} \int (\nabla \cdot \mathbf{F}) dV = \frac{\partial}{\partial V} \int (\nabla \cdot \mathbf{F}) R d\phi d\ell_p \frac{d\psi}{|\nabla\psi|} \\
 &= \frac{\partial}{\partial V} \oint \mathbf{F} \cdot \frac{\nabla V}{|\nabla V|} R d\phi d\ell_p \quad (\text{by Gauss}) \\
 &= \frac{\partial}{\partial V} 2\pi \oint \mathbf{F} \cdot \nabla V \frac{\partial\psi}{\partial V} \frac{R d\ell_p}{|\nabla\psi|} \\
 &= \frac{\partial}{\partial V} \langle \mathbf{F} \cdot \nabla V \rangle
 \end{aligned} \tag{C.1}$$

Consider a surface of constant poloidal flux, of which each point of the boundary is moving with velocity \mathbf{u}_ψ . For this surface we can state

$$\frac{\partial\psi}{\partial t} + \mathbf{u}_\psi \cdot \nabla\psi = 0 \tag{C.2}$$

Now for a general scalar field $F(t, x, y, z)$ define scalar $H(t) = \int_V F dV$ where V is the volume enclosed by a flux surface $\psi = cst$ moving with speed \mathbf{u}_ψ , then

$$\left. \frac{\partial H}{\partial t} \right|_{\psi=cst} = \int_V \frac{\partial F}{\partial t} dV + \oint_S F \mathbf{u}_\psi \cdot d\mathbf{S}_\psi = \int_V \frac{\partial F}{\partial t} dV + \oint_S F \mathbf{u}_\psi \cdot \frac{\nabla\psi}{|\nabla\psi|} dS_\psi \tag{C.3}$$

Using this theorem, we can express the time rate of change of toroidal flux Φ enclosed by a surface S of constant poloidal flux $\psi = cst$ as:

$$\begin{aligned} \left. \frac{\partial \Phi}{\partial t} \right|_{\psi=cst} &= \frac{1}{2\pi} \frac{\partial}{\partial t} \int_V \mathbf{B} \cdot \nabla \phi dV \\ &= \frac{1}{2\pi} \int_V \frac{\partial \mathbf{B}}{\partial t} \cdot \nabla \phi dV + \frac{1}{2\pi} \oint_S (\mathbf{B} \cdot \nabla \phi) (\mathbf{u}_\psi \cdot \nabla \psi) \frac{dS}{|\nabla \psi|} \end{aligned} \quad (\text{C.4})$$

Poloidal electric field

We can rewrite the first term of (C.4), using Faraday's law

$$\begin{aligned} \int_V \frac{\partial \mathbf{B}}{\partial t} \cdot \nabla \phi dV &= - \int_V ((\nabla \times \mathbf{E}) \cdot \nabla \phi) dV \\ &= - \int_V \nabla \cdot (\mathbf{E} \times \nabla \phi) dV \\ &= - \oint_S (\mathbf{E} \times \nabla \phi) \cdot \frac{\nabla \psi}{|\nabla \psi|} dS \quad (\text{by Gauss}) \\ &= - \oint_S \mathbf{E} \cdot (\nabla \phi \times \nabla \psi) \frac{dS}{|\nabla \psi|} \\ &= -2\pi \oint_S \mathbf{E} \cdot \mathbf{B}_p \frac{dS}{|\nabla \psi|} \end{aligned} \quad (\text{C.5})$$

Toroidal electric field

To rewrite the second term of (C.4), one uses the radial component of Ampère's law

$$\begin{aligned} \nabla \psi \cdot \frac{\partial \mathbf{B}}{\partial t} &= -\nabla \psi \cdot (\nabla \times \mathbf{E}) \\ &= \nabla \cdot (\nabla \psi \times \mathbf{E}_\phi) \quad \text{since } \nabla \psi \cdot (\nabla \times \mathbf{E}_p) = 0 \\ &= \nabla \cdot (\nabla \psi \times \nabla \phi R E_\phi) \\ &= -\nabla \cdot (2\pi \mathbf{B}_p R E_\phi) \\ -\mathbf{B} \cdot \nabla \frac{\partial \psi}{\partial t} &= -\mathbf{B} \cdot \nabla (2\pi R E_\phi) \quad \text{since } (B_\phi R \nabla \phi) \cdot \nabla (R E_\phi) = 0 \end{aligned} \quad (\text{C.6})$$

Therefore,

$$\frac{\partial \psi}{\partial t} = 2\pi R E_\phi \quad (\text{C.7})$$

and, using (C.2)

$$\mathbf{u}_\psi \cdot \nabla \psi = -2\pi R E_\phi \quad (\text{C.8})$$

Combining (C.5) and (C.8) into (C.4) we finally get

$$\left. \frac{\partial \Phi}{\partial t} \right|_{\psi=cst} = - \oint_S (\mathbf{E} \cdot \mathbf{B}_p + B_\phi E_\phi) \frac{dS}{|\nabla \psi|} \quad (\text{C.9})$$

$$= - \oint_S (\mathbf{E} \cdot \mathbf{B}) \frac{dS}{|\nabla \psi|} \quad (\text{C.10})$$

$$= - \frac{\partial V}{\partial \psi} \langle \mathbf{E} \cdot \mathbf{B} \rangle \quad (\text{C.11})$$

Rate of change of poloidal flux

This can be related to the time rate of change of the poloidal flux as follows:

$$\left. \frac{\partial \psi}{\partial t} \right|_{\Phi=cst} = \left. \frac{\partial \psi}{\partial V} \frac{\partial V}{\partial \Phi} \frac{\partial \Phi}{\partial t} \right|_{\psi=cst} \quad (\text{C.12a})$$

$$\left. \frac{\partial \psi}{\partial t} \right|_{\rho} + \left. \frac{\partial \psi}{\partial \rho} \frac{\partial \rho}{\partial t} \right|_{\Phi} = - \frac{\partial V}{\partial \Phi} \langle \mathbf{E} \cdot \mathbf{B} \rangle \quad (\text{C.12b})$$

$$\left. \frac{\partial \psi}{\partial t} \right|_{\rho} - \frac{\rho \dot{B}_0}{2B_0} \frac{\partial \psi}{\partial \rho} = -2\pi \frac{R_0^2 \langle \mathbf{E} \cdot \mathbf{B} \rangle}{T \langle R_0^2 / R^2 \rangle} \quad (\text{using (6.23)}) \quad (\text{C.12c})$$

The last equation is equivalent to (44) in the ASTRA manual (Pereverzev et al. 2002). At this stage it is useful to define a cylinder-equivalent magnetic and electric field (Hinton et al. 1976)

$$B_{po} = \frac{1}{2\pi R_0} \frac{\partial \psi}{\partial \rho} \quad (\text{C.13})$$

$$E_o = \frac{R_0 \langle \mathbf{E} \cdot \mathbf{B} \rangle}{T \langle R_0^2 / R^2 \rangle} \quad (\text{C.14})$$

from which we see that, for $\dot{B}_0 = 0$, equation (C.12c) becomes:

$$\frac{\partial B_{po}}{\partial t} = - \frac{\partial E_o}{\partial \rho} \quad (\text{C.15})$$

Which is similar to Faraday's law for a cylindrical system.

Ohm's law

We can then write the longitudinal Ohm's law as

$$\langle \mathbf{j} \cdot \mathbf{B} \rangle = \sigma_{\parallel} \langle \mathbf{E} \cdot \mathbf{B} \rangle + \langle \mathbf{j}_{ni} \cdot \mathbf{B} \rangle \quad (\text{C.16})$$

where $\mathbf{j}_{ni} = \mathbf{j}_{bs} + \mathbf{j}_{cd}$ is the non-inductive component of the current density, decomposed into bootstrap (plasma self-driven) and current drive (externally driven) parts. Equivalently:

$$\sigma_{\parallel} \frac{\langle \mathbf{E} \cdot \mathbf{B} \rangle}{B_0} = \frac{\langle \mathbf{j} \cdot \mathbf{B} \rangle}{B_0} - \frac{\langle \mathbf{j}_{bs} \cdot \mathbf{B} \rangle}{B_0} - \frac{\langle \mathbf{j}_{cd} \cdot \mathbf{B} \rangle}{B_0} \quad (\text{C.17})$$

$$\text{or } \sigma_{\parallel} E_{\parallel} = j_{\parallel} - j_{bs} - j_{cd} \quad (\text{C.18})$$

Parallel current

As a final step we need to rewrite the term $j_{\parallel} = \frac{\langle \mathbf{j} \cdot \mathbf{B} \rangle}{B_0}$ in terms of ψ :

$$\begin{aligned}
 \frac{\langle \mathbf{j} \cdot \mathbf{B} \rangle}{B_0} &= \frac{T}{2\pi\mu_0 B_0} \langle \nabla \cdot (\nabla\psi/R^2) \rangle + \frac{1}{2\pi\mu_0 B_0} \langle \nabla T \cdot \nabla\psi/R^2 \rangle \\
 &= \frac{1}{2\pi\mu_0 B_0} \left(\frac{4\pi^2 T}{V'} \frac{\partial}{\partial\rho} G_2 \frac{\partial\psi}{\partial\rho} + \frac{4\pi^2 V'}{4\pi^2} \left\langle \frac{(\nabla\rho)^2}{R^2} \right\rangle \frac{\partial T}{\partial\rho} \frac{\partial\psi}{\partial\rho} \right) \\
 &= \frac{2\pi R_0 J^2}{\mu_0 V'} \left(\frac{1}{J} \frac{\partial}{\partial\rho} G_2 \frac{\partial\psi}{\partial\rho} + \frac{G_2}{J^2} \frac{\partial J}{\partial\rho} \frac{\partial\psi}{\partial\rho} \right) \\
 &= \frac{2\pi R_0 J^2}{\mu_0 V'} \frac{\partial}{\partial\rho} \left(\frac{G_2}{J} \frac{\partial\psi}{\partial\rho} \right)
 \end{aligned} \tag{C.19}$$

Where we have introduced the flux quantities

$$J = \frac{T}{R_0 B_0}, \quad G_2 = \frac{V'}{4\pi^2} \left\langle \left(\frac{(\nabla\rho)^2}{R^2} \right) \right\rangle, \quad V' = \frac{\partial V}{\partial\rho}. \tag{C.20}$$

The poloidal flux diffusion equation

Finally, combining (C.17), (C.19) and (C.12c) the poloidal flux diffusion equation reads

$$\boxed{\sigma_{\parallel} \left(\frac{\partial\psi}{\partial t} + \frac{\rho \dot{B}_0}{2B_0} \frac{\partial\psi}{\partial\rho} \right) = \frac{R_0 J^2}{\mu_0 \rho} \frac{\partial}{\partial\rho} \left(\frac{G_2}{J} \frac{\partial\psi}{\partial\rho} \right) - \frac{V'}{2\pi\rho} (j_{bs} + j_{cd})} \tag{C.21}$$

which is the last equation of (59) in (Pereverzev et al. 2002).

C.1.2 Derivation of the particle transport equation

For an arbitrary plasma species α , let n_{α} be the local particle density of the species and \mathbf{u}_{α} be the local velocity of the particles. The continuity equation for this species is stated as

$$\frac{\partial n_{\alpha}}{\partial t} + \nabla \cdot (n_{\alpha} \mathbf{u}_{\alpha}) = s_{\alpha} \tag{C.22}$$

Here s_{α} is a localized particle source. We now wish to write an equation for the density associated with the particles contained inside a toroidal flux surface. For this purpose we start by taking the volume integral of this expression over a volume enclosed by one such toroidal flux surface.

$$\int \frac{\partial n_{\alpha}}{\partial t} dV + \oint n_{\alpha} \mathbf{u}_{\alpha} \cdot \nabla\Phi \frac{dS}{|\nabla\Phi|} = \int s_{\alpha} dV \tag{C.23}$$

Using (C.3), and the fact that $\nabla\rho \parallel \nabla\Phi$:

$$\frac{\partial}{\partial t} \Big|_{\Phi} \int n_{\alpha} dV + \oint n_{\alpha} (\mathbf{u}_{\alpha} - \mathbf{u}_{\Phi}) \cdot \nabla\rho \frac{dS}{|\nabla\rho|} + \int s_{\alpha} dV \tag{C.24}$$

Using the definition of the flux surface average (6.18),

$$\frac{\partial}{\partial t} \Big|_{\Phi} \int \langle n_{\alpha} \rangle V' d\rho + V' \langle n_{\alpha} (\mathbf{u}_{\alpha} - \mathbf{u}_{\Phi}) \cdot \nabla\rho \rangle = \int \langle s_{\alpha} \rangle V' d\rho \tag{C.25}$$

then taking the radial derivative

$$\frac{\partial}{\partial t} \Big|_{\Phi} [\langle n_{\alpha} \rangle V'] + \frac{\partial}{\partial \rho} \underbrace{[V' \langle n_{\alpha} (\mathbf{u}_{\alpha} - \mathbf{u}_{\Phi}) \cdot \nabla \rho \rangle]}_{\Gamma_{\alpha}} = \underbrace{\langle s_{\alpha} \rangle}_{S_{\alpha}} V' \quad (\text{C.26})$$

where we define the particle flux Γ_a . Finally writing the time derivative on at constant ρ :

$$\frac{1}{V'} \left(\frac{\partial}{\partial t} + \frac{\dot{B}_0}{2B_0} \frac{\partial}{\partial \rho} \right) (\langle n_{\alpha} \rangle V') + \frac{1}{V'} \frac{\partial}{\partial \rho} \Gamma_{\alpha} = S_{\alpha} \quad (\text{C.27})$$

Appendix D

Details of the RAPTOR code

D.1 Implementation using finite elements

This section contains some details of the numerical implementation which were not included in the main text.

D.1.1 Finite Element Method

Consider the general case of a time-varying, inhomogeneous partial differential equation of the form

$$m(\rho, t) \frac{\partial y}{\partial t} = \frac{\partial}{\partial \rho} \left[g(\rho, t) \frac{\partial y}{\partial \rho} \right] + k(\rho) j(\rho, t), \quad (\text{D.1})$$

where $y(\rho, t) : \mathbb{R} \times \mathbb{R} \rightarrow \mathbb{R}$, $0 \leq \rho \leq \rho_e$ and $t_0 \leq t \leq t_f$. The infinite-dimensional problem in ρ is transformed into a finite-dimensional problem using the Finite Element approach (for which a vast literature exists, e.g. (Hughes 1987)). An important advantage of using finite element methods is that the basis functions can easily be modified, and also that the order of spatial derivatives of the elements involved are, as we shall see, one order lower than the order of the PDE.

First, let us approximate the solution by

$$y(\rho, t) \approx \sum_{\alpha=1}^{n_{sp}} \hat{y}_\alpha(t) \Lambda_\alpha(\rho). \quad (\text{D.2})$$

We choose polynomial B-splines (de Boor 2001) on a finite support as finite elements Λ_α . Choosing a set of (possibly irregularly spaced) *knots* $0 = x_1 < \dots < x_{n_{kts}} = \rho_e$ the basis functions are defined recursively as

$$\Lambda_\alpha^0(\rho) = 1 \text{ if } x_\alpha \leq \rho < x_{\alpha+1}, \quad 0 \text{ otherwise}, \quad (\text{D.3})$$

$$\Lambda_\alpha^p = w_{\alpha-1}^p \Lambda_{\alpha-1}^{p-1} + (1 - w_\alpha^p) \Lambda_\alpha^{p-1}, \quad (\text{D.4})$$

$$w_\alpha^p = \frac{\rho - x_\alpha}{x_{\alpha+p} - x_\alpha}. \quad (\text{D.5})$$

Where p is the order of the spline. We obtain non-periodic splines by defining additional knots on the domain boundary: $x_{-p+1} = \dots = x_1$ and $x_{n_{kts}+p} = x_{n_{kts}+p-1} = \dots = x_{n_{kts}}$. For a given spline order and set of knots we can construct $n_{sp} = p + n_{kts} - 1$ unique

splines. Note that as a result of the finite support of the elements, $\Lambda_\alpha^p(\rho) \neq 0$ if and only if $x_{\alpha-p} < \rho < x_{\alpha+1}$.

Substituting this into (D.1)

$$\sum_{\alpha=1}^{n_{sp}} m \frac{d\hat{y}_\alpha(t)}{dt} \Lambda_\alpha(\rho) = \sum_{\alpha=1}^{n_{sp}} \hat{y}_\alpha(t) \frac{\partial}{\partial \rho} \left[g \frac{\partial \Lambda_\alpha(\rho)}{\partial \rho} \right] + kj, \quad (\text{D.6})$$

where we have dropped the (ρ, t) dependencies for notational simplicity. We can construct the weak form by projecting the equation for each α onto a trial function Λ_β and by integrating over the domain

$$\sum_{\alpha=1}^{n_{sp}} \frac{d\hat{y}_\alpha(t)}{dt} \int_0^{\rho_e} m \Lambda_\beta \Lambda_\alpha \, d\rho = \sum_{\alpha=1}^{n_{sp}} \hat{y}_\alpha(t) \int_0^{\rho_e} d\rho \left(\Lambda_\beta \frac{\partial}{\partial \rho} \left[g \frac{\partial \Lambda_\alpha}{\partial \rho} \right] \right) + \int_0^{\rho_e} d\rho \Lambda_\beta kj \quad (\text{D.7})$$

$$\sum_{\alpha=1}^{n_{sp}} \frac{d\hat{y}_\alpha(t)}{dt} \underbrace{\int_0^{\rho_e} m \Lambda_\beta \Lambda_\alpha \, d\rho}_{M_{\beta\alpha}(t)} = - \sum_{\alpha=1}^{n_{sp}} \hat{y}_\alpha(t) \underbrace{\left[\int_0^{\rho_e} g \frac{\partial \Lambda_\beta}{\partial \rho} \frac{\partial \Lambda_\alpha}{\partial \rho} \, d\rho \right]}_{=D_{\beta\alpha}} \quad (\text{D.8})$$

$$+ \underbrace{\left[g \Lambda_\beta \frac{\partial y}{\partial \rho} \right]_0^{\rho_e}}_{=l_\beta} + \underbrace{\left[\int_0^{\rho_e} \Lambda_\beta kj \, d\rho \right]}_{=s_\beta}. \quad (\text{D.9})$$

Note that by integrating by parts, we were able to reduce the order of the maximum radial derivative to be evaluated. This yields an equation for each β , of the form:

$$\sum_{\alpha=1}^{n_{sp}} M_{\beta\alpha} \frac{d\hat{y}_\alpha}{dt} = \sum_{\alpha=1}^{n_{sp}} -D_{\beta\alpha} \hat{y}_\alpha + l_\beta + s_\beta, \quad (\text{D.10})$$

which can be written in matrix form as

$$\mathbf{M} \frac{d\hat{\mathbf{y}}}{dt} = -\mathbf{D}\hat{\mathbf{y}} + \mathbf{l} + \mathbf{s}, \quad (\text{D.11})$$

where $\mathbf{M} \in \mathbb{R}^{n_{sp} \times n_{sp}}$, $\mathbf{D} \in \mathbb{R}^{n_{sp} \times n_{sp}}$, $\mathbf{l} \in \mathbb{R}^{n_{sp}}$, $\mathbf{s} \in \mathbb{R}^{n_{sp}}$ and $\hat{\mathbf{y}} \in \mathbb{R}^{n_{sp}}$. As a consequence of the finite support of the basis functions, the matrices have limited bandwidth. Furthermore, the finite element basis functions Λ_α and Λ_β are usually chosen such that $\Lambda_\alpha = \Lambda_\beta \, \forall \alpha = \beta$, in which case the above matrices become symmetric.

D.1.2 Finite element matrix expressions

With the method above, the flux transport and electron energy transport equations (7.10), (7.11) are rewritten to matrix form (7.20), (7.21). The matrix coefficients are given below,

with the boundary conditions included where appropriate.

$$[M_\psi]_{\beta\alpha} = \int_0^{\rho_e} m_\psi \Lambda_\alpha \Lambda_\beta d\rho \quad \forall \alpha, \beta \in [1, \dots, n_{sp}] \quad (\text{D.12})$$

$$[D_\psi]_{\beta\alpha} = \begin{cases} \int_0^{\rho_e} d_\psi \frac{\partial \Lambda_\alpha}{\partial \rho} \frac{\partial \Lambda_\beta}{\partial \rho} d\rho & \text{if } (\beta \neq n_{sp}) \text{ and } (\alpha \neq n_{sp}) \\ \int_0^{\rho_e} d_\psi \frac{\partial \Lambda_\alpha}{\partial \rho} \frac{\partial \Lambda_\beta}{\partial \rho} d\rho + d_{BC} & \text{if } (\beta = n_{sp}) \text{ or } (\alpha = n_{sp}) \end{cases} \quad (\text{D.13})$$

$$[M_{T_e}]_{\beta\alpha} = \begin{cases} \int_0^{\rho_e} m_{T_e} \Lambda_\alpha \Lambda_\beta d\rho & \text{if } \beta \neq n_{sp} \\ 0 & \text{if } \beta = n_{sp} \end{cases} \quad (\text{D.14})$$

$$[D_{T_e}]_{\beta\alpha} = \begin{cases} \int_0^{\rho_e} d_{T_e} \frac{\partial \Lambda_\alpha}{\partial \rho} \frac{\partial \Lambda_\beta}{\partial \rho} d\rho & \text{if } \beta \neq n_{sp} \\ 1 & \text{if } \beta = n_{sp} \text{ or } \alpha = n_{sp} \\ 0 & \text{if } \beta = n_{sp} \text{ or } \alpha \neq n_{sp} \end{cases} \quad (\text{D.15})$$

$$[B_\psi]_{\beta i} = \begin{cases} \int_0^{\rho_e} S_{i,\psi} \Lambda_\beta d\rho & \text{if } i \in [1, \dots, m] \\ b_{BC} & \text{if } (\beta = n_{sp}) \text{ or } (i = m + 1) \\ 0 & \text{if } (\beta \neq n_{sp}) \text{ or } (i = m + 1) \end{cases} \quad (\text{D.16})$$

$$[B_{T_e}]_{\beta i} = \begin{cases} \int_0^{\rho_e} S_{i,\psi} \Lambda_\beta d\rho & \text{if } i \in [1, \dots, m] \\ 0 & \text{if } i = m + 1 \end{cases} \quad (\text{D.17})$$

$$[f_\psi]_\beta = \int_0^{\rho_e} f_\psi \Lambda_\beta d\rho \quad (\text{D.18})$$

$$[f_{T_e}]_\beta = \begin{cases} \int_0^{\rho_e} f_{T_e} \Lambda_\beta d\rho & \text{if } \beta \neq n_{sp} \\ \int_0^{\rho_e} f_{T_e} \Lambda_\beta d\rho + T_{e,edge} & \text{if } \beta = n_{sp} \end{cases} \quad (\text{D.19})$$

The terms d_{BC} and b_{BC} depend on the choice of the boundary condition used.

$$d_{BC} = \begin{cases} \mu_0/L_{ext} & \text{if Eq.(6.33) is used} \\ 0 & \text{if Eq.(6.34) is used} \end{cases} \quad (\text{D.20})$$

$$b_{BC} = \begin{cases} \mu_0/L_{ext} & \text{if Eq.(6.33) is used} \\ \mu_0 & \text{if Eq.(6.34) is used} \end{cases} \quad (\text{D.21})$$

D.1.3 Numerical integration using Legendre-Gauss quadrature

The integrals appearing in (D.12)-(D.19) are evaluated numerically using Gaussian quadrature (Press et al. 1996). Note that due to the finite support of the basis functions the terms are identically zero except pairs of indices α, β satisfying $\alpha - p \leq \beta \leq \alpha + 1$ where p is the order of the spline. For this set of combinations of α, β , the integrals can be computed efficiently using Gaussian quadrature. On the i th interval $[x_i, x_{i+1}]$ between two knots, let us define the set of n_g Gauss points $x_{i,j}^g$ for $j = [1, 2, \dots, n_g]$, then define the function $z(x) = (2x - x_{i+1} - x_i)/(x_{i+1} - x_i)$ which linearly maps the interval $x \in [x_i, x_{i+1}]$ to $z \in [-1, 1]$. Now the j th Gauss point is the point for which $z(x_{i,j}^g)$ is the j th zero of the normalized Legendre polynomial of order n_g . The corresponding set of weights $w_{i,j}^g$ are given by

$$w_{i,j}^g = 2(1 - z(x_{i,j}^g)^2)^{-1} [L'_{n_g}(z(x_{i,j}^g))]^{-2} \quad (\text{D.22})$$

where L'_{n_g} is the derivative of that same Legendre polynomial. Then we can approximate the integral

$$\int_{x_i}^{x_{i+1}} f(x) dx \approx \sum_{j=1}^{n_g} w_{i,j}^g f(x_{i,j}^g) \quad (\text{D.23})$$

The integral (D.12), for example, is then given by:

$$\int_{\rho} m(\rho, t) \Lambda_{\alpha}(\rho) \Lambda_{\beta}(\rho) d\rho \approx \sum_{i=i_{\min}}^{i_{\max}} \sum_{j=1}^{n_g} w_{i,j}^g \Lambda_{\alpha}(x_{i,j}^g) \Lambda_{\beta}(x_{i,j}^g) m(x_{i,j}^g, t) \quad (\text{D.24})$$

Here i_{\min} and i_{\max} are the indices of the intervals delimiting the domain where $\Lambda_{\alpha} > 0$. Using n_g points exactly integrates up to polynomial order $2n_g - 1$, thus choosing $n_g = 4$ provides exact integration of the products of up to order 7 (Note that the integrands include a product of two cubic spines which gives order ≥ 6). Thus one needs to evaluate radial quantities on $(n_{kts} - 1)n_g$ radial points. Separating the time-varying part of $m(\rho, t) = \tilde{m}(\rho) \sigma_{\parallel}(\rho, t)$ where $\tilde{m}(\rho) = (\mu_0 \rho / (J(\rho)^2 R_0))$ we can write each element of $\mathbf{M}_{\psi,k}$ as an inner product

$$[M_{\psi}(t_k)]_{\beta\alpha} \approx \boldsymbol{\xi}_{\alpha,\beta}^T \bar{\boldsymbol{\sigma}}_{\alpha}(t) \quad (\text{D.25})$$

where

$$\boldsymbol{\xi}_{\alpha,\beta} = \begin{pmatrix} w_{i_{\min},1}^g \Lambda_{\alpha}(x_{i_{\min},1}^g) \Lambda_{\beta}(x_{i_{\min},1}^g) \tilde{m}(x_{i_{\min},1}^g) \\ \vdots \\ w_{i_{\min},n_g}^g \Lambda_{\alpha}(x_{i_{\min},n_g}^g) \Lambda_{\beta}(x_{i_{\min},n_g}^g) \tilde{m}(x_{i_{\min},n_g}^g) \\ w_{i_{\min}+1,1}^g \Lambda_{\alpha}(x_{i_{\min}+1,1}^g) \Lambda_{\beta}(x_{i_{\min}+1,1}^g) \tilde{m}(x_{i_{\min}+1,1}^g) \\ \vdots \\ w_{i_{\min}+1,n_g}^g \Lambda_{\alpha}(x_{i_{\min}+1,n_g}^g) \Lambda_{\beta}(x_{i_{\min}+1,n_g}^g) \tilde{m}(x_{i_{\min}+1,n_g}^g) \\ \vdots \\ w_{i_{\max},n_g}^g \Lambda_{\alpha}(x_{i_{\max},n_g}^g) \Lambda_{\beta}(x_{i_{\max},n_g}^g) \tilde{m}(x_{i_{\max},n_g}^g) \end{pmatrix}, \quad (\text{D.26})$$

and

$$\bar{\boldsymbol{\sigma}}_{\alpha}(t) = \begin{pmatrix} \sigma_{\parallel}(x_{i_{\min},1}^g, t) \\ \vdots \\ \sigma_{\parallel}(x_{i_{\min},n_g}^g, t) \\ \sigma_{\parallel}(x_{i_{\min}+1,1}^g, t) \\ \vdots \\ \sigma_{\parallel}(x_{i_{\min}+1,n_g}^g, t) \\ \vdots \\ \sigma_{\parallel}(x_{i_{\max},n_g}^g, t) \end{pmatrix} \quad (\text{D.27})$$

The row vectors $\boldsymbol{\xi}_{\alpha,\beta}^T$ for all combinations (α, β) corresponding to a nonzero element of \mathbf{M}_{ψ} can be combined into a band-structured matrix $\boldsymbol{\Xi}$. Then defining $\bar{\boldsymbol{\sigma}}(t)^T = [\sigma_{\parallel}(x_{1,1}^g)^T, \dots, \sigma_{\parallel}(x_{n_{kts}-1,n_g}^g)^T]^T$, i.e. the vector containing the values of σ_{\parallel} on all Gauss points on all intervals, we can compute *all* the elements of \mathbf{M}_{ψ} with a single matrix-vector product $\boldsymbol{\Xi} \bar{\boldsymbol{\sigma}}(t)$. The elements are then assigned to their corresponding indices. The key

advantage is that the entire matrix Ξ can be pre-computed once the equilibrium, knots and finite elements have been defined. In the time loop, which needs to be executed rapidly, it is only necessary to calculate $\sigma_{\parallel}(t)$ on the grid of $(n_{kts} - 1)n_g$ Gauss points, perform one matrix multiplication and assign the resulting elements to their respective indices positions in the matrix to construct \mathbf{M}_{ψ} .

Generalizing this approach to the other terms, we see for example that \mathbf{D}_{ψ} and \mathbf{B}_{Te} can be entirely pre-calculated as no terms in the integrand depend on time, while for example \mathbf{f}_{ψ} requires calculating j_{bs} at the Gauss points and can be obtained in a similar way as for \mathbf{M}_{ψ} .

Gaussian quadrature can also be applied when computing surface and volume integrals, necessary for evaluating integral quantities such as W_i and I_{BS} . Taking a general example, $Q_i(\rho) = \int_0^{\rho} q(\rho)d\rho$ can be evaluated by writing $Q(x_l) = \sum_{i=1}^l \sum_{j=1}^{n_g} w_{i,j}^g q(x_{i,j}^g)$. After some algebra, this summation can be recast into a matrix multiplication involving a lower-triangular matrix containing weights and a vector containing all the elements $q(x_{i,j}^g)$.

D.2 Interpretative mode

The preparation for real-time computations is done in MATLAB including (i) loading a pre-defined equilibrium, (ii) pre-computing the finite element basis functions and matrices required for differentiation and integration, and (iii) preparing variables used later for assembling the elements of the linear system. The time loop of the interpretative-RAPTOR code is implemented both in MATLAB and in SIMULINK. The first version is provided mainly for testing and debugging, while the second one allows the code to be converted to C for real-time execution. This is then used in the real-time simulations described in Chapter 8.

In both cases, the T_e profile evolution has to be specified in time – more precisely, the time evolution of the \hat{T}_e spline coefficients must be specified. This can be given either from post-shot experimental data or from real-time diagnostic measurements. A schematic representation of the program workflow for interpretative-RAPTOR is described below.

D.2.1 Program workflow

The workflow of interpretative-RAPTOR and RT-RAPTOR are shown in Figure D.1. One starts by running the configuration script `RAPTOR_config.m` and modifying default parameters as necessary. Then the `RAPTOR` model and `params` structures contain all the necessary information for either the RT-RAPTOR SIMULINK model or an equivalent MATLAB script `RAPTOR_interpretative.m`. When used in RT mode, the `.mdl` is compiled into a shared object library and sent to the RT node where it should be executed. For each shot, the `.mdl`, the configuration files, and all the RT input/output data are stored to the TCv database so new models can be tested on old data.

D.2.2 Algorithm breakdown

Based on the efficient methods to calculate the time-varying matrices and the outputs at each time step, presented in the previous section, we now give an overview of a typical interpretative (RT-)RAPTOR calculation:

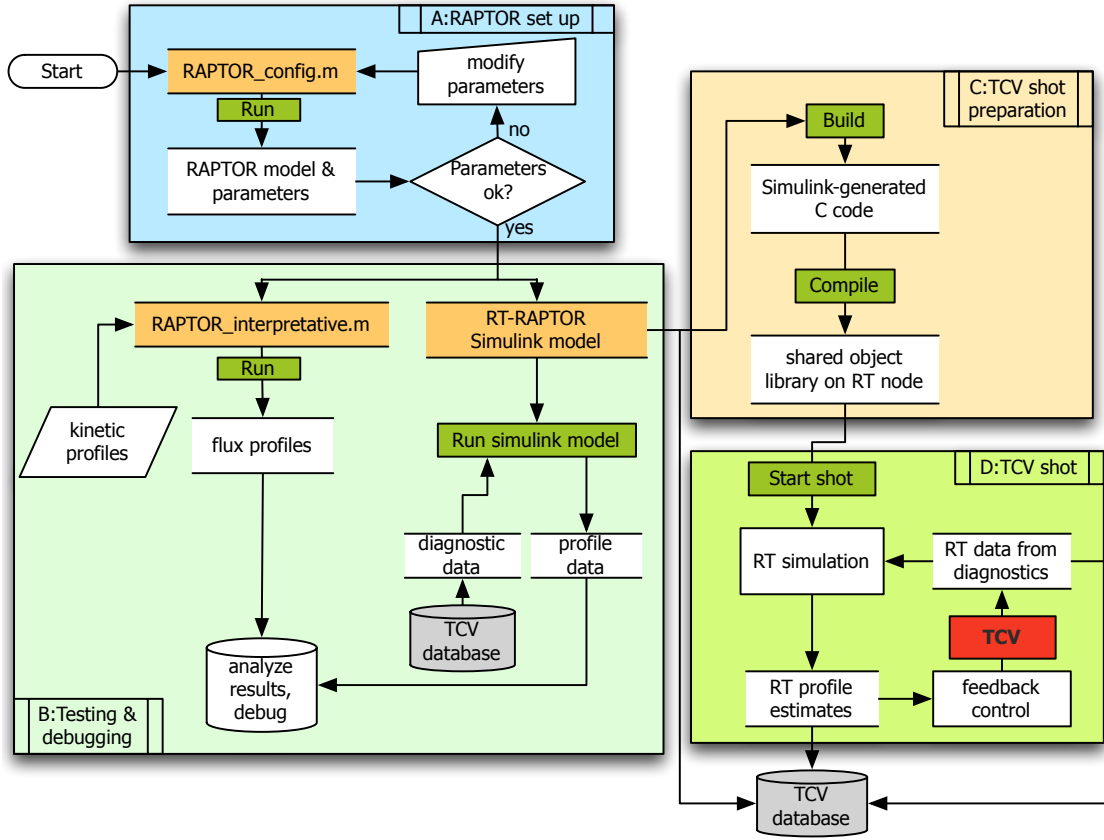


Figure D.1: Interpretative-RAPTOR and RT-RAPTOR workflow, also representative of typical operation of the TCV SCD real-time control system using SIMULINK. Blocks A-B represent off-line preparatory steps, while C, D are automatically performed during the shot preparation and during the shot itself.

1. Define spline order, knot locations, time grid and other model parameters, compute Gauss grid points
2. Choose a reference equilibrium, compute fixed geometric terms.
3. Compute all pre-calculable matrices.
4. Choose an initial condition $\hat{\psi}_0$.
5. Execute the time loop for each time step $k = [0, M]$
 - Calculate time-varying profiles: Given values of $\hat{\psi}$, T_e , n_e and their spatial derivatives at time step k on the grid of Gauss points, calculate $\sigma_{||}$ (7.5), j_{bs} (7.7), j_{aux} (7.2) on the same points.
 - Assemble the linear system: Use the method described in D.1.3 to calculate $\mathbf{M}_{\psi,k}$ and $\mathbf{s}_{\psi,k}$.
 - Solve the linear system (7.38) using Cholesky factorization to obtain $\hat{\psi}_{k+1}$
 - Compute necessary outputs as shown in Section 6.4.4

6. Compute additional post-run outputs if necessary

All the pre and post-processing steps, respectively (1-4) and (6), are implemented in MATLAB (Fig.D.1, block A). The real-time step (v) has been implemented both in MATLAB and SIMULINK (Fig.D.1 block B). The SIMULINK version is then automatically converted to C code, compiled for the TCV control system and is the part that runs in real-time during a TCV shot (Fig.D.1 blocks C,D). This is also described in Appendix A.

D.3 Predictive mode

D.3.1 Newton iterations

In this section we show the Newton iterations needed to solve (7.45), which reads

$$\tilde{f}_k \equiv \tilde{f}(x_{k+1}, x_k, u_k) = 0 \quad \forall k$$

Each Newton iteration at each time step requires knowledge of the Jacobian:

$$\mathcal{J}_{k+1}^k = \frac{\partial \tilde{f}_k}{\partial x_{k+1}} \quad (\text{D.28})$$

written in full as

$$\frac{\partial \tilde{f}_k}{\partial x_{k+1}} = \begin{bmatrix} \frac{\partial \tilde{F}_k}{\partial \psi_{k+1}} & \frac{\partial \tilde{F}_k}{\partial T_{e,k+1}} \\ \frac{\partial \tilde{G}_k}{\partial \psi_{k+1}} & \frac{\partial \tilde{G}_k}{\partial T_{e,k+1}} \end{bmatrix} \quad (\text{D.29})$$

with

$$\frac{\partial \tilde{F}_k}{\partial \psi_{k+1}} = - \left[\frac{M_\psi}{\Delta t} + \theta (-D_\psi + \frac{\partial f_\psi}{\partial \psi}) \right]_k \quad (\text{D.30})$$

$$\frac{\partial \tilde{F}_k}{\partial T_{e,k+1}} = \theta \left[-\frac{\partial M_\psi}{\partial T_e} \frac{(\psi_{k+1} - \psi_k)}{\Delta t} + \frac{\partial B_\psi}{\partial T_e} u_k + \frac{\partial f_\psi}{\partial T_e} \right]_k \quad (\text{D.31})$$

$$\frac{\partial \tilde{G}_k}{\partial \psi_{k+1}} = \theta \left[-\frac{\partial D_{T_e}}{\partial \psi} + \frac{\partial f_{T_e}}{\partial \psi} \right]_k + \frac{1}{\Delta t} \frac{\partial f_{T_e}}{\partial \psi} \Big|_k \quad (\text{D.32})$$

$$\frac{\partial \tilde{G}_k}{\partial T_{e,k+1}} = - \left[\frac{M_{T_e}}{\Delta t} - \theta \frac{\partial D_{T_e}}{\partial T_e} \right]_k \quad (\text{D.33})$$

Each of the terms in the above equations are computed from the analytical derivatives of the various expressions (7.12) - (7.17) using the chain rule. The descent direction is obtained from the solution of the linear system

$$\mathcal{J}_{k+1}^k d = \tilde{f}_k, \quad (\text{D.34})$$

which requires factoring the Jacobian (e.g. computing the LU decomposition). As an initial estimate we use the backwards difference $x_{k+1}^{(0)} = x_k + (x_k - x_{k-1})$. Calculating \tilde{f} with these values will give a nonzero result. Subsequent estimates for x_{k+1} , yielding progressively smaller values of \tilde{f} are then obtained by updating the previous estimate by

$$x_{k+1}^{(i+1)} = x_{k+1}^{(i)} + \tau d. \quad (\text{D.35})$$

We usually take the full Newton step by setting $\tau = 1$. This procedure is iterated by recomputing the Jacobian for the new estimate $x_{k+1}^{(i+1)}$, solving for the descent direction d , and repeating the process. The iterations are stopped upon reaching the condition

$$\|\tilde{f}_k\| < \epsilon_{Newton} \quad (\text{D.36})$$

where ϵ_{Newton} is a predefined (very small, $\sim 10^{-9}$) tolerance level. Typically, only a few iterations are necessary depending on the size of the time step. The algorithm is summarized in Algorithm 1.

Algorithm 1 Predictive-RAPTOR integration algorithm: implicit time steps including forward sensitivity analysis

given $u_k \forall k$, initial state x_0 and initial state sensitivity $\partial x_0 / \partial p$.

for each time step $k = 0 \dots M$ **do**

 First guess $x_{k+1}^{(0)} = x_k + (x_k - x_{k-1})$; $i = 0$

repeat

 Evaluate $\tilde{f}_k^{(i)}(x_{k+1}^{(i)}, x_k, u_k)$ (Function residual)

 Evaluate $\mathcal{J}_{k+1} = \partial \tilde{f}_k / \partial x_{k+1}$ (Jacobian)

 Solve Eq. (D.34) for d (Newton direction)

 Update $x_{k+1}^{(i+1)} = x_{k+1}^{(i)} + \tau d$ (Newton step)

$i \leftarrow i + 1$

until $\tilde{f}_k^{(i)} < \epsilon_{Newton}$

 Set $x_{k+1} = x_{k+1}^{(i)}$

 Evaluate $\mathcal{J}_k = \partial \tilde{f}_k / \partial x_k$

 Solve Eq.(7.46) for $\partial x_{k+1} / \partial p$ (Forward sensitivity)

end for

D.3.2 Convergence studies

To test the numerical performance and convergence properties of this algorithm, a series of benchmarks has been carried out. The benchmarks are based on the example presented in Section 9.3.2. We do not calculate the state sensitivities in these runs and focus only on the performance of the state integration algorithm by varying some numerical parameters of the simulation. We examine the effect of (i) the number of knots in the radial grid (n_{kts} in Eq.(7.19)), (ii) the time step size (Δt in Eq.(7.42)), and (iii) the tolerance in the implicit Newton loop (ϵ_{Newton} in Eq.(D.36)).

After each simulation, we collect values of both ψ and T_e on a grid of spatial and temporal points $\rho_N = [0, 1]$ and $t = [0, 10, 20, \dots, 50]$ ms in vectors $\boldsymbol{\psi}_{out}^{(i)}$ and $\mathbf{T}_{eout}^{(i)}$ for different simulation runs $i \in [1, 2, \dots]$, with the first run being the most accurate. The relative error for the i th run is defined as

$$e_{\psi}^{(i)} = \frac{\|\boldsymbol{\psi}_{out}^{(i)} - \boldsymbol{\psi}_{out}^{(1)}\|_2}{\|\boldsymbol{\psi}_{out}^{(i)}\|_2}, \quad e_{T_e}^{(i)} = \frac{\|\mathbf{T}_{eout}^{(i)} - \mathbf{T}_{eout}^{(1)}\|_2}{\|\mathbf{T}_{eout}^{(i)}\|_2} \quad (\text{D.37})$$

The results are shown in Figure D.2 and are discussed below:

- Fig.D.2a shows the convergence properties expected for a third order spatial discretization (giving $e \sim 1/n_{kts}^3$). Notice that already for $n_{sp} = 11$ the relative error is less than 1%, so it is possible to use a relatively coarse ρ grid without losing too much accuracy. This is due to the fact that the profiles in this simulation do not feature excessive spatial detail. Using more spatially localized current drive sources would require using a (locally) denser grid. The computation time is shown in Fig.D.2b to increase roughly linearly with the number of spatial grid points. This is thanks to the band structure of the various matrices: for splines of order d , $2d + 1$ diagonals are populated, and the number of elements to be computed therefore scales as $\sim (2d + 1)n_{kts}$ for large n_{kts} . Figures D.3d-f show a collection of profiles obtained during these simulations and confirm that choosing $n_{kts} \geq 11$ is sufficient.
- Figures D.2c,d show a linear decrease of the error with decreasing time step size, as expected from a first-order method. However comparing the temporal step size with the confinement time, which is ~ 5 ms, it is remarkable that already a 1ms step size gives relatively good results (with a few % error). This is due to the robust numerical properties of the implicit method used. A further illustration of the effect of decreasing Δt is given in Fig.D.3a,b,c, where the difference between the characteristic current diffusion and confinement time scales is also apparent. As expected, the computational time scales linearly with the number of time points in the simulation.
- Figures D.2e,f show the effect of the Newton step tolerance. As expected, the error scales linearly with ϵ_{Newton} as this parameter directly affects the error tolerance of each time step. Due to the quadratic convergence of the Newton algorithm, the computation time scales very weakly with this parameter (Figure D.2d).

We illustrate the typical computational times for the simulations shown in this paper. Consider the simulations in Section 9.3 where we chose $\Delta t = 1$ ms, $n_{kts} = 11$ and $\epsilon = 10^{-6}$. With these numbers, a single Predictive-RAPTOR profile evolution (101 time steps) takes about 1 second, and a full nonlinear trajectory optimization with 9 parameters takes approximately 3 minutes with the system specifications listed in the caption of Figure D.2.

D.4 Discretization of the optimization problem

To solve the optimization problem numerically we need to write the problem (9.28)-(9.33) in discrete-time form. The discretization of the state equation (9.30) has already been treated in Section 7.5.1. It remains to discretize the time-dependent control parametrization (9.31) cost (9.28) and state constraint (9.33). We proceed by applying the same approximations as when discretizing the state dynamics: $\dot{x}(t) = (x_{k+1} - x_k)/\Delta t$.

The control vector parametrization (9.31) becomes simply $u_k = \mathbf{P}(t_k)p$. For the cost (9.28), let the reference profiles $l_{ref}, T_{e,ref}$ be given on the set of knot points $[\rho_1, \rho_2, \dots, \rho_{n_{kts}}]$. Recalling that $x = [\hat{\psi}; \hat{\mathbf{T}}_e]$, the cost function terms (9.11) and (9.13)

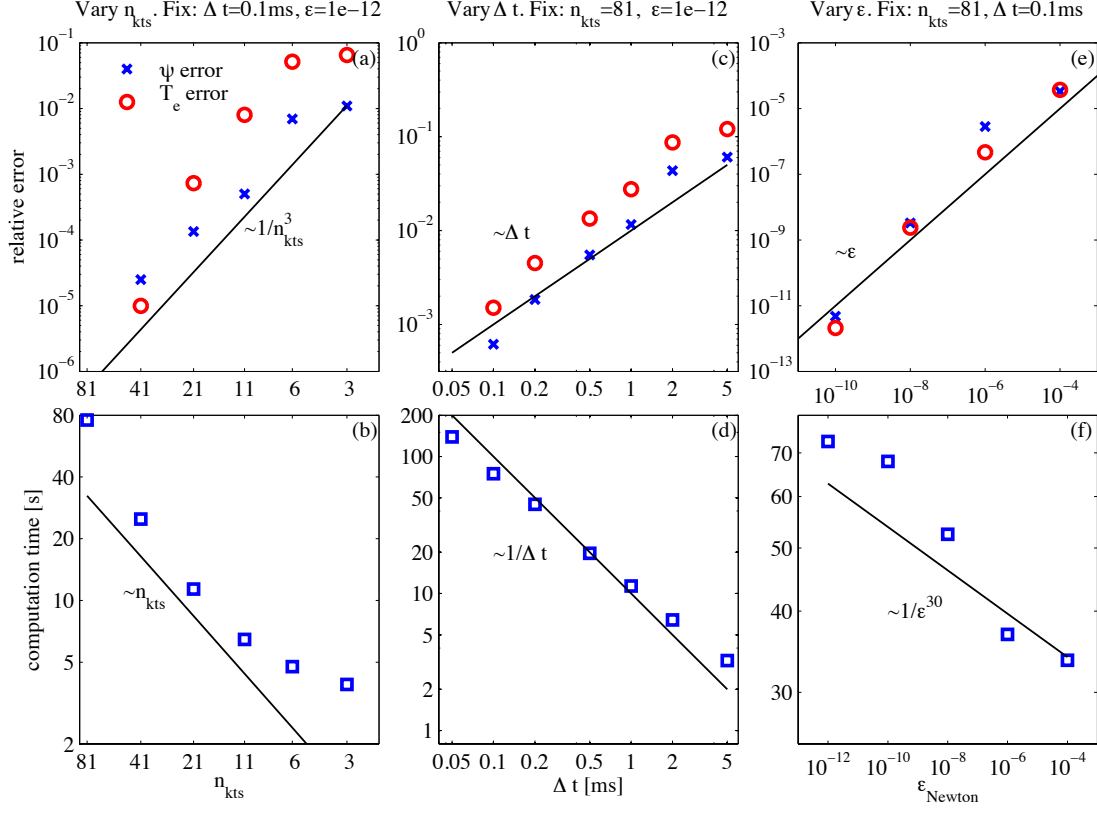


Figure D.2: Numerical convergence tests of the Predictive-RAPTOR transport simulations using backwards (implicit) Euler time integration and cubic spline finite elements. As can be expected, we see cubic convergence in the number of spatial grid points (a). Linear convergence in the time step size (b) and linear convergence with the implicit iteration tolerance (c). Computation times (for all the simulation steps, but excluding the simulation set-up) scale less than quadratically with the spatial grid size, linearly with the time step size and very weakly with the implicit iteration tolerance. These calculations were done on an Intel®Xeon(R) X5560 2.80GHz CPU, with Fedora 12 64bit LINUX, Predictive-RAPTOR implemented in MATLAB v.7.10

become:

$$J_l = \nu_l \sum_{i=1}^{n_{kts}} [W_l(\rho_i)(\mathbf{c}_l(\rho_i)\psi_M - \iota_{ref}(\rho_i))]^2 \quad (\text{D.38})$$

$$J_{ss} = \nu_{ss} \sum_{i=1}^{n_{kts}} \left[W_{ss}(\rho_i) \mathbf{c}_{\Lambda'}(\rho_i) \frac{\psi_{M+1} - \psi_M}{\Delta t} \right]^2, \quad (\text{D.39})$$

and similarly for the other terms, where $\mathbf{c}_l(\rho_i)$ and $\mathbf{c}_{\Lambda'}(\rho_i)$ are defined in (7.31), (7.32) and W_l is the weighting function appearing in (9.11)

The $\iota < \iota_{lim}$ constraint is discretized by taking a trapezoidal approximation to the integrals on ρ , resulting in

$$c_{\iota < \iota_{lim}}(t_k) = \frac{1}{2} \sum_{i=2}^{n_{kts}} (\rho_i - \rho_{i-1}) \left(\max\{0, \mathbf{c}_l^T(\rho_i) \hat{\psi}_k - \iota_{lim}\} \dots \quad (\text{D.40}) \right.$$

$$\left. + \max\{0, \mathbf{c}_l^T(\rho_{i-1}) \hat{\psi}_k - \iota_{lim}\} \right) \quad (\text{D.41})$$

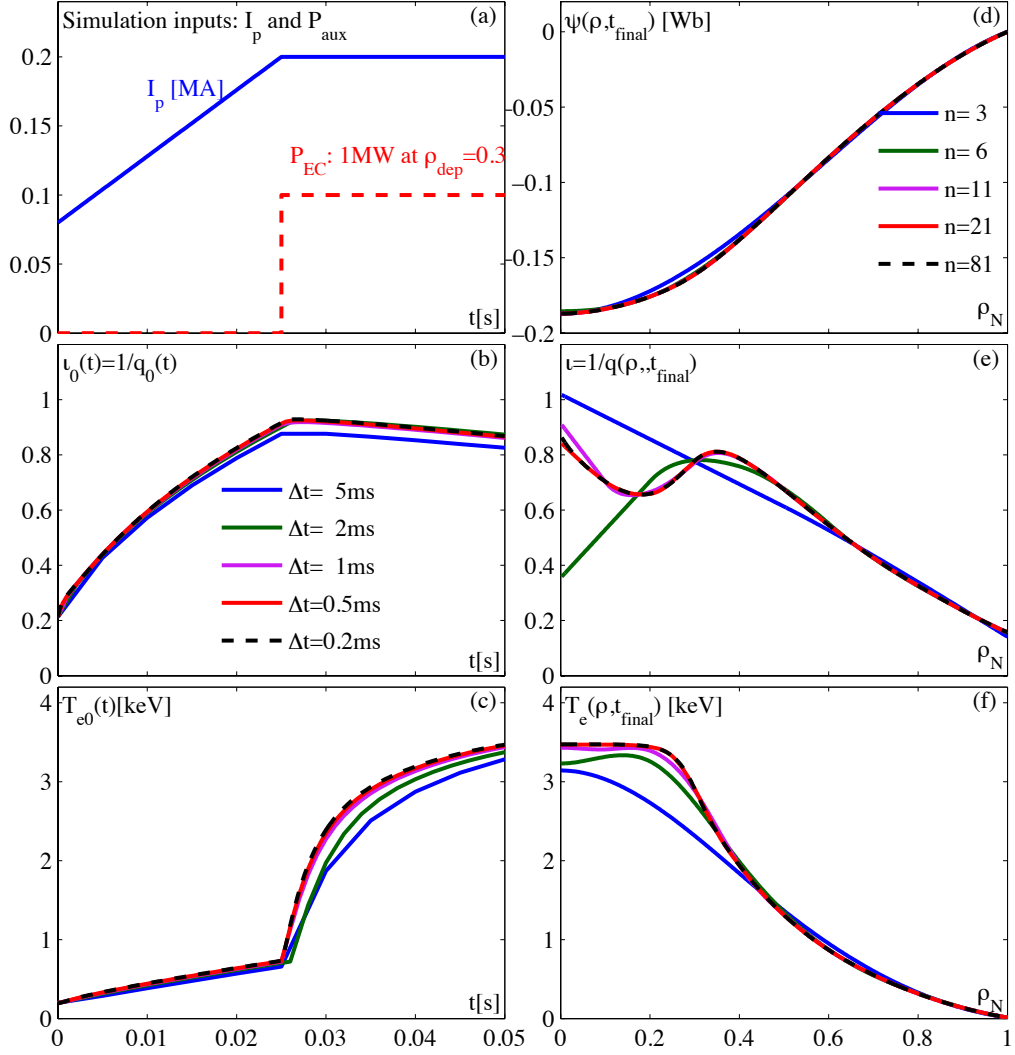


Figure D.3: Time traces and spatial profiles of benchmark simulations using Predictive-RAPTOR, investigating the profiles obtained depending on the spatial and temporal resolutions in the simulations. The time trajectories of I_p and P_{EC} are shown in (a). A first set of simulations (b,c) uses a high number of spatial points $n_{kts} = 81$ but different time resolution Δt . The time evolution of $\nu_0 = 1/q_0$ (b) and T_{e0} (c) is shown for each simulation. From (c), we can conclude that a time step of ≈ 0.5 ms is appropriate even for rapid transients. A second set of simulations (d,e,f), use a very small time grid $\Delta t = 0.1$ ms while the number of (equidistant) spatial knot points is varied. The right panels show, at the final time, the profiles of ψ (d), ν (e) and T_e (f) obtained for the various grids. This shows that one needs n_{kts} sufficiently high to correctly model the structure in the ν profile due to the localized off-axis ECCD.

$$C_{l < \nu_{lim}} = \frac{1}{2} \sum_{k=1}^M (t_k - t_{k-1}) \left([c_{l < \nu_{lim}}(t_k)]^2 + [c_{l < \nu_{lim}}(t_{k-1})]^2 \right) - \epsilon \quad (\text{D.42})$$

Similarly, the edge voltage constraint becomes

$$\frac{1}{2} \sum_{k=1}^M \left[(t_k - t_{k-1}) \left([c_{U_{pl}}(t_k)]^2 + [c_{U_{pl}}(t_{k-1})]^2 \right) \right] - \epsilon \quad (\text{D.43})$$

with

$$c_{U_{pl}}(t_k) = \max\{0, U_{pl,\min} - \mathbf{v}^T(\boldsymbol{\psi}_{k+1} - \boldsymbol{\psi}_k)/\Delta t\} \quad (\text{D.44})$$

where \mathbf{v}^T is a row vector of zeros except for the last entry which is 1. Similar expressions are used for the gradients of the state constraints (9.26),(9.27).

D.5 Importing MHD equilibria from CHEASE

The quantities J , G_1 , G_2 , $V' = \partial V/\partial \rho$ in RAPTOR, depend on the fixed 2D MHD equilibrium. They can be obtained from an MHD equilibrium code such as CHEASE (Lutjens et al. 1996). This section explains how the relevant profiles (in MKSA) are obtained from the the outputs of CHEASE (in dimensionless units).

D.5.1 CHEASE output definitions

In the CHEASE output, the following flux-surface averaged quantities are defined:

$$\{C_0, C_1, C_2, C_3\} = \oint \left\{ \frac{1}{R}, 1, \frac{1}{R^2}, \frac{|\nabla\psi|^2}{4\pi^2 R^2} \right\} \frac{d\ell_p}{B_p} \quad (\text{D.45})$$

where care must be taken for C_3 since $\psi^{ASTRA} = 2\pi\psi^{CHEASE}$. Also, CHEASE uses normalized units, where lengths are normalized by R_0 and magnetic fields by B_0 . Therefore, in MKSA, the terms read:

$$\{C_0, C_1, C_2, C_3\} = \oint \left\{ \frac{R_0}{R}, 1, \frac{R_0^2}{R^2}, \frac{|\nabla\psi|^2}{4\pi^2 B_0^2 R^2} \right\} \frac{B_0 d\ell_p}{R_0 B_p} \quad (\text{D.46})$$

or

$$\oint \left\{ \frac{1}{R}, 1, \frac{1}{R^2}, \frac{|\nabla\psi|^2}{R^2} \right\} \frac{d\ell_p}{B_p} = \left\{ \frac{C_0}{B_0}, \frac{R_0 C_1}{B_0}, \frac{C_2}{R_0 B_0}, 4\pi^2 R_0 B_0 C_3 \right\}. \quad (\text{D.47})$$

Other quantities available in CHEASE are $T(\psi)$, which is equal to J in ASTRA (since it is normalized as $T^{CHEASE} = \frac{T^{MKSA}}{R_0 B_0}$), as well as the normalized poloidal field $\langle B_p^2 \rangle = \langle B_{p,MKSA}^2 \rangle / B_0^2$.

Note that the CHEASE output contains further (redundant) quantities, which could also be used. In particular, $q = JC_2/2\pi$ and $\langle B_{p,MKSA}^2 \rangle = \mu_0 I_p(\rho) B_0 / R_0 C_1$.

D.5.2 RAPTOR quantities in terms of CHEASE outputs

The equilibrium-dependent quantities in the flux transport equation (6.26) are ρ , V' , J , G_2/J (6.27)–(6.29). These quantities will now be written in terms of $C_0, C_1, C_2, C_3, J, \langle B_p^2 \rangle$, available from CHEASE.

$$\frac{G_2}{J} = \frac{V'}{4\pi^2 J} \left\langle \left(\frac{(\nabla\rho)^2}{R^2} \right) \right\rangle \quad (\text{D.48})$$

$$= \frac{1}{4\pi^2 J} \frac{\partial V}{\partial \rho} \frac{\partial \rho}{\partial \psi} \frac{\partial \rho}{\partial \psi} \left\langle \left(\frac{(\nabla\psi)^2}{R^2} \right) \right\rangle \quad (\text{D.49})$$

$$= \frac{1}{J} \frac{\partial V}{\partial \psi} \frac{\partial \rho}{\partial \psi} \langle B_p^2 \rangle B_0^2 \quad (\text{D.50})$$

Now

$$\frac{\partial V}{\partial \psi} = \oint \frac{d\ell_p}{|B_p|} = \frac{R_0}{B_0} C_1 \quad (\text{D.51})$$

Furthermore,

$$\frac{\partial \rho}{\partial \psi} = \frac{\partial \rho}{\partial \Phi} \frac{\partial \Phi}{\partial V} \frac{\partial V}{\partial \psi} \quad (\text{D.52})$$

Using (6.23) and (6.24),

$$\frac{\partial \rho}{\partial \psi} = \frac{1}{2\pi\rho B_0} \frac{T}{2\pi} \underbrace{\left\langle \frac{1}{R^2} \right\rangle}_{=C_2/(R_0^2 C_1)} \frac{\partial V}{\partial \psi} = \frac{J C_2}{4\pi^2 \rho B_0} \quad (\text{D.53})$$

Combining the terms, we obtain

$$\frac{G_2}{J} = \frac{1}{J} \frac{C_1 R_0}{B_0} \frac{J C_2}{4\pi^2 \rho B_0} \langle B_p^2 \rangle B_0^2 \quad (\text{D.54})$$

$$= \frac{R_0}{4\pi^2 \rho} C_1 C_2 \langle B_p^2 \rangle. \quad (\text{D.55})$$

The term appearing in the current source can be rewritten as:

$$\frac{V'}{2\pi\rho} = \frac{4\pi^2 \rho}{J R_0 \langle 1/R^2 \rangle} \frac{1}{2\pi\rho} = \frac{2\pi}{J R_0} \frac{R_0^2 C_1}{C_2} = \frac{2\pi}{J} \frac{R_0 C_1}{C_2} \quad (\text{D.56})$$

We need the edge value of (non-normalized) ρ . To calculate $\rho_e = \sqrt{\frac{\Phi_e}{\pi B_0}}$, use (6.22).

$$\Phi(\psi) = \frac{1}{2\pi} \int_0^V \frac{I}{R^2} dV = \frac{I}{2\pi} \int_0^\psi \left(\oint \frac{1}{R^2} \frac{d\ell_p}{B_p} \right) d\psi = \frac{I}{2\pi R_0 B_0} \int_0^\psi C_2 d\psi \quad (\text{D.57})$$

so

$$\Phi_e = \frac{J}{2\pi} \int_0^{\psi_e} C_2 d\psi \quad (\text{D.58})$$

For the T_e equation, we require the term $G_1 = V' \langle (\nabla \rho)^2 \rangle$. This is rewritten as

$$V' \langle (\nabla \rho)^2 \rangle = \frac{\partial V}{\partial \rho} \left(\frac{\partial \rho}{\partial \psi} \right)^2 \langle (\nabla \psi)^2 \rangle = \frac{\partial V}{\partial \psi} \frac{\partial \rho}{\partial \psi} \langle (\nabla \psi)^2 \rangle \quad (\text{D.59})$$

and, using (D.51) and (D.53),

$$V' \langle (\nabla \rho)^2 \rangle = \frac{R_0 J C_1 C_2}{B_0^2 4\pi^2 \rho} \langle (\nabla \psi)^2 \rangle \quad (\text{D.60})$$

Note that $\langle (\nabla \psi)^2 \rangle = 4\pi^2 B_0^2 R_0^2 \langle (\nabla \psi)^2 \rangle_{CHEASE}$

Appendix E

TENEX: kinetic profiles from X-ray diagnostics

This appendix provides further details on the nonlinear neural-network mapping used to reconstruct profiles of \tilde{T}_e ($= T_e(\rho)/T_{e0}$) and n_e based on DMPX (soft X-ray) and FIR (line integrated density) measurements, briefly introduced in Section 8.2.1

We first build a database of several shots spanning a range of different heating conditions but similar shape. In practice, about 15 shots, corresponding to approximately 300 time points, were found sufficient as long as the heating conditions were sufficiently diverse. We collect both the post-shot processed and fitted Thomson profiles for $T_e(\rho)$ and $n_e(\rho)$ every 20ms, and the (lowpass filtered) raw data from all DMPX and FIR channels corresponding to the same time points. The data is collected into matrices, the columns of which contain data for each time point, for example

$$\mathbf{M}_{FIR} = [\mathbf{m}_{FIR}(t_1), \dots, \mathbf{m}_{FIR}(t_P)] \in \mathbb{R}^{n_d \times n_P} \quad (\text{E.1})$$

where n_P represents the total number of time points available in the database, n_d is the number of diagnostic channels and $\mathbf{m}_{FIR}(t_1)$ is the vector of acquired FIR values (one data point for each chord) at the time t_1 . Similarly we construct matrices \mathbf{M}_{DMPX} , \mathbf{M}_{n_e} and $\mathbf{M}_{\tilde{T}_e}$.

To reduce the dimensionality of the problem, the data is parametrized by writing each data vector as a sum of basis functions

$$\mathbf{m}(t_j) = \sum_{i=1}^{n_{bas}} \mathbf{b}_i d_i(t_j). \quad (\text{E.2})$$

The basis functions are determined as the minimum least-square error fit to the data by computing the singular value decomposition of each matrix and retaining the dominant n_{bas} vectors spanning the matrix column space. Typical values for n_{bas} are 3 or 4 and this number may be different for each diagnostic. Thus, each matrix can be approximated as $\mathbf{M} \approx \mathbf{B}\mathbf{D}$, where $\mathbf{B} \in \mathbb{R}^{n_d \times n_{bas}}$ is a matrix containing the first n_{bas} orthogonal singular vectors and $\mathbf{D} \in \mathbb{R}^{n_{bas} \times n_P}$ is the matrix of basis function coefficients. Now for each data vector $\mathbf{m}(t_j)$ the corresponding basis function coefficients are given by $\mathbf{d}(t_j) = \mathbf{B}^+ \mathbf{m}(t_j)$ where $\mathbf{B}^+ = (\mathbf{B}^T \mathbf{B})^{-1} \mathbf{B}^T$ denotes the pseudo-inverse of \mathbf{B} . This procedure gives us a set

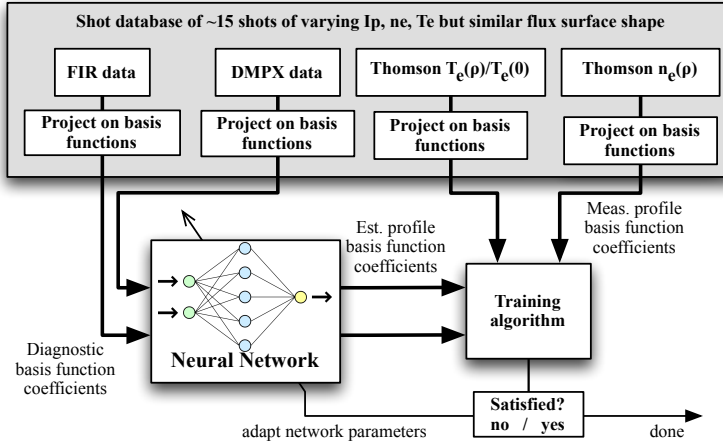


Figure E.1: Schematic representation of the training phase of the “TENEX” algorithm for determining estimates of T_e and n_e profiles from DMPX soft-X ray and FIR interferometer diagnostics. The basis function coefficients for the T_e/T_{e0} and n_e profile are the output of a Neural Network, trained on data from previous shots.

of input and output vectors

$$\mathbf{d}_{in}(t_j) = \begin{bmatrix} \mathbf{d}_{FIR}(t_j) \\ \mathbf{d}_{DMPX}(t_j) \end{bmatrix} \in \mathbb{R}^{2n_{bas}}, \quad \mathbf{d}_{out}(t_j) = \begin{bmatrix} \mathbf{d}_{n_e}(t_j) \\ \mathbf{d}_{T_e}(t_j) \end{bmatrix} \in \mathbb{R}^{2n_{bas}} \quad (\text{E.3})$$

$\forall j \in [1, \dots, n_p]$ (Time points in the database). We now attempt to find the nonlinear mapping $\mathcal{N} : \mathbb{R}^{2n_{bas}} \rightarrow \mathbb{R}^{2n_{bas}}$ such that $\sum_j \|\mathbf{d}_{out}(t_j) - \mathcal{N}(\mathbf{d}_{in}(t_j))\|_2^2$ is minimized. For \mathcal{N} we use a neural network which is trained on the available data set using standard techniques (Haykin 1999) such as the Levenberg-Marquardt optimization algorithm, separating the data set into training, validation and test samples with suitable stopping criteria based on the validation set to avoid over-fitting. Once the neural network parameters have been optimized the network can be used to map a fresh input set of real-time DMPX and FIR measurements to estimated profiles of $n_e(\rho)$ and $\tilde{T}_e(\rho) = T_e(\rho)/T_{e0}$ profile. The overall method is illustrated schematically in Figure E.1.

Acknowledgements

I could not have wished for better thesis supervisors than Tim Goodman and Olivier Sauter. While popular literature characterizes typical PhD supervisors as heartless monsters with no regard for their students, I could trust in the constant support and encouragement from not one, but two excellent supervisors. Bending a fanatic control engineer into a plasma physicist must not have been an easy task, but in end I am glad we walked down this physics path. As a control engineer, *and* soon-to-be physicist, I finally understand that the truth is in the middle and we need the best of both worlds to move ahead. I would not have gotten here without you both. And not only are you the best supervisors in the world, you are also great mentors, colleagues and friends. Thank you for pointing me in the right direction whenever I risked getting lost. Thank you for letting me stray off the beaten path to explore the forests containing rapacious dinosaurs. Thank you for that constantly open door, for the willingness to discuss anything at any time, for your patience, your support and encouragement when I needed it most.

I also owe a debt of gratitude to the outstanding work of my friend and colleague James Paley, who built the new TCV real-time control system. Without his work, none of the experimental results shown in this thesis would have been obtained. It was a pleasure working with you the first few years and I truly missed our collaboration in the final phases.

It is an absolute privilege to have been allowed so much operating time on a fantastic machine like TCV. The things I have learned here I could not have learned elsewhere, and I am grateful to the CRPP for trust placed upon this young and naïve student. I am also grateful to not have been caned upon misplacing a couple of megajoules of microwave energy, or rattling the steering mirror mechanisms a bit more than strictly necessary.

I also take this opportunity to thank everyone in and around the control room: the Pilots (PF, Karpushov, Yanis, Ugo), all the PdJs, DDJs, GdJs (in particular Miguel) and Xavier Llobet, but also all the engineers and technicians (I mention Pascal and Claude, but the complete list is much longer) for the tremendous work maintaining and running TCV. Without your efforts, nothing would be possible.

I have learnt much from the excellent physicists on the TCV team, in particular (but not only) Stefano Coda, Basil Duval and Jean-Marc Moret. I have also greatly benefited from discussions with many other CRPP scientists and staff, in particular Jo Lister, Stefano Alberti, Jonathan Graves, Tony Cooper, Xavier Llobet, Stephan Brunner, Philippe Marmillod and Trach-Minh Tran. For the RAPTOR work, I received valuable help from G. Rozza and A. Manzoni of CMCS/EPFL, Philippe Müllhaupt, G. François and S. Willson of LA/EPFL.

I would also like to warmly thank T. Shimozuma, S. Kubo, Y. Yoshimura, T. Mutoh

and all the other friends at NIFS in Japan for the unforgettable experience during our collaboration. It was an honor and pleasure to collaborate with your team and work on such an amazing device as LHD.

The teaching duties have been a welcome distraction, and I have enjoyed the interaction with students while myself learning more and more every year. I am grateful to Dr. S. Alberti, Prof. A. Fasoli and Prof. M.Q. Tran for having me as teaching assistant in their courses. Thanks to the CRPP secretariat, in particular to Edith, Séverine and Heidi, for all the help and support.

I also thank the CRPP steering committee for accepting my candidacy as a PhD student, and Stefano Coda in particular for replying to that application e-mail just in time. I thank my thesis examination committee, especially Prof. H. Zohm. and Dr. E. Joffrin who came to Lausanne to provide their judgement.

It would have not been the same without my friends and colleague PhD students who have accompanied me on this journey: Mattia, Loïc, Kees, David W., Alice, Silvia, Theo, Andreas, Janos, Martin, Silvano, Francesco, Thibaut, Jonathan, Christian T., Karim, Lucia. Thankfully we were well-introduced into the tricks of the trade by past generations of students: Costanza, Ale B., Ale M., Seb, Xavier, Barbora, Nicolas, Christian Schlatter, Emiliano, Sun-hee. And now we gladly pass the gauntlet to the new generation: Doohyun, Annamaria, Josef, Fabio, Daniele, Wubie, Joaquim, David P. But let us not forget postdocs of past and present: with people like Wouter and Bao, TCV is in good hands.

All work and no play makes F a dull boy, and oh have we played: Mattia, GP, Ale, Marzia, Ludo, Gigi, Claudia, thanks for being my extended family in Lausanne, I hope this is just the beginning. Thanks to co-immigrants from Delft: Martijn and Kees, my landmarks in the midst of changing winds. Un grand merci aussi à mes amis suisses, en particulier les amis du CjL: pour moi, la Suisse, c'est vous. Gli amici da sempre: Gabo, Pazzo, Aldo e gli altri monumenti che sono la mia Punta Ala. Mijn vrienden in Nederland, teveel om hier op te noemen, maar jullie weten wie jullie zijn. E naturalmente la mia famiglia, mia madre, mio papà e mio fratello.

Finally, thanks to the Punta Ala Sbrock Project, Jalapeño Project, Randall Munroe, Nicholas Gurewitch, Dick Valentine, Virgilio Savona, Stefano Belisari, Guy-Manuel de Homem-Christo and Thomas Bangalter, Jan Lundgren, Antony Hegarthy, the Casady sisters, Steve Jobs and Mark Zuckerberg and other artists for providing the necessary creative input to keep me running.

Lausanne, 18th October 2011

Glossary

| | |
|--|---|
| CRPP | Centre des Recherches en Physique des Plasmas |
| DMPX | see MPX |
| ECCD | Electron Cyclotron Current Drive |
| EC(R)H | Electron Cyclotron (Resonance) Heating |
| ELM | Edge Localized Mode |
| $(\cdot)_{\text{FF}}$ or $(\cdot)_{\text{ff}}$ | feedforward |
| FIR | Far InfraRed interferometer |
| H-mode | High confinement mode |
| HFS | High field side |
| ICRH | Ion Cyclotron Resonance Heating |
| IOH | Ohmic coil current control mode |
| ITER | “The Way” in Latin. International tokamak experiment under construction in Cadarache, France (formerly: acronym for International Thermonuclear Experimental Reactor) |
| LFS | Low Field Side |
| l.h.s | Left hand side |
| LIUQE | TCV offline equilibrium reconstruction code (EQUIL spelt in reverse) |
| MCF | Magnetically Confined Fusion |
| MPX | (Duplex) Multi-wire Proportional X-ray diagnostic (also known as DMPX) |
| NBI | Neutral Beam Injector/Injection |
| NTM | Neoclassical Tearing Mode |
| OH | Ohmic |
| PLL | Phase Locked Loop |
| PF | Poloidal field |
| RAPTOR | RApid Plasma Transport Simulator |
| r.h.s | Right hand side |
| SCD | Système de Contrôle Distribué (TCV distributed digital real-time control system) |
| TCV | Tokamak à Configuration Variable |
| TF | Toroidal field |

Bibliography

- Albajar, F. et al. (2005). “Importance of electron cyclotron wave energy transport in ITER.” In: *Nuclear Fusion* 45.7, p. 642. URL: <http://stacks.iop.org/0029-5515/45/i=7/a=012>.
- Alberti, S. et al. (2005). “Third-harmonic, top-launch, ECRH experiments on TCV tokamak.” In: *Nuclear Fusion* 45.11, pp. 1224–1231. URL: <http://stacks.iop.org/0029-5515/45/1224>.
- Alberti, S. et al. (2011). “THz-Instrumentation development for gyrotron-DNP applications: from source to sample.” In: *Third International Symposium on Dynamic Nuclear Polarization*. EPFL, Lausanne, Switzerland.
- Ambrosino, G. and R. Albanese (2005). “Magnetic control of plasma current, position, and shape in Tokamaks: a survey or modeling and control approaches.” In: *Control Systems, IEEE* 25.5, pp. 76–92. ISSN: 1066-033X. DOI: 10.1109/MCS.2005.1512797.
- Anderson, B.D.O. and J.B. Moore (1979). *Optimal filtering*. Mineola, NY (USA): Dover Publications.
- Angioni, C. et al. (Feb. 2002). “Neutral beam stabilization of sawtooth oscillations in JET.” In: *Plasma Physics and Controlled Fusion* 44, pp. 205–222. DOI: 10.1088/0741-3335/44/2/305.
- Angioni, C. et al. (2003). “Effects of localized electron heating and current drive on the sawtooth period.” In: *Nuclear Fusion* 43.6, pp. 455–468. URL: <http://stacks.iop.org/0029-5515/43/455>.
- Ariola, M. and A. Pironti (2008). *Magnetic Control of Tokamak Plasmas*. Springer.
- Artaud, J.F. et al. (2010). “The CRONOS suite of codes for integrated tokamak modelling.” In: *Nuclear Fusion* 50.4, p. 043001. URL: <http://stacks.iop.org/0029-5515/50/i=4/a=043001>.
- Artsimovich, L.A. (1972). “Tokamak devices.” In: *Nuclear Fusion* 12.2, p. 215. URL: <http://stacks.iop.org/0029-5515/12/i=2/a=012>.
- Åstrom, Karl J. and Björn Wittenmark (1997). *Computer-Controlled Systems: theory and design*. third. Upper Saddle River, New Jersey: Prentice Hall.
- Barana, O. et al. (2007). “Integration of advanced feedback control techniques on Tore Supra.” In: *Fusion Engineering and Design* 82.5-14. Proceedings of the 24th Symposium on Fusion Technology - SOFT-24, pp. 1023–1029. ISSN: 0920-3796. DOI: DOI:10.1016/j.fusengdes.2007.05.054. URL: <http://www.sciencedirect.com/science/article/pii/S0920379607002852>.
- Barry, S., C. Nieswand, and S.L. Prunty (1997). “Far-infrared polarimetry on the TCV tokamak.” In: *Proceedings of the 8th international symposium on Laser-aided Plasma Diagnostics (LAPD-8)*. Doorwerth, The Netherlands.

BIBLIOGRAPHY

- Barton, J. E. et al. (Nov. 2010). “Closed-Loop Simulation of Model-Based Current Profile Control with the DIII-D Plasma Control System.” In: *APS Meeting Abstracts*, 9051P–+.
- Berkel, M. van et al. (2011). “Real-time wavelet detection of crashes in limit cycles of non-stationary fusion plasmas.” In: *Fusion Engineering and Design* In Press, Corrected Proof, pp. –. ISSN: 0920-3796. DOI: DOI:10.1016/j.fusengdes.2011.07.002. URL: <http://www.sciencedirect.com/science/article/pii/S0920379611005084>.
- Berrino, J. et al. (2005). “Electron cyclotron emission temperature fluctuations associated with magnetic islands and real-time identification and control system.” In: *Nuclear Fusion* 45.11, pp. 1350–1361. URL: <http://stacks.iop.org/0029-5515/45/1350>.
- Blanchard, P et al. (2002). “High field side measurements of non-thermal electron cyclotron emission on TCV plasmas with ECH and ECCD.” In: *Plasma Physics and Controlled Fusion* 44.10, p. 2231. URL: <http://stacks.iop.org/0741-3335/44/i=10/a=310>.
- Blum, J. (1989). *Numerical Simulation and Optimal Control in Plasma Physics with Applications to Tokamaks*. Series in Modern Applied Mathematics. Paris: Wiley Gauthier-Villars.
- Blum, J, C Boulbe, and B Faugeras (2008). “Real-time plasma equilibrium reconstruction in a Tokamak.” In: *Journal of Physics: Conference Series* 135.1, p. 012019. URL: <http://stacks.iop.org/1742-6596/135/i=1/a=012019>.
- Boozer, Allen H. (1998). “What is a stellarator?” In: 5.5, pp. 1647–1655. ISSN: 1070664X. DOI: DOI:10.1063/1.872833. URL: <http://dx.doi.org/doi/10.1063/1.872833>.
- Bortolon, A. et al. (Dec. 2006). “Observation of Spontaneous Toroidal Rotation Inversion in Ohmically Heated Tokamak Plasmas.” In: *Physical Review Letters* 97.23, pp. 235003–+. DOI: 10.1103/PhysRevLett.97.235003.
- Breslau, J.A. et al. (2011). “Onset and saturation of a non-resonant internal mode in NSTX and implications for AT modes in ITER.” In: *Nuclear Fusion* 51.6, p. 063027. URL: <http://stacks.iop.org/0029-5515/51/i=6/a=063027>.
- Bryson, Arthur E. and Yu-Chi Ho (1975). *Applied Optimal Control*. New York: Taylor & Francis.
- Budny, R.V. et al. (2008). “Predictions of H-mode performance in ITER.” In: *Nuclear Fusion* 48.7, p. 075005. URL: <http://stacks.iop.org/0029-5515/48/i=7/a=075005>.
- Burckhart, A et al. (2010). “Inter-ELM behaviour of the electron density and temperature pedestal in ASDEX Upgrade.” In: *Plasma Physics and Controlled Fusion* 52.10, p. 105010. URL: <http://stacks.iop.org/0741-3335/52/i=10/a=105010>.
- Burdakov, A V, A A Ivanov, and E P Kruglyakov (2010). “Modern magnetic mirrors and their fusion prospects.” In: *Plasma Physics and Controlled Fusion* 52.12, p. 124026. URL: <http://stacks.iop.org/0741-3335/52/i=12/a=124026>.
- Buttery, R. J. et al. (2002). “Neoclassical Tearing Physics in the Spherical Tokamak MAST.” In: *Phys. Rev. Lett.* 88.12, p. 125005. DOI: 10.1103/PhysRevLett.88.125005.
- Cacuci, Dan G. (1981). “Sensitivity theory for nonlinear systems. I. Nonlinear functional analysis approach.” In: *Journal of Mathematical Physics* 22.12, pp. 2794–2802. DOI: 10.1063/1.525186. URL: <http://link.aip.org/link/?JMP/22/2794/1>.
- Callen, D. et al. (1987). In: *Plasma Physics and Controlled Nuclear Fusion Research*. Vol. 2. Kyoto, Japan: IAEA, Vienna, p. 157.

- Camenen, Y. et al. (2007a). “Current profile tailoring using localized electron cyclotron heating in highly elongated TCV plasmas.” In: *Nuclear Fusion* 47, p. 586. DOI: 10.1088/0029-5515/47/7/010.
- Camenen, Y. et al. (2007b). “Impact of plasma triangularity and collisionality on electron heat transport in TCV L-mode plasmas.” In: *Nuclear Fusion* 47.7, pp. 510–516. URL: <http://stacks.iop.org/0029-5515/47/510>.
- Camenen, Y. et al. (Dec. 2010). “Experimental demonstration of an up-down asymmetry effect on intrinsic rotation in the TCV tokamak.” In: *Plasma Physics and Controlled Fusion* 52.12, pp. 124037–+. DOI: 10.1088/0741-3335/52/12/124037.
- Canal, Gustavo (2011). “Coupling Between Sawteeth and Tearing Modes in TCV.” In: *38th EPS Conference on Plasma Physics, 27 June - 1 July, Strasbourg, France*.
- Carrera, R., R. D. Hazeltine, and M. Kotschenreuther (Apr. 1986). “Island bootstrap current modification of the nonlinear dynamics of the tearing mode.” In: *Physics of Fluids* 29, pp. 899–902. DOI: 10.1063/1.865682.
- Chapman, I T (2011). “Controlling sawtooth oscillations in tokamak plasmas.” In: *Plasma Physics and Controlled Fusion* 53.1, p. 013001. URL: <http://stacks.iop.org/0741-3335/53/i=1/a=013001>.
- Chapman, I T et al. (2007). “The physics of sawtooth stabilization.” In: *Plasma Physics and Controlled Fusion* 49.12B, B385. URL: <http://stacks.iop.org/0741-3335/49/i=12B/a=S35>.
- Chapman, I. T. et al. (Oct. 2010). “Empirical scaling of sawtooth period for onset of neoclassical tearing modes.” In: *Nuclear Fusion* 50.10, pp. 102001–+. DOI: 10.1088/0029-5515/50/10/102001.
- Chu, M S and M Okabayashi (2010). “Stabilization of the external kink and the resistive wall mode.” In: *Plasma Physics and Controlled Fusion* 52.12, p. 123001. URL: <http://stacks.iop.org/0741-3335/52/i=12/a=123001>.
- Cirant, S. et al. (2006). “Modulated ECCD experiments on TCV.” In: *21th IAEA Fusion Energy Conference*. Paper EX/P3-3. Chengdu, China. URL: <http://www-pub.iaea.org/MTCD/Meetings/Announcements.asp?ConfID=149>, <http://crpplocal.epfl.ch/pinboard/papers/068011201.pdf>.
- Coda, S et al. (2000). “High-power ECH and fully non-inductive operation with ECCD in the TCV tokamak.” In: *Plasma Physics and Controlled Fusion* 42.12B, B311–B321. URL: <http://stacks.iop.org/0741-3335/42/B311>.
- Coda, S. et al. (2003). “Electron cyclotron current drive and suprathreshold electron dynamics in the TCV tokamak.” In: *Nuclear Fusion* 43.11, pp. 1361–1370. URL: <http://stacks.iop.org/0029-5515/43/1361>.
- Coda, S. et al. (2007). “The physics of electron internal transport barriers in the TCV tokamak.” In: *Nuclear Fusion* 47.7, pp. 714–720. URL: <http://stacks.iop.org/0029-5515/47/714>.
- Coda, S. et al. (2008). “Fully Bootstrap Discharge Sustainment in Steady State in the TCV Tokamak.” In: *IAEA Conference 2008*. Geneva, Switzerland, EX/2–3.
- Coda, S. and the TCV Team (2010). “Progress and Scientific Results in the TCV Tokamak.” In: *23rd IAEA Fusion Energy Conference*. Daejeon, Korea.
- Connor, J.W. et al. (2004). “A review of internal transport barrier physics for steady-state operation of tokamaks.” In: *Nuclear Fusion* 44.4, R1. URL: <http://stacks.iop.org/0029-5515/44/i=4/a=R01>.

BIBLIOGRAPHY

- Crotinger, J.A. et al. (1997). *UCRL-ID-126284*. Tech. rep. LLNL.
- de Boor, C. (2001). *A Practical Guide to Splines*. Vol. 27. Applied Mathematical Science. Springer-Verlag, New York.
- De Lazzari, D. and E. Westerhof (2009). “On the merits of heating and current drive for tearing mode stabilization.” In: *Nuclear Fusion* 49.7, 075002 (8pp). URL: <http://stacks.iop.org/0029-5515/49/075002>.
- de Vries, P. C. et al. (May 2011). “Survey of disruption causes at JET.” In: *Nuclear Fusion* 51.5, pp. 053018–+. DOI: 10.1088/0029-5515/51/5/053018.
- Decker, J and Y Peysson (2004). *Report EUR-CEA-FC-1736*. Tech. rep. Euratom-CEA.
- Degeling, A. W. et al. (June 2003a). “ELM Dynamics in TCV H-modes.” In: *Plasma Physics*. Ed. by I. S. Falconer, R. L. Dewar, & J. Khachan. Vol. 669. American Institute of Physics Conference Series, pp. 223–227. DOI: 10.1063/1.1593906.
- Degeling, A. W. et al. (Sept. 2003b). “Magnetic triggering of ELMs in TCV.” In: *Plasma Physics and Controlled Fusion* 45, pp. 1637–1655. DOI: 10.1088/0741-3335/45/9/306.
- Donaldson, T. P. (Dec. 1978). “Theory of foil-absorption techniques for plasma X-ray continuum measurements.” In: *Plasma Physics* 20, pp. 1279–1289. DOI: 10.1088/0032-1028/20/12/005.
- Doyle, E.J. et al. (2007). “Chapter 2: Plasma confinement and transport.” In: *Nuclear Fusion* 47.6, S18. URL: <http://stacks.iop.org/0029-5515/47/i=6/a=S02>.
- Duval, B. P. et al. (2010). “Momentum Transport in TCV Across Sawteeth Events.” In: *23rd IAEA Fusion Energy Conference*. Daejeon, Korea.
- Erba, M. et al. (1998). “Validation of a new mixed Bohm/gyro-Bohm model for electron and ion heat transport against the ITER, Tore Supra and START database discharges.” In: *Nuclear Fusion* 38.7, p. 1013. URL: <http://stacks.iop.org/0029-5515/38/i=7/a=305>.
- Esposito, B. et al. (2011). “Avoidance of disruptions at high β_N in ASDEX Upgrade with off-axis ECRH.” In: *Nuclear Fusion* 51.8, p. 083051. URL: <http://stacks.iop.org/0029-5515/51/i=8/a=083051>.
- Evans, T. E. et al. (June 2004). “Suppression of Large Edge-Localized Modes in High-Confinement DIII-D Plasmas with a Stochastic Magnetic Boundary.” In: *Physical Review Letters* 92.23, pp. 235003–+. DOI: 10.1103/PhysRevLett.92.235003.
- Fable, E et al. (2006). “Inward thermodiffusive particle pinch in electron internal transport barriers in TCV.” In: *Plasma Physics and Controlled Fusion* 48.9, p. 1271. URL: <http://stacks.iop.org/0741-3335/48/i=9/a=001>.
- Farina, D (2005). *GRAY: a quasi-optical ray tracing code for electron cyclotron absorption and current drive in tokamaks [PDF] from cnr.it*. Tech. rep. IFP-CNR Internal Report FP.
- Favez, J-Y et al. (2005). “Improving tokamak vertical position control in the presence of power supply voltage saturation.” In: *Plasma Physics and Controlled Fusion* 47.10, p. 1709. URL: <http://stacks.iop.org/0741-3335/47/i=10/a=008>.
- Felici, F. (2011). *ECPOL: an object-oriented ECH polarization propagation code*. Tech. rep. CRPP.
- Felici, F. et al. (2009a). “Real-time feedback control of millimeter-wave polarization for LHD.” In: *Review of Scientific Instruments* 80.1, p. 013504. DOI: 10.1063/1.3073735.

- Felici, F. et al. (2009b). “Self-consistent simulation of tearing modes during ECCD experiments on TCV.” In: *36th EPS Conference on Plasma Physics, Sofia, Bulgaria, 29 June - 03 July*.
- Felici, F. et al. (Oct. 2010a). “Feedback control of ECRH polarization on LHD.” In: *Nuclear Fusion* 50.10, pp. 105003–+. DOI: 10.1088/0029-5515/50/10/105003.
- Felici, F. et al. (Nov. 2010b). “RAPTOR: Optimization, real-time simulation and control of the tokamak q profile evolution using a simplified transport model.” In: *APS Meeting Abstracts*, 9090P–+.
- Felici, F. and O. Sauter (2011). “Nonlinear model-based optimization of actuator trajectories for tokamak plasma profile control.” In: *Submitted to Plasma Physics and Controlled Fusion*.
- Felici, F. et al. (2011a). “Optimization, real-time simulation and feedback control of tokamak plasma profiles on TCV.” In: *38th EPS Conference on Plasma Physics, 27 June - 1 July, Strasbourg, France*.
- Felici, F. et al. (2011b). “Real-time physics-model-based simulation of the current density profile in tokamak plasmas.” In: *Nuclear Fusion* 51.8, p. 083052. URL: <http://stacks.iop.org/0029-5515/51/i=8/a=083052>.
- Felton, R. et al. (2005). “Real-time measurement and control at JET experiment control.” In: *Fusion Engineering and Design* 74.1-4. Proceedings of the 23rd Symposium of Fusion Technology - SOFT 23, pp. 561–566. ISSN: 0920-3796. DOI: DOI:10.1016/j.fusengdes.2005.06.286. URL: <http://www.sciencedirect.com/science/article/pii/S0920379605003352>.
- Ferron, J.R. et al. (1998). “Real time equilibrium reconstruction for tokamak discharge control.” In: *Nuclear Fusion* 38.7, p. 1055. URL: <http://stacks.iop.org/0029-5515/38/i=7/a=308>.
- Ferron, J.R. et al. (2006). “Feedback control of the safety factor profile evolution during formation of an advanced tokamak discharge.” In: *Nuclear Fusion* 46, p. L13. DOI: 10.1088/0029-5515/46/10/L01.
- Firestone, M.A. and C.E. Kessel (1991a). “Electromagnetic And Kinetic Control Of A Tokamak Reactor.” In: *Plasma Science, 1991. IEEE Conference Record - Abstracts., 1991 IEEE International Conference on*, pp. 193–194. DOI: 10.1109/PLASMA.1991.695738.
- (1991b). “Plasma kinetic control in a tokamak.” In: *Plasma Science, IEEE Transactions on* 19.1, pp. 29–41. ISSN: 0093-3813. DOI: 10.1109/27.62364.
- Fitzpatrick, Richard (1995). “Helical temperature perturbations associated with tearing modes in tokamak plasmas.” In: *Physics of Plasmas* 2.3, pp. 825–838.
- Franke, Stefan (1997). “Application of Thomson scattering at 1.06mm as a diagnostic for spatial profile measurements of electron temperature and density on the TCV tokamak.” PhD thesis. Lausanne, Switzerland: EPFL.
- Franklin, Gene F and J. David Powell (2002). *Feedback control of dynamic systems*. fourth. Upper Saddle River, New Jersey: Prentice Hall.
- Friedberg, Jeffrey P. (1987). *Ideal Magnetohydrodynamics*. Modern perspectives in energy. 233 Spring Street, New York: Plenum Press. ISBN: 0-306-42512-2.
- Fujita, T. et al. (2001). “Quasisteady High-Confinement Reversed Shear Plasma with Large Bootstrap Current Fraction under Full Noninductive Current Drive Condition in JT-60U.” In: *Phys. Rev. Lett.* 87.8, p. 085001. DOI: 10.1103/PhysRevLett.87.085001.

BIBLIOGRAPHY

- Fujita, T. and the JT-60 team (2006). “Steady state operation research in JT-60U with extended pulse length.” In: *Nuclear Fusion* 46.3, S3. URL: <http://stacks.iop.org/0029-5515/46/i=3/a=S02>.
- Fujita, Takaaki (2010). “Tokamak equilibria with nearly zero central current: the current hole.” In: *Nuclear Fusion* 50.11, p. 113001. URL: <http://stacks.iop.org/0029-5515/50/i=11/a=113001>.
- Furth, Harold P., John Killeen, and Marshall N. Rosenbluth (1963). “Finite-Resistivity Instabilities of a Sheet Pinch.” In: *Physics of Fluids* 6.4, pp. 459–484. DOI: 10.1063/1.1706761. URL: <http://link.aip.org/link/?PFL/6/459/1>.
- Furth, H.P., P.H. Rutherford, and H. Selberg (1973). “Tearing mode in the cylindrical tokamak.” In: *The Physics of Fluids* 16.7, pp. 1054–1063.
- Gantenbein, G. et al. (2000). “Complete Suppression of Neoclassical Tearing Modes with Current Drive at the Electron-Cyclotron-Resonance Frequency in ASDEX Upgrade Tokamak.” In: *Phys. Rev. Lett.* 85.6, pp. 1242–1245. DOI: 10.1103/PhysRevLett.85.1242.
- Garcia, J. and G. Giruzzi (May 2010). “Critical Behavior of Magnetically Confined Plasma Regimes.” In: *Physical Review Letters* 104.20, pp. 205003–+. DOI: 10.1103/PhysRevLett.104.205003.
- Genacchi, G. and A. Taroni (1988). *JETTO: a free boundary plasma transport code*. RT/TIB 5. ENEA.
- Glasser, A. H., J. M. Greene, and J. L. Johnson (1975). “Resistive instabilities in general toroidal plasma configurations.” In: *Physics of Fluids* 18.7, pp. 875–888. DOI: 10.1063/1.861224. URL: <http://link.aip.org/link/?PFL/18/875/1>.
- Goedbloed, J.P. and S. Poedts (2004). *Principles of Magnetohydrodynamics; with Applications to Laboratory and Astrophysical Plasmas*. Cambridge: Cambridge University Press.
- Goedbloed, J.P., R. Keppens, and S. Poedts (2010). *Advanced Magnetohydrodynamics; with Applications to Laboratory and Astrophysical Plasmas*. Cambridge: Cambridge University Press.
- Goeler, S. von, W. Stodiek, and N. Sauthoff (1974). “Studies of Internal Disruptions and $m = 1$ Oscillations in Tokamak Discharges with Soft—X-Ray Techniques.” In: *Phys. Rev. Lett.* 33.20, pp. 1201–1203. DOI: 10.1103/PhysRevLett.33.1201.
- Golub, Gene H. and Charles F. Van Loan (1996). *Matrix Computations*. ISBN: 0-8018-5413-X. London, UK: The Johns Hopkins University Press.
- Goodman, T P et al. (2005). “Safety factor profile requirements for electron ITB formation in TCV.” In: *Plasma Physics and Controlled Fusion* 47.12B, B107–B120. URL: <http://stacks.iop.org/0741-3335/47/B107>.
- Goodman, T. P. and the TCV team (May 2008). “Experience in integrated control of the multi-megawatt electron cyclotron heating system on the TCV tokamak: the first decade.” In: *Nuclear Fusion* 48.5, pp. 054011–+. DOI: 10.1088/0029-5515/48/5/054011.
- Goodman, T. P. et al. (2008). “First measurements of oblique ECE with a real-time movable line of sight on TCV.” In: *FUSION SCIENCE AND TECHNOLOGY* 53.1. 14th Joint Workshop on Electron Cyclotron Emission and Electron Cyclotron Resonance Heating, Santorini, GREECE, MAY 09-12, 2006, 196–207. ISSN: 1536-1055.

- Goodman, T. P. et al. (June 2011). “Sawtooth Pacing by Real-Time Auxiliary Power Control in a Tokamak Plasma.” In: *Physical Review Letters* 106.24, pp. 245002–+. DOI: 10.1103/PhysRevLett.106.245002.
- Goodman, T.P. et al. (2007). “Co- and Counter - viewing oblique ECE measurements during ECH and ECCD on the TCV tokamak.” In: *34th EPS Conference on Plasma Physics, Warsaw Congress Centre, Poland, 02 July 2007*.
- Gormezano, C et al. (2004). “Hybrid advanced scenarios: perspectives for ITER and new experiments with dominant RF heating.” In: *Plasma Physics and Controlled Fusion* 46.12B, B435. URL: <http://stacks.iop.org/0741-3335/46/i=12B/a=037>.
- Gormezano, C. et al. (2007). “Chapter 6: Steady state operation.” In: *Nuclear Fusion* 47.6, S285. URL: <http://stacks.iop.org/0029-5515/47/i=6/a=S06>.
- Grad, H. and H. Rubin (1958). “Hydromagnetic Equilibria and Force-Free Fields.” In: *Proceedings of the 2nd UN Conf. on the Peaceful Uses of Atomic Energy*. Vol. 31. IAEA. Geneva, p. 190.
- Graves, J P et al. (2005). “Sawtooth control in fusion plasmas.” In: *Plasma Physics and Controlled Fusion* 47.12B, B121–B133. URL: <http://stacks.iop.org/0741-3335/47/B121>.
- Graves, J. P. et al. (2009). “Sawtooth-Control Mechanism using Toroidally Propagating Ion-Cyclotron-Resonance Waves in Tokamaks.” In: *Phys. Rev. Lett.* 102.6, p. 065005. DOI: 10.1103/PhysRevLett.102.065005.
- Grigorenko, Ilya (2006). *Optimal Control And Forecasting of Complex Dynamical Systems*. World Scientific Publishing Company.
- Hammett, Gregory W. and Francis W. Perkins (1990). “Fluid moment models for Landau damping with application to the ion-temperature-gradient instability.” In: *Phys. Rev. Lett.* 64.25, pp. 3019–3022. DOI: 10.1103/PhysRevLett.64.3019.
- Harvey, R. W. et al. (May 2002). “Radial Transport and Electron-Cyclotron-Current Drive in the TCV and DIII-D Tokamaks.” In: *Physical Review Letters* 88.20, pp. 205001–+. DOI: 10.1103/PhysRevLett.88.205001.
- Hawryluk, R J (1980). In: *Physics of Plasmas Close to Thermonuclear Conditions*. Ed. by B. Coppi. Vol. 1, p. 19.
- Haykin, S. (1999). *Neural Networks: A Comprehensive Foundation, second edition*. Second. Upper Saddle River, New Jersey: Prentice Hall.
- Hegna, C. C. (1998). “The physics of neoclassical magnetohydrodynamic tearing modes.” In: *Physics of Plasmas* 5.5, pp. 1767–1774. DOI: 10.1063/1.872846. URL: <http://link.aip.org/link/?PHP/5/1767/1>.
- Hender, T.C. et al. (2007). “Chapter 3: MHD stability, operational limits and disruptions.” In: *Nuclear Fusion* 47.6, S128–S202. URL: <http://stacks.iop.org/0029-5515/47/S128>.
- Henderson, M. A. et al. (2004). “Rapid and Localized Electron Internal-Transport-Barrier Formation During Shear Inversion in Fully Noninductive TCV Discharges.” In: *Physical Review Letters* 93.21, 215001, p. 215001. DOI: 10.1103/PhysRevLett.93.215001. URL: <http://link.aps.org/abstract/PRL/v93/e215001>.
- Hennen, B A et al. (2010). “Real-time control of tearing modes using a line-of-sight electron cyclotron emission diagnostic.” In: *Plasma Physics and Controlled Fusion* 52.10, p. 104006. URL: <http://stacks.iop.org/0741-3335/52/i=10/a=104006>.

BIBLIOGRAPHY

- Hinton, F. L. and R. D. Hazeltine (1976). “Theory of plasma transport in toroidal confinement systems.” In: *Rev. Mod. Phys.* 48.2, pp. 239–308. DOI: 10.1103/RevModPhys.48.239.
- Hofmann, F. (1988). “FBT - a free-boundary tokamak equilibrium code for highly elongated and shaped plasmas.” In: *Computer Physics Communications* 48.2, pp. 207 – 221. ISSN: 0010-4655. DOI: DOI:10.1016/0010-4655(88)90041-0. URL: <http://www.sciencedirect.com/science/article/B6TJ5-46DF8X2-37/2/a7064d1131afc8b1fdec3bbaa41a177>.
- Hofmann, F. and G. Tonetti (1988). “Tokamak equilibrium reconstruction using faraday rotation measurements.” In: *Nuclear Fusion* 28.10, p. 1871.
- Hofmann, F. and S.C. Jardin (1990). “Plasma shape and position control in highly elongated tokamaks.” In: *Nuclear Fusion* 30.10, p. 2013. URL: <http://stacks.iop.org/0029-5515/30/i=10/a=003>.
- Hofmann, F et al. (1994). “Creation and control of variably shaped plasmas in TCV.” In: *Plasma Physics and Controlled Fusion* 36.12B, B277. URL: <http://stacks.iop.org/0741-3335/36/i=12B/a=023>.
- Hofmann, F. et al. (1998). “Feedback stabilization of axisymmetric modes in the TCV tokamak using active coils inside and outside the vacuum vessel.” In: *Nuclear Fusion* 38.3, p. 399. URL: <http://stacks.iop.org/0029-5515/38/i=3/a=306>.
- Hofmann, F. et al. (2000). “Vertical position control in TCV: Comparison of model predictions with experimental results.” In: *Nuclear Fusion* 40.4, p. 767. URL: <http://stacks.iop.org/0029-5515/40/i=4/a=302>.
- Hofmann, F et al. (2001). “Stability and energy confinement of highly elongated plasmas in TCV.” In: *Plasma Physics and Controlled Fusion* 43.12A, A161. URL: <http://stacks.iop.org/0741-3335/43/i=12A/a=312>.
- Horton, L D et al. (2004). “ITER-relevant H-mode physics at ASDEX Upgrade.” In: *Plasma Physics and Controlled Fusion* 46.12B, B511. URL: <http://stacks.iop.org/0741-3335/46/i=12B/a=042>.
- Hughes, Thomas J. R. (1987). *The finite element method*. New Jersey, USA: Prentice Hall.
- Humphreys, D. A. et al. (2006). “Active control for stabilization of neoclassical tearing modes.” In: *Physics of Plasmas* 13.5, 056113, p. 056113. DOI: 10.1063/1.2173606. URL: <http://link.aip.org/link/?PHP/13/056113/1>.
- Humphreys, D.A. et al. (2007). “Development of ITER-relevant plasma control solutions at DIII-D.” In: *Nuclear Fusion* 47.8, p. 943. URL: <http://stacks.iop.org/0029-5515/47/i=8/a=028>.
- Imbeaux, F. et al. (2011a). “Current ramps in tokamaks: from present experiments to ITER scenarios.” In: *Nuclear Fusion* 51.8, p. 083026. URL: <http://stacks.iop.org/0029-5515/51/i=8/a=083026>.
- Imbeaux, F. et al. (2011b). “Real-time control of the safety factor profile diagnosed by magneto-hydrodynamic activity on the Tore Supra tokamak.” In: *Nuclear Fusion* 51.7, p. 073033. URL: <http://stacks.iop.org/0029-5515/51/i=7/a=073033>.
- Isayama, A et al. (2000). “Complete stabilization of a tearing mode in steady state high- β_p H-mode discharges by the first harmonic electron cyclotron heating/current drive on JT-60U.” In: *Plasma Physics and Controlled Fusion* 42.12, p. L37. URL: <http://stacks.iop.org/0741-3335/42/i=12/a=102>.

- Isayama, A. et al. (2007). “Stabilization of neoclassical tearing modes by electron cyclotron current drive in JT-60U.” In: *Nuclear Fusion* 47.8, p. 773. URL: <http://stacks.iop.org/0029-5515/47/i=8/a=007>.
- Isayama, A. et al. (2009). “Neoclassical tearing mode control using electron cyclotron current drive and magnetic island evolution in JT-60U.” In: *Nuclear Fusion* 49.5, p. 055006. URL: <http://stacks.iop.org/0029-5515/49/i=5/a=055006>.
- Jacquinet, J. and the JET team (Mar. 1999). “Deuterium-tritium operation in magnetic confinement experiments: results and underlying physics.” In: *Plasma Physics and Controlled Fusion* 41, A13–A46.
- Jardin, S. C., N. Pomphrey, and J. Delucia (1986). “Dynamic modeling of transport and positional control of tokamaks.” In: *Journal of Computational Physics* 66.2, pp. 481–507. ISSN: 0021-9991. DOI: DOI:10.1016/0021-9991(86)90077-X. URL: <http://www.sciencedirect.com/science/article/pii/002199918690077X>.
- Jardin, S.C., M.G. Bell, and N. Pomphrey (1993). “TSC simulation of Ohmic discharges in TFTR.” In: *Nuclear Fusion* 33.3, p. 371. URL: <http://stacks.iop.org/0029-5515/33/i=3/a=I01>.
- Jenkins, Thomas G. et al. (2010). “Calculating electron cyclotron current drive stabilization of resistive tearing modes in a nonlinear magnetohydrodynamic model.” In: *Physics of Plasmas* 17.1, 012502, p. 012502. DOI: 10.1063/1.3276740. URL: <http://link.aip.org/link/?PHP/17/012502/1>.
- Joffrin, E et al. (2003). “Integrated scenario in JET using real-time profile control.” In: *Plasma Physics and Controlled Fusion* 45.12A, A367. URL: <http://stacks.iop.org/0741-3335/45/i=12A/a=024>.
- Joffrin, E. et al. (July 2005). “The ‘hybrid’ scenario in JET: towards its validation for ITER.” In: *Nuclear Fusion* 45, pp. 626–634. DOI: 10.1088/0029-5515/45/7/010.
- Joffrin, E. et al. (2007). “Integrated plasma controls for steady state scenarios.” In: *Nuclear Fusion* 47.12, p. 1664. URL: <http://stacks.iop.org/0029-5515/47/i=12/a=004>.
- Joffrin, E. et al. (2010). “High confinement hybrid scenario in JET and its significance for ITER.” In: *23rd IAEA Fusion Energy Conference, Daejeon, Korea*. IAEA-CN-165/EX/1-1. Daejeon, South Korea.
- Khalil, Hassan K. (2001). *Nonlinear Systems*. 3rd ed. Prentice-Hall, Inc.
- Khayrutdinov, R. R. and V. E. Lukash (1993). “Studies of Plasma Equilibrium and Transport in a Tokamak Fusion Device with the Inverse-Variable Technique.” In: *Journal of Computational Physics* 109.2, pp. 193–201. ISSN: 0021-9991. DOI: DOI:10.1006/jcph.1993.1211. URL: <http://www.sciencedirect.com/science/article/pii/S0021999183712118>.
- Kim, S. H. et al. (Oct. 2009). “Full tokamak discharge simulation of ITER by combining DINA-CH and CRONOS.” In: *Plasma Physics and Controlled Fusion* 51.10, pp. 105007–+. DOI: 10.1088/0741-3335/51/10/105007.
- Klimanov, I. et al. (2005). “Electron cyclotron emission spectrometry on the Tokamak à Configuration Variable.” In: 76.9, p. 093504. ISSN: 00346748. DOI: DOI:10.1063/1.2042667. URL: <http://dx.doi.org/doi/10.1063/1.2042667>.
- Klimanov, I. et al. (Mar. 2007). “BRIEF COMMUNICATION: Generation of suprathermal electrons during sawtooth crashes in a tokamak plasma.” In: *Plasma Physics and Controlled Fusion* 49, pp. 1–+. DOI: 10.1088/0741-3335/49/3/L01.
- Koslowski, H.R. et al. (2001). “MHD studies in radiating mantle plasmas on JET.” In: *21st EPS Conference on Plasma Physics, Funchal (PT), 18-22 June*.

BIBLIOGRAPHY

- Kritz, A.H. et al. (1982). In: *Proc. 3rd Int. Symp. on Heating in Toroidal Plasmas*. Vol. II. Brussels, p. 707.
- La Haye, R. J. (2006). “Neoclassical tearing modes and their control.” In: *Physics of Plasmas* 13.5, 055501, p. 055501. DOI: 10.1063/1.2180747. URL: <http://link.aip.org/link/?PHP/13/055501/1>.
- La Haye, R. J. and O. Sauter (July 1998). “Threshold for metastable tearing modes in DIII-D.” In: *Nuclear Fusion* 38, pp. 987–999. DOI: 10.1088/0029-5515/38/7/303.
- La Haye, R.J. et al. (2005). “Higher stable beta by use of pre-emptive electron cyclotron current drive on DIII-D.” In: *Nuclear Fusion* 45.11, p. L37. URL: <http://stacks.iop.org/0029-5515/45/i=11/a=L02>.
- La Haye, R.J. et al. (2006). “Cross-machine benchmarking for ITER of neoclassical tearing mode stabilization by electron cyclotron current drive.” In: *Nuclear Fusion* 46.4, p. 451. URL: <http://stacks.iop.org/0029-5515/46/i=4/a=006>.
- La Haye, R.J., A. Isayama, and M. Maraschek (2009). “Prospects for stabilization of neoclassical tearing modes by electron cyclotron current drive in ITER.” In: *Nuclear Fusion* 49.4, p. 045005. URL: <http://stacks.iop.org/0029-5515/49/i=4/a=045005>.
- Lang, P. T. et al. (May 2004). “ELM pace making and mitigation by pellet injection in ASDEX Upgrade.” In: *Nuclear Fusion* 44, pp. 665–677. DOI: 10.1088/0029-5515/44/5/010.
- Lauret, M. et al. (2011). “Demonstration of sawtooth period locking with power modulation in TCV plasmas.” In: *Submitted to Physical Review Letters*.
- Lazarus, E.A., J.B. Lister, and G.H. Neilson (1990). “Control of the vertical instability in tokamaks.” In: *Nuclear Fusion* 30.1, p. 111. URL: <http://stacks.iop.org/0029-5515/30/i=1/a=010>.
- Lazzari, D. De and E. Westerhof (2010). “On the merits of heating and current drive for tearing mode stabilization.” In: *Nuclear Fusion* 50.7, p. 079801. URL: <http://stacks.iop.org/0029-5515/50/i=7/a=079801>.
- Lennholm, M. et al. (2009). “Demonstration of Effective Control of Fast-Ion-Stabilized Sawteeth by Electron-Cyclotron Current Drive.” In: *Phys. Rev. Lett.* 102.11, p. 115004. DOI: 10.1103/PhysRevLett.102.115004.
- Lennholm, M. et al. (July 2011). “Feedback control of the sawtooth period through real time control of the ion cyclotron resonance frequency.” In: *Nuclear Fusion* 51.7, pp. 073032–+. DOI: 10.1088/0029-5515/51/7/073032.
- Lindl, J. D. and E. I. Moses (May 2011). “Special Topic: Plans for the National Ignition Campaign (NIC) on the National Ignition Facility (NIF): On the threshold of initiating ignition experiments.” In: *Physics of Plasmas* 18.5, pp. 050901–+. DOI: 10.1063/1.3591001.
- Lister, J.B. et al. (1997). “The control of tokamak configuration variable plasmas.” In: *Fusion Technology* 32.3. cited By (since 1996) 32, pp. 321–373. URL: <http://www.scopus.com/inward/record.url?eid=2-s2.0-0031272843&partnerID=40&md5=46eddddea076f5d52ea558debbe6baec0>.
- Ljung, Lennart (1999). *System Identification, Theory for the User*. Second. Upper Saddle River, New Jersey: Prentice-Hall. ISBN: 0-13-656695-2.
- Luce, T. C. et al. (2004). “High performance stationary discharges in the DIII-D tokamak.” In: *Physics of Plasmas* 11.5, pp. 2627–2636. DOI: 10.1063/1.1704644. URL: <http://link.aip.org/link/?PHP/11/2627/1>.

- Lutjens, H., A. Bondeson, and O. Sauter (1996). “The CHEASE code for toroidal MHD equilibria.” In: *Computer Physics Communications* 97.3, pp. 219–260. ISSN: 0010-4655. DOI: 10.1016/0010-4655(96)00046-X.
- Lütjens, Hinrich, Jean-François Luciani, and Xavier Garbet (2001). “Curvature effects on the dynamics of tearing modes in tokamaks.” In: 8.10, pp. 4267–4270. ISSN: 1070664X. DOI: DOI:10.1063/1.1399056. URL: <http://dx.doi.org/doi/10.1063/1.1399056>.
- Lyon, J.F. et al. (1990). “Stellarators.” In: *Nuclear Fusion* 30.9, p. 1695. URL: <http://stacks.iop.org/0029-5515/30/i=9/a=004>.
- Maget, P. et al. (2010). “Modelling of (2,1) NTM threshold in JET advanced scenarios.” In: *Nuclear Fusion* 50.4, p. 045004. URL: <http://stacks.iop.org/0029-5515/50/i=4/a=045004>.
- Maraschek, M et al. (2003). “Scaling of the marginal β_p of neoclassical tearing modes during power ramp-down experiments in ASDEX Upgrade.” In: *Plasma Physics and Controlled Fusion* 45.7, p. 1369. URL: <http://stacks.iop.org/0741-3335/45/i=7/a=322>.
- Maraschek, M. et al. (2005). “Active control of MHD instabilities by ECCD in ASDEX Upgrade.” In: *Nuclear Fusion* 45.11, pp. 1369–1376. URL: <http://stacks.iop.org/0029-5515/45/1369>.
- Maraschek, M. et al. (2007). “Enhancement of the Stabilization Efficiency of a Neoclassical Magnetic Island by Modulated Electron Cyclotron Current Drive in the ASDEX Upgrade Tokamak.” In: *Physical Review Letters* 98.2, 025005, p. 025005. URL: <http://link.aps.org/abstract/PRL/v98/e025005>.
- Martin, Y. R., A. W. Degeling, and J. B. Lister (May 2002). “Search for determinism in ELM time series in TCV.” In: *Plasma Physics and Controlled Fusion* 44.26, A260000–A382.
- Martin, Y. R. et al. (Dec. 2003). “Accessibility and properties of ELMy H-mode and ITB plasmas in TCV.” In: *Plasma Physics and Controlled Fusion* 45.26, A260000–A365. DOI: 10.1088/0741-3335/45/12A/023.
- Martin, Y. R., L. Porte, and S. Alberti (May 2006). “Third harmonic EC heating of ELMy H-mode in TCV.” In: *Plasma Physics and Controlled Fusion* 48.26, A260000–A169. DOI: 10.1088/0741-3335/48/5A/S15.
- Matsuda, K. (Feb. 1989). “Ray tracing study of the electron cyclotron current drive in DIII-D using 60 GHz.” In: *IEEE Transactions on Plasma Science* 17, pp. 6–11. DOI: 10.1109/27.21664.
- Moreau, D. and I. Voitsekhovitch (1999). “Plasma control issues for an advanced steady state tokamak reactor.” In: *Nuclear Fusion* 39.5, p. 685. URL: <http://stacks.iop.org/0029-5515/39/i=5/a=308>.
- Moreau, D. et al. (2008). “A two-time-scale dynamic-model approach for magnetic and kinetic profile control in advanced tokamak scenarios on JET.” In: *Nuclear Fusion* 48.10, p. 106001. URL: <http://stacks.iop.org/0029-5515/48/i=10/a=106001>.
- Moreau, D. et al. (2011). “Plasma models for real-time control of advanced tokamak scenarios.” In: *Nuclear Fusion* 51.6, p. 063009. URL: <http://stacks.iop.org/0029-5515/51/i=6/a=063009>.
- Moret, J.-M. et al. (1997). “Influence of Plasma Shape on Transport in the TCV Tokamak.” In: *Phys. Rev. Lett.* 79.11, pp. 2057–2060. DOI: 10.1103/PhysRevLett.79.2057.
- Moret, J.-M. et al. (June 1998). “Magnetic measurements on the TCV Tokamak.” In: *Review of Scientific Instruments* 69, pp. 2333–2348. DOI: 10.1063/1.1148940.

BIBLIOGRAPHY

- Morrow-Jones, J. et al. (1993). “Use of tokamak dynamics models for digital filtering and control.” In: *Fusion Engineering, 1993., 15th IEEE/NPSS Symposium on*. Vol. 1, 219–222 vol.1. DOI: 10.1109/FUSION.1993.518318.
- Mueck, A. et al. (Apr. 2007). “Demonstration of Electron-Bernstein-Wave Heating in a Tokamak via O-X-B Double-Mode Conversion.” In: *Physical Review Letters* 98.17, pp. 175004–+. DOI: 10.1103/PhysRevLett.98.175004.
- Murari, A. et al. (2009). “Unbiased and non-supervised learning methods for disruption prediction at JET.” In: *Nuclear Fusion* 49.5, p. 055028. URL: <http://stacks.iop.org/0029-5515/49/i=5/a=055028>.
- Nave, M.F.F. and J.A. Wesson (1990). “Mode locking in tokamaks.” In: *Nuclear Fusion* 30.12, p. 2575. URL: <http://stacks.iop.org/0029-5515/30/i=12/a=011>.
- Nikkola, P. et al. (Nov. 2003). “Modelling of the electron cyclotron current drive experiments in the TCV tokamak.” In: *Nuclear Fusion* 43, pp. 1343–1352. DOI: 10.1088/0029-5515/43/11/006.
- Nocedal, Jorge and Stephen Wright (2006). *Numerical Optimization*. Second. Springer Series in Operations Research and Financial Engineering. Springer.
- Ogata, K. (2002). *Modern Control Systems*. 4th. Prentice Hall.
- Oikawa, T. et al. (2005). “Evolution of the Current Density Profile Associated with Magnetic Island Formation in JT-60U.” In: *Physical Review Letters* 94. DOI: 10.1103/PhysRevLett.94.125003.
- Oosterbeek, J. W. et al. (Sept. 2008). “A line-of-sight electron cyclotron emission receiver for electron cyclotron resonance heating feedback control of tearing modes.” In: *Review of Scientific Instruments* 79.9, pp. 093503–+. DOI: 10.1063/1.2976665.
- Ou, Y. et al. (2007). “Towards model-based current profile control at DIII-D.” In: *Fusion Engineering and Design* 82.5-14. Proceedings of the 24th Symposium on Fusion Technology - SOFT-24, pp. 1153–1160. ISSN: 0920-3796. DOI: DOI:10.1016/j.fusengdes.2007.04.016. URL: <http://www.sciencedirect.com/science/article/B6V3C-4NYBMFM-1/2/fa0bf0cc42e00f56a0dca3a2e4fb68e8>.
- Ou, Y et al. (2008). “Design and simulation of extremum-seeking open-loop optimal control of current profile in the DIII-D tokamak.” In: *Plasma Physics and Controlled Fusion* 50.11, 115001 (24pp). URL: <http://stacks.iop.org/0741-3335/50/115001>.
- Ou, Y. et al. (2010a). “Optimal Tracking Control of Current Profile in Tokamaks.” In: *Control Systems Technology, IEEE Transactions on*. ISSN: 1063-6536. DOI: 10.1109/TCST.2010.2046640.
- Ou, Yongsheng, Chao Xu, and E. Schuster (2010b). “Robust Control Design for the Poloidal Magnetic Flux Profile Evolution in the Presence of Model Uncertainties.” In: *Plasma Science, IEEE Transactions on* 38.3, pp. 375–382. ISSN: 0093-3813. DOI: 10.1109/TPS.2009.2038476.
- Ouarit, H. et al. (2011). “Validation of plasma current profile model predictive control in tokamaks via simulations.” In: *Fusion Engineering and Design* In Press, Corrected Proof, pp. –. ISSN: 0920-3796. DOI: DOI:10.1016/j.fusengdes.2011.03.078. URL: <http://www.sciencedirect.com/science/article/B6V3C-52NSTY4-3/2/2d9a19f1eb1cd2c72c8fa4815bb1e893>.
- Paley, J I, S Coda, and the TCV Team (2007). “Real time control of the plasma current and elongation in tokamaks using ECRH actuators.” In: *Plasma Physics and Controlled Fusion* 49.10, pp. 1735–1746. URL: <http://stacks.iop.org/0741-3335/49/1735>.

- Paley, J. I. et al. (2009). “From profile to sawtooth control: developing feedback control using ECRH/ECCD systems on the TCV tokamak.” In: *Plasma Physics and Controlled Fusion* 51.12, 124041 (11pp). URL: <http://stacks.iop.org/0741-3335/51/124041>.
- Paley, J. I. et al. (May 2009). “Real time control of the sawtooth period using EC launchers.” In: *Plasma Physics and Controlled Fusion* 51.5, pp. 055010–+. DOI: 10.1088/0741-3335/51/5/055010.
- Paley, J.I. et al. (2010). “Architecture and commissioning of the TCV distributed feedback control system.” In: *17th IEEE-NPSS Real Time Conference (RT)*, pp. 1–6. DOI: 10.1109/RTC.2010.5750487.
- Pankin, Alexei et al. (2004). “The tokamak Monte Carlo fast ion module NUBEAM in the National Transport Code Collaboration library.” In: *Computer Physics Communications* 159.3, pp. 157–184. ISSN: 0010-4655. DOI: DOI:10.1016/j.cpc.2003.11.002. URL: <http://www.sciencedirect.com/science/article/pii/S0010465504001109>.
- Park, Y S and A S Welander (2006). “Real-time determination of magnetic island location for neoclassical tearing mode control in DIII-D.” In: *Plasma Physics and Controlled Fusion* 48.9, pp. 1447–1454. URL: <http://stacks.iop.org/0741-3335/48/1447>.
- Peeters, A. G. (Dec. 2000). “The bootstrap current and its consequences.” In: *Plasma Physics and Controlled Fusion* 42, B231–B242.
- Pereverzev, G. V. and P.N. Yushmanov (2002). *ASTRA Automated System for TRansport Analysis in a Tokamak*. Tech. rep. 5/98. IPP Report.
- Petty, C.C. et al. (2004a). “Complete suppression of the $m = 2 / n = 1$ neoclassical tearing mode using electron cyclotron current drive in DIII-D.” In: *Nuclear Fusion* 44.2, pp. 243–251. URL: <http://stacks.iop.org/0029-5515/44/243>.
- Petty, C.C. et al. (2004b). “Onset and suppression of 2/1 NTM in DIII-D.” In: *Proceedings of the 20th International Conference on Fusion Energy, Villamoura (PT)*. EX/7-3.
- Peysson, Y and J Decker (2008). *Report EUR-CEA-FC-1739*. Tech. rep. EURATOM-CEA.
- Pfeiffer, W. W. et al. (Dec. 1980). *ONETWO: A computer code for modeling plasma transport in Tokamaks*. Tech. rep.
- Pietrzyk, Z. A. et al. (2001). “Long-Pulse Improved Central Electron Confinement in the TCV Tokamak with Electron Cyclotron Heating and Current Drive.” In: *Phys. Rev. Lett.* 86.8, pp. 1530–1533. DOI: 10.1103/PhysRevLett.86.1530.
- Piras, F. (2011). Private communication.
- Piras, F., J.-M. Moret, and J.X. Rossel (2010a). “Measurement of the magnetic field errors on TCV.” In: *Fusion Engineering and Design* 85.5, pp. 739–744. ISSN: 0920-3796. DOI: DOI:10.1016/j.fusengdes.2010.04.049. URL: <http://www.sciencedirect.com/science/article/pii/S0920379610001900>.
- Piras, F. et al. (2010b). ““Snowflake” H Mode in a Tokamak Plasma.” In: *Phys. Rev. Lett.* 105.15, p. 155003. DOI: 10.1103/PhysRevLett.105.155003.
- Pironti, A. and M. Walker (2005). “Control of tokamak plasmas: introduction to a special section.” In: *Control Systems, IEEE* 25.5, pp. 24–29. ISSN: 1066-033X. DOI: 10.1109/MCS.2005.1512793.
- (2006). “Control of tokamak plasmas. II.” In: *Control Systems, IEEE* 26.2, pp. 30–31. ISSN: 1066-033X. DOI: 10.1109/MCS.2006.1615270.
- Pitts, R. et al. (Mar. 2001). “Divertor geometry effects on detachment in TCV.” In: *Journal of Nuclear Materials* 290, pp. 940–946. DOI: 10.1016/S0022-3115(00)00461-X.

BIBLIOGRAPHY

- Pitts, R. A. et al. (Oct. 2003). “ELM driven divertor target currents on TCV.” In: *Nuclear Fusion* 43, pp. 1145–1166. DOI: 10.1088/0029-5515/43/10/017.
- Pitts, R. A. et al. (June 2007). “Parallel SOL flow on TCV.” In: *Journal of Nuclear Materials* 363, pp. 505–510. DOI: 10.1016/j.jnucmat.2006.12.065.
- Pitzschke, Andreas (2011). “Pedestal Characteristics and MHD Stability of H-Mode Plasmas in TCV.” PhD thesis. EPFL, Lausanne, Switzerland.
- Pletzer, A., A. Bondeson, and R.L. Dewar (1994). “Linear Stability of Resistive MHD modes: Axisymmetric Toroidal Computation of the Outer Region Matching Data.” In: *Journal of Computational Physics* 115, pp. 530–549.
- Pochelon, A. et al. (2001). “Plasma shape effects on sawtooth/internal kink stability and plasma shaping using electron cyclotron wave current profile tailoring in TCV.” In: *Nuclear Fusion* 41.11, p. 1663. URL: <http://stacks.iop.org/0029-5515/41/i=11/a=316>.
- Polevoi, A.R. et al. (2002). In: *Proceedings of the 19th International Conference on Fusion Energy, Lyon (FR)*. IAEA, Vienna, CT/P-08.
- Poli, E., A. G. Peeters, and G. V. Pereverzev (2001). “TORBEAM, a beam tracing code for electron-cyclotron waves in tokamak plasmas.” In: *Computer Physics Communications* 136.1-2, pp. 90–104. ISSN: 0010-4655. DOI: DOI:10.1016/S0010-4655(01)00146-1. URL: <http://www.sciencedirect.com/science/article/pii/S0010465501001461>.
- Poli, E. et al. (2002). “Reduction of the Ion Drive and ρ_θ^* Scaling of the Neoclassical Tearing Mode.” In: *Phys. Rev. Lett.* 88.7, p. 075001. DOI: 10.1103/PhysRevLett.88.075001.
- Popov, A. M. et al. (2002a). “Simulation of neoclassical tearing modes in the DIII-D tokamak. II. Suppression by radially localized electron cyclotron current drive.” In: 9.10, pp. 4229–4240. ISSN: 1070664X. DOI: DOI:10.1063/1.1505843. URL: <http://dx.doi.org/doi/10.1063/1.1505843>.
- (2002b). “Simulation of neoclassical tearing modes (NTMs) in the DIII-D tokamak. I. NTM excitation.” In: 9.10, pp. 4205–4228. ISSN: 1070664X. DOI: DOI:10.1063/1.1505842. URL: <http://dx.doi.org/doi/10.1063/1.1505842>.
- Porcelli, F, D Boucher, and M N Rosenbluth (1996). “Model for the sawtooth period and amplitude.” In: *Plasma Physics and Controlled Fusion* 38.12, pp. 2163–2186. URL: <http://stacks.iop.org/0741-3335/38/2163>.
- Porte, L. et al. (Aug. 2007). “Plasma dynamics with second and third-harmonic ECRH and access to quasi-stationary ELM-free H-mode on TCV.” In: *Nuclear Fusion* 47, pp. 952–960. DOI: 10.1088/0029-5515/47/8/029.
- Prater, R. (2004). “Heating and current drive by electron cyclotron waves.” In: *Physics of Plasmas* 11.5, pp. 2349–2376. DOI: 10.1063/1.1690762. URL: <http://link.aip.org/link/?PHP/11/2349/1>.
- Prater, R. et al. (2007). “Stabilization and prevention of the 2/1 neoclassical tearing mode for improved performance in DIII-D.” In: *Nuclear Fusion* 47.5, p. 371. URL: <http://stacks.iop.org/0029-5515/47/i=5/a=001>.
- Press, William H. et al. (1996). *Numerical Recipes*. Second. New York: Cambridge University Press.
- Raju, D (2011). Private communication.
- Raju, D, O Sauter, and J B Lister (2003). “Study of nonlinear mode coupling during neoclassical tearing modes using bispectrum analysis.” In: *Plasma Physics and Con-*

- trolled Fusion* 45.4, pp. 369–378. DOI: 10.1088/0741-3335/45/4/304. URL: <http://stacks.iop.org/0741-3335/45/369>.
- Ramponi, G., E. Lazzaro, and S. Nowak (Sept. 1999). “On the stabilization of neoclassical tearing modes by electron cyclotron waves.” In: *Physics of Plasmas* 6, pp. 3561–3570. DOI: 10.1063/1.873633.
- Ramponi, G. et al. (2008). “Physics analysis of the ITER ECW system for optimized performance.” In: *Nuclear Fusion* 48.5, p. 054012. URL: <http://stacks.iop.org/0029-5515/48/i=5/a=054012>.
- Rattá, G.A. et al. (2010). “An advanced disruption predictor for JET tested in a simulated real-time environment.” In: *Nuclear Fusion* 50.2, p. 025005. URL: <http://stacks.iop.org/0029-5515/50/i=2/a=025005>.
- Rebut, P.H., P.P. Lallia, and M.L. Watkins (1989). In: *Plasma Physics and Controlled Nuclear Fusion Research 1988 (Proc. 12th Int. Conf. Nice, 1988)*. Vol. 2. IAEA, Vienna, p. 191.
- Reimerdes, H. et al. (2002). “From Current-Driven to Neoclassically Driven Tearing Modes.” In: *Phys. Rev. Lett.* 88.10, p. 105005. DOI: 10.1103/PhysRevLett.88.105005.
- Reux, C. et al. (Sept. 2010). “Experimental study of disruption mitigation using massive injection of noble gases on Tore Supra.” In: *Nuclear Fusion* 50.9, pp. 095006–+. DOI: 10.1088/0029-5515/50/9/095006.
- Rossel, J et al. (2011). “Edge localized mode control by electron cyclotron waves in a Tokamak plasma.” In: *Submitted to Physical Review Letters*.
- Rutherford, P. H. (1973). “Nonlinear growth of the tearing mode.” In: *Physics of Fluids* 16.11, pp. 1903–1908. DOI: 10.1063/1.1694232. URL: <http://link.aip.org/link/?PFL/16/1903/1>.
- Ryutov, D D (1988). “Open-ended traps.” In: *Soviet Physics Uspekhi* 31.4, p. 300. URL: <http://stacks.iop.org/0038-5670/31/i=4/a=R02>.
- Sauter, O. et al. (1997). “Beta limits in long-pulse tokamak discharges.” In: *Physics of Plasmas* 4.5, pp. 1654–1664. DOI: 10.1063/1.872270. URL: <http://link.aip.org/link/?PHP/4/1654/1>.
- Sauter, O., C. Angioni, and Y. R. Lin-Liu (1999a). “Neoclassical conductivity and bootstrap current formulas for general axisymmetric equilibria and arbitrary collisionality regime.” In: *Physics of Plasmas* 6.7, pp. 2834–2839. DOI: 10.1063/1.873240. URL: <http://link.aip.org/link/?PHP/6/2834/1>.
- Sauter, O. et al. (1999b). “Sawtooth period simulations of TCV discharges.” In: *Proc. Joint Varenna - Lausanne Int. Workshop on Theory of Fusion Plasmas Varenna, Italy, August 31 - September 4, 1998*. Vol. ISPP-18, pp. 403–408.
- Sauter, O. et al. (2001). “Steady-state fully noninductive operation with electron cyclotron current drive and current profile control in the tokamak à configuration variable (TCV).” In: 8.5, pp. 2199–2207. ISSN: 1070664X. DOI: DOI:10.1063/1.1355317. URL: <http://dx.doi.org/doi/10.1063/1.1355317>.
- Sauter, O. et al. (2002a). “Control of Neoclassical Tearing Modes by Sawtooth Control.” In: *Phys. Rev. Lett.* 88.10, p. 105001. DOI: 10.1103/PhysRevLett.88.105001.
- Sauter, O et al. (2002b). “Marginal β -limit for neoclassical tearing modes in JET H-mode discharges.” In: *Plasma Physics and Controlled Fusion* 44.9, pp. 1999–2019. DOI: 10.1088/0741-3335/44/9/315. URL: <http://stacks.iop.org/0741-3335/44/1999>.

BIBLIOGRAPHY

- Sauter, O. et al. (2005). “Inductive Current Density Perturbations to Probe Electron Internal Transport Barriers in Tokamaks.” In: *Physical Review Letters* 94.10, 105002, p. 105002. DOI: 10.1103/PhysRevLett.94.105002. URL: <http://link.aps.org/abstract/PRL/v94/e105002>.
- Sauter, O. et al. (Nov. 2010). “Experimental studies of ECRH/ECCD effects on Tearing Mode stability using the new TCV real-time control system.” In: *APS Meeting Abstracts*, 9075P–+.
- Sauter, O et al. (2010). “On the requirements to control neoclassical tearing modes in burning plasmas.” In: *Plasma Physics and Controlled Fusion* 52.2, p. 025002. URL: <http://stacks.iop.org/0741-3335/52/i=2/a=025002>.
- Scarabosio, A. et al. (May 2006). “Toroidal plasma rotation in the TCV tokamak.” In: *Plasma Physics and Controlled Fusion* 48, pp. 663–683. DOI: 10.1088/0741-3335/48/5/012.
- Scarabosio, A, A Pochelon, and Y Martin (2007). “Plasma shape stabilization of current rise MHD instabilities in TCV.” In: *Plasma Physics and Controlled Fusion* 49.7, p. 1041. URL: <http://stacks.iop.org/0741-3335/49/i=7/a=007>.
- Schlatter, Christian (2009). “Turbulent ion heating in TCV tokamak plasmas. Turbulent ion heating in TCV tokamak plasmas. Turbulent ion heating in the TCV tokamak.” PhD thesis. Lausanne, Switzerland: EPFL.
- Sevillano, Goretti et al. (2011). “Observer-based real-time control for the poloidal beta of the plasma using diamagnetic measurements in Tokamak fusion reactors.” In: *Proceedings of the 50th IEEE Conference on Decision and Control and European Control Conference, Orlando, FL, USA*.
- Shafranov, V. D. (1958). “On Magnetohydrodynamical Equilibrium Configurations.” In: *Soviet Journal of Experimental and Theoretical Physics* 6, pp. 545–+.
- Shimada, M. et al. (2007). “Chapter 1: Overview and summary.” In: *Nuclear Fusion* 47.6, S1. URL: <http://stacks.iop.org/0029-5515/47/i=6/a=S01>.
- Silva, Miguel et al. (2011). “Fast polarizers installation for ECRH and ECE in TCV.” In: *Fusion Engineering and Design* In Press, Corrected Proof, pp. –. ISSN: 0920-3796. DOI: DOI:10.1016/j.fusengdes.2011.01.043. URL: <http://www.sciencedirect.com/science/article/pii/S092037961100055X>.
- Singer, C. E. et al. (1988). “Baldur: A one-dimensional plasma transport code.” In: *Computer Physics Communications* 49.2, pp. 275–398. ISSN: 0010-4655. DOI: DOI:10.1016/0010-4655(88)90012-4. URL: <http://www.sciencedirect.com/science/article/pii/0010465588900124>.
- Sips, A C C et al. (2002). “Progress towards steady-state advanced scenarios in ASDEX Upgrade.” In: *Plasma Physics and Controlled Fusion* 44.5A, A151. URL: <http://stacks.iop.org/0741-3335/44/i=5A/a=311>.
- Sips, A. C. C. et al. (May 2005). “Advanced scenarios for ITER operation.” In: *Plasma Physics and Controlled Fusion* 47.26, A260000–A40. DOI: 10.1088/0741-3335/47/5A/003. eprint: [arXiv:physics/0410263](http://arxiv.org/abs/physics/0410263).
- Smyshlyaev, Andrey and Miroslav Krstic (2010). *Adaptive Control of Parabolic PDEs*. Princeton, NJ (USA): Princeton Univeristy Press.

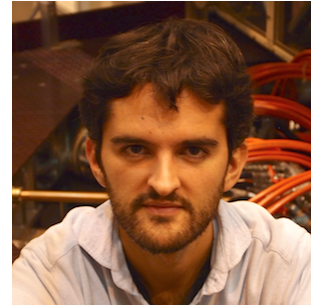
- Söldner, F X and the JET Team (1997). “Shear optimization experiments with current profile control on JET.” In: *Plasma Physics and Controlled Fusion* 39.12B, B353. URL: <http://stacks.iop.org/0741-3335/39/i=12B/a=027>.
- Sontag, Eduardo D. (1998). *Mathematical Control Theory*. second. Vol. 6. Texts in Applied Mathematics. New York (USA): Springer.
- Sushkov, A. et al. (Feb. 2008). “High-resolution multiwire proportional soft x-ray diagnostic measurements on TCV.” In: *Review of Scientific Instruments* 79.2, pp. 023506–+. DOI: 10.1063/1.2833822.
- Suttrop, W. et al. (June 2011). “First Observation of Edge Localized Modes Mitigation with Resonant and Nonresonant Magnetic Perturbations in ASDEX Upgrade.” In: *Physical Review Letters* 106.22, pp. 225004–+. DOI: 10.1103/PhysRevLett.106.225004.
- Suzuki, T. et al. (2008). “Off-axis current drive and real-time control of current profile in JT-60U.” In: *Nuclear Fusion* 48.4, p. 045002. URL: <http://stacks.iop.org/0029-5515/48/i=4/a=045002>.
- Teo, K.L., C.J. Goh, and K.H. Wong (1991). *A unified computational approach to optimal control problems*. Pitman Monographs and Surveys in Pure and Applied Mathematics. John Wiley & Sons Inc.
- Troyon, F. et al. (Jan. 1984). “MHD-Limits to Plasma Confinement.” In: *Plasma Physics and Controlled Fusion* 26, pp. 209–215. DOI: 10.1088/0741-3335/26/1A/319.
- Turco, F. and T.C. Luce (2010). “Impact of the current profile evolution on tearing stability of ITER demonstration discharges in DIII-D.” In: *Nuclear Fusion* 50.9, p. 095010. URL: <http://stacks.iop.org/0029-5515/50/i=9/a=095010>.
- Turri, G et al. (2008). “MHD as trigger of electron temperature oscillations in ECCD discharges in TCV.” In: *Plasma Physics and Controlled Fusion* 50.6, 065010 (13pp). URL: <http://stacks.iop.org/0741-3335/50/065010>.
- Udintsev, V. S. et al. (2007). “Recent Electron Cyclotron Emission Results on TCV.” In: *Fusion Science and Technology* 52.2, pp. 161–168.
- Udintsev, V S et al. (2008). “Global plasma oscillations in electron internal transport barriers in TCV.” In: *Plasma Physics and Controlled Fusion* 50.12, 124052 (12pp). URL: <http://stacks.iop.org/0741-3335/50/124052>.
- Volpe, F. A. G. et al. (2009). “Advanced techniques for neoclassical tearing mode control in DIII-D.” In: *Physics of Plasmas* 16.10, 102502, p. 102502. DOI: 10.1063/1.3232325. URL: <http://link.aip.org/link/?PHP/16/102502/1>.
- Waelbroeck, F. L., J. W. Connor, and H. R. Wilson (2001). “Finite Larmor-Radius Theory of Magnetic Island Evolution.” In: *Phys. Rev. Lett.* 87.21, p. 215003. DOI: 10.1103/PhysRevLett.87.215003.
- Wagner, F et al. (2010). “On the heating mix of ITER.” In: *Plasma Physics and Controlled Fusion* 52.12, p. 124044. URL: <http://stacks.iop.org/0741-3335/52/i=12/a=124044>.
- Waltz, R. E. et al. (1997). “A gyro-Landau-fluid transport model.” In: *Physics of Plasmas* 4.7, pp. 2482–2496. DOI: 10.1063/1.872228. URL: <http://link.aip.org/link/?PHP/4/2482/1>.
- Weisen, H. et al. (1997). “Effect of plasma shape on confinement and MHD behaviour in the TCV tokamak.” In: *Nuclear Fusion* 37.12, p. 1741. URL: <http://stacks.iop.org/0029-5515/37/i=12/a=I07>.

BIBLIOGRAPHY

- Weisen, H. et al. (2002). “Shape dependence of sawtooth inversion radii and profile peaking factors in TCV L mode plasmas.” In: *Nuclear Fusion* 42.2, p. 136. URL: <http://stacks.iop.org/0029-5515/42/i=2/a=303>.
- Wesson, John (2004). *Tokamaks*. Third edition. Vol. 118. International series of monographs on physics. New York (USA): Oxford Science Publications. ISBN: 0-19-8509227.
- Westerhof, E. (1990). “Tearing mode stabilization by local current density perturbations.” In: *Nuclear Fusion* 30.6, pp. 1143–1147.
- Westerhof, E. et al. (Nov. 2002). “Control of sawteeth and triggering of NTMs with ion cyclotron resonance frequency waves in JET.” In: *Nuclear Fusion* 42, pp. 1324–1334. DOI: 10.1088/0029-5515/42/11/306.
- Wijnands, T. et al. (June 1997). “Feedback control of the current profile on Tore Supra.” In: *Nuclear Fusion* 37, pp. 777–791. DOI: 10.1088/0029-5515/37/6/I06.
- Wilson, H. R. et al. (1996). “Threshold for neoclassical magnetic islands in a low collision frequency tokamak.” In: *Physics of Plasmas* 3.1, pp. 248–265. ISSN: 1070664X. DOI: DOI:10.1063/1.871830.
- Witrant, E et al. (2007). “A control-oriented model of the current profile in tokamak plasma.” In: *Plasma Physics and Controlled Fusion* 49.7, pp. 1075–1105. URL: <http://stacks.iop.org/0741-3335/49/1075>.
- Witvoet, G. et al. (2011). “Numerical demonstration of injection locking of the sawtooth period by means of modulated EC current drive.” In: *Nuclear Fusion* 51.10, p. 103043. URL: <http://stacks.iop.org/0029-5515/51/i=10/a=103043>.
- Witvoet, G. et al. (July 2011). “Systematic design of a sawtooth period feedback controller using a Kadomtsev-Porcelli sawtooth model.” In: *Nuclear Fusion* 51.7, pp. 073024–+. DOI: 10.1088/0029-5515/51/7/073024.
- Xu, C. et al. (2010a). “Ramp-Up-Phase Current-Profile Control of Tokamak Plasmas via Nonlinear Programming.” In: *Plasma Science, IEEE Transactions on* 38.2, pp. 163–173. ISSN: 0093-3813. DOI: 10.1109/TPS.2009.2037626.
- Xu, Chao, Yongsheng Ou, and E. Schuster (2010b). “Transport Parameter Estimations of Plasma Transport Dynamics Using the Extended Kalman Filter.” In: *Plasma Science, IEEE Transactions on* 38.3, pp. 359–364. ISSN: 0093-3813. DOI: 10.1109/TPS.2009.2038220.
- Zeeland, M.A. Van et al. (2008). “Tearing mode structure in the DIII-D tokamak through spectrally filtered fast visible bremsstrahlung imaging.” In: *Nuclear Fusion* 48.9, p. 092002. URL: <http://stacks.iop.org/0029-5515/48/i=9/a=092002>.
- Zhang, Y. et al. (June 2011). “Prediction of disruptions on ASDEX Upgrade using discriminant analysis.” In: *Nuclear Fusion* 51.6, pp. 063039–+. DOI: 10.1088/0029-5515/51/6/063039.
- Zohm, H. (2006). “The physics base for NTM stabilisation by ECCD in ITER.” In: *14th Workshop on ECE and ECRH Santorini, Greece*.
- Zohm, H. et al. (1999). “Experiments on neoclassical tearing mode stabilization by ECCD in ASDEX Upgrade.” In: *Nuclear Fusion* 39.5, p. 577. URL: <http://stacks.iop.org/0029-5515/39/i=5/a=101>.
- Zohm, H. et al. (2007). “Control of MHD instabilities by ECCD: ASDEX Upgrade results and implications for ITER.” In: *Nuclear Fusion* 47.3, pp. 228–232. DOI: 10.1088/0029-5515/47/3/010. URL: <http://stacks.iop.org/0029-5515/47/228>.

- Zucca, C et al. (2009a). “Current density evolution in electron internal transport barrier discharges in TCV.” In: *Plasma Physics and Controlled Fusion* 51.1, 015002 (16pp). URL: <http://stacks.iop.org/0741-3335/51/015002>.
- Zucca, C et al. (2009b). “Modulation of electron transport during swing ECCD discharges in TCV.” In: *Plasma Physics and Controlled Fusion* 51.12, p. 125009. URL: <http://stacks.iop.org/0741-3335/51/i=12/a=125009>.
- Zucca, Costanza (2009). “Modeling and control of the current density profile in tokamaks and its relation to electron transport.” PhD thesis. EPFL, Lausanne, Switzerland.

Curriculum Vitae



Federico Felici

PERSONAL

- Full name: Federico Alberto Alfredo FELICI
- Born: 17th May 1982 in Leiden (The Netherlands)
- Nationality: Italian and Dutch
- E-mail: ffelici@gmail.com

EDUCATION

École Polytechnique Fédérale de Lausanne (EPFL), Switzerland

Ph.D., Plasma Physics 2007-2011
Centre des Recherches en Physique des Plasmas (CRPP)

- Thesis Topic: *Real-time control of tokamak plasmas*
- Advisers: Dr. O. Sauter and Dr. T.P. Goodman
- Areas of study: Plasma physics, tokamak physics and control, plasma control using EC systems, MHD control, profile control, plasma transport simulations, real-time simulations, optimal control, EC polarization control.
- Several visits to the [National Institute for Fusion Science \(Japan\)](#) for research collaboration on feedback control of EC systems on the Large Helical Device.

Technische Universiteit Delft, The Netherlands

MSc., Systems & Control (*Cum Laude*) 2003-2005
Delft Center for Systems & Control

- Thesis Topic: *Subspace identification of LPV systems*
- Adviser: Prof. M. Verhaegen
- Areas of study: Control systems, system identification, intelligent control, model predictive control, robust control, optimal control, neural networks.
- Exchange year to Università di Bologna, Italy (Erasmus programme, 2003-2004)

BSc., Aerospace engineering (*Cum Laude*) 1999-2003

Het Rijnlands Lyceum Oegstgeest, The Netherlands

High School 1994-1999

- Subjects: Dutch, English, Math, Physics, Chemistry, Economics, Latin, Greek
- International Baccalaureate A2 English Second Language exam

OTHER RESEARCH EXPERIENCE **Visiting researcher** Sep. – Dec. 2006
IDSIA institute for Artificial Intelligence, Lugano, Switzerland

- Adviser: Prof. J. Schmidhuber
- Area of Study: *Recurrent neural networks for time-series identification.*

Assistant Researcher Dec. 2005 – Jun. 2006
Delft Center for Systems and Control

- Supervisor: Prof. M. Verhaegen
- Area of study: *Subspace identification of LPV systems using periodic scheduling sequences*

GRADUATE LEVEL COURSES

- Physics of Magnetically confined plasmas
- Advanced theory of plasma
- Advanced topics in Numerical Modeling for PDEs
- The economics of technology policy
- Nonlinear control (L. Marconi, Università di Bologna, 2004)
- Identification and control of LPV systems (DISC summer school, 2006)

HONORS AND AWARDS

- EPFL prize for dedication to teaching assistant duties (2009)
- VSB Fonds: 4000€ grant for 4-month post-master research stay at IDSIA.
- Nominated finalist for “KIVI-NIRIA Regeltechniek prijs” 2006 (Prize for best MSc thesis in control engineering)
- Nominated finalist for best junior presentation award, 25th Benelux Meeting on Systems & Control (2006)
- High school award for best results in science subjects (1999).

TEACHING EXPERIENCE

Teaching assistant for several EPFL BSc. and MSc. classes. Responsible for preparation of exercises and solutions, assistant during exercise sessions.

- General Physics I, II
- Plasma Physics I (Dr. S. Alberti, 3rd year BSc. Physics)
- Nuclear Fusion and Plasma Physics (Prof. A. Fasoli and Prof. M.Q. Tran, 1st year MSc. Nuclear Engineering)

SKILLS

- Proficient in MATLAB and SIMULINK including several toolboxes.
- Good knowledge of LabView, C, Linux/UNIX, InDesign, MediaWiki, L^AT_EX.
- Good knowledge of real-time signal processing software and hardware concepts, control systems technology.

LANGUAGES

- Italian and Dutch: Native speaker (bilingual)
- English: Fluent in speech and writing
- French: Fluent in speech, excellent writing

ACTIVITIES

- Initiative for reinstating regular PhD student seminars at CRPP (2010)
- Member of local organizing committee of the IAEA Fusion Energy Conference in Geneva, responsible for exposition by ITER domestic agencies (2008).
- Co-developer of new internal wiki page for CRPP. Now routinely used as main exchange platform for internal information including the TCV experiment (2007)
- Active member of student organization Augustinus in Leiden. Several leading positions in committees for 1500 member student organisation (2000-2006)

SELECTED
REFEREED
JOURNAL
PUBLICATIONS

- F. Felici, O. Sauter, S. Coda, et al. (2011b). "Real-time physics-model-based simulation of the current density profile in tokamak plasmas". In: *Nuclear Fusion* 51.8, p. 083052. URL: <http://stacks.iop.org/0029-5515/51/i=8/a=083052>
- T. P. Goodman, F. Felici, O. Sauter, et al. (June 2011). "Sawtooth Pacing by Real-Time Auxiliary Power Control in a Tokamak Plasma". In: *Physical Review Letters* 106.24, pp. 245002–+. DOI: 10.1103/PhysRevLett.106.245002
- M. Lauret, F. Felici, G. Witvoet, et al. (2011). "Demonstration of sawtooth period locking with power modulation in TCV plasmas". In: *Submitted to Physical Review Letters*
- F. Felici and O. Sauter (2011). "Nonlinear model-based optimization of actuator trajectories for tokamak plasma profile control". In: *Submitted to Plasma Physics and Controlled Fusion*
- F. Felici, T. Shimozuma, S. Kubo, et al. (Oct. 2010). "Feedback control of ECRH polarization on LHD". In: *Nuclear Fusion* 50.10, pp. 105003–+. DOI: 10.1088/0029-5515/50/10/105003
- F. Felici, T. Goodman, O. Sauter, et al. (2009). "Real-time feedback control of millimeter-wave polarization for LHD". In: *Review of Scientific Instruments* 80.1, p. 013504. DOI: 10.1063/1.3073735
- F. Felici, J-W. van Wingerden, and M. Verhaegen (2007). "Subspace identification of MIMO LPV systems using a periodic scheduling sequence". In: *Automatica* 43.10, pp. 1684–1697. ISSN: 0005-1098. DOI: 10.1016/j.automatica.2007.02.027

SELECTED
CONFERENCE
PRESENTATIONS

- F. Felici, O. Sauter, S. Coda, et al. (2011a). "Optimization, real-time simulation and feedback control of tokamak plasma profiles on TCV". In: *38th EPS Conference on Plasma Physics, 27 June - 1 July, Strasbourg, France* (Oral presentation)
- F. Felici, O. Sauter, T. Goodman, et al. (Nov. 2010). "RAPTOR: Optimization, real-time simulation and control of the tokamak q profile evolution using a simplified transport model". In: *APS Meeting Abstracts, 9090P–+* (Poster presentation)
- O. Sauter, F. Felici, T. Goodman, et al. (Nov. 2010). "Experimental studies of ECRH/ECCD effects on Tearing Mode stability using the new TCV real-time control system". In: *APS Meeting Abstracts, 9075P–+* (Poster presentation)
- F. Felici, O. Sauter, T.P. Goodman, et al. (2009). "Self-consistent simulation of tearing modes during ECCD experiments on TCV". In: *36th EPS Conference on Plasma Physics, Sofia, Bulgaria, 29 June - 03 July* (Poster presentation)
- F. Felici, E. Asp, S. Cirant, et al. (2009). "Recent results of ECRH/ECCD experiments on TCV". In: *18th International Toki Conference, Gifu, Japan* (Oral presentation)
- F. Felici, C. Zucca, T.P. Goodman, et al. (2008). "Safety factor profile influence on tearing mode stability in TCV". In: *Swiss Physical Society Annual Meeting, Geneva* (Oral presentation)
- Federico Felici, Jan-Willem van Wingerden, and Michel Verhaegen (2007). "Dedicated periodic scheduling sequences for LPV system identification". In: *European Control Conference, Kos, Greece* (Oral presentation)

A more extensive publication list can be found on <http://people.epfl.ch/federico.felici>